New Series

LANDOLT-BÖRNSTEIN

Numerical Data and Functional Relationships in Science and Technology

GROUP III

VOLUME 32

Condensed Matter

Magnetic Properties of Metals

Supplement to Volume 19

SUBVOLUME D

Rare Earth Elements, Alloys and Compounds

Springer

2 Magnetic properties of rare earth elements, alloys and compounds

2.1 Rare earth elements

2.1.1 Introduction

Since our previous review work in Landoldt-Börnstein, Group III, Crystal and Solid State Physics, Vol. 19d1, p. 1 (1991) [91D], a numerous amount of experimental and theoretical work on the magnetic properties of rare earth elements, alloys and compounds have been reported. Although the investigation of the magnetic structures of the rare earth has been an active area of research for nearly 30 years, the field has recently attracted new interest, due largely to the development of high-resolution X-ray and neutron magnetic diffraction techniques. Erbium, for example, has the most complex phase diagram of any of the heavy rare earths (Fig. 335 in [91D]). The gradual way in which the picture of its magnetic structure has been refined in successive studies (Fig. 255) is typical of the steady progress that has been made in our understanding of all of the rare earth metals (see also as an example, Fig. 146 for Dy, Fig. 209 for Ho or Fig. 256 for Er and Ref. [94J] where new updated neutron diffraction studies of the magnetic phase diagrams of some heavy rare earth elements, are displayed). In spite of the new data in this chapter, for a main survey of this type of results the reader is referred to [91D]. Compared with [91D], the present survey includes the comprehensive review of high temperature magnetic susceptibility of the light lanthanides (see Figs. 1, 3 for Ce, Fig. 26 for Sm or Fig. 35 for Eu and Gd). However, most of the recent investigations are dealing with the magnetic properties of rare earth elements in their artificial form like ultrathin films or multilayer superstructures [93J]. Many papers are also dedicated to the surface magnetic behaviour mostly of Gd, Dy, Tb and Er deposited on the surface of nonmagnetic metals (Fig. 95 for Gd, Fig. 144 for Tb, Fig. 174 for Dy, Figs. 284 and 291 for Er) [91W, 91B2]. It is well known that the magnetic order can be modified at the surface of a ferromagnetic material (see Fig. 71). The loss of the transitional symmetry perpendicular to the surface plane and the reduced atomic coordination can result in magnetic interactions which differ from those in the bulk. It is to be expected that the magnetic ordering will be weakened at the surface by the reduced atomic coordination.

Contrary to these expectations the enhanced surface ordering temperatures and the surface magnetic reconstruction (SMR) (i. e., a different orientation of the spins at the surface than in the bulk) (see Fig. 72) are among the most intriguing phenomena found in surface magnetism [93T1]. As an example, in Fig. A the results obtained from the spin-resolved photoemission experiment performed on ultrathin Gd films grown on W(110) are shown [93V]. The results indicate that the in-plane ordering temperature of the surface is by 80 K higher than that of the inner layers. These data show also a complex and unexpected temperature dependence of the magnetization. At high temperatures the polarization of 4f states at the surface differs from that of the underlaying layers. Extensive studies have failed to demonstrate the existence of such phenomenon in 3d transition metals. Evidence for an enhanced surface ordering temperature T_S over the bulk Curie temperature T_B was found by Rau et al. [86R] on polycrystalline Gd surfaces as is shown in Fig. 47. A similar observation has been reported for epitaxial Tb films (Fig. 142 and Ref. [89R]. In a nearest–neighbor Ising model with bulk coupling constant J, there exists a critical value of the surface coupling

constant J_s, above which the surface orders at temperature (T_S) higher than the bulk Curie temperature (T_B). In this case the surface critical behaviour at T_S is known as a "surface transition". For $T_B < T < T_S$ the surface behaves as a two-dimensional system, with the magnetic order decaying almost exponentially within the bulk (see Figs. 52 and 70). There also exist a few experimental cases for which $T_S < T_B$. Farle et al. [87F] reported that the Curie temperature depends on the film thickness; T_C of a Gd monolayer on W(110) is 20 K below T_C for bulk sample.

It is worthwhile to point out that, despite of these findings, the mechanism responsible for the enhancement of the surface Curie temperature in these systems is still not at all understood in terms of fundamental atomic properties.

The synthesis of artificially layered materials has attracted much attention in the last decade. The discovery of techniques to produce multilayers of rare earth elements that alternate with the non-magnetic hexagonal structure elements Y or Lu (see Fig. B) has opened up broad new opportunities to study the magnetic coupling in rare earth systems. Y and Lu have similar physical and electronic properties to the magnetic heavy rare earth and, because of the relatively small mismatch between the basal plane lattice parameters (e.g. 1.6 % for Dy and Y), good epitaxial growth is achieved. Artificial single crystal superlattices of Gd–Y, Dy–Y, Er–Y, and Ho–Y, have been produced and extensively studied (Figs. 80, 168, 283 or 238). These and similar systems offer a near ideal opportunity to investigate the magnetic exchange couplings and interaction strengths in a system consisting of magnetically concentrated layers (e.g. Dy) interleaved, in a controlled fashion, with magnetically "dead" layers (e.g. Y, Lu). It should be noted that such a system is unique and can never be simulated by bulk dilute alloys because of the attendant reduction in the average exchange interaction with the decreased density of magnetic ions, and the probability of some nearest neighbours even in very dilute samples.

Magnetic long-range coupling in layered metallic structures has become a key issue in thin-film magnetism since the observation of oscillatory exchange coupling across non-ferromagnetic spacer layers [86S, 86G]. Although this phenomenon was first discovered in rare earth superlattices most studies today deal with transition metal systems because of their technological relevance to magnetic storage devices. The present theoretical understanding of transition metal multilayers has been developed on the basic of detailed observations revealing, e.g. short-period oscillations not extend beyond several atomic planes [91U] as well as 90^o coupling [91R].

In metallic RE systems, due to the localised nature of the 4f electrons, the exchange coupling is well described by the Heisenberg Hamiltonian $H = - JS_iS_j$, where J denotes the effective coupling strength between the localised 4f-spin moments S_i and S_j. The exchange coupling in rare earth metals is indirect, relatively long range, mediated through the 6s and 5d conduction electrons it is oscillatory and usually described in a Ruderman-Kittel-Kasuya-Yosida picture. Hence, magnetic superlattices containing magnetic rare earth elements, e.g. Gd or Dy, alternating with a nonmagnetic analogue such as Y, Lu, W, would seem to be promising systems for investigating the modulation effects derived from a long-range interlayer exchange coupling. The Y, Lu or other nonmagnetic metal block (Zr, Mo) does not simply act as an inert spacer between the blocks of magnetic material. Instead, it is found that there is a phase shift, proportional to the length of the Y, Lu or W block, introduced between neighbouring magnetically active (Gd, Dy or Tb) blocks.

Neutron and X-ray studies of the rare earth films and miltilayers have revealed a rich complex magnetic phases which could not have been predicted from the behaviour of the pure bulk magnetic systems [91M]. This is caused due to the lattice strain and clamping originating at layer interfaces as is shown in Fig. C. This epitaxial strains and clamping imposed at the film-substrate interfaces alters the detailed temperature dependence of the magnetic structures most notably by the introduction of multiphase coexistence. Moreover, while the crystal symmetries of the film remain unchanged from the bulk, the lattice and magnetic correlation lengths are reduced, consistent with a high degree of disorder. This disorder may play a significant role in the resulting magnetic order. Indeed, in the low temperature Er/Y superstructure the magnetic correlation lengths are comparable to the unit-cell size of magnetic structures and two new magnetic wave vectors falling between 5/21 and 1/4 were observed (see Fig. 284 and Ref. [97H]). It has been found that the driving energy for the ferromagnetic transition in Er mulitilayers varies linearly with strain [91B], implying that strain effects are more important than even the artificial modulation of multilayers. The complexity of these interfaces and their dependence on growth conditions, continue to challenge systematic studies.

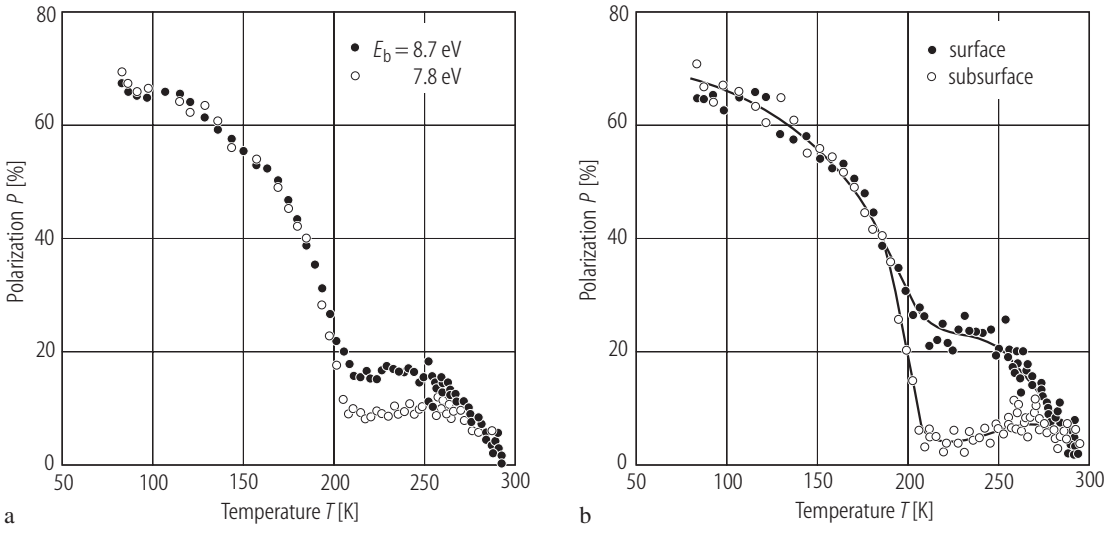

Fig. A. Spin polarization of the surface (black dots) and subsurface (open dots) 4f emission as reflections of the surface magnetization. The subsurface in-plane magnetization decreases abruptly near 280 K. Between 210 K and 290 K the in-plane ferromagnetic order decays rapidly below the surface one [93V].

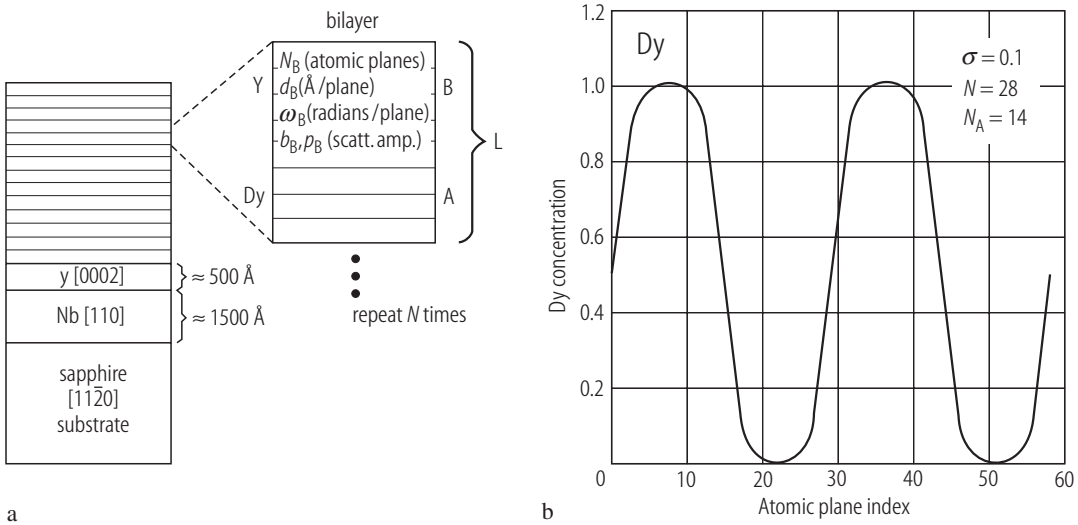

Fig. B. (**a**) Schematic drawing of the rare earth multilayer structure. The expanded view of a Y/Dy bilayer lists the physical parameters characterizing the individual A(Dy) and B(Y) layers. Y will grow epitaxially on (110)Nb in 4:3 atomic registration sequence. The resulting interface strains are relieved through a thick Y layer applied over the Nb before commencing the growth of the alternate Dy and Y layers. (**b**) Composition profile of the multilayer obtained from analysis of the neutron scattering data. The data confirms that interdiffusion is limited to two atomic planes on either side of the interface [89R].

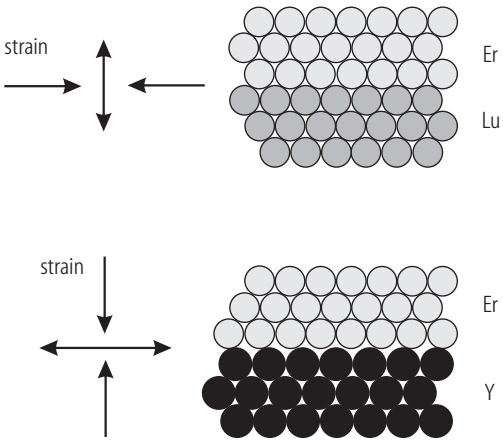

Fig. C. Schematic drawing of the strain in the Er films near the film-substrate interfaces [97H].

Acknowledgement

We would like to thank L. Folcik and A. Hackemer for their helpful technical assistance.

References

86G Grünburg, P., Schreiber, R., Pang, Y., Brodsky, M.B., Sowers, H.: Phys. Rev. Lett. **57** (1986) 2442

86R Rau, C., Eichner, S.: Phys. Rev. B **34** (1986) 6347

86S Salamon, M.B., Sinha, S., Rhyne, J.J., Cunningham, J.E., Erwin, R.W., Borchers, J., Flynn, C.P.: Phys. Rev. Lett. **56** (1986) 259

87F Farle, M., Baberschke, K.: Phys. Rev. Lett. **58** (1987) 511

89R Rhyne, J.J., Erwin, R.W., Borchers, J., Salamon, M.B., Du, R., Flynn, C.P.: Physica B **159** (1989) 111

91B Borchers, J.A., Salamon, M.B., Erwin, R.W., Rhyne, J.J., Du, R.R., Flynn, C.P.: Phys. Rev. B **43** (1991) 3123

91B2 Bucher, J.P., Douglass, D.C., Bloomfield, L.A.: Phys. Rev. Lett. **66** (1991) 3052

91D Drulis, H., Drulis, M., in: Landoldt- Börnstein, NS (Wijn, H.P.J., ed.), Berlin, Heidelberg, New York : Springer, Vol.III/19d1 (1991), p.1

91M Majkrzak, C.F., Kwo, J., Hong, M., Yafet, Y., Gibbs, D., Chien, C.L., Bohr, J.: Adv. Phys. **40** (1991) 99

91R Rührig, M., Schäfer, R., Hubert, A., Mosler, R., Wolf, J.A., Demokritov, S., Grűnberg, P.: Phys. Status Solidi (a) **125** (1991) 635

91U Unguris, J., Celotta, R.J., Pierce, D.T.: Phys. Rev. Lett. **67** (1991) 140

91W Ruqian Wu, Freeman, A.J.: J. Magn. Magn. Mater. **99** (1991) 81

93J Jehan, D.A., McMorrow, D.F., Cowley, R.A., Ward, R.C.C., Wells, M.R., Hagmann, N., Clausen, K.N.: Phys. Rev. B **48** (1993) 5594

93T1 Tang, H., Weller, D., Walker, T.G., Scott, J.C., Chappert, C., Hopster, H., Pang, A.W., Dessau, D.S., Pappas, D.P.: Phys. Rev. Lett. **71** (1993) 444

93V Vescovo, E., Carbone, C., Rader, O.: Phys. Rev. B **48** (1993) 7731

94J Jehan, D.A., McMorrow, D.F., Simpson, J.A., Cowley, R.A., Swaddling, P.P., Clausen, K.N.: Phys. Rev. B **50** (1994) 3085

97H Helgsen, G., Tanaka, Y., Hill, J.P., Wochner, P., Gibbs, D., Flynn, C.P., Salamon, M.B. Phys. Rev. B **56** (1997) 2635

2.1.2 Survey

Survey of magnetic, electrical, spectroscopic, thermal and mechanical properties of rare earth metals.

Structure	Spin ordering	Θ [K]	T_C [K]	T_N [K]	p_s [μ_B]	p_{eff} [μ_B/R]	Remarks	Ref.
Cerium (Ce)							**LBIII/19d1, pages 48-54**	
Ce $f_{cc} \rightarrow b_{cc}$		–50				2.58 (750K) 3.21 (1850K)	high temperature susceptibility $\chi_m(T)$, Fig. 3	87K1
dhcp poly					2.4		$\sigma(H)$ at 4.2, 20, 30 K, Fig. 6 molecular field, CEF, exchange interaction	87L
γCe αCe		 600					magnetic susceptibility vs. T, Fig. 2 no-crystal field effects $B_4^0 = 0$, $B_6^0 = 0$, conduction electron susceptibility $\chi_P = 0.75 \cdot 10^{-6}$ cm^{3}g^{-1} $\chi(T)$ and crystal electric field (CEF) parameters, Fig. 1 $\chi_P = 0.75 \cdot 10^{-6}$ cm^{3}g^{-1} $B_4^0 = 3.64$ K, $B_6^0 = 0.06$ K CEF level scheme: $\Gamma_7 = 0$ $\Gamma_8 = 230$ meV, $\Gamma_8' = 490$ meV $\Gamma_6 = 545$ meV, $\Gamma_7' = 355$ meV	88O
Ce γ-bulk (d=100Å) or amorphous (d=5Å)					0.2(100Å) 1(15Å)		$\sigma(H)$ at 2 K, Fig. 4 thin multilayers, Ce/Ta d_{Ce} = 5 Å, 15 Å, 100 Å $\sigma(T)$ at 5 T ‖ sample plane, Fig. 5	96A

Structure	Spin ordering	Θ [K]	T_C [K]	T_N [K]	p_s [μ_B]	p_{eff} [μ_B/R]	Remarks	Ref.
Praseodymium (Pr)							**LBIII/19d1, pages 55-72**	
hcp→bcc		0				3.62 (750K) 4.47 (1850K)	high temperature susceptibility, Fig. 3	87K1
dhcp poly					2.4		σ(H) at 4.2 K, 20 K, 30 K molecular field, CEF, Fig. 6 exchange interaction	87L
Neodymium (Nd)							**LBIII/19d1, pages 73-86**	
hcp→bcc		0				3.71 (750K) 4.81 (1850K)	high temperature susceptibility, Fig. 3	87K1
hcp				19.9			quadrupole-q magnetic structure below 4.5 K, Fig. 8 $q_1 = 0.106$, $q_2 = 0.116$ $q_3 = 0.181$, $q_4 = 0.184$	89F
dhcp					1.96 ($H\|\|a$) 2.09 ($H\|\|b$) 1.41 ($H\|\|c$)		wavevectors vs. applied field at 1.8 K, Fig. 10 magnetic satellite vs. T at $H = 0$, Fig. 11, magnetic phase diagram $H \parallel a$ and b axis, Fig. 15 T_N vs. H^2, Fig. 16 thermal expansion vs. T, $H \parallel a$ Fig. 17 $H \parallel b$, Fig. 18 magnetostriction vs. applied field $H \parallel a$, Fig. 19 $H \parallel b$, Fig. 20	91Z

Structure	Spin ordering	Θ [K]	T_C [K]	T_N [K]	p_s [μ_B]	p_{eff} [μ_B/R]	Remarks	Ref.
dhcp							multi-q modulated magnetic structure, cubic and hexagonal sites, Fig. 7 basal plane component and magnetic transition temperatures, Fig. 12 magnetic satellites, temperature evolution for (100) point, Fig. 13	94L
							magnetic phase diagram under pressure, Fig. 14 magnetic neutron diffraction	96W2
	double q						magnetic X-ray diffraction, Fig. 21	96W
superlattice epitaxial 582nm [Nd(3.2nm)/ Y(2nm)]$_{120}$	cubic site ordering 8K			27			ZFC magnetization vs. T, Fig. 22 FC magnetization vs. T, Fig. 23 magnetic moment of hexagonal site vs. Nd concentration, Fig. 24 magnetic moment vs. T, hexagonal and cubic sites, Fig. 25	97E
dhcp bulk	helimagnetic			32				
bulk dhcp				19.9			2-q structure, between 19.1 K and 8.2 K 4-q structure below 6 K, Fig. 9	97G
Samarium (Sm)							**LBIII/19d1, pages 87-90**	
hcp→bct							magnetic susceptibility, high temperature range, Fig. 26	87K1

Structure	Spin ordering	Θ [K]	T_C [K]	T_N [K]	p_s [μ_B]	p_{eff} [μ_B/R]	Remarks	Ref.
dhcp s.c. poly	spin-reorientation transition						specific heat, temperature dependence 2 K…32 K, Fig. 34 anomalies at: 9.6 K, 13.7 K, 20.4 K excess entropy: (4.0 ± 0.5) J mol^{-1}K^{-1} for 9 K…10 K (1.14 ± 0.1) J mol^{-1}K^{-1} for 13.7 K peak (0.114 ± 0.02) J mol^{-1}K^{-1} for 20.4 K peak	89S
dhcp							neutron scattering intermultiplet transition in Sm^3, Fig. 29 form factor in Sm^{3+}, Fig. 30, Fig. 31, Fig. 33 spin-orbit transition in Sm metal, Fig. 32 $^6H_{5/2}\rightarrow{}^6H_{7/2}$ 135 meV $\rightarrow{}^6F_{1/2}$ 760 meV $\rightarrow{}^6F_{3/2}$ 780 meV $\rightarrow{}^6F_{5/2}$ 850 meV $\rightarrow{}^6F_{7/2}$ 930 meV	93N
bct→fcc						4…5.5	magnetic moment, ultra-high-pressure Fig. 27 energy calculation of the Bain path (energy vs. *c*/*a* ratio), Fig. 28	93S1
Europium (Eu)							**LBIII/19d1, pages 91-97**	
Eu/Se superlattice	AF→spin flop state transition, H_{cr} at 3750G, 2150G, 1000G						Mössbauer spectra vs. applied pressure at 44 K, Fig. 36 isomer shift, Fig. 37 hyperfine field, Fig. 38, Fig. 39 valence change of 0.5 electron intermediate-valence state	87F1
hcp-bcc transition							high temperature susceptibility, 750 K…1850 K, Fig. 35	87K1

Structure	Spin ordering	Θ [K]	T_C [K]	T_N [K]	p_s [μ_B]	p_{eff} [μ_B/R]	Remarks	Ref.
Eu/Se superlattice	AF→spin flop state transition, H_{cr} at 3750G, 2150G, 1000G						magnetic properties of Eu/Se, magnetization vs. applied field at 1.9 K, Fig. 40 magnetic anisotropy K_u, T_N vs. d (Se-Eu distance), $H_{cr} \propto d^{-0.8}$ $K_u \propto d^{-0.5}$ $J \propto d^{-1.1}$ magnetization vs. T, Fig. 41 magnetic phase diagram, Fig. 42	98D
Gadolinium (Gd)							**LBIII/19d1, pages 98-108**	
		Fig. 56	291.85				spin dynamics critical exponents PAC spectra, Fig. 57	86Ch
		317			7.55	7.98	magnetization in the pulsed field, Fig. 45 magnetization vs. T at different fields, Fig. 46 effective field constant, $\gamma = (5.0 \pm 0.41) \cdot 10^3$ g cm^{-3} magnetocaloric effect, Fig. 64 short range order parameter, Fig. 58	86P
		310					surface ferromagnetic order spontanous magnetization, Fig. 47	86R
Gd(0001)/W(110) monolayer 80Å (27 layers)			292.5 (bulk) 288(2) (80Å) 281(1) (Θ_A=1.6) 271(1) (Θ_A=0.8)				electron-spin-resonance study, Fig. 111, Fig. 112 g = 1.97, $\Delta H/\Delta T$ = 5 Oe K^{-1} EPR intensity, Fig. 113	87F

Structure	Spin ordering	Θ [K]	T_C [K]	T_N [K]	p_s [μ_B]	p_{eff} [μ_B/R]	Remarks	Ref.
							heat capacity, $0 < T < 16$ K, Fig. 62 $C_p(T) = (4.48\ T + 1.37\ T^{1.5} + 0.404\ T^3)$ mJK^{-1}mol^{-1} $\gamma = (4.48 \pm 0.07)$ mJK^{-2}mol^{-1}, $\Theta_D = (169 \pm 1)$ K	87H
$[Gd_{NGd}/Y_{N\gamma}]_M$ superlattice N_{Gd}=10 N_Y=6-24 M=76;225							magnetic properties magnetization vs. magnetic field, $T = 12$ K, Fig. 80 magnetization - temperature dependence, $0 < T < 300$ K, Fig. 81 remanence and saturation field oscillatory dependence, Fig. 83 oscillatory period: 7 atomic layers overall oscillation range: 20 atomic layers	87K
thin films over glass							T_C vs. annealing temperature, Fig. 69 273 K < T_C < 293 K	88N
Gd(001)/W(110) monolayer 80Å (≈27 layers)							EPR magnetic resonance near T_C field vs. T, Fig. 114 anisotropy coefficient $N_\perp = 0.692(1)$ for monolayer	89F
s.c.		317(39)					magnetic susceptibility, Fig. 49 $g_{anis} = 2.52 \cdot 10^{-4}$, $g_{iso} = 5.28 \cdot 10^{-3}$	89G
hcp s.c.							muon spin rotation, $0 < T < 300$ K, Fig. 61	90H
Gd(0001)/W(110)							ac susceptibility, Fig. 97 Hopkinsen effect, $T_H = (289 \pm 1)$ K	90S

Structure	Spin ordering	Θ [K]	T_C [K]	T_N [K]	p_s [μ_B]	p_{eff} [μ_B/R]	Remarks	Ref.
Gd(0001)/W(110) films, d=30Å							photoemission, Fig. 106, surface state $5d_{3x^2-r^2}$	91L
Gd					7.0		Compton profile, Fig. 55 spin polarization $(0.53 \pm 0.08)\ \mu_B$/at	91S
hcp Gd(0001) surface							antiferromagnetic coupling surface layer against FM bulk, energy Gd(0001) slab vs. distance to adjacent underlayer, Fig. 70 d_{FM}= 5.55 au; d_{AFM}= 5.77 au	91W
Gd(0001)/Gd hcp	AF/FM						magnetic configuration for a 6-layer Gd(0001) slab, Fig. 71 localized d_{z^2} state	91W1
Gd(0001)/W(110) films, d=20Å							surface-state binding energy, Fig. 108	92D
Gd(0001)/W(110)							surface magnetism, Fig. 101 photoemission spectra, Fig. 103	92M
Gd/Nb films d_{Gd}=11-10^3Å							magnetooptic Kerr effect 2 K < T < 295 K, $\mu_0 H$ < 0.3 T remanent magnetization, Fig. 84 in-plane magnetization M_r, coercive field H_c, Fig. 85 domain temperature vs. film thickness $\Delta T_C / T_{C(\infty)} \propto d^{-\lambda}$, $\lambda \approx 1.6$	93P

Structure	Spin ordering	Θ [K]	T_C [K]	T_N [K]	p_s [μ_B]	p_{eff} [μ_B/R]	Remarks	Ref.
Gd(0001)/W(110) films, d=80Å							4f photoemission at 50 K, Fig. 59, Fig. 60 $^4f^6 - {}^7F_J$ transition Gd-4f photoemission spectra, Fig. 105 $h\nu$ = 200 eV	93S2
Gd(0001)/W(110) films, hcp							magnetic reconstruction of Gd(0001) surface, Fig. 72 photoemission from 4f core vs. T, Fig. 107 surface ordering T_{CS} =(353 ± 2) K bulk ordering T_{CB} = 293 K	93T1
Gd(0001)/W(110)			353(2)				photoelectron spectroscopy, Fig. 102	93V
Gd(0001)/W(110)							ac susceptibility, Fig. 98, Fig. 100	94A
Gd(0001)/W(110) films, d=10-100nm							annealing effects on coercive field, Fig. 95 MOKE hysteresis loops, Fig. 109	94P
Gd(0001)/W(110) d=80Å							core-level photoemission, Fig. 104 spin-orbit splitting Δ_{SO}(4d) = 4.8 eV	95A
Gd(0001)/W(110) films, d=10-130nm hcp							magnetic reorientation, Kerr effect, coercive field, $H_C(T)$, $H \| a$and effective anisotropy, Fig. 73, Fig. 96 remanent magnetization vs. T, Fig. 94 in-plane susceptibility vs. T, 120 K < T < 300 K, d = 28…130 nm, Fig. 99	95B1

Structure	Spin ordering	Θ [K]	T_C [K]	T_N [K]	p_s [μ_B]	p_{eff} [μ_B/R]	Remarks	Ref.
Gd/Y films d=3-1000Å							magnetic measurements, 2 K < T < 300 K, 0.01 T ≤H ≤ 0.3 T, magnetization vs. T at T > 100 K and H = 0.01 T, Fig. 74 saturation magnetization vs. T, Fig. 77 remanence vs. T, Fig. 78 4 K < T < 300 K, d = 4…1000 Å magnetization vs. magnetic field, Fig. 79 coercive field $H_C(T)$, Fig. 82, $\Delta T_C \propto d^{-1.6}$	95G
s.c.							magnetic entropy, Fig. 67	96D
Gd/Mo multilayers 3.3nm						7.63	interface pinning missing moment vs. d_{Mo}, Fig. 87 magnetization vs. field at 5.5 K < T < 250 K range, Fig. 88 magnetization at 5 K, Fig. 89	96H
Gd/W mulitlayers					7.63		finite-size effects saturation magnetization, Fig. 68 $M_s = 2017 - 2112 \times (1/d_{Gd})$ magnetization of Gd/W vs. H, Fig. 90 Curie temperature vs. layer thickness, Fig. 91 $[T_C(\infty) - T_C(d)]/T_C(\infty) = (d/d_0)^{-\lambda}$, λ = 1.5	96J
hcp						5.1 8.0	plastic deformation magnetization vs. H, Fig. 50 magnetization vs. T, 50 K < T < 350 K, Fig. 51	96M
Gd/W multilayers d_W=18Å 8Å<d_{Gd}<85Å						6.1	average moment per Gd, vs. layer thickness, Fig. 92 total moment per Gd layer, Fig. 93	97L

Structure	Spin ordering	Θ [K]	T_C [K]	T_N [K]	p_s [μ_B]	p_{eff} [μ_B/R]	Remarks	Ref.
film, d=100Å			490				EPR spectra, Fig. 115 signal intensity, Fig. 116 linewidth, Fig. 117 g value vs. T, Fig. 118 exchange FM interaction inside layer $J = 0.07 \cdot 10^{-3}$ eV	97T
s.c.					7.63		magnetization vs. H and T, H || [0001], Fig. 43 H || [1010], Fig. 44 ac magnetic susceptibility H || [0001] and [1010], Fig. 52, Fig. 53, Fig. 54, Fig. 64	98D
			291				heat capacity in magnetic field, Fig. 63 magnetocaloric effect, s.c., Fig. 65 magnetic entropy vs. T, Fig. 66 $\Delta T_C \approx 6$ K/T	98D
ultrathin films			155				spontaneous magnetization, Fig. 48 suppression ΔT_C vs. thickness d, Fig. 75 $\Delta T_C \propto d^{-1}$ magnetic hysteresis loop, Fig. 76	98G
Terbium (Tb)							**LBIII/19d1, pages 109-128**	
			T_{Cb}= 220K	T_{Nb}= 228K			top most surface layer electron spin polarization vs. T, Fig. 142 surface Curie temperature T_{Cs} = 248 K	88R
(100) platelet							neutron diffraction topography, Fig. 120 helimagnetic-ferromagnetic phase coexistence	89B

Structure	Spin ordering	Θ [K]	T_C [K]	T_N [K]	p_s [μ_B]	p_{eff} [μ_B/R]	Remarks	Ref.
s.c.							magnetic phase diagram from elasticity modulus, Fig. 119	89K
s.c.							magnetocaloric effect, magnetic phase diagram, *H-T*, Fig. 126 H_w = 0.099 T, T_w = 228.5 K	89N
s.c.	F→HAF Θ_1=210-222K HAF→P Θ_2=223.3-230K	236					ac magnetic susceptibility $\chi'(T)$ the wall energy $E_w/2 \mid B_2 \mid \sigma^2$, Fig. 128 thermal modulation wave $\parallel b$ axis, Fig. 137	91McK
hcp	F spiral phase		220	232		9.9(1)	pressure effect on critical fields, paramagnetic Curie temperatures, efficient magnetic moment $\sigma(H)$, $0 < H < 14$ kOe, $H \parallel a$, Fig. 130; magnetic phase diagram, 200 K < T < 235 K, Fig. 131 $\sigma(T)$; $H \parallel b$ as function of pressure, Fig. 132 $\Delta\sigma$-effect vs. magnetic field, $H \parallel a$ 150 K < T < 230 K, Fig. 133 volume magnetostriction, $\omega(\sigma^2)$, Fig. 139 magnetostriction vs. T, $H \parallel b$ and $H \parallel a$, Fig. 140, Fig. 141 $d\Theta_1/dp = -1.17 \cdot 10^{-9}$ K cm^{2}dyn^{-1} $d\Theta_2/dp = -0.8 \cdot 10^{-9}$ K cm^{2}dyn^{-1} magnetic anisotropy constant in the base plane, K_6 $(1/K_6)\,(\partial K_6/\partial p) = 0.61 \cdot 10^{-11}$cm^{2}dyn^{-1}	91N1
hcp	F spiral phase		220	232	9.0	9.34	X-ray scattering study, magnetic wavevector vs. T, Fig. 124 turn angle per layer: $17^o < \omega < 21.8^o$ for 220 K < T < 235 K	92G

Structure	Spin ordering	Θ [K]	T_C [K]	T_N [K]	p_s [μ_B]	p_{eff} [μ_B/R]	Remarks	Ref.
hcp			225	231			neutron diffraction study, turn angle vs. T, Fig. 123 T_N and T_C vs. pressure, Fig. 129 dT_N/dp = –0.82 K/kbar dT_C/dp = –1.28 K/kbar $\omega_C d\omega_i/dp$ = 0.01/kbar	92K
			221	229			time dependent effects ac magnetic susceptibility, Fig. 134 χ' vs. H, Fig. 135 χ' vs. T, Fig. 136	93McK
s.c.					9.3		inelastic neutron scattering under pressure, magnon dispersion at 90 K magnon dispersion $\parallel c$ axis at 90 K, Fig. 121 interplaner exchange parameters, Fig. 122 energy gap Δ = 1.44 meV at 4.3 kbar Δ = 2 meV at 15.2 kbar	94K
Tb(0001)/W(110) film, 150Å thick							photoemission experiments 4f core-level photoemission spectra, at 110 K, Fig. 143	95A
Tb/Y superlattices Tb(26Å)/Y(44Å)×50							magnetization vs. T 215 K < T < T_1, Fig. 144	95D
s.c			221 F→HAF				magnetization vs. T, 50 K < T < 250 K, $H \parallel a$, Fig. 125 magnetic entropy change, $H \parallel a$, Fig. 127	96D
			221 F→HAF	230 HAF→P			Magnetostriction vs. T, Fig. 138	97M

Structure	Spin ordering	Θ [K]	T_C [K]	T_N [K]	p_s [μ_B]	p_{eff} [μ_B/R]	Remarks	Ref.
Dysprosium (Dy)							**LBIII/19d1, pages 129-149**	
Dy/M bilayer d_{Dy}=70-100Å						10.4(5)	X-ray analysis and magnetic measurements, Fig. 176 magnetization σ vs. H at 10 K, Fig. 179 $M = M(0)\,(1 - BT^{3/2}e^{-\Delta/T})$, Δ: anisotropy gap, 150 K < Δ < 210 K for Dy/Y Δ = constant = 20 K for Dy	87B
Dy/Y superlattices $[Dy_{15}/Y_{14}]_{64}$ $[Dy_9/Y_8]_{90}$				176 163	7.6 H state		neutron diffraction analysis, magnetic diffraction peaks vs. T, 10 K < T < 160 K, Fig. 170 magnetic peaks at T = 10 K, Q = 1.96, 2.04 and 2.12 Å^{-1}, field dependence of the helical state, neutron diffraction, Fig. 171 field induced ferromagnetism, magnetization measurements along the easy and hard directions, Fig. 178 zero field diffraction ‖ c axis interplanar space and turn angle vs. T, Fig. 188 turn angle $\omega_Y = 52^o = 0.29\,\pi \equiv$ wavevector = 0.31 Å turn angle $\omega_{Dy}(T) = 0.175\,\pi(31.5^o)$ at 10 K average turn angle for Dy/Y superlattice: 33.5°	87E
Dy/Y multilayers d_{Dy}=16 planes d_Y =10-22 planes							long-range helical spin-ordering neutron diffraction studies along (000l), T dependence, Fig. 169 coherent Dy layer moment vs. T, 0 < T < 180 K, Fig. 177	87R
			91.1(2) 92.1	180.6(1)			calorimetric study, s.c., energy change at AF, F and HAF transition temperatures, Fig. 161 energy peak = 7 Jmol^{-1} the latent heat (35 ± 2) Jmol^{-1} at 91.1 K	88Å

Structure	Spin ordering	Θ [K]	T_C [K]	T_N [K]	p_s [μ_B]	p_{eff} [μ_B/R]	Remarks	Ref.
	spiral AF					10.6	L_{III} absorption edge magnetic scattering, Fig. 167 wavevector $\tau = 0.24c^*$ at 176 K $\tau = 0.15c^*$ at 83 K $E = 7.798$ keV	89I
Dy/Y							magnetic multilayers neutron scattering $[Dy_{14}/Y_{22}]_{89}$, Fig. 168	89R1
Dy/Y superlattice							neutron scattering studies, peak intensity, ferromagnetic and helical components vs. magnetic field, Fig. 172 magnetic satellites for $[Dy_{12}/Y_9]_{100}$ at 10 K, Fig. 173 net layer magnetic moment vs. T, $0 < T < 180$ K, Fig. 181 magnetic coherence length ξ as a function Y thickness, Fig. 189	89R
s.c.			85	178			magnetocaloric effect and pressure influence specific magnetization and critical field, $H\|\|a$, Fig. 149, $\sigma(H)$, Fig. 150 volume magnetostriction ω for $H\|\|a$, Fig. 158, Fig. 159 magnetoelastic energy change, magnetic anisotropy, elastic energy and energy barrier.in HAFM→FM transition, Fig. 162 magnetocaloric effect $H \parallel a$ and b axis, Fig. 166 total entropy, 140 K < T < 200 K, Fig. 163, Fig. 164, magnetic entropy vs. applied field $\parallel a$ axis, Fig. 165 Néel point T_N, $dT_N/dp = -6 \cdot 10^{-10}$ K cm^{2}dyn^{-1} Curie point T_C, $dT_C/dp = -13 \cdot 10^{-10}$ K cm^{2}dyn^{-1}, tricritical point ≈ 165 K	91N

Structure	Spin ordering	Θ [K]	T_C [K]	T_N [K]	p_s [μ_B]	p_{eff} [μ_B/R]	Remarks	Ref.
Dy/M M=Ta,Lu,Y,Co nanostruct. multilayers							magnetic properties magnetization σ vs. H, Fig. 180 –50 kOe < H < 50 kOe, thickness dependence magnetization, σ vs. T, Fig. 182 intrinsic anisotropy K_u, thickness dependence $K_u = 1.4 \cdot 10^7$erg cm^3 at 4.2 K $K_u = 2 \cdot 10^6$erg cm^3 at 300 K	91S
s.c.			90	180			c axis magnetic moment ac susceptibility $H \parallel b$ and c axis, Fig. 155 magnetization vs. T, Fig. 157	91W2
Dy/Lu films			85(bulk) 100 (400Å) 125 (145Å) 175(40Å)				neutron diffraction magnetic coherence length vs. number Lu interlayers, Fig. 191 magnetization vs. T, Fig. 192 multipeak structure at 100 K magnetic coherence of 1.5 bilayers turn angle $\omega = 28^o \pm 1°$ per Dy plane interlayer coherence lost at 80 Å of Lu energy barrier between helical and ferromagnetic state is proportional to $(1 - \cos \omega)^2 / \cos \omega$, 28° < ω < 35 T_N for Dy/Lu	93B
hcp	ω=43° per layer at T_N ω=26.5° per layer at T_C			178 (bulk)	10.33		magnetic properties, Lu/Dy trilayers magnetization vs. T, 0 < T < 200 K, Fig. 193 p_{Dy} vs. H, Fig. 194 $T_C = T_N$ for 40 Å film	93B1

Structure	Spin ordering	Θ [K]	T_C [K]	T_N [K]	p_s [μ_B]	p_{eff} [μ_B/R]	Remarks	Ref.
Dy/Zr $[Dy(x\text{Å})/Zr(30\text{Å})]_n$, 8<x<30Å			75				magnetic measurements magnetization vs. T, $0 < T < 300$ K, Fig. 197 hysteresis loops at 10 K, Fig. 198 volume anisotropy energy $K_u \approx -5 \cdot 10^9$ erg cm^{-3} surface anisotropy energy $K_s \approx 200$ erg cm^{-2}	93L
Dy/Lu epitaxial 50Å thick	HAF→F			175			magnetic phase diagram for epitaxial Dy magnetization, σ vs. H, Fig. 175 H-T vs. basal plane strain ε, Fig. 187 magnetic spiral, $q = 0.1$ Å^{-1} (10 planes)	93T
Dy/Sc hcp $c\text{-}[Dy(25\text{Å})/Sc(40\text{Å})]_{60}$ $c\text{-}[Dy(14\text{Å})/Sc(21\text{Å})]_{85}$			150 147 100				neutron diffraction experiments, Fig. 200 magnetization vs. T for ZFC and FC for $H \parallel c$, and $H \perp c$, Fig. 201	93T2
Dy/Lu				167			neutron diffraction studies difraction scans at 150 and 170 K, Fig. 190	94R
Dy/Sc superlattice $Dy(20\text{Å})/Sc(x\text{Å})_{64}$ 20<x<60Å				43 (40%Dy)			magnetoresistance studies, Fig. 199	94T2

Structure	Spin ordering	Θ [K]	T_C [K]	T_N [K]	p_s [μ_B]	p_{eff} [μ_B/R]	Remarks	Ref.
Dy/Cu(111) films Dy(20Å)/Cu(100Å)×30 Dy(40Å)/Cu(100)×20							magnetic relaxation measurements magnetization vs. T and vs. H, Fig. 195, anisotropy studies ZFC and FC blocking temperatures: T_B = 2.5 K for Dy(20Å) T_B = 25 K for Dy(40Å)	94T3
Dy(0001)/W(110) film, 150Å thick							photoemission experiments 4f core-level photoemission spectra, at 55 K, Fig. 174	95A
s.c.	helical→para magnetic phase transition						neutron diffraction, ultrasonic studies, intensity of (0,0,2–δ) reflection vs. T, Fig. 148 ultrasonic velocity, v_{33} and attenuation coefficient, α_{33}, Fig. 160	95dP
Dy/Zr multilayers $[Dy(xÅ)/Zr(30Å)]_n$ 6<x<30Å							magnetization results, Fig. 196 $0 < T < 300$ K	95L
							magnetization process, X-ray diffraction study, diffraction pattern at 0, 3 kOe and 8 kOe and 95 K, Fig 147 FM phase volume fraction, Fig. 156	95S
							magnetization vs. T, s.c. , $H \parallel a$, Fig. 151	96D
	fan		85	179			ac calorimetry, specific heat measurements phase diagram, $0 < H \parallel a < 17$ kOe, Fig. 145	96I

Structure	Spin ordering	Θ [K]	T_C [K]	T_N [K]	p_s [μ_B]	p_{eff} [μ_B/R]	Remarks	Ref.
1$\bar{1}$02 Dy/Y superlattice							neutron diffraction measurements magnetization vs. T, Fig. 186 $0 < T < 300$ K	96T-B
							magnetic phase diagram H-T, Fig. 146 magnetization measurements vs. T, Fig. 152, Fig. 153 for $H \parallel b$ magnetization vs. applied field, $H \parallel b$, Fig. 154 $T_{a\text{-}ha} = 93$ K, F (angular)→AF (helical) $T_{ha\text{-}p} = 180$ K, AF→P (paramagnetic)	97A
Dy_n/Y_{15} $5<n<25$							magnetoelastic stress, $B \parallel a$, in applied field, $0 < \mu_0 H < 12$ T magnetoelastic stress isotherms, Fig. 183	97dM
Dy/Y	helimagnetic spiral						magnetic measurements, neutron scattering interplane turn angles temperature dependence $0 < T < 175$ K, Fig. 184 heli- and ferromagnetic phase ranges vs. T, Fig. 185	97T-B
Holmium (Ho)							**LBIII/19d1, pages 150-164**	
hcp	conical spiral		20	131		10	magnetic X-ray scattering turn angle ≈ 50° / layer at T_N turn angle ≈ 30° / layer at T_C modulation wavevector q/c^*, Fig. 209	85G
							magnetic X-ray scattering layer commensurate structure, in $17 < T < 25$ K, Fig. 208 magnetic wavevector	86B

Structure	Spin ordering	Θ [K]	T_C [K]	T_N [K]	p_s [μ_B]	p_{eff} [μ_B/R]	Remarks	Ref.
	helical			133			elastic neutron diffraction elastic constant c_{44} annd c_{66}, temperature dependence, Fig. 232 and Fig. 233 commensurate lock-in transition at 17.8 K anomalies at T_N = 133 K, 97.4 K, 24.5 K, 19.8 K and T_C = 17.8 K	88B1
hcp							elastic neutron scattering; 18 < T < 30 K magnetic structure for b = 5 (q = 1/5c*), Fig. 206	88C
dhcp s.c.	flat spiral→ conical spiral at 19.46K						specific heat temperature dependence, Fig. 234 2 K…32 K, peak at 19.46 K; latent heat (2.7 ± 0.3) J mol^{-1} excess entropy: (0.14 ± 0.02) J mol^{-1}K^{-1} peak at 17.3 K excess entropy: (0.10 ± 0.02) J mol^{-1}K^{-1}	89S
hcp	incommen- surate spiral					10.3	magnetic X-ray scattering magnetic satellite evolution vs. T 17 < T < 25 K, Fig. 210	90B1
s.c.							magnetic measurements, magnetic moment vs. T, $H \parallel b$, Fig. 227	90B2
	helifan						magnetic energy vs. magnetic field at 50.2 K and $H \parallel b$, Fig. 211 theoretical neutron-diffraction pattern at 50 K, Fig. 212 magnetic structure sequence: helix→helifan(3/2)→fan→ferro as field increases	90J

Structure	Spin ordering	Θ [K]	T_C [K]	T_N [K]	p_s [μ_B]	p_{eff} [μ_B/R]	Remarks	Ref.
hcp	spiral→conical at 16K		16	132			spin-slip structures magnetization measurements magnetic phase diagram $H \parallel a$, Fig. 202, $4 < T < 140$ K; $\mu_0 H$ up to 55 T H-T diagram along the c axis, Fig. 205 magnetization vs. T, Fig. 224 and Fig. 225 anomalies at 20 K, 24 K at 42 K for $H \parallel b$ and anomaly at 98 K for $H \parallel c$ spin slip spacing of 11, 8, 5 and 2 layers	90W text
hcp	$q_m=(5/11)c^*$			132			dispersion relationship, neutron experiments, spin wave gap in $q = (5/11)c^* \approx 0.6$ meV spin wave dispersion at 19.5 K, Fig. 214 $B_2^0 = 0.029$ meV, $B_6^0 = -0.956 \cdot 10^{-6}$ $B_6^6 = 9.210 \cdot 10^{-6}$	91McM
	conical		20	132	p_{ab}=9.5 p_c=1.7		susceptibility measurements temperature dependence of p conical-to-ferromagnetic transition, Fig. 226 temperature dependence of p, para-to-helical antiferromagnetic transition, Fig. 228	91S2
							neutron diffraction studies helifan (3/2) structure at 50 K, Fig. 213	92J
s.c.	cone q=1/6c^*			133			neutron diffraction measurements neutron scattering intensity at 25 K $H \parallel b$ axis, $H = 0.25$ T, Fig. 221	92J1

Structure	Spin ordering	Θ [K]	T_C [K]	T_N [K]	p_s [μ_B]	p_{eff} [μ_B/R]	Remarks	Ref.
s.c.	helical-to-conical structure				1.53(1) $H\|\|c$ at 4.2K		neutron diffraction around 20 K, magnetization vs. T, $5 < T < 45$ K, Fig. 223 temperature evolution: intensity and width, interplane turn angle around 20 K transition, Fig. 219	92P
Ho/Lu Ho_{40}/Lu_{15} Ho_{20}/Lu_{15}	cone phase τ=1/6c*		40(5)				neutron diffraction experiments novel ferromagnrtic phase turn angle vs. T, $0 < T < 120$ K, Fig. 250 Lu layer turn angle: 40°/ layer	93S
hcp				131.2	10		neutron scattering magnetic critical fluctuations neutron-scattering scans at (0,0,2,–τ) and (0,0,τ), Fig. 215, Fig. 216 turn angle per plane along c axis: $\phi \approx 50°$	94T3
s.c.	spiral-to-conical phase						X-ray magnetic scattering, magnetic modulation wavevector vs. T, $0 < T < 140$ K, Fig. 217	94H
	helimagnetic						neutron diffraction studies spiral wavevector τ vs. T $124 \text{ K} < T < 133$ K in 3 T $H \parallel b$ axis, Fig. 218 lock-in $\tau = 5/18$	94T

Structure	Spin ordering	Θ [K]	T_C [K]	T_N [K]	p_s [μ_B]	p_{eff} [μ_B/R]	Remarks	Ref.
Ho/Y superlattice $(Ho_{40}Y_{15})_{40}$							X-ray and neutron diffraction measurements neutron scattering vs. T $10 < T < 130$ K, Fig. 235 turn angle-temperature dependence film and bulk Ho, Fig. 242 turn angle vs. lattice thickness, Fig. 241	94C
							helix turn angle α wavevector k_H , Fig. 243	95A1
							neutron diffraction, ultrasonic studies intensity of (0,0,2-δ) reflection vs.T, Fig. 220 ultrasonic velocity v_{33} and attenuation coefficient α_{33}, Fig. 229 velocity v_{33} vs. T along c axis, Fig. 230	95dP
Ho/Zr multilayers Ho(30Å)/Zr(30Å)							magnetization in high magnetic field, magnetization and magnetoresistance vs. magnetic field at 4.2 K, Fig. 244 and at 50 K, Fig. 246 magnetoresistance oscillation vs. Zr layers thickness, Fig. 245	95R
Ho/Lu superlattice							magnetic phase diagram H || ab, $(Ho_{40}/Lu_{15})_{50}$, $(Ho_{20}/Lu_{10})_{50}$, Fig. 240	
							low-temperature magnetic structure at 19.5 K, Fig. 207	95S2

Structure	Spin ordering	Θ [K]	T_C [K]	T_N [K]	p_s [μ_B]	p_{eff} [μ_B/R]	Remarks	Ref.
Ho_n/Lu_m superlattice n=11-31 m=19-50							magnetic phase diagram $0 < \mu_0 H < 1$ T, $0 < T < 140$ K, Fig. 238 Number of layers / T_C [K] / T_N [K] / H to F field [T] 11.5 / 40 / 118 / 0.8 12 / 34 / 120 / 1.0 17.5 / 27 / 127 / 1.6 21 / 27 / - / 1.7 31 / 26 / 127 / 2.0	95T1
Ho/Y superlattice	*c* axis cone						magnetic susceptibility, magnetic phase diagram, $H \parallel b$, $0 < T < 140$ K, 3000 Å-film, Fig. 237 Néel temperature change with Y thickness, Fig. 236	95T2
s.c.	τ=(5/18)*c**			132.9			ultrasonic measurements elastic constant c_{33} and α_{33} of 5/18 lock-in plane, Fig. 231	95V
Ho/Lu superlattice	H→F→fan		20 40				magnetoelastic stress magnetic phase diagrams, Fig. 253	96A1
$[Ho_6/Lu_6]_{100}$ superlattice							magnetoelastic stress isotherms $0 < \mu_0 H < 12$ T, Fig. 239	96dM

Structure	Spin ordering	Θ [K]	T_C [K]	T_N [K]	p_s [μ_B]	p_{eff} [μ_B/R]	Remarks	Ref.
Ho/Sc superlattice ($Ho_n/Sc_{m.}$) n=20-30 m=10-40			50(5)	127(2) 132(5) 125(3)			neutron diffraction technique Ho_{30}/Sc_{20}; 4/23c* Ho_{20}/Sc_{20}; 1/6c* Ho_{20}/Sc_{40}; 2/11c* neutron scattering at 4 K, Fig. 251 turn angle vs. T, Fig. 252	97B-J
							magnetoresistance H-T phase diagram, $H \parallel b$ 2 K < T < 140 K; H up to 5.5 T, Fig. 203	97G1
	helicon						critical lattice versus magnetic field magnetic field dependence of c-lattice parameter, $0 < \mu_0 H < 6$ T, Fig. 222	97O
Ho/Lu superlattice (Ho_n/Lu_{15})× 50 n=8-85 planes c/2 superation							magnetoelastic stress temperature dependence, at 12 T, Fig. 247 magnetoelastic stress vs. Ho number planes at 10 K and 12 T, Fig. 248 stress isotherms vs. applied field, $H \parallel b$ easy axis, Fig. 249	98dM
Erbium (Er)							**LBIII/19d1, pages 165-174**	
Monocrystal 10<d<70nm							magnetic susceptibility, Fig. 272	87C
$[Er_{23}/Y_{19}]_{100}$		$\Theta_{\parallel}$=33		$T_{N\parallel}$=77 $T_{N\perp}$=25		9.9	magnetometer measurements magnetization vs. T, $H \parallel c$ H = 5 kOe, Fig. 289	88B

Structure	Spin ordering	Θ [K]	T_C [K]	T_N [K]	p_s [μ_B]	p_{eff} [μ_B/R]	Remarks	Ref.
			19.2	85			scanning microcalorimetry, ferromagnetic first order transition, Fig. 276, Fig. 277 the latent heat, $\Delta H_L = (18.5 \pm 1)$ J mol^{-1} three endothermic peaks within 21 K < T < 26 K at 25.3 K: $\Delta H_L = (1.2 \pm 0.3)$ J mol^{-1} at 21.6 K: $\Delta H_L = (0.5 \pm 0.3)$ J mol^{-1} two peaks in 50 K < T < 55 K range 53.4 K: $\Delta H_L = (1.3 \pm 0.3)$ J mol^{-1}) 50.8 K: $\Delta H_L = (0.7 \pm 0.3)$ J mol^{-1})	89Å
Er/Y superlattice [Er_{32}/Y_{21}]				78(1)			neutron diffraction studies magnetic peaks, Fig. 282 magnetoelastic energy 1.4 K/atom	89R
Er/Y multilayers				84	8.5		turn angles and magnetic moment vs. T, Fig. 283 0 < T < 80 K T_N = 78 K for [Er_{32}/Y_{21}] T_N = 78.5 K for [Er_{23}/Y_{19}] T_N = 72.5(10) K for [Er_{13}/Y_{26}]	89R1
hcp			18	81			magnetic X-ray scattering magnetic satellite intensity vs. T in 0 < T < 60 K, Fig. 260	90B1
Er/Y superlattice d_{Er}=375-14.500Å d_Y=175-2200Å				$T_{N\|\|}$=45 $T_{N\perp}$=28			structural and magnetic properties schematic drawing of Er/Y super lattice, Fig. 281 field dependence of magnetization for 9500 Å films, Fig. 279 critical field vs. film thickness at 10 K and 20 K, Fig. 278 magnetization vs. magnetic field 0 < H < 40 kOe, Fig. 287 critical field vs. T, Fig. 286 saturation moment at 10 K, 208 G cm^{3}g^{-1} for [$Er_{23.5}$ / Y_{19}]$_{100}$	91B

Structure	Spin ordering	Θ [K]	T_C [K]	T_N [K]	p_s [μ_B]	p_{eff} [μ_B/R]	Remarks	Ref.
Er/Lu d=400-9500Å			21				magnetization vs. T, $H \parallel c$; $0 < T < 100$ K, Fig. 291 modulated spin state vs. T, Fig. 261	91B1
s.c.				8.2			spin-slip transition magnetization vs. magnetic field, $0 < H < 30$ kOe, Fig. 266 tricritical point at $T = 68$ K spin-slip structure; $\tau = 5/21, 5/24, 5/27$	91G
s.c.				84			magnetoelastic effects c_{33} temperature dependence, $0 < T < 90$ K, Fig. 292 sharp points at T_N , $T_N = 52$ K and $T_C = 18$ K c_{11} and α_{11} between 15 K $< T <$ 60 K lock-in structure, $b = 7$ evidence, Fig. 293	92E
hcp	Cone lock-in q=(1/4)c* CAM				7.0 $\parallel c$, 4.5 in base plane		magnetic structure neutron scattering along c axis wavevector vs. T, Fig. 262 lock-in cone structures vs. T, Fig. 264 magnetic moments in intermediate phase q = (1/4)c* $p_{xy} = 4.3\ \mu_B$; $p_z = 7.3\ \mu_B$	92L
	LSW FS helical		20	85			magnetic phase transition magnetization vs. T, Fig. 265 transitions: paramagnetic→antiferromagnetic→helical→ferromagnetic spiral(FS) $Q_2 = 85$ K, $Q_B = 52$ K, $Q_1 = 20$ K $p_\parallel = 7.8\ \mu_B$, $p_\perp = 4.4\ \mu_B$ at 6 K wavevector = 5/21 at $T < 18$ K	92S

Structure	Spin ordering	Θ [K]	T_C [K]	T_N [K]	p_s [μ_B]	p_{eff} [μ_B/R]	Remarks	Ref.
			19				heat capacity studies zero-field (1.5 K…20 K) heat capacity, Fig. 275 zero-field (20 K…80 K) heat capacity, Fig. 274 electronic coefficient: $\gamma = (8.7 \pm 0.1)$ mJ mol^{-1}K^{-2} $\Theta_D = (176.9 \pm 0.4)$ K Five anomalies at: 25.1 K, 17.5 K, 42 K, 48.9 K, 51.4 K $C = \alpha T^{-2} + 0.585\ T^{-3} - 0.120\ T^{-4} + \gamma T + \beta T^3 + dT^3\exp(-\Delta/T)$ at $H = 0$ $H = 0$ $\quad$ $\mu_0 H = 10$ T $c = 18$ mJK/ g·atom $\quad$ 37 mJK/g·atom $\gamma = 8.7$ mJK/g·atom $\quad$ 100.5 mJK/g·atom $\beta = 0.351$ mJK/g·atom $\quad$ 351 mJK/g·atom $d = 8.9$ mJK/g·atom $\quad$ 3.8 mJK/g·atom Δ(K) = 11.6 K $\quad$ 9.1 K	93P1
							neutron diffraction studies spin configuration at 4.5 kbar and at 11.5 kbar, Fig. 259	93K
							neutron scattering magnetization measurements phase diagram (H-T), $0 < H < 50$ kOe; $0 < T < 60$ K, Fig. 256 stages of collapsing $q = 2/7c^*$ structure vs. magnetic field, Fig. 258 magnetization vs. field; $H \parallel a$ axis, at 10 K; Fig. 267 phase diagram in a basal plane, Fig. 268	94J
s.c.							X-ray diffraction; 4.2 K < T < 100 K H-T phase diagram vs. crystallographic directions, Fig. 257	95B

Structure	Spin ordering	Θ [K]	T_C [K]	T_N [K]	p_s [μ_B]	p_{eff} [μ_B/R]	Remarks	Ref.
s.c.				82(1)			high pressure neutron diffraction at 11.5 kbar and 14 kbar modulation wavevector $Q = q(2\pi/c)$ vs. T, Fig. 263 magnetic moment distribution at 4.5 K at r_n in the n'th basal plane $p_x(r_n) / \mu_B = 4.41\cos(r_n \cdot Q + \pi/2)$ $p_y(r_n) / \mu_B = 0$ $p_z(r_n) / \mu_B = 10.16\cos(r_n \cdot Q + 0) +$ $3.33\cos(r_n \cdot Q + \pi) + 2.67\cos(r_n \cdot 5Q + 0) + 1.83\cos(r_n \cdot 7Q + \pi)$	95K
							X-ray diffraction study first order magnetic transition, Fig. 273	95T
s.c.			18	$T_{N\parallel}$=89 $T_{N\perp}$=53			magnetic transition identification magnetization, ac susceptibility, electrical resistance, thermal expansion studies ac susceptibility vs. T, $0 < T < 100$ K, Fig. 270, Fig. 269 $T_{N\parallel} = 52.5$ K, $T_{N\perp} = 87.9$ K spin-slip transition at: 26.6 K, 28.5 K, 29.7 K, 35.8 K, 43.0 K and 51.0 K, magnetization vs. T, $H \parallel c$ and b axis, Fig. 271 spin-slip transition at: 26.8 K, 29.1 K, 34.4 K, 41.7 K, 51.3 K $T_C = 19.5$ K, $T_{N\parallel} = 87.4$ K	95W

Structure	Spin ordering	Θ [K]	T_C [K]	T_N [K]	p_s [μ_B]	p_{eff} [μ_B/R]	Remarks	Ref.
			19	87 53			*b* axis magnetic phase diagram, Fig. 254 transition at: 22 K, 42 K, 48 K 53 K($T_{N\perp}$) and 87 K($T_{N\parallel}$)	96W2

q	Structure	*T* [K]
5/21	F	18 (T_C)
1/4	2(44)	18-25
6/23	2(444443)	25.5-28.5
5/19	2(44443)	29
4/15	2(4443)	32.5-35.5
3/11	2(443)	40
2/7	2(43)	49.5-52.5

epitaxial Er s.c. *d*=2000Å							magnetization vs. magnetic field, $0 < H < 30$ kOe at 10 K, Fig 288 critical field vs. *T*, Fig. 290 magnetization vs. *T*, at 200 G, Fig. 280	96C
Er_m/Y_{15} 10<m<30							magnetoelastic stress measurements magnetoelastic isotherms, in field $0 < \mu_0 H < 12$ *T*, $H \parallel a$, Fig. 285 conical→fan structure transition, at $\mu_0 H_{cr1} = 3$ T fan→FN structure transition at $\mu_0 H_{cr2} = 8$ T FN→F structure transition at $\mu_0 H_{cr3} = 12$ T	97dM
films *d*>>1μm Er/Y Er/Lu				86			X-ray scattering magnetic wavevector vs. *T*, Fig. 284 two new magnetic phases with vectors 11/45 and 6/25 $\tau \approx 0.283$ at $T_N = 86$ K $\tau \approx 0.292$ at 52 K	97H

Structure	Spin ordering	Θ [K]	T_C [K]	T_N [K]	p_s [μ_B]	p_{eff} [μ_B/R]	Remarks	Ref.
s.c.				$T_{N\parallel}$ $T_{N\perp}$			magnetic phase diagram, Fig. 254 magnetoresistance measurements, c axis 10 K < T < 100 K, $\mu_0 H$ < 5.5 T	97W
Thulium (Tm)							**LBIII/19d1, pages 175-179**	
hcp			25	54	7		X-ray diffraction studies L_{III} absorption edge, Fig. 305 E = 8648 eV	90B
				56			magnetization s.c. temperature dependence vs. magnetic field 0 < T < 80 K, Fig. 296 4 - 3 seven-layers ferrimagnetism, p_s = 1 μ_B	90D
	seven layer ferrimagnetic antiphase at 5K			58.5			magnetic excitations, inelastic neutron studies constant-κ scans at κ = (1,1,ξ) (ξ = 0, 0.3, 0.8), Fig. 300 dispersion gap (≈ 8meV)	90F-B

Structure	Spin ordering	Θ [K]	T_C [K]	T_N [K]	p_s [μ_B]	p_{eff} [μ_B/R]	Remarks	Ref.
s.c.	pora→AF→ CAM→ferri →ferro		33	58	1.025 (ferri) 7.06 (ferro)		magnetic transitions T_m s.c. magnetization, ac susceptibility and calorimetric measurements isothermal magnetization at 5 K, $H \parallel a$ and $H \parallel b$ axis, Fig. 295 critical field for ferri→ferro transition 33 kOe ferrimagnetic saturation moment; p_s = 1.025 μ_B/atom ferromagnetic saturation moment, p_s = 7.07 μ_B/atom ac susceptibility vs. T, Fig. 298, 299 antiferromagnetic transition at 58 K endothermic peak at 33.4 K with $\Delta H_L = (0.8 \pm 0.2)$ J mol^{-1}, Fig. 306	91Å
				57.5			inelastic neutrons scattering crystal-field levels, Fig. 297 $B_2^0 = -0.096,\ B_4^0 = 0,\ B_6^0 = -0.92 \cdot 10^{-5},\ B_6^6 = 8.86 \cdot 10^{-5}$ meV the inter planer exchange coupling coefficient: $J_0 = 0.098$, $J_1 = 0.057$, $J_2 = -0.022$, $J_3 = -0.025$, $J_4 = -0.010$, $J_5 = -0.002$ meV spin wave and transverse phonon dispersion, Fig. 301	91McE
s.c.				56			magnetostriction measurements thermal expansion, $0 < T < 80$ K, Fig. 303 magnetostriction vs. magnetic field $0 < \mu_0 H < 8$ T, Fig. 302 three transitions at: 4.2 K for $\mu_0 H = 2.82$ T, 3.35 T and 3.61 T above T_N at 59.3 K one transition: $\mu_0 H = 5.33$ T	92Z

Structure	Spin ordering	Θ [K]	T_C [K]	T_N [K]	p_s [μ_B]	p_{eff} [μ_B/R]	Remarks	Ref.
s.c.					6.6		magnetoresistance and magnetization studies magnetic phase diagram, $B \parallel c$ axis, Fig. 294 isothermal magnetization, $0 < \mu_0 H < 7$ T and magnetoresistance, Fig. 304 moment in ferromagnetic state $p = 0.12$ μ_B spin-wave energy gap 8.5 meV in ferrimagnetic state and 6.7 meV in ferromagnetic phase	98E

References

74W Wells, P., Lanchester, P.C., Jones, D.W., Jordan, R.G.: J. Phys. F **4** (1974) 1729

85G Gibbs, D., Moncton, D.E., D'Amico, K.L., Bohr, J., Grier, B.H.: Phys. Rev. Lett. **55** (1985) 234

85T Tsang,T-W., Gschneidner jr., K.A., Schmidt, F.A., Thome, D.K.: Phys. Rev. B **31** (1985) 235

86B Bohr, J., Gibbs, D., Moncton, D.E., D'Amico, K.L.: Physica A **140** (1986) 349

86Ch Chowdhury, A.R., Collins, G.S., Hohenemser, C.: Phys. Rev. B **33** (1986) 5070

86G Grünburg, P., Schreiber, R., Pang, Y., Brodsky, M.B., Sowers, H.: Phys. Rev. Lett. **57** (1986) 2442

86P Ponomarev, B.K.: J. Magn. Magn. Mater. **61** (1986) 129

86R Rau, C., Eichner, S.: Phys. Rev. B **34** (1986) 6347

86S Salamon, M.B., Sinha, S., Rhyne, J.J., Cunningham, J.E., Erwin, R.W., Borchers, J., Flynn, C.P.: Phys. Rev. Lett. **56** (1986) 259

87B Borchers, J., Sinha, S., Salamon, M.B., Du, R., Flynn, C.P., Rhyne, J.J., Erwin, R.W.: J. Appl. Phys. **61** (1987) 4049

87C Cowen, R.A., Stolzman, B., Averback, R.S., Hahn, H.: J. Appl. Phys. **61** (1987) 3317

87E Erwin, R.W., Rhyne, J.J., Salamon, M.B., Borchers, J., Sinha, S., Du, R., Cunningham, J. E., Flynn, C.P.: Phys. Rev. B **35** (1987) 6808

87F Farle, M., Baberschke, K.: Phys. Rev. Lett. **58** (1987) 511

87F1 Farrell, J.N., Taylor, R.D.: Phys. Rev. Lett. **58** (1987) 2478

87H Hill, R.W., Collocott, S.J., Gschneidner jr., K.A., Schmidt, F.A.: J. Phys. F **17** (1987) 1867

87K Kwo, J., Hong, F.J., DiSalvo, F.J., Waszczak, J.V., Majkrzak, C.F.: Phys. Rev. B **35** (1987) 7295

87K1 Konovalov, S.V., Singer, V.V., Radovskij, I.Z., Geld, P.V.: Solid State Phys. **29** (1987) 1768

87L Leyarovski, E., Marachkov, J., Gilewski, A., Mydlarz, T.: Phys. Rev. B **35** (1987) 8674

87R Rhyne, J.J., Erwin, R.W., Borchers, J., Sinha, S., Salamon, M.B., Du, R., Flynn, C.P.: J. Appl. Phys. **61** (1987) 4043

88Å Åström, H.U., Benediktsson, G.: J. Phys. F **18** (1988) 2113

88B Borchers, J.A., Salamon, M.B., Du, R., Flynn, C.P., Rhyne, J.J., Erwin, R.W.: J. Appl. Phys. **63** (1988) 3458

88B1 Bates, S., Patterson, C., McIntyre, G.J., Palmer, S.B., Mayer, A., Cowley, R.A., Melville, R.: J. Phys. C **21** (1988) 4125

88C Cowley, R.A., Bates, S.: J. Phys. C **21** (1988) 4113

88N Nakamura, O., Baba, K., Ishii, H., Takeda, T.: J. Appl. Phys. **64** (1988) 3614

88O Orlov, V.G., Kurchatov, I.V.: Solid State Commun. **67** (1988) 689

88R Rau, C., Jin, C., Robert, M.: J. Appl. Phys. **63** (1988) 3667

89Å Âström, H.U., Benediktsson, G.: J. Phys. Condens. Matter **1** (1989) 4381

89B Baruchel, J., Sandonis, J. Pearce, A.: Physica B **156-157** (1989) 765

89F Forgan, E.M., Gibbons, E.P., McEwen, K.A., Fort, D.: Phys. Rev. Lett. **62** (1989) 470

89F1 Farle, M., Berghaus, A., Baberschke, K.: Phys. Rev. B **39** (1989) 4838

89G Geldart, D.J., Hargraves, P., Fujiki, N.M., Dunlap, R.A.: Phys. Rev. Lett. **62** (1989) 2728

89I Isaacs, E.D., McWhan, D.B., Siddons, D.P., Hastings, J.B., Gibbs, D.: Phys. Rev. B **40** (1989) 9336

89K Kataev, G.I., Sattarov, M.R.,Tishin, A.M.: Phys. Status Solidi (a) **114** (1989) K79

89N Nikitin, S.A., Tishin, A.M., Bykhover, S.E.: Phys. Status Solidi (a) **114** (1989) K99

89R Rhyne, J.J., Erwin, R.W., Borchers, J., Salamon, M.B., Du, R., Flynn, C.P.: Physica B **159** (1989) 111

89R1 Rhyne, J.J., Erwin, R.W., Borchers, J., Salamon, M.B., Du, R., Flynn, C.P.: Phys. Scr. T **29** (1989) 31

89S Stewart, A.M., Collocott, S.J.: J. Phys.: Condens. Matter **1** (1989) 677

90B Bohr, J. Gibbs, D., Huang, K.: Phys. Rev. B **42** (1990) 4322

90B1 Bohr, J.: J. Magn. Magn. Mater. **83** (1990) 530

90B2 Burhanov, G.S., Volkozub, A.V., Snigirev, O.V., Tishin, A.M., Chistykov, O.D.: Solid State Phys. **32** (1990) 2483

90D Daou, J.N., Burger, J.P., Vajda, P., Chouteau, G., Tur, R.: J. Phys.: Condens. Matter **2** (1990) 7897

90F-B Fernandez-Baca, J.A., Niclow, R.M., Rhyne, J.J.: J. Appl. Phys. **67** (1990) 5283

90H Hartmann, O., Wäppling, R., Karlsson, E., Kalvius, G.M., Asch, L., Litterst, F.J., Aggarwal, K., Münch, K.H., Gygax, F.N., Schenck, A.: Hyperfine Interactions **64** (1990) 369

90J Jensen, J., Mackintosh, A. R.: Phys. Rev. Lett. **64** (1990) 2699

90S Salas, F.H., Mirabal-Garcia, M.: Phys. Rev. B **41** (1990) 10859

90W Willis, F., Ali, N., Steinitz, M.O., Mojtaba Kahrizi, Tindall, D.A.: J. Appl. Phys. **67** (1990) 5277

91Å Åström, H.U., Noguest, J., Nicolaides, G.K., Rao, K.V., Benediktsson, G.: J. Phys.: Condens. Matter **3** (1991) 7395

91B Borchers, J.A., Salamon, M.B., Erwin, R.W., Rhyne, J.J., Du, R.R., Flynn, C.P.: Phys. Rev. B **43** (1991) 3123

91B1 Beach, R.S., Borchers, J.A., Erwin, R.W., Rhyne, J.J., Matheny, A., Flynn, C.P., Salamon, M.B.: J. Appl. Phys. **69** (1991) 4335

91B2 Bucher, J.P., Douglass, D.C., Bloomfield, L.A.: Phys. Rev. Lett. **66** (1991) 3052

91D Drulis, H., Drulis, M., in: Landoldt- Börnstein, NS (Wijn, H.P.J., ed.), Berlin, Heidelberg, New York : Springer, Vol.III/19d1 (1991), p.1

91G Godovikov, S.K., Nikitin, S.A., Tishin, A.M.: Phys. Lett. A **158** (1991) 265

91M Majkrzak, C.F., Kwo, J., Hong, M., Yafet, Y., Gibbs, D., Chien, C.L., Bohr, J.: Adv. Phys. **40** (1991) 99

91L Dongqi Li, Hutchings, C.W., Dowben, P.A., Hwang, C., Rong-Tzong Wu, Onellion, M., Andrews, A.B., Erskine, J.L.: J. Magn. Magn. Mater. **99** (1991) 85

91McE McEwen, K.A., Steigenberger, U., Jensen, J.: Phys. Rev. B **43** (1991) 3298

91McK McKenna, T.J., Campbell, S.J., Chaplin, D.H., Wilson, G.V.H.: J. Phys.: Condens. Matter **3** (1991) 1855

91McM McMorrow, D.F., Patterson, C., Godfrin, H., Jehan, D.A.: Europhys. Lett. **15** (1991) 541

91N Nikitin, S.A., Tishin, A.M., Leontiev, P.I.: J. Magn. Magn. Mater. **92** (1991) 405

91N1 Nikitin, S.A., Tishin, A.M., Bezdushnyi, R.V., Spichkin, Yu.I., Red'ko, S.V.: J. Magn. Magn. Mater. **92** (1991) 397

91R Rührig, M., Schäfer, R., Hubert, A., Mosler, R., Wolf, J.A., Demokritov, S., Grűnberg, P.: Phys. Status Solidi (a) **125** (1991) 635

91S Nobuhiko Sakai, Yoshikazu Tanaka, Fumitake Itoh, Hiroshi Sakurai, Hiroshi Kawata, Toshiaki Iwazumi: J. Phys. Soc. Jpn. **60** (1991) 1201

91S1 Shan, Z.S., Jacobsen, B., Liou, S.H., Sellmyer, D.J.: J. Appl. Phys. **69** (1991) 5289

91S2 Snigirev, O.V., Tishin, A.M., Volkozub, A.V.: J. Magn. Magn. Mater. **94** (1991) 342

91U Unguris, J., Celotta, R.J., Pierce, D.T.: Phys. Rev. Lett. **67** (1991) 140

91W Ruqian Wu, Freeman, A.J.: J. Magn. Magn. Mater. **99** (1991) 81

91W1 Ruqian Wu, Chun Li, Freeman, A.J., Fu, C.L.: Phys. Rev. B **44** (1991) 9400

91W2 Willis, F., Ali, N.: J. Appl. Phys. **69** (1991) 5694

91Z Zochowski, S.W., McEwen, K.A., Fawcett, E.: J. Phys.: Condens. Matter **3** (1991) 8079

92D Dongqi Li, Jiandi Zhang, Dowben, P.A., Onellion, M.: Phys. Rev. B **45** (1992) 7272

92E Eccleston, R.S., Palmer, S.B.: J. Phys.: Condens. Matter **4** (1992) 10037

92G Gehring, P.M., Rebelsky, L., Gibbs, D., Shirane, G.: Phys. Rev. B **45** (1992) 243

92J Jensen, J., Mackintosh, A.R.: J. Magn. Magn. Mater. **104-107** (1992) 1481

92J1 Jehan, D.A., McMorrow, D.F., Cowley, R.A., McIntyre, G.J.: Europhys. Lett. **17** (1992) 553

92K Kawano, S., Achiwa, N., Onodera, A., Nakai, Y.: Physica B **180-181** (1992) 46

92L Lin, H., Collins, M.F., Holden, T.M., Wei, W.: Phys. Rev. B **45** (1992) 12873

92M Mulhollan, G.A., Garrison, K., Erskine, J.L.: Phys. Rev. Lett. **69** (1992) 3240

92P Pearce, A., Baruchel, J., Kulda, J.: Phys. Status Solidi (b) **172** (1992) 443

92S Snigirev, O.V., Tishin, A.M., Volkozub, A.V.: J. Magn. Magn. Mater. **111** (1992) 149

92Z Zochowski, S.W., McEwen, K.A.: J. Magn. Magn. Mater. **104-107** (1992) 1515

93B Beach, R.S., Borchers, J.A., Matheny, A., Erwin, R.W., Salamon, M.B., Everitt, B., Pettit, K., Rhyne, J.J., Flynn, C.P.: Phys. Rev. Lett. **70** (1993) 3502

93B1 Beach, R.S., Matheny, A., Salamon, M.B., Flynn, C.P., Borchers, J.A., Erwin, R.W., Rhyne, J.J.: J. Appl. Phys. **73** (1993) 6901

93J Jehan, D.A., McMorrow, D.F., Cowley, R.A., Ward, R.C.C., Wells, M.R., Hagmann, N., Clausen, K.N.: Phys. Rev. B **48** (1993) 5594

93K Kawano, S., Lebech, B., Achiwa, N.: J. Phys.: Condens. Matter **5** (1993) 1535

93L Luche, M.C., Baudry, A., Boyer, P.: J. Magn. Magn. Mater. **121** (1993) 148

93McK McKenna, T.J., Campbell, S.J., Chaplin, D.H., Wilson, G.V.H.: J. Magn. Magn. Mater. **124** (1993) 105

93N Needham, L.M., Williams, W.G., Taylor, A.D.: J. Phys.: Condens. Matter **5** (1993) 2591

93P Paschen, U., Sürgers, C., v. Löhneysen, H.: Z. Phys. B **90** (1993) 289

93P1 Pecharsky, V.K., Gschneidner jr., K.A., Fort, D.: Phys. Rev. B **47** (1993) 5063

93S Swaddling, P.P., McMorrow, D.F., Simpson, J.A., Wells, M.R., Ward, R.C.C., Clausen, K.N.: J. Phys.:Condens. Matter **5** (1993) L481

93S1 Söderlind, P., Eriksson, O., Wills, J.M., Johansson, B.: Phys. Rev. B **48** (1993) 9212

93S2 Starke, K., Navas, E., Baumgarten, L., Kaindl, G.: Phys. Rev. B **48** (1993) 1329

93T Tsui, F., Flynn, C.P.: Phys. Rev. Lett. **71** (1993) 1462

93T1 Tang, H., Weller, D., Walker, T.G., Scott, J.C., Chappert, C., Hopster, H., Pang, A.W., Dessau, D.S., Pappas, D.P.: Phys. Rev. Lett. **71** (1993) 444

93T2 Tsui, F., Flynn, C.P., Beach, R.S., Borchers, J.A., Erwin, R.W., Rhyne, J.J.: J. Appl. Phys. **73** (1993) 6904

93V Vescovo, E., Carbone, C., Rader, O.: Phys. Rev. B **48** (1993) 7731

94A Aspelmeier, A., Gerhardter, F., Baberschke, K.: J. Magn. Magn. Mater. **132** (1994) 22

94C Cowley, R.A., McMorrow, D.F., Simpson, A., Jehan, D., Swaddling, P., Ward, R.C.C., Wells, M.R.: J. Appl. Phys. **76** (1994) 6274

94F Farle, M., Lewis, W.A.: J. Appl. Phys. **75** (1994) 5604

94H Helgesen, G., Hill, J.P., Thurston, T.R., Gibbs, D., Kwo, J., Hong, M.: Phys. Rev. B **50** (1994) 2990

94J Jehan, D.A., McMorrow, D.F., Simpson, J.A., Cowley, R.A., Swaddling, P.P., Clausen, K.N.: Phys. Rev. B **50** (1994) 3085

94K Kawano, S., Fernandez-Baca, J.A., Nicklow, R.M.: J. Appl. Phys. **75** (1994) 6060

94L Lebech, B., Wolny, J., Moon, R.M.: J. Phys. Condens. Matter **6** (1994) 5201

94P Pang, A.W., Berger, A., Hopster, H.: Phys. Rev. B **50** (1994) 6457

94R Rhyne, J.J., Salamon, M.B., Flynn, C.P., Erwin, R.W., Borchers, J.A.: J. Magn. Magn. Mater. **129** (1994) 39

94T Tindall, D.A., Adams, C.P., Steinitz, M.O., Holden, T.M.: J. Appl. Phys. **75** (1994) 6318

94T1 Tsui, F., Uher, C., Flynn, C.P.: Phys. Rev. Lett. **72** (1994) 3084

94T2 Tejada, J., Zhang, X.X., Ferrater, C.: Z. Phys. B **94** (1994) 245

94T3 Thurston, T.R., Helgesen, G., Hill, J.P., Gibbs, D., Gaulin, B.D., Simpson, P.J.: Phys. Rev. B **49** (1994) 15730

95A Arenholz, E., Navas, E., Starke, K., Baumgarten, L., Kaindl, G.: Phys. Rev. B **51** (1995) 8211

95A1 Andrianov, A.V.: J. Magn. Magn. Mater. **140-144** (1995) 749

95B Bulatov, A.S., Dolzhenko, V.F., Korniets, A.V.: J. Magn. Magn. Mater. **147** (1995) 403

95B1 Berger, A., Pang, A.W., Hopster, H.: Phys. Rev. B **52** (1995) 1078

95D Dufour, C., Dumesnil, K., Vergnat, M., Mangin, Ph., Marchal, G., Hennion, M.: J. Magn. Magn. Mater. **140-144** (1995) 771

95dP Du Plessis, P. de V., Venter, A.M., Brits, G.H.F.: J. Phys.: Condens.Matter **7** (1995) 9863

95G Gajdzik, M., Paschen, U., Sürgers, C., v. Löhneysen, H.: Z. Phys. B **98** (1995) 541

95K Kawano, S., Sørensen, S. Aa., Lebech, B., Achiwa, N.: J. Magn. Magn. Mater. **140-144** (1995) 763

95L Luche, M.C., Baudry, A., Boyer, P., Rouvière, J.L., Fermon, C., Miramond, C.: J. Magn. Magn. Mater. **150** (1995) 175

95R Raquet, B., Sdaq, A., Broto, J.M., Rakoto, H., Ousset, J.C., Askenazy, S., Baudry, A., Boyer, P., Luche, M.C., Khmou, A.: Physica B **211** (1995) 335
95S Shinoda, Y., Tajima, K.: J. Phys. Soc. Jpn. **64** (1995) 1334
95S1 Swaddling, P.P., McMorrow, D.F., Cowley, R.A., Simpson, J.A., Wells, M.R., Ward, R.C.C., Clausen, K.N., Collins, M.F., Buyers, W.J.L.: J. Magn. Magn. Mater. **140-144** (1995) 783
95S2 Simpson, J.A., McMorrow, D.F., Cowley, R.A., Jehan, D.A.: J. Magn. Magn. Mater. **140-144** (1995) 751
95T Tajima, K., Shinoda, Y., Tadakuma, M.: J. Magn. Magn. Mater. **140-144** (1995) 765
95T1 Tomka, G.J., de Groot, P.A.J., Rainford, B.D., Wells, M.R., Ward, R.C.C., Arnaudas, J.I.: J. Magn. Magn. Mater. **140-144** (1995) 785
95T2 Tomka, G.J., de Groot, P.A.J., Rainford, B.D., Wells, M.R., Ward, R.C.C., del Moral, A.: J. Magn. Magn. Mater. **140-144** (1995) 777
95V Venter, A.M., du Plessis, P. de V.: J. Magn. Magn. Mater. **140-144** (1995) 757
95W Watson, B., Ali, N.: J. Phys.: Condens. Matter **7** (1995) 4713
96A Aoki, Y., Sato, H., Komaba, Y., Kobayashi, Y., Sugawara, H., Yokoyama, T., Hanyu, T.: Phys. Rev. B **54** (1996) 12172
96A1 Arnaudas, J.I., del Moral, A., Ciria, M., Tomka, G.J., de la Fuente, C., de Groot, P.A.J., Ward, R.C.C., Wells, M.R.: J. Magn. Magn. Mater. **156** (1996) 421
96C Conover, M.J., Kaldowsky, A., Flynn, C.P.: Phys. Rev. B **53** (1996) R2938
96D Dan'kov, S.Y., Spichkin, Yu.I., Tishin, A.M.: J. Magn. Magn. Mater. **152** (1996) 208
96dM del Moral, A., Arnaudas, J.I., Ciria, M., Wells, M.R., Ward, R.C.C.: J. Magn. Magn. Mater. **157-158** (1996) 539
96H Harkins, J.V., Donovan, P.: J. Magn. Magn. Mater. **156** (1996) 224
96I Izawa, T., Tajima, K., Yamamoto, Y., Fujii, M., Fujimaru, O., Shinoda, Y.: J. Phys. Soc. Jpn. **65** (1996) 2640
96J Jiang, J.S., Chien, C.L.: J. Appl. Phys. **79** (1996) 5615
96M Mulyukov, Kh.Ya., Korznikova, G.F., Nikitin, S.A.: J. Magn. Magn. Mater. **153** (1996) 241
96T-B Theis-Bröhl, K., Ritley, K.A., Flynn, C.P., Hamacher, K., Kaiser, H., Rhyne, J.J.: J. Appl. Phys. **79** (1996) 4779
96W Watson, D., Forgan, E.M., Nuttall, W.J., Stirling, W.G., Fort, D.: Phys. Rev. B **53** (1996) 726
96W1 Watson, B., Ali, N.: J. Phys.: Condens. Matter **8** (1996) 1797
96W2 Watson, D., Forgan, E.M., Nuttall, W.J., Sokol, P.E., Shaikh, S.J., Zochowski, S.W., Fort, D.: J. Phys.: Condens. Matter **8** (1996) 5049
97A Alkhafaji, M.T., Ali, N.: J. Alloys Compounds **250** (1997) 659
97B-J Bryn-Jacobsen, C., Cowley, R.A., McMorrow, D.F., Goff, J.P., Ward, R.C.C., Wells, M.R.: Physica B **234-236** (1997) 495
97dM del Moral, A., Ciria, M., Arnaudas, J.I., Ward, R.C.C., Wells, M.R.: J. Appl. Phys. **81** (1997) 5311
97E Everitt, B.A., Salamon, M.B., Borchers, J.A., Erwin, R.W., Rhyne, J.J., Park, B.J., O'Donovan, K.V., McMorrow, D.F., Flynn, C.P.: Phys. Rev. B **56** (1997) 5452
97G Goff, J.P., Bryn-Jacobsen, C., McMorrow, D.F., Ward, R.C.C., Wells, M.R.: Phys. Rev. B **55** (1997) 12537
97G1 Gebhardt, J.R., Baer, R.A., Ali, N.: J. Alloys Compounds **250** (1997) 655
97H Helgsen, G., Tanaka, Y., Hill, J.P., Wochner, P., Gibbs, D., Flynn, C.P., Salamon, M.B. Phys. Rev. B **56** (1997) 2635
97L Li, Yi, Polaczyk, C., Kapoor, J., Riegel, D.: J. Magn. Magn. Mater. **165** (1997) 165
97M Mulyukov, K.Ya, Korznikova, G.F., Sharipov, I.Z.: Phys. Status Solidi (a) **161** (1997) 493
97O Ohsumi, H., Tajima, K., Wakabayashi, N., Shinoda, Y., Kamishima, K., Goto, T.: J. Phys. Soc. Jpn. **66** (1997) 1896
97T Tishin, A.M., Koksharov, Yu.A., Bohr, J., Khomutov, G.B.: Phys. Rev. B **55** (1997) 11064
97T-B Theis-Bröhl, K., Ritley, K.A., Flynn, C.P., Van Nostrand, J.E., Cahill, D.G., Hamacher, K., Kaiser, H., Rhyne, J.J.: J. Magn. Magn. Mater. **166** (1997) 27
97W Watson, B., Ali, N.: J. Alloys Compounds **250** (1997) 662

98D Dan'kov, S.Yu., Tishin, A.M., Pecharsky, V.K., Gschneidner jr., K.A.: Phys. Rev. B **57** (1998) 3478
98dM de Moral, A., Ciria, M., Arnaudas, J.I., Wells, M.R., Ward, R.C.C., de la Fuente, C.: J. Phys.: Condens. Matter **10** (1998) L139
98E Ellerby, M., McEwen, K.A., Jensen, J.: Phys. Rev. B **57** (1998) 8416
98G Gajdzik, M., Trappmann, T., Sürgers, C., v. Löhneysen, H.: Phys. Rev. B **57** (1998) 3525
98O Ono, T., Ishii, T., Tanuma, S., Yoshida, I.: Solid State Commun. **105** (1998) 93

2.1.3 Figures

2.1.3.1 Cerium

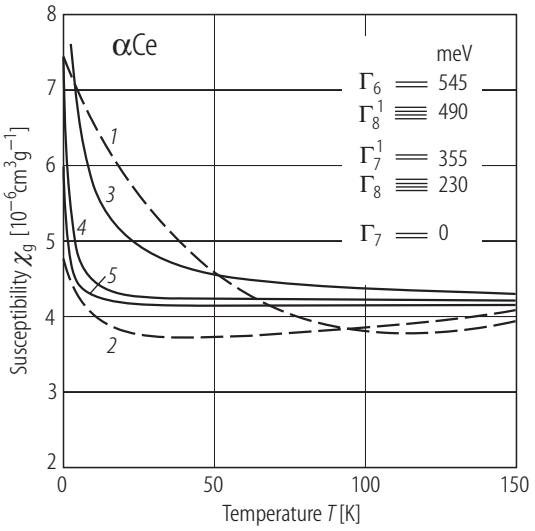

Fig. 1. Magnetic susceptibility of αCe. The dashed curves *1* and *2* are experimental data. The solid curves were calculated at ζ = 900 K, Θ = 600 K and χ_P = $0.75 \cdot 10^{-6}$ cm^3 g^{-1}. The CEF parameters varied as follows: (*3*): B_{40}^L = 4.53 K, B_{60}^L = 0; (*4*): B_{40}^L = 3.64 K, B_{60}^L = 0.06 K; (*5*): B_{40}^L = 3.1 K, B_{60}^L = 0.11 K. The inset shows the level scheme corresponding to the CEF parameters for curve (*4*). ζ: spin-orbit coupling parameter, χ_P: Pauli contribution [88O].

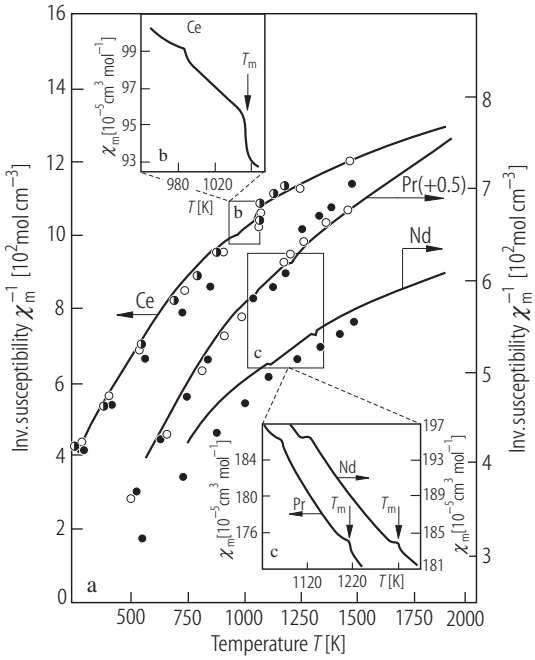

Fig. 3. Temperature dependence of the susceptibility for Ce, Pr and Nd for the high temperatures. The anomalies connected with the structure phase transitions and with the melting point (T_m) are visible. The solid lines are also experimental data [87K1].

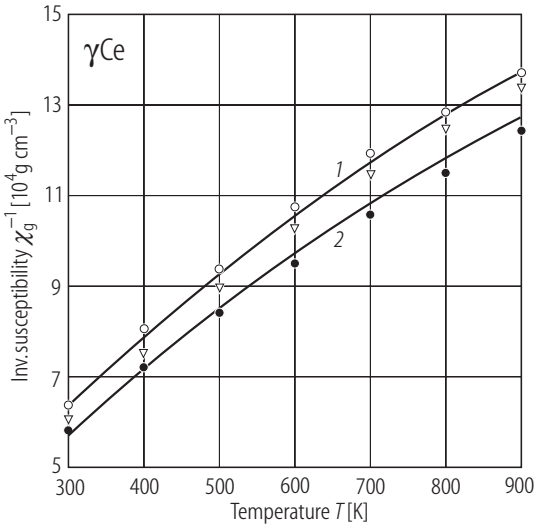

Fig. 2. Inverse magnetic susceptibility of γCe. The solid curves were calculated for the following values of parameters: (*1*): ζ = 900 K, B_{40}^L = 0, B_{60}^L = 0, Θ = 85 K, χ_P = $0.75\ 10^{-6}$ cm^3 g^{-1}; (*2*): ζ = 875 K, B_{40}^L = 0, B_{60}^L = 0, Θ = 50 K, χ_P = $1\ 10^{-6}$ cm^3 g^{-1}. ζ: spin-orbit coupling parameter, χ_P: Pauli contribution [88O].

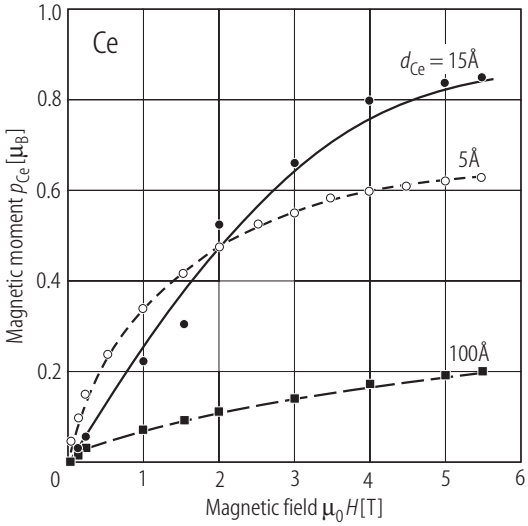

Fig. 4. Magnetization curves obtained at 2 K for Ce thin layers with d_{Ce} = 5, 15 and 100 Å [96A].

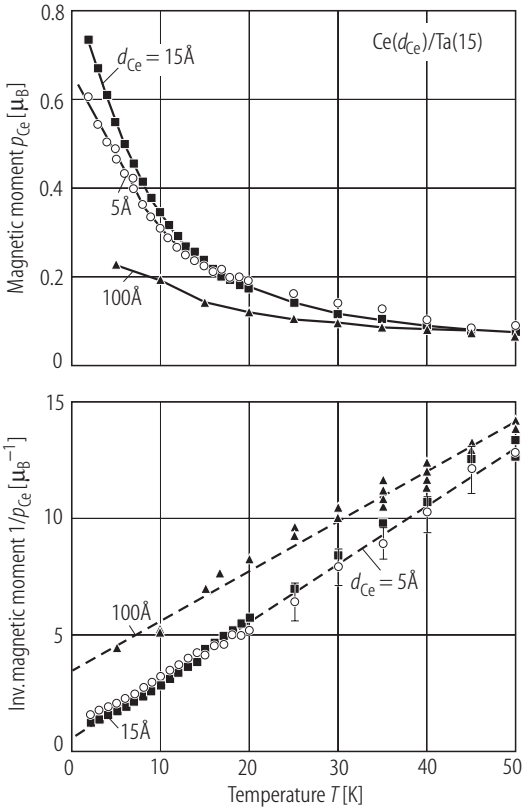

Fig. 5. Temperature dependence of magnetic moment p_{Ce} and $1/p_{Ce}$ for Ce thin layers with d_{Ce} = 5, 15 and 100 Å obtained at a field of 5 T applied parallel to the sample plane [96A].

References

87K1 Konovalov, S.V., Singer, V.V., Radovskij, I.Z., Geld, P.V.: Solid State Phys. **29** (1987) 1768

88O Orlov, V.G., Kurchatov, I.V.: Solid State Commun. **67** (1988) 689

96A Aoki, Y., Sato, H., Komaba, Y., Kobayashi, Y., Sugawara, H., Yokoyama, T., Hanyu, T.: Phys. Rev. B **54** (1996) 12172

2.1.3.2 Praseodymium

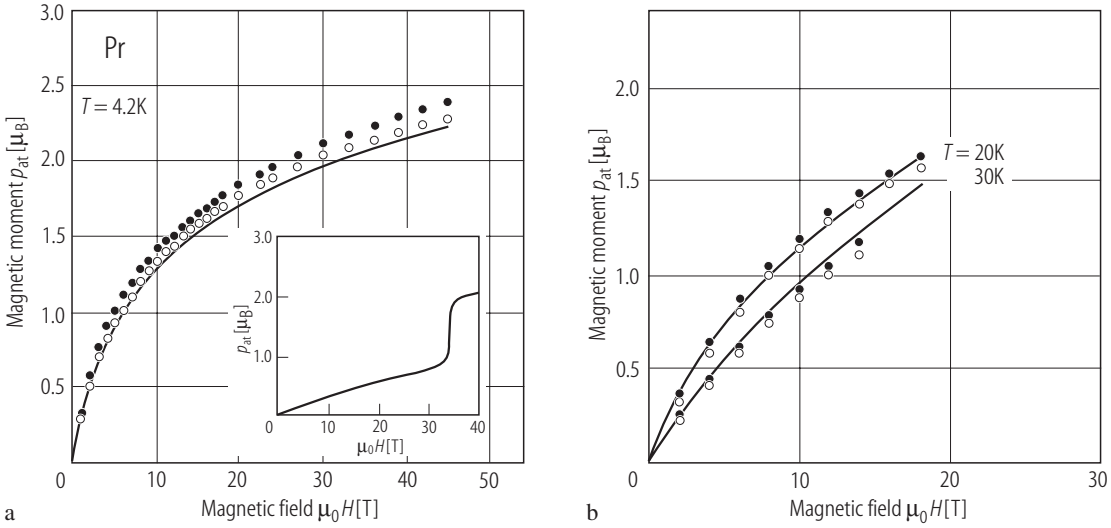

Fig. 6. Magnetization of polycrystalline Pr: (**a**) at 4.2 K, (**b**) at 20 K and 30 K. Open circles: annealed sample; solid circles: unannealed sample. Solid lines represent calculated results for the molecular field approximation considering Hamiltonian for the hexagonal and cubic ions with effective exchange parameters J_{cc} = 0.14 meV, $J_{hc} \equiv J_{ch}$= 0.19 meV, J_{hh} = 0.17 meV. In the inset the calculated magnetization for a single crystal with magnetic field along the *c* axis [87L].

References

87L Leyarovski, E., Marachkov, J., Gilewski, A., Mydlarz, T.: Phys. Rev. B **35** (1987) 8674

2.1.3.3 Neodymium

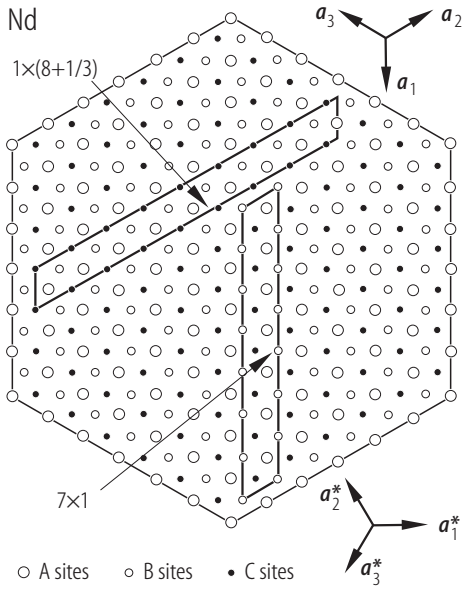

Fig. 7. Projection of all atoms in the dhcp lattice on a single hexagonal plane. Cubic A sites and hexagonal B and C sites are shown. The hold parallelograms indicate the 7x1 and 1x(8+1/3) commensurate magnetic unit cells, respectively. Also shown are the real ($\boldsymbol{a}_i$, i = 1, 2, 3) and the reciprocal lattice unit vectors ($\boldsymbol{a}_i$*, i = 1, 2, 3). If the crystal structure dominates the formation of the incipient magnetic order a commensurate modulated magnetic structure would be described by vector that connects hexagonal sites only. This is illustrated by the 7x1 magnetic unit cell. As the temperature is lowered the order on the hexagonal sites induces a moment on the cubic sites. The magnetic structure to be commensurate would be as is illustrated in figure where the 1x(8+1/3) magnetic unit cell corresponds to (q_x, q_y) = (3/25,0) [94L].

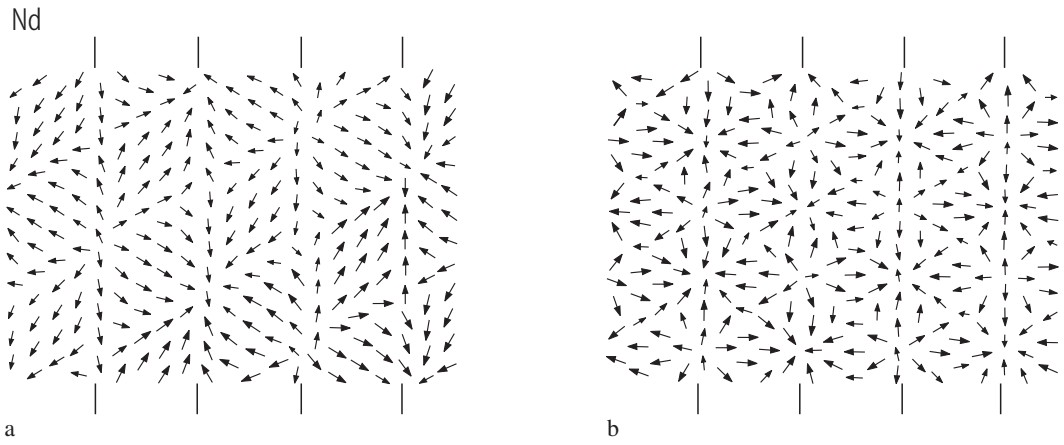

Fig. 8. Single layer moment patterns of double-$\boldsymbol{q}$ structure of dhcp Nd: (**a**) from $\boldsymbol{q}_1$ and $\boldsymbol{q}_2$; (**b**) from $\boldsymbol{q}_3$ and $\boldsymbol{q}_4$ .The moments associated with $\boldsymbol{q}_1$ and $\boldsymbol{q}_2$ are on "hexagonal" layer and those with $\boldsymbol{q}_3$ and $\boldsymbol{q}_4$ are on the cubic layer, respectively of the dhcp lattice [89F].

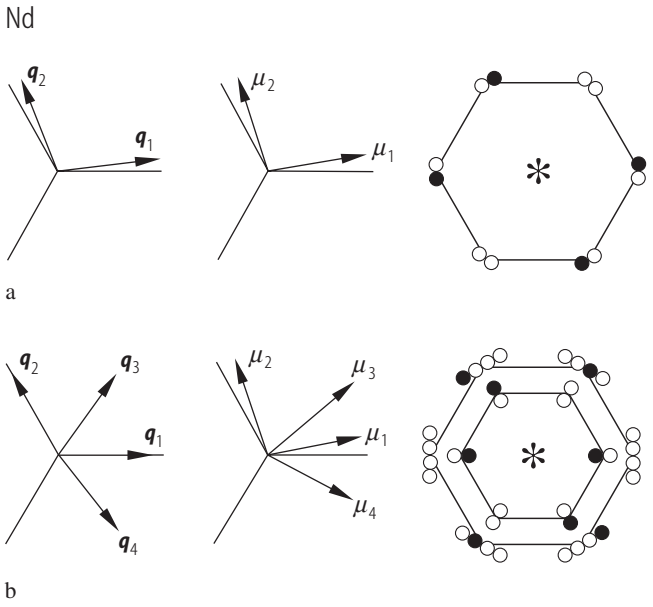

Fig. 9. Basal plane projections of modulation vectors, moment amplitudes, and the corresponding diffraction pattern around a nuclear Bragg point (*) in Nd. (**a**) for the 2-***q*** structure and (**b**) for the 4-***q*** structure. Full circles result from the arrows shown, and solid circles arise from domain averaging [97G].

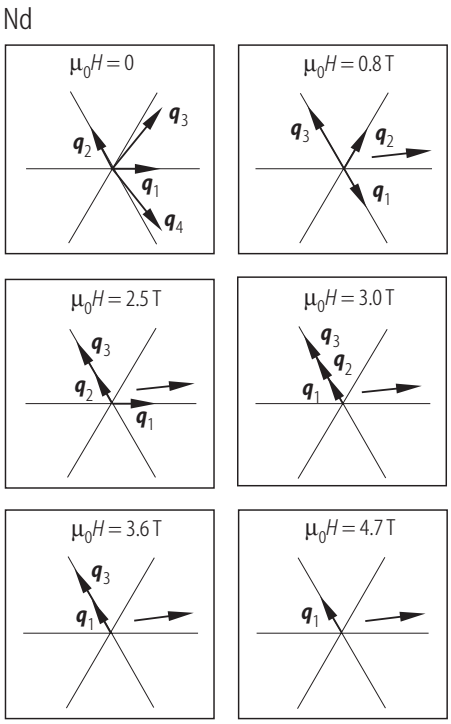

Fig. 10. Schematic representation of the wave vectors associated with the various magnetic phases of Nd at $T \approx 1.8$ K. The arrow indicates the direction of the applied magnetic field [91Z].

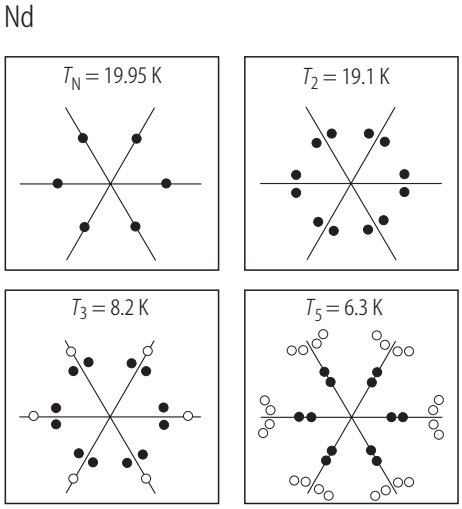

Fig. 11. Schematic representation of the magnetic satellite reflections observed around (100) at various temperatures and zero applied magnetic field in Nd metal. The solid and open circles denote the hexagonal and cubic satellites, respectively [91Z].

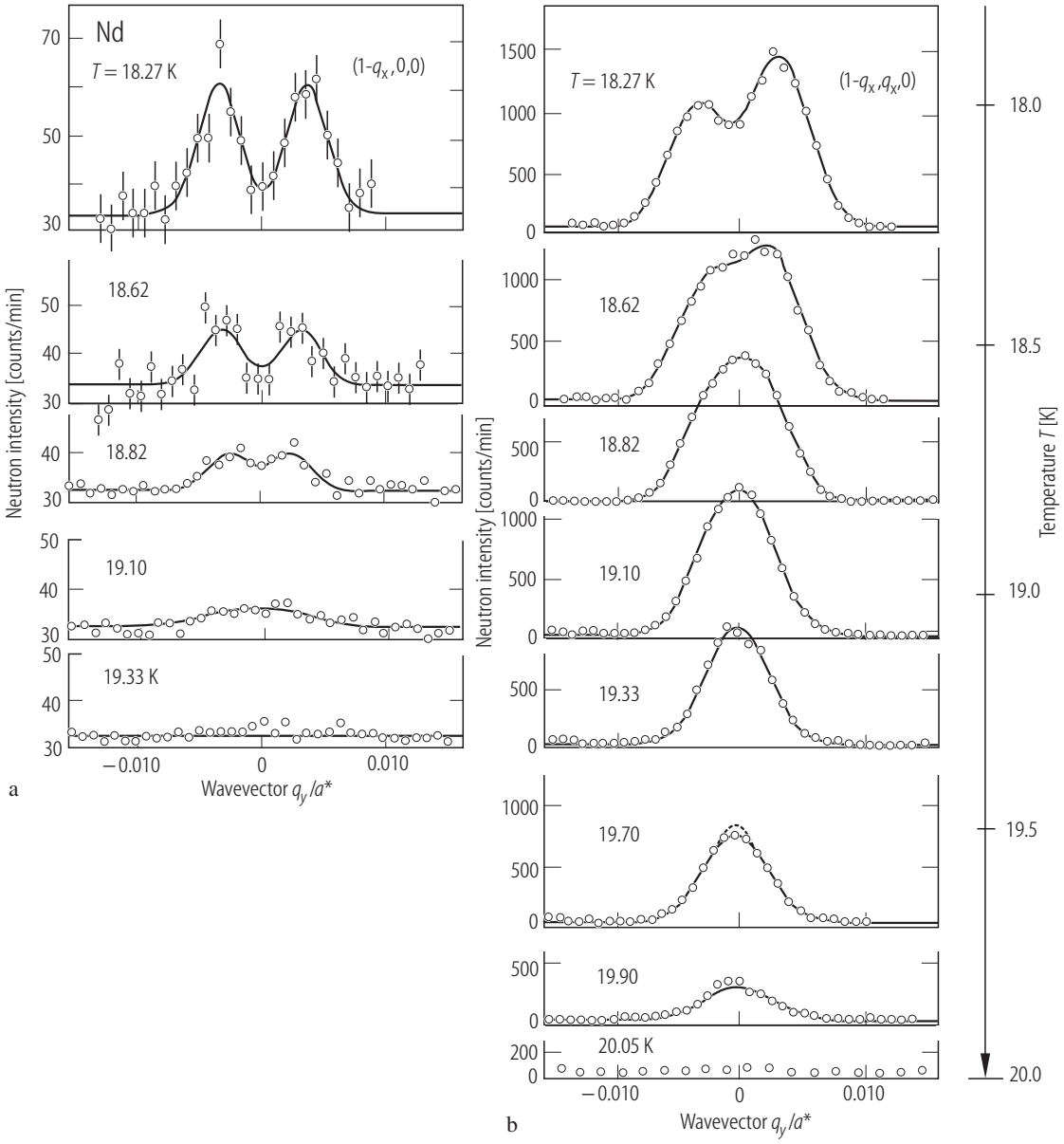

Fig. 13. Temperature evolution of the magnetic satellites near the (100) reciprocal lattice point measured on heating in Nd. The data show the transition from the single-q state near T_N to the two-q state appearing below $T_N \approx 9.1$ K [94L].

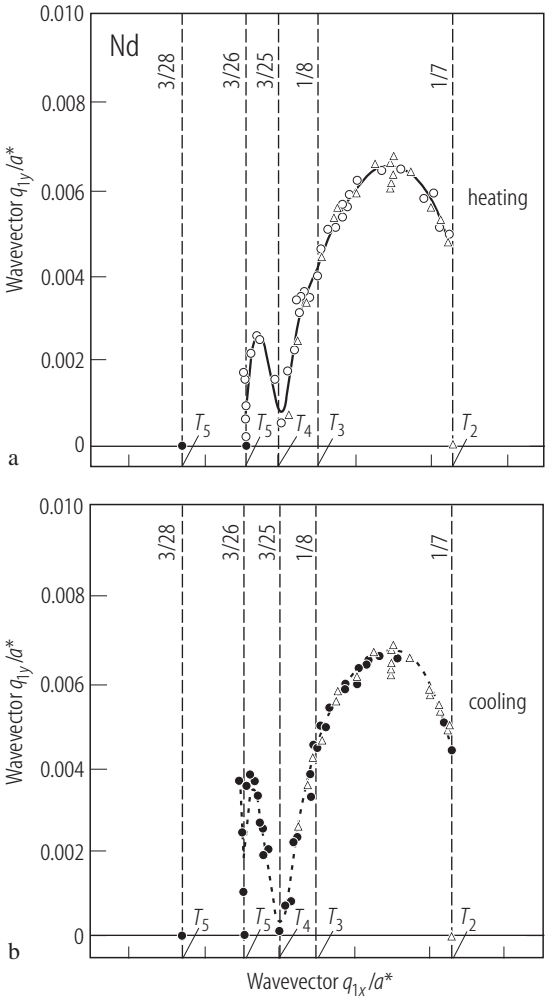

Fig. 12. Basal plane components of the modulation vector describing the magnetic structure in pure Nd metal. The q_{1y} component is shown as function of the q_{1x} component in Nd metal. The temperature is an implicit parameter for both axes and T_2 corresponds to (q_{1x}, q_{1y}) = (1/7, 0). The numbers against the dashed lines indicate the commensurate values of q_{1x}. The transition temperatures T_N and T_2 - T_5 correspond approximately to 19.3, 17.9, 10.5, 7.7, and 6.3 K on heating and to 19.1, 17.9, 8.7, 6.8, and 5.2 K on cooling. (**a**) and (**b**) correspond to heating and cooling, respectively. The stars correspond to (q_x, q_y) calculated for the higher-order commensurate structures [94L].

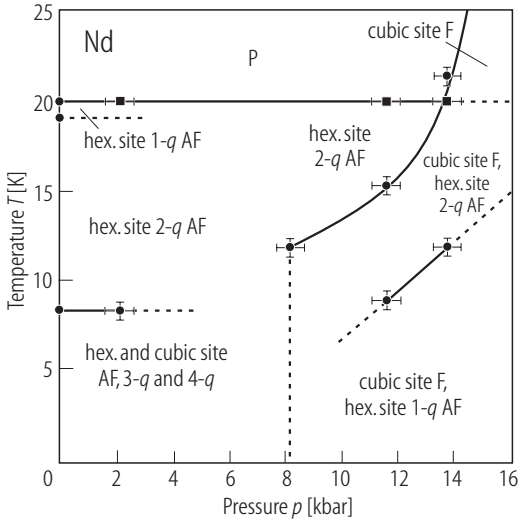

Fig. 14. Magnetic phase diagram of Nd under pressure. Where hexagonal or cubic sites are not mentioned they are disordered [96W2].

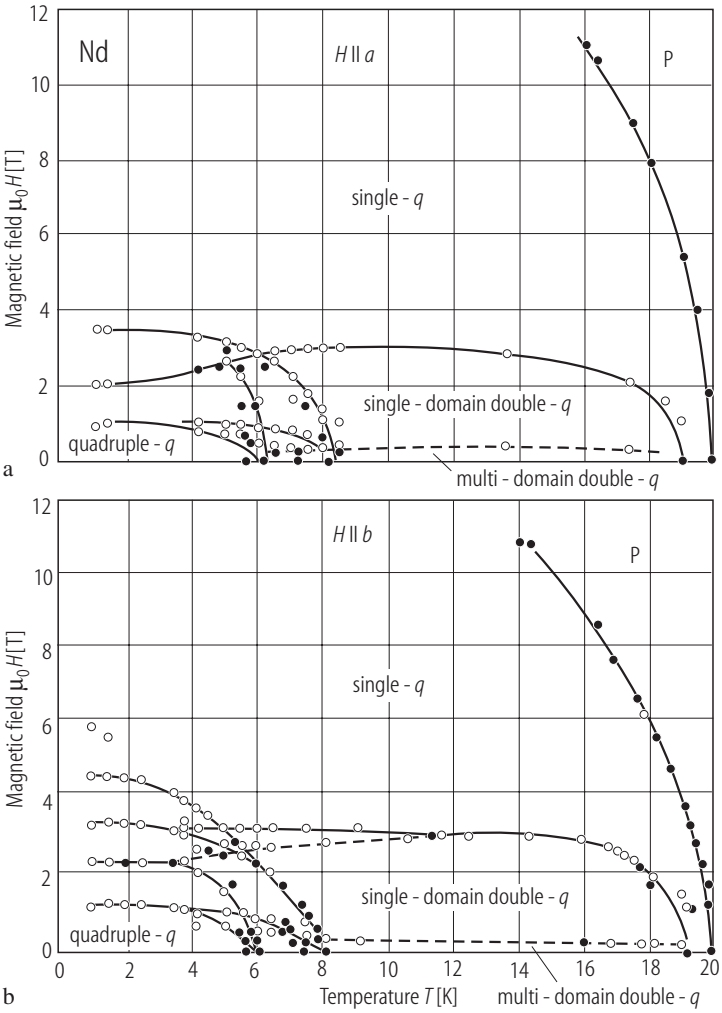

Fig. 15. (**a**) Magnetic phase diagram of Nd, measured with the magnetic field along the *a* axis, (**b**) with the magnetic field along the *b* axis. Data are taken from thermal expansion (solid circles) and magnetostriction (open circles) experiments, respectively [91Z].

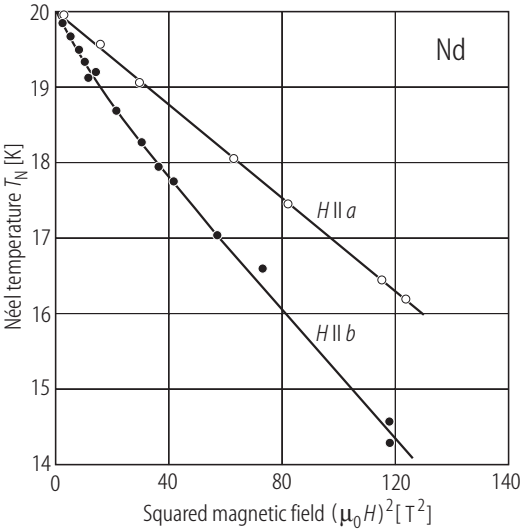

Fig. 16. T_N vs. H^2 for magnetic fields along the *a* and *b* axes of Nd [91Z].

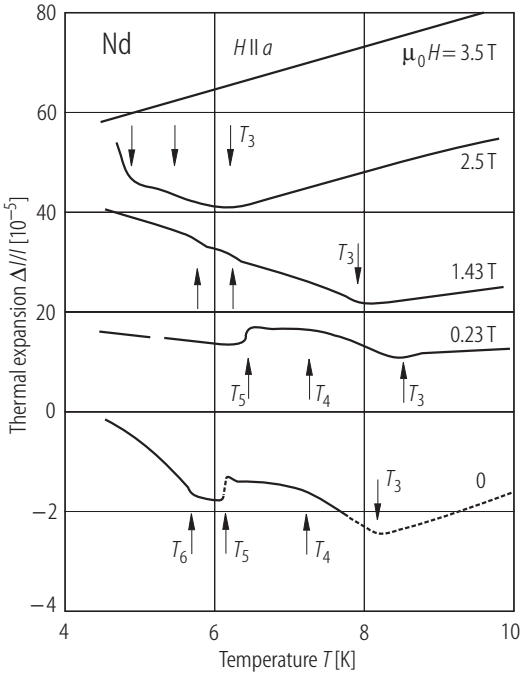

Fig. 17. Thermal expansion of Nd, measured along the *a* axis, at $H = 0.0$, 0.23, 1.43, 2.5, and 3.5 T. Note the change of scale for $H > 0$ [91Z].

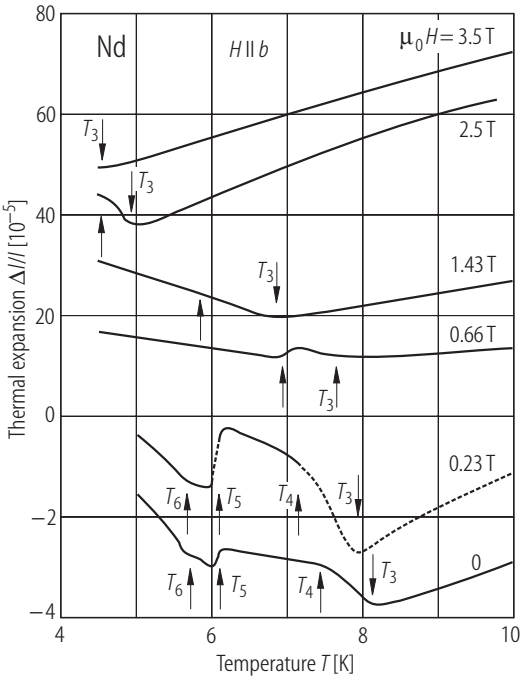

Fig. 18. Thermal expansion of Nd, measured along the *b* axis, at $H = 0$, 0.23, 0.66, 1.43, 2.5, and 3.5 T. Note the change of scale for $H > 0.23$ T [91Z].

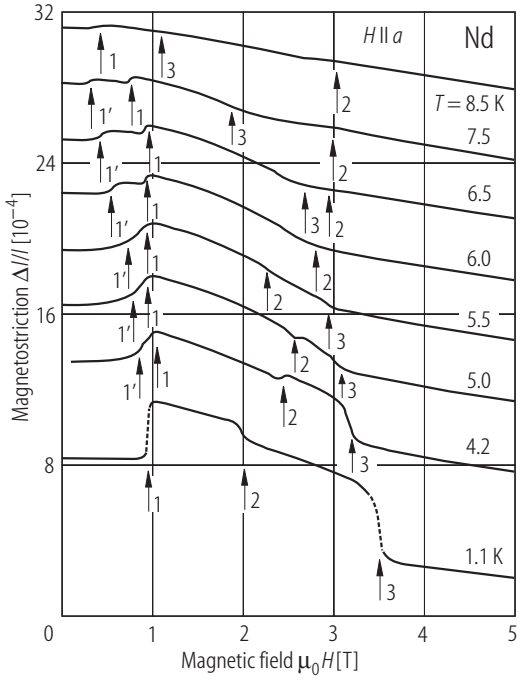

Fig. 19. Magnetostriction of Nd, measured in increasing field along the *a* axis, for various temperatures. Average values of the magnetic fields indicated by arrows are
(1) 1.15 T; (2) 2.2 T; (3) 3.2 T; (4) 4.4 T [91Z].

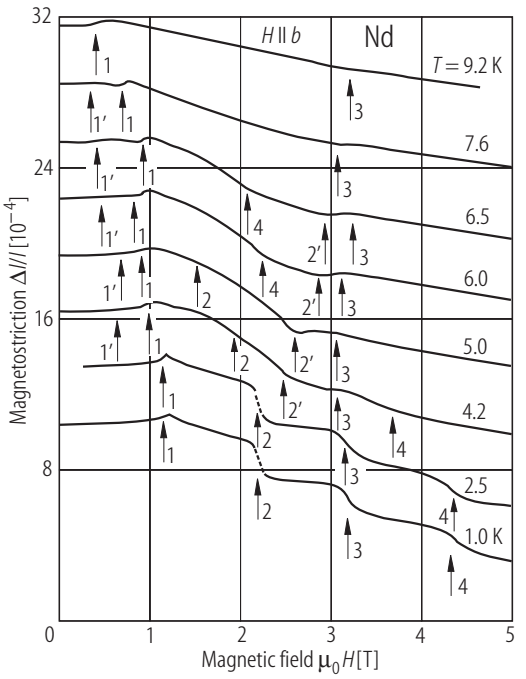

Fig. 20. Magnetostriction of Nd, measured in increasing field along the *b* axis, for various temperatures. Average values of the magnetic fields indicated by arrows are
(1) 1.15 T; (2) 2.2 T; (3) 3.2 T; (4) 4.4 T [91Z].

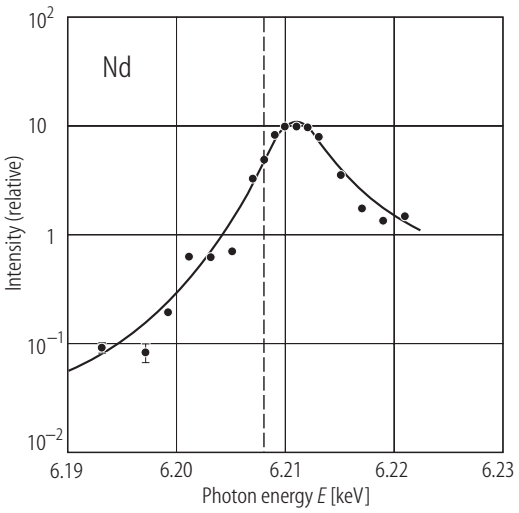

Fig. 21. High resolution magnetic X-ray diffraction of antiferromagnetic ordering in the neodymium metal, near the LII and LIII absorption edges. The vertical line indicates the positions of the absorption edges in zero magnetic field [96W].

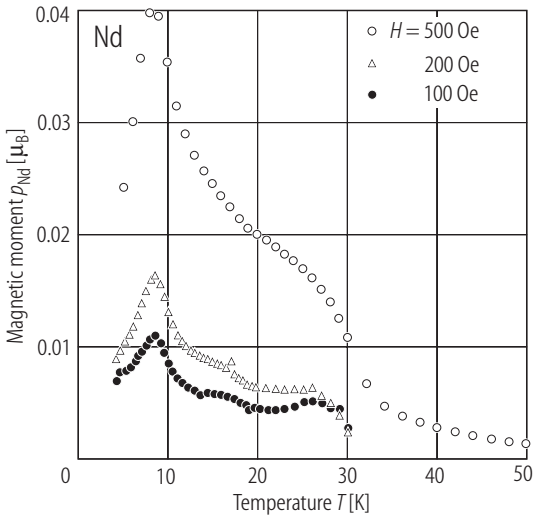

Fig. 22. Zero-field cooled magnetization of the 582 nm Nd film with the field along the (100) easy axis. The anomaly near 27 K is associated with the Néel point, which is significantly higher than in bulk Nd; the peak near 8 K arises from cubic-site ordering [97E].

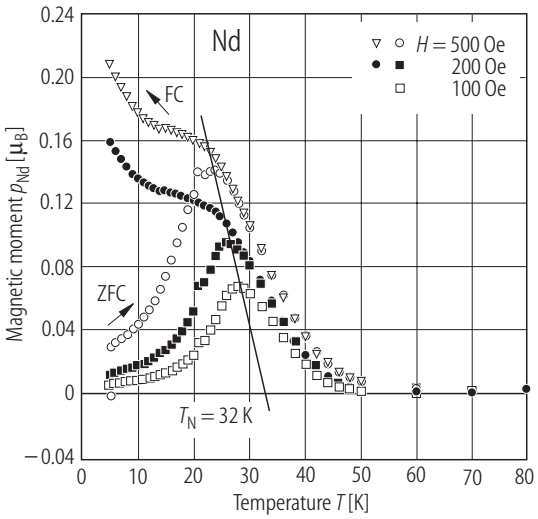

Fig. 23. Field-cooled and zero-field cooled data on a [Nd (3.2 nm)/Y (2 nm)]$_{120}$ superlattice. The Néel temperature extrapolated to a zero-field has 32 K, much above the bulk value of 19.9 K [97E].

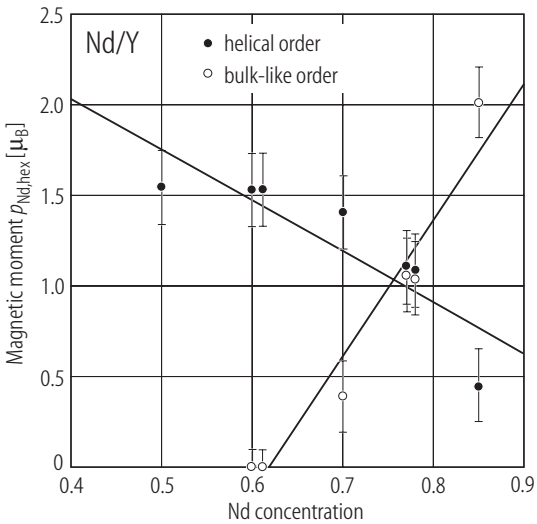

Fig. 25. Magnetic moment per hexagonal site associated with helimagnetic order and the moment per atom associated with bulk-like order of hexagonal sites vs. the Nd concentration in the Nd/Y superlattices. The Nd atoms are in the dhcp structure in all samples [97E].

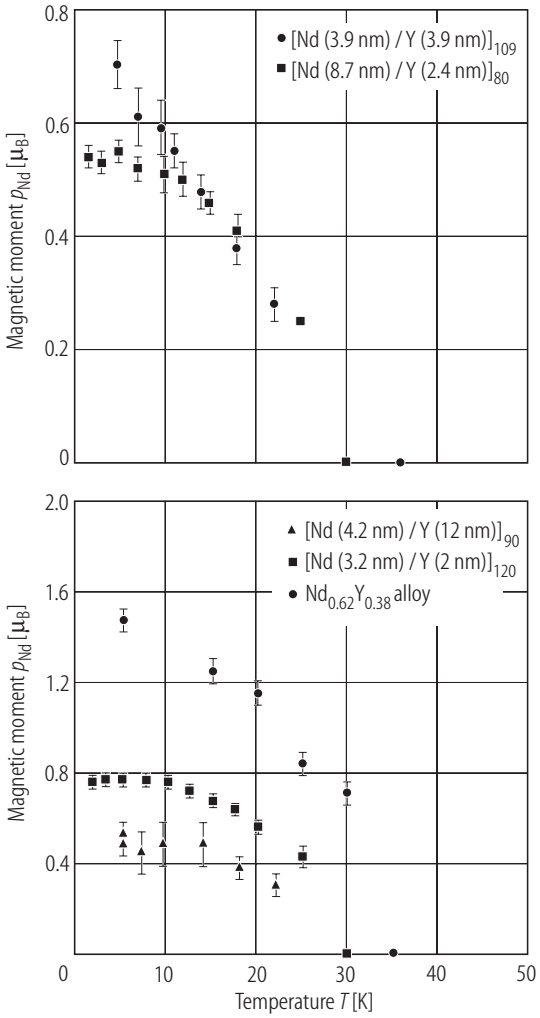

Fig. 24. Temperature dependence of the magnetic moment per Nd atom (hexagonal and cubic sites) that orders in the helimagnetic structure for several Nd/Y superlattices and the alloy sample. The temperatures at which this component vanishes agree semiquantitatively with the Néel temperatures from the magnetization data [97E].

References

89F Forgan, E.M., Gibbons, E.P., McEwen, K.A., Fort, D.: Phys. Rev. Lett. **62** (1989) 470

91Z Zochowski, S.W., McEwen, K.A., Fawcett, E.: J. Phys.: Condens. Matter **3** (1991) 8079

94L Lebech, B., Wolny, J., Moon, R.M.: J. Phys. Condens. Matter **6** (1994) 5201

96W Watson, D., Forgan, E.M., Nuttall, W.J., Stirling, W.G., Fort, D.: Phys. Rev. B **53** (1996) 726

96W2 Watson, D., Forgan, E.M., Nuttall, W.J., Sokol, P.E., Shaikh, S.J., Zochowski, S.W., Fort, D.: J. Phys.: Condens. Matter **8** (1996) 5049

97E Everitt, B.A., Salamon, M.B., Borchers, J.A., Erwin, R.W., Rhyne, J.J., Park, B.J., O'Donovan, K.V., McMorrow, D.F., Flynn, C.P.: Phys. Rev. B **56** (1997) 5452

97G Goff, J.P., Bryn-Jacobsen, C., McMorrow, D.F., Ward, R.C.C., Wells, M.R.: Phys. Rev. B **55** (1997) 12537

2.1.3.4 Samarium

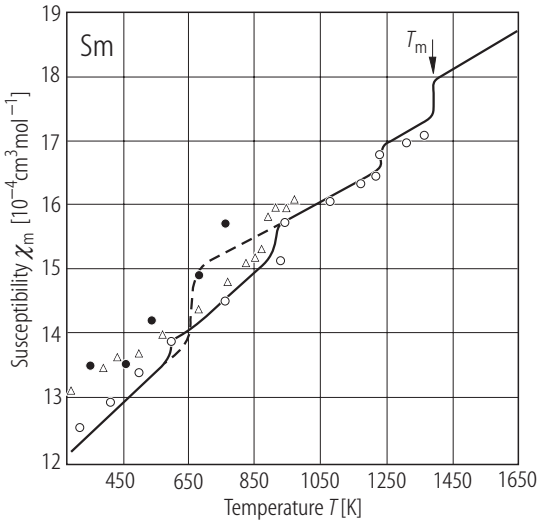

Fig. 26. Magnetic susceptibility vs. temperature of Sm metal at higher temperatures. The anomalies reflect the structural phase transitions and the melting point T_m. The data collected from several papers cited in [87K1].

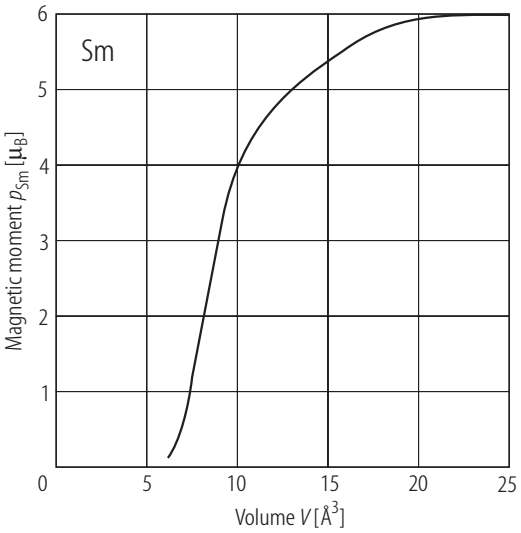

Fig. 27. Calculated spin moment for the itinerant ferromagnetic state of Sm as a function of volume. At sufficiently low volumes (Mbar) the moment disappears and Sm metal is a 4f delocalized paramagnet [93S1].

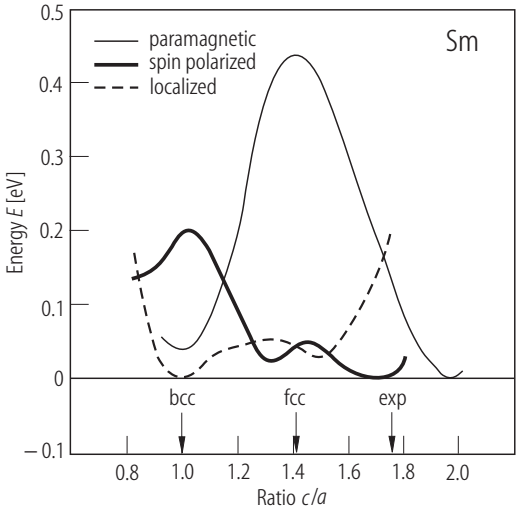

Fig. 28. Total energy (at $T = 0$) of the bct structure as a function of the c/a ratio for both delocalized and trivalent Sm at a volume compression $V/V_0 = 0.37$. The thin solid and bold lines refer to a treatment of the 4f electrons as itinerant-paramagnetic and itinerant-ferromagnetic, respectively. The dotted line represents the localized phase [93S1].

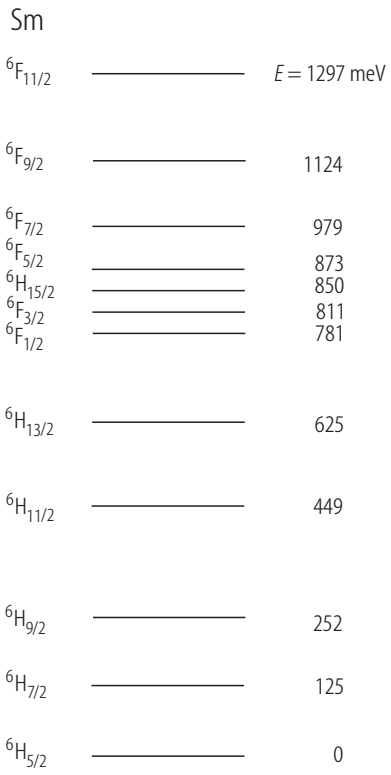

Fig. 29. Multiplet levels for Sm^{3+} ion calculated for Sm metal [93N].

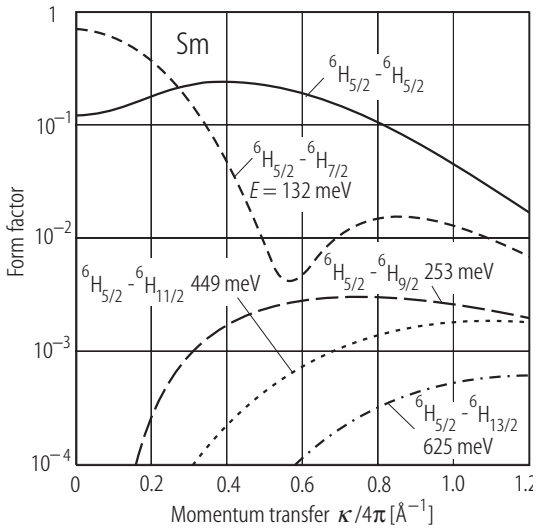

Fig. 30. Form factor predictions for spin-orbit transition in Sm^{3+} as a function of neutron momentum transfer κ[93N].

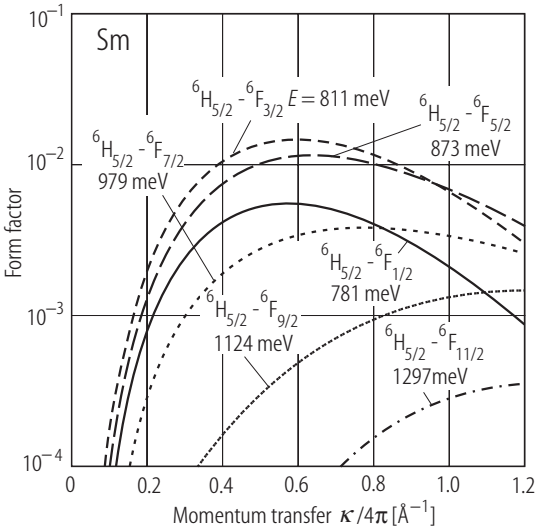

Fig. 31. Form factor predictions for H → F intermultiplet transition in Sm^{3+} as a function of κ[93N].

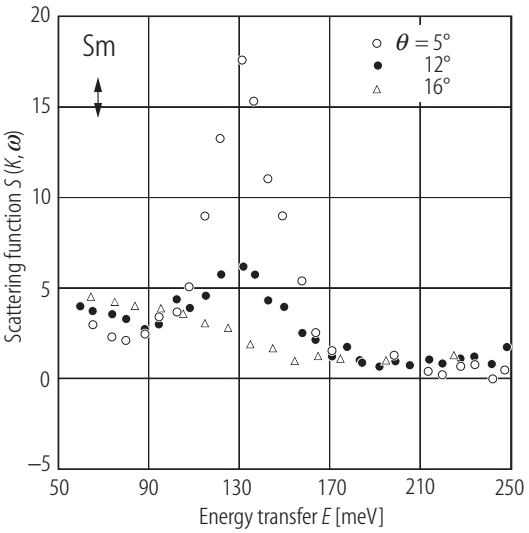

Fig. 32. $^6H_{5/2} \rightarrow {}^6H_{7/2}$ spin-orbit transition in Sm metal observed at angles of 5°, 12°, 16° with an incident energy of 6/8 meV in neutron scattering experiment [93N].

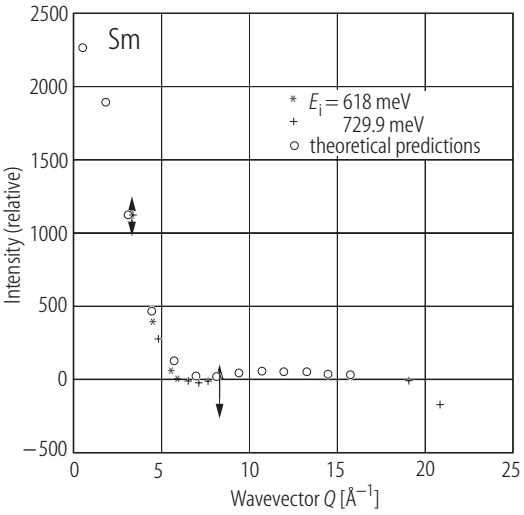

Fig. 33. Plot of the experimental and theoretical form factor for the $^6H_{5/2} \rightarrow {}^6H_{7/2}$ transition in Sm metal. None of the other (see Fig. 30) spin-orbit transition were observed [93N].

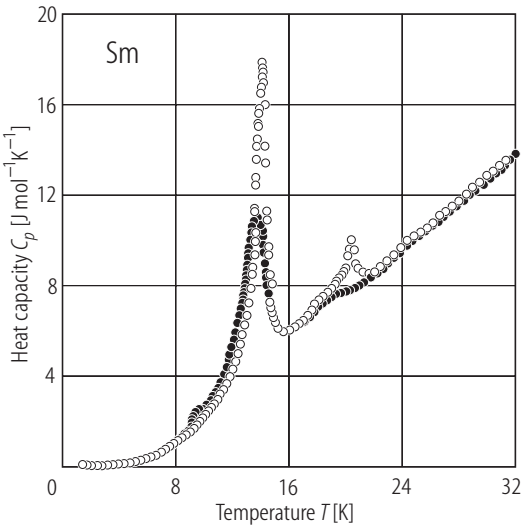

Fig. 34. Specific heat C_p, of the two samarium samples (SmIV-99.89 at%; SmV-99.98 at% purity) in the temperature range: 0…32 K. The effect of increasing impurity contents reduce the amplitudes of the transition [89S].

References

87K1 Konovalov, S.V., Singer, V.V., Radovskij, I.Z., Geld, P.V.: Solid State Phys. **29** (1987) 1768

89S Stewart, A.M., Collocott, S.J.: J. Phys.: Condens. Matter **1** (1989) 677

93N Needham, L.M., Williams, W.G., Taylor, A.D.: J. Phys.: Condens. Matter **5** (1993) 2591

93S1 Söderlind, P., Eriksson, O., Wills, J.M., Johansson, B.: Phys. Rev. B **48** (1993) 9212

2.1.3.5 Europium

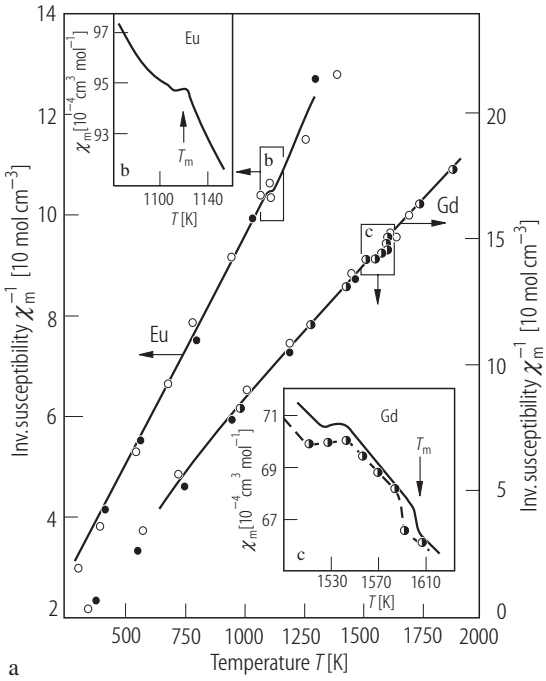

Fig. 35. Magnetic susceptibilities as a function of the temperature for Eu and Gd in the high temperature range beyond the melting temperatures (T_m). In the insets the details near transition temperatures are shown. The anomaly at $T = 15.35$ K for Gd reflects the hcp → bcc transition [87K1].

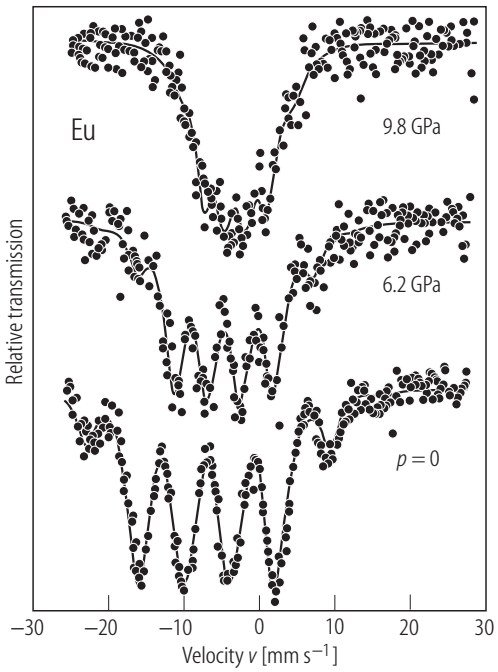

Fig. 36. Mössbauer spectra of ^{151}Eu metal at 44 K and 0, 6.2, and 9.8 GPa applied pressure. The single-line SmF_3 source is at 44 K. The centroid of the pattern moves in accordance with changes in the f-shell occupation [87F1].

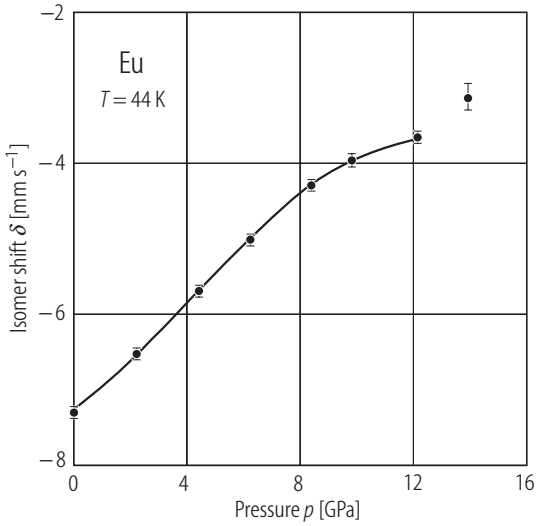

Fig. 37. Mössbauer isomer shift of ^{151}Eu in metal vs. $^{151}SmF_3$ as a function of pressure at 44 K. Source and absorber are at the same temperature [87F1].

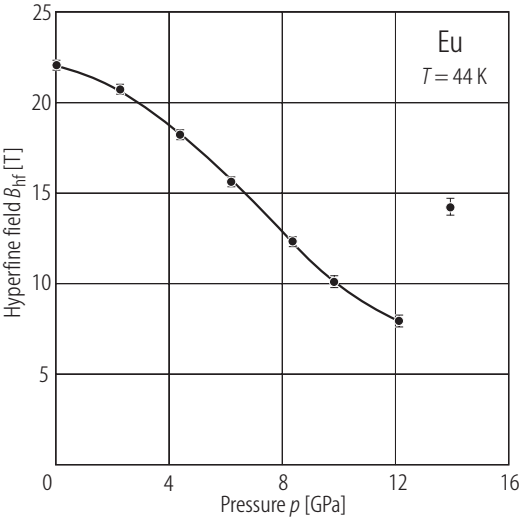

Fig. 38. Pressure dependence of the magnetic hyperfine field at the nucleus of ^{151}Eu in Eu metal at 44 K [87F1].

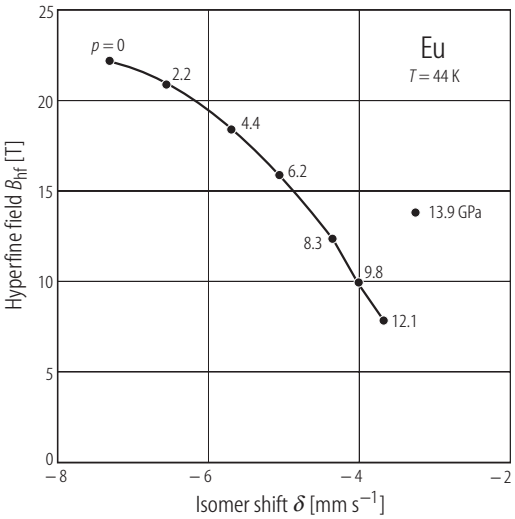

Fig. 39. Comparison of the isomer shift and magnetic hyperfine field for Eu metal at 44 K and high pressure. Pressures are marked along the curve. The extrapolated isomer shift of about – 3 mm s^{-1} for zero hyperfine field corresponds to a valence change of about 0.5 electron. It is shown that in Eu metal at high pressure and below the Néel temperature, the intermediate valence and magnetic ordering phenomena coexist [87F1].

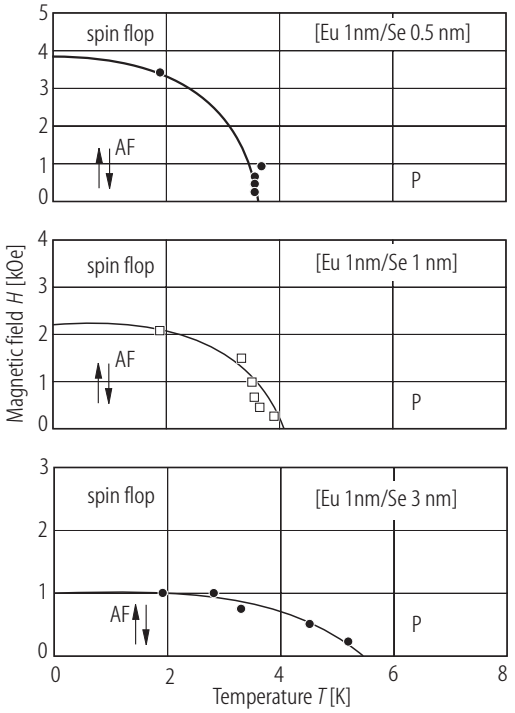

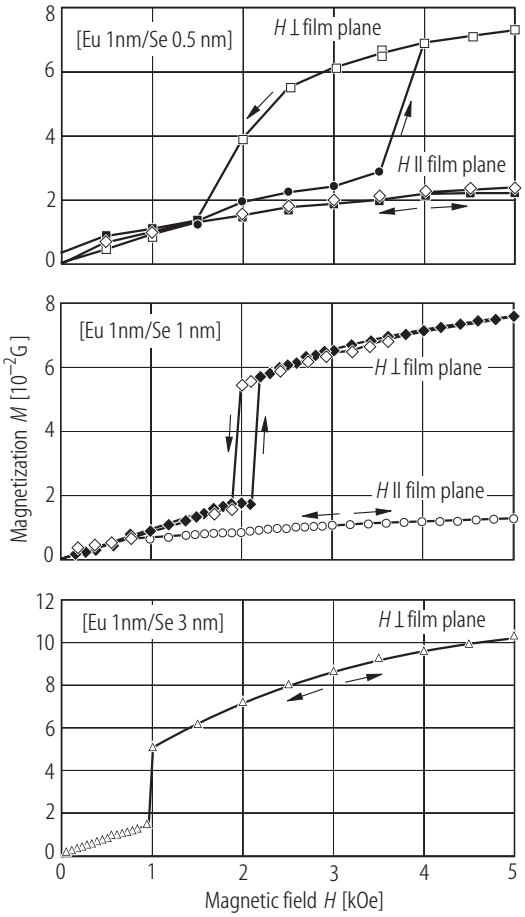

Fig. 40. Magnetization process of Eu/Se superlattice at 1.9 K [98O].

Fig. 42. Magnetic phase diagrams of Eu/Se superlattice [98O].

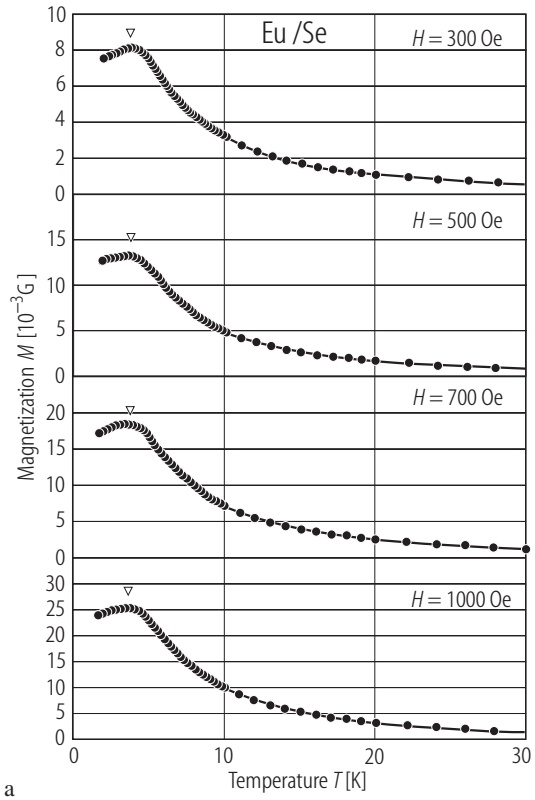

a

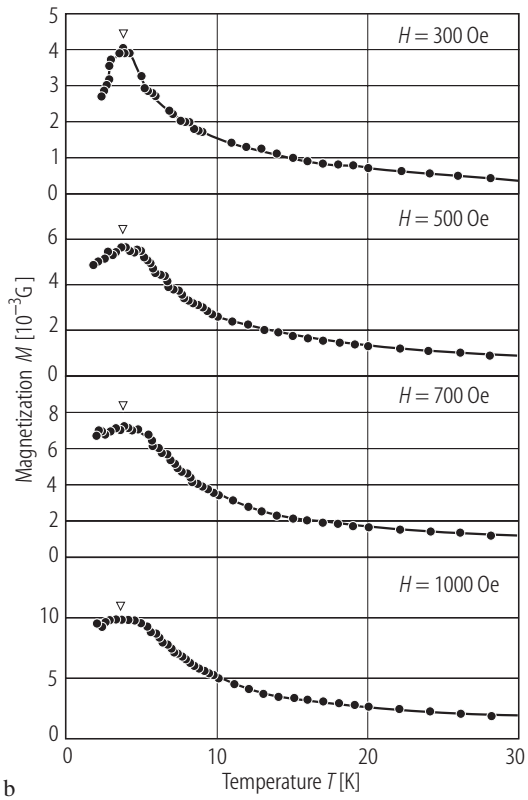

b

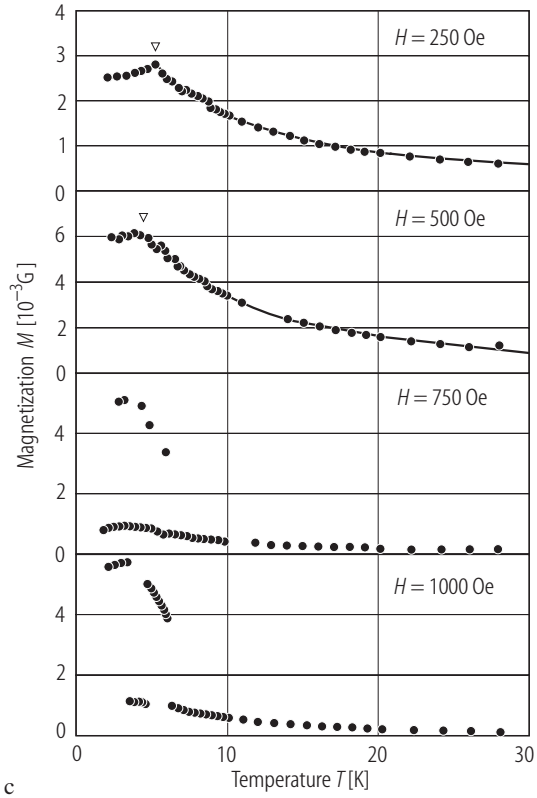

c

Fig. 41. (**a**)Temperature dependence of the magnetization of [Eu 1nm/Se 0.5 nm]; (**b**) the [Eu 1 nm/Se 1 nm] and (**c**) the [Eu 1 nm/Se 3 nm] of the Eu thin film samples on the Se substrate in the magnetic field $H \perp$ film plane [98O].

References

87F1 Farrell, J.N., Taylor, R.D.: Phys. Rev. Lett. **58** (1987) 2478

87K1 Konovalov, S.V., Singer, V.V., Radovskij, I.Z., Geld, P.V.: Solid State Phys. **29** (1987) 1768

98O Ono, T., Ishii, T., Tanuma, S., Yoshida, I.: Solid State Commun. **105** (1998) 93

2.1.3.6 Gadolinium

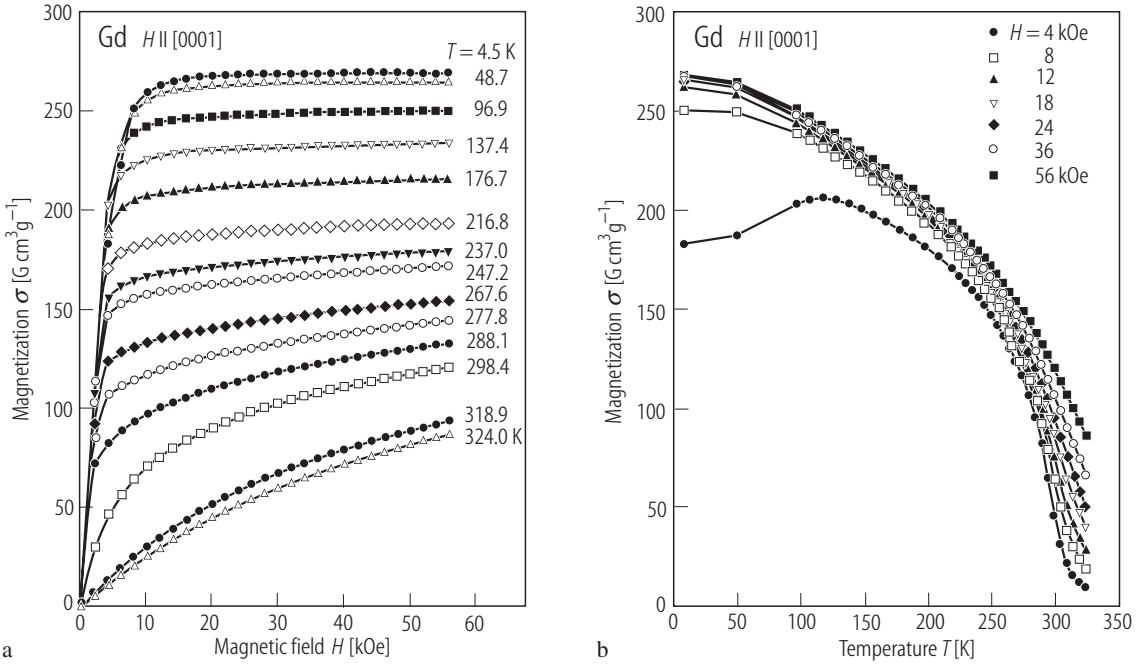

Fig. 43. (**a**) Magnetization of a Gd single crystal as a function of field at selected temperatures, and (**b**) magnetization of Gd vs. temperature at selected dc fields, with the field parallel to the [0001] direction [98D].

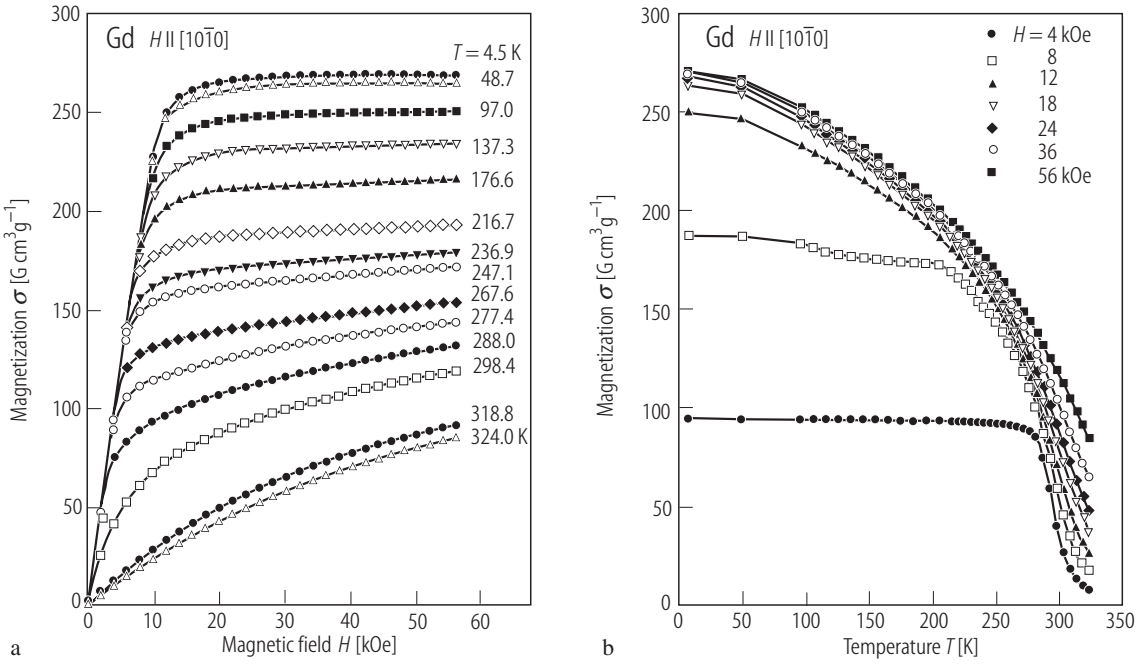

Fig. 44. (**a**) Magnetization of a Gd single crystal as a function of field at selected temperatures, and (**b**) magnetization of Gd vs. temperature at selected dc fields with the field parallel to the [10$\bar{1}$0] direction [98D].

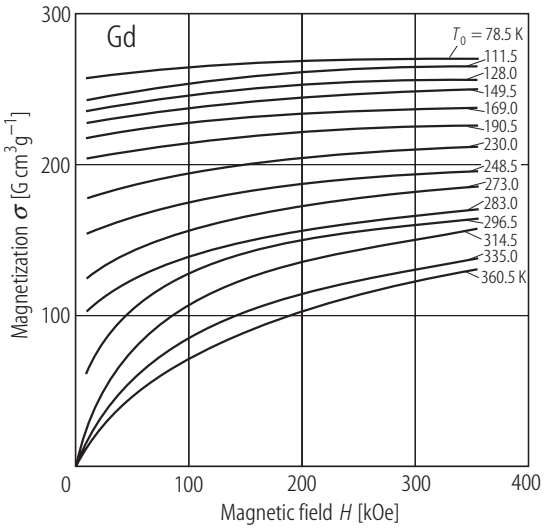

Fig. 45. Magnetization adiabates for Gd single crystal in the 0.01s pulsed field up to 360 kOe at different values of the initial temperature of the sample in K. At 360.5 K that is almost 70 K above the Curie point. In the field of 360 kOe the Gd magnetization exceeds its spontaneous magnetization at 273 K, i.e., by 20 K below the Curie temperature [86P].

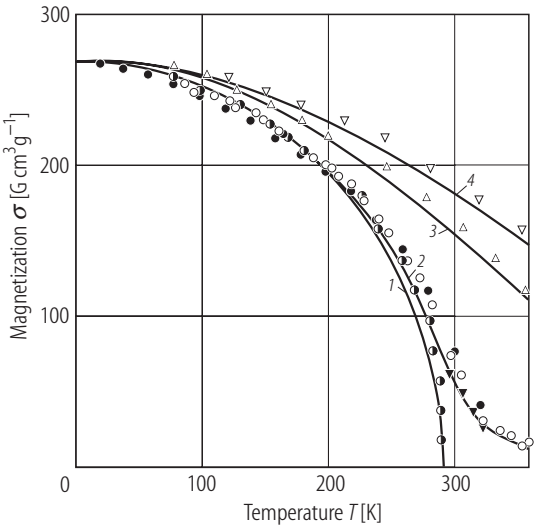

Fig. 46. Temperature dependencies of magnetization of Gd at different values of the external field $H = 0$ (half-filled circles); H = 17 kOe (open circles); 200 kOe (open triangles up); 360 kOe (open triangles down), 17 kOe (solid circles). The solid lines are calculated in the effective field approximation with
(*1*) $H = 0$; (*2*) H = 17 kOe; (*3*) 200 kOe; (*4*) 360 kOe; solid triangles: σ_{eff} (with a short-range order contribution at temperatures higher than T_C) [86P].

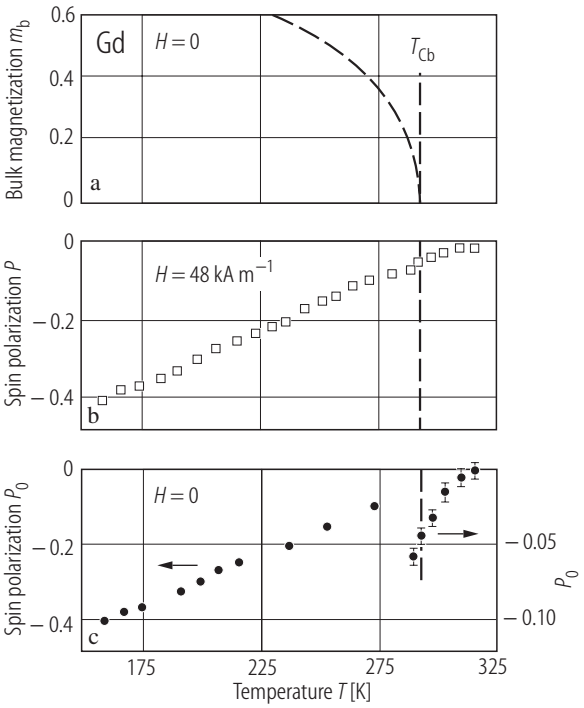

Fig. 47. (**a**) Temperature dependence of the bulk spontaneous magnetization m_b (T, H = 0) for Gd normalized to the bulk saturation magnetization. (**b**) temperature dependence of the electron-spin polarization (ESP) at the topmost layer of atomically clean surfaces of Gd for H = 48 kA m^{-1}. (**c**) Temperature dependence of the spontaneous electron-spin polarization $P_0(T)$ using T_{Cb} = 315 K for the extrapolation. The results shown demonstrate that, for Gd, the topmost surface layer is magnetically ordered while the bulk is disordered. The Gd surface long-range ferromagnetic order exists far above the bulk Curie temperature T_{Cb}= 292.5 K [86R].

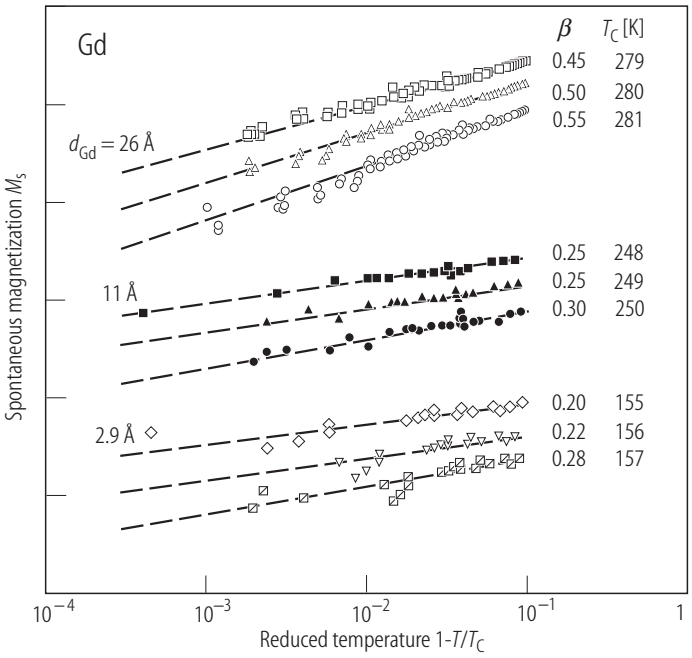

Fig. 48. Log-log plot of the spontaneous magnetization M_s (B = 10 mT) vs. reduced temperature ($1 - T/T_C$) for Gd thin film samples prepared at T_s = 473 K. The dashed lines illustrate a behavior M_s (d_{Gd}). Sample thickness is d_{Gd} = 26, 11, and 2.9 Å (from top to bottom data set). Data are shifted vertically for clarity [98G].

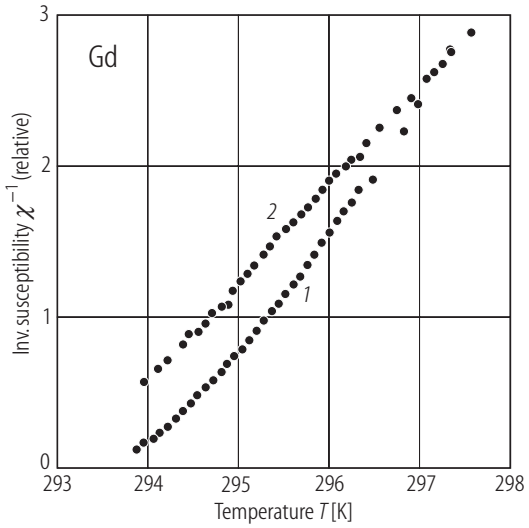

Fig. 49. Inverse magnetic susceptibility χ^{-1}, as a function of temperature for a single crystal of Gd measured along the c axis (plot *1*) and in the basal plane (plot *2*) [89G].

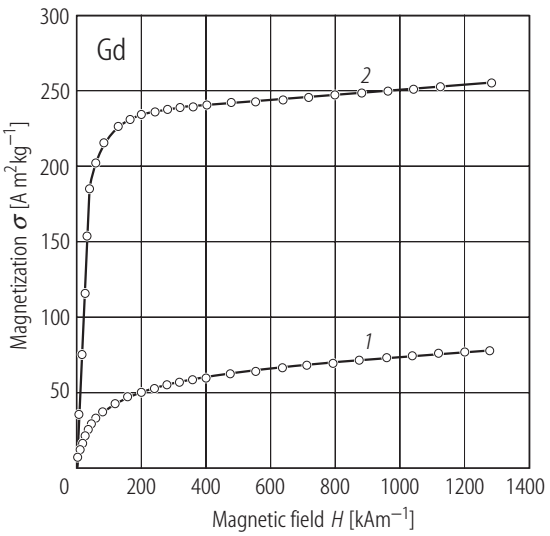

Fig. 50. Magnetization curves for Gd plots deformed on Bridgman anvil-type unit under a pressure of 4 GPa at room temperature (*1*) and annealed (*2*) in a vacuum of $1.3 \cdot 10^{-2}$ Pa at different temperatures for 30 min measured at 77 K [96M].

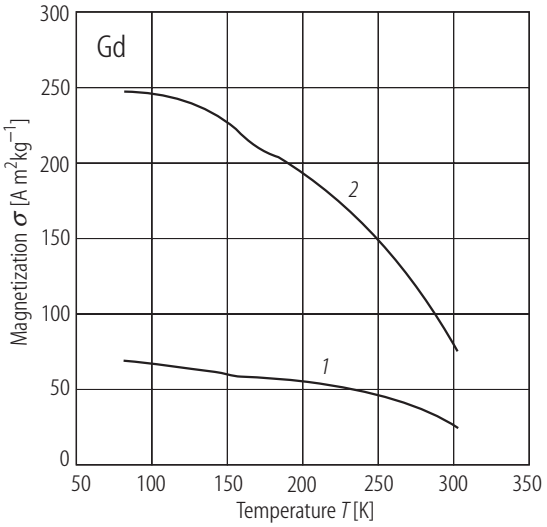

Fig. 51. Temperature dependence of the magnetization $\sigma(T)$ for Gd as-deformed (*1*) and annealed (*2*) states. For details see Fig. 50 [96M].

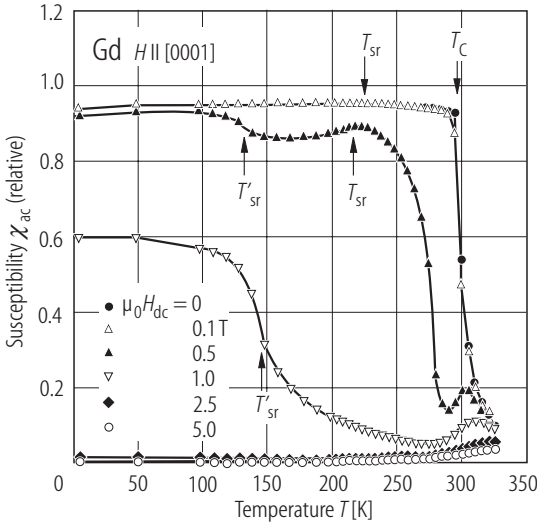

Fig. 52. AC magnetic susceptibility of a Gd single crystal in bias dc fields with the ac and dc fields parallel to the [0001] direction [98D]. $\mu_0 H_{ac}$ = 0.25 mT, ν = 250 Hz.

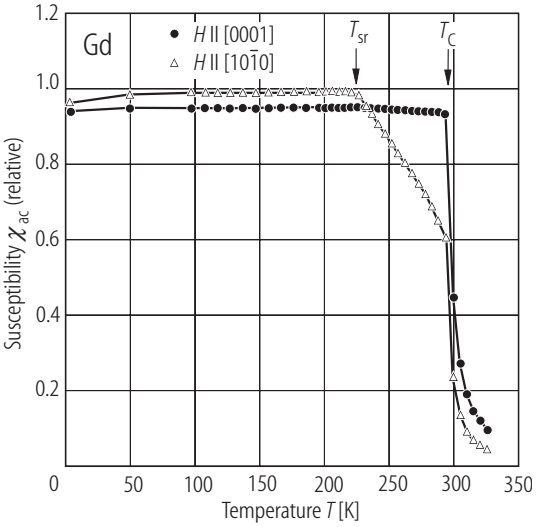

Fig. 53. AC magnetic susceptibility of Gd single crystals with the ac field parallel to the [0001] and [10$\bar{1}$0] directions. T_{sr} and T_C are the spin-reorientation and Curie temperatures, respectively [98D]. $\mu_0 H_{dc}$ = 0, $\mu_0 H_{ac}$ = 0.5 mT, ν = 250 Hz.

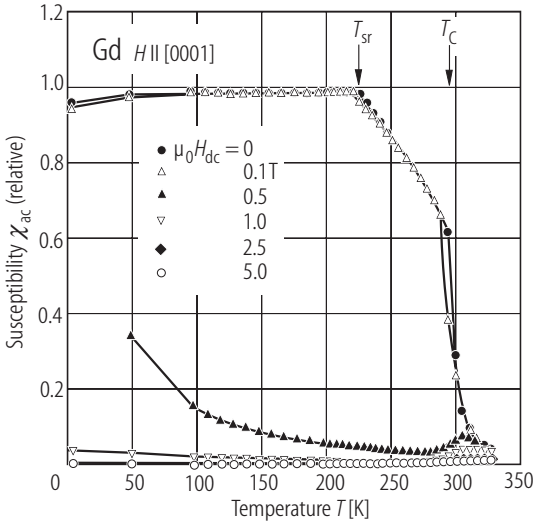

Fig. 54. AC magnetic susceptibility of a Gd single crystal in bias dc fields with the ac and dc fields parallel to the [10$\bar{1}$0] direction [98D]. $\mu_0 H_{ac}$ = 2.5 Oe, ν = 250 Hz.

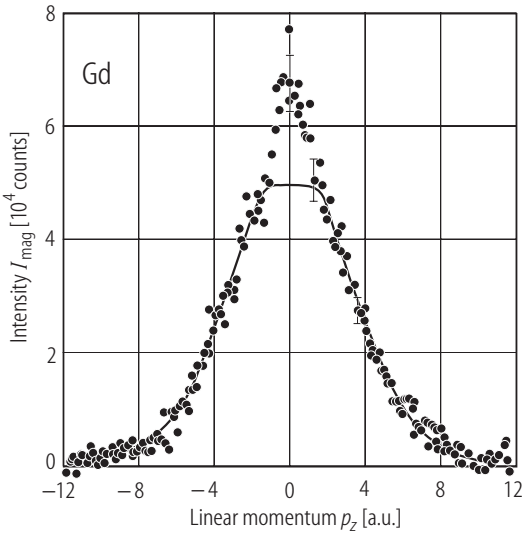

Fig. 55. Magnetic-electron Compton profile of ferromagnetic Gd at 106 K measured with circularly polarized synchrotron-radiation X-rays of 45.2 keV. The solid line is the relativistic Hartree-Fock impulse Compton profile of atomic 4f electrons and corresponds to 7 μ_B/at. The remaining area corresponds to 0.53(8) μ_B/at is only slightly smaller than the expected conduction-electron magnetic moment 0.63 μ_B/at [91S].

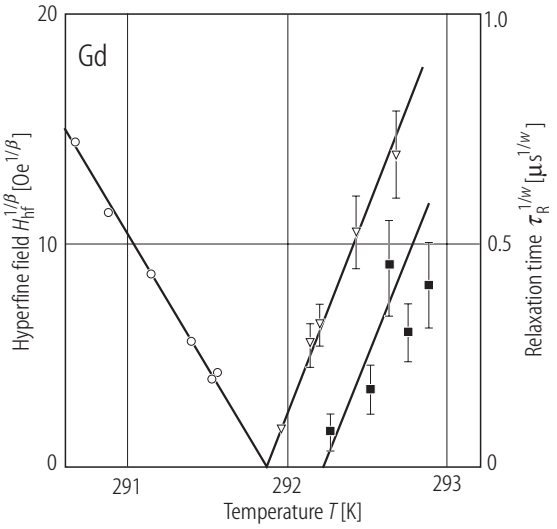

Fig. 56. Determination of T_C via Gd ^{111}In PAC data. The data are presented as linearized plots of the hyperfine field below T_C (left scale), and the nuclear relaxation rate above T_C (right scale). w is the critical exponent. The open circles and triangles represent the hyperfine field and nuclear relaxation rate for single-crystal natural Gd samples, and determine T_C to be 291.85 K by two independent methods. The solid squares represent nuclear relaxation rates obtained for a piece of polycrystalline ^{160}Gd used in the Mössbauer experiments and determine T_C to be 292.2(1) K [86Ch].

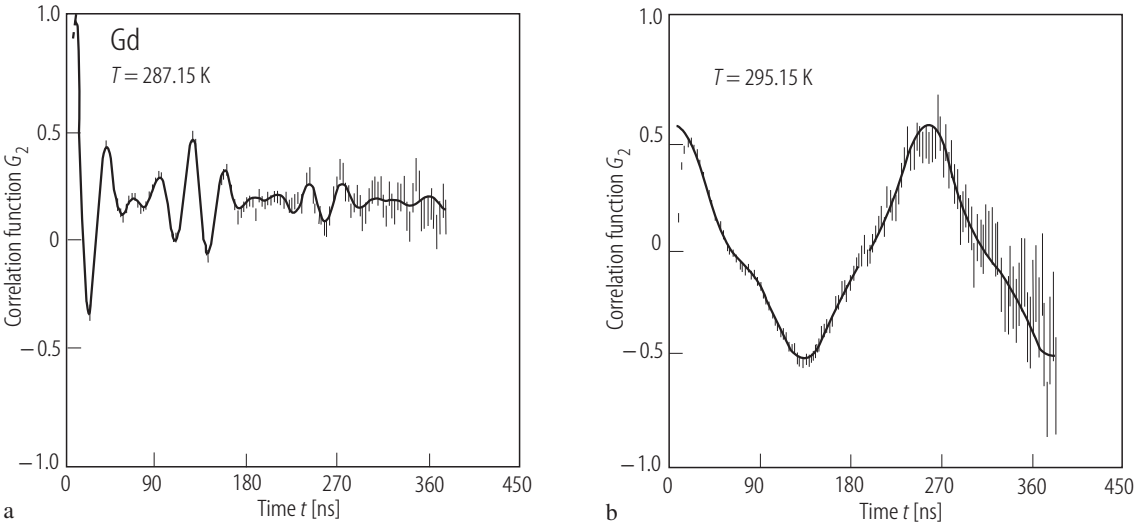

Fig. 57. Typical perturbed angular correlation (PAC) spectra below (**a**) and above (**b**) the Curie temperature. Below T_C the spectra may be fitted by a combined magnetic-quadruple interaction; above T_C the spectra are described by a pure quadruple interaction [86Ch].

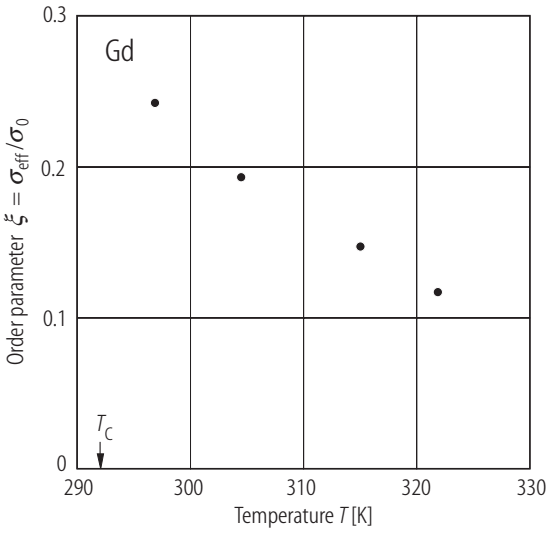

Fig. 58. Short-range order parameter in Gd above Curie temperature. σ_0 = 268.4 G cm^3 g^{-1} is the spontaneous magnetization of Gd at 0 K [86P].

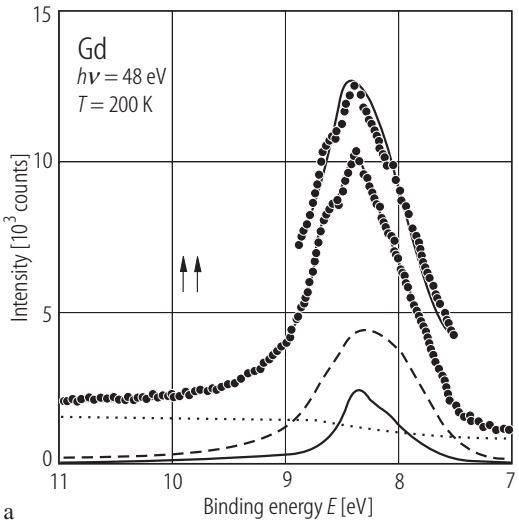

a

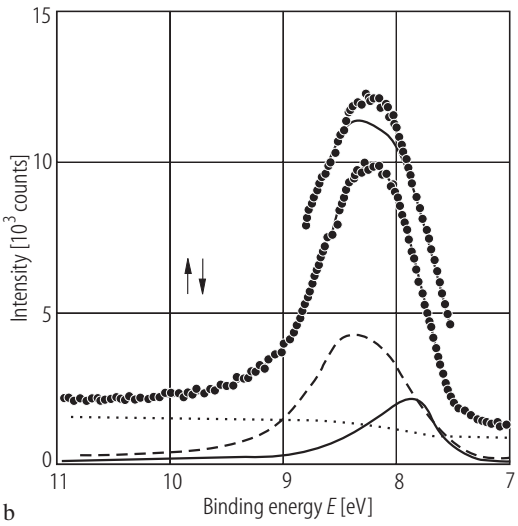

b

Fig. 59. Gd-4f PE spectra taken with circularly polarized 48-eV photons for (**a**) parallel (ΔM_J = + 1) and (**b**) antiparallel (ΔM_J = – 1) orientation between photon spin and sample magnetization. The (0001) surface layer component (uppermost solid subspectra) is ferromagnetically aligned to the bulk of Gd (lower solid subspectra). The dashed components, which are identical in spectra (**a**) and (**b**), represent the sum of the paramagnetic bulk (dotted lines) and surface signals (dashed lines) due to unpolarized light and the finite sample temperature. The solid curves through the peaks displaced vertically represent the best-fit results for hypothetical antiferromagnetic alignment of surface layer and bulk [93S2].

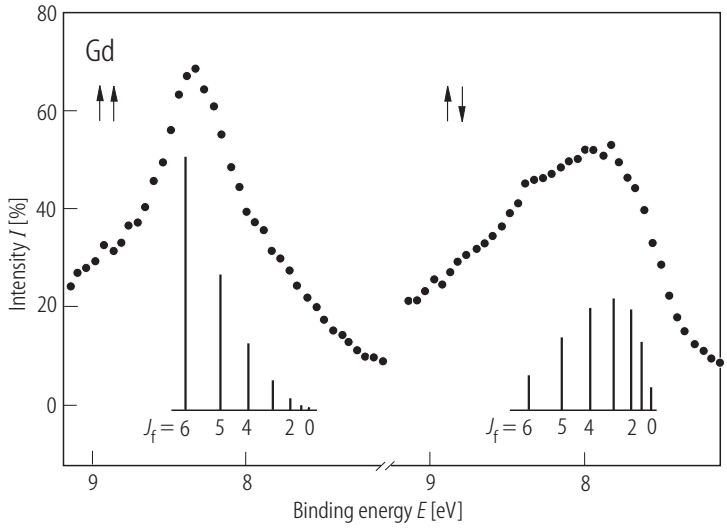

Fig. 60. Calculated relative intensities of the 4 $f^6 - {}^7F_J$ final state photoemission multiplet components for (**a**) $\parallel$ ($\Delta M_J = +1$) and (**b**) $\perp$ ($\Delta M_J = -1$) orientation between photon spin and sample magnetization. For comparison, the experimental spectra normalized to 100 % circular polarization, are also given [93S2].

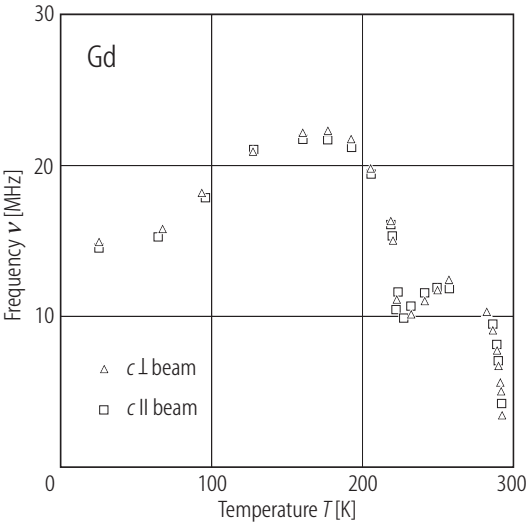

Fig. 61. Temperature dependence of the muon spin rotation frequency in a single crystal sphere of Gd metal below T_C [90H].

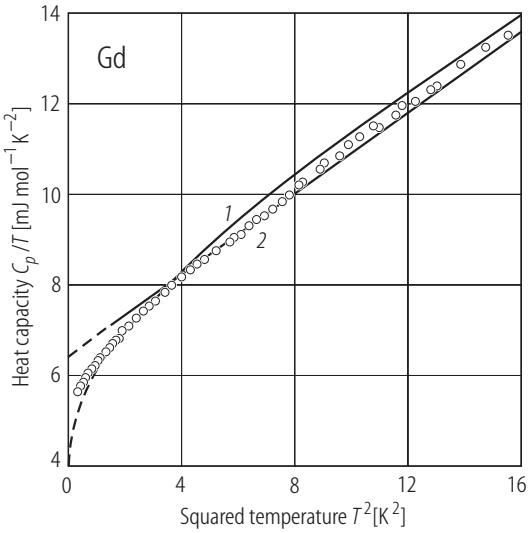

Fig. 62. Heat capacity of electrotransported Gd: curve *1*, circles: from the results of [74W]; *2*: from the results of [85T]. [87H].

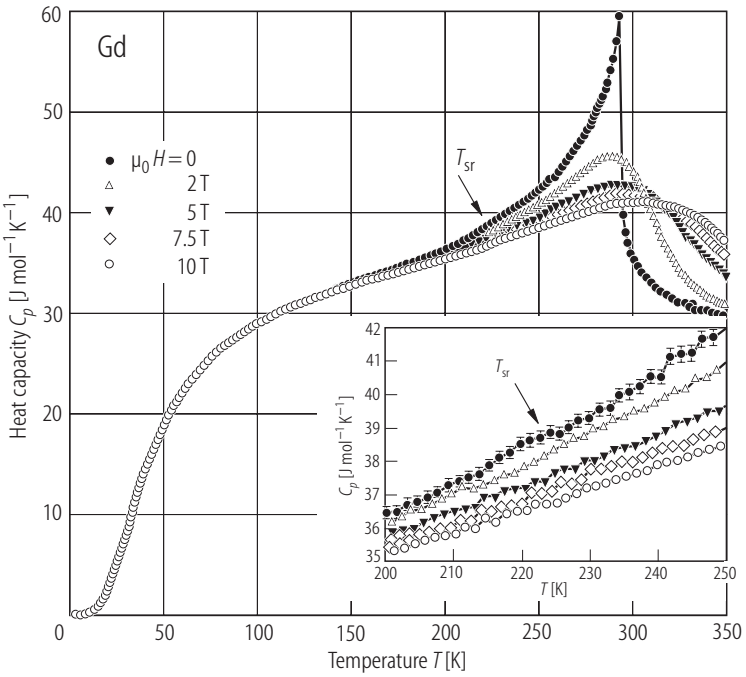

Fig. 63. Heat capacity of single-crystal Gd with the magnetic field applied parallel to the [0001] direction. The inset clarifies the details near the spin reorientation transition T_{sr}. The error bars are shown for the zero-field heat capacity in the inset. The arrows point to the anomaly at T_{sr} [98D].

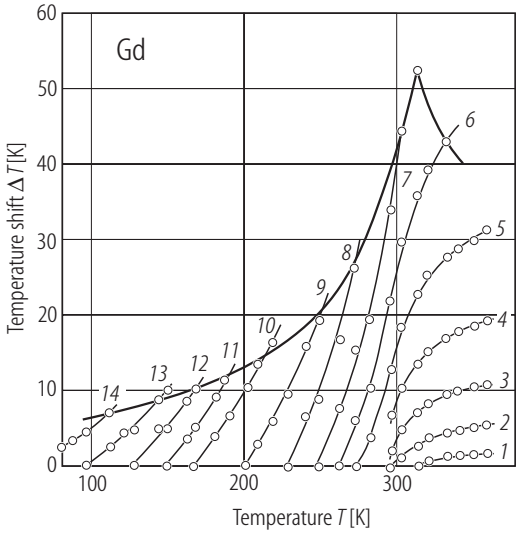

Fig. 64. Temperature dependencies of the magnetocaloric effect in Gd at fields up to 360 kOe with account taken of the short-range order above T_C. The thick line is the calculation in the constant field H = 360 kOe. The thin lines are the calculations at constant magnetization values σ in G cm^3 g^{-1}: (*1*) 40; (*2*) 60; (*3*) 80; (*4*) 100; (*5*) 120; (*6*) 140; (*7*) 160; (*8*) 180; (*9*) 200; (*10*) 220; (*11*) 230; (*12*) 240; (*13*) 250; (*14*) 260 [86P].

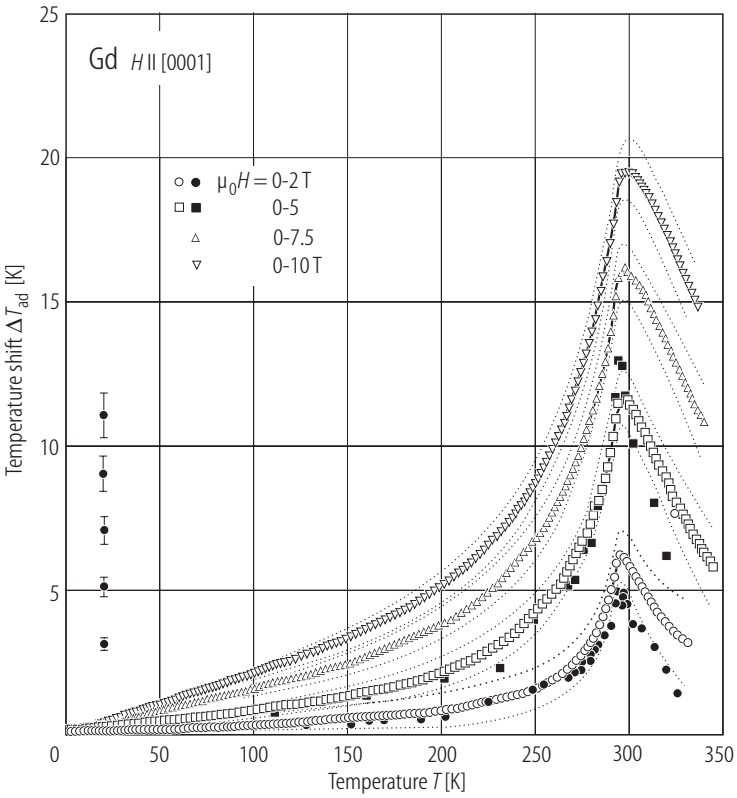

Fig. 65. Magnetocaloric effect in single crystal Gd with the magnetic field applied parallel to the [0001] direction. The error bars on the left-hand side of the figure indicate the uncertainty in the direct measurements (± 7 %) [98D]. Open symbols: calculated from C_p data, solid symbols: experimental, dotted lines: range due to errors in C_p.

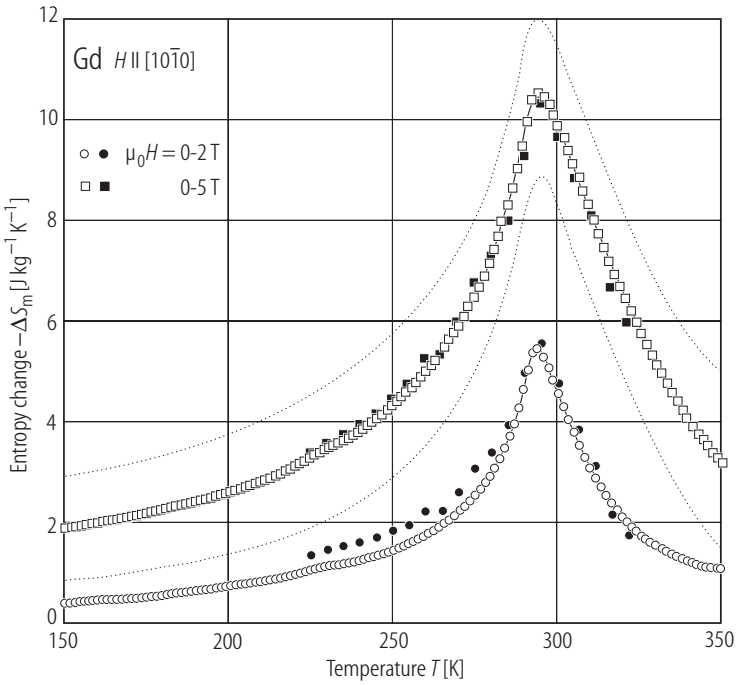

Fig. 66. Magnetic entropy change in single crystal Gd with the magnetic field applied parallel to the [10$\bar{1}$0] direction as determined from heat-capacity (open symbols) and magnetization (solid symbols) measurements. Dotted lines: range due to errors in C_p [98D].

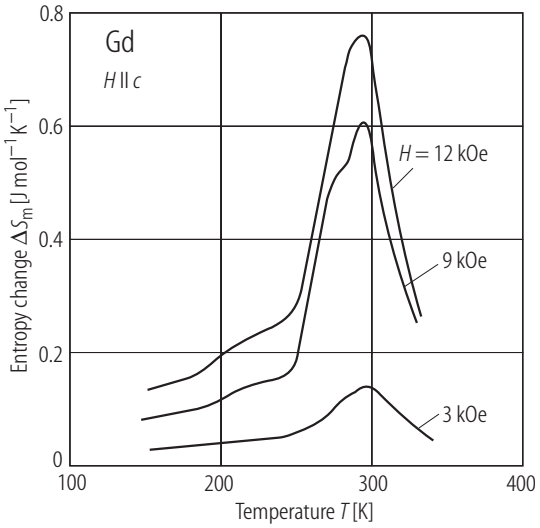

Fig. 67. Temperature dependence of the magnetic entropy change for Gd monocrystal ($H||c$): H = 12 kOe, 9 kOe and 3 kOe [96D].

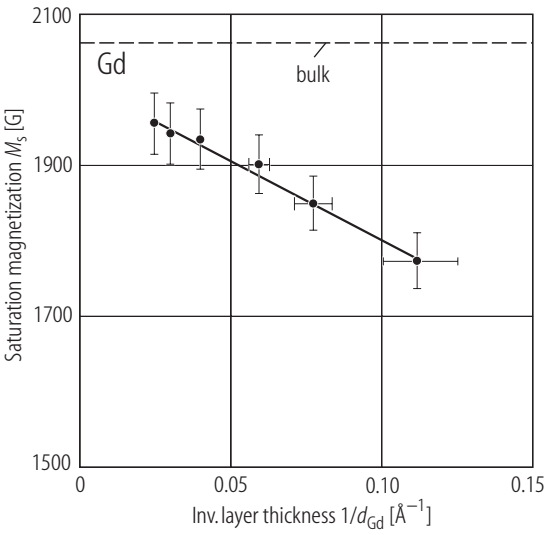

Fig. 68. Saturation magnetization of Gd (M_s) as a function of inverse Gd layer thickness ($1/d_{Gd}$) for a series of annealed multilayers. The dotted line represent the bulk Gd magnetization [96J].

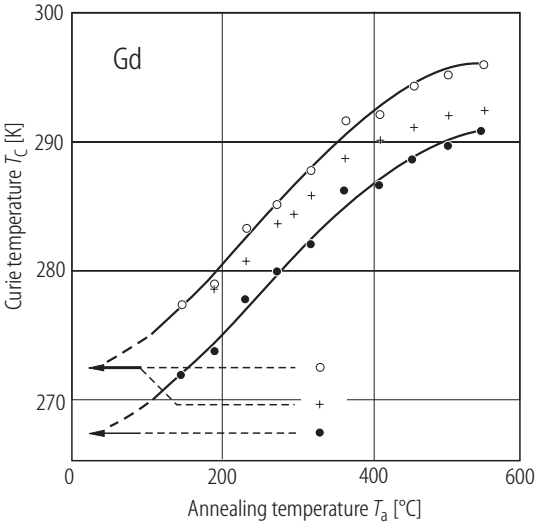

Fig. 69. Curie temperature T_C of thin films of Gd grown on a glass substrate vs. annealing temperature T_a. Open circles show T_C values determined from the Arrott plot, closed circles from Graham's plot and crosses from resistance data. Arrows indicate values for the as-deposited sample [88N].

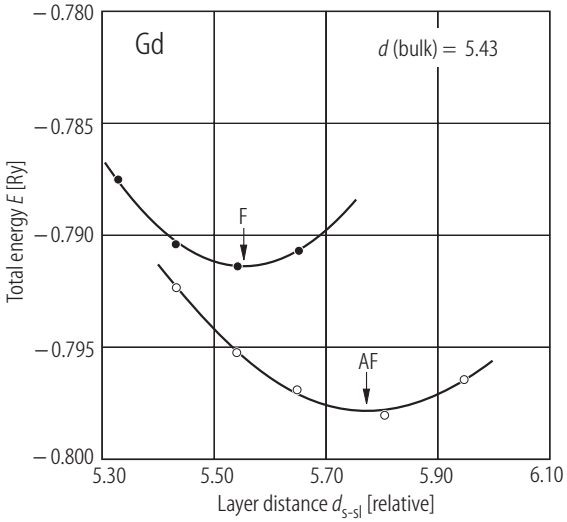

Fig. 70. Theoretical total energy of the Gd(0001) slab vs. the distance between the surface and adjacent underlayer. Solid circles stand for the FM state, and open circles are for the AFM states. Arrows show the equilibrium positions obtained by total energy minimization [91W].

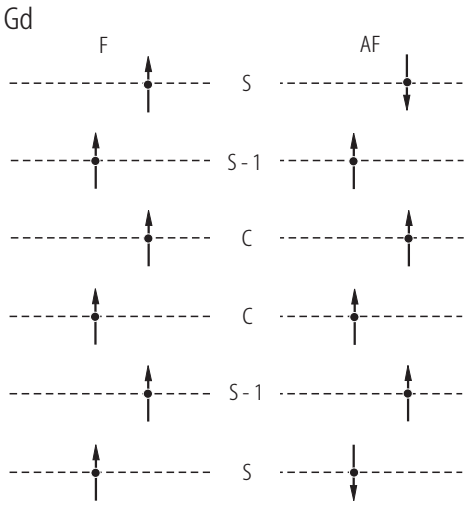

Fig. 71. Schematic ferromagnetic and antiferromagnetic configurations for a six-layer Gd(0001) slab [91W1].

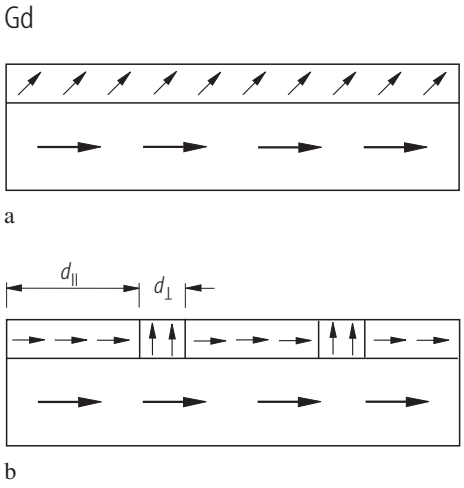

Fig. 72. Possible domain configurations for both in-plane and perpendicular surface magnetism of Gd(001) films. Panel (**a**) shows a magnetic state with canted spins on the surface, and panel (**b**) shows a combination of perpendicular and in-plane domains [93T1].

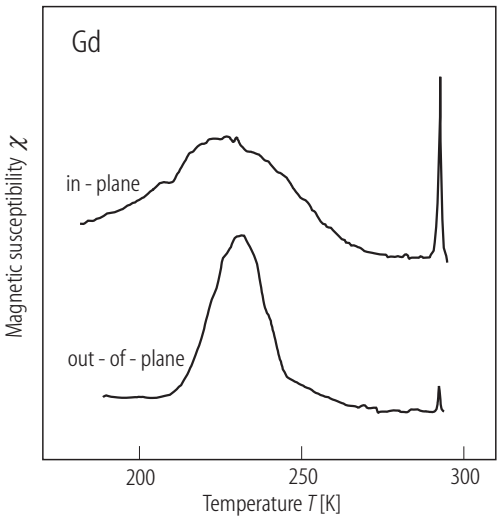

Fig. 73. Comparison between the temperature dependence in-plane and out-of-plane susceptibility for a 130 nm thick Gd film [95B1].

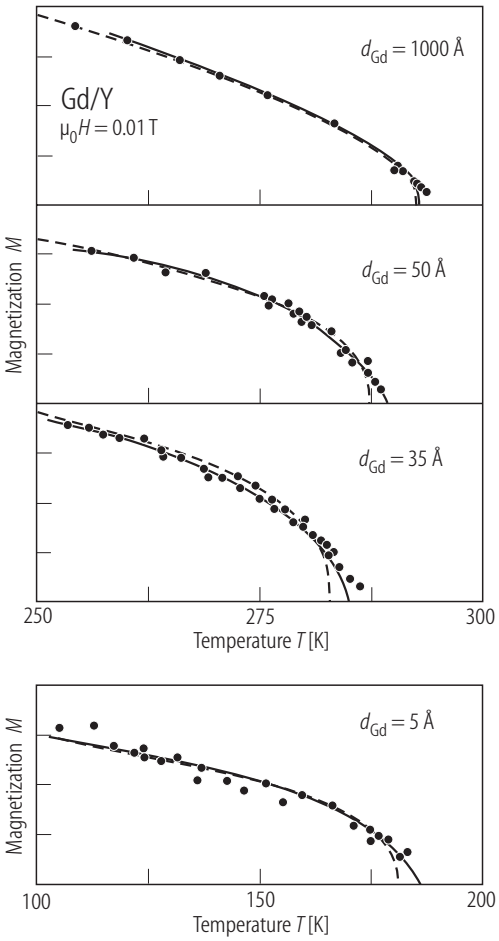

Fig. 74. Magnetization M for Gd/Y films measured in a small field of $\mu_0 H = 0.01$ T as a function of temperature. The Curie temperature is determined by extrapolating the $M(0.01\ \mathrm{T})$ vs. temperature curve to $M = 0$ [95G].

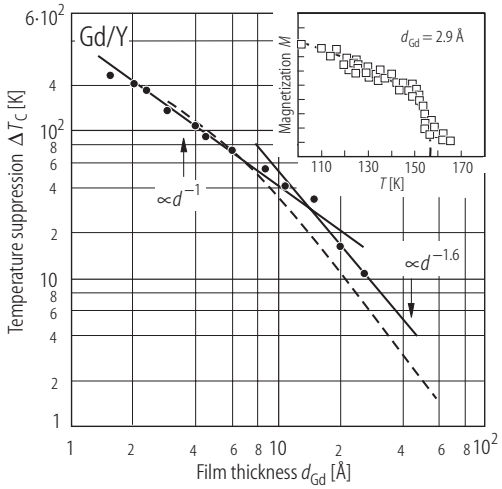

Fig. 75. Suppression ΔT_C of the Curie temperature as a function of Gd/Y film thickness d_{Gd}. Solid circles: experimental data (T_s = 473 K); dashed line: generalized mean-field theory for Heisenberg ferromagnets. Solid lines illustrate $d_{Gd}^{-1.6}$ and d_{Gd}^{-1} dependence. The inset shows the determination of T_C by extrapolating the magnetization $M(T)$ measured in a small external field $\mu_0 H = 10$ mT to $M(T_C) = 0$ for $d_{Gd} = 2.9$ Å (dashed line). For this sample the extrapolation is nearly identical to a power-law fit with $\beta = 0.23$ [98G].

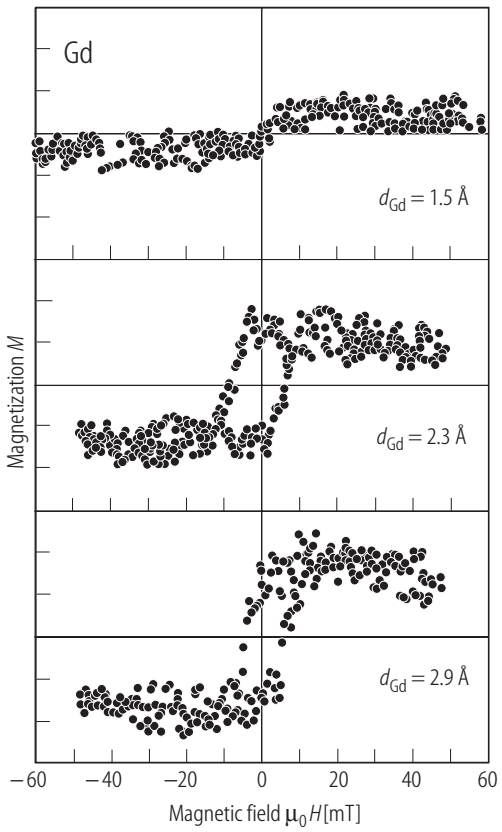

Fig. 76. Hysteresis loops, i.e. magnetization M vs. applied magnetic field $\mu_0 H$, obtained by the magneto-optical Kerr effect (MOKE) measurements on Gd films (T_s = 473 K) with d_{Gd} = 1.5, 2.3, and 2.9 Å at T = 5 K…7 K [98G].

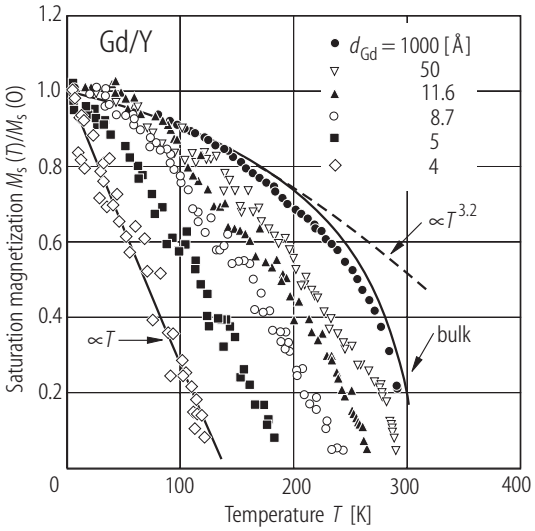

Fig. 77. Temperature dependence of saturation magnetization M_s for various Gd/Y film thicknesses (substrate temperature T_s = 300 °C for all samples) [95G].

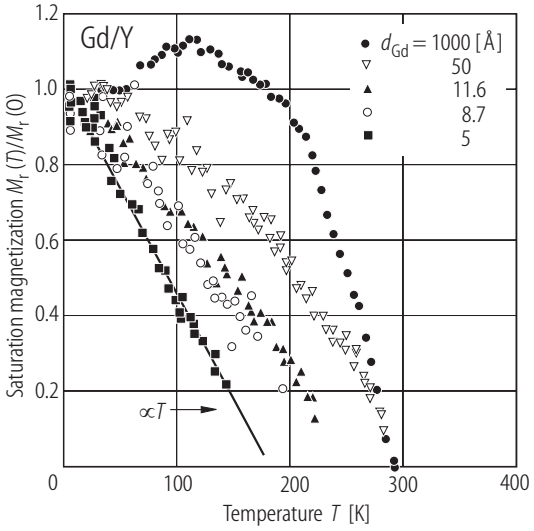

Fig. 78. Temperature dependence of remanence M_r for various (Gd/Y) film thickness (substrate temperature T_s = 300 °C for all samples) [95G].

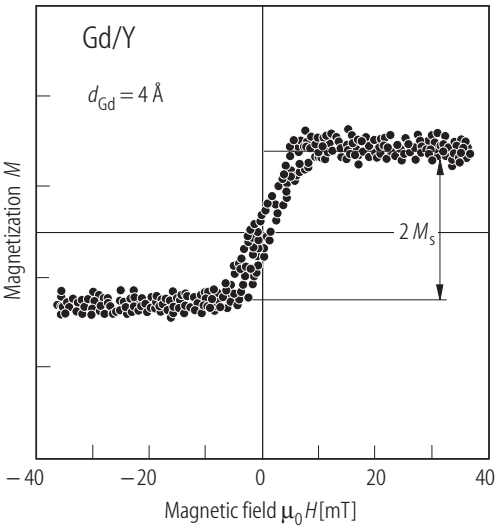

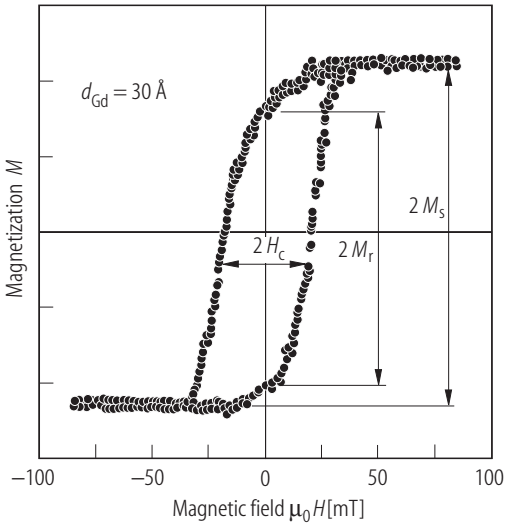

Fig. 79. Hysteresis loops of magnetization M vs. applied magnetic field obtained by the magnetooptic Kerr effect (MOKE) measurements on thin Gd films on an Y buffer layer with d_{Gd} = 30 Å and 4 Å covered with a 100 Å Y protective top layer at $T \approx 50$ K. Saturation magnetization M_s, remanence M_r, and coercivity H_c are indicated [95G].

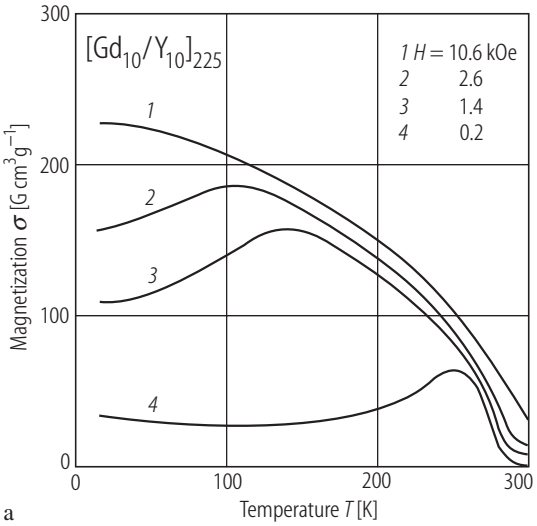

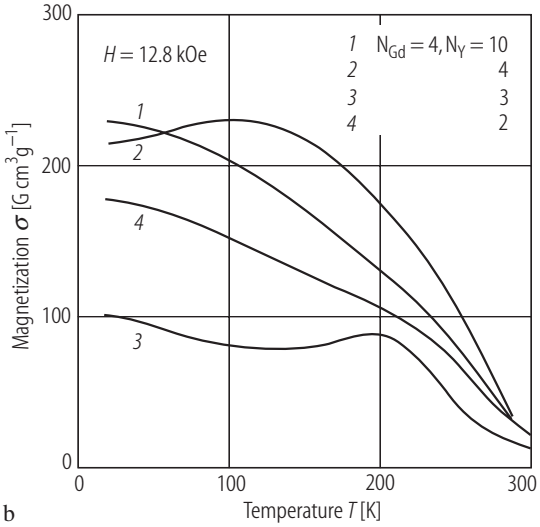

Fig. 81. (**a**) Temperature dependence of the magnetic moment ot the $(10Gd/10Y)_{225}$ superlattice in a series of applied fields. (**b**) The temperature dependence of the magnetic moment of the (4/2), (4/3), (4/4), and (4/10) superlattices in an applied field of 12.8 kOe [87K].

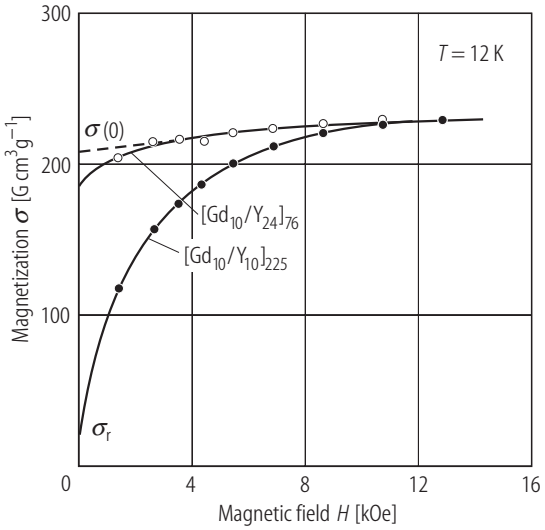

Fig. 80. The in-plane magnetization curves at 12 K for the synthetic superlattices consisting $(10Gd/24Y)_{76}$ and $(10Gd/10Y)_{225}$ [87K].

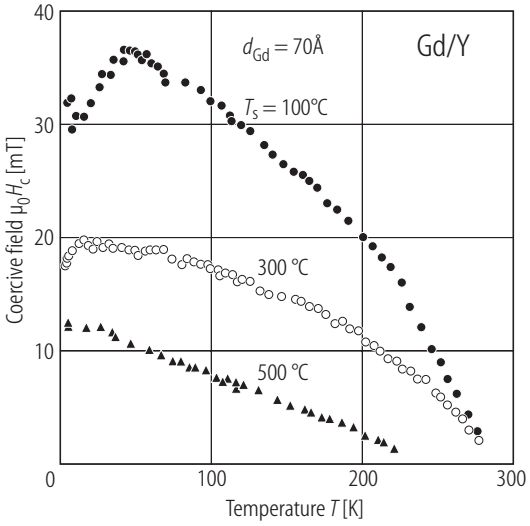

Fig. 82. Coercive field $H_c(T)$ for Gd/Y films prepared with different substrate temperatures T_s and a constant film thickness d_{Gd} = 70 Å [95G].

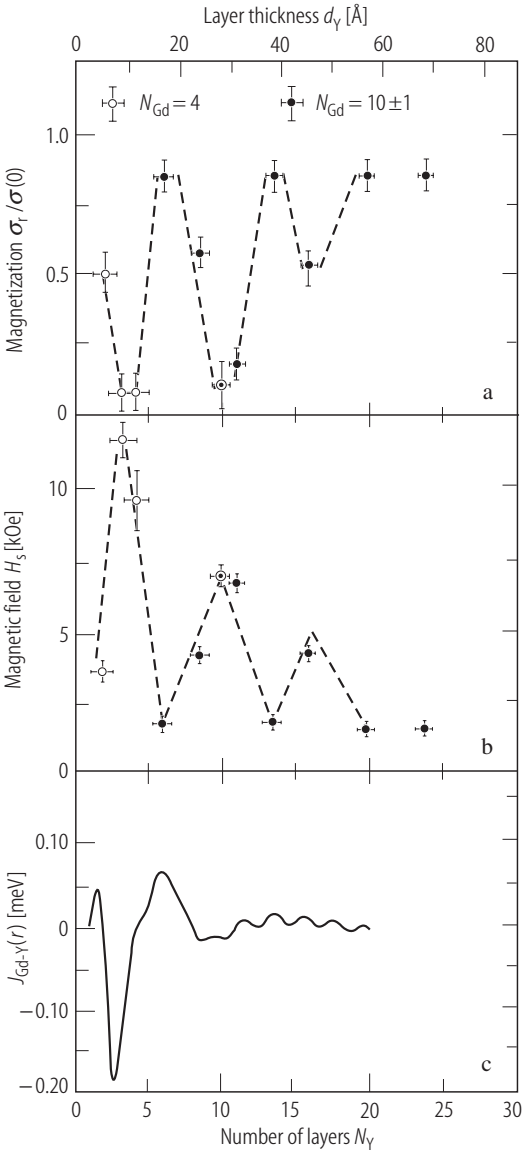

Fig. 83. The oscillatory dependence of (**a**) remanent magnetization $\sigma_r/\sigma(0)$ and (**b**) saturation field H_s, on N_Y (number of Yttrium atomic layers) in two series of superlattices (Gd - Y) with $N_{Gd} = 4$, and $N_{Gd} = 10 \pm 1$. The dashed lines are guide to the eyes. (**c**) The calculated functional dependence of $J_{Gd\text{-}Y}$ on N_Y [87K].

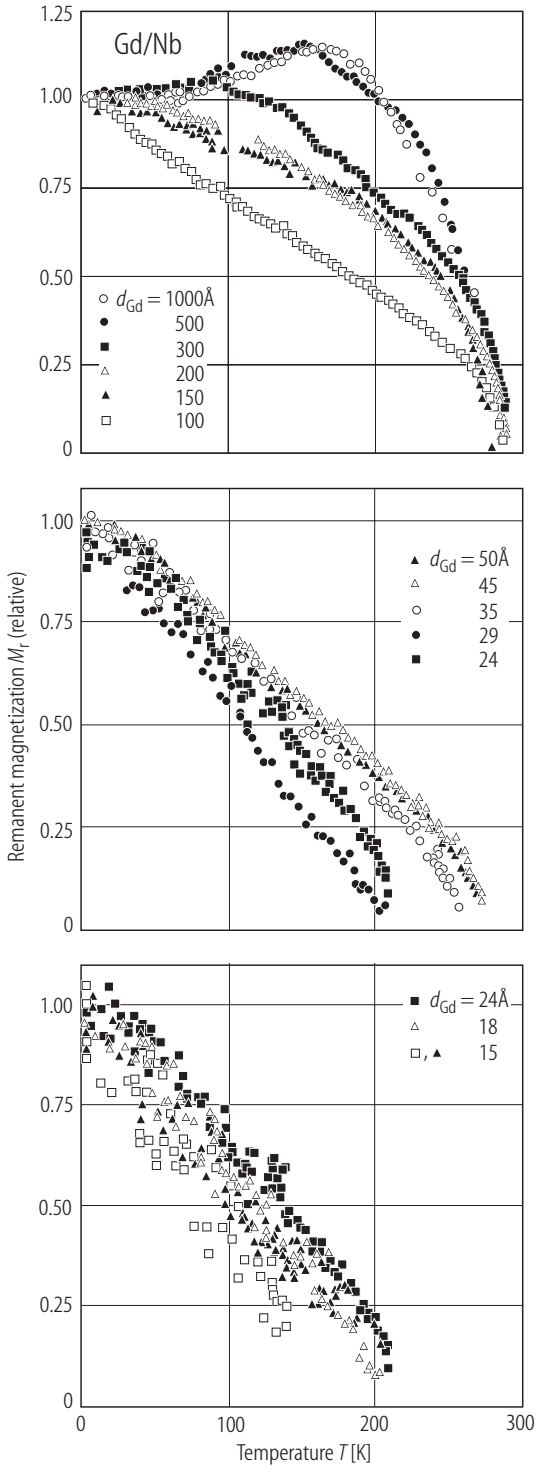

Fig. 84. Temperature dependence of the in-plane remanent magnetization M_r of Gd/Nb films with thickness between 15 and 1000 Å. The curves are normalized to the same value at $T = 0$ K [93P].

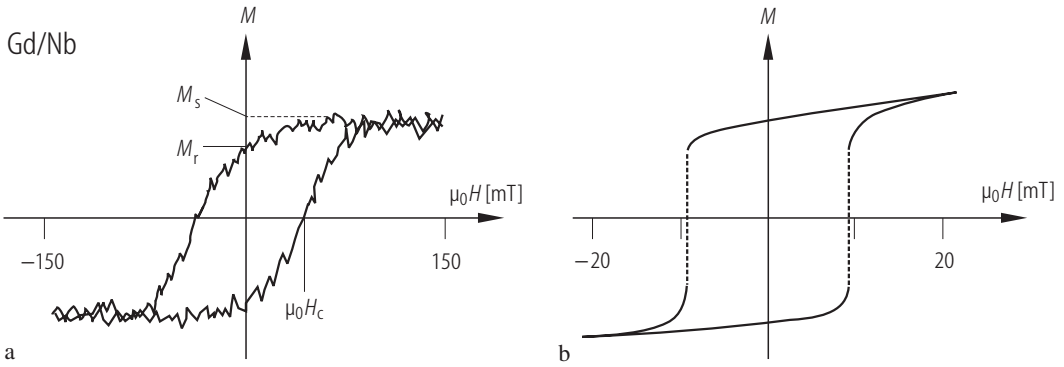

Fig. 85. Hysteresis curves of two Gd/Nb films with (**a**) d_{Gd} = 15 Å at T = 51 K and (**b**) d_{Gd}=1000 Å at T = 55 K. In-plane components of the remanent magnetization M_r, coercive field H_c and saturation magnetization M_s are indicated in (**a**) [93P].

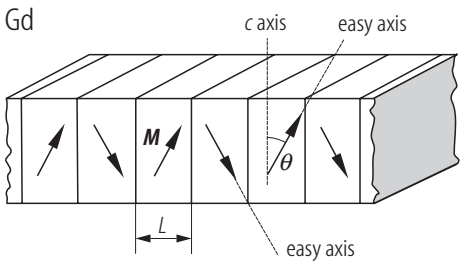

Fig. 86. Model of the domain pattern used to explain the temperature dependence of the remanence and coercivity shown in Fig. 84 and 85 [93P].

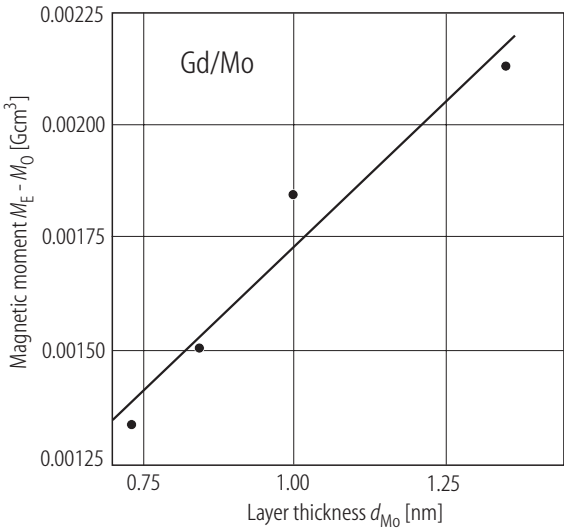

Fig. 87. The difference between the expected saturation moment, M_E, and the maximum observed moment, M_0, at 5.5 K, plotted as a function of Mo layer thickness of Gd/Mo multilayers [96H].

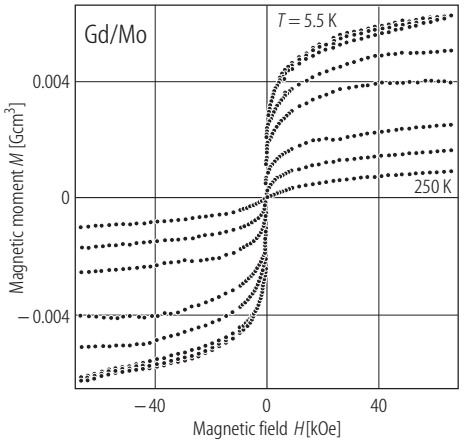

Fig. 88. Magnetization of a Gd/Mo multilayer (d_{Gd} = 3.6 nm, d_{Mo} = 1.0 nm) at 5.5, 10, 20, 50, 80, 150, 200 and 250 K [96H].

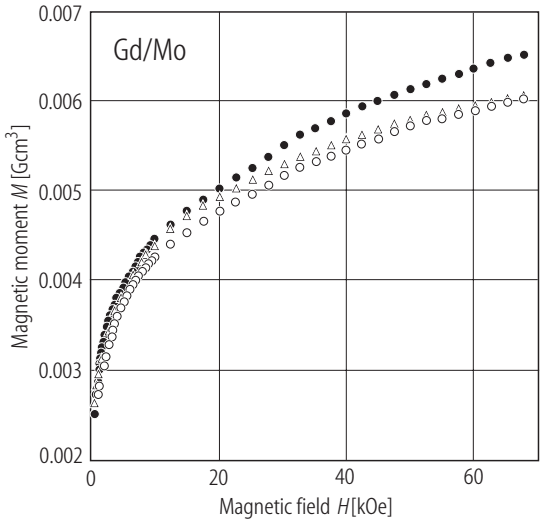

Fig. 89. Magnetization of three Gd/Mo multilayers measured at 5 K. Mo layer thicknesses are (open circles) 0.73 nm; (solid circles) 0.84 nm; (open triangles) 1.35 nm [97H].

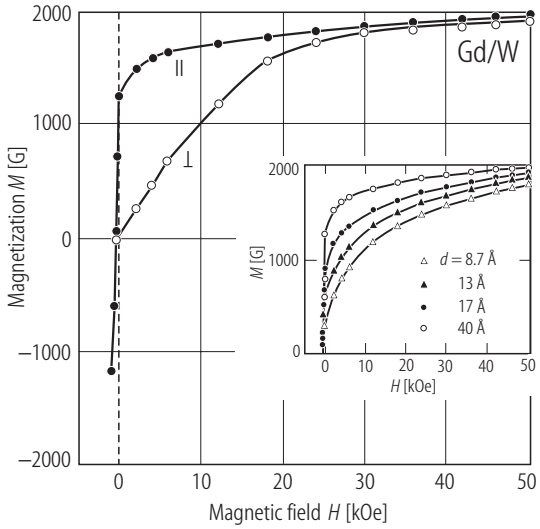

Fig. 90. Gd magnetization curves at 1.7 K for annealed $Gd_{32\ Å}/W_{26\ Å}$ with the field applied parallel and perpendicular to the sample plane. Inset: magnetization of Gd for multilayers with 8.7, 13, 17, and 40 Å Gd layers [96J].

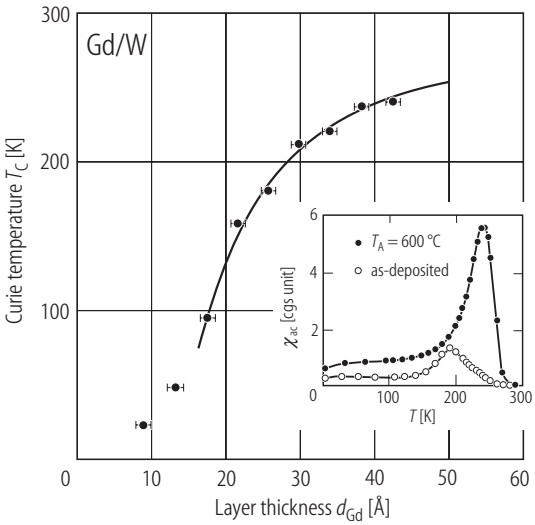

Fig. 91. Curie temperature as a function of the Gd layer thickness for a series of Gd/W multilayers with d_W = 26 Å annealed at 600 °C. The solid curve is a fit to the finite-size scaling law. Inset: Temperature dependence of the ac susceptibility (in cgs units) of the as-deposited and annealed $Gd_{40\ Å}/W_{26\ Å}$ samples [96J].

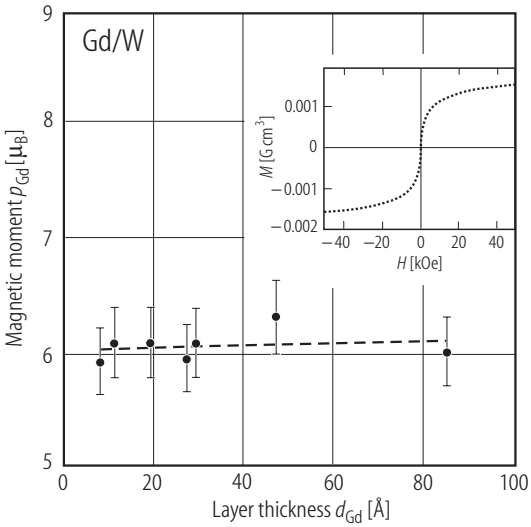

Fig. 92. Average magnetic moment per Gd atom in Gd/W multilayers as a function of the Gd layer thickness. Inset: Magnetic hysteresis loop at 5 K for the $Gd_{19\ Å}/W_{18\ Å}$ multilayer [97L].

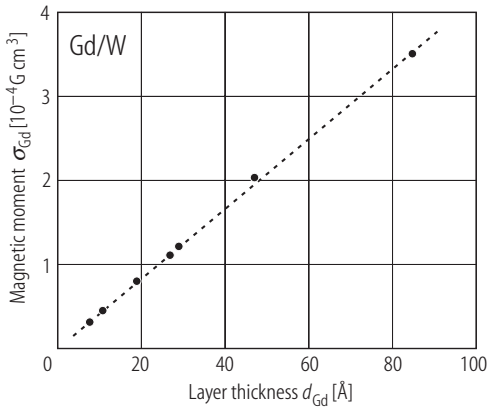

Fig. 93. Total magnetic moment per Gd layer at 5 K as a function of Gd layer thickness [97L].

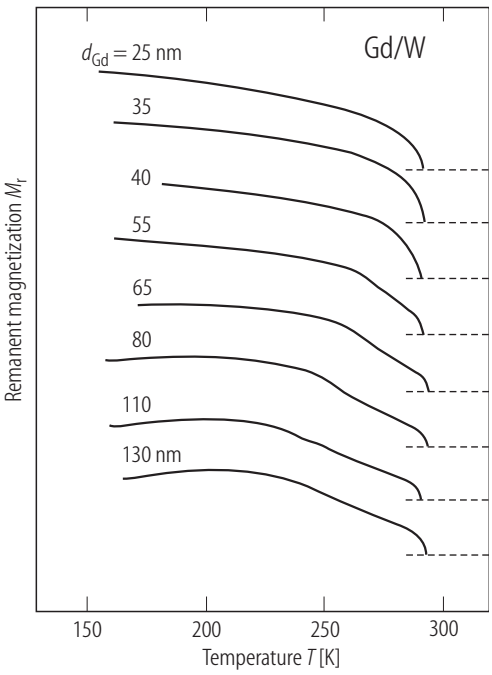

Fig. 94. Remanent magnetization as a function of temperature for Gd on W(110) films of different thickness [95B1].

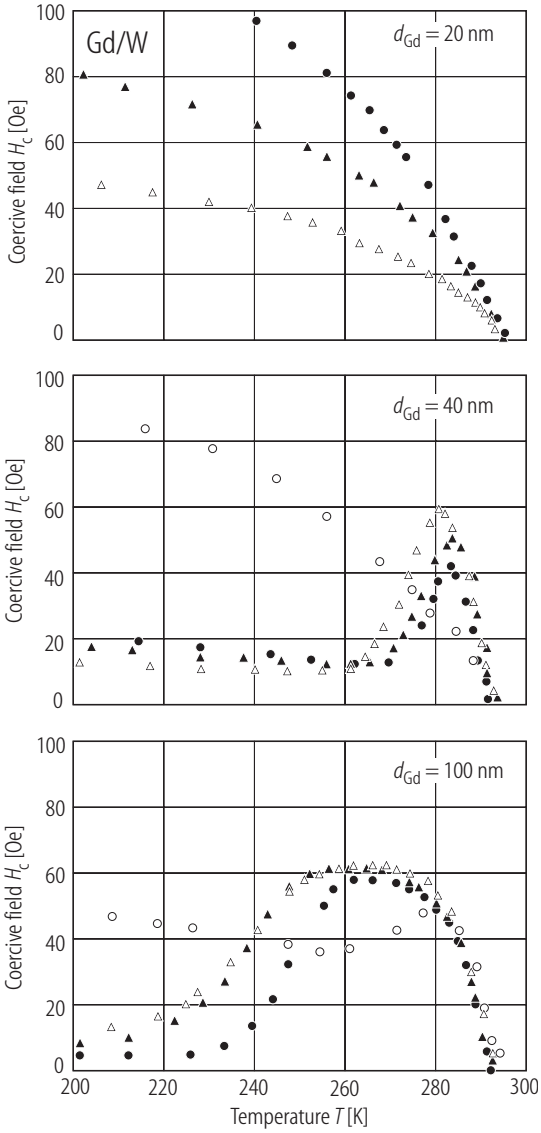

Fig. 95. Coercive field as a function of temperature for three different films on W(110) (thickness as indicated), after annealing to various temperatures (open circles: T_{an} = 570 K; solid circles: T_{an} = 670 K; solid triangles: T_{an} = 770 K; open triangles: T_{an} = 870 K) [94P].

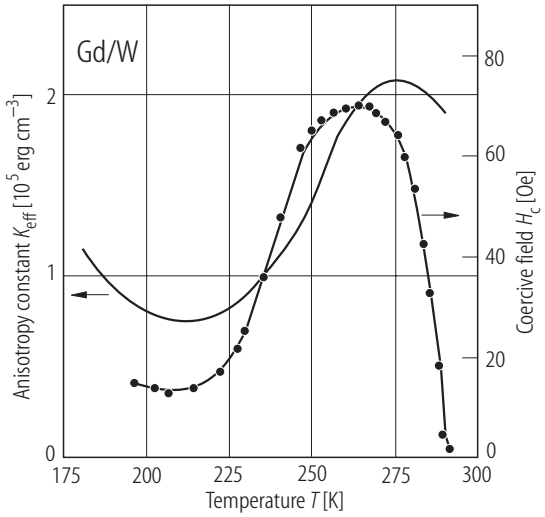

Fig. 96. Comparison between the coercive field $H_c(T)$ for 130 nm thick Gd on W(110) surface and the effective anisotropy $K_{eff}(T)_4$ for bulk Gd [95B1].

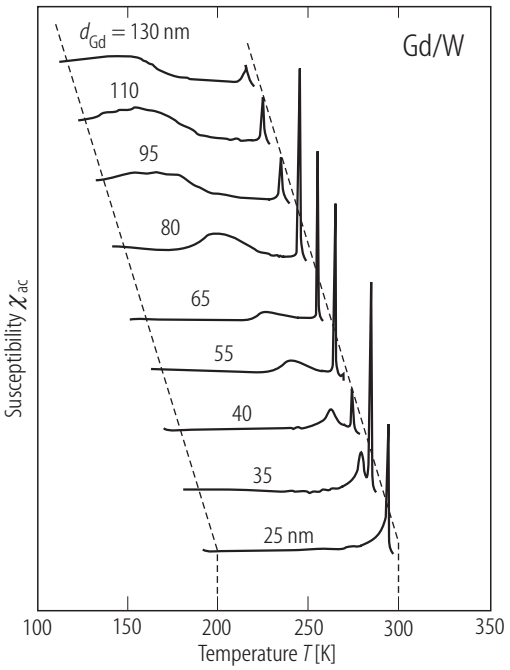

Fig. 99. In-plane susceptibility as a function of temperature for Gd/W(110) films of various thickness registered by the magneto-optical response of the surface to a small in-plane ac field. In addition to the peak caused by the ferromagnetic-paramagnetic phase transition, the magnetization reorientation peak is present [95B1].

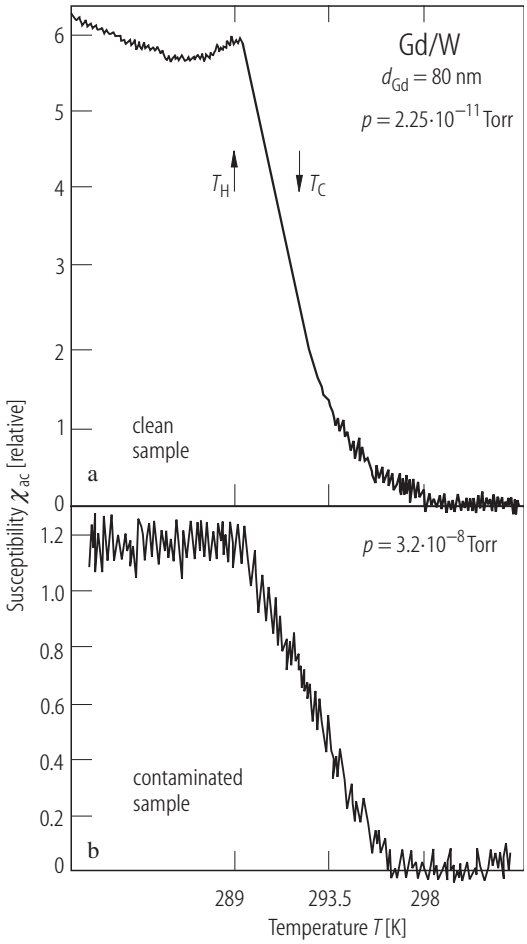

Fig. 97. (**a**) AC magnetic susceptibility of a clean Gd(0001) film 80 nm thick on to W(110) surfaces as a function of temperature T_C and T_H refer to the Curie and Hopkinson temperatures, respectively. (**b**) ac magnetic susceptibility of the same sample as in (**a**), after contamination. The abruptness of the drop in χ within 4 K above Hopkinson maximum indicates the presence of a first-order (SEMO) transition, i.e., the coexistence of an ordered surface with a disordered bulk [90S].

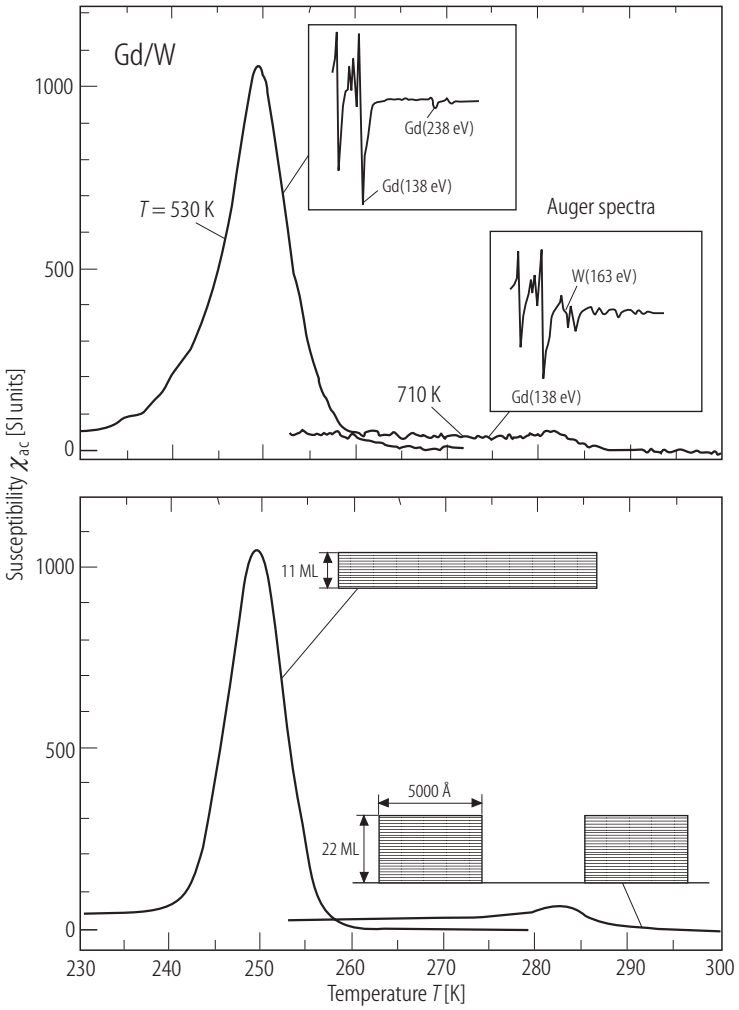

Fig. 98. Upper panel: $\chi_{ac}(T)$ and Auger spectra of 11 ML Gd/W(110) first annealed at 530 K, then at 710 K. The occurrence of a W Auger signal after annealing to 710 K is accompanied by a drastically reduced χ peak closer to T_C (bulk). Lower panel: simulated χ_{ac} for the mass equivalent of 11 monolayers (ML) [94A].

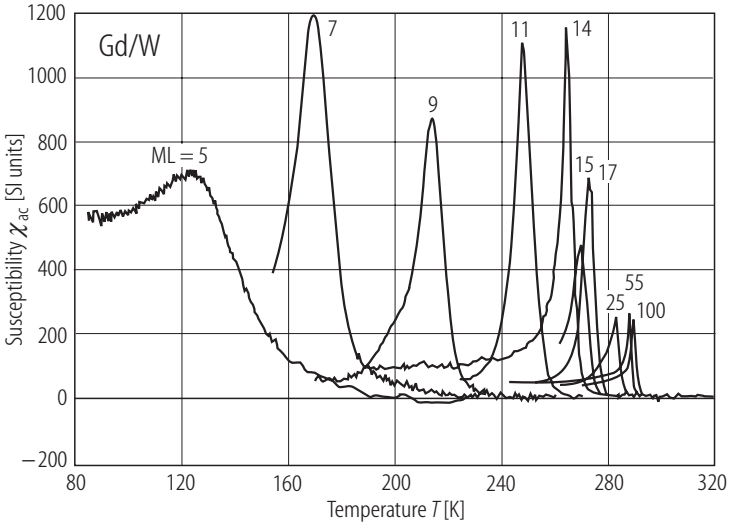

Fig. 100. χ_{ac} peaks of different Gd(0001)/W(110) film thickness grown at T_s = 320 K carefully annealed without changing the layer-by-layer ML (monolayer) [94A].

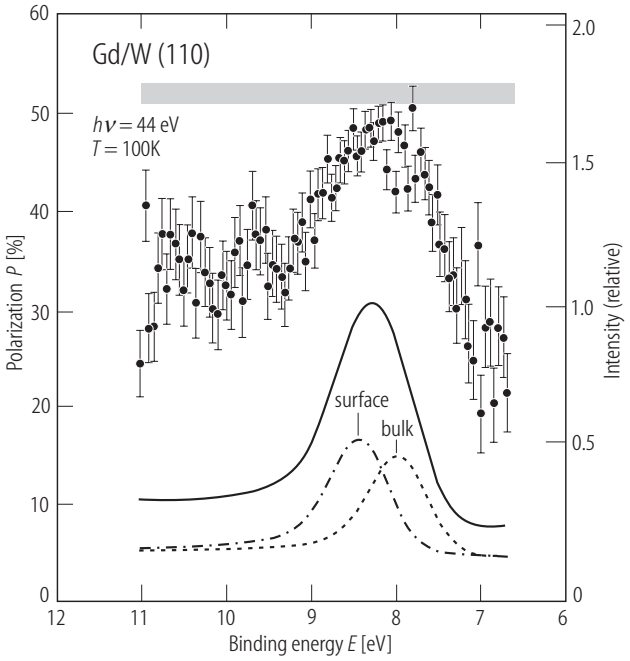

Fig. 101. 4f core level normal emission intensity and polarization data taken from Gd/W(110). The total intensity shown is separated into the bulk and surface contributions. The shaded bar at the top of the figure delineates the range of the total 4f polarization as calculated from the fit line shapes [92M].

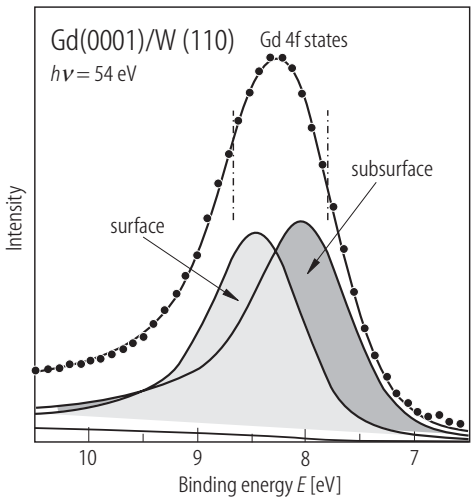

Fig. 102. Photoemission spectrum (circles) of the Gd 4f emission. The continuous line through the data points is the result of the curve fitting based on the decomposition into surface (light shadowed) and subsurface (dark shadowed) contributions [93V].

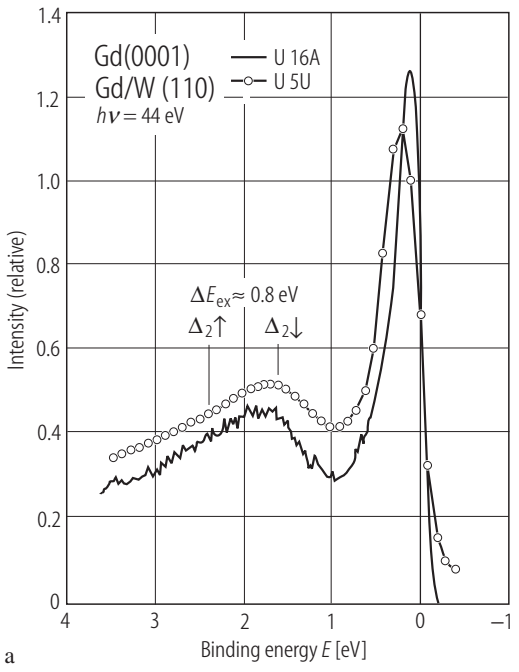

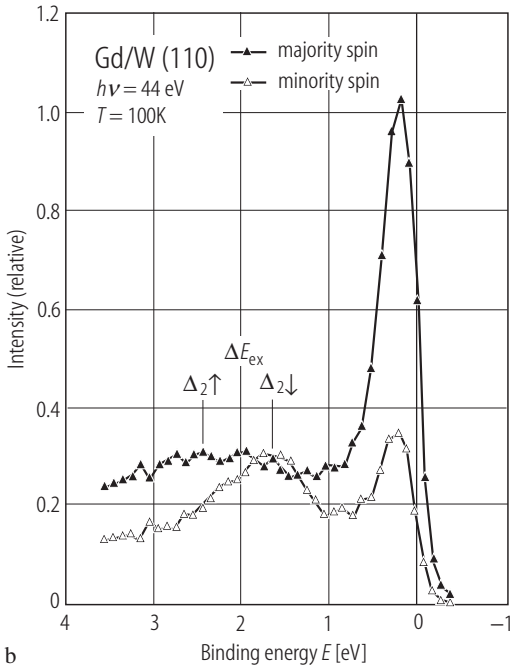

Fig. 103. (**a**) Angle-resolved valence-band photoemission spectra from the surfaces of Gd(0001) and Gd/W(110) multilayer acquired at the U16A and U5U beam lines, respectively. (**b**) Spin-resolved intensities obtained from the U5U data of (**a**) [92M].

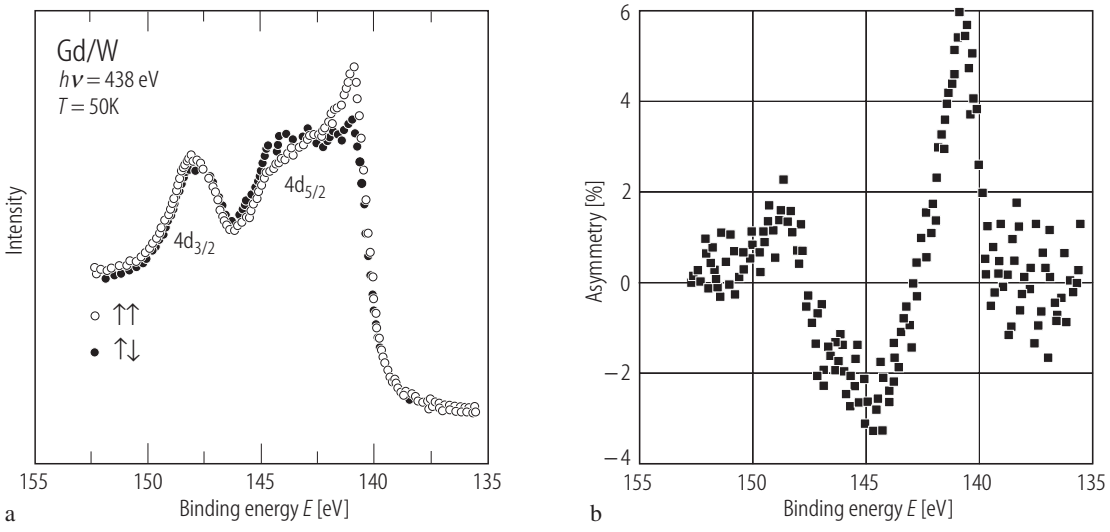

Fig. 104. (**a**) Gd 4d core-level photoemission (PE) spectra ($h\nu$ = 438 eV) obtained from a remanently magnetize Gd(0001)/W(110) film (thickness 80 Å: T = 50 K). Open (solid) circles are for nearly parallel (antiparallel) orientation of photon spin and sample magnetization. The MCD (magnetic circular dichroism) asymmetry derived from the raw data is plotted in (**b**) [95A].

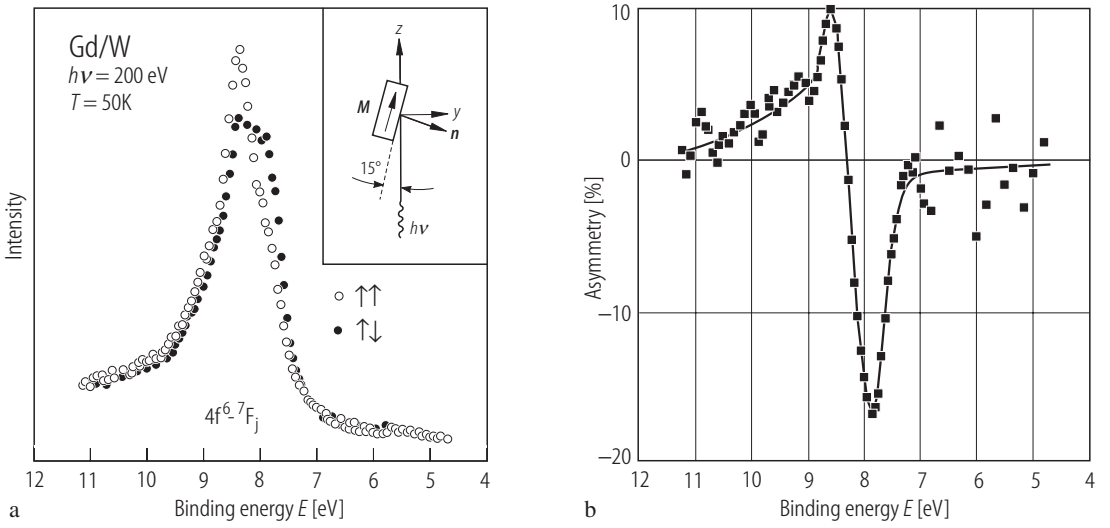

Fig. 105. (**a**) Gd-4f photoemission spectra ($h\nu$ = 200 eV) of a remanently magnetized Gd(0001)/W(110) film (thickness ≅ 80 Å: T ≅ 50 K). The open (solid) circles are for parallel (antiparallel) orientation of photon spin and sample magnetization. (**b**) Asymmetry $(I_{\uparrow\uparrow} - I_{\uparrow\downarrow})/(I_{\uparrow\uparrow} + I_{\uparrow\downarrow})$ calculated from the raw experimental spectra in (**a**). The inset gives schematically the experimental geometry [93S2].

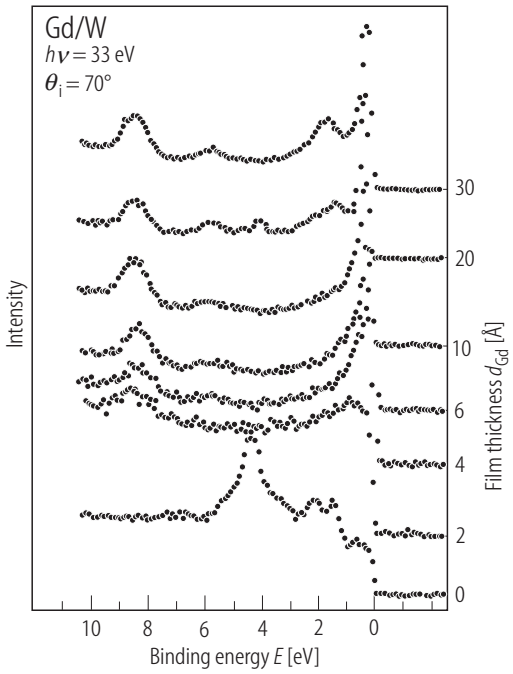

Fig. 106. Photoemission spectra of Gd overlayers on W(110). The photoelectrons were collected normal to the surface and the light is p-polarized, so that the relative signal from the surface state increased relative to the other bands. For the very thin Gd films, there are two prominent features: the 4f levels at a binding energy of 8.6 eV and the 5d bands near the Fermi energy. For photoemission in the normal direction ($k_{\|} = 0$) the Gd 5d bands become resolved into at least two distinct features with increasing coverage [91L].

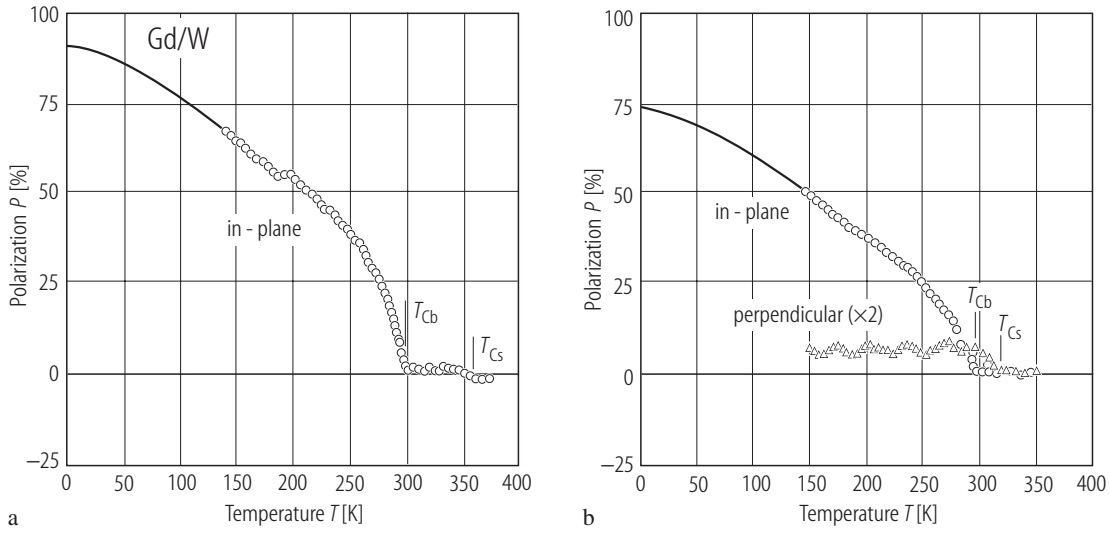

Fig. 107. Spin resolved photoemission polarization from the Gd 4f core levels vs. temperature taken with $h\nu$ = 149 eV. The data in panel (**a**) were taken from a 400 Å film of Gd grown on W(110) at 300 K and annealed to 825 K for 3.5 min, while the panel (**b**) data are from a film grown at 673 K. T_{Cs} and T_{Cb} indicate the surface and bulk magnetic ordering temperatures, respectively. An extrapolation to zero temperature is shown using a $T^{3/2}$ fit with prefactors of $1.6 \cdot 10^{-4}$ and $1.8 \cdot 10^{-4}$ deg$^{-3/2}$ for (**a**) and (**b**), respectively. For comparison, the bulk Gd prefactor is $0.98 \cdot 10^{-4}$ deg$^{-3/2}$ [93T1].

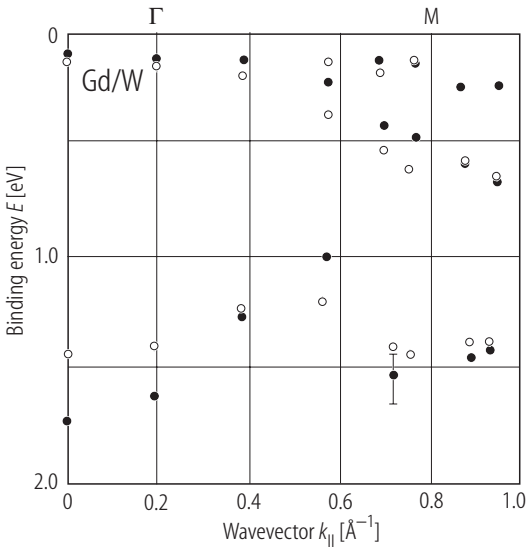

Fig. 108. The experimental band structure from Γ to M of the surface Brillouin zone from spectra taken at a photon energy of 33 eV at various emission angles. The results are shown for the two temperatures of 295 K (solid circles) and 235 K (open circles). The results are for a 20-Å film of Gd on W(110) [92D].

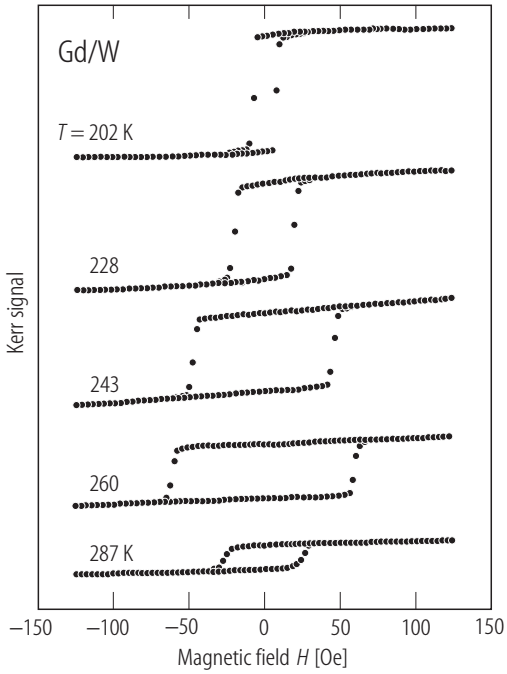

Fig. 109. Temperature-dependent hysteresis loops measured on a 100-nm Gd film on W(110) after annealing to 770 K. The hysteresis loops exhibit a nonvanishing slope outside the magnetization reversal region around H_c. This effect indicates that the easy axis of magnetization for Gd(0001) films is not in the surface plane [94 P].

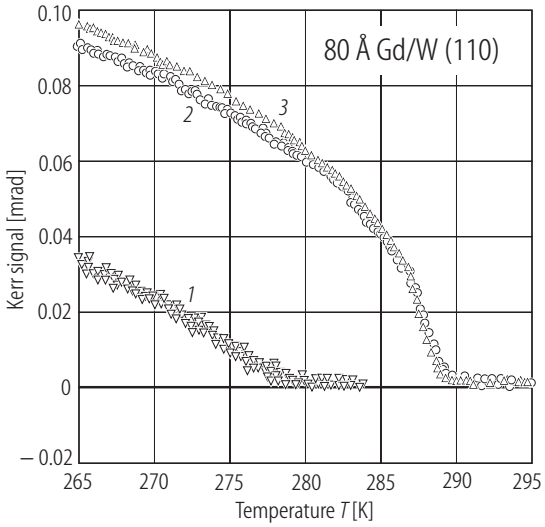

Fig. 110. Remanent magnetization of 80 Å Gd(0001) on W(110) for different annealing steps: (*1*) as-deposited 310 K, (*2*) 620 K, (*3*) 820 K. The as-deposited films have a reduced Curie temperature T_C = 273 K, which gradually shifts up to the bulk T_C of Gd upon annealing [94F].

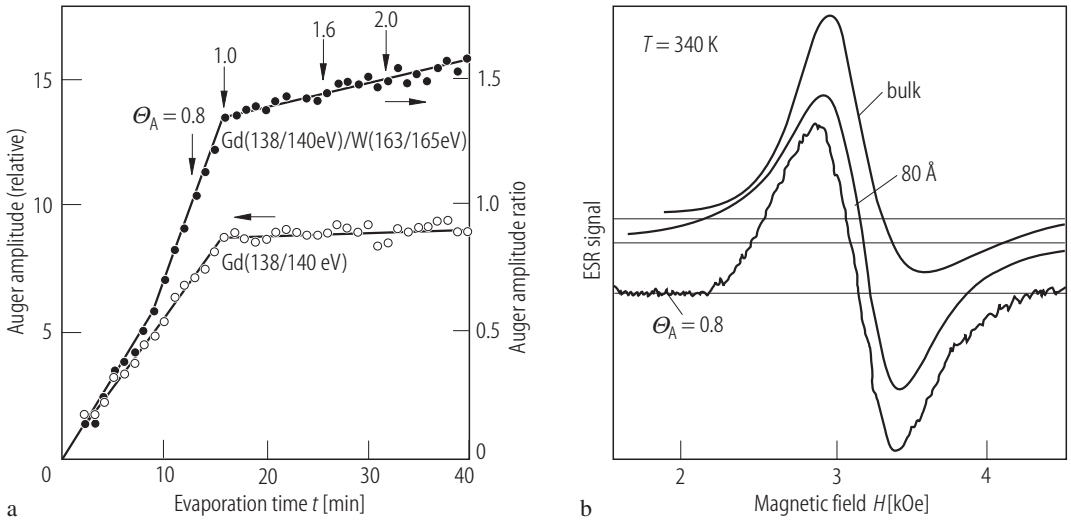

Fig. 111. The Auger amplitude of Gd and the Auger amplitude ratio Gd/W as functions of evaporation time. An adsorbate coverage of $\Theta_A = 1$ corresponds to a hcp Gd (0001) close-packed monolayer on W(110). The substrate temperature during evaporation was $T_s = 450$ °C. (**b**) ESR absorption spectra for a 18-μm (bulk), 80-Å, and $\Theta_A = 0.8$ Gd adsorbate layer, far in the paramagnetic regime. The microwave frequency is 9.30 GHz and H_0 lies in the surface plane [87F].

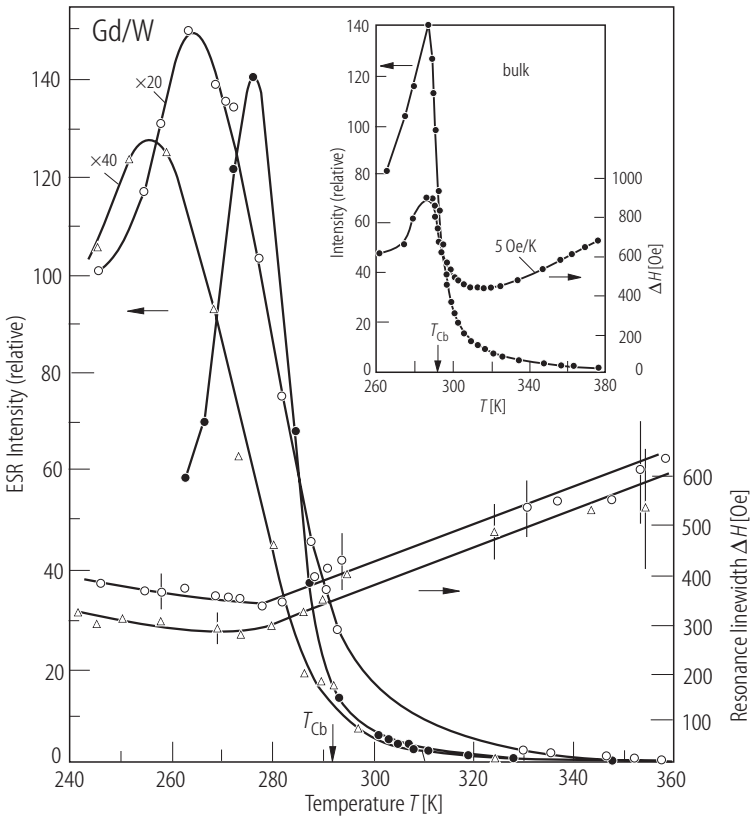

Fig. 112. ESR intensity and linewidth as functions of temperature for 80 Å (solid circles), $\Theta_A = 1.6$ (open squares), and $\Theta_A = 0.8$ (open triangles) of Gd/W (110). The gain factors for $\Theta_A = 0.8$ and $\Theta_A = 1.6$ are 40 and 20 with respect to the 80 Å data. For comparison the corresponding data of a bulk foil (solid circles) are shown in the inset. $T_{Cb} = 292.5$ K. The inflection points of the ESR intensity curves are a strong evidence for a ferromagnetic ordering of the monolayer. Θ_A is an adsorbate coverage parameter [87F].

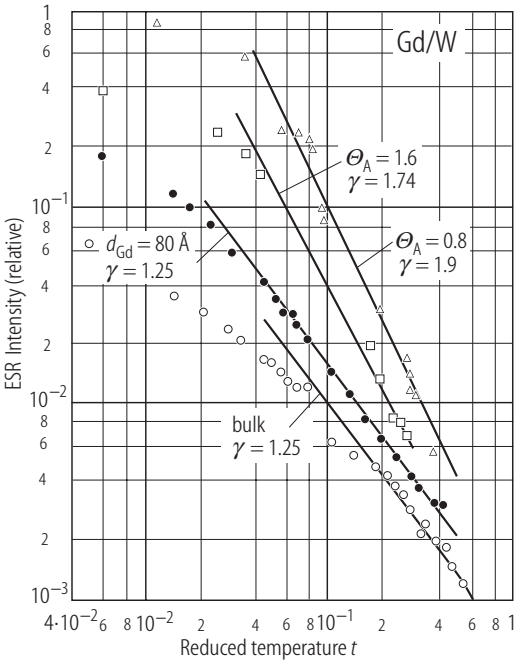

Fig. 113. Log-log plot of the ESR intensity [$\alpha\chi(0)$] of Gd on W(110) for $T > T_C$. Straight lines are best fits by a power law $\chi(0) \alpha t^{-\gamma}$, where $t = (T - T_C)/T_C$ with $\gamma \approx 1.8$ for a monolayer and $\gamma \cong 1.25$ for an 80 Å film. This agrees well with the theoretical γ of 2D ($\gamma = 1.8$) and 3D ($\gamma = 1.25$) Ising system, respectively. Θ_A is the adsorbate coverage [87F].

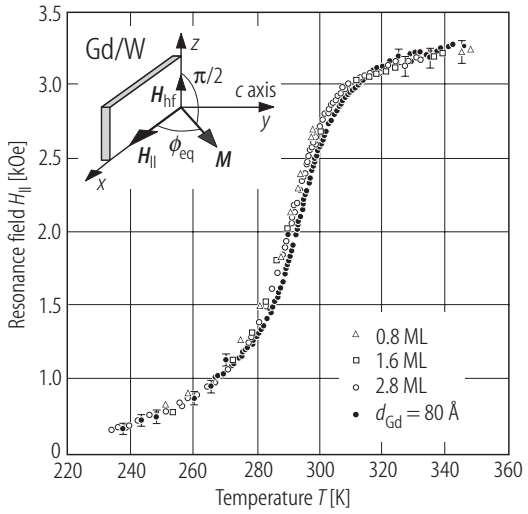

Fig. 114. Magnetic resonance fields at 9 GHz for epitaxial layers Gd (0001)/W(110) as a function of temperature for various thicknesses of magnetic monolayer (ML). The dc magnetic field $H_{||}$ is applied in the film plane (inset). In uniaxial symmetry the orientation of M is given by ϕ_{eq}. For all layer thicknesses a shift to lower magnetic fields with decreasing temperature is observed. This shift to lower resonance fields indicates that the effective magnetization M_{eff} inverses in the plane when the temperature is lowered through T_C.The magnetization lies completely in the film plane ($\phi_{eq} = 0$) opposite to the behaviour of bulk Gd [89F1].

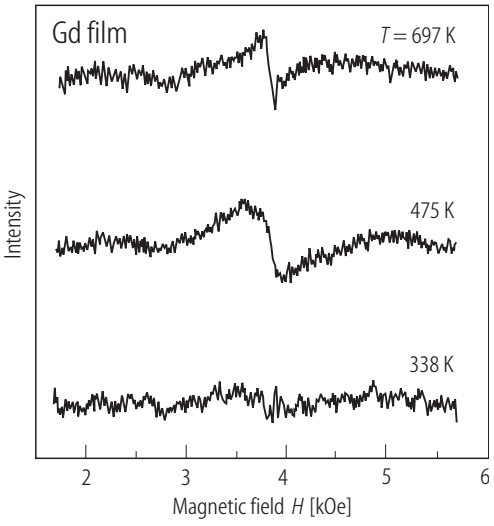

Fig. 115. EPR spectra of Gd-containing Langmuir-Blodgett (LB) film during heating. The plane of the film is perpendicular to the external magnetic field [97T].

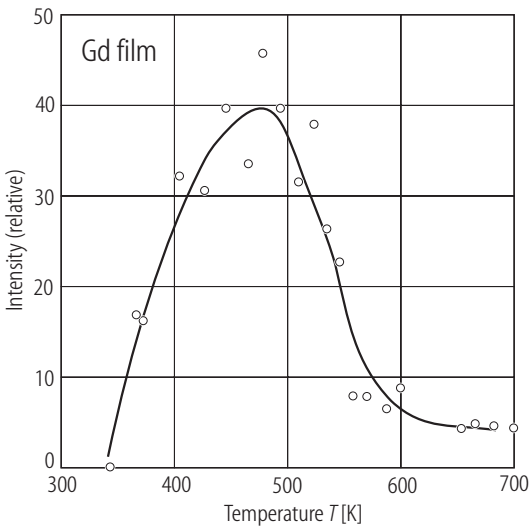

Fig. 116. Temperature dependencies of the EPR signal intensity in Gd-containing LB film during heating. Solid line is guide for the eye [97T].

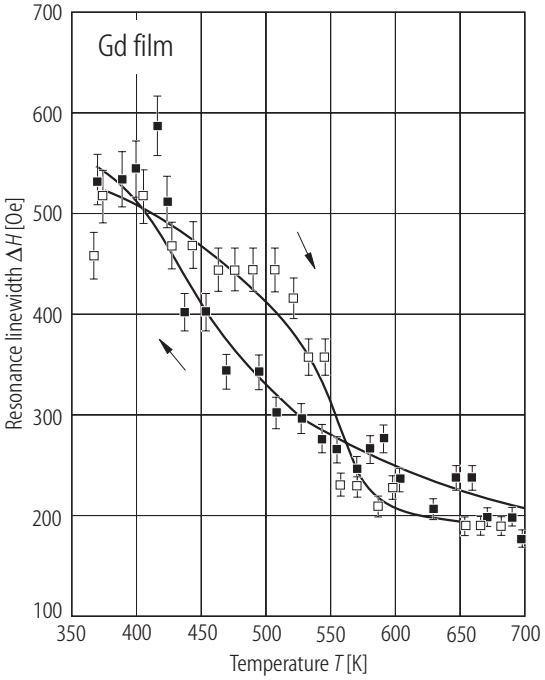

Fig. 117. Linewidth of the EPR line as a function of temperature in Gd-containing LB film. Open and closed squares denote temperature increasing and decreasing processes, correspondingly [97T].

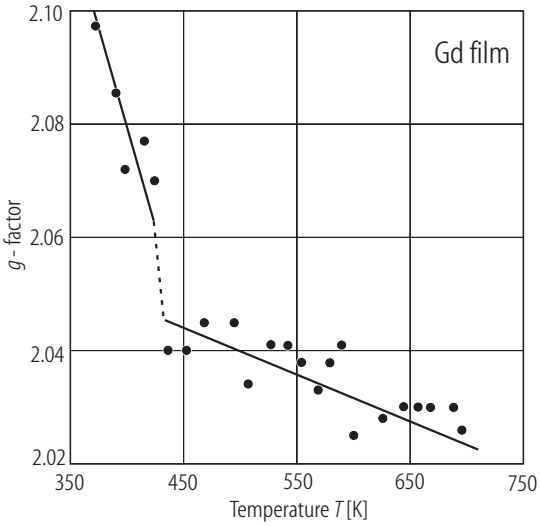

Fig. 118. *g* value of the EPR line in Gd-containing LB film as a function of temperature during cooling [97T].

References

74W Wells, P., Lanchester, P.C., Jones, D.W., Jordan, R.G.: J. Phys. F **4** (1974) 1729

85T Tsang,T-W., Gschneidner jr., K.A., Schmidt, F.A., Thome, D.K.: Phys. Rev. B **31** (1985) 235

86Ch Chowdhury, A.R., Collins, G.S., Hohenemser, C.: Phys. Rev. B **33** (1986) 5070

86P Ponomarev, B.K.: J. Magn. Magn. Mater. **61** (1986) 129

86R Rau, C., Eichner, S.: Phys. Rev. B **34** (1986) 6347

87F Farle, M., Baberschke, K.: Phys. Rev. Lett. **58** (1987) 511

87H Hill, R.W., Collocott, S.J., Gschneidner jr., K.A., Schmidt, F.A.: J. Phys. F **17** (1987) 1867

87K Kwo, J., Hong, F.J., DiSalvo, F.J., Waszczak, J.V., Majkrzak, C.F.: Phys. Rev. B **35** (1987) 7295

88N Nakamura, O., Baba, K., Ishii, H., Takeda, T.: J. Appl. Phys. **64** (1988) 3614

89F1 Farle, M., Berghaus, A., Baberschke, K.: Phys. Rev. B **39** (1989) 4838

89G Geldart, D.J., Hargraves, P., Fujiki, N.M., Dunlap, R.A.: Phys. Rev. Lett. **62** (1989) 2728

90H Hartmann, O., Wäppling, R., Karlsson, E., Kalvius, G.M., Asch, L., Litterst, F.J., Aggarwal, K., Münch, K.H., Gygax, F.N., Schenck, A.: Hyperfine Interactions **64** (1990) 369

90S Salas, F.H., Mirabal-Garcia, M.: Phys. Rev. B **41** (1990) 10859

91L Dongqi Li, Hutchings, C.W., Dowben, P.A., Hwang, C., Rong-Tzong Wu, Onellion, M., Andrews, A.B., Erskine, J.L.: J. Magn. Magn. Mater. **99** (1991) 85

91S Nobuhiko Sakai, Yoshikazu Tanaka, Fumitake Itoh, Hiroshi Sakurai, Hiroshi Kawata, Toshiaki Iwazumi: J. Phys. Soc. Jpn. **60** (1991) 1201

91W Ruqian Wu, Freeman, A.J.: J. Magn. Magn. Mater. **99** (1991) 81

91W1 Ruqian Wu, Chun Li, Freeman, A.J., Fu, C.L.: Phys. Rev. B **44** (1991) 9400

92D Dongqi Li, Jiandi Zhang, Dowben, P.A., Onellion, M.: Phys. Rev. B **45** (1992) 7272

92M Mulhollan, G.A., Garrison, K., Erskine, J.L.: Phys. Rev. Lett. **69** (1992) 3240

93P Paschen, U., Sürgers, C., v. Löhneysen, H.: Z. Phys. B **90** (1993) 289

93S2 Starke, K., Navas, E., Baumgarten, L., Kaindl, G.: Phys. Rev. B **48** (1993) 1329

93T1 Tang, H., Weller, D., Walker, T.G., Scott, J.C., Chappert, C., Hopster, H., Pang, A.W., Dessau, D.S., Pappas, D.P.: Phys. Rev. Lett. **71** (1993) 444

93V Vescovo, E., Carbone, C., Rader, O.: Phys. Rev. B **48** (1993) 7731

94A Aspelmeier, A., Gerhardter, F., Baberschke, K.: J. Magn. Magn. Mater. **132** (1994) 22

94F Farle, M., Lewis, W.A.: J. Appl. Phys. **75** (1994) 5604

94P Pang, A.W., Berger, A., Hopster, H.: Phys. Rev. B **50** (1994) 6457

95A Arenholz, E., Navas, E., Starke, K., Baumgarten, L., Kaindl, G.: Phys. Rev. B **51** (1995) 8211

95B1 Berger, A., Pang, A.W., Hopster, H.: Phys. Rev. B **52** (1995) 1078

95G Gajdzik, M., Paschen, U., Sürgers, C., v. Löhneysen, H.: Z. Phys. B **98** (1995) 541

96D Dan'kov, S.Y., Spichkin, Yu.I., Tishin, A.M.: J. Magn. Magn. Mater. **152** (1996) 208

96H Harkins, J.V., Donovan, P.: J. Magn. Magn. Mater. **156** (1996) 224

96J Jiang, J.S., Chien, C.L.: J. Appl. Phys. **79** (1996) 5615

96M Mulyukov, Kh.Ya., Korznikova, G.F., Nikitin, S.A.: J. Magn. Magn. Mater. **153** (1996) 241

97H Helgsen, G., Tanaka, Y., Hill, J.P., Wochner, P., Gibbs, D., Flynn, C.P., Salamon, M.B. Phys. Rev. B **56** (1997) 2635

97L Li, Yi, Polaczyk, C., Kapoor, J., Riegel, D.: J. Magn. Magn. Mater. **165** (1997) 165

97T Tishin, A.M., Koksharov, Yu.A., Bohr, J., Khomutov, G.B.: Phys. Rev. B **55** (1997) 11064

98D Dan'kov, S.Yu., Tishin, A.M., Pecharsky, V.K., Gschneidner jr., K.A.: Phys. Rev. B **57** (1998) 3478

98G Gajdzik, M., Trappmann, T., Sürgers, C., v. Löhneysen, H.: Phys. Rev. B **57** (1998) 3525

2.1.3.7 Terbium

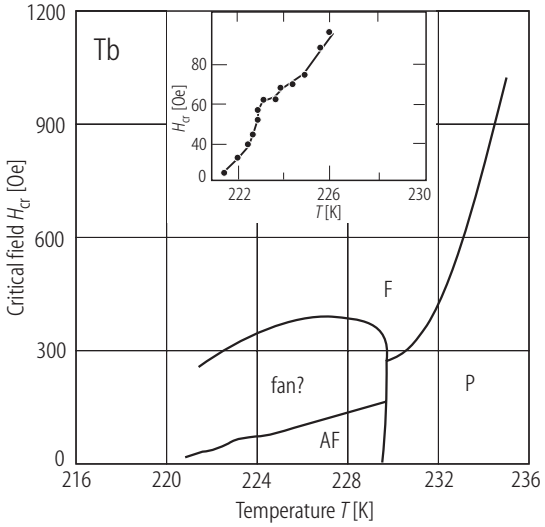

Fig. 119. Magnetic phase diagram of Tb single crystal determined from the elasticity modulus measured by means of the flexural oscillation method at frequencies of 1 kHz to 2 kHz in a spinoidal magnetic field up to 2.5 kOe. The inset shows the anomaly in the temperature dependence of the critical field of helical antiferromagnetic structure destruction [89K].

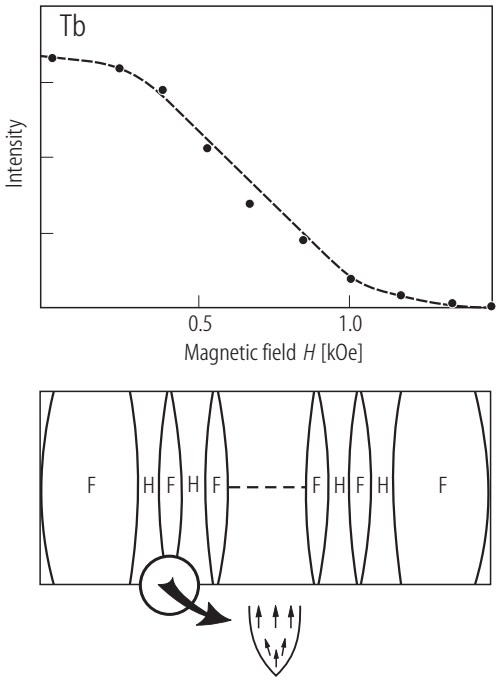

Fig. 120. Evolution as a function of the applied magnetic field of the magnetic satellite integrated intensity from a rectangular platelet shaped crystal of Tb. In the inset a schematic drawing of the interfaces observed, as well as the assumed magnetization rotation near the tips of the needle shaped ferromagnetic regions are illustrated. The helimagnetic phase region occupies the whole sample at zero field, whereas the ferromagnetic phase does it for an applied field higher than 0.15 T [89B].

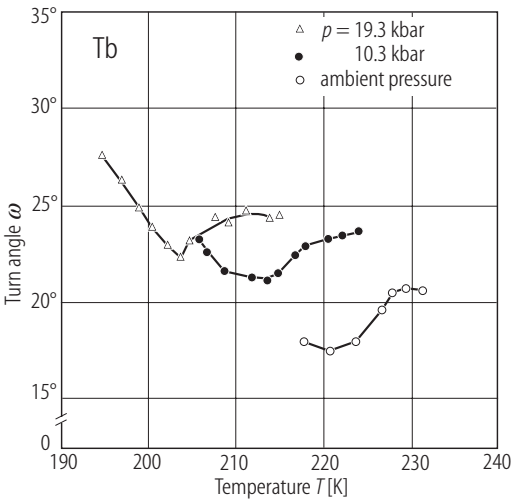

Fig. 123. Temperature dependence of turn angles of the helical structure of Tb under pressure 10.3 kbar and 19.3 kbar, on the warming process [92K].

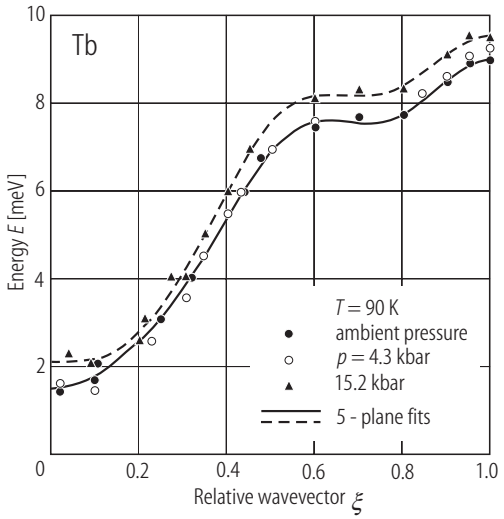

Fig. 121. Magnon dispersion relations for ferromagnetic Tb along the *c* axis at 90 K at ambient pressure and under 4.3 and 15.2 kbar. The solid and dotted lines shown in this figure represent the result of a least-squares fit [94K].

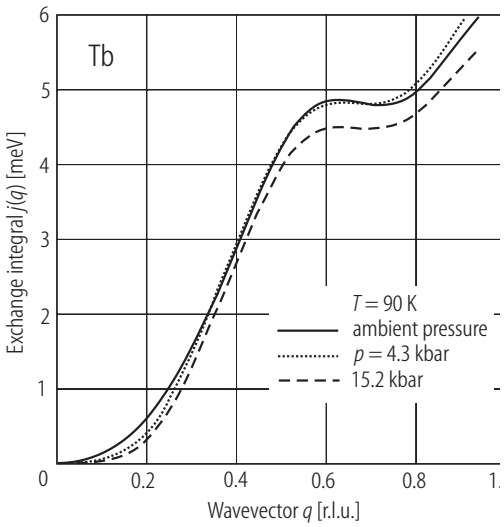

Fig. 122. The Fourier transformed exchange $j(q) = J\,[J(q) - J(0)]$ in the *c* direction deduced for ferromagnetic Tb from the magnon measurements at 90 K under (**a**) ambient pressure, (**b**) 4.3 kbar, and (**c**) 15.2 kbar. The values of q are expressed in reciprocal lattice units (r.l.u.) [94K].

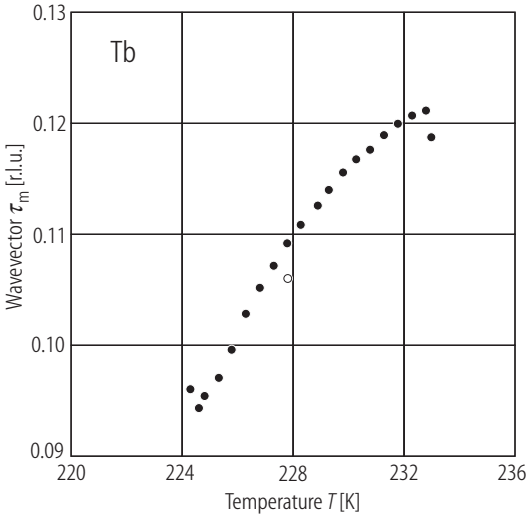

Fig. 124. Temperature dependence of the magnetic modulation wavevector τ_m of Tb. The open circle indicates the change in τ_m after quenching the sample from well into the paramagnetic state. Here 1 r.l.u. = 1.1036 $Å^{-1}$. Over the entire temperature range the modulation warevector τ_m lies between 0.0947 and 0.1213 r.l.u. corresponding to the variation in the turn angle from 17.0° to 21.8° [92G].

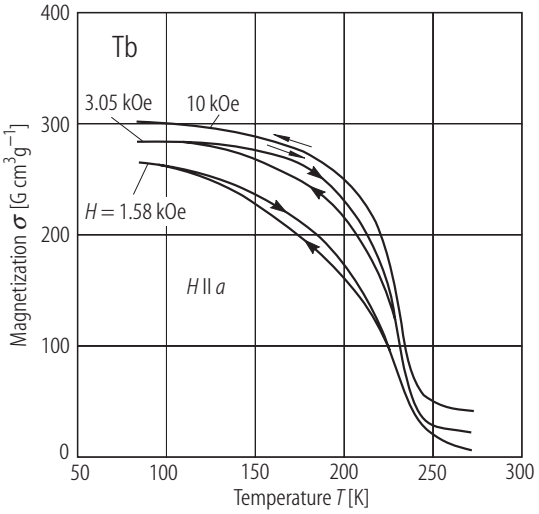

Fig. 125. Temperature dependence of the magnetization of Tb monocrystal in the case of fixed magnetic fields ($H||a$): H = 1.58, 3.05, and 10 kOe [96D].

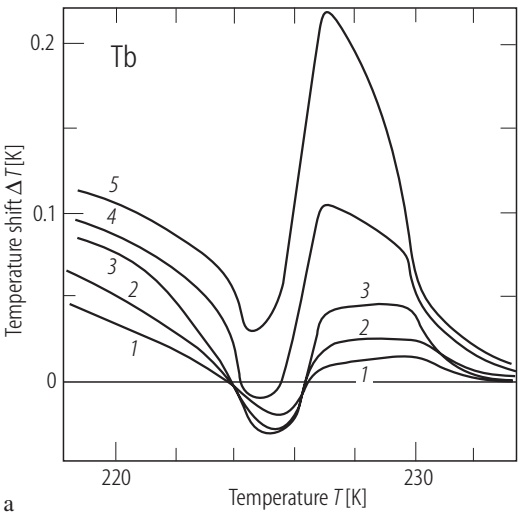

a

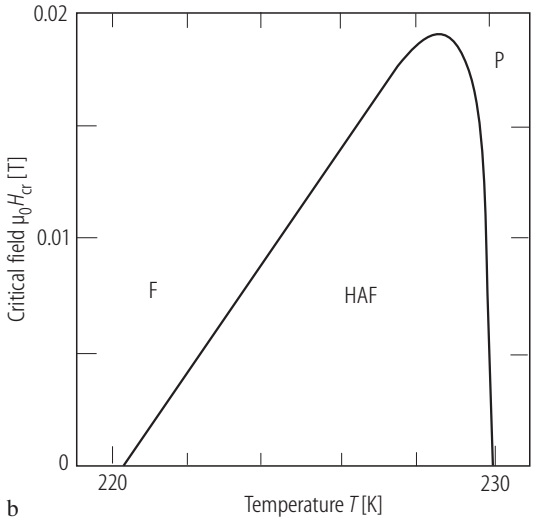

b

Fig. 126. (**a**) Dependence of the magnetocaloric effect (MCE) in Tb single crystals on temperature in a field || b; $\mu_0 H$ = 0.02 (*1*), 0.025 (*2*), 0.03 (*3*), 0.035 (*4*), 0.04 T (*5*).(**b**) Magnetic phase diagram of Tb single crystals determined from MCE results. P: paramagnetic phase; HAF: helical antiferromagnetic structure; F: ferromagnetic phase [89N].

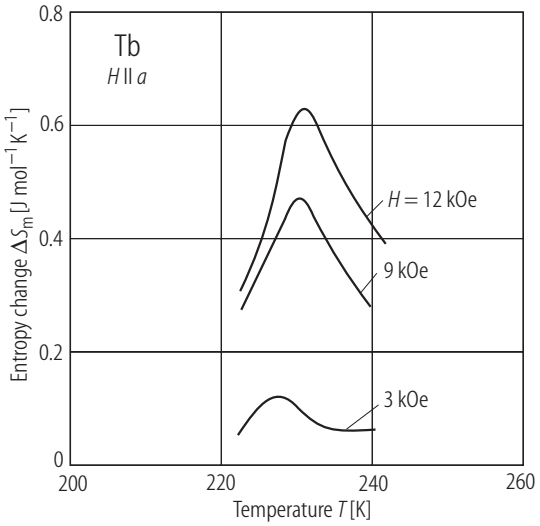

Fig. 127. Temperature dependence of the magnetic entropy change for Tb monocrystal ($H \| a$): H = 12, 9 and 3 kOe [96D].

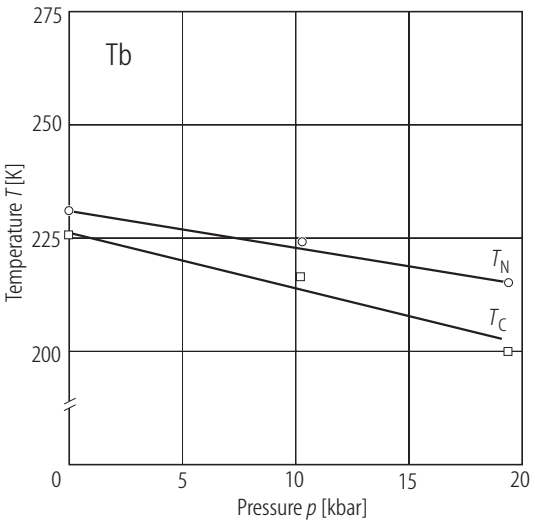

Fig. 129. Pressure dependence of transition Néel temperature, T_N and T_C (transition of the helix-planar ferromagnetic) for Tb studied by neutron diffraction [92K].

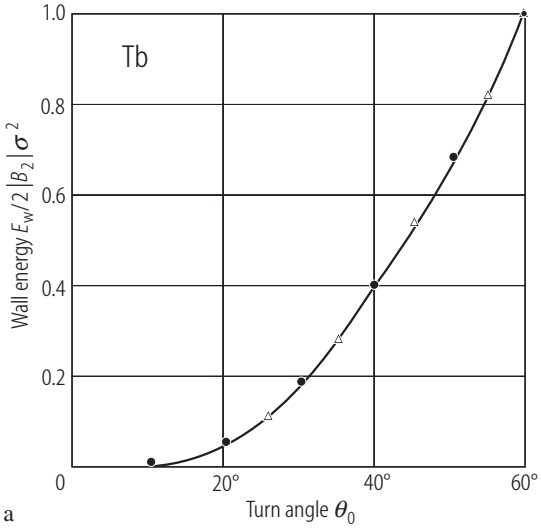

a

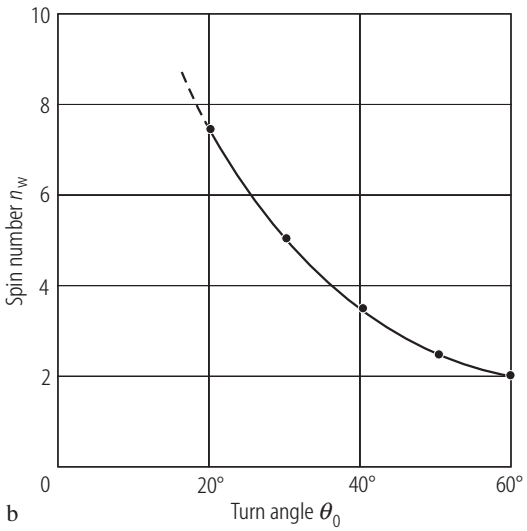

b

Fig. 128. (**a**) Minimum value of the domain wall energy $E_w/2\,|B_2|\,\sigma^2$ for Tb metal plotted as a function of turn angle θ_0. Open symbols indicate previous results.

(**b**) A plot of n_w for the minimum energy of an AF domain wall as a function of θ_0 (n_w is the number of spins in the wall) [91McK].

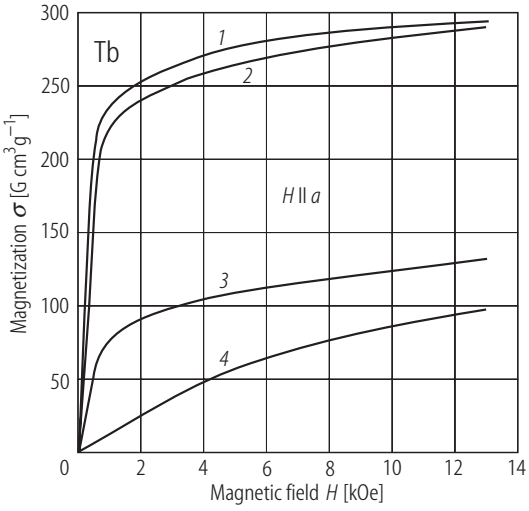

Fig. 130. Curves of the Tb single crystal magnetization at $H||a$ and various pressures:
(*1*) $T = 80$ K, $p = 10^6$ dyn cm^{-2};
(*2*) $T = 80$ K, $p = 8 \cdot 10^9$ dyn cm^{-2};
(*3*) $T = 228$ K, $p = 10^6$ dyn cm^{-2};
(*4*) $T = 228$ K, $p = 9.5 \cdot 10^9$ dyn cm^{-2} [91N1].

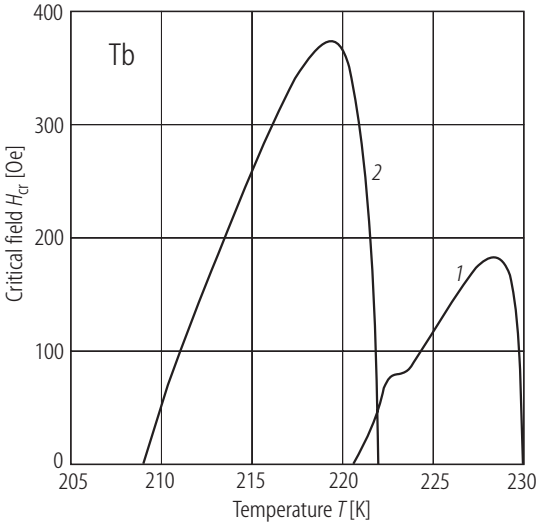

Fig. 131. Magnetic phase diagram of a Tb single crystal under pressure:
(*1*) $p = 10^6$ dyn cm^{-2} and (*2*) 10^{10} dyn cm^{-2} [91N1].

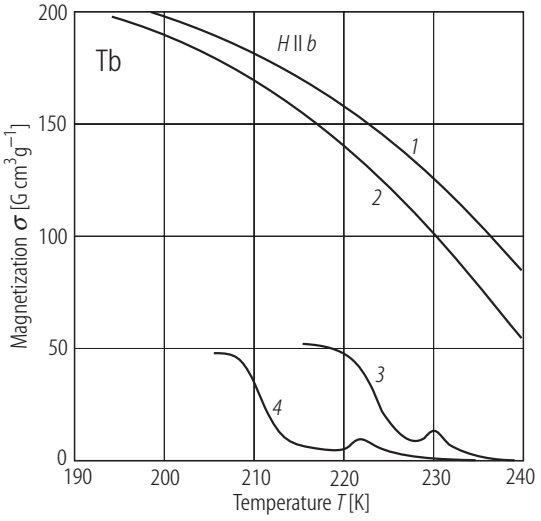

Fig. 132. Dependence of specific magnetization of a Tb single crystal for $H||b$ (easy axis) on temperature at different values of magnetic field and pressure:
(*1*) $H = 13$ kOe, $p = 10^6$ dyn cm^{-2};
(*2*) $H = 100$ Oe , $p = 10^{10}$ dyn cm^{-2};
(*3*) $H = 100$ Oe, $p = 10^6$ dyn cm^{-2};
(*4*) $H = 100$ Oe, $p = 10^{10}$dyn cm^{-2} [91N1].

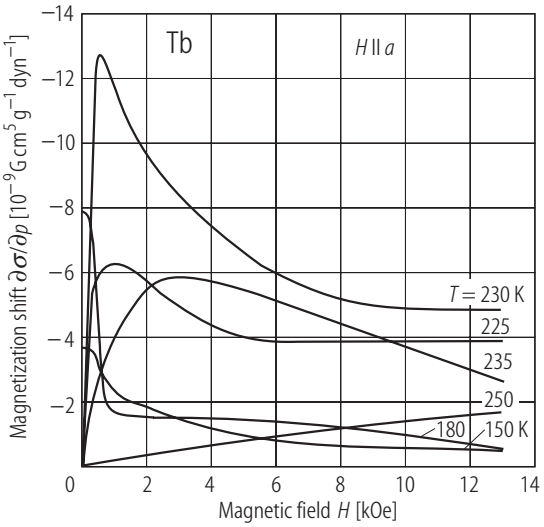

Fig. 133. Dependence of the Tb $\Delta\sigma = (\sigma - \sigma_0)$ effect on the magnetic field $H||a$: σ is the specific magnetization at temperature T and pressure p; σ_0 is the magnetization at 0 K [91N1].

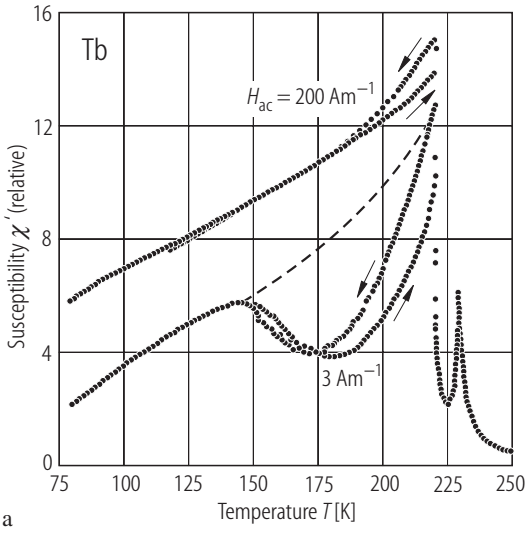

a

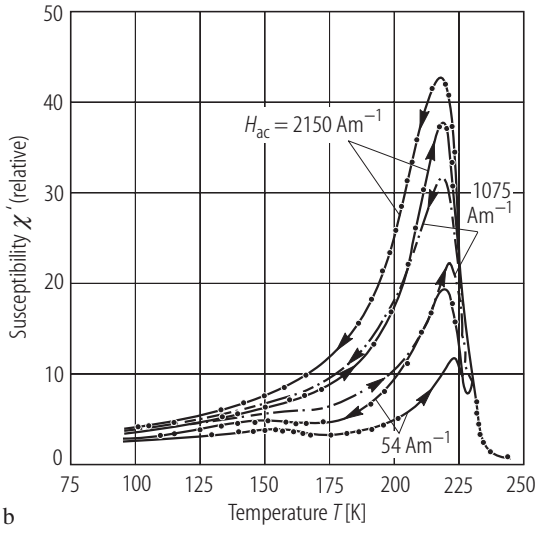

b

Fig. 134. Warming and cooling ac susceptibility runs (≈ 0.2 K min^{-1}) for (**a**) single crystal Tb, H_{ac} = 3 A m^{-1} and 200 A m^{-1}, ν = 1 kHz), and (**b**) for polycrystalline Tb primary field H_{ac} = 54 A m^{-1} (full line), 1075 A m^{-1} (broken line) and 2150 A m^{-1} (full line); ν = 100 Hz). Besides the transitions at T_N = 229 K from paramagnetism to helical spin antiferromagnetism a broad peak in susceptibility at 150 K is observed [93McK].

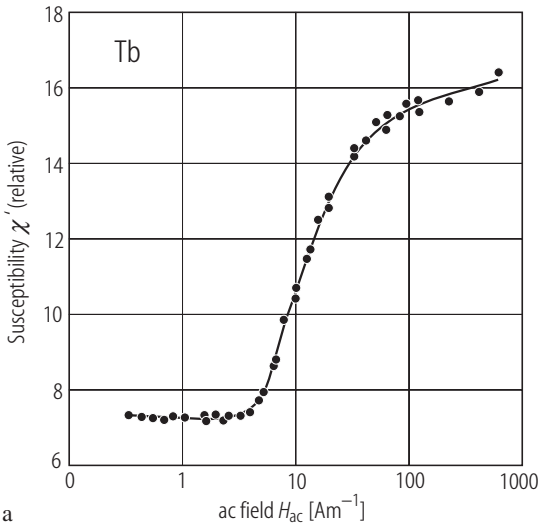

a

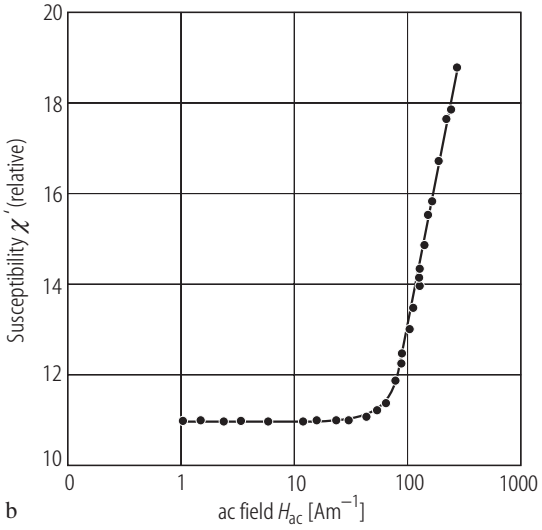

b

Fig. 135. Field dependence of χ' for (**a**) single crystal Tb at a constant temperature (T ≈ 207 K) in the ferromagnetic region (ν = 99 Hz), and (**b**) for polycrystalline Tb at T ≈ 204 K (ν = 493 Hz) [93McK].

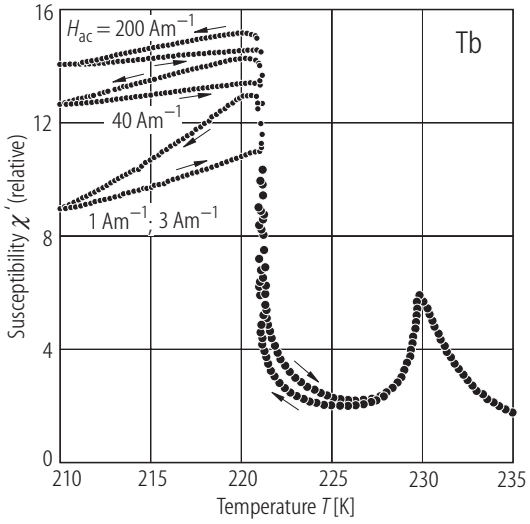

◀

Fig. 136. ac magnetic susceptibility of single crystal Tb as a function of temperature in the critical region for several applied fields:
H_{ac} = 1, 3, 40 and 200 Am^{-1}. The warming runs were started at $T \approx 210$ K. All experiments were performed at a rate of ≈ 0.15 K min^{-1} and at a primary frequency ν = 1 kHz [93McK].

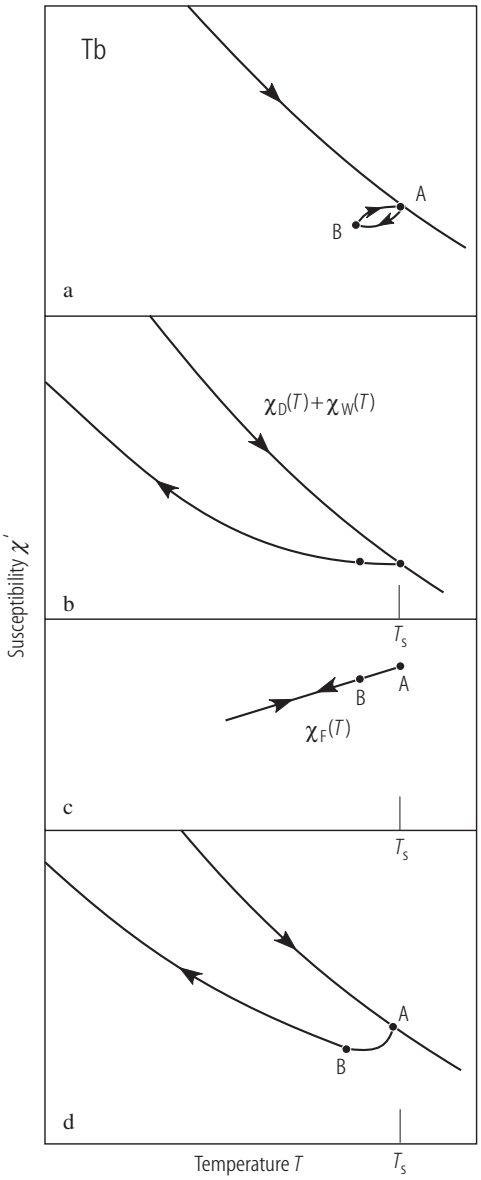

◀

Fig. 137. (**a**) Schematic representation of the behaviour of susceptibility in a temperature modulation cycle AB on warming from the ferromagnetic region to the AF region of Tb metal. Such an effect is expected when the observed polarity of $S_\uparrow \equiv (\Delta\chi'/\Delta T)_\uparrow$ is opposite to that of the analytical derivative $(d\chi'/dT)_\uparrow$. (**b**) Illustration of the hysteresis expected in $\chi_D(T) + \chi_W(T)$ for warming to a temperature T_s in the AF region followed by recooling. Points A and B indicate the limits of a temperature modulation cycle. (**c**) Plot of the temperature dependence of the contribution to susceptibility of $\chi_F(T)$ (or of $\chi_{WF}(T)$), (**d**) Predicted behaviour of $\chi'(T)$. χ_D: susceptibility within the spiral spin domains, χ_W and χ_{WF}: AF- and F- domain walls contribution, respectively, χ_F: F-islands contribution [91McK].

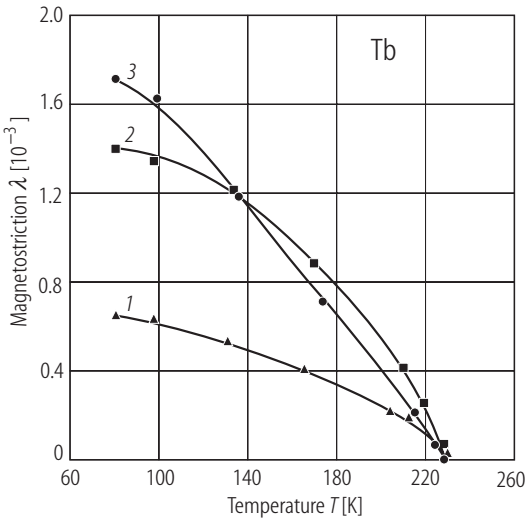

◀

Fig. 138. Temperature dependence of magnetostriction of Tb measured in a field 980 kA m^{-1}: (*1*) submicrocrystalline state, (*2*) after annealing at 573 K, (*3*) after annealing at 1073 K [97M].

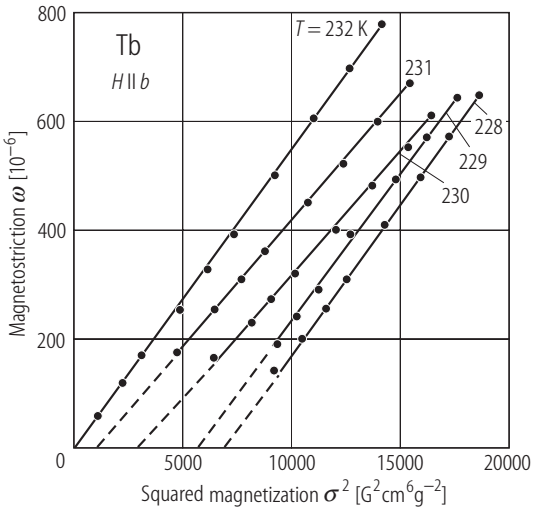

Fig. 139. Dependence of the Tb volume magnetostriction on the square of a specific magnetization value in the vicinity of the Néel point in the magnetic field $H \| b$: T = 232, 231, 230, 229, and 228 K [91N1].

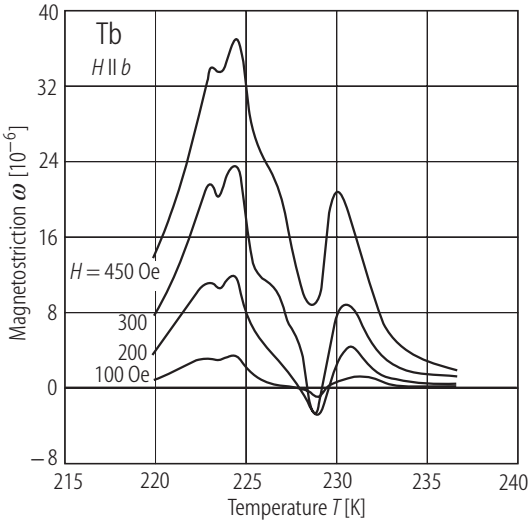

Fig. 140. Dependence of the Tb volume magnetostriction on temperature in the magnetic field $H \| b$ [91N1].

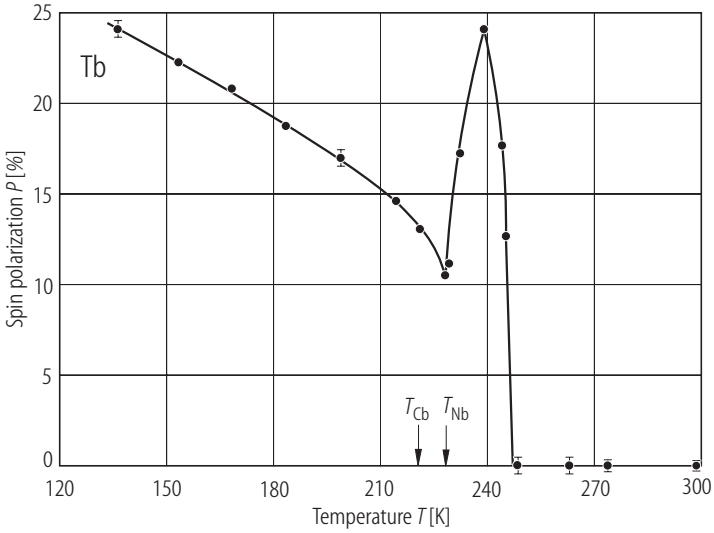

Fig. 142. Magnetic order at surfaces of Tb metal investigated by electron capture spectroscopy (ECS) which probes the electron spin polarisation of the topmost surface layer of 1 mm-thick Tb samples as function of temperature. T_{Cb} denotes the bulk Curie temperature as determined using ferromagnetic induction and the magnetooptical Kerr effect. T_{Nb} denotes the bulk Néel temperature of Tb [88R].

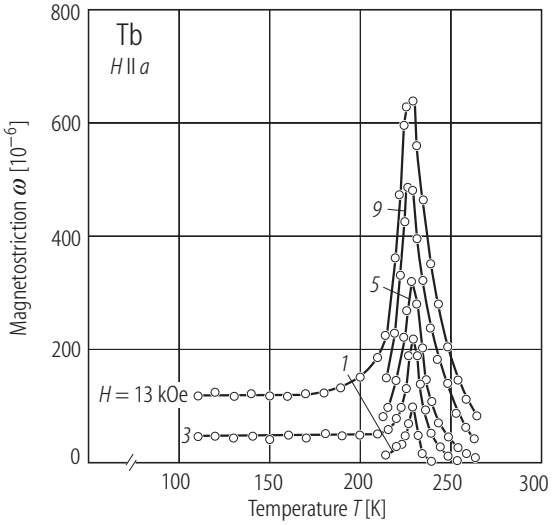

Fig. 141. Dependence of the Tb volume magnetostriction on temperature in the magnetic field $H \| a$: H = 13, 9, 5, 3, and 1 kOe [91N1].

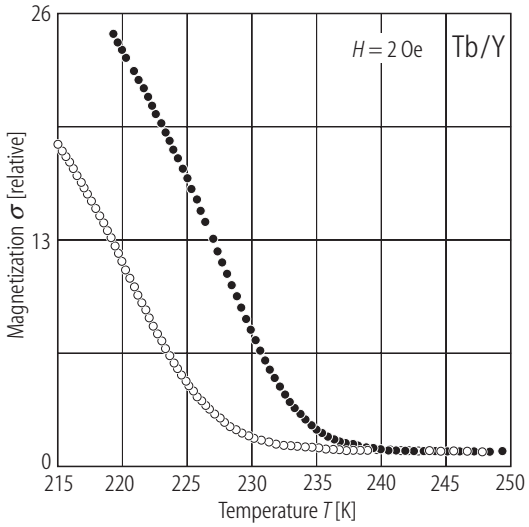

Fig. 144. Thermal dependence of the magnetization of 1000 Å Tb film epitaxially grown on Y (solid circles), and Tb (26 Å)/Y(44 Å) superlattice (open circles) under 2 Oe magnetic applied in the basal plane. Tb directly undergoes a transition from the paramagnetic phase to the ferromagnetic one whereas there is no ferromagnetic long range order in the superlattice [95D].

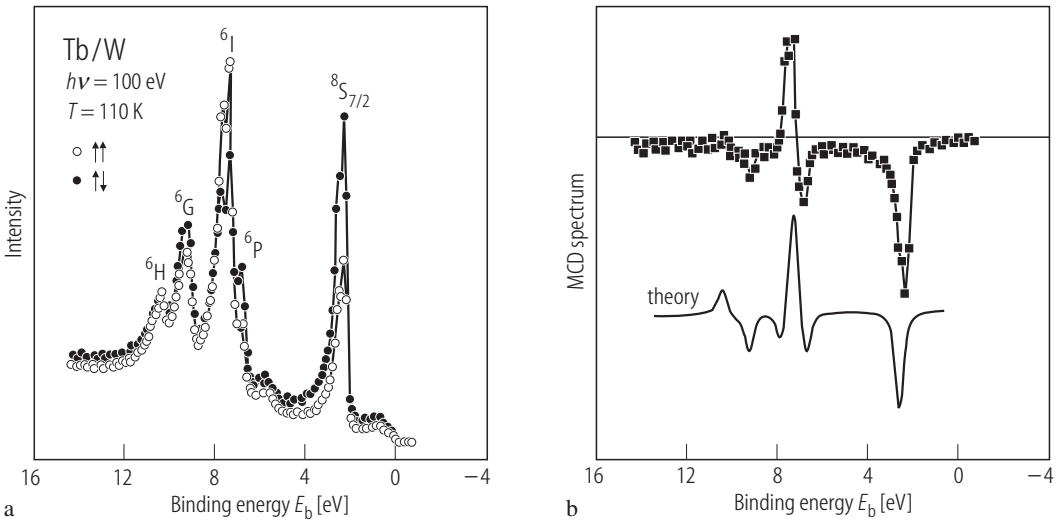

Fig. 143. (**a**) Tb 4f photoemission (PE) spectra ($h\nu$ = 100 eV) of a remanently magnetized Tb(0001)/W(110) film (150 Å thick; T = 110 K). Open (solid) circles are for nearly parallel (antiparallel) orientation of photon spin and sample magnetization. (**b**) Solid squares: Intensity difference of the experimental magnetic circular dichroism (MCD) spectra in (**a**); the solid curve at the bottom of (**b**) reproduces the theoretical MCD spectrum [95A].

References

88R Rau, C., Jin, C., Robert, M.: J. Appl. Phys. **63** (1988) 3667

89B Baruchel, J., Sandonis, J. Pearce, A.: Physica B **156-157** (1989) 765

89K Kataev, G.I., Sattarov, M.R.,Tishin, A.M.: Phys. Status Solidi (a) **114** (1989) K79

89N Nikitin, S.A., Tishin, A.M., Bykhover, S.E.: Phys. Status Solidi (a) **114** (1989) K99

91McK McKenna, T.J., Campbell, S.J., Chaplin, D.H., Wilson, G.V.H.: J. Phys.: Condens. Matter **3** (1991) 1855

91N1 Nikitin, S.A., Tishin, A.M., Bezdushnyi, R.V., Spichkin, Yu.I., Red'ko, S.V.: J. Magn. Magn. Mater. **92** (1991) 397

92G Gehring, P.M., Rebelsky, L., Gibbs, D., Shirane, G.: Phys. Rev. B **45** (1992) 243

92K Kawano, S., Achiwa, N., Onodera, A., Nakai, Y.: Physica B **180-181** (1992) 46

93McK McKenna, T.J., Campbell, S.J., Chaplin, D.H., Wilson, G.V.H.: J. Magn. Magn. Mater. **124** (1993) 105

94K Kawano, S., Fernandez-Baca, J.A., Nicklow, R.M.: J. Appl. Phys. **75** (1994) 6060

95A Arenholz, E., Navas, E., Starke, K., Baumgarten, L., Kaindl, G.: Phys. Rev. B **51** (1995) 8211

95D Dufour, C., Dumesnil, K., Vergnat, M., Mangin, Ph., Marchal, G., Hennion, M.: J. Magn. Magn. Mater. **140-144** (1995) 771

96D Dan'kov, S.Y., Spichkin, Yu.I., Tishin, A.M.: J. Magn. Magn. Mater. **152** (1996) 208

97M Mulyukov, K.Ya, Korznikova, G.F., Sharipov, I.Z.: Phys. Status Solidi (a) **161** (1997) 493

2.1.3.8 Dysprosium

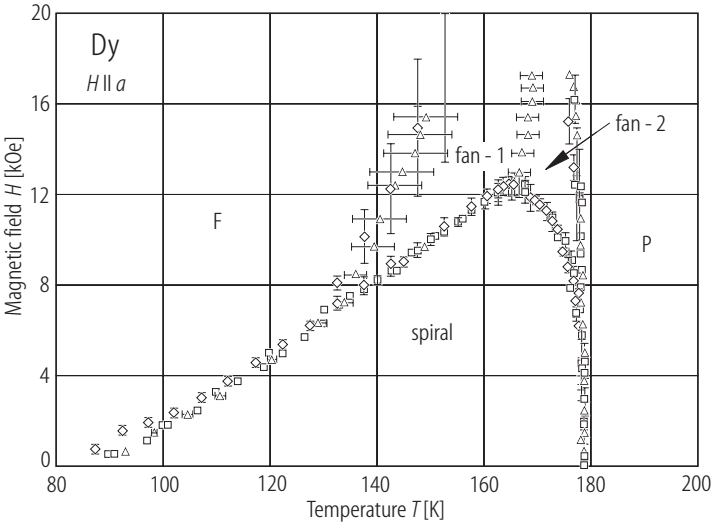

Fig. 145. Magnetic phase diagram of Dy determined from anomalies in specific heat. Magnetic field is applied along the *a* axis [96I].

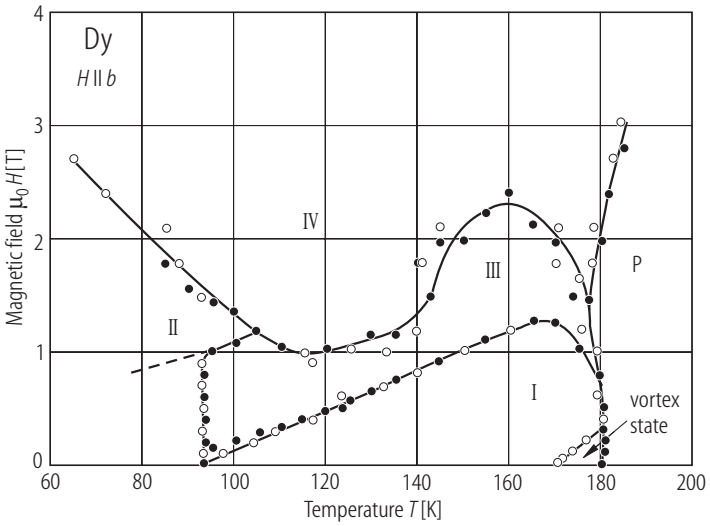

Fig. 146. Magnetic phase diagram of single crystal Dy with an applied field along the *b* axis. Five magnetic phases below the paramagnetic (P) phase are indicated, I-helical antiferromagnetic phase, II-angular ferromagnetic phase, III-fan phase, IV-collinear ferromagnetic phase, and the so-called vortex state. Open circles represent the data from magnetization as a function of temperature at fixed applied magnetic fields and solid circles represent the data from magnetization as a function of field at fixed temperatures [97A].

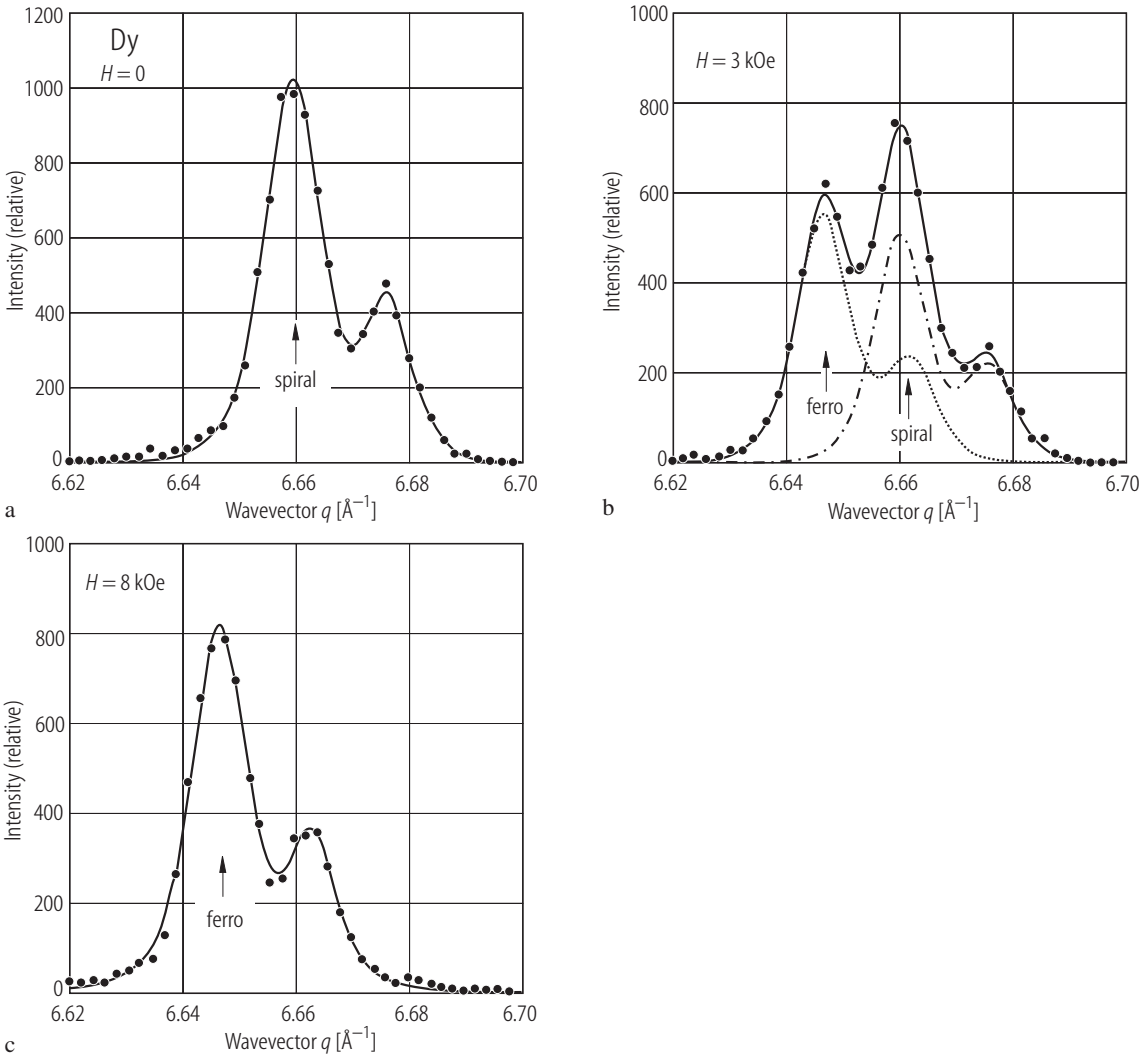

Fig. 147. Magnetic field dependence of the X-ray diffraction pattern of Dy at $T = 95$ K where the phase transition induced by magnetic field takes place. The (006) diffraction pattern along the c*-direction. (**a**) $H = 0$ (virgin state). Only a single hexagonal phase appears. Two peaks are caused by $K\alpha_1$ and $K\alpha_2$ lines of Cu target. The arrow indicates the position of hexagonal phase reflected by $K\alpha_1$ line. (**b**) $H = 3$ kOe. The diffraction profile for the coexistence of hexagonal and orthorhombic phases. Two arrows correspond to the hexagonal and orthorhombic phase reflected by $K\alpha_1$ line. (**c**) $H = 8$ kOe. The diffraction pattern corresponds to a single orthorhombic phase. The arrow corresponds to the orthorhombic phase reflected by $K\alpha_1$ line. The coexistence of the spiral and ferromagnetic phase is a typical case of the first order phase transition from spiral to ferromagnetic structure [95S].

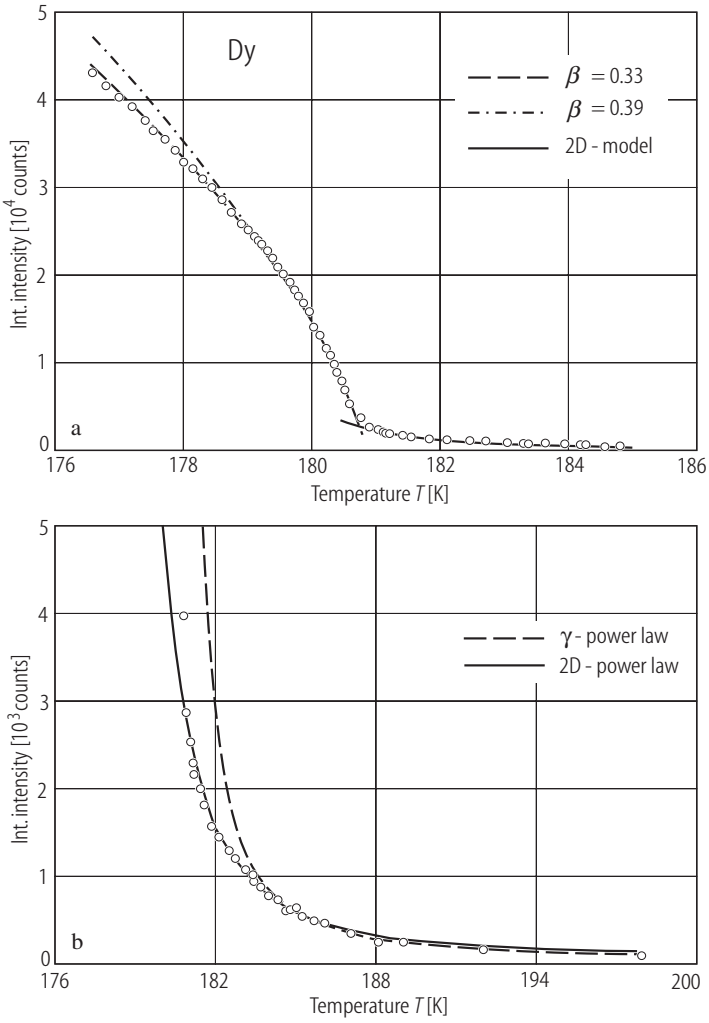

Fig. 148. Integrated intensity for the (0,0,2–δ) neutron reflection vs. temperature for Dy. In (**a**) fits to $(t_-)^{2\beta}$ dependence of the spontaneous magnetization in the ordered region and to a 2D-planar spin model in the paramagnetic region. In (**b**) fits to the persistent intensity observed in the paramagnetic region are indicated [95dP].

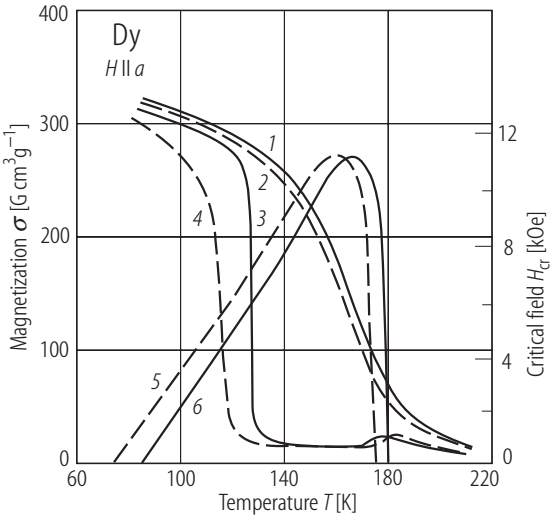

Fig. 149. Temperature dependencies of the specific magnetization and critical field H_{cr} for a Dy single crystal at $H \| a$ (the easy magnetization direction) and for various pressures; (*1*): H = 12 kOe, $p = 10^6$ dyn cm^{-2}; (*2*): H = 12 kOe, $p = 10^{10}$ dyn cm^{-2}; (*3*): H = 5 kOe, $p = 10^6$ dyn cm^{-2}; (*4*): H = 5 kOe, $p = 10^{10}$ dyn cm^{-2}; critical fields: (*5*) $p = 10^{10}$ dyn cm^{-2}, (*6*) $p = 10^6$ dyn cm^{-2}. The magnetic field shifts the temperature Θ_1 towards higher and the pressure towards lower temperature [91N].

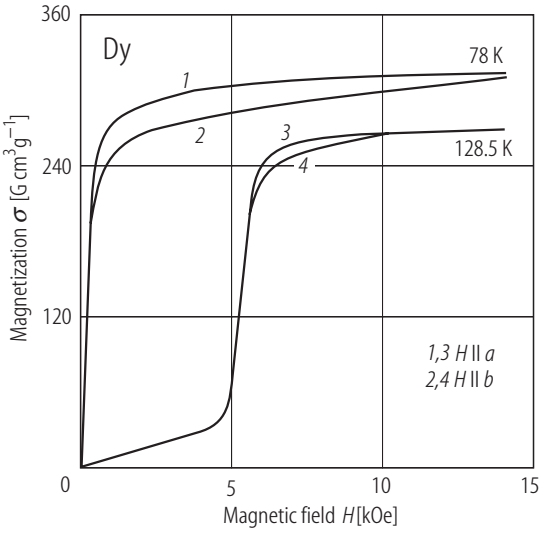

Fig. 150. Dependence of specific magnetization σ on the field under atmospheric pressure for a Dy single crystal. The sharp increase of σ at the critical value H_{cr} is caused by the destruction of helicoidal antiferromagnetism (see curves *3* and *4*) [91N].

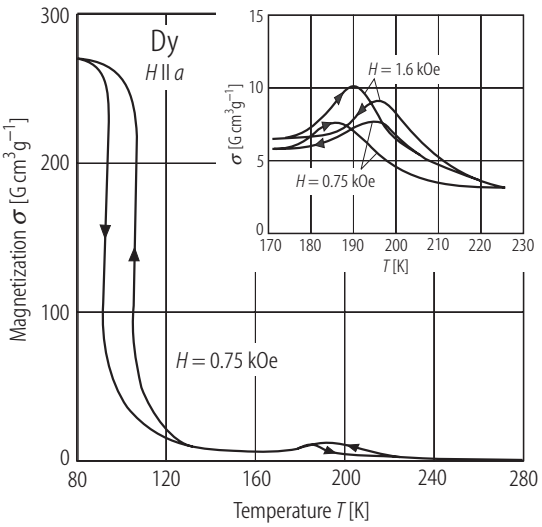

Fig. 151. Temperature dependence of the magnetization of Dy monocrystal in the case a fixed magnetic field of 0.75 kOe ($H \| a$). Inset: H = 1.6 kOe and 0.75 kOe [96D].

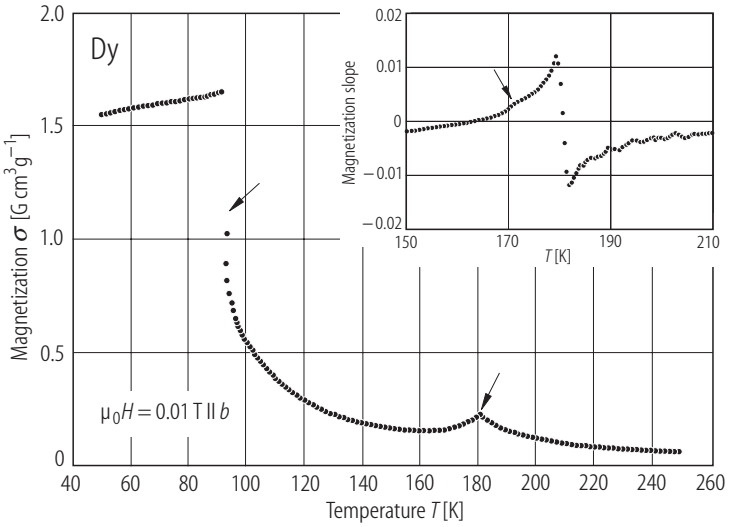

Fig. 152. Magnetization of Dy as a function of temperature at 0.01 T along the *b* axis, arrows indicate magnetic transitions. The inset is the slope of magnetization, the arrow shows the vortex transition [97A].

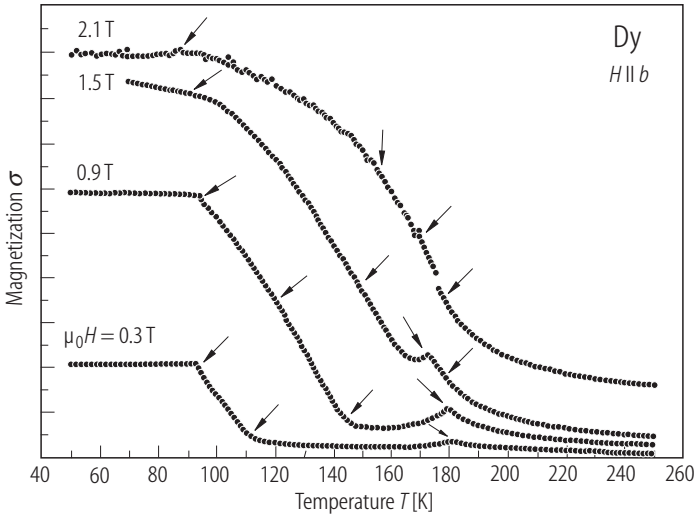

Fig. 153. Magnetization of Dy as a function of temperatures at $\mu_0 H = 0.3$, 0.9, 1.5, and 2.1 T along the b axis, arrows indicate magnetic transitions {97A].

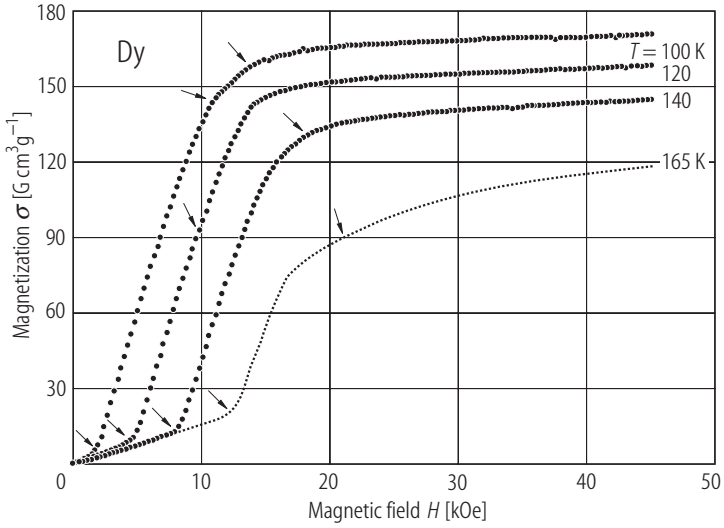

Fig. 154. Magnetization of Dy as a function of field along the b axis at T = 100, 120, 140, and 165 K, arrows indicate magnetic transitions [97A].

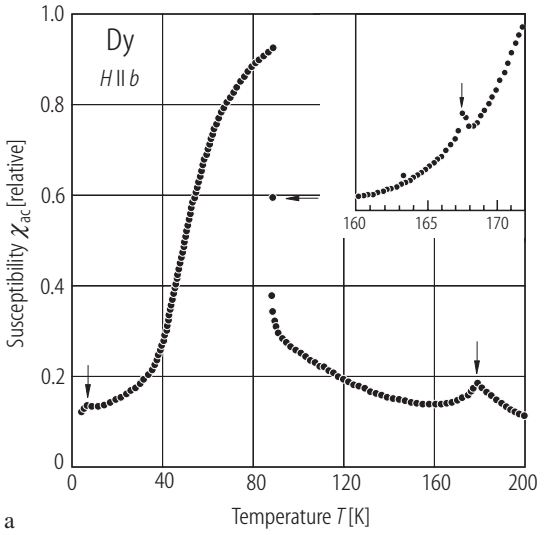

a

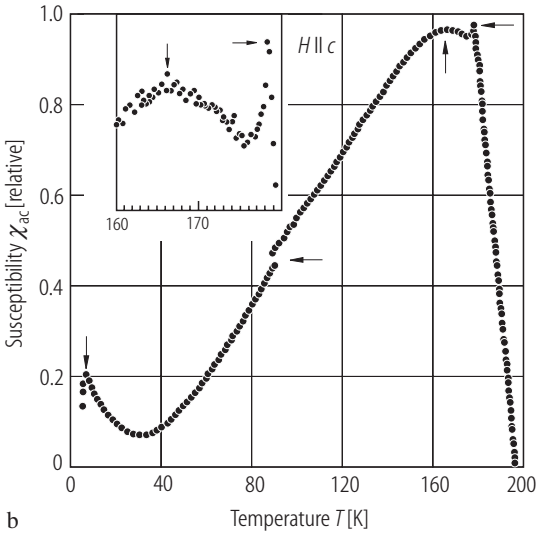

b

Fig. 155. Alternate-current susceptibility (χ_{ac} arbitrary units) of single-crystal Dy along the *b* (**a**) and *c* axis (**b**). T_C, T_N and the anomalies near 6.5 and 167 K are shown by arrows. The insets show the anomalies near 167 K. The anomaly is most likely due to the so-called "vortex state" of Dy what means that the long-range order associated with the antiferromagnetic state has not fully developed [91W2].

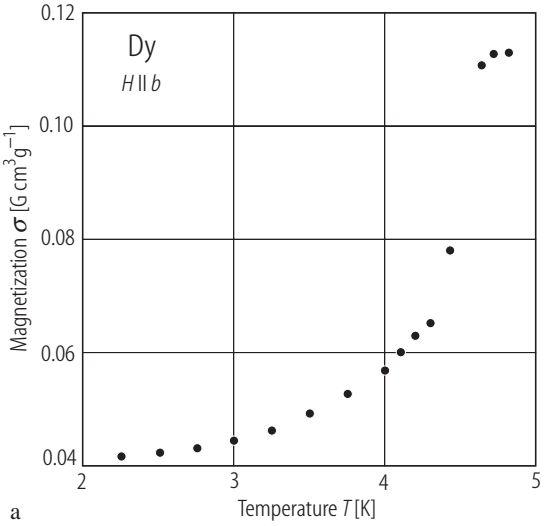

a

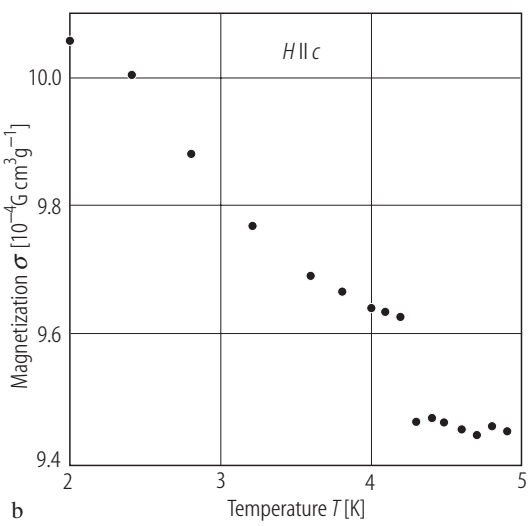

b

Fig. 157. Magnetization as a function of temperature along the *b* (**a**) and *c* axis (**b**) of single crystal Dy in an applied field (0.002 T). The anomalies in the magnetization at $T = 4.3$ K and ac susceptibility at $T = 6.5$ K are due to a lifting of a component of the magnetic moment of Dy onto the *c* axis [91W2].

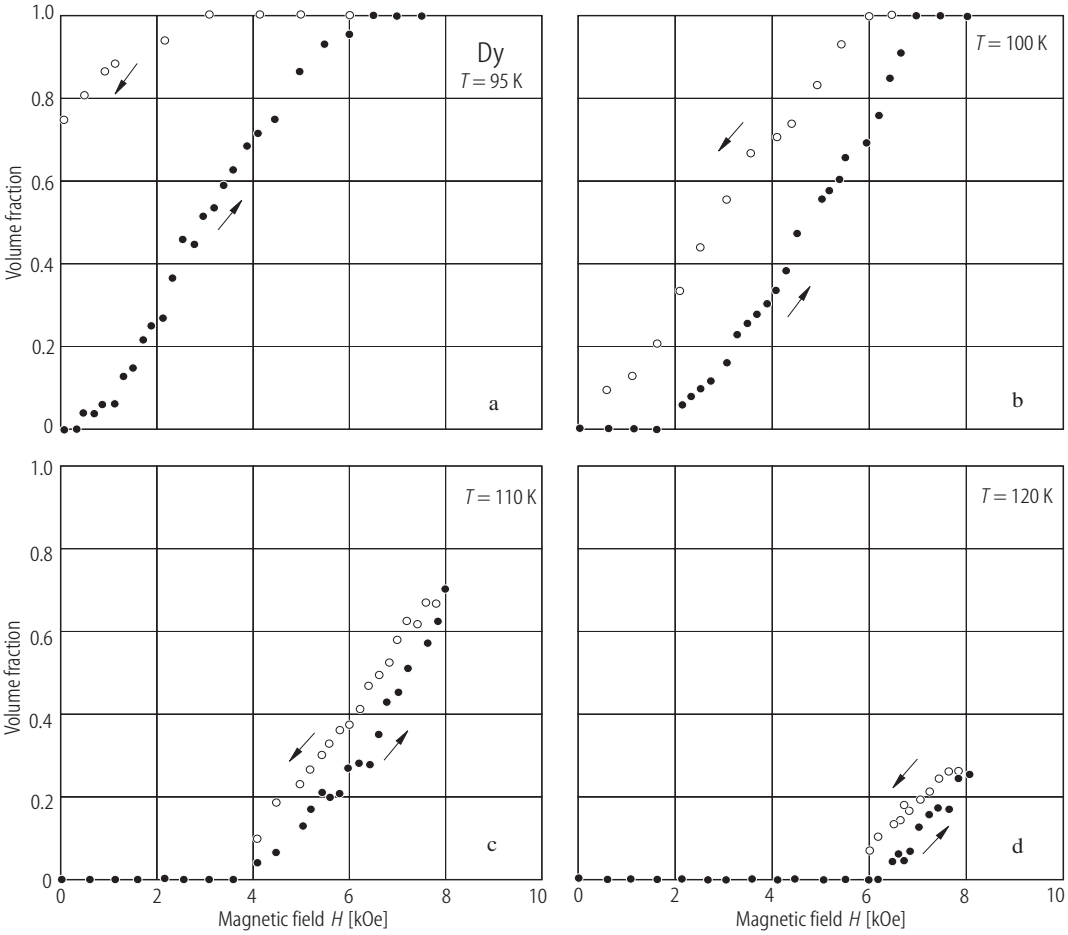

Fig. 156. Magnetic field dependence of the volume fraction of the orthorhombic (ferromagnet) phase. The abscissa is the external field. The hysteresis becomes small as the temperature is increased. (**a**) $T = 95$ K. Most of the crystal structure remains at orthorhombic in the remanent state. (**b**), (**c**), (**d**) are the results for $T = 100$ K, 110 K, and 120 K, respectively [95S].

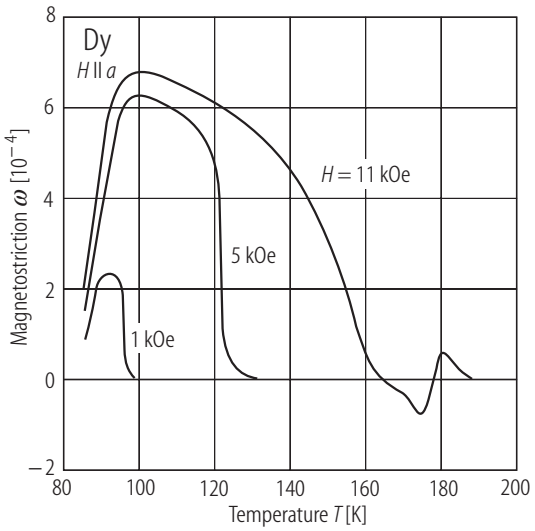

Fig. 158. Temperature dependence of the volume magnetostriction ω of a Dy single crystal at $H \| a$: $H = 11$, 5 and 1 kOe [91N].

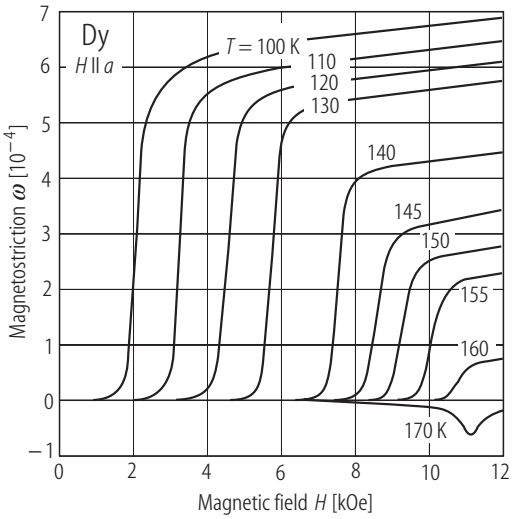

Fig. 159. Dependencies of volume magnetostriction ω on the magnetic field for a Dy single crystal at $H \| a$ [91N].

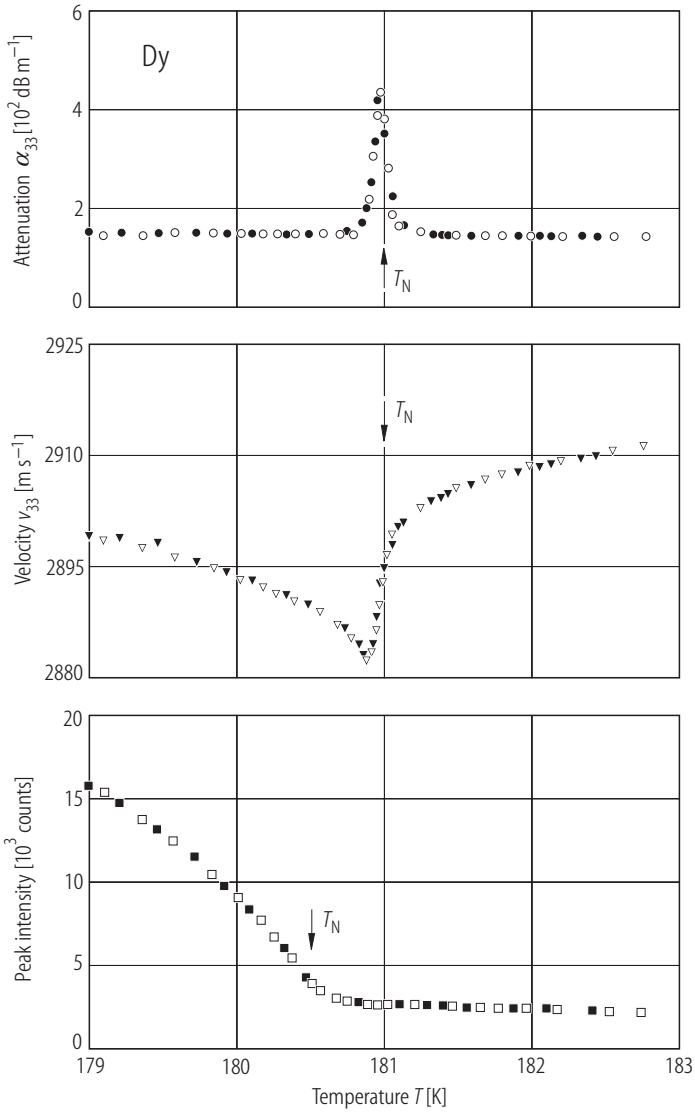

Fig. 160. Helical-paramagnetic phase transition in Dy. Simultaneously measured ultrasonic velocity v_{33} and attenuation α_{33}, and peak scattered neutron intensity vs. temperature for single-crystal Dy. The longitudinal ultrasonic wave was propagated along the c axis and neutrons probed the $(0, 0.2 - \delta)$ satellite. Open symbols indicate measurements taken during the cooling and closed symbols refer to the subsequent heating run [95dP].

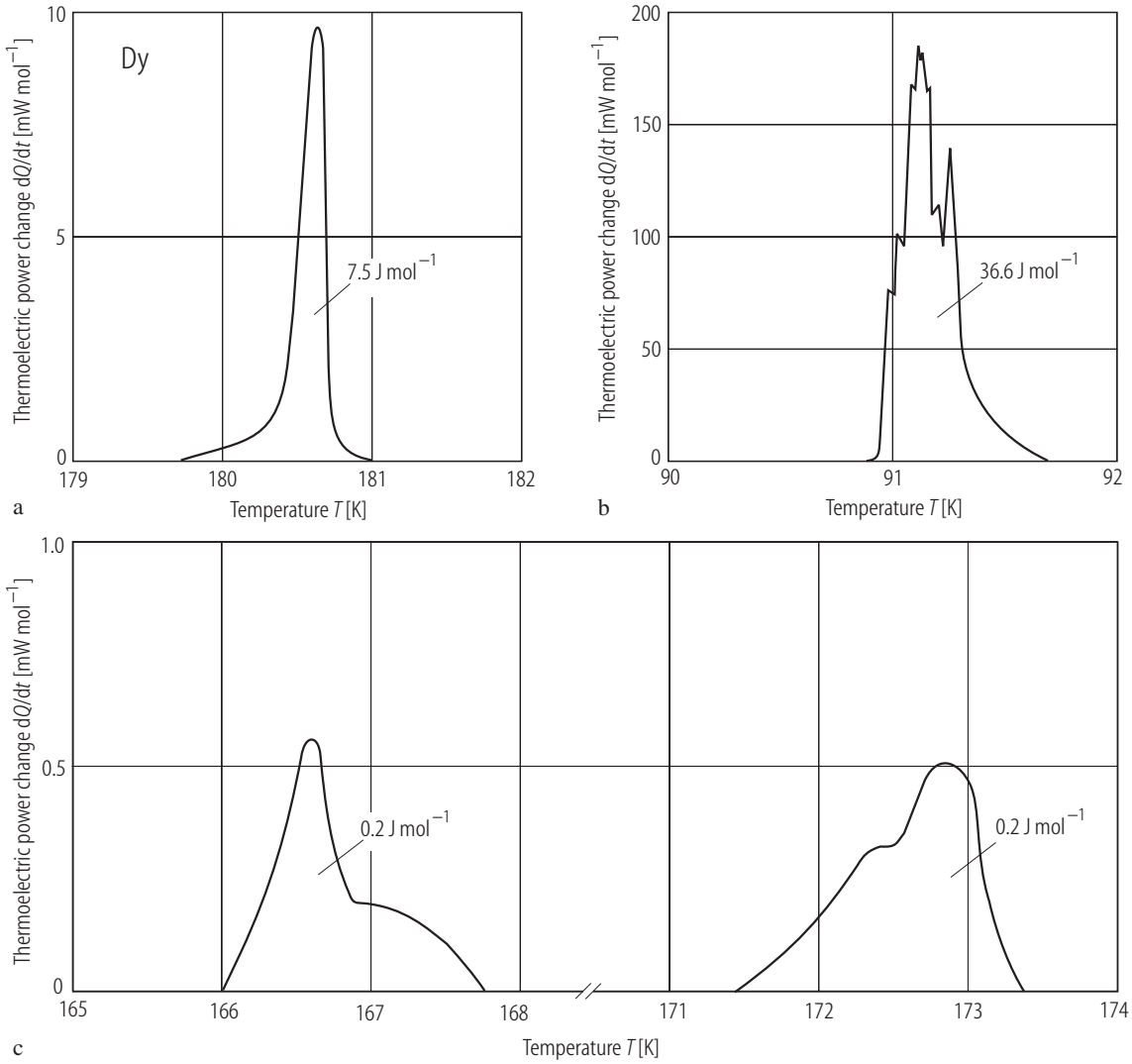

Fig. 161. Investigation of the nature of the magnetic transitions in high-purity Dy with a high-resolution microcalorimeter. Change in energy content of Dy as a function of temperature (**a**) at the antiferromagnetic transition, (**b**) at the ferromagnetic transition, (**c**) in the helical regime. The splitting of the curve T_C into number of smaller peaks can arise from domain-related effects [88Å].

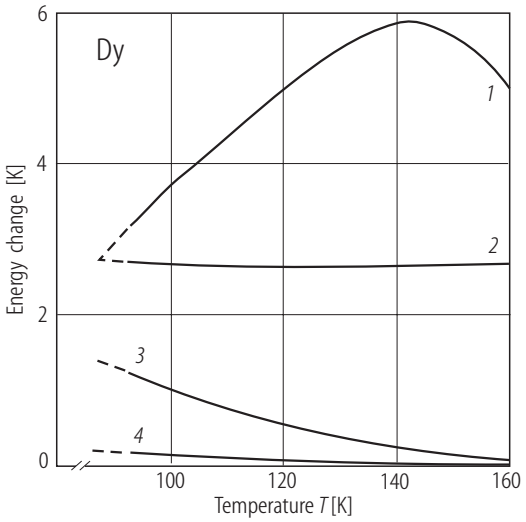

Fig. 162. Temperature dependencies of the change of (*1*) exchange energy ΔE_{exch}, (*2*) magnetoelastic energy ΔE_{me}, (*3*) energy of magnetic anisotropy $\Delta E_A{}^b$, and (*4*) elastic energy $\Delta E_{me}{}^b$ in Dy during magnetic phase transition of the first type helicoidal antiferromagnetism-ferromagnetism [91N].

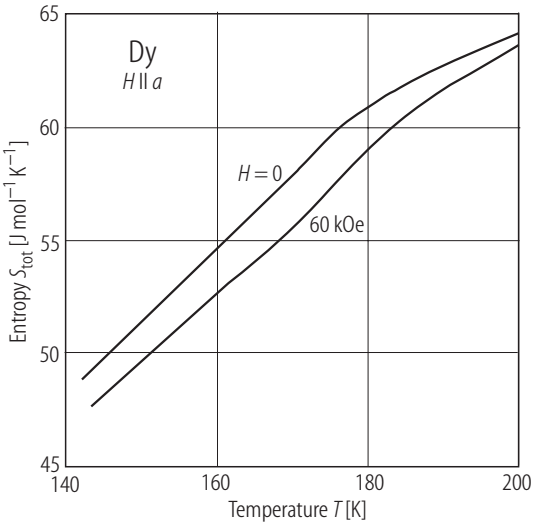

Fig. 163. Temperature dependence of the total entropy of Dy single crystal at $H = 0$ and 60 kOe ($H \| a$) [91N].

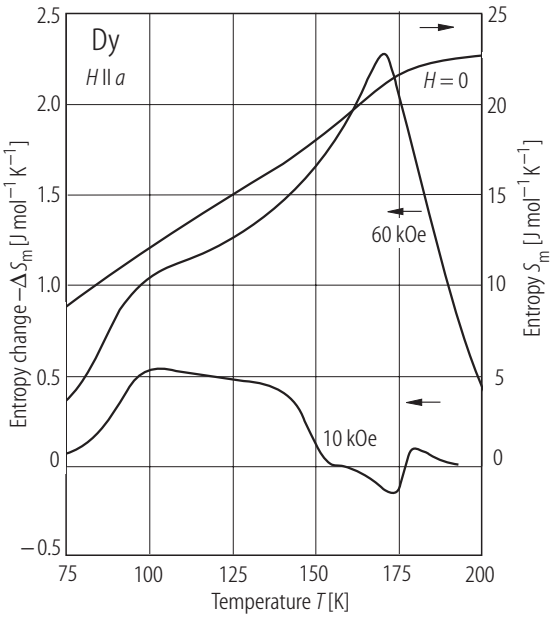

Fig. 164. Temperature dependence of the change in the magnetic part of the entropy in a Dy single crystal in the field applied along the *a* axis: H = 10 kOe, 60 kOe, and temperature dependence of the magnetic part of Dy in a zero field [91N].

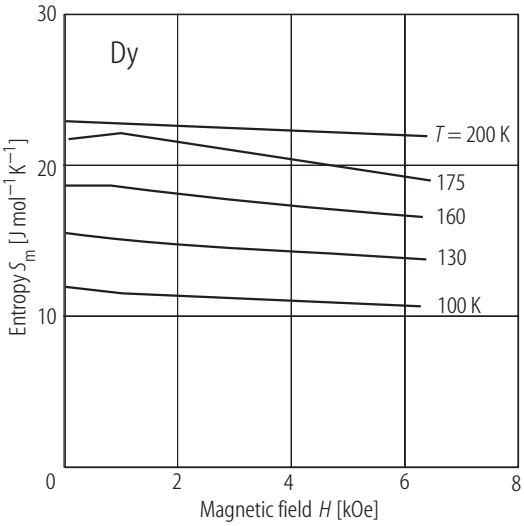

Fig. 165. Dependence of the magnetic part of the entropy S_m (H, T) of a Dy single crystal on the field applied along the a axis [91N].

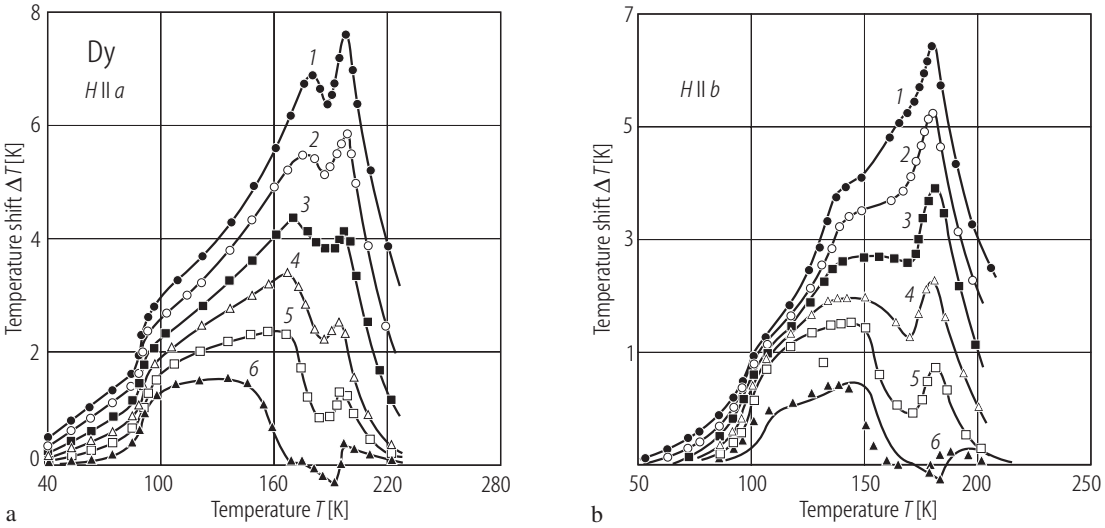

Fig. 166. Temperature dependencies of the magnetocaloric effect in a Dy single crystal in fields applied (**a**) along the a axis and (**b**) along the b axis : H = 60 kOe (*1*), 50 kOe (*2*), 40 kOe (*3*), 30 kOe (*4*), 20 kOe (*5*), 10 kOe (*6*) [91N].

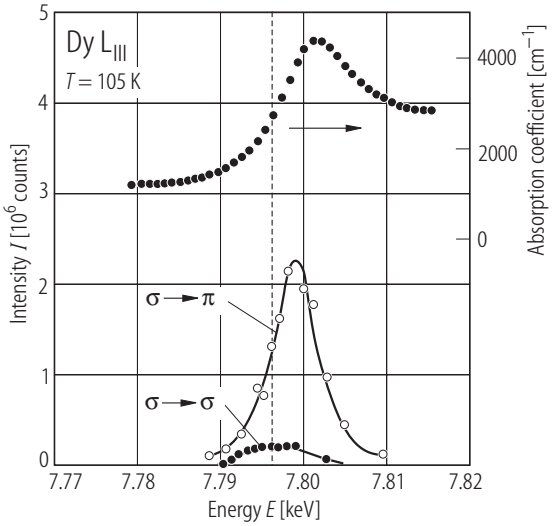

Fig. 167. Resonance enhancement of the magnetic scattering about the L_{III} absorption edge of Dy at the first-harmonic (0, 0.2+τ) with a total intensity that was $3 \cdot 10^{-5}$ weaker than the charge peak at the (0, 0.2). Upper curve shows the absorption profile for a Dy foil taken with a singly bent, asymmetrically cut Ge(111) monochromator. Lower curves show the integrated intensity of the (0, 0, 2+τ) magnetic satellite for both scattered polarisation: σ to π and σ to σ. The intensity of the magnetic satellite drops by a factor of 90 when the incident X-ray energy is tuned below the absorption edge to $E = 7.668$ keV [89I].

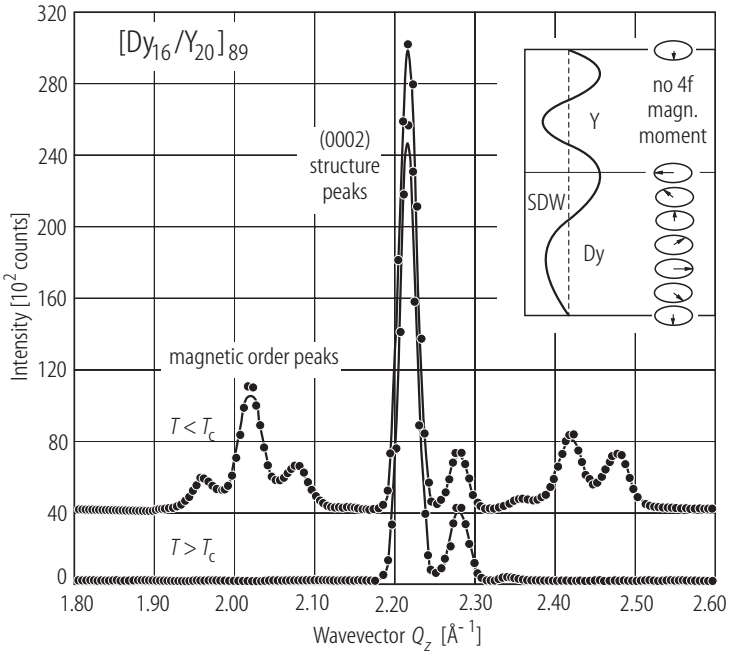

Fig. 168. Scattered neutron intensity for a scan along the c^* direction (Q_z) in a $[Dy_{16}/Y_{20}]_{89}$ multilayer above and below the helimagnetic ordering temperature 167 K (shown as T_C). For $T > T_C$ the small peak to the right of (0002) is a bilayer harmonic. Below T_C the fundamental and two bilayer harmonics are shown for both Q^- (≈ 2.02 Å^{-1}) and for Q^+(≈ 2.42 Å^{-1}) magnetic satellites. For the multilayer structure see Fig. B. The right inset schematically depicts the Dy 4f local moment configuration and the long-range conduction electron spin density wave in both Dy and Y [89R1].

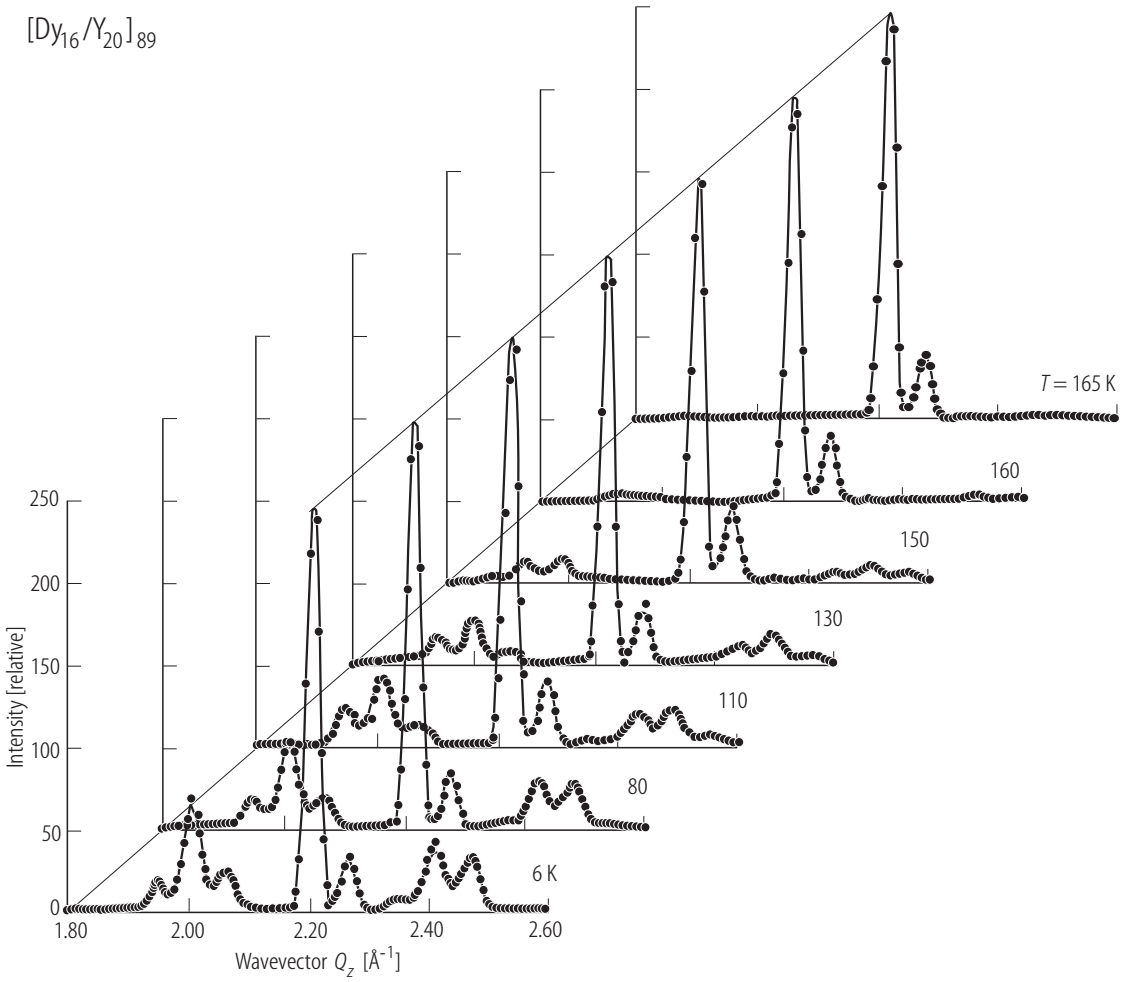

Fig. 169. Neutron diffraction scans around the (0002) principal Bragg peak which is also the propagation's direction (K) for the incommensurate helical magnetic order for the $[Dy_{16}/Y_{20}]_{89}$ multistructure for several temperature below T_C = 167 K. Note the temperature independence of the (0002) peak at Q_2 = 2.215 Å^{-1}. The small peak to the right of the (0002) is a bilayer harmonic. The fundamental and two bilayer harmonics are shown for both Q^{-1}(≈2.02 Å^{-1}) and for Q^{+}(≈2.42 Å^{-1}) magnetic satellites and are observed to be temperature dependent. The presence of the fully resolved Q^{-1} satellites makes it immediately obvious that the magnetism is coherent over many multilayer periods. The coherence range can be calculated from the width of the magnetic peaks [87R].

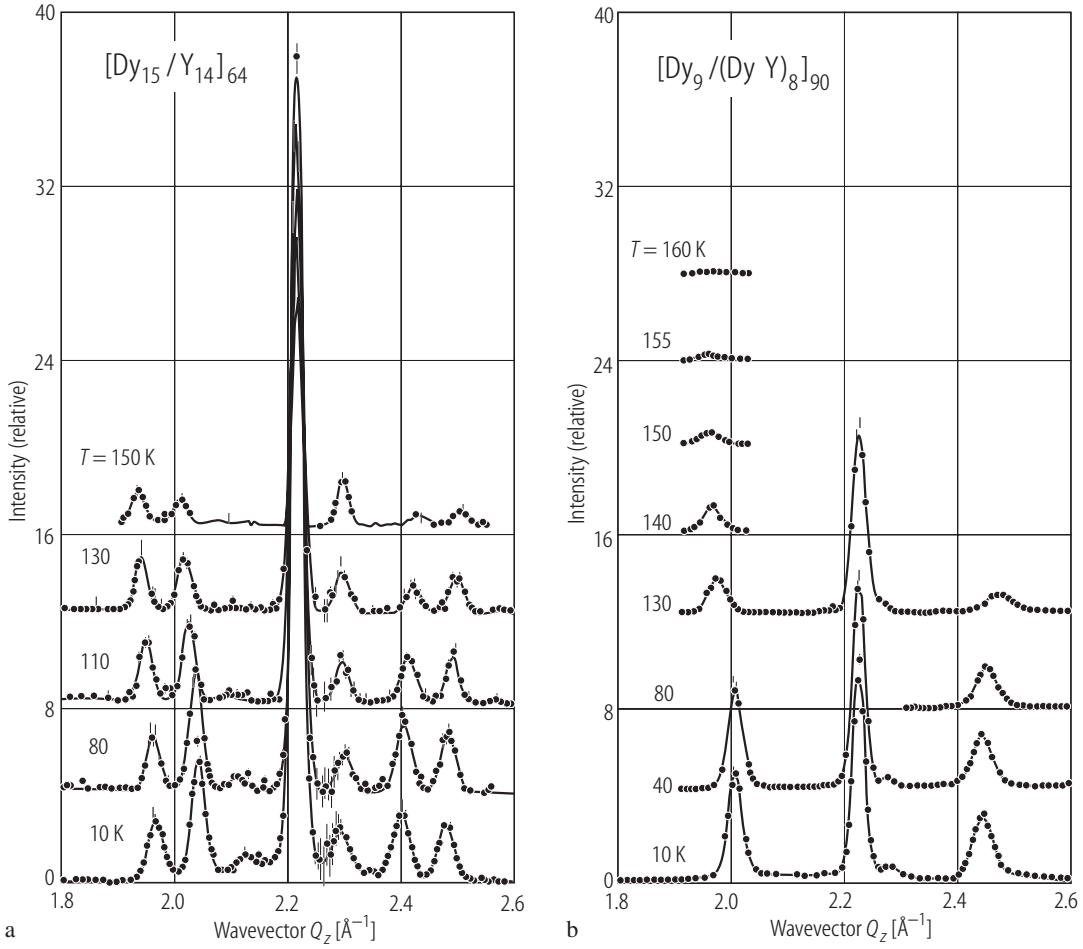

Fig. 170. The (000l) scans in the neutron diffraction experiments for:
(**a**) $[Dy_{15}/Y_{14}]_{14}$ and (**b**) $[Dy_9/(DyY)_8]_{90}$ made up of about 15 growth planes of Dy atoms followed by 14 planes o Y atoms. The second sample has 90 layers, each layer consisting of 90 Dy atomic planes and 8 $Dy_{0.5}Y_{0.5}$ alloy planes. As the temperature is lowered additional peaks of magnetic origin appear on either side of τ_0. In sample (**b**) only two additional peaks are found in the zone about the primary nuclear peak and the scattering pattern is identical to that found in the conventional helimagnetic phase such as bulk Dy. In sample (**a**), by contrast, a triad of magnetic peaks appear on either side of τ_0 below 175 K [87E].

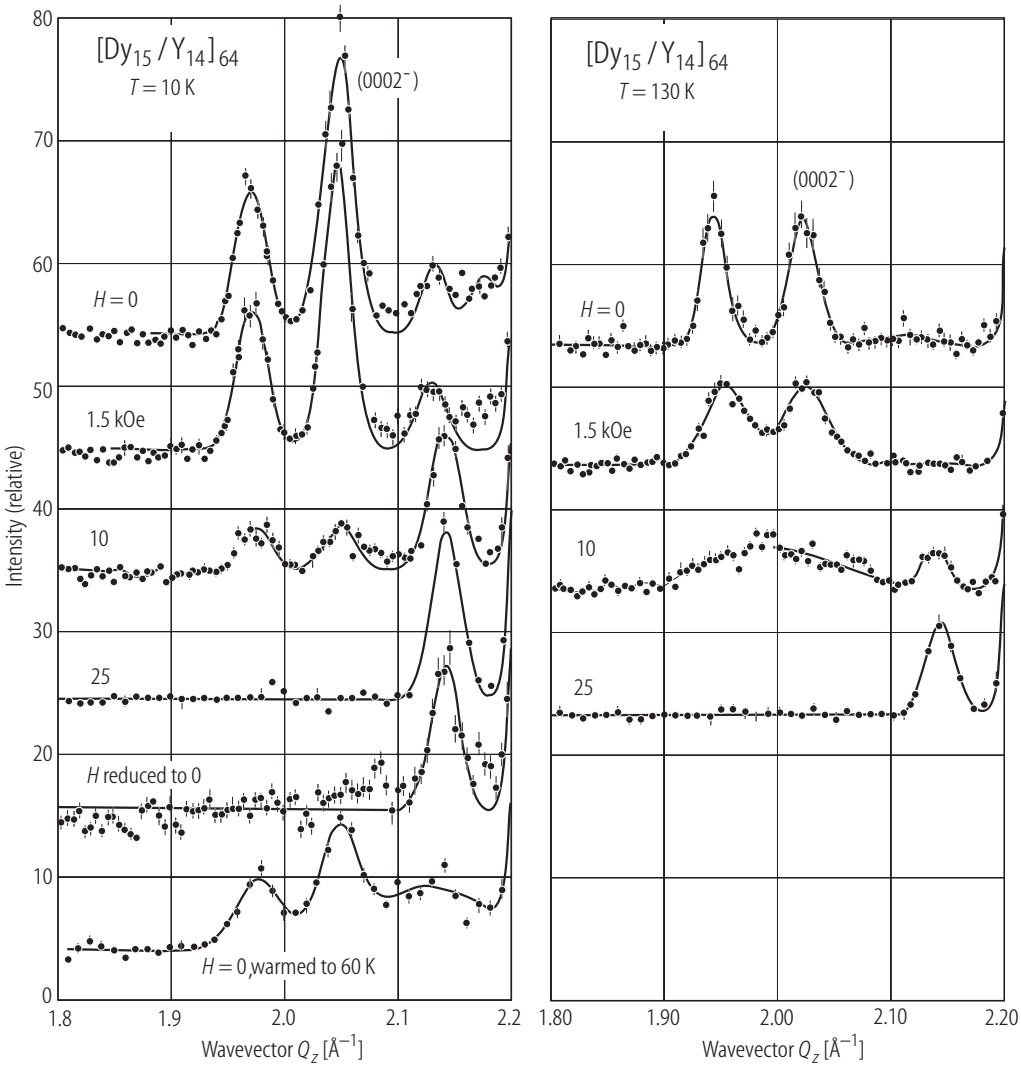

Fig. 171. Field dependence of the helimagnetic state is shown for sample $Dy_{15}/Y_{14}]_{64}$ at temperatures of 10 and 130 K with the field along the easy direction. At low temperature the magnetic satellite intensity decreases for fields above about 1.5 kOe with complete ferromagnetic saturation by 25 kOe. Very little broadening of the magnetic satellites is observed at 10 K. However, at 130 K the first effect of the applied field is to broaden the magnetic satellites, and a field of 10 kOe is sufficient to limit the helimagnetic coherence to a single bilayer. The helimagnetic state is not reformed at low temperature, but can be regained upon warming, although with a shorter coherence length than the zero-field cooled state [87E].

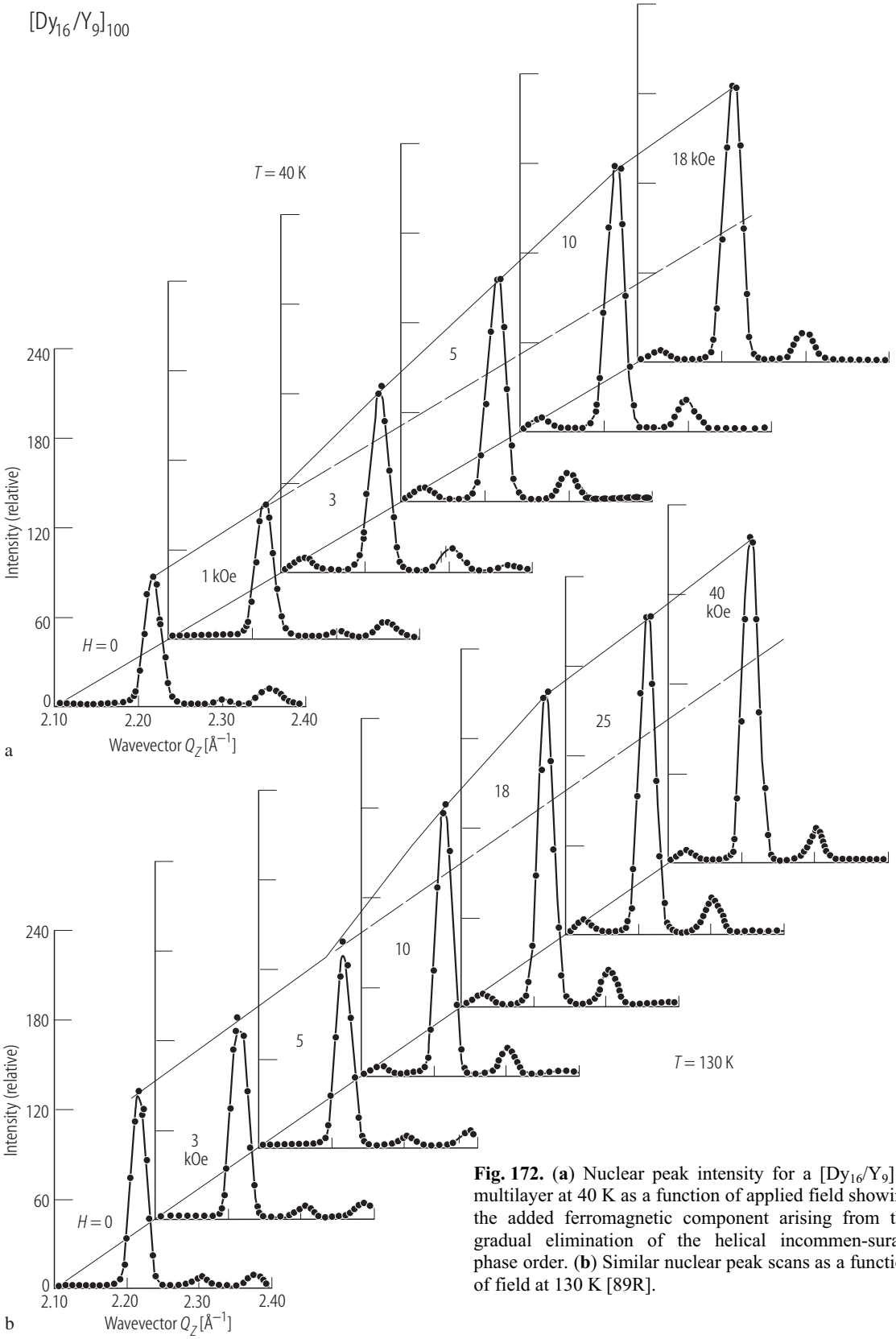

Fig. 172. (**a**) Nuclear peak intensity for a $[Dy_{16}/Y_9]_{100}$ multilayer at 40 K as a function of applied field showing the added ferromagnetic component arising from the gradual elimination of the helical incommen-surate phase order. (**b**) Similar nuclear peak scans as a function of field at 130 K [89R].

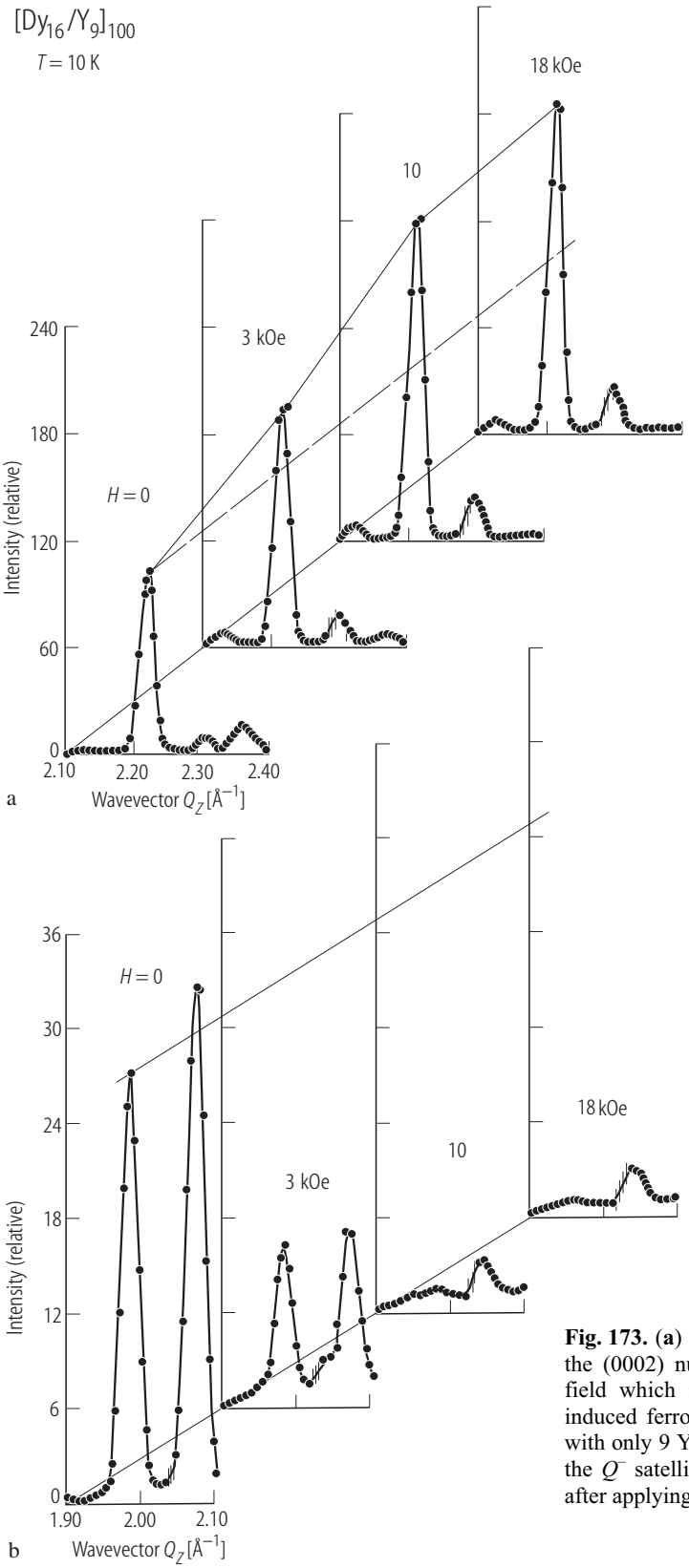

Fig. 173. (**a**) Excess ferromagnetic intensity remains on the (0002) nuclear peaks following application of the field which indicates the strong metastability of the induced ferromagnetic state at 10 K for the multilayer with only 9 Y planes. (**b**) Residual intensity for $H = 0$ at the Q^- satellite positions in the $[Dy_{16}/Y_9]_{100}$ multilayer after applying each of the fields shown [89R].

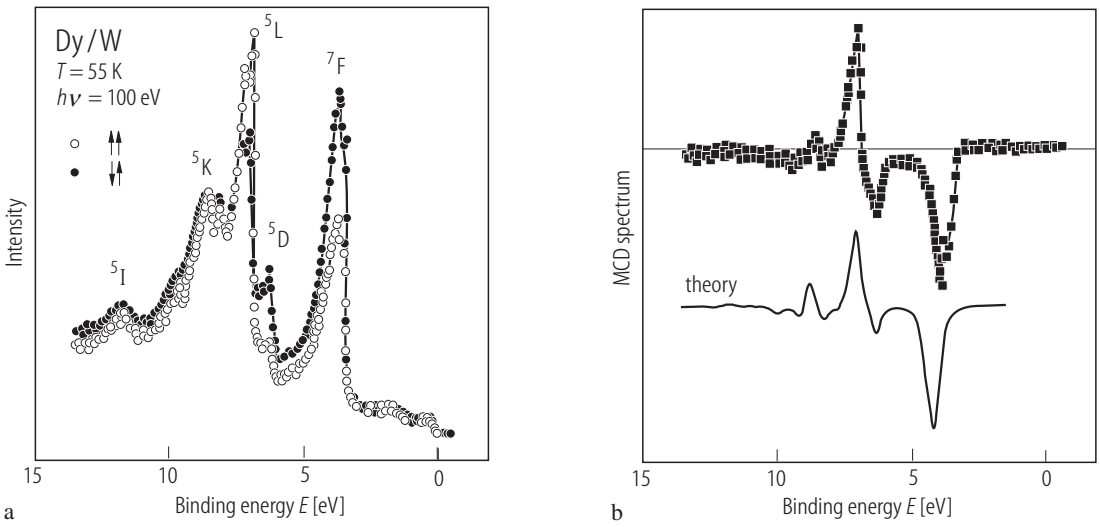

Fig. 174. (**a**) Dy 4f photoemission (PE) spectra ($h\nu$ = 100 eV) of a remanently magnetized Dy(0001)/W(110) film (150 Å thick; T = 55 K). Open (solid) dots are for nearly parallel (antiparallel) orientation of photon spin and sample magnetization. (**b**) Solid squares: Intensity difference of the experimental magnetic circular dichroism spectra in (**a**), the solid curve at the bottom of (**b**) represents the theoretical MCD spectrum [95A].

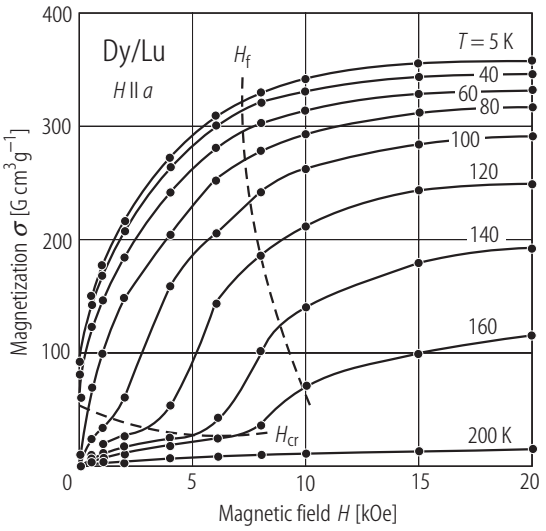

Fig. 175. Field dependent magnetization curves for the field-cooled $(Y_{0.45}Lu_{0.55})_{1500Å}/Dy_{50Å}/(Y_{0.45}Lu_{0.55})_{100Å}$ superstructure grown along the [0001] direction at various temperatures. The magnetic field was applied along one of the a axis in the growth plane. Note that above T_C = 90 K the magnetization exhibits a low field anomaly at H_{cr} before its rapid rise to saturation. The critical fields H_{cr} and H_f are indicated by dashed lines [93T].

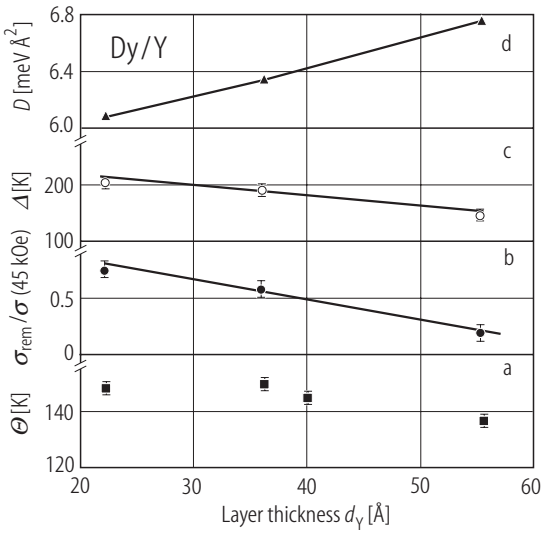

Fig. 176. (**a**) Curie temperature Θ obtained from a Curie-Weiss law fit above the paramagnetic transition at 2 kOe, (**b**) the fractional remanence magnetization, σ_{rem} at 10 K after saturation in a field of 45 kOe, and (**c**) the spin-wave anisotropy gap and (**d**) the spin-wave stiffness D obtained from fits of the saturation magnetization to spin-wave dispersion relations, all as functions of Y layer thickness in single-crystal superlattice of Dy and Y [87B].

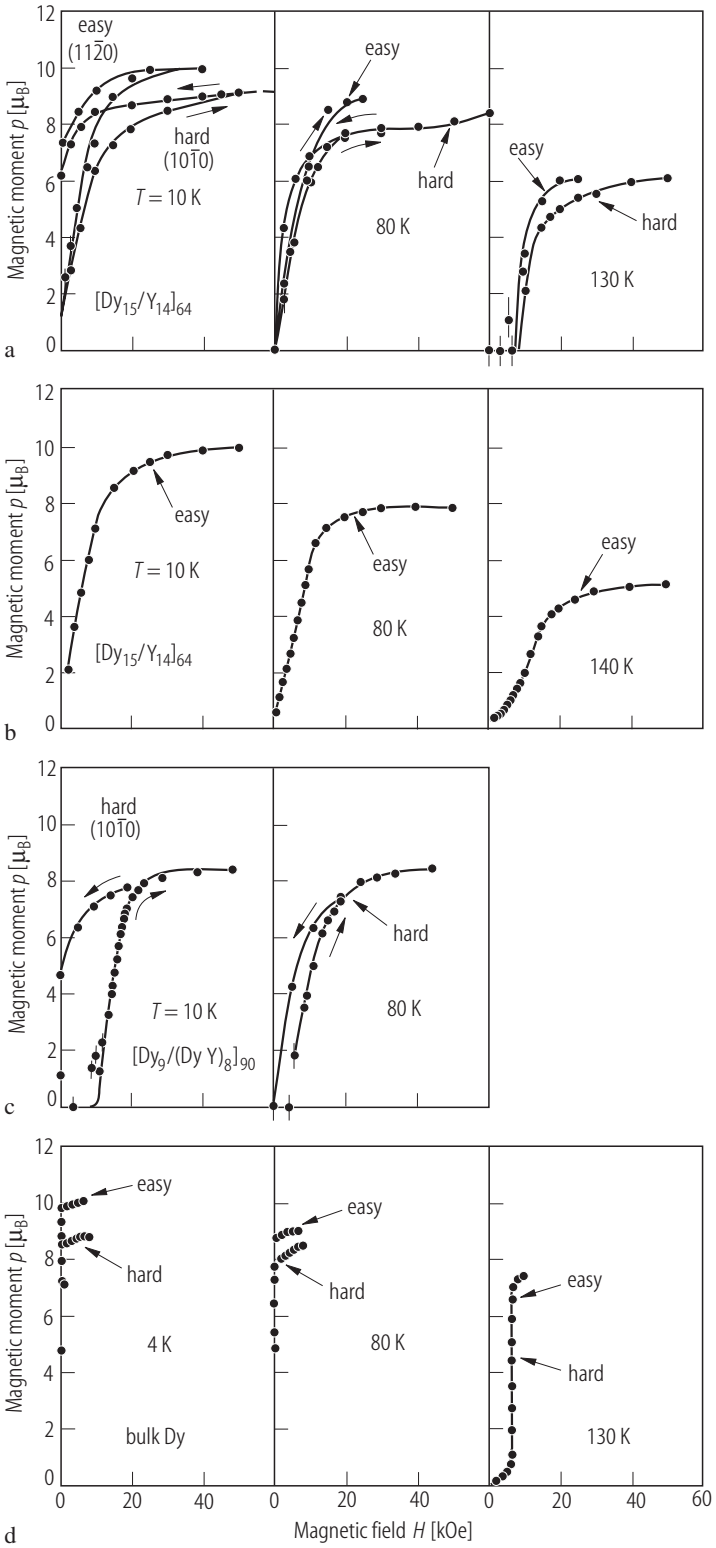

Fig. 178. (**a**) Magnetization of $[D_{15}/Y_{14}]_{64}$ sample from neutron experiment for fields applied along the easy and hard directions in the basal plane. (**b**) Magnetometer measurements on the same sample. (**c**) $[Dy_9/(DyY)]_{90}$ multilayer. The basal-plane anisotropy is observed to be similar to that of bulk Dy shown in (**d**). At low temperatures the slope of the curves is clearly not demagnetization limited, and the first-order transition from the helimagnetic to ferromagnetic states in bulk Dy is not as sharp in the superlattice [87E].

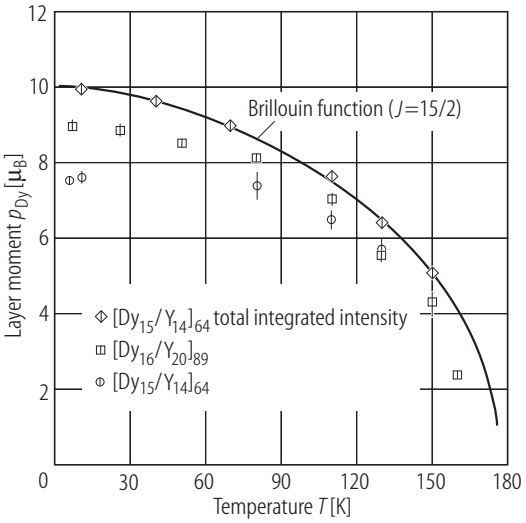

Fig. 177. Temperature dependence of the coherent Dy layer moment in $[Dy_{16}/Y_{20}]_{89}$ and $[Dy_{15}/Y_{14}]_{64}$ compared to a Brillouin function. Also shown is the total integrated magnetic intensity for $[Dy_{15}/Y_{14}]_{64}$ [87R].

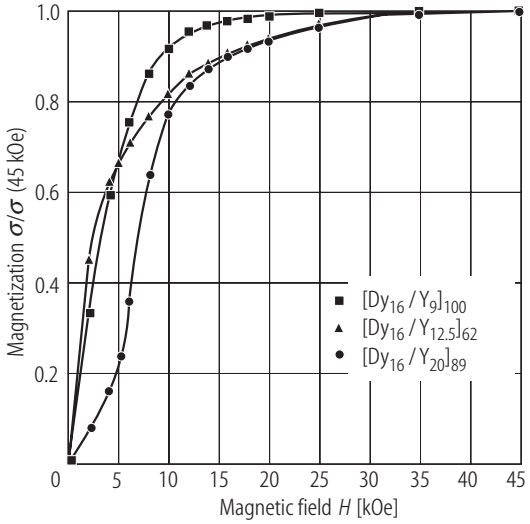

Fig. 179. Field-cooled magnetization σ as a function of applied field at 10 K for the three superlattices as indicated. All results have been scaled by the value of the magnetization at 45 kOe unlike pure Dy, the initial susceptibility shows metamagnetic behavior at low fields [87B].

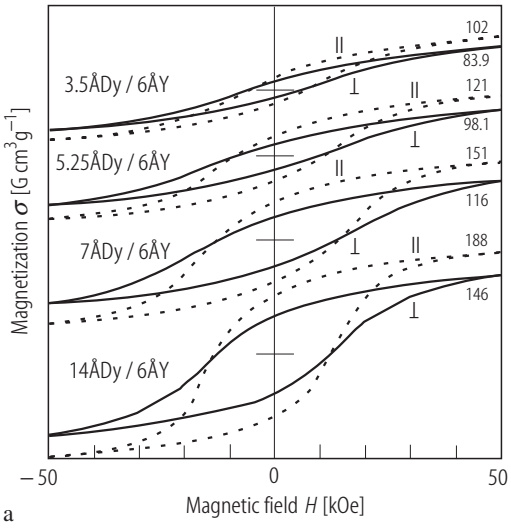

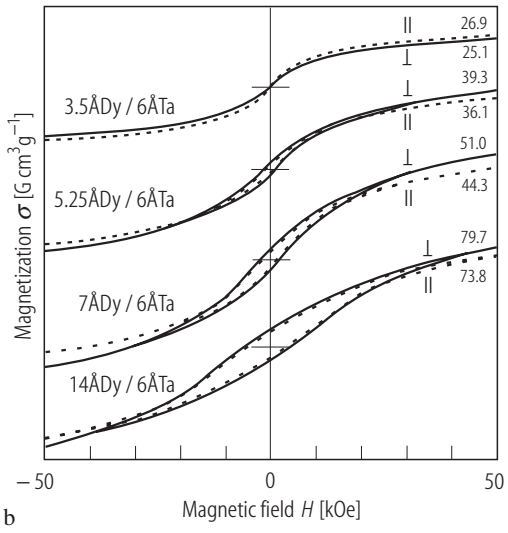

Fig. 180. (**a**) Layers-thickness dependence of hysteresis loops for Dy/6ÅTa and (**b**) for Dy/6ÅY superstructure at 5 K. Figure shows that all Dy/Y samples have $\sigma_{||} > \sigma_{\perp}$, i.e., in-plane anisotropy [91S1].

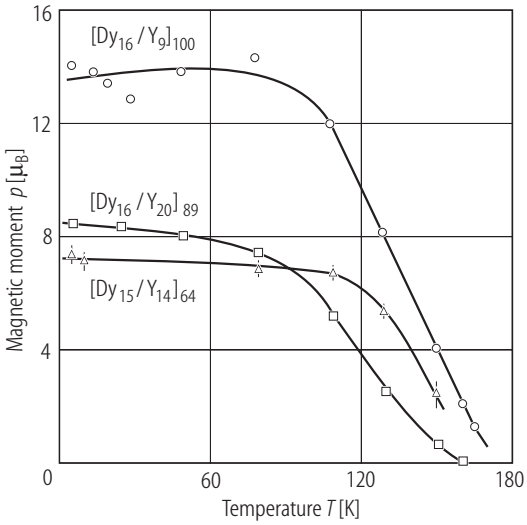

Fig. 181. Uncompensated net layer moment resulting from incomplete helices in Dy layers. In an applied field this net moment is a pseudo-random order parameter coupled to the external field which is suggested to destroy the long-range coherence for T approaching T_N [89R].

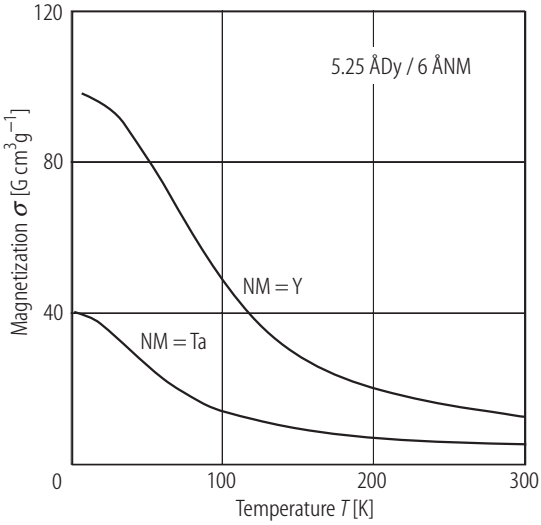

Fig. 182. Temperature dependence of magnetization at H = 55 kOe for 5.25ÅDy/6ÅTa and 5.25ÅDy/6ÅY multilayer superstructure. All the magnetization comes from Dy but is strongly effected by the Ta and Y atoms [91S1].

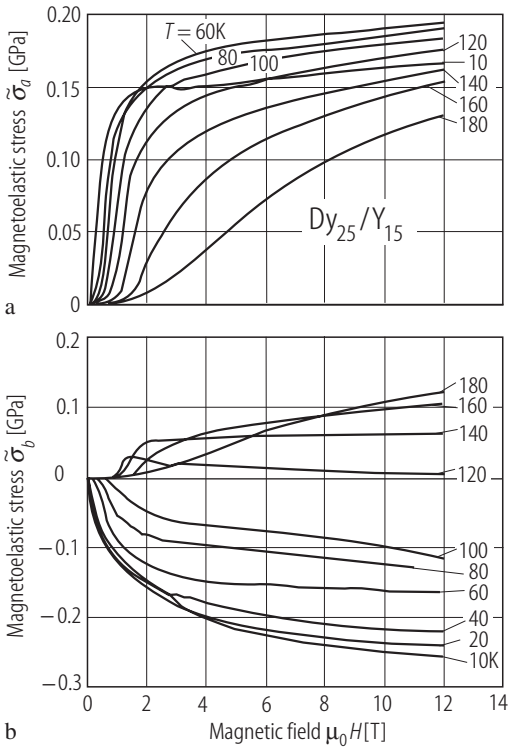

Fig. 183. Magnetoelastic stress isotherms for SL $(Dy_{25}/Y_{15})\times 50$ superlattices. $\tilde{\sigma}_a$ (**a**) and $\tilde{\sigma}_b$ (**b**) correspond to SL clamping along the a and b axes [97dM].

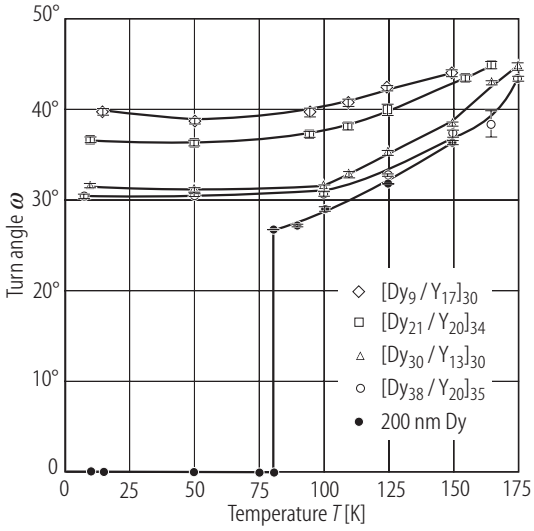

Fig. 184. Temperature dependence of interplane turn angles of the helimagnetic spiral for Dy/Y superlattices and 200 nm thick Dy film. The values are weighted averages of the turn angles of the Dy and the Y layers [97T-B].

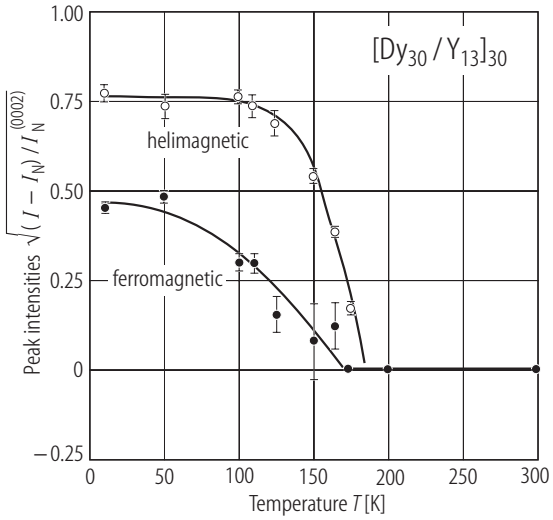

Fig. 185. Dy/Y superlattices. Temperature dependencies of the magnetic peak relative intensities. The solid circles represent the ferromagnetic moment component derived from the square root of the excess integrated intensities of the (0002) peak at different temperatures normalized by its average value above T_N. The open circles represent the helimagnetic component derived from the square root of the integrated intensity of the $(0002)^-$ and the $(0002)^+$ helimagnetic satellites normalized to the (0002) nuclear peak intensity [97T-B].

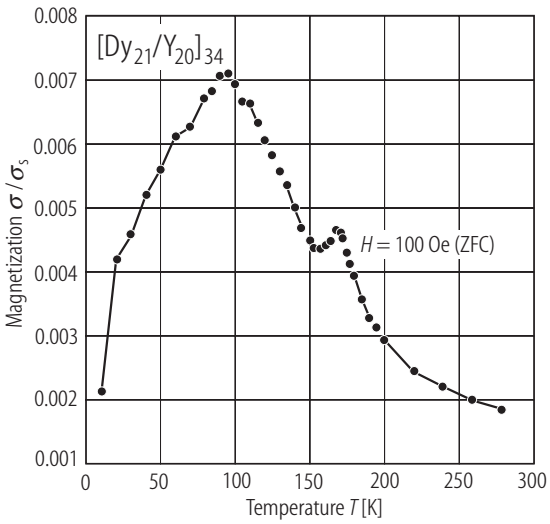

Fig. 186. Zero field cooled SQUID magnetization measurement for the superlattice $[Dy_{21}/Y_{20}]_{34}$. The measurement was performed with increasing temperature from 10 K at a magnetic field of 100 Oe [96T-B].

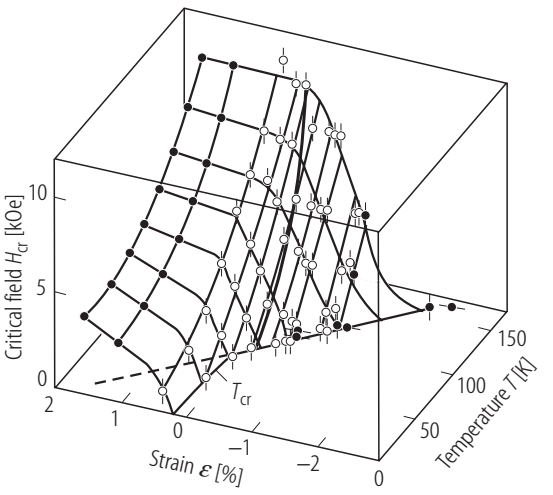

Fig. 187. Magnetic phase diagram for epitaxial Dy thin films grown along the *c* axis. The phase boundary corresponds to the locus of critical field H_{cr}. T_{cr} is defined where the phase boundary intersects the T-ε plane at zero field. The open circles are data points for $(Y_xLu_{1-x})_{1500Å}/Dy_{50Å}/(Y_xLu_{1-x})_{100Å}$ sandwich films. The dashed line through the nearly linear part of the T_{cr} curve indicates the equivalent bulk uniaxial behavior [93T].

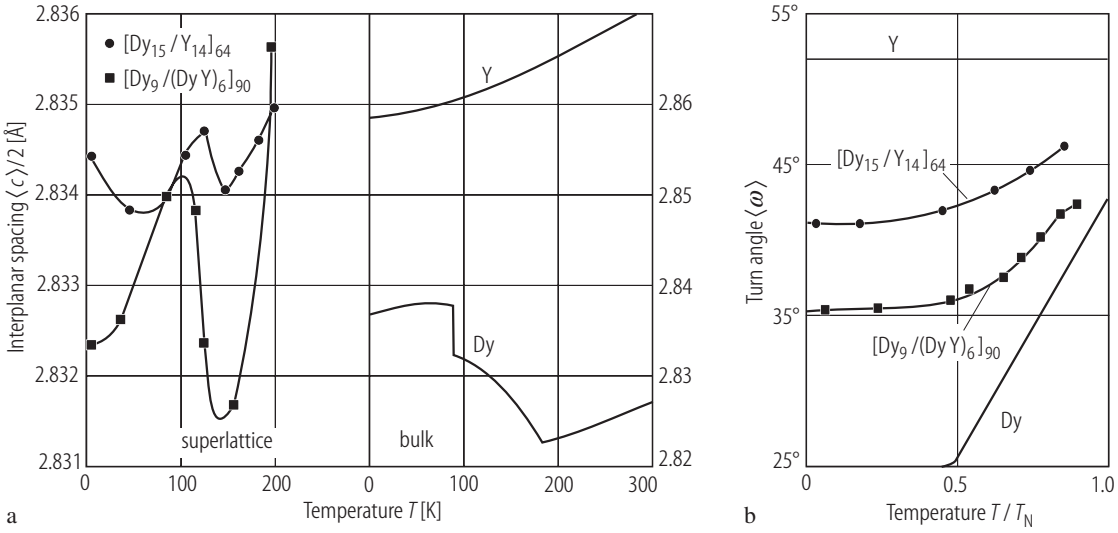

Fig. 188. (**a**) Average interplanar spacing along the *c* axis obtained from the position of the primary nuclear Bragg peak. The temperature dependence in the Dy/Y superlattice is a weighted average of the behavior in the constituent materials. Note the change of scale when comparing to the bulk materials. (**b**) shows the average turn angle in the superlattices as well as in the bulk materials [87E].

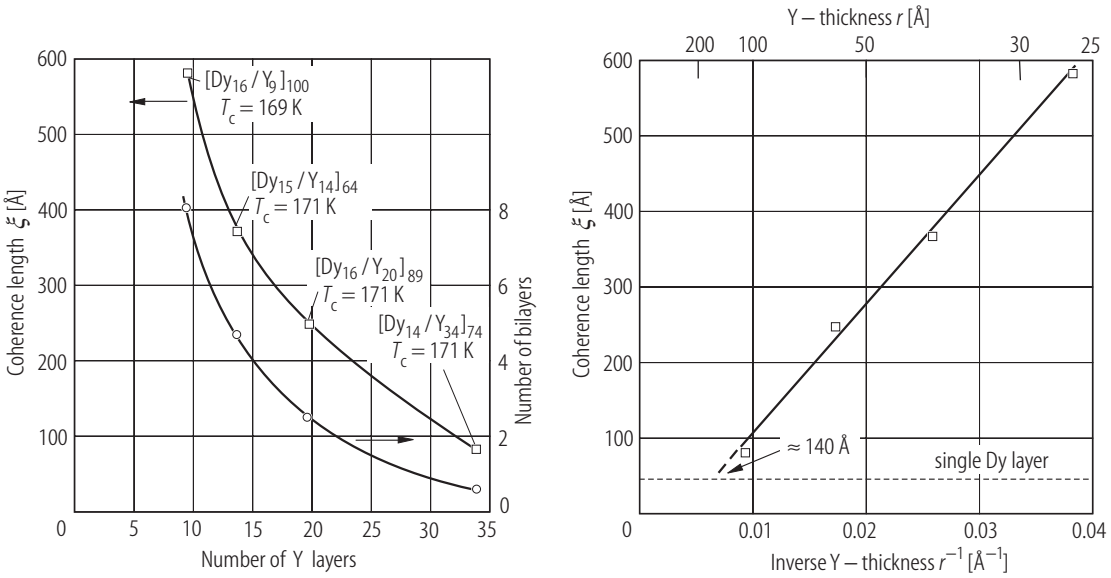

Fig. 189. (Left) Magnetic coherence length ξ (in both Å and number of complete bilayers) obtained from the intrinsic Q width of the magnetic satellite peaks as a function of Y thickness for the four samples. (Right) Linear inverse dependence of the coherence length on the Y interlayer thickness. The extrapolated ξ drops to a single Dy layer at 140 Å. In the figures T_c denotes the helical ordering temperature [89R].

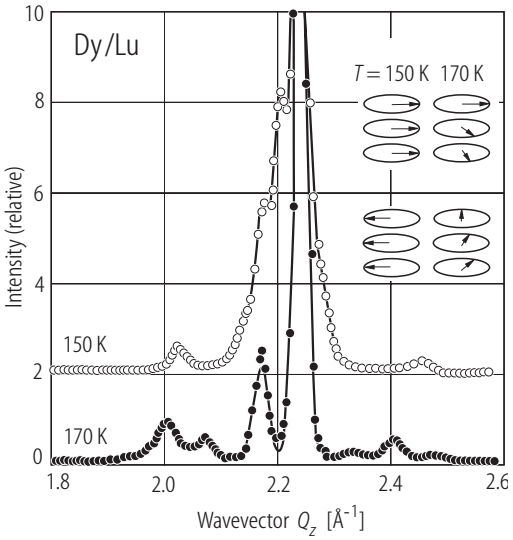

Fig. 190. Diffraction scans for a Dy/Lu superlattice [94R].

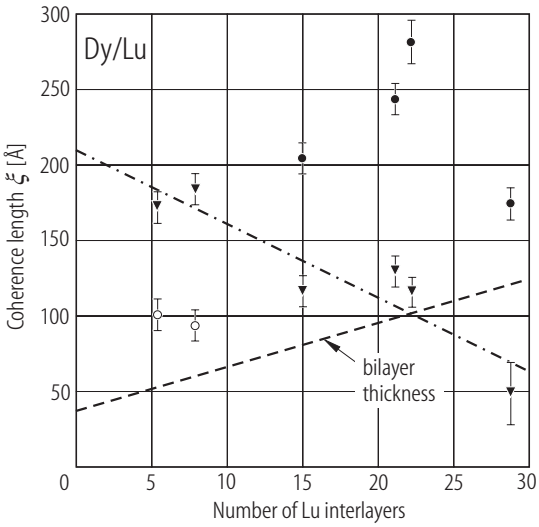

Fig. 191. Magnetic coherence length vs. number of Lu interlayers for spiral (triangles), aligned ferromagnetic layers (open circles), and antialigned layers (solid circles). The actual spacing is 2.77Å/Lu layer [93B].

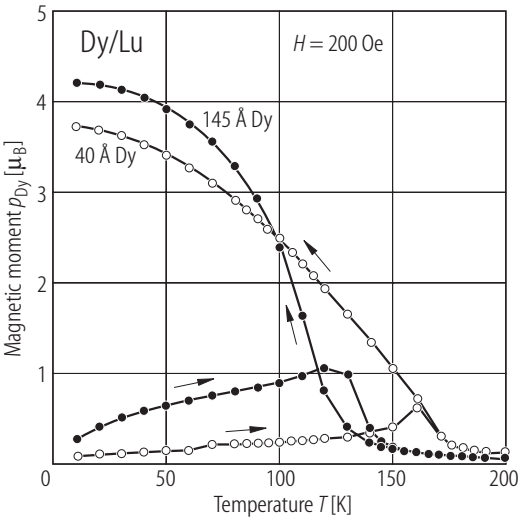

Fig. 193. Magnetic moment of Lu(500Å)/(145Å)Dy/Lu(500Å) (solid circles) and Lu/40ÅDy/Lu (open circles) trilayers as a function of temperature. Both field-cooled (200 Oe) and zero-field-cooled data are shown. Arrows indicate whether the temperature was being raised or lowered. The thermal hysteresis in the FM transition of the 145 Å film is probably connected to structural distortion occurring at T_c. The Dy helical magnetic order yields to ferromagnetism (FM) at temperatures almost double T_c = 85 K of the bulk element [93B1].

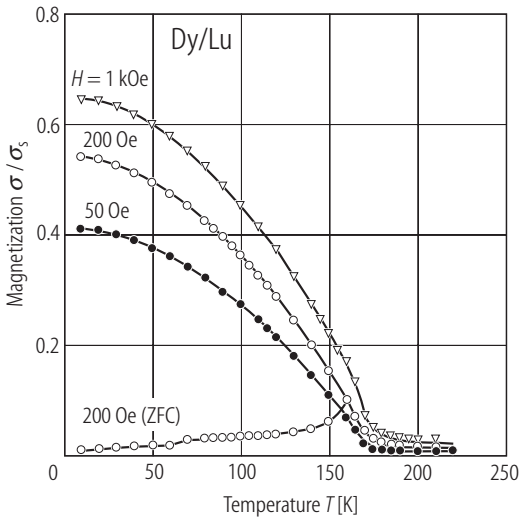

Fig. 192. FC magnetization vs. temperature for the 40 Å Dy layer (sandwich between 500 Å slabs of Lu (Lu/40Å - Dy/Lu) in the fields of 50 Oe, 200 Oe (FC and ZFC) and 1 kOe [93B].

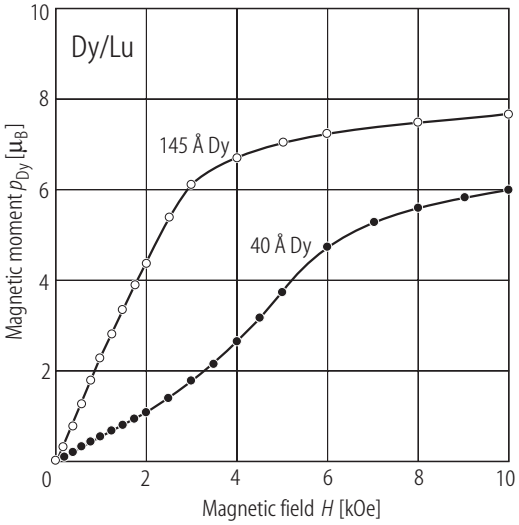

Fig. 194. Zero-field-cooled magnetization (at T = 10 K) vs. field for the 40ÅLu- and 145ÅDy/Lu films. The field required to saturate the magnetization is large for thinner films, exceeding 10 kOe for the 40 Å sample. The saturation moment p_s for the 40 Å sample is 65 % of p_s bulk Dy [93B1].

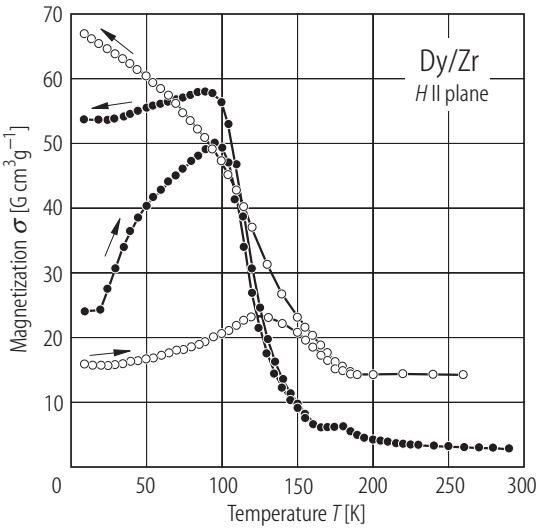

Fig. 196. Temperature dependence of the magnetization for zero-field-cooled, field-cooled Zr(200Å)/Dy(600Å) (solid circles) and Zr(200Å)/Dy(100Å) (open circles) samples. The applied field (500 Oe) was in film plane. The sense of variation of temperature is indicated by arrows [95L].

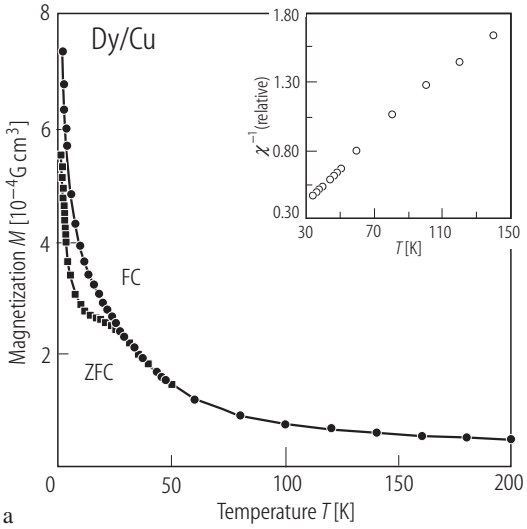

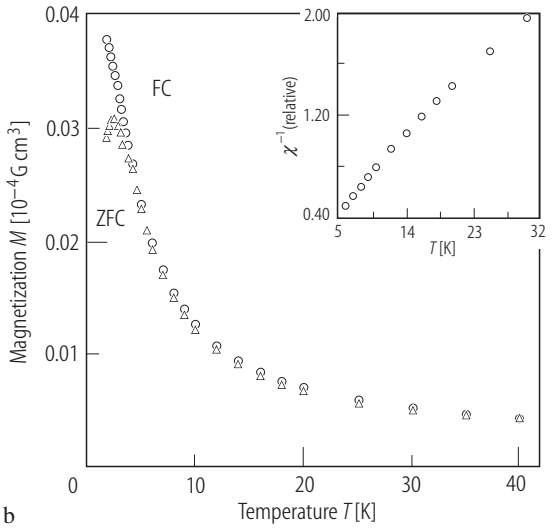

Fig. 195. (**a**) Low field $M(T)$ data for Dy/Cu multilayers deposited on to crystalline Cu(111) with the composition $[Cu(100Å)/Dy(20Å)]_{30}$. Inset: χ^{-1} vs. T. (**b**) Low field $M(T)$ data for $[Cu(100Å)/Dy(40Å)]_{20}$ sample. Inset: χ^{-1} vs. T [94T2].

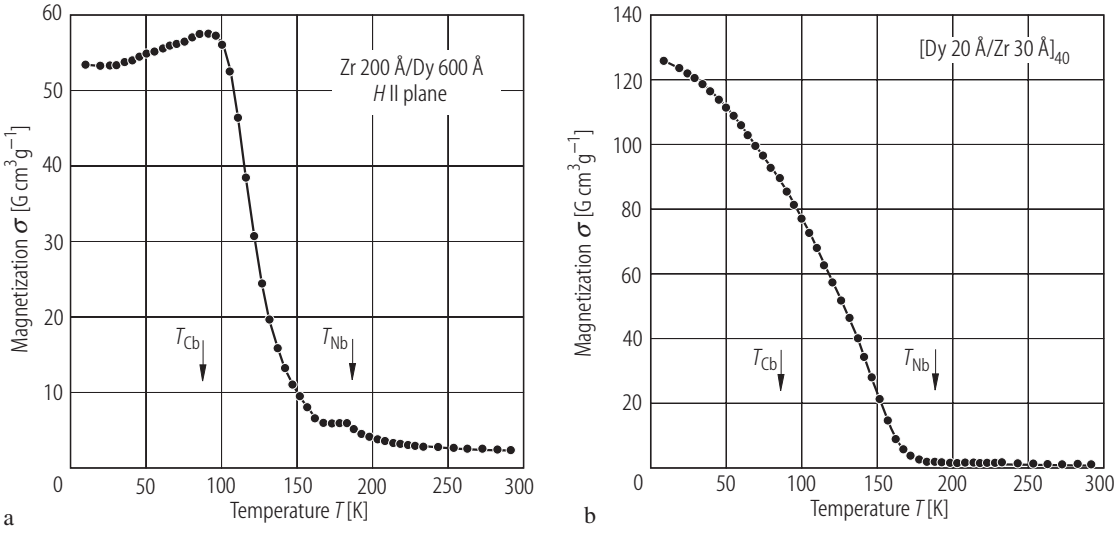

Fig. 197. (**a**) Temperature dependence of magnetization measured in the bilayer Zr(200Å)/Dy(600Å) and (**b**) [Dy(20Å)/Zr(30Å)]$_{40}$ grown on Si(111) after previous depositions of a 600Å-thick Zr buffer layer. Both samples were field-cooled. The magnetic field (500 Oe) was applied parallel to the layer plane [93L].

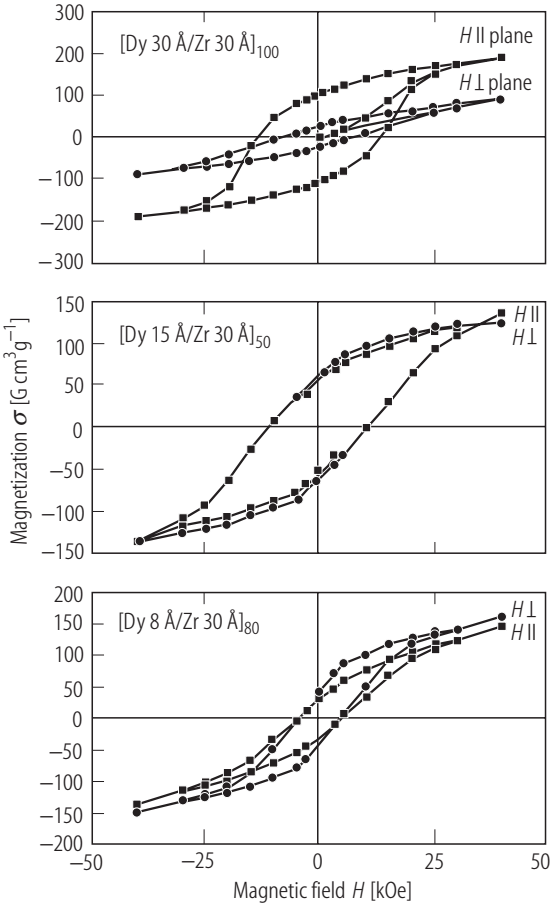

Fig. 198. Hysteresis loops measured at 10 K in multilayers [Dy(xÅ)/Zr(30Å)]$_n$ (x = 30, 15 and 8), for applied fields parallel and perpendicular to the layer plane [93L].

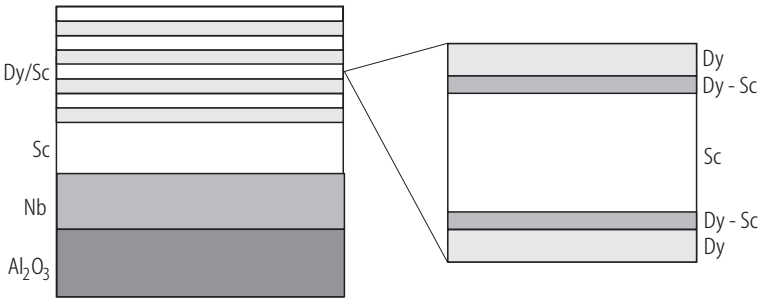

Fig. 199. Sketch of the Dy/Sc superlattice (SL) with the enlarged section to the right indicating the Dy-Sc alloyed layers on both sides of each Sc layers [94T1].

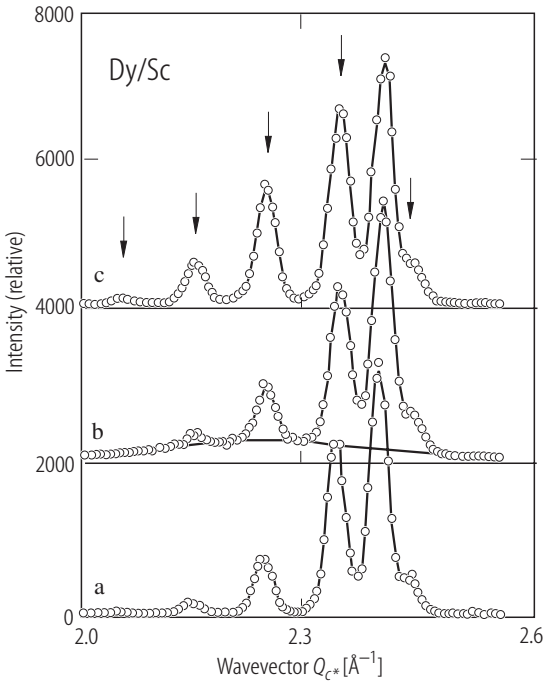

Fig. 200. Neutron diffraction from c-[$Dy_{25Å}/Sc_{40Å}]_{66}$ for scans along the [0002] diffraction (**a**) nuclear intensity at 160 K showing five structural superlattice sidebands and (0002) Sc reflection from the buffer layer; (**b**) zero-field scan at 10 K showing the short-ranged ferromagnetic order along the growth direction that is indicated by the thick line underneath the unchanged structural superlattice peaks; and (**c**) zero-field-cooled scan at 10 K, and at 60 kOe field applied along the *a* axis showing the magnetic superlattice intensities on top of structural peaks, indicating a coherent ferromagnetic order with vanishing short-ranged order [93T2].

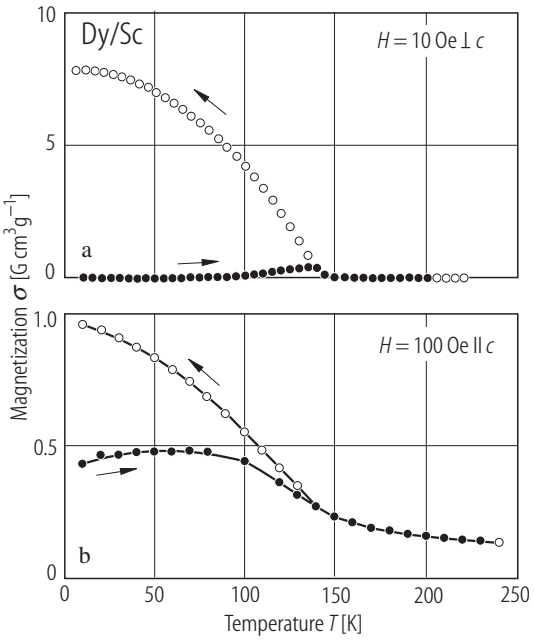

Fig. 201. Temperature dependence of the field-cooled (open circles) and zero-field-cooled (solid circles) magnetizations for c-[$Dy_{25Å}/Sc_{40Å}]_{66}$: (**a**) 10 Oe field applied perpendicular to the *c* axis, and (**b**) 100 Oe field applied along the *c* axis [93T2].

References

87B Borchers, J., Sinha, S., Salamon, M.B., Du, R., Flynn, C.P., Rhyne, J.J., Erwin, R.W.: J. Appl. Phys. **61** (1987) 4049

87E Erwin, R.W., Rhyne, J.J., Salamon, M.B., Borchers, J., Sinha, S., Du, R., Cunningham, J. E., Flynn, C.P.: Phys. Rev. B **35** (1987) 6808

87R Rhyne, J.J., Erwin, R.W., Borchers, J., Sinha, S., Salamon, M.B., Du, R., Flynn, C.P.: J. Appl. Phys. **61** (1987) 4043

88Å Åström, H.U., Benediktsson, G.: J. Phys. F **18** (1988) 2113

89I Isaacs, E.D., McWhan, D.B., Siddons, D.P., Hastings, J.B., Gibbs, D.: Phys. Rev. B **40** (1989) 9336

89R Rhyne, J.J., Erwin, R.W., Borchers, J., Salamon, M.B., Du, R., Flynn, C.P.: Physica B **159** (1989) 111

89R1 Rhyne, J.J., Erwin, R.W., Borchers, J., Salamon, M.B., Du, R., Flynn, C.P.: Phys. Scr. T **29** (1989) 31

91N Nikitin, S.A., Tishin, A.M., Leontiev, P.I.: J. Magn. Magn. Mater. **92** (1991) 405

91S1 Shan, Z.S., Jacobsen, B., Liou, S.H., Sellmyer, D.J.: J. Appl. Phys. **69** (1991) 5289

91W2 Willis, F., Ali, N.: J. Appl. Phys. **69** (1991) 5694

93B Beach, R.S., Borchers, J.A., Matheny, A., Erwin, R.W., Salamon, M.B., Everitt, B., Pettit, K., Rhyne, J.J., Flynn, C.P.: Phys. Rev. Lett. **70** (1993) 3502

93B1 Beach, R.S., Matheny, A., Salamon, M.B., Flynn, C.P., Borchers, J.A., Erwin, R.W., Rhyne, J.J.: J. Appl. Phys. **73** (1993) 6901

93L Luche, M.C., Baudry, A., Boyer, P.: J. Magn. Magn. Mater. **121** (1993) 148

93T Tsui, F., Flynn, C.P.: Phys. Rev. Lett. **71** (1993) 1462

93T2 Tsui, F., Flynn, C.P., Beach, R.S., Borchers, J.A., Erwin, R.W., Rhyne, J.J.: J. Appl. Phys. **73** (1993) 6904

94R Rhyne, J.J., Salamon, M.B., Flynn, C.P., Erwin, R.W., Borchers, J.A.: J. Magn. Magn. Mater. **129** (1994) 39

94T1 Tsui, F., Uher, C., Flynn, C.P.: Phys. Rev. Lett. **72** (1994) 3084

94T2 Tejada, J., Zhang, X.X., Ferrater, C.: Z. Phys. B **94** (1994) 245

95A Arenholz, E., Navas, E., Starke, K., Baumgarten, L., Kaindl, G.: Phys. Rev. B **51** (1995) 8211

95L Luche, M.C., Baudry, A., Boyer, P., Rouvière, J.L., Fermon, C., Miramond, C.: J. Magn. Magn. Mater. **150** (1995) 175

95S Shinoda, Y., Tajima, K.: J. Phys. Soc. Jpn. **64** (1995) 1334

95dP Du Plessis, P. de V., Venter, A.M., Brits, G.H.F.: J. Phys.: Condens.Matter **7** (1995) 9863

96D Dan'kov, S.Y., Spichkin, Yu.I., Tishin, A.M.: J. Magn. Magn. Mater. **152** (1996) 208

96I Izawa, T., Tajima, K., Yamamoto, Y., Fujii, M., Fujimaru, O., Shinoda, Y.: J. Phys. Soc. Jpn. **65** (1996) 2640

96T-B Theis-Bröhl, K., Ritley, K.A., Flynn, C.P., Hamacher, K., Kaiser, H., Rhyne, J.J.: J. Appl. Phys. **79** (1996) 4779

97A Alkhafaji, M.T., Ali, N.: J. Alloys Compounds **250** (1997) 659

97T-B Theis-Bröhl, K., Ritley, K.A., Flynn, C.P., Van Nostrand, J.E., Cahill, D.G., Hamacher, K., Kaiser, H., Rhyne, J.J.: J. Magn. Magn. Mater. **166** (1997) 27

97dM del Moral, A., Ciria, M., Arnaudas, J.I., Ward, R.C.C., Wells, M.R.: J. Appl. Phys. **81** (1997) 5311

2.1.3.9 Holmium

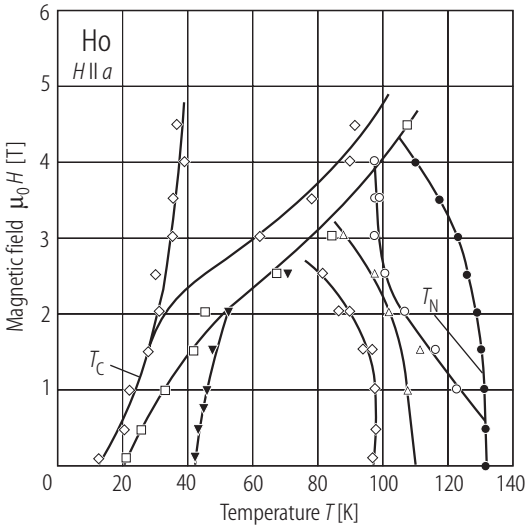

Fig. 202. Magnetic phase diagram of Ho single crystal along the *a* axis. The phase transition temperatures are mapped out as magnetic field vs. temperature. The transition temperatures are determined by temperature dependence of magnetization measurements in constant magnetic fields along the *a* axis. The T_C transition splits into two parts at a field of 2 T whereas T_N transition splits into two parts at 0.5 T. The rest of the curves in the figure represent the transitions between various spin-slip structures [90W].

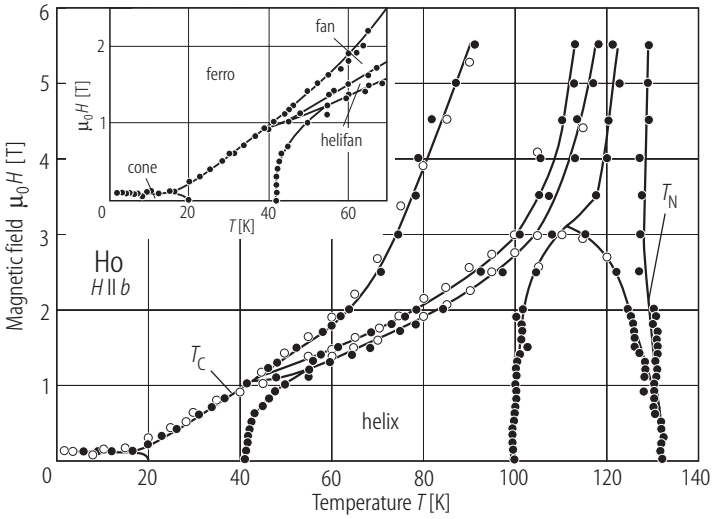

Fig. 203. *H-T* phase diagram of single crystal Ho for applied magnetic field along the *b* axis. Closed circles indicate data from resistance vs. temperature measurements, and open circles indicate data from magneto-resistance vs. field measurements. The inset shows the *H-T* phase diagram for temperatures below 70 K. The curves not labelled in the figure attribute to the transitions to various spin-slip structures [97G1].

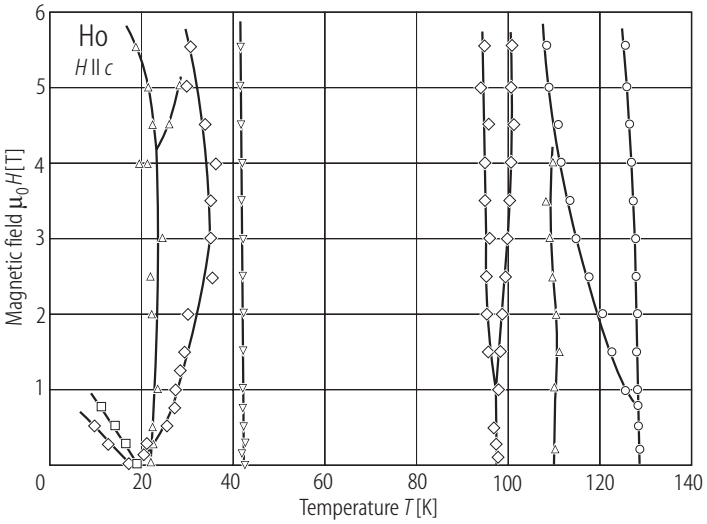

Fig. 205. Magnetic phase diagram of Ho single crystal along the *c* axis. The phase transition temperatures are mapped out as field vs. temperature. The transition temperatures are determined by temperature dependence of magnetization measurements in constant magnetic field along the *c* axis. There are two separate transitions observed. One occurred at a temperature just below the 20 K anomaly and the other occurred near 25 K. In addition to T_C, T_N and the anomalies attributed to spin-slip structures the additional anomaly near 110 K was observed. The anomalies at 20, 42 and 98 K are attributed to various spin-slip structures [90W].

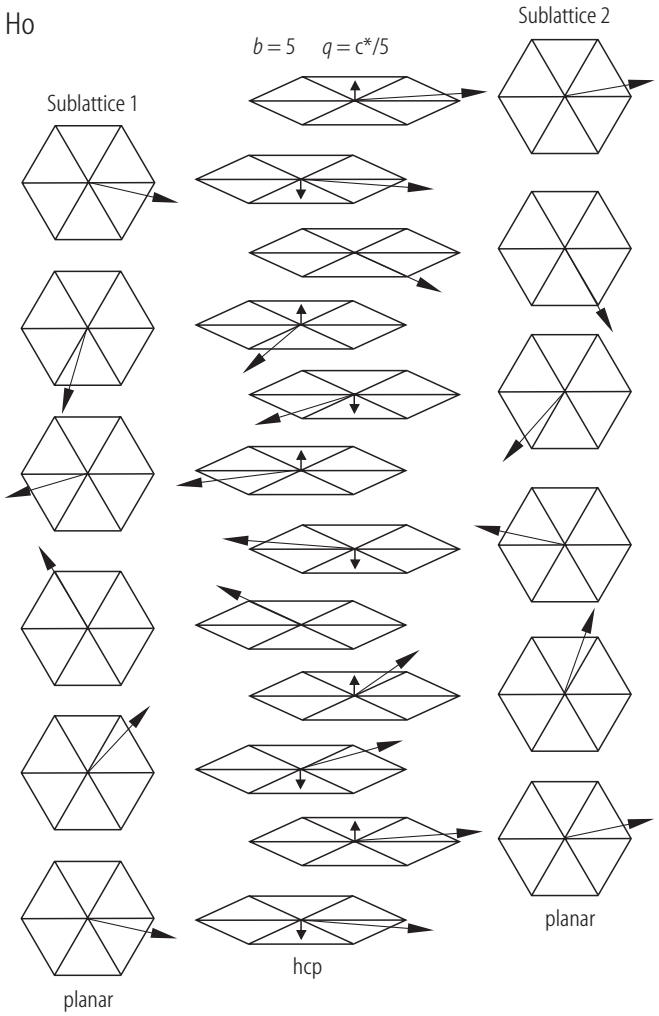

Fig. 206. A pictorial representation of Ho magnetic structure with Debye-Waller factor $b = 5(q = 1/5\ c^*)$ for temperatures between 30 and 18 K just above the transition to a ferromagnetic cone phase with a wavevector of 1/6 c^*. The sublattices are viewed together as they would appear in the hcp structure and separately in planar relief. The arrows denote sublattice spin orientation. One of the possible antiferromagnetic arrangements for the *c* axis moments is also indicated [88C].

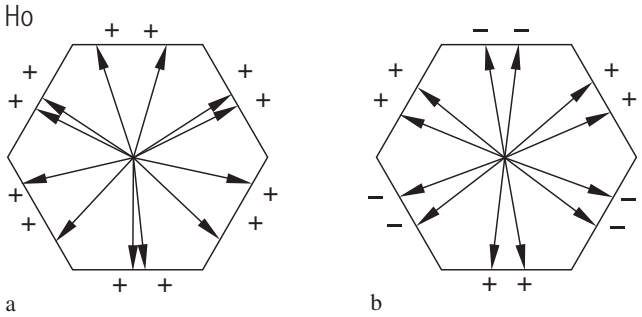

Fig. 207. Basal-plane projections of moments in the 1/6 *c** phase. At low temperatures, the structure is that of (**a**), with moments having two values of bunching angle and tilt alternately. The tilts are the same direction along *c* and the larger tilt is marked +. The bunching angles are not to scale. Moments in (**b**) have equal and opposite tilts out of the basal plane, indicated + and –, and this represents the structure near the transition at 19.5 K [95S2].

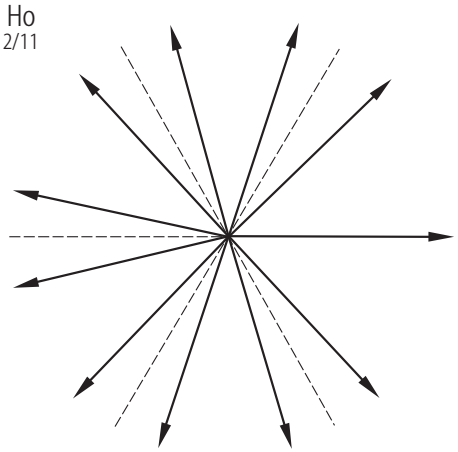

Fig. 208. A schematic and simplified drawing of the directions of the atomic moments in the 11 atomic layer commensurate 2/11 structure. The dotted lines indicate the 6 easy directions in the basal plane of the hcp crystal structure [86B].

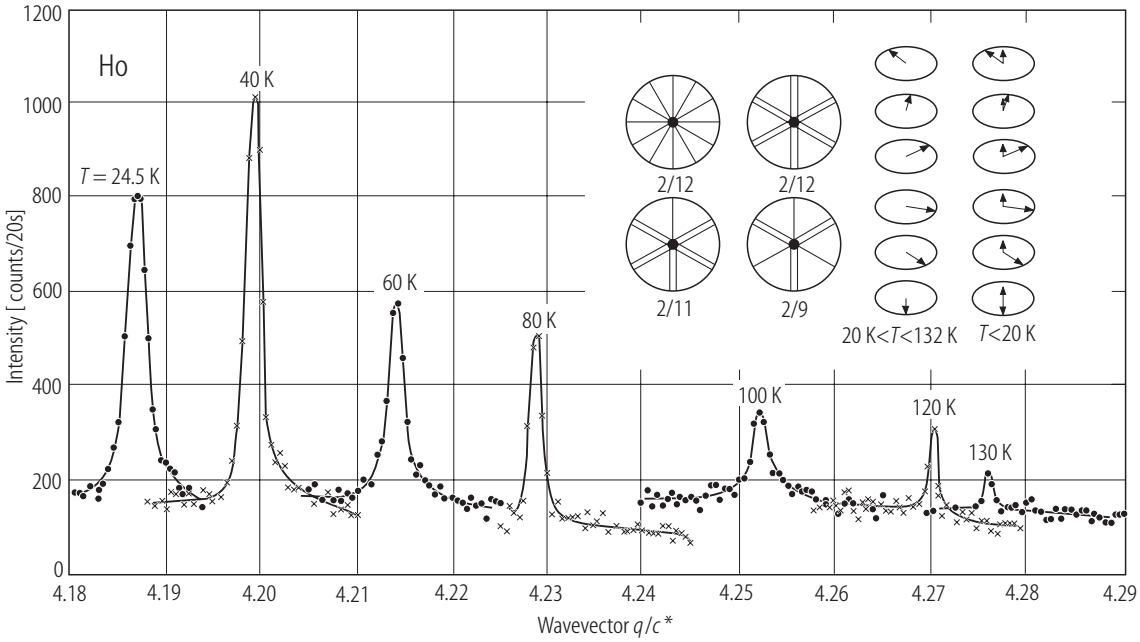

Fig. 209. Temperature dependence of the Ho $(004)^+$ magnetic satellite taken with synchrotron radiation. Inset: Right, schematic representation of the magnetic structure of Ho. Left, projections of the magnetic unit cell for different spin-slip structures. For simplicity the doublet has been drawn as two parallel spins [85G].

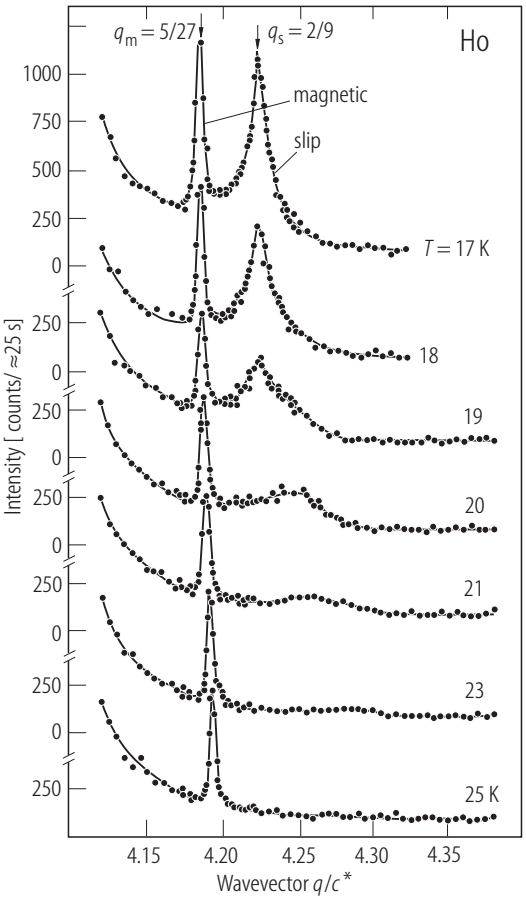

Fig. 210. Magnetic X-ray scattering in Ho metal. The magnetic order below the Néel point is an incommensurate spiral in which each basal plane of the hexagonal closed packed (hcp) crystal structure orders ferromagnetically. Moments in successive basal planes are rotated relative to each other by the turn-angle of the antiferromagnetic magnetic spiral. This leads to a diffraction pattern with satellites of magnetic origin along the 001 direction above and below the Bragg points of the crystal lattice. Figure shows the satellite in Ho above the (004) Bragg peak. In addition to the sharp magnetic satellite an initially broad second peak appears at a higher wavevector. At lower temperatures when the magnetic period approaches 5/27 the additional peak becomes sharper and well defined [90B1].

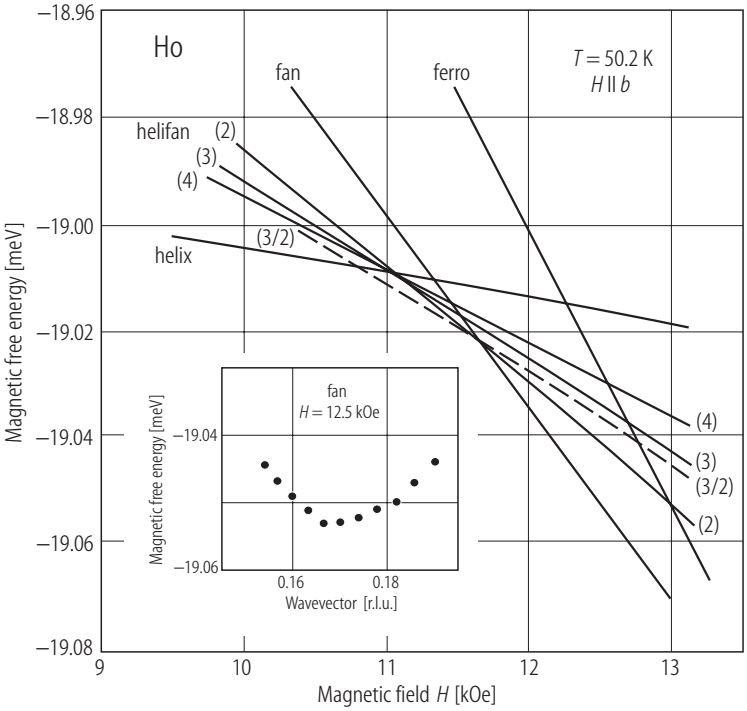

Fig. 211. Magnetic free energy, for different magnetic structures in Ho at 50 K, as a function of the magnetic field along an easy *b* axis. The free energy is in each case minimized with respect to the wave vector which characterised the structure, as illustrated for the fan phase in the inset [90J].

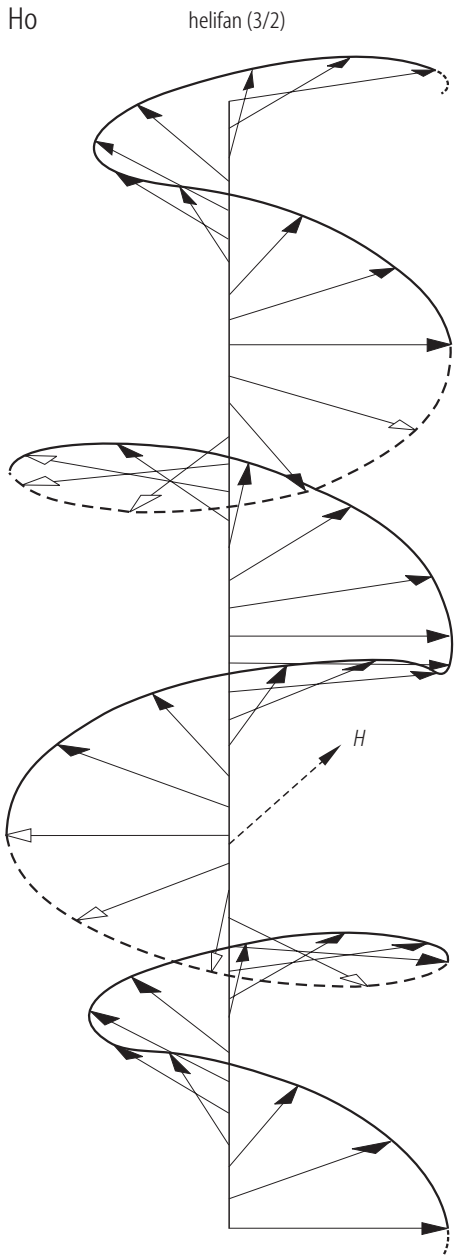

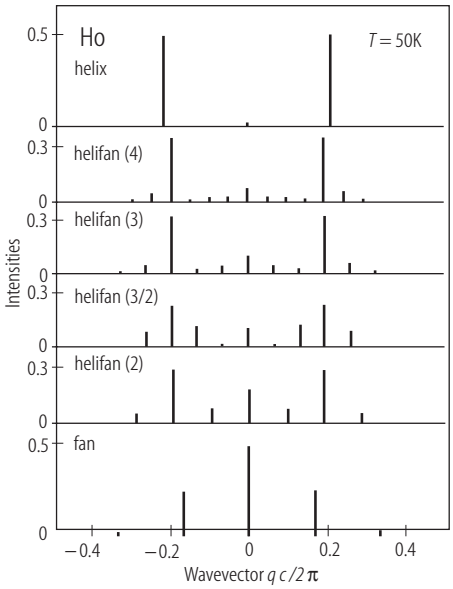

Fig. 212. Neutron-diffraction patterns predicted for the different periodic structures at 50 K. The scattering vector is assumed to lie along the *c* axis. The structures are calculated with a field of 11 kOe along the *b* axis [90J].

Fig. 213. Helifan (3/2) structure in Ho at 50 K. The moments lie in planes normal to the *c* axis and their relative orientations are indicated by arrows. A magnetic field of 11 kOe is applied in the basal plane, and moments with components respectively parallel and antiparallel to the field are designated by filled and open arrow heads. This component of the moments has a periodicity which is 3/2 that of the corresponding helix, and the helicity of the structure changes regularly [92J].

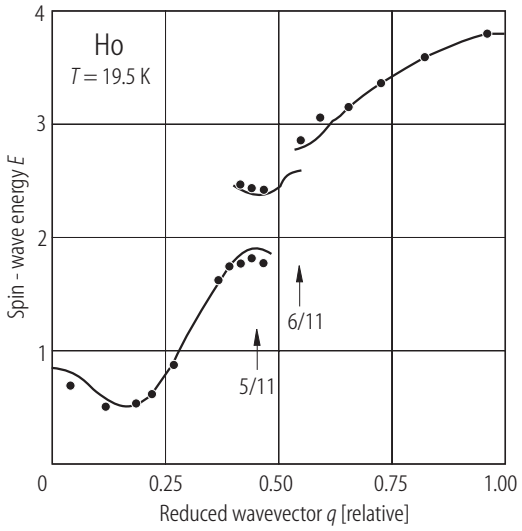

Fig. 214. Spin-wave dispersion relation along (00l) of Ho in its one-spin-slip phase at 19.5 K. The presence of a gap of 0.6 meV at q = 5/11 c^* is clearly shown [91McM].

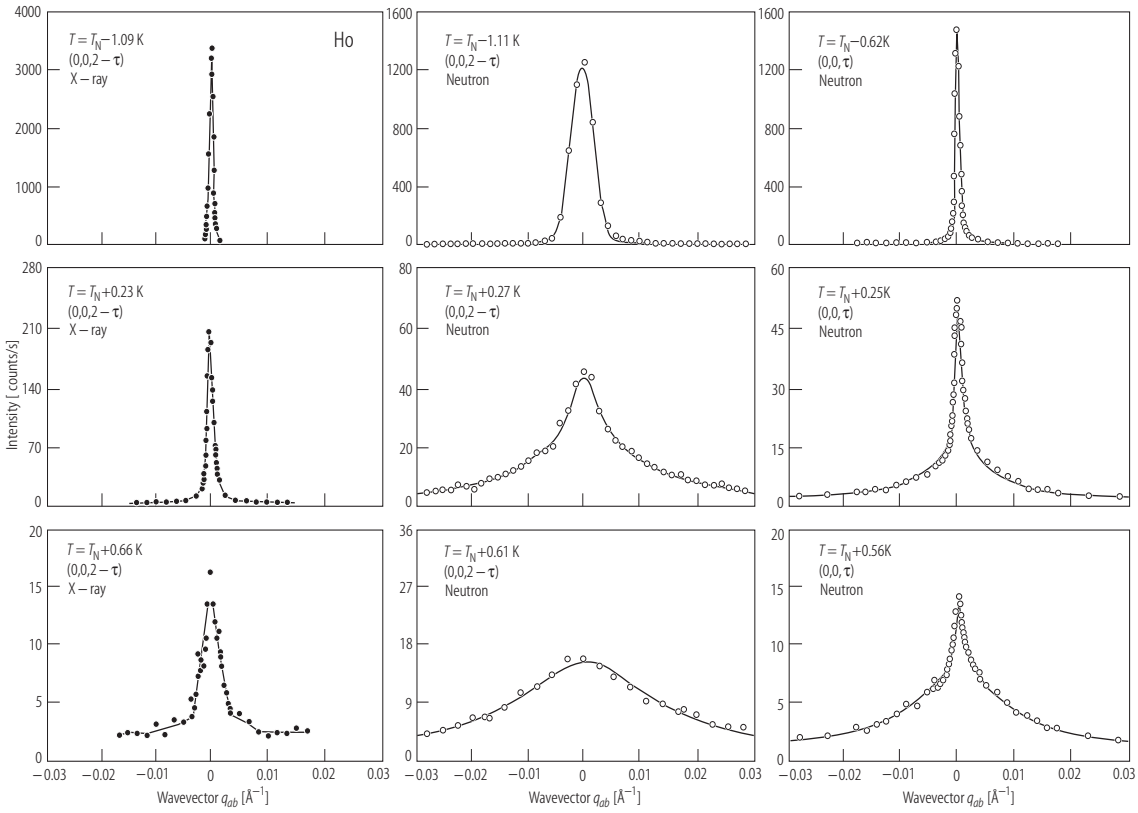

Fig. 215. Transverse X-ray- and neutron-scattering scans taken at the (0,0,2–τ) and (0,0,τ) magnetic peak positions of Ho. The scans in the top row of the figure were taken at temperatures below the transition and represent the resolution of the different experimental configurations. The centre and bottom rows show critical scattering observed at temperatures above the transition. The solid lines represent fits to the Lorentzian plus squared-Lorentzian line shape [94T3].

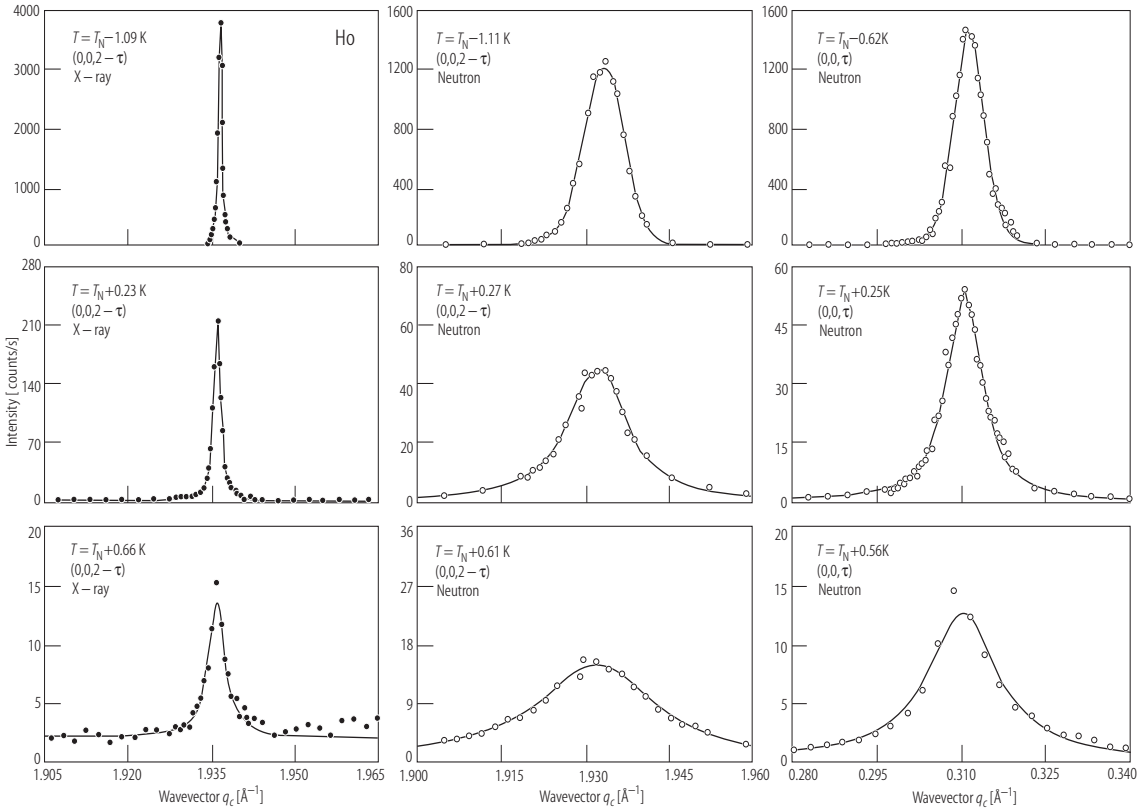

Fig. 216. Longitudinal X-ray- and neutron-scattering scans taken under identical conditions to those of Fig. 215 for Ho sample [94T3].

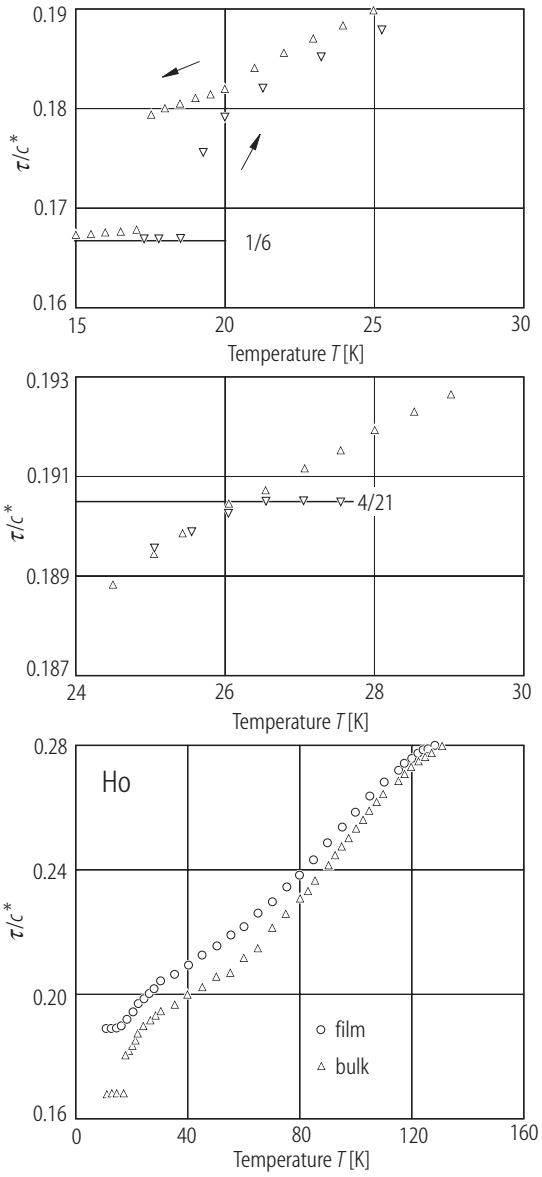

Fig. 218. Neutron diffraction studies of the lock-in behaviour of the spiral wavevector of Ho τ vs. temperature in a 3 T *b*-axis applied magnetic field. τ values of 5/18 and 8/29 are shown by dashed lines. These data clearly support the lock-in transition from a paramagnetic phase directly to a commensurate phase with $\tau = 5/18 = 0.2778$ [94T].

Fig. 217. Magnetic modulation wavevector τ (in c^* units) vs. temperature for the bulk and film Ho samples. The two upper figures show the hysteresis measured near the spiral-to-conical transition of the bulk sample and a lock-in transformation which was observed in the bulk sample after the temperature was cycled in a loop around $T = 27$ K. Close to T_N, $\tau = 0.28$ for both samples, which corresponds to an average turn angle $\delta = \tau \times 180° = 50.4°$ between moments in neighbouring planes along the *c* axis. Near $T_C = 17.0$ K, the bulk sample exhibits a lock-in transition to $\tau = 1/6$, which corresponds to the spiral-to-conical phase transformation. The latter is marked by an abrupt change in wave vector from $\tau = 0.1795$ at 17.5 K to $\tau = 0.1677 \pm 0.0010$ at 17 K. When the temperature of the bulk sample is raised from 10 K, the conical- to-spiral transition occurs at a higher temperature ($T_C' = 19$ K) than for cooling cycles. A lock-in transition to $\tau = 4/21$ was observed in the experiments in a separate cycling of the temperature in a loop around 27 K [94H].

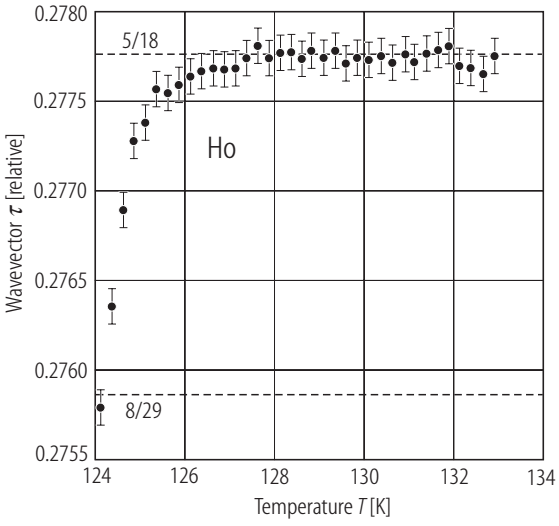

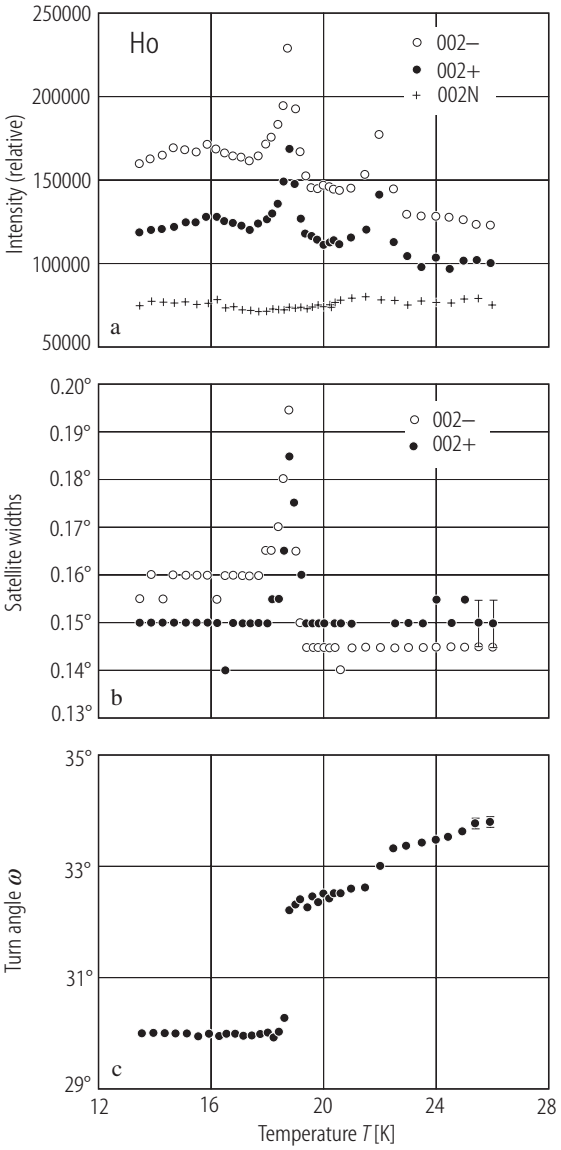

Fig. 219. Temperature evolution of (**a**) integrated intensities (in arbitrary units) of the 0 0 2±τ and (002) nuclear reflections, (**b**) widths of the 0 0 2±τ reflections, and (**c**) interplanar turn angle, of a (*b*, *c*) Ho sample in *b*-axis applied field of 0.025 T [92P].

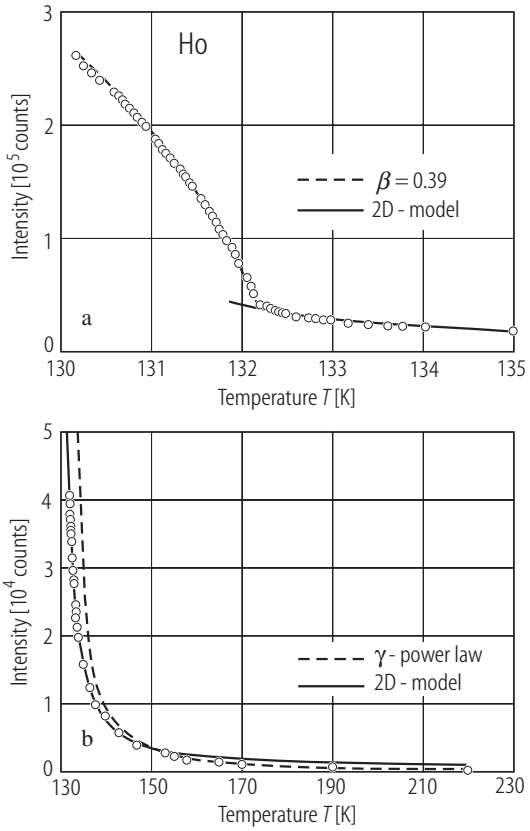

Fig. 220. Integrated intensity for the (0, 0.2–δ) reflection vs. temperature for Ho helical to paramagnetic phase transition. In (**a**) fits to a $t^{2\beta}$ dependence of the spontaneous magnetization in the ordered region and to a 2D-planar spin model in the paramagnetic region. In (**b**) fits to the persistent intensity observed in the paramagnetic region [95dP].

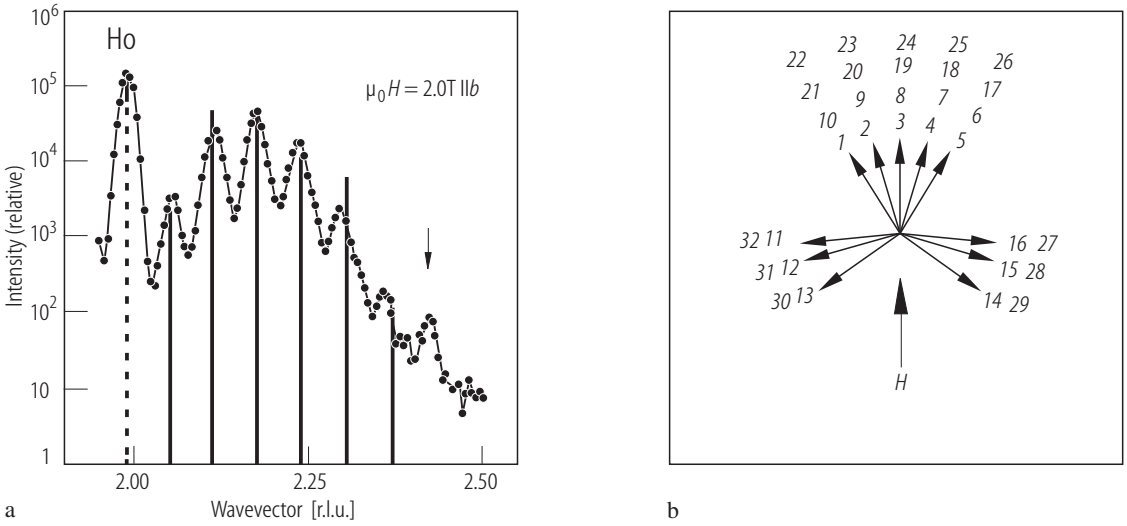

Fig. 221. (**a**) Scattered-neutron intensity observed in a scan of the neutron wavevector transfer along [00l] peak of Ho neutron diffraction pattern at 40 K in a field of 2.0 T applied along the easy *b* axis. The solid vertical lines represent the intensity calculated for a helifan (3/2) structure, with 20 moments having a component aligned along the field and 12 moments with a component anti-aligned. (**b**) A representation of the helifan (3/2) structure which was found to give the best fit to the data shown in (**a**). The arrows point in the direction of the moments and have been projected onto the basal plane. They are numbered in the order in which they occur along the c axis. Note: the changes of helicity at moments numbered *6* and *22* [92J1].

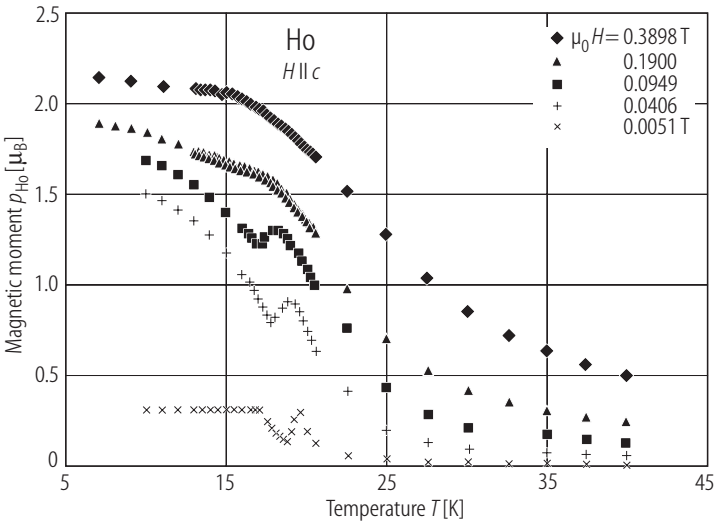

Fig. 223. Temperature variation of Ho single crystal magnetization as a function of the applied *c*-axis field. The results give evidence for the existence of a net *c*-axis magnetic moment and hence a low temperature (< 25 K) conical phase in Ho [92P].

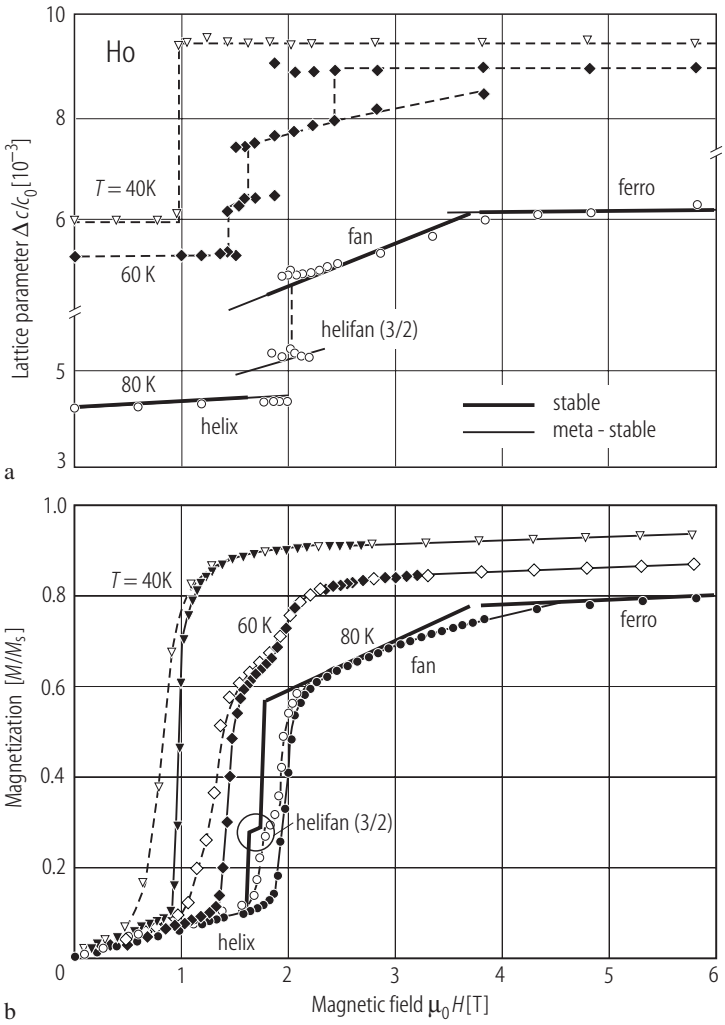

Fig. 222. (**a**) Magnetic field dependence of the *c*-lattice parameter in Ho metal at various temperatures. The solid thick and thin lines are calculated results for the stable and metastable phases, respectively, at 80 K. (**b**) Magnetization curves at various temperatures. The solid line is calculated result for the stable phase at 80 K. The helifan phase is stable between 1.69 and 1.73 T. Open symbols and dotted lines are the results obtained with decreasing magnetic field [97O].

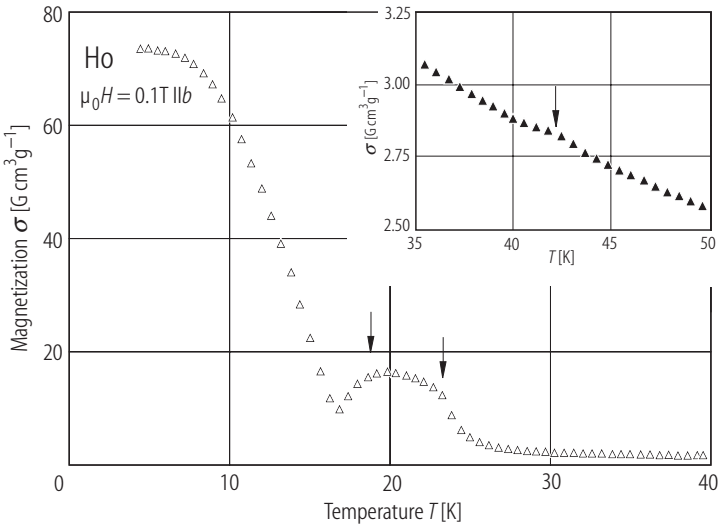

Fig. 224. Magnetization as a function of temperature from 5 to 40 K for magnetic field of 0.1 T along the *b* axis of Ho single crystal. The arrows show 20 K and 24 K anomalies. The inset shows the expanded σ vs. T region between 35 and 50 K. The arrow indicates the 42 K anomaly [90W].

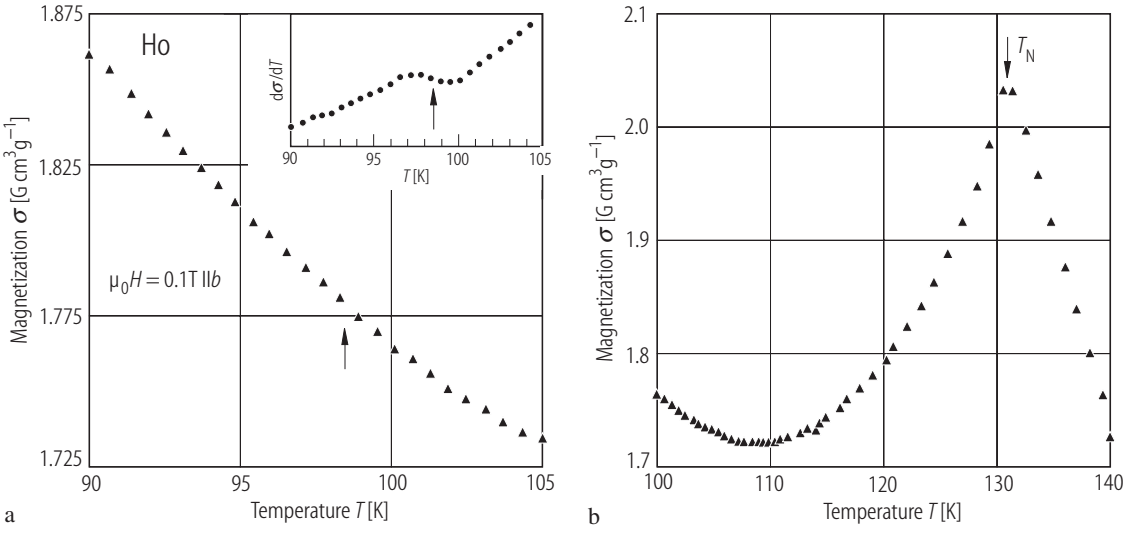

Fig. 225. (**a**) Magnetization as function of temperature from 90 K to 105 K for a magnetic field of 0.1 T along the *b* axis . The inset of (**a**) shows dσ/dT vs. T. The arrows indicate the 98 K anomaly. (**b**) Magnetization σ as function of temperature between 100 K and 140 K for a magnetic field of 0.1 T along the *b* axis. The peak is in the Néel temperature [90W].

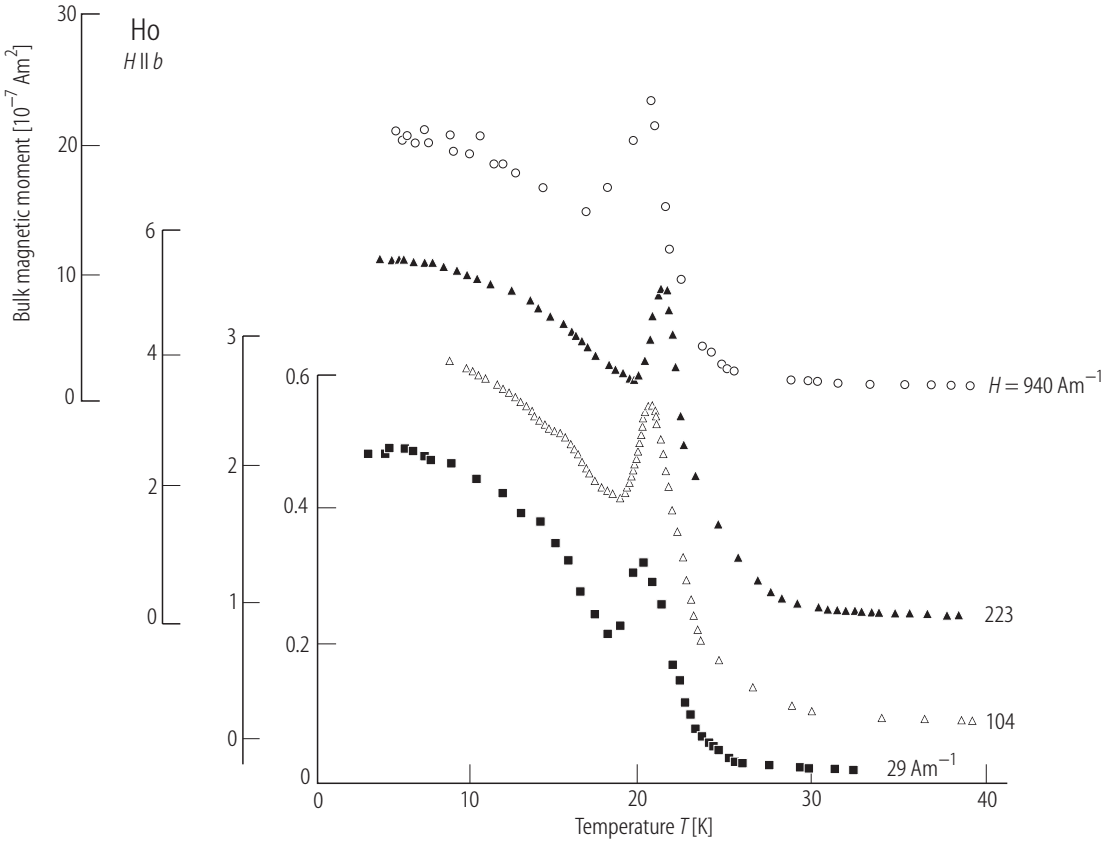

Fig. 226. Temperature dependencies of the magnetic moment of a Ho single crystal on sample heating in magnetic field. H = 29, 104, 223, and 940 A m^{-1}, with $H \| b$ [91S2].

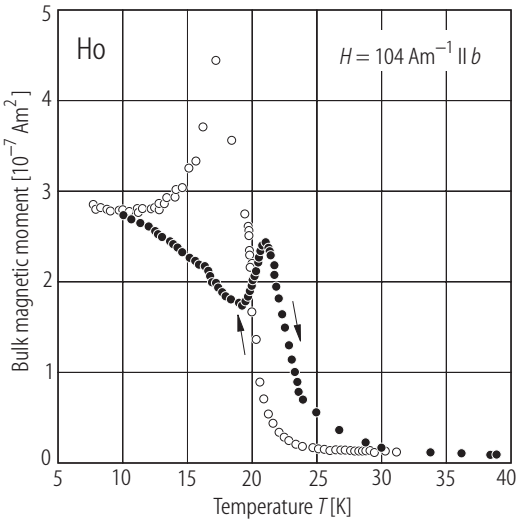

Fig. 227. Temperature dependence of the magnetic moment of Ho single crystal in the warming and cooling runs in the magnetic field H = 104 A m^{-1}. $H||b$ in the temperature range where the helimagnetic-ferromagnetic phase takes place. The hysteresis observed is an evidence of the first-order transition [90B2].

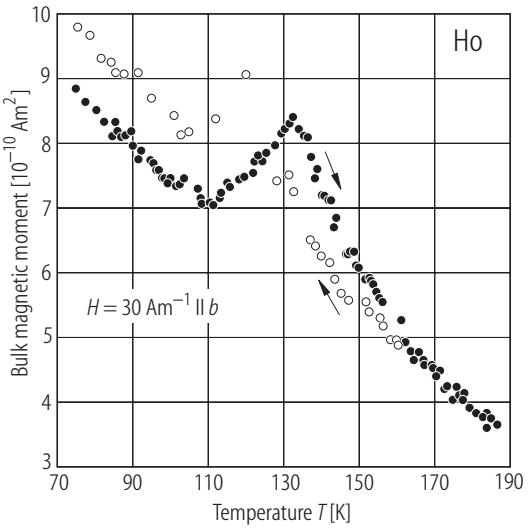

Fig. 228. Temperature dependencies of the magnetic moment of a Ho single crystal on sample cooling and heating in the fields H = 30 A m^{-1}. in the vicinity of the paramagnetism-helicoidal antiferromagnetism phase transition ($H||b$) [91S2].

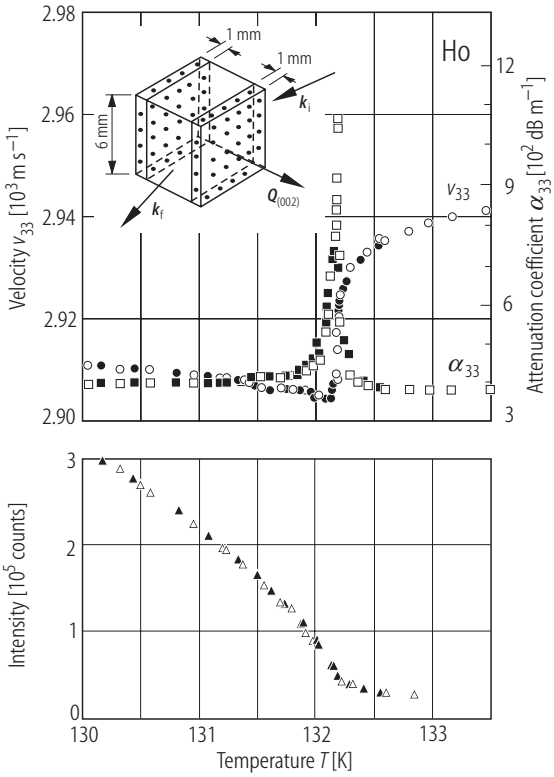

Fig. 229. Simultaneously measured ultrasonic velocity v_{33} and attenuation α_{33} and integrated neutron intensity vs. temperature for the Ho crystal. The longitudinal ultrasonic wave was propagated along the c axis and neutrons probed the (0, 0.2–δ) satellite while passing through the bulk of the crystal on account of the Cd-masking arrangement. Open symbols refer to cooling and closed symbols refer to the subsequent heating run [95dP].

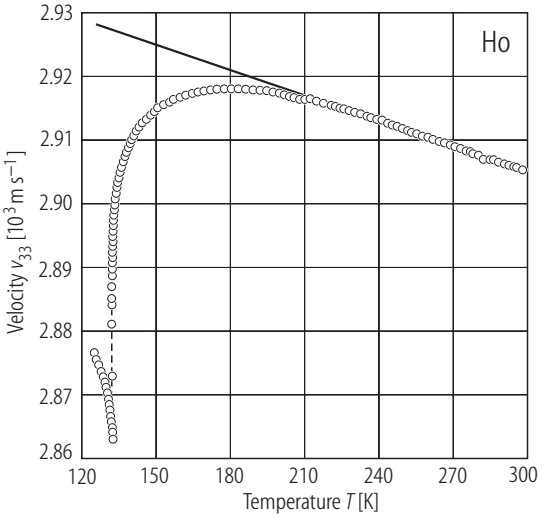

Fig. 230. Longitudinal velocity v_{33} vs temperature for ultrasonic waves propagated along the c axis of crystal Ho. The solid line represents the "normal" temperature dependence expected for a non-magnetic crystal in the temperature region of interest [95dP].

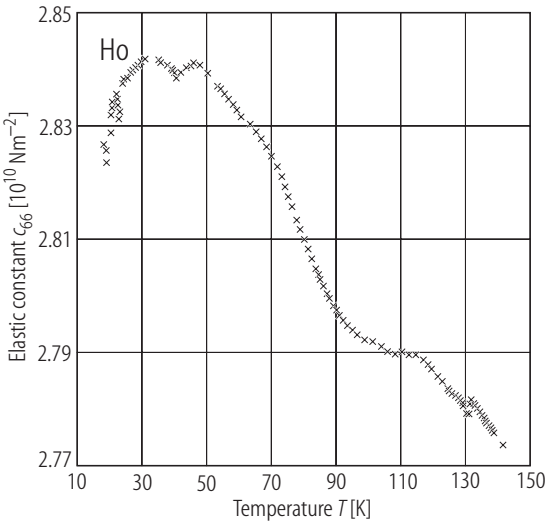

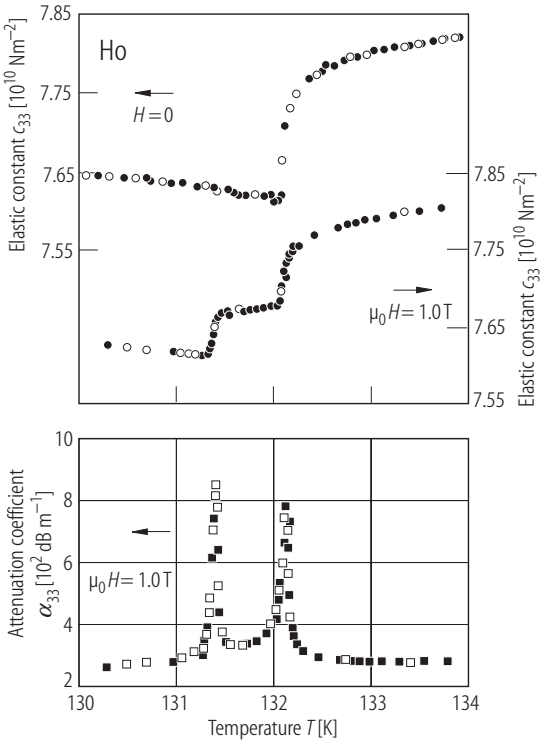

Fig. 231. Temperature dependence of the longitudinal elastic constant c_{33} for Ho measured by the pulse echo overlap method. Anomalies in elastic constant c_{33} and attenuation coefficient α_{33} indicating the extent of the $\tau = 5/18\ c^*$ lock-in below T_N in an applied field of 1 T. Results obtained in a cooling run are indicated by open symbols and during a heating run by closed symbols [95V].

Fig. 233. Temperature dependence of the elastic constant c_{66} of Ho measured by propagating shear waves down the a axis polarised perpendicular to c in the range 10 - 150 K [88B1].

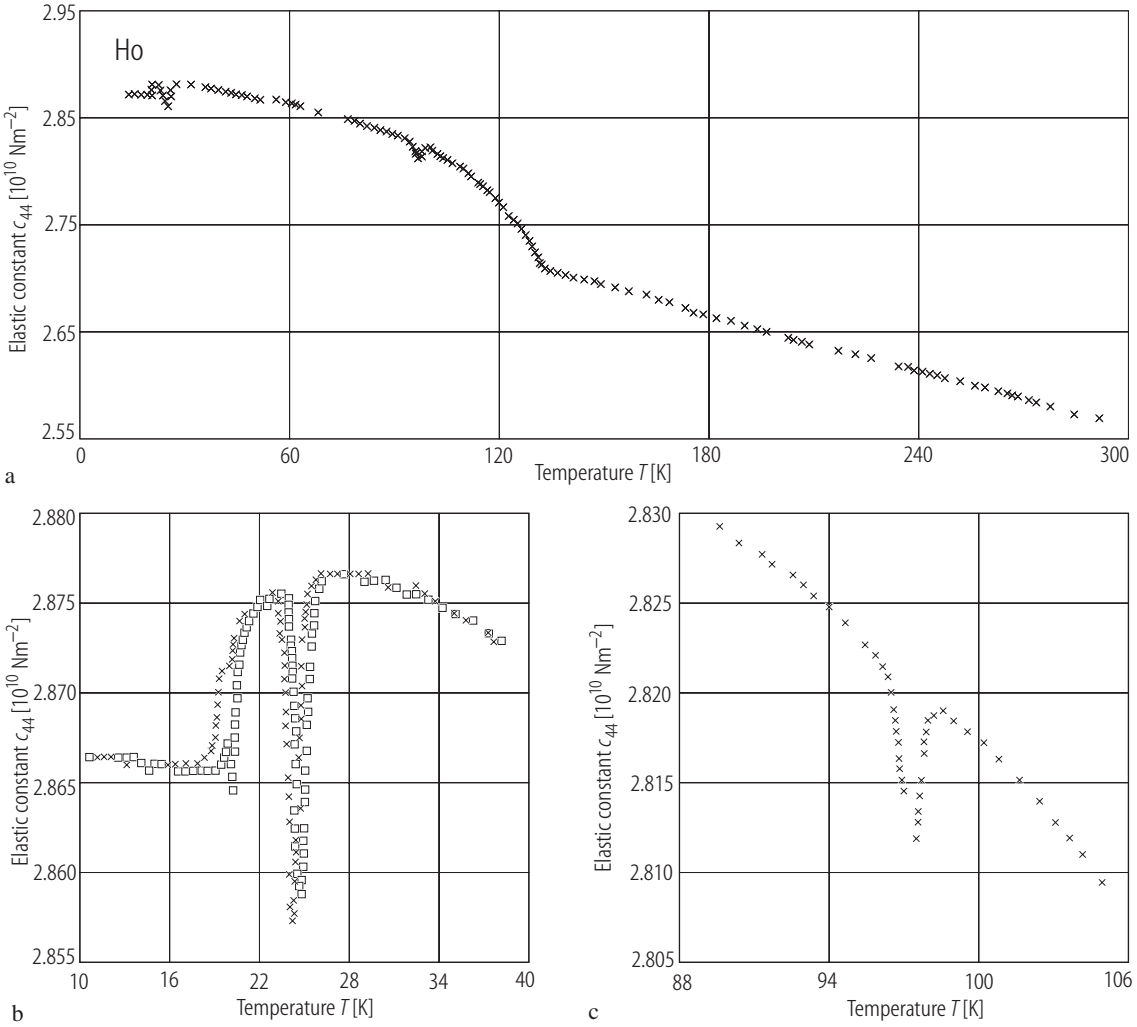

Fig. 232. Temperature dependence of the elastic constant c_{44} (shear waves polarised parallel to c). (**a**) 4.2 – 300 K, (**b**) 7 – 40 K, (**c**) 88 – 106 K. Crosses: cooling, squares: warming. The small step and dip around 19.8 K indicate the dual nature of the low-temperature transition [88B1].

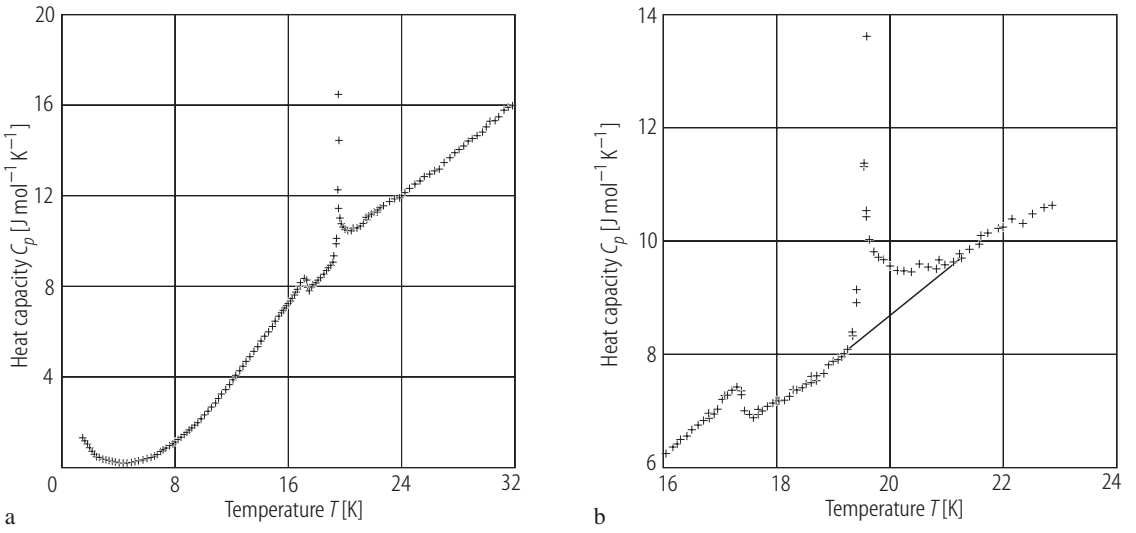

Fig. 234. Specific heat, C_p, of Ho in the temperature range: (**a**) 0 - 32 K; (**b**): 16 - 23 K. The narrowness (0.03 K) of the peak at 19.46 K suggest its discontinuance [89S].

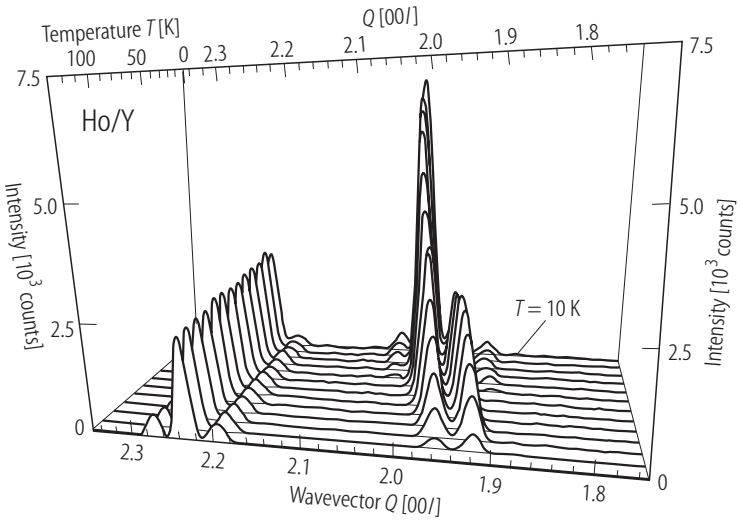

Fig. 235. Neutron-scattering intensity observed from a $(Ho_{40}Y_{15})_{50}$ superlattice along (00l) at a series temperatures at intervals of 10 K from 130 to 10 K. The nuclear (002) scattering is temperature independent and the magnetic scattering grows with decreasing temperature. Note that even at 120 K, the magnetic scattering is two peaks showing long-range coherence [94C].

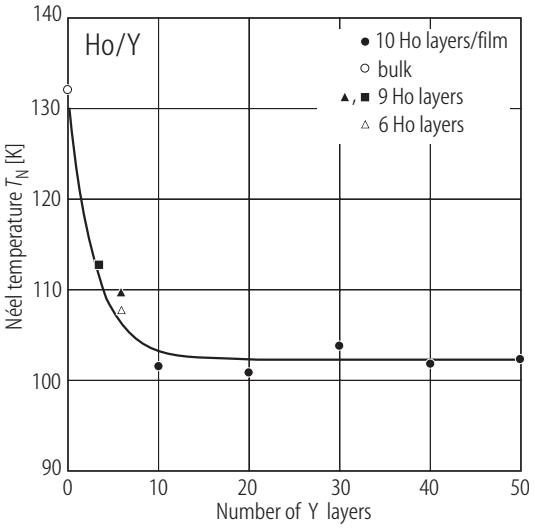

Fig. 236. Néel temperature dependence on Y layer thickness in Ho/Y superlattice structure. Notice a lower Néel temperature than in a bulk Ho [95T2].

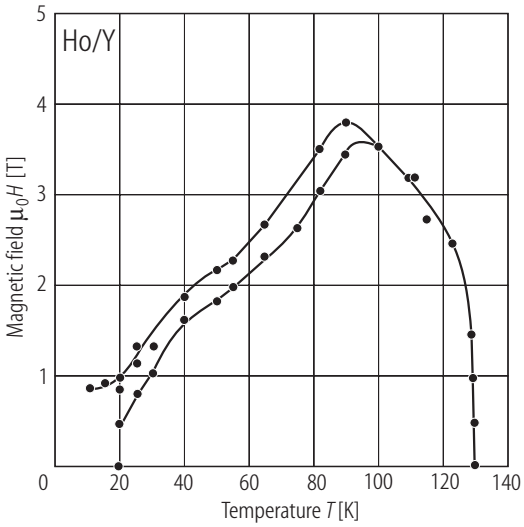

Fig. 237. *b* axis magnetic phase diagram of a 3000 Å Ho film [95T2].

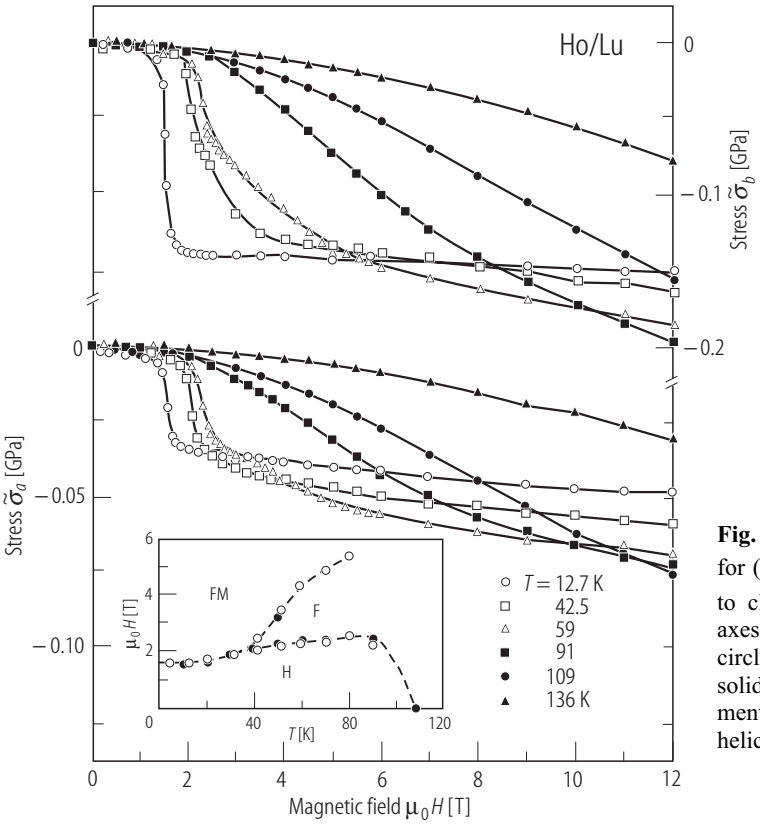

Fig. 239. Magnetoelastic stress isotherms for $(Ho_6/Lu_6)_{100}$: $\tilde{\sigma}_a$ and $\tilde{\sigma}_b$ correspond to clamping along *a*- and *b*- superlattice axes. Inset: magnetic phase diagram (open circles: from magnetoelastic stress and solid circles: from magnetization measurements; ferromagnetic (FM), fan (F), and helical phases (H) [96dM].

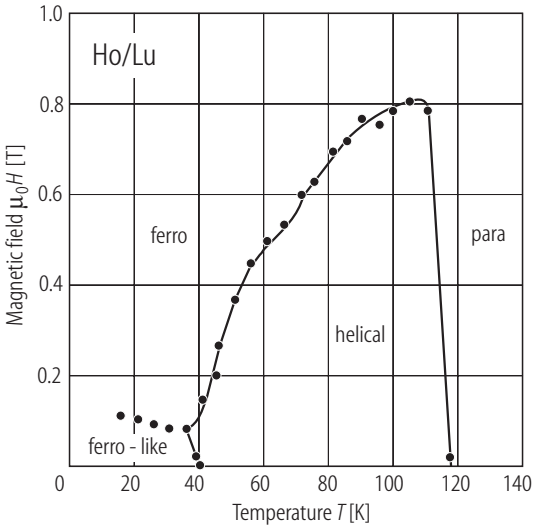

Fig. 238. Magnetic phase diagram of $(11Ho/50Lu)_{50}$ superstructure with magnetic field H applied in the b direction investigated by vibrating sample magnetometry [95T1].

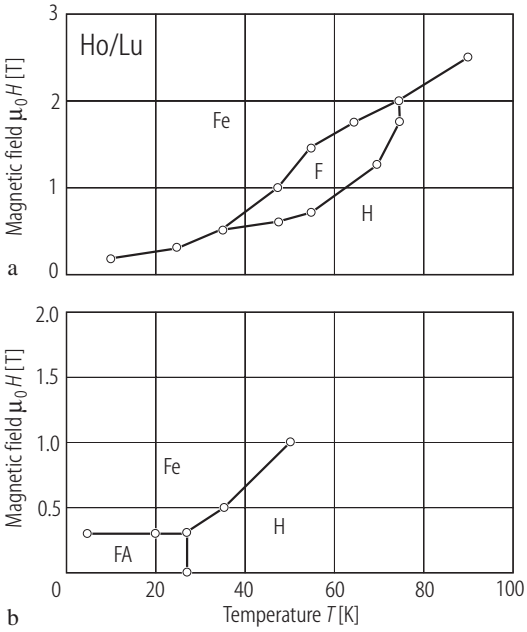

Fig. 240. Magnetic phases of (**a**) $(Ho_{40}Lu_{15})_{50}$ and (**b**) $(Ho_{20}Lu_{10})_{50}$ superlattices in a basal plane magnetic field. Fe: ferromagnetic, H: basal plane helix, FA: ferromagnetic ordering with antiferromagnetic coupling between blocks and fan phase (F) [95S1].

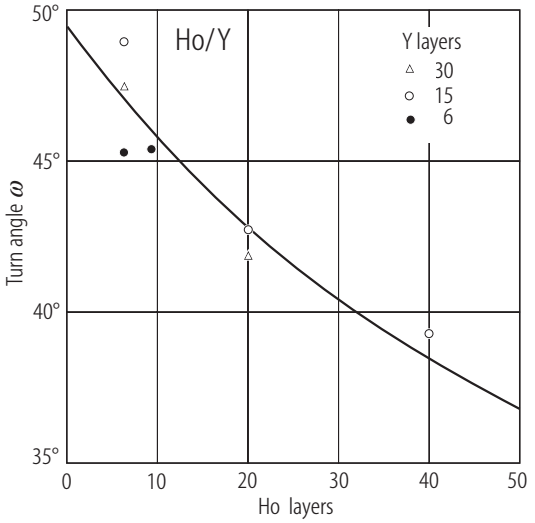

Fig. 241. Turn angle ω for Ho in various superlattices showing that at least for thick superlattices, ω is largely independent of the Y thickness and that ω is close to a commensurate spin-slip value [94C].

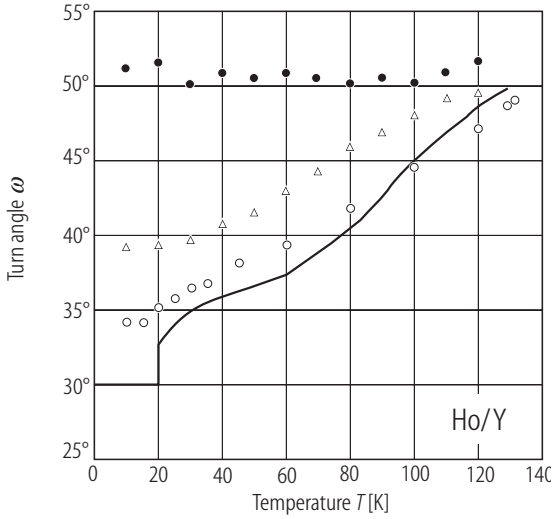

Fig. 242. Temperature dependence of the turn angles ω for successive Ho (triangles) and Y (solid circles) layers of the $Ho_{40}Y_{15}$ superlattice. Also shown is ω (open circles) for an epitaxially grown Ho film and for bulk Ho (solid line) [94C].

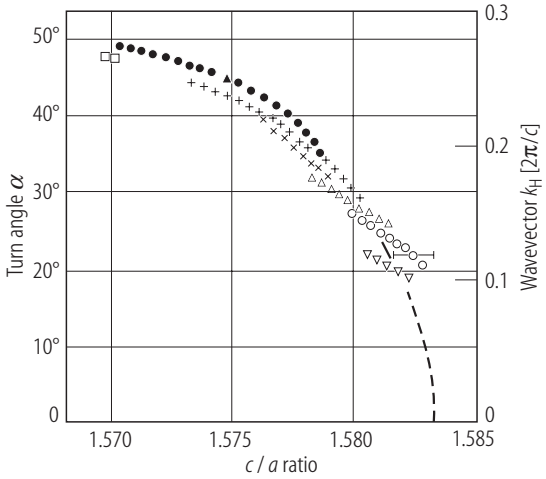

Fig. 243. Helix turn angle α and the helix wavevector k_H vs. c/a ratio of the crystalline lattice Ho (solid circles), Dy (+), Er (solid triangle), Tb (open triangles, downward), $Tb_{91}Y_9$ (open circles), $Tb_{84}Y_{16}$ (open triangles, upright), $Tb_{69}Y_{31}$ (x), $Tb_{39}Y_{61}$ (squares). Composition in at %. Dashed curve is a square root fit [95A1].

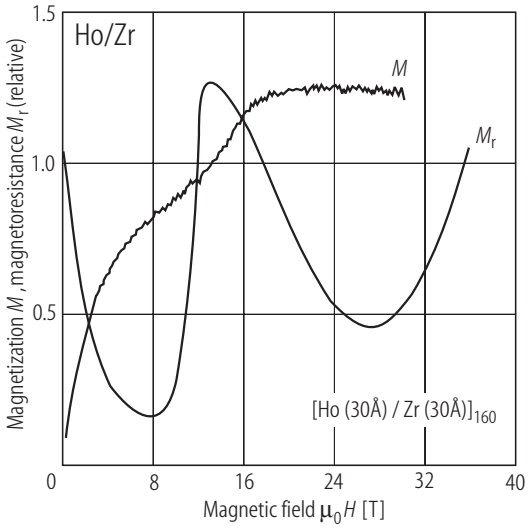

Fig. 244. Typical magnetization and magnetoresistance with a magnetic field perpendicular to the plane at 4.2 K for Ho/Zr multilayers. Both results point out a large magnetic transition around 11 T. This transition would be related to the closing of the conical or helical magnetic configurations finally producing ferromagnetic alignment along the direction of the field [95R].

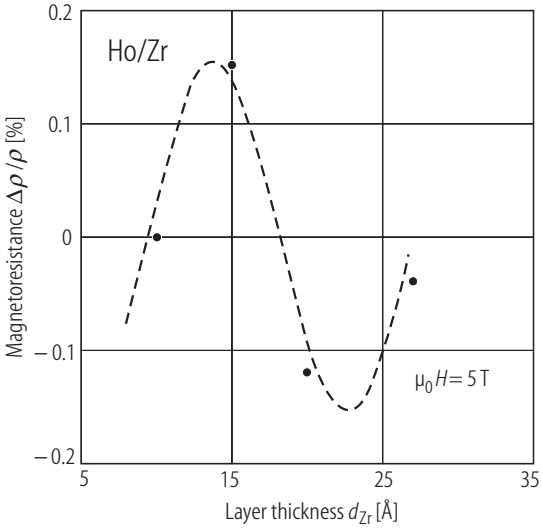

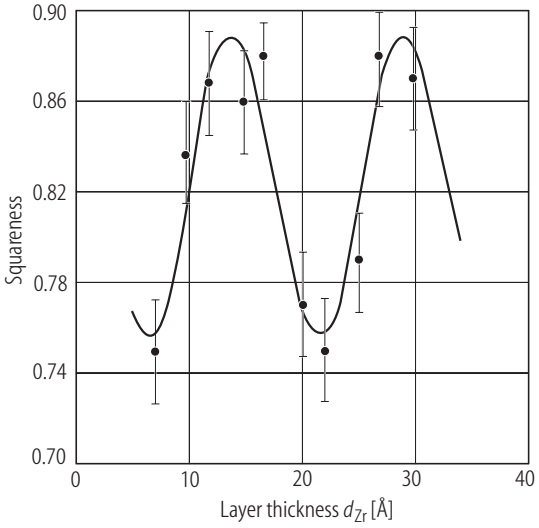

Fig. 245. Oscillation of magnetoresistance for [Ho(30Å)/Zr(xÅ)]×20 multilayers. The right figure shows the squareness of the hysteresis loops of same samples [95R].

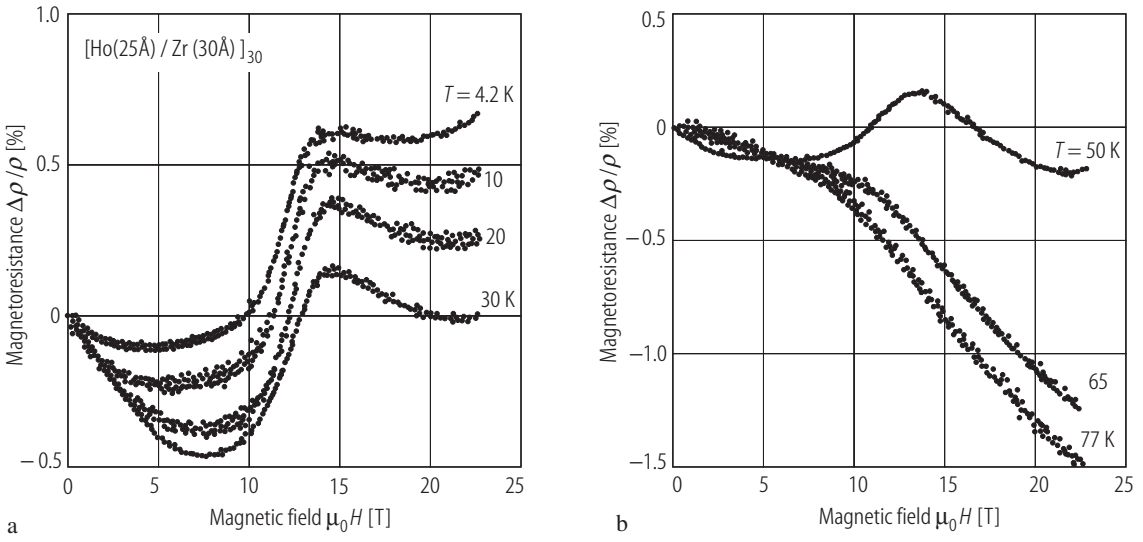

Fig. 246. Typical magnetoresistance for Ho/Zr multilayers at (**a**) low temperature showing a sharp magnetic transition and (**b**) temperature higher than 50 K [95R].

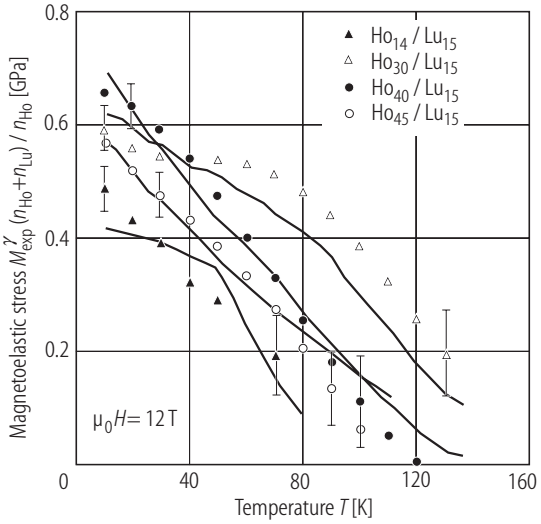

Fig. 247. Variation with temperature of the magnetoelastic stress M^{γ}_{exp} (12 T), multiplied by $(n_{Ho} + n_{Lu})/n_{Ho}$, for the $(Ho_n/Lu_{15})\times50$ superlattices, with n_{Ho} = 14, 30, 40, 45. The lines are the scaling with the reduced magnetization [98dM].

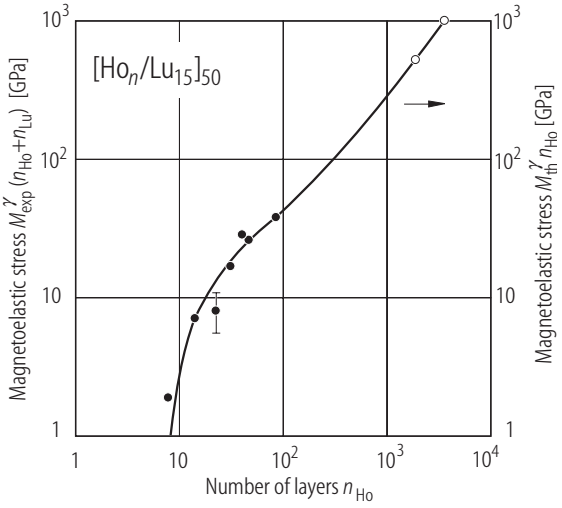

Fig. 248. Variation of the basal plane cylindrical symmetry breaking magnetoelastic stress, M^{γ}_{exp}, at 10 K and at an applied magnetic field of 12 T, multiplied by $(n_{Ho} + n_{Lu})$ (solid circles), against n_{Ho} (where n_{Ho} and n_{Lu} respectively are the number of atomic planes in the Ho and Lu blocks), for the $(Ho_n/Lu_{15})\times50$ superlattices. M^{γ}_{exp} multiplied by the same factor is plotted for $5\cdot10^3$ Å and 10^4 Å thick Ho films (open circles) [98dM].

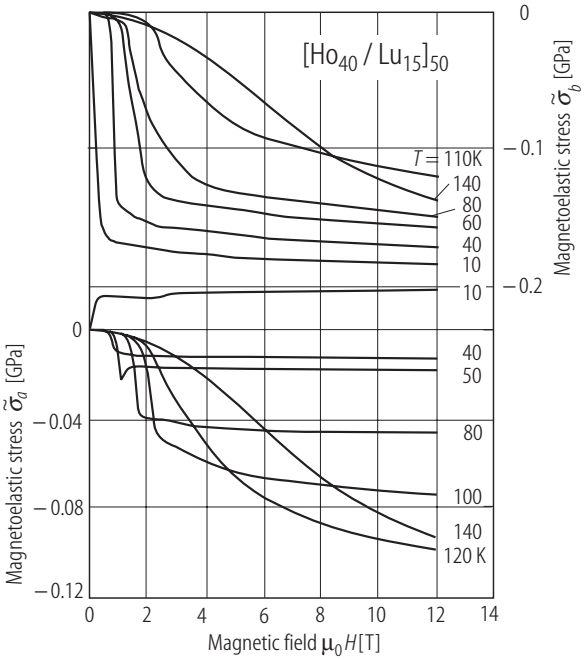

Fig. 249. Magnetoelastic stress measured isotherms for the superlattice (SL) $(Ho_{40}/Lu_{15})\times 50$. $\tilde{\sigma}_a$ and $\tilde{\sigma}_b$ respectively correspond to the SL clamping along the *a* and *b* axes of the hexagonal structure, with magnetic field applied along the *b* easy axis [98dM].

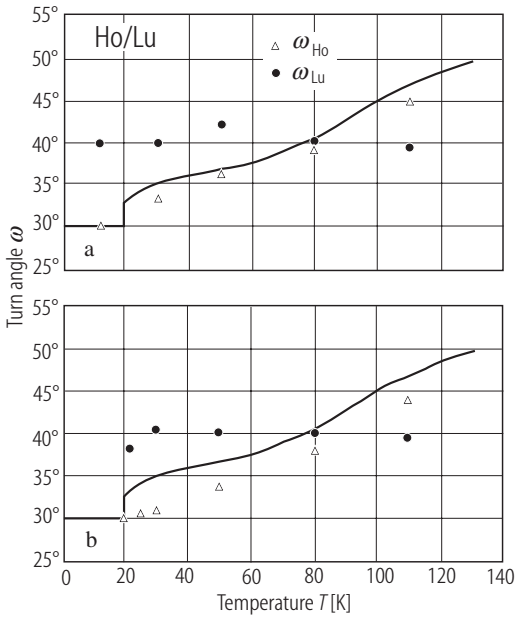

Fig. 250. Temperature dependence of the turn angle ω_{Ho} in Ho and ω_{Lu} in Lu for the (**a**) $(Ho_{40}/Lu_{15})_{50}$ and (**b**) $(Ho_{20}/Lu_{15})_{50}$ superlattices. The full curves are the turn angle measured in bulk Ho [93S].

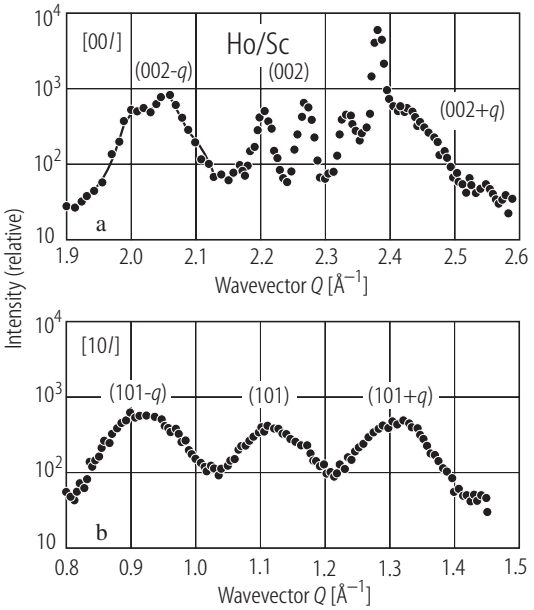

Fig. 251. Neutron scattering observed at T = 4 K from sample Ho_{30}/Sc_{10} with wavevector transfer, Q along (**a**) [00*l*], and (**b**) [10*l*]. The structure of the scattering at (002-*q*) suggests coherence of the magnetic ordering along [00*l*] [97B-J].

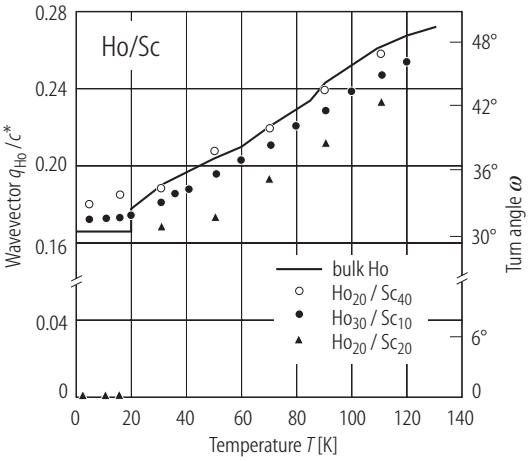

Fig. 252. Temperature dependence of the Ho turn angle per plane, $\omega_{Ho}(q_{Ho})$ in Ho/Sc superlattices [97B-J].

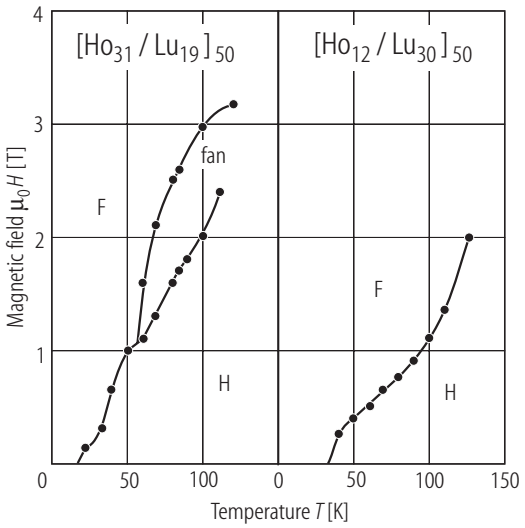

Fig. 253. Magnetic phase diagrams for $[Ho_{31}Lu_{19}]_{50}$ and $[Ho_{12}Lu_{30}]_{50}$ superlattices [96A1].

References

85G Gibbs, D., Moncton, D.E., D'Amico, K.L., Bohr, J., Grier, B.H.: Phys. Rev. Lett. **55** (1985) 234

86B Bohr, J., Gibbs, D., Moncton, D.E., D'Amico, K.L.: Physica A **140** (1986) 349

88B1 Bates, S., Patterson, C., McIntyre, G.J., Palmer, S.B., Mayer, A., Cowley, R.A., Melville, R.: J. Phys. C **21** (1988) 4125

88C Cowley, R.A., Bates, S.: J. Phys. C **21** (1988) 4113

89S Stewart, A.M., Collocott, S.J.: J. Phys.: Condens. Matter **1** (1989) 677

90B1 Bohr, J.: J. Magn. Magn. Mater. **83** (1990) 530

90B2 Burhanov, G.S., Volkozub, A.V., Snigirev, O.V., Tishin, A.M., Chistykov, O.D.: Solid State Phys. **32** (1990) 2483

90J Jensen, J., Mackintosh, A. R.: Phys. Rev. Lett. **64** (1990) 2699

90W Willis, F., Ali, N., Steinitz, M.O., Mojtaba Kahrizi, Tindall, D.A.: J. Appl. Phys. **67** (1990) 5277

91McM McMorrow, D.F., Patterson, C., Godfrin, H., Jehan, D.A.: Europhys. Lett. **15** (1991) 541

91S2 Snigirev, O.V., Tishin, A.M., Volkozub, A.V.: J. Magn. Magn. Mater. **94** (1991) 342

92J Jensen, J., Mackintosh, A.R.: J. Magn. Magn. Mater. **104-107** (1992) 1481

92J1 Jehan, D.A., McMorrow, D.F., Cowley, R.A., McIntyre, G.J.: Europhys. Lett. **17** (1992) 553

92P Pearce, A., Baruchel, J., Kulda, J.: Phys. Status Solidi (b) **172** (1992) 443

93S Swaddling, P.P., McMorrow, D.F., Simpson, J.A., Wells, M.R., Ward, R.C.C., Clausen, K.N.: J. Phys.:Condens. Matter **5** (1993) L481

94C Cowley, R.A., McMorrow, D.F., Simpson, A., Jehan, D., Swaddling, P., Ward, R.C.C., Wells, M.R.: J. Appl. Phys. **76** (1994) 6274

94H Helgesen, G., Hill, J.P., Thurston, T.R., Gibbs, D., Kwo, J., Hong, M.: Phys. Rev. B **50** (1994) 2990

94T Tindall, D.A., Adams, C.P., Steinitz, M.O., Holden, T.M.: J. Appl. Phys. **75** (1994) 6318

94T3 Thurston, T.R., Helgesen, G., Hill, J.P., Gibbs, D., Gaulin, B.D., Simpson, P.J.: Phys. Rev. B **49** (1994) 15730

95A1 Andrianov, A.V.: J. Magn. Magn. Mater. **140-144** (1995) 749

95R Raquet, B., Sdaq, A., Broto, J.M., Rakoto, H., Ousset, J.C., Askenazy, S., Baudry, A., Boyer, P., Luche, M.C., Khmou, A.: Physica B **211** (1995) 335

95S1 Swaddling, P.P., McMorrow, D.F., Cowley, R.A., Simpson, J.A., Wells, M.R., Ward, R.C.C., Clausen, K.N., Collins, M.F., Buyers, W.J.L.: J. Magn. Magn. Mater. **140-144** (1995) 783

95S2 Simpson, J.A., McMorrow, D.F., Cowley, R.A., Jehan, D.A.: J. Magn. Magn. Mater. **140-144** (1995) 751

95T1 Tomka, G.J., de Groot, P.A.J., Rainford, B.D., Wells, M.R., Ward, R.C.C., Arnaudas, J.I.: J. Magn. Magn. Mater. **140-144** (1995) 785

95T2 Tomka, G.J., de Groot, P.A.J., Rainford, B.D., Wells, M.R., Ward, R.C.C., del Moral, A.: J. Magn. Magn. Mater. **140-144** (1995) 777

95V Venter, A.M., du Plessis, P. de V.: J. Magn. Magn. Mater. **140-144** (1995) 757

95dP Du Plessis, P. de V., Venter, A.M., Brits, G.H.F.: J. Phys.: Condens.Matter **7** (1995) 9863

96A1 Arnaudas, J.I., del Moral, A., Ciria, M., Tomka, G.J., de la Fuente, C., de Groot, P.A.J., Ward, R.C.C., Wells, M.R.: J. Magn. Magn. Mater. **156** (1996) 421

96dM del Moral, A., Arnaudas, J.I., Ciria, M., Wells, M.R., Ward, R.C.C.: J. Magn. Magn. Mater. **157-158** (1996) 539

97B-J Bryn-Jacobsen, C., Cowley, R.A., McMorrow, D.F., Goff, J.P., Ward, R.C.C., Wells, M.R.: Physica B **234-236** (1997) 495

97G1 Gebhardt, J.R., Baer, R.A., Ali, N.: J. Alloys Compounds **250** (1997) 655

97O Ohsumi, H., Tajima, K., Wakabayashi, N., Shinoda, Y., Kamishima, K., Goto, T.: J. Phys. Soc. Jpn. **66** (1997) 1896

98dM de Moral, A., Ciria, M., Arnaudas, J.I., Wells, M.R., Ward, R.C.C., de la Fuente, C.: J. Phys.: Condens. Matter **10** (1998) L139

2.1.3.10 Erbium

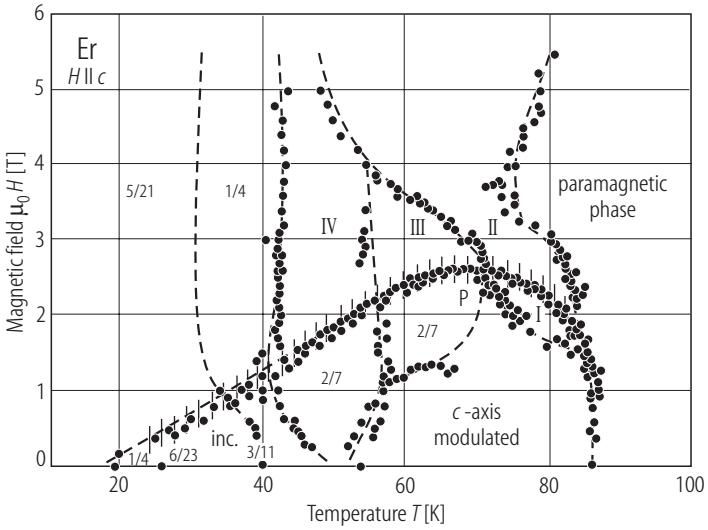

Fig. 254. The *c*-axis magnetic phase diagram of single crystal Er in the temperature range from 10 K to 100 K and in applied *c*-axis magnetic fields from 0 to 5.50 T. Solid circles represent transitions. Dashed lines have been added to suggest transition lines. Regions with unknown structure have been labelled with Roman numerals; inc.: incommensurate phase [97W].

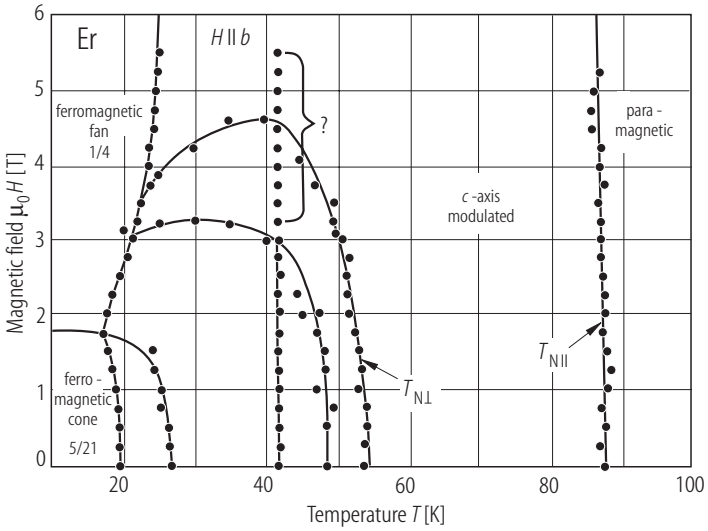

Fig. 255. The *b*-axis magnetic phase diagram of Er between 10 K and 100 K up to 5.5 T from the resistance and magnetoresistance measurements. Solid circles represent transitions. Lines are used to suggest transition. Reduced *c*-axis wavevectors (1/4, 5/21) are indicated [96W1].

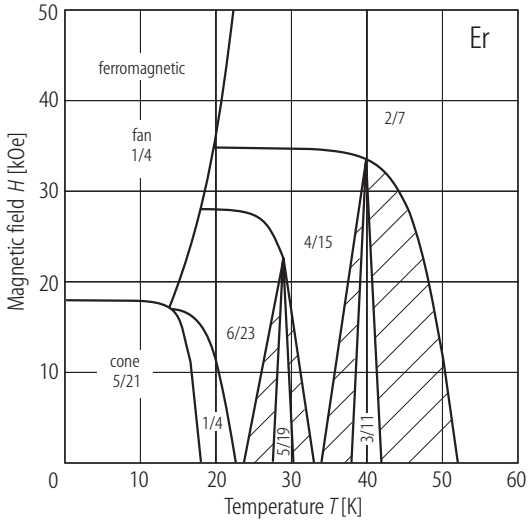

Fig. 256. Schematic phase diagram of Er in a basal-plane field determined from neutron diffraction. The shaded regions represent incommensurable values of the modulation wavevector [94J].

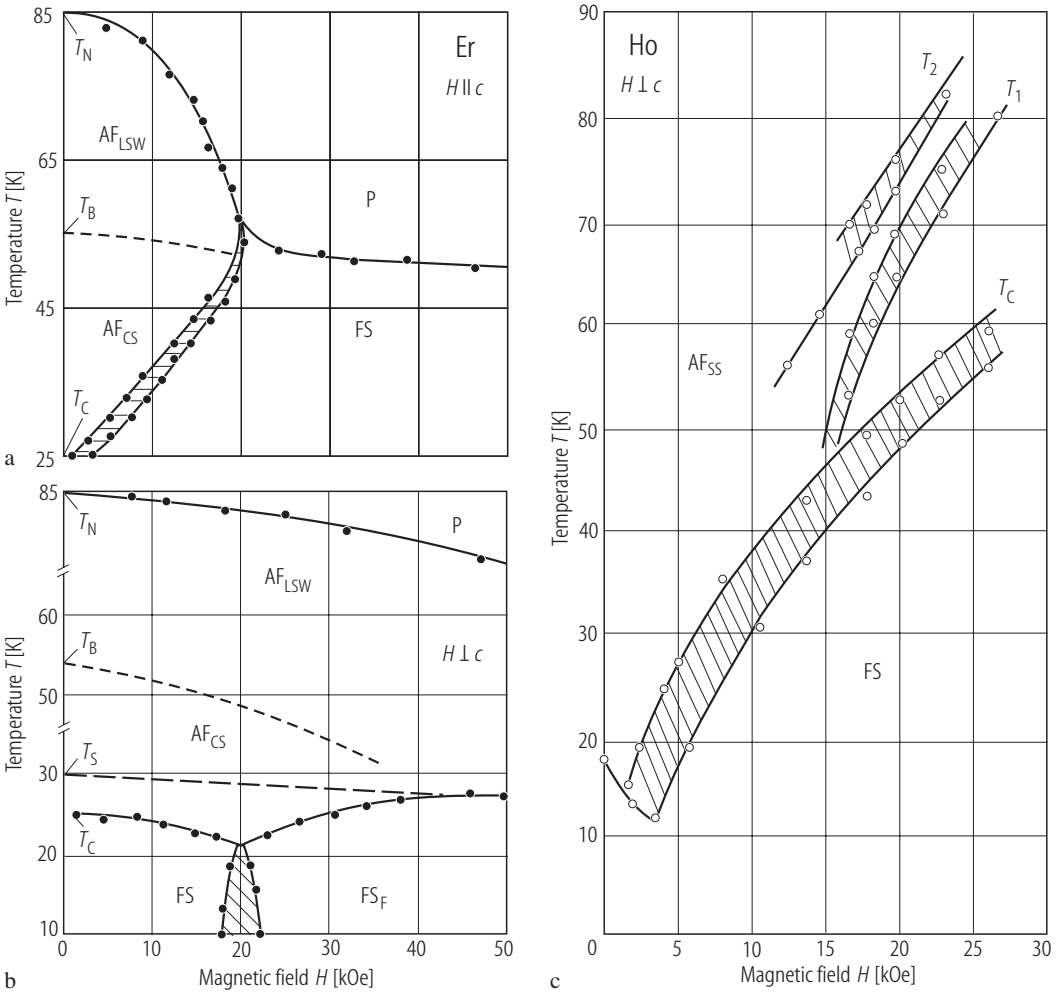

Fig. 257. *H-T* phase diagrams for (**a**) Er orientation $H \| c$, (**b**) Er with $H \perp c$ orientation and (**c**) Ho for $H \perp c$ orientation. The shaded portion stands for the heterophase state (HS) [95B].

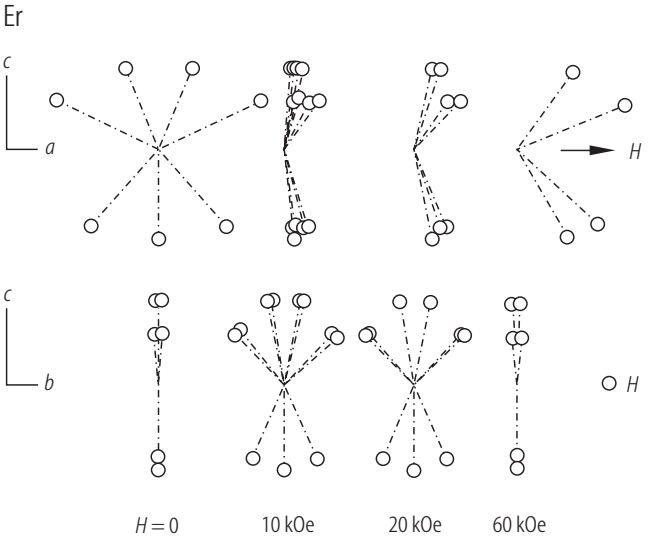

Fig. 258. Calculated stages in the collapse of the $q_c = (2/7)c^*$ structure of Er with a magnetic field along the *a* axis at 35 K. Scaling: *a* to *c* 2:1, and *b* to *c* 1:1 [94J].

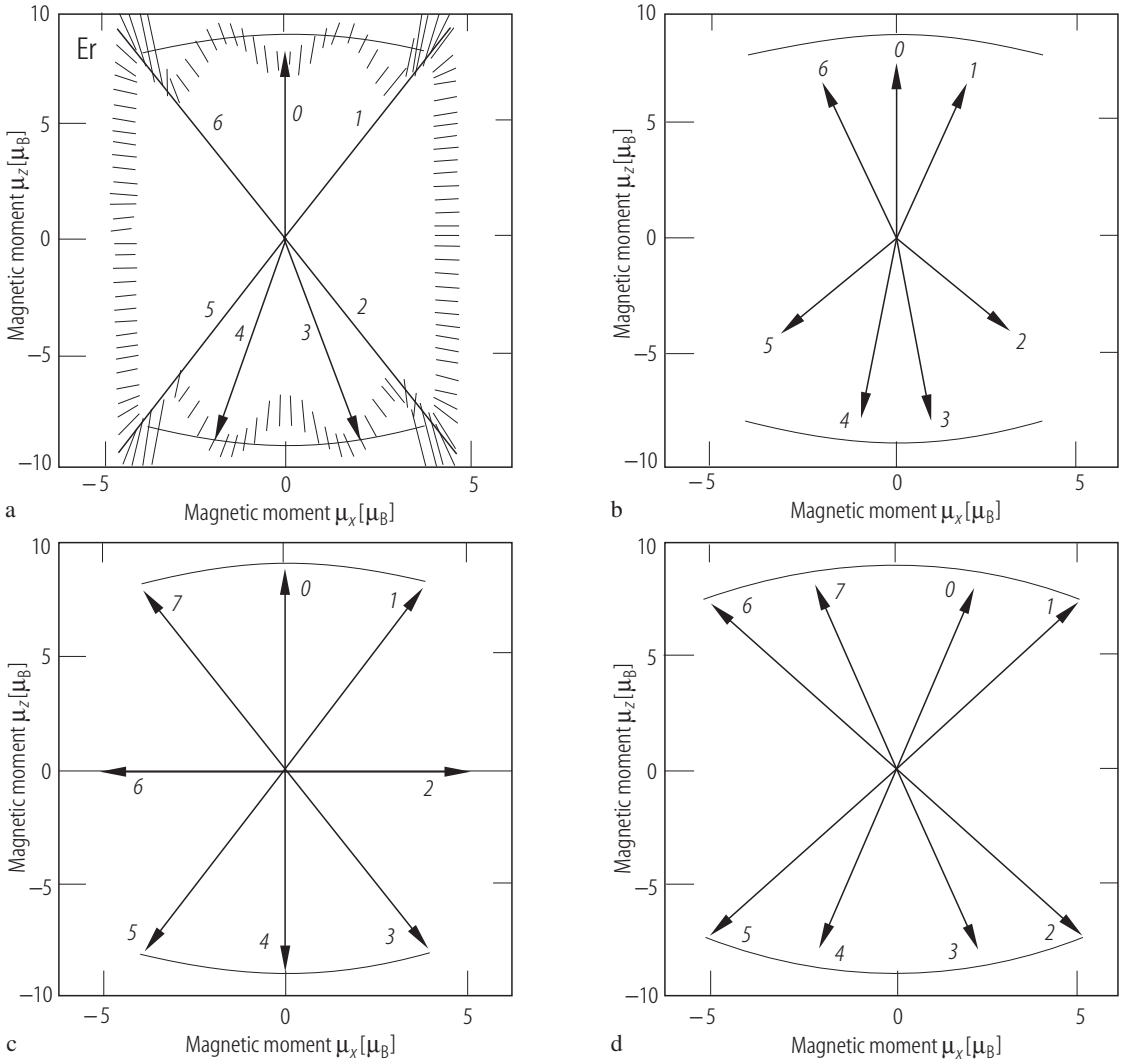

Fig. 259. Spin configuration for a cycloidal structure of Er at 4.5 K and at 11.5 kbar hydrostatic pressure determined by the neutron diffraction studies. The moments have been projected onto the *zz*-plane and displaced to a common origin. The numbers i = *0*, *1*, *2*, *6*, *7* refer to spins in the i-th layer of atoms. The moment components along the y axis were assumed to be zero. The two arcs mark the 9 μ_B upper limits of the total Er moment per atom. The borders of the hatched areas in (**a**) are given by the two curves calculated for an incommensurate structure by using the upper and lower limits for the ordered moment amplitudes. Figures (**c**) and (**d**) show similar diagrams derived for Er at 22 K and at ambient pressure. Figure (**b**) shows the spin configuration for Er at ambient pressure and 49 K [93K].

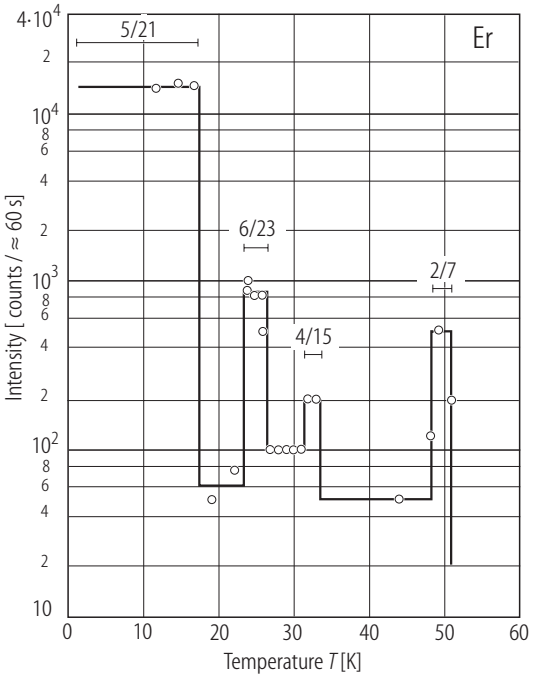

Fig. 260. Peak intensity of the scattering at the magnetic satellite above the (002) Bragg point in Er. The intensity is enhanced at temperatures where the magnetic wavevector corresponds to a structure with a ferromagnetic component. The 2/7 structure has 3 spins up followed by 4 spins down. The 4/15 structure has, 4 up and 4 down. Similarly for the 6/23 structure. The 5/21 structure is the conical structure which occurs below the Curie point [90B1].

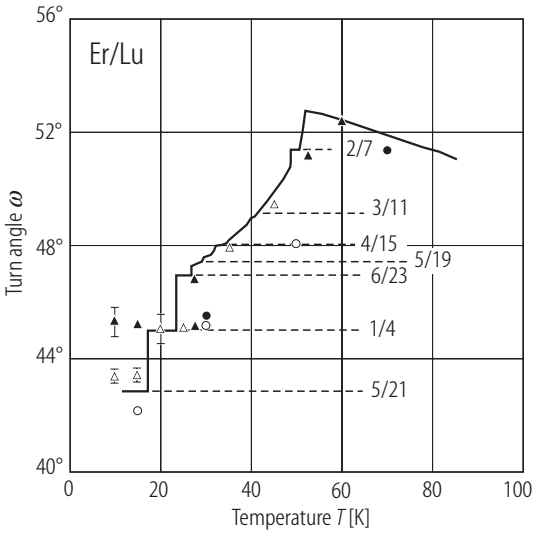

Fig. 261. Phase angle of the modulated spin state measured as a function of temperature in zero field. Open symbols correspond to the basal plane spiral and closed symbols to the *c*-axis modulation. Data for the 600 Å Er/Lu film (circles), the 9500 Å film (triangles), and for bulk Er (solid line) are shown for comparison. The commensurate spin states in bulk are labelled following the notation of Gibbs [91B1].

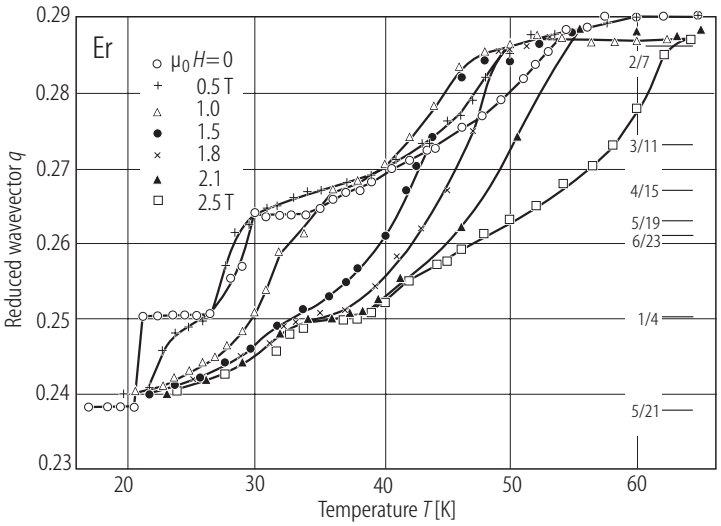

Fig. 262. Magnitude of the wavevector q as a function of temperature at different fields applied along the c axis for Er single-crystal. Lock-ins at 5/21, 1/4**,** and 5/19 in zero field, at 1/4 in a field of above 1.8 T and at 2/7 in a field 2.1 T can be seen. The rational fractions on the right are zero field lock-ins predicted by the *c*-axis spin-slip model [92L].

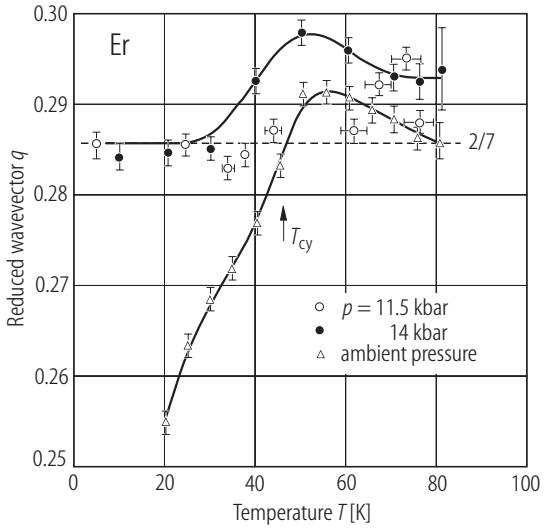

Fig. 263. Temperature dependence of the modulation wavevector $Q = q(2\pi/c)$ obtained from the displacement between (1 1 $l\pm q$) satellites of Er neutron pattern. At 4.5 K, $q = 2/7$ for 11.5 and 14 kbar. Below 18 K, $q = 5/21$ at ambient pressure [95K].

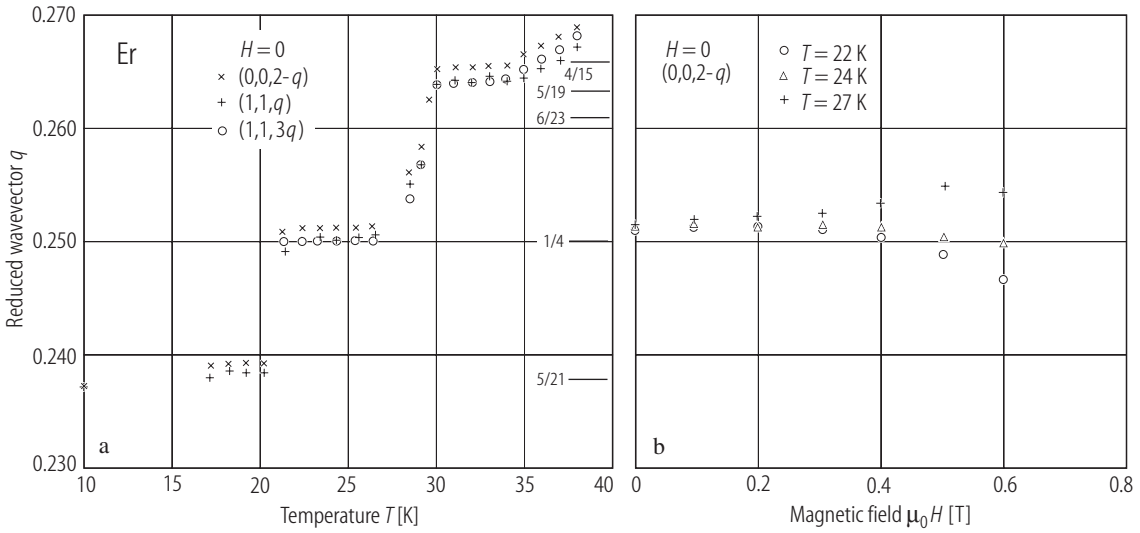

Fig. 264. (**a**) Lock-ins in zero field along the [00*l*] and [11*l*] directions. (**b**) Wavevector q as a function of field near the $q = (1/4)c^*$ in the intermediate phase of the Er metal [92L].

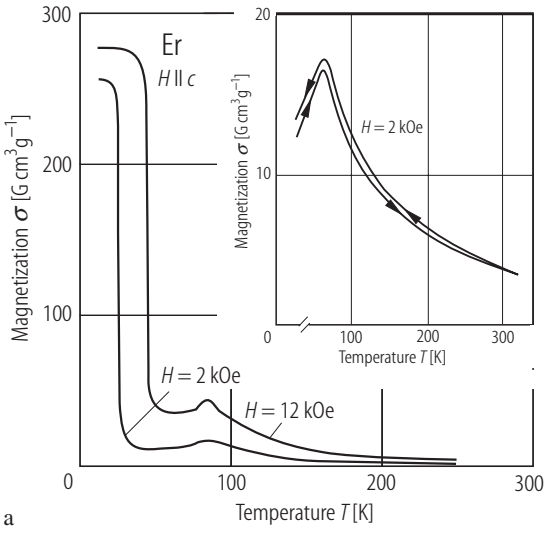

a

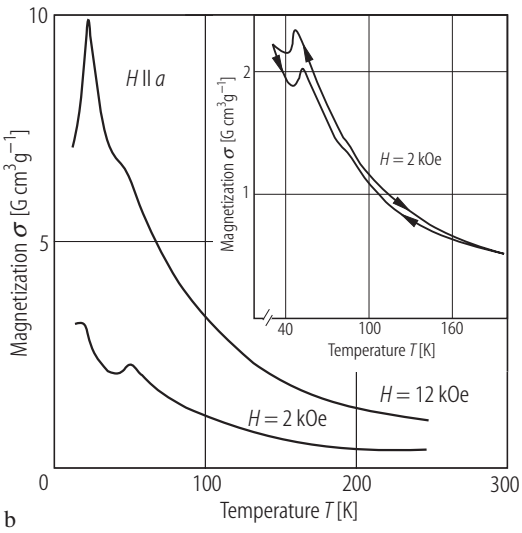

b

Fig. 265. (**a**) Temperature dependencies $\sigma(T)$ of Er in the field $H\|c$ in cooling the sample at 12 kOe and 2 kOe. Hysteresis of $\sigma(T)$ near the temperature 82 K is shown in the inset on an enlarged scale. (**b**) Temperature dependencies $\sigma(T)$ of Er in the field $H\|a$ in cooling the sample at 12 kOe and 2 kOe. Hysteresis of $\sigma(T)$ near 82 K is shown in the inset on an enlarged scale. Both in the case $H\|c$ and $H\|a$ the magnetization hysteresis in the vicinity of 82 K does exist. In the field $H\|c$ no maximum of magnetization is observed at 52 K where the LSW – CS transition occurs [92S].

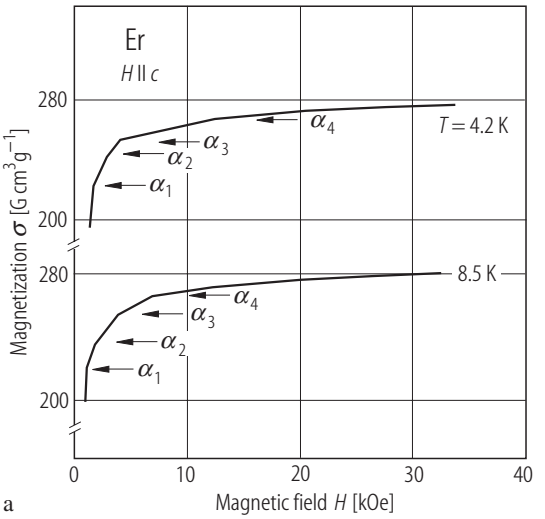

a

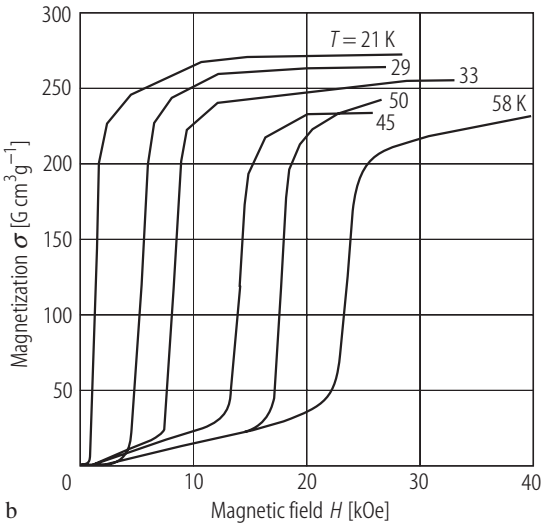

b

Fig. 266. Measured field dependencies of the magnetization of Er single crystal in the field applied along the axis of easy magnetization, the c axis. In the region of weak fields four bends are observed (α_i) [91G]. (**a**) T = 4.2 and 8.5 K, (**b**) 21 K < T < 58 K.

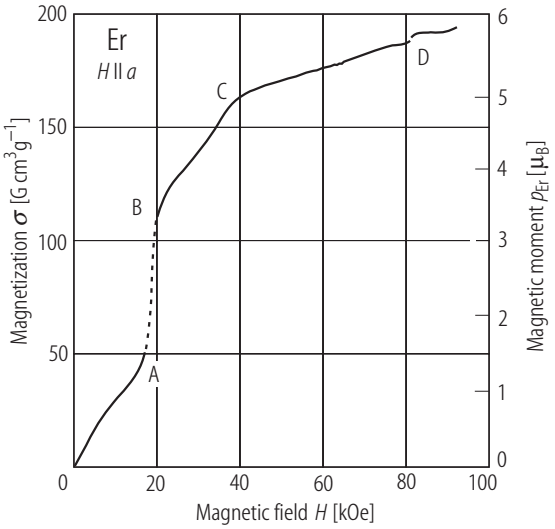

Fig. 267. The *a* axis magnetization of Er at 10 K vs. a basal-plane magnetic field applied to *c*-axis conical structure. Between the origin and A slight distortion of the conical structure takes place. Between A and B the large jump in magnetization corresponds to a first-order transition from cone to a "fan" structure. In this fan phase, the basal-plane moments are no longer ordered helically as in the cone but are arranged with a large component along the applied field (*a* axis) and small modulated component transverse to the field (*b* axis). Between B and C the fan angle closes up and the fan harmonics been progressively weaker. At about 45 kOe there is no longer a basal-plane component transverse to the applied field and the c axis moment begins to be pulled down into the basal plane. This process continues until the kink in magnetization data at D [94J].

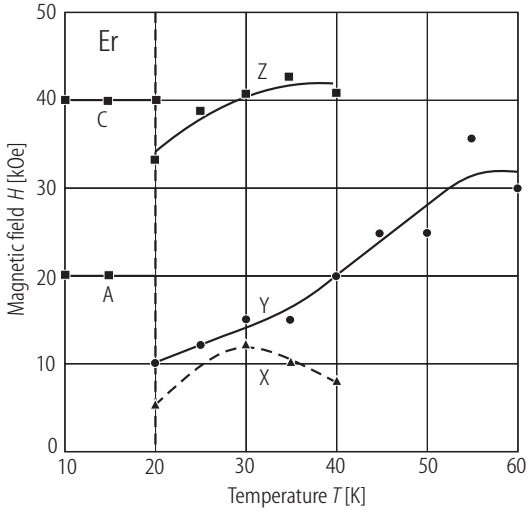

Fig. 268. Schematic phase diagram of Er in a basal-plane field determined from the magnetization study. The letters show how the phase boundaries relate to the magnetization data in Fig. 267 [94J].

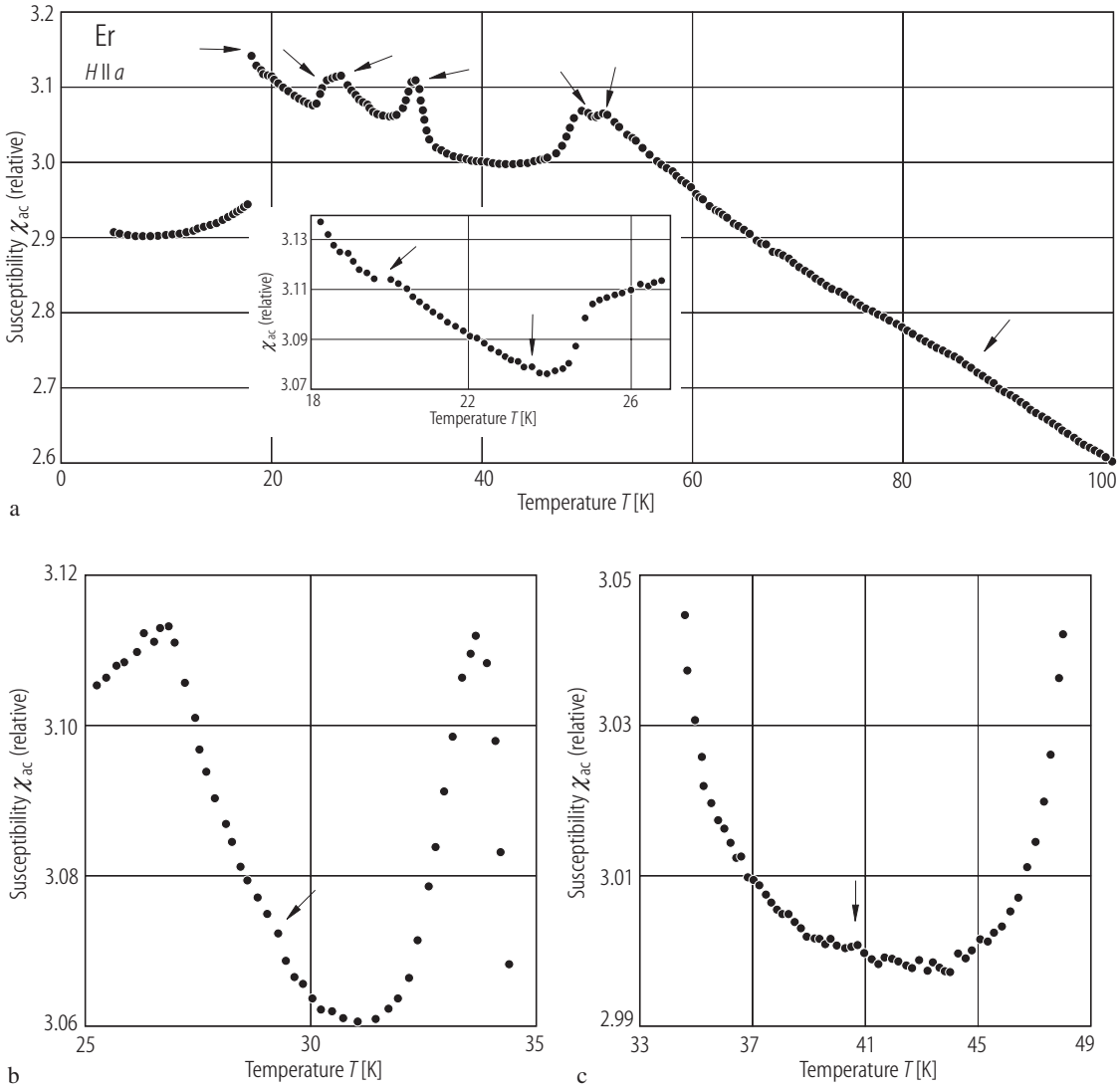

Fig. 269. (**a**) ac susceptibility (χ_{ac}, in arbitrary units) of single-crystal Er in the temperature range from 5 K to 100 K along the *a* axis. The inset shows χ_{ac} vs. *T* for the *a* axis near 22 K. (**b**) χ_{ac} vs. *T* for Er along the *a* axis near 30 K. (**c**) χ_{ac} vs. *T* for Er along the *a* axis near 41 K [95W].

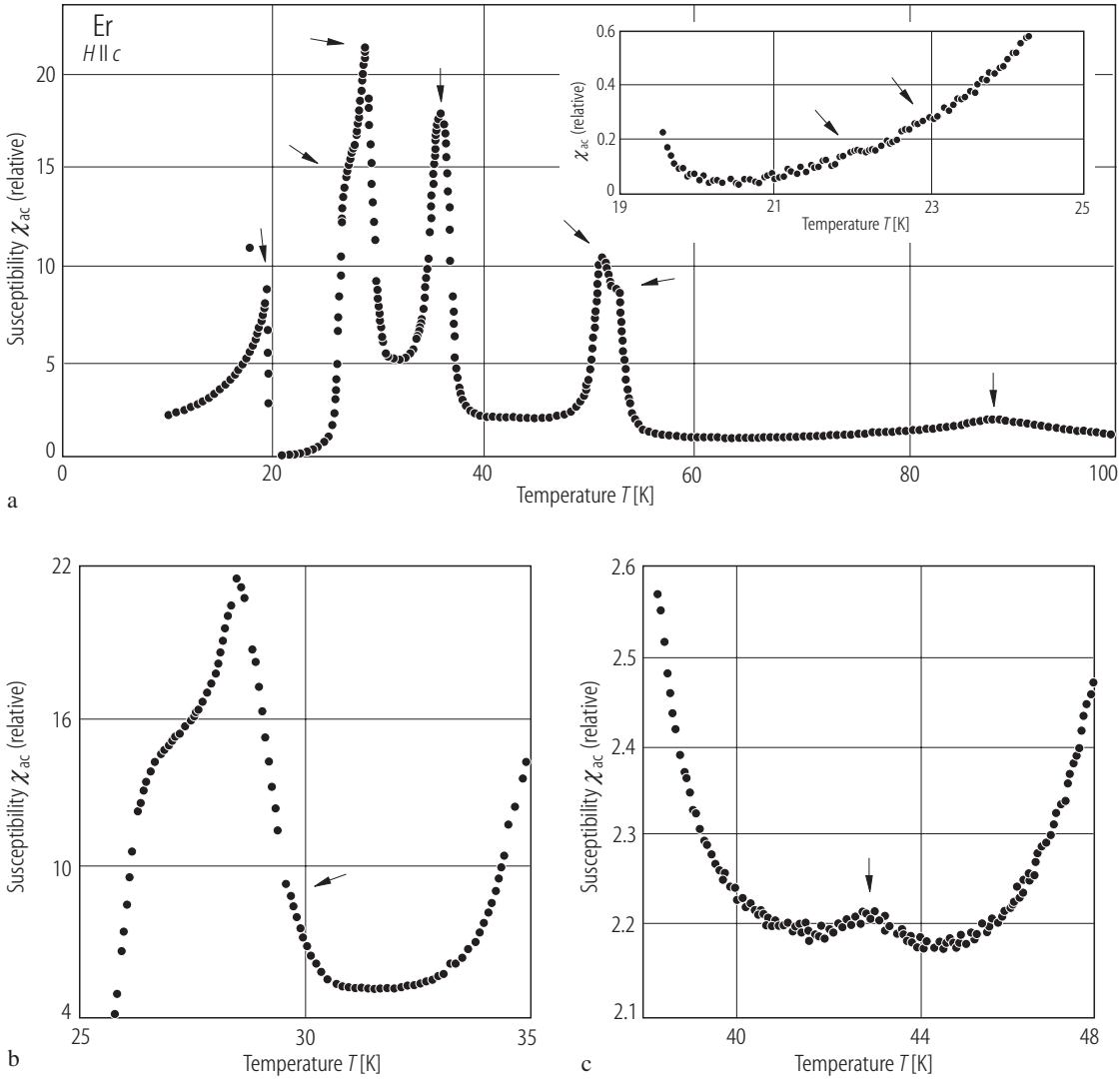

Fig. 270. (**a**) ac susceptibility (χ_{ac}, in arbitrary units) of single-crystal Er in the temperature range from 10 K to 100 K along the *c* axis. The inset shows χ_{ac} vs. *T* for the *c* axis near 22 K. (**b**) χ_{ac} vs. *T* along the *c* axis for Er near 30 K. (**c**) χ_{ac} vs. *T* for Er along the *c* axis near 42 K. Anomalies are indicated by arrows [95W].

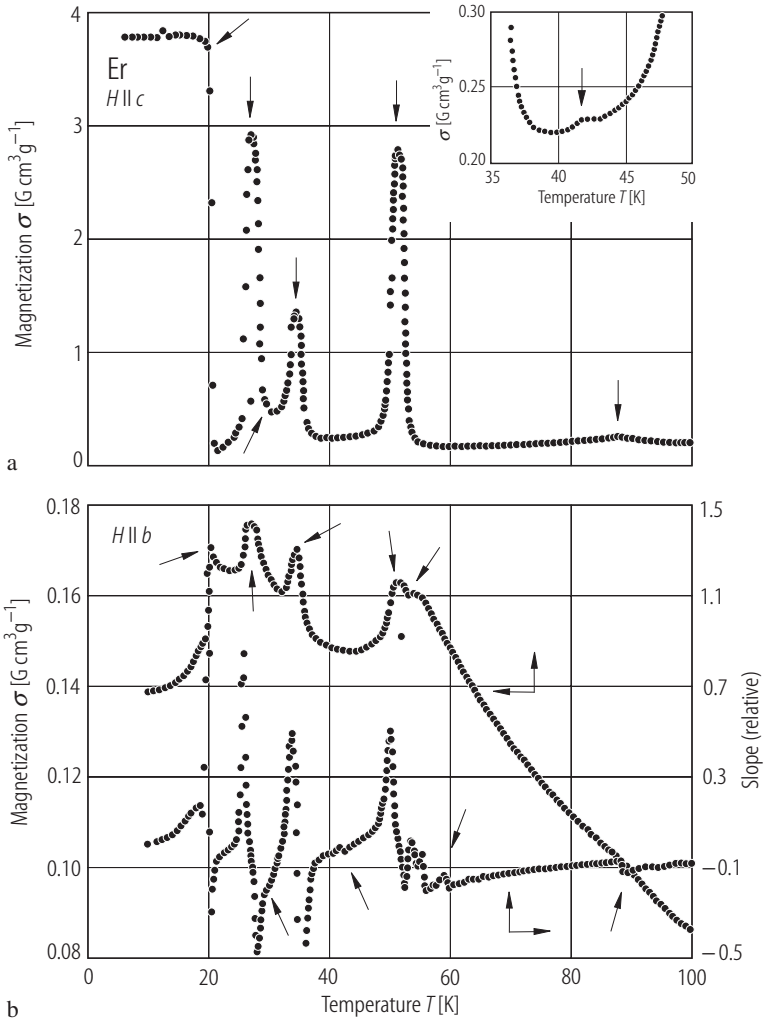

Fig. 271. (**a**) Magnetization σ of single-crystal Er along the *c* axis as a function of temperature in a constant magnetic field of 100 G. The inset shows σ against *T* for the *c* axis near 42 K. (**b**) The upper curve is the magnetization of Er along the *b* axis as a function of temperature for a constant magnetic field of 100 G. The lower curve is the slope of the *b* axis σ-*T* plot for Er [95W].

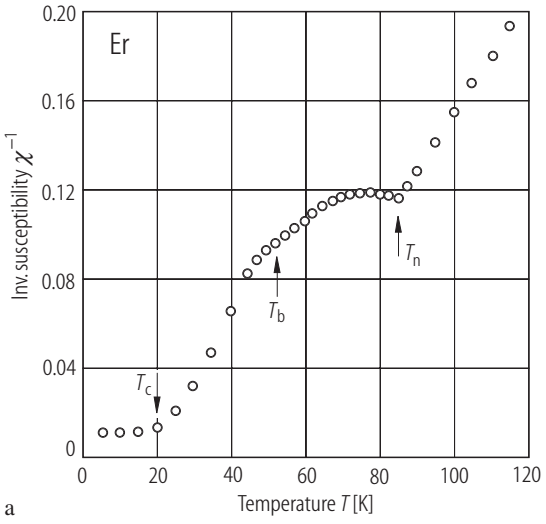

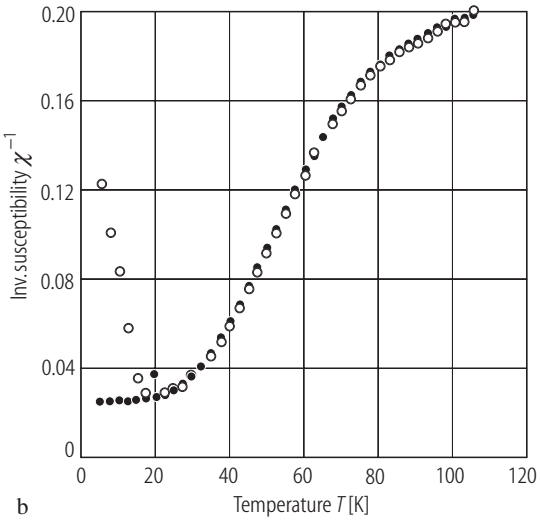

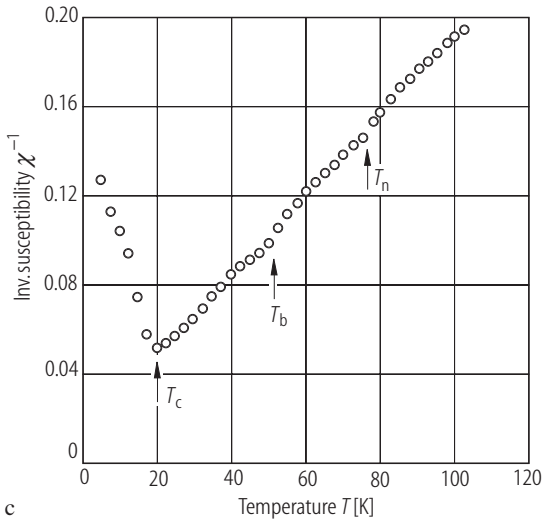

Fig. 272. (**a**) Reciprocal of the susceptibility of a polycrystalline Er metal. All known three phase transitions are visible. (**b**) Reciprocal susceptibility of pure Er particles slowly evaporated and condensed in the inert gas. The two high-temperature phase transitions are absent but superparamagnetic or spin-glass-like behaviour appears. (**c**) Reciprocal susceptibility of a rapidly evaporated sample. Note the shift in the high-temperature phase transitions and the supermagnetic behaviour below T_C [87C].

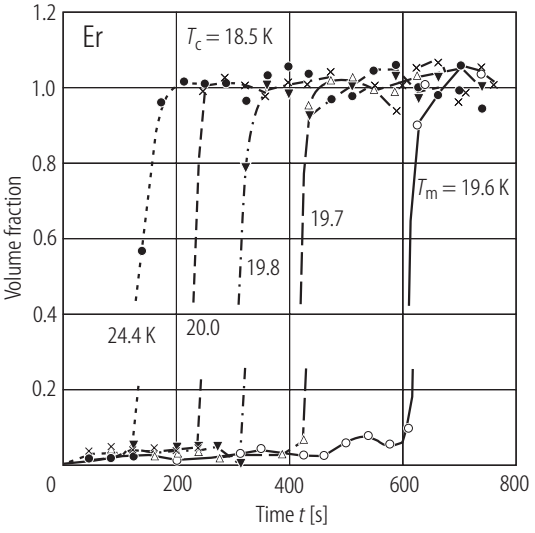

Fig. 273. Time evolution for the volume fraction of cycloidal magnetic phase in Er as an evidence of the first-order phase transitions from cycloidal to one ferromagnetic studied by X-ray diffraction. Temperature of the sample is heated from 13 K to T_m just above T_C [95T].

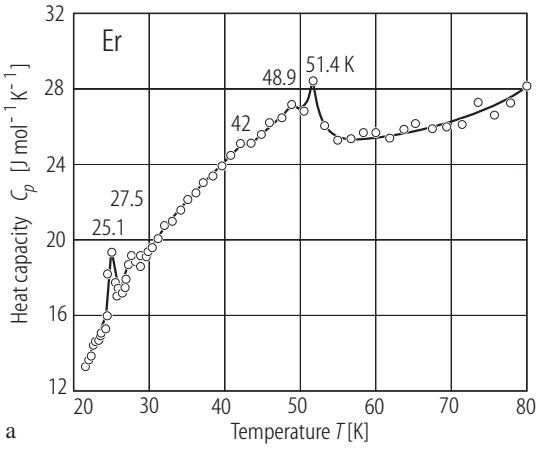

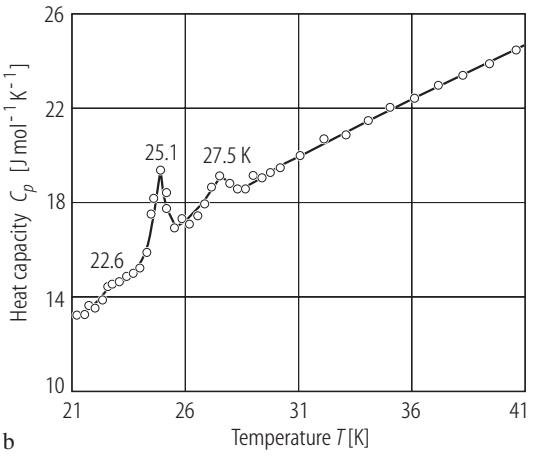

Fig. 274. Heat capacity of Er in a region of (**a**) 20 - 80 K and (**b**) 21 - 41 K. The maximum located at 51.4 K is evidence of the antiferromagnetic phase transition due to the basal plane moment ordering. The small anomaly at 48.9 K is a spin-slip transition which is associated with the magnetic wavevector 2/7. Similarly the flat step at 42 K is also evidence of the spin-slip transition with $\tau_m = 3/11$. Two transitions at 27.5 and 25.1 K are due to spin-slip transformations with $\tau_m = 5/19$ and $\tau_m = 4/15$, respectively [93P1].

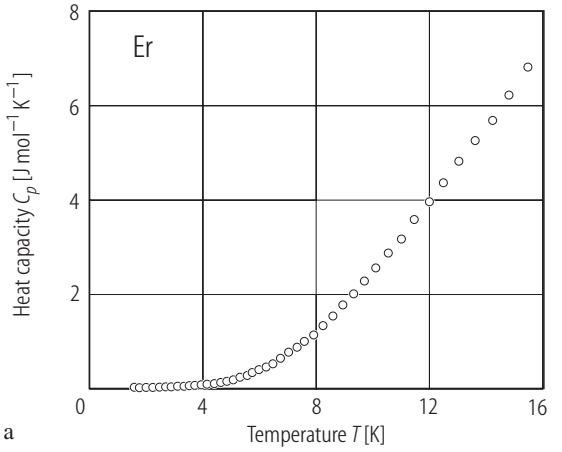

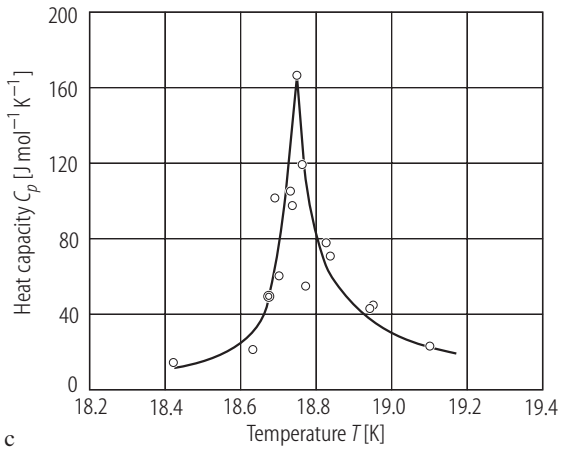

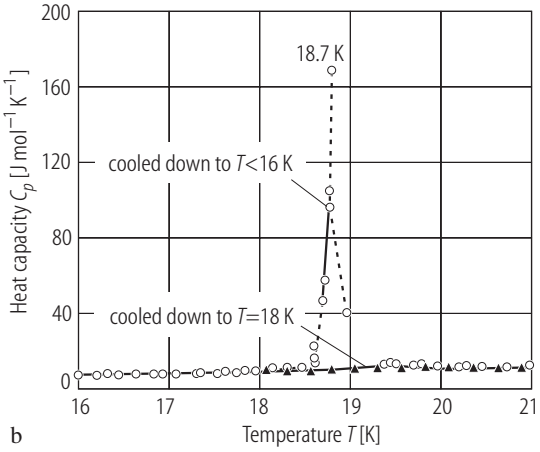

Fig. 275. Heat capacity of Er in a region of (**a**) 1.5 - 16 K, (**b**) 16 - 21 K, and (**c**) 18.4 - 19.1 K. The anomaly at 18.7 K (**c**) is associated with the antiferromagnetic to ferromagnetic transition [93P1].

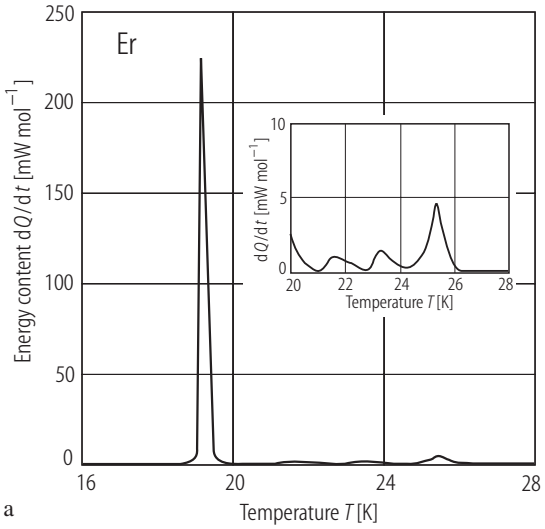

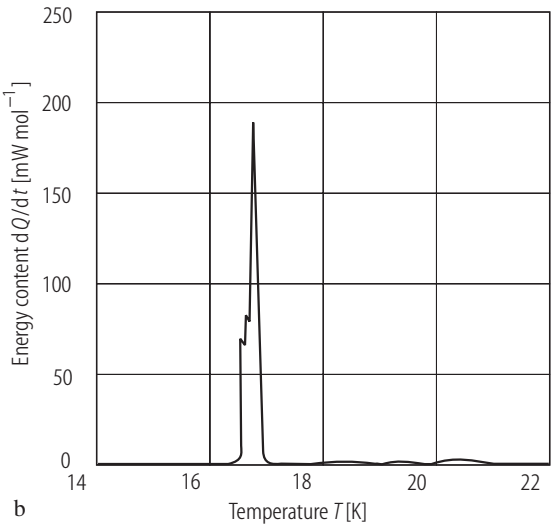

Fig. 276. Change in energy content of Er at the ferromagnetic transition as measured with a scanning calorimeter: (**a**) increasing temperature and (**b**) decreasing temperature. The large peak below 20 K caused by the ferromagnetic transition corresponds to an energy of (18.5 ± 1.0) J mol^{-1}. The inset shows a blow-up of the energy scale between 20 and 26 K. The energy of the peak at 25 K is (1.2 ± 0.3) J mol^{-1} [89Å].

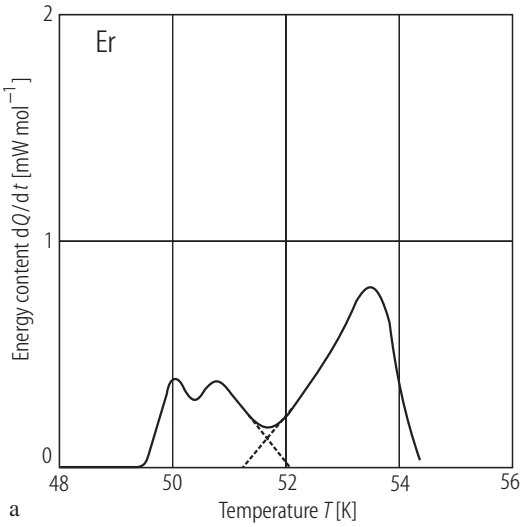

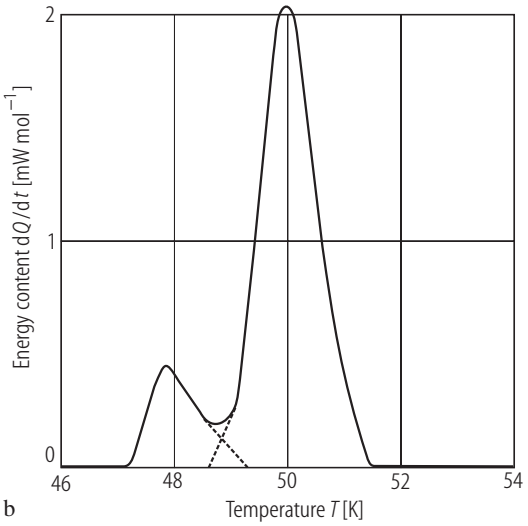

Fig. 277. Change in an energy content of Er near the basal-plane ordering temperature for (**a**) increasing temperature and (**b**) decreasing temperature. The energy of the larger peaks is (1.3 ± 0.3) J mol^{-1} [89Å].

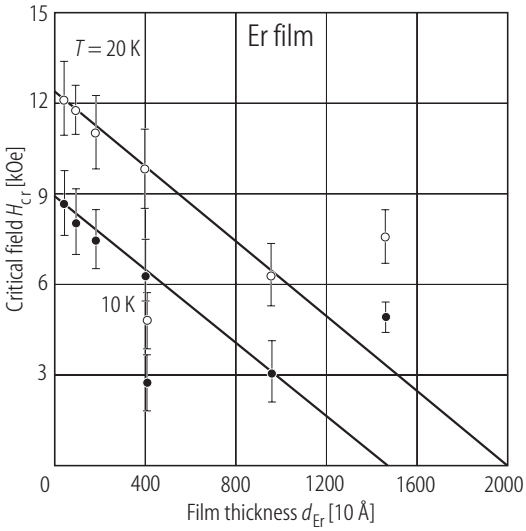

Fig. 278. Critical field vs. Er film thickness at 10 K (solid circles) and 20 K (open circles). The critical fields were obtained from plots of the magnetization vs. field for each film. The solid lines mark linear extrapolations of the data to $H_{cr} = 0$ kOe [91B].

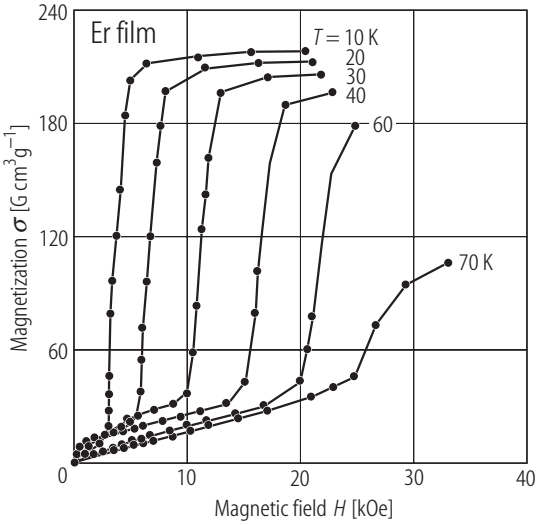

Fig. 279. Field dependence of the magnetization for the 9500-Å Er film at various temperatures. The *c*-axis fields have been corrected for demagnetization effects [91B].

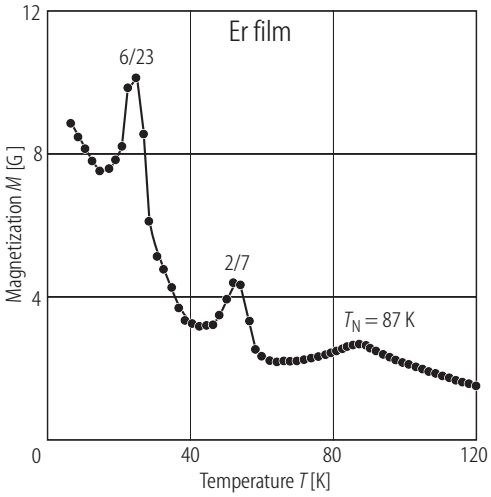

Fig. 280. Magnetization of the strain-free film sample vs. temperature in a small (200 G) applied magnetic field. Below its Néel temperature, Er has a helimagnetic *c*-axis modulated magnetic structure. In this state each Er atom has a magnetic moment aligned along the *c* axis , and the sign of the moment oscillates with a period of about eight atomic layers. The two peaks on the left are quite sharp and can be associated with known spin-slip states in which the oscillations lock to the lattice before completing a harmonic cycle, thus leaving a small net magnetic moment [96C].

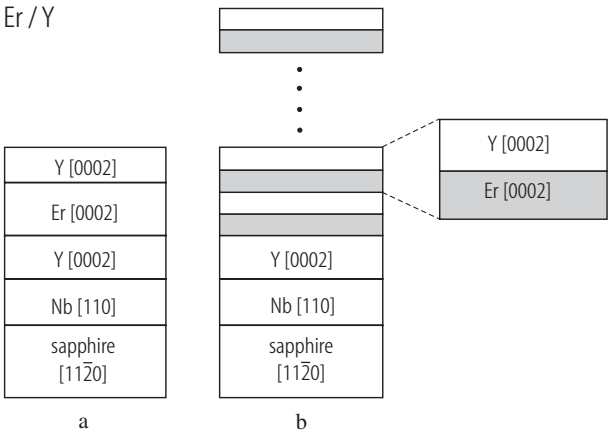

Fig. 281. Schematic drawing of (**a**) an Er thin films and (**b**) an Er/Y superlattice [91B].

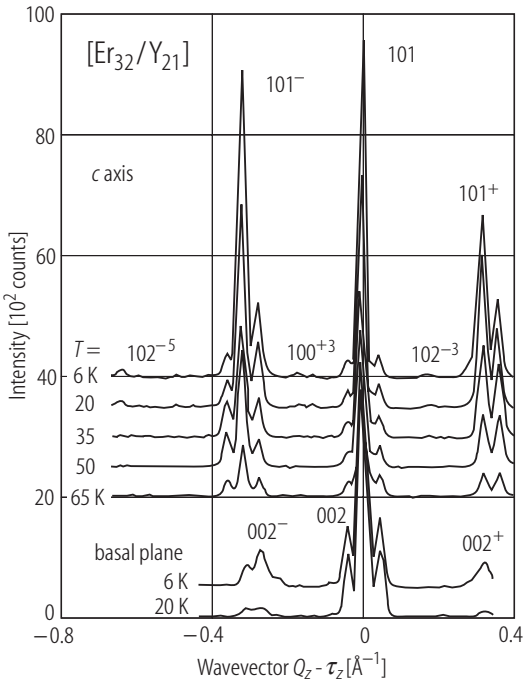

Fig. 282. Neutron diffraction scans along the c^* direction, through (101*1) and (0002) for [Er_{32}/Y_{21}] show the development of a linear-spin-density-wave state with moments along the c axis, which then "squares-up" on lowering the temperature as indicated by the appearance of higher order harmonics. Below about 30 K, the order of the basal-plane components, is indicated by the satellites of (0002). This ordering has a different turn angle than the c-axis component [89R].

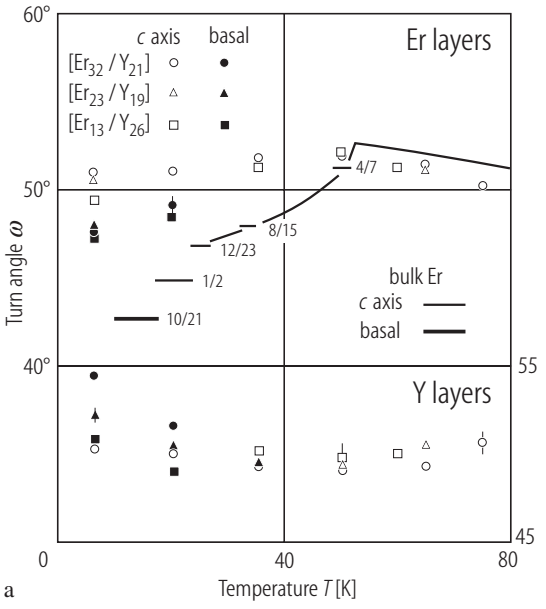

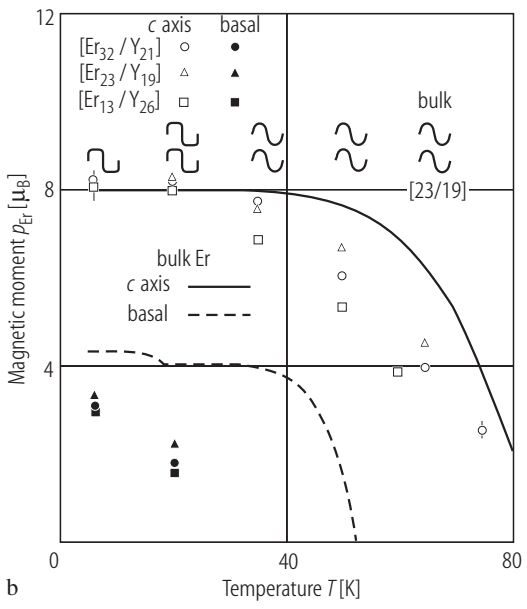

Fig. 283. (**a**) Turn angles in the Er and Y layers are shown and compared to bulk Er. In the Er layers ω is "clamped" near the high-temperature lock-in value of bulk Er ($2\pi/7$). The basal plane ω which appears at low temperature has a somewhat lower value than the c-axis ω. The ω in the Y layers is near the 50° found in other superlattices and dilute Y alloys. The total phase shift across the Y layers is not a sample multiple of π (**b**). The c-axis and basal-plane moments obtained for the superlattices [Er_{32}/Y_{21}], [Er_{23}/Y_{19}], [Er_{13}/Y_{26}], (T_N = 78.0, 78.5, and (72.2 ± 1) K, respectively) are shown along with the values for bulk Er (T_N = 84 K). The ordering temperature for the basal-plane components is about half of the value in Er, and the saturation moment reaches only 8.5 μ_B obtained for Er [89R1].

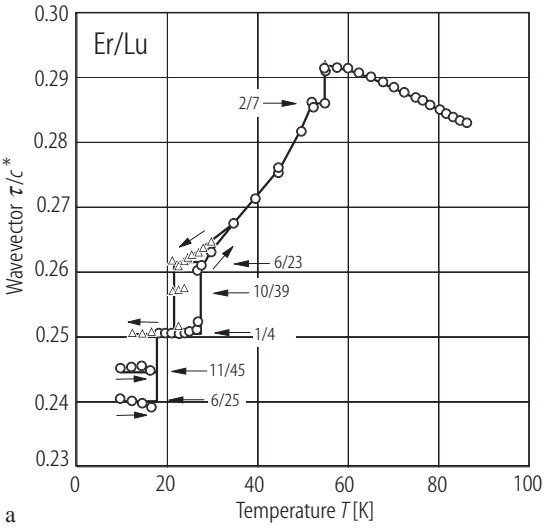

a

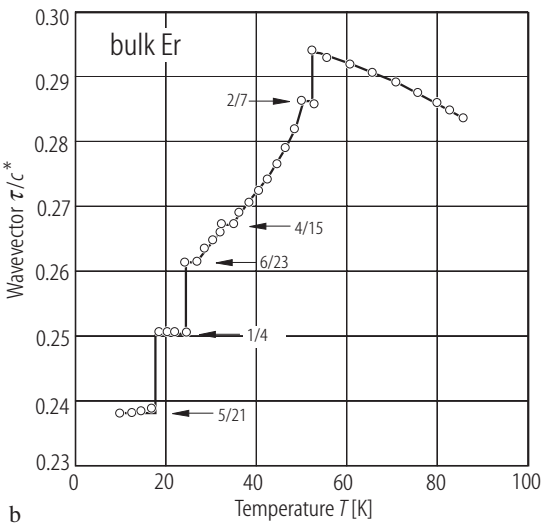

b

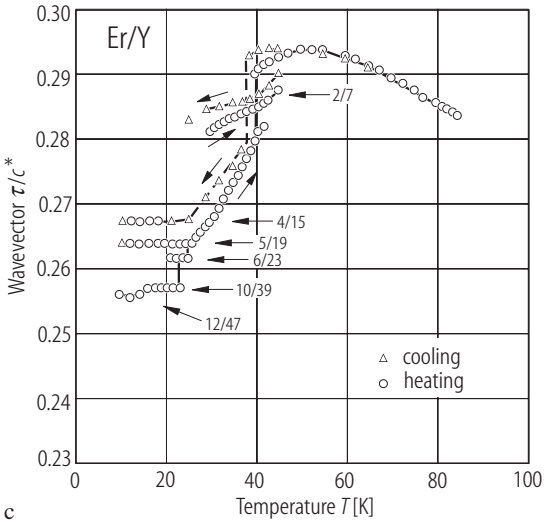

c

Fig. 284. Magnetic wavevector τ of Er as a function of temperature for an Er film on a Lu substrate (**a**), for bulk Er (**b**), and for an Er film on a Y substrate (**c**). Small arrows are used to indicate the hysteresis found between measurements done on heating and cooling of the sample [97H].

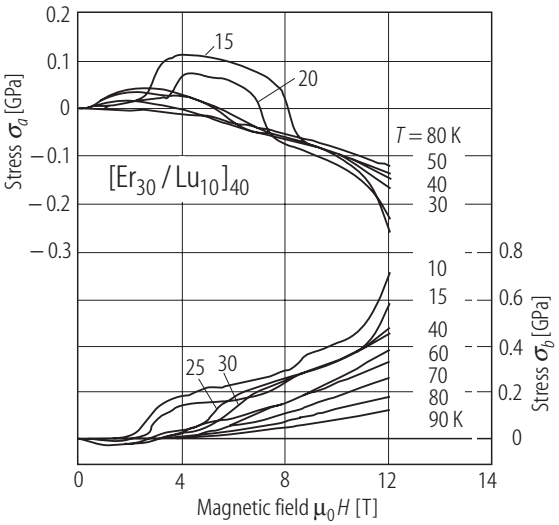

Fig. 285. Magnetoelastic stress isotherms for SL $(Er_{30}/Lu_{10})\times 40$ superlattices. σ_a and σ_b correspond to SL clamping along the *a* and *b* axes [97dM].

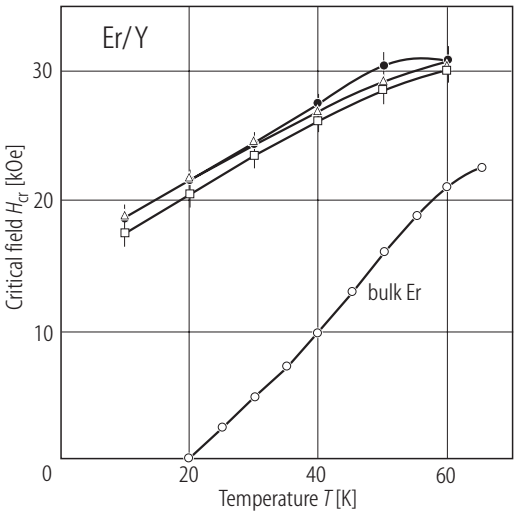

Fig. 286. Critical field plotted as a function of temperature for $[Er_{23.5}/Y_{19}]_{100}$ (squares), $[Er_{13.5}/Y_{25}]_{100}$ (solid circles),and $[Er_{31.5}/Y_{21}]_{60}$ (triangles). The bulk Er values (open circles) are shown for comparison [91B].

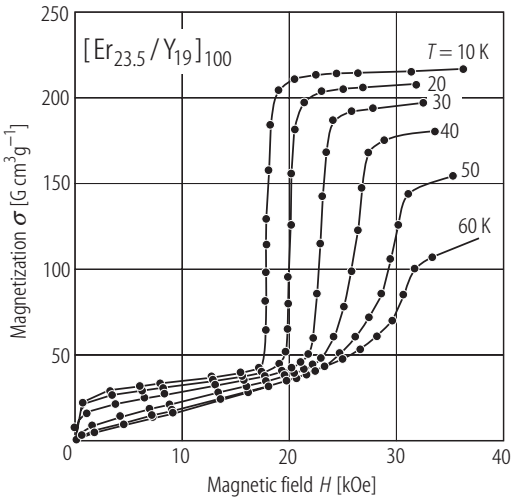

Fig. 287. Field dependence of the magnetization for $[Er_{23.5}/Y_{19}]_{100}$ superlattice at various temperatures. The *c*-axis fields have been corrected for demagnetization effects [91B].

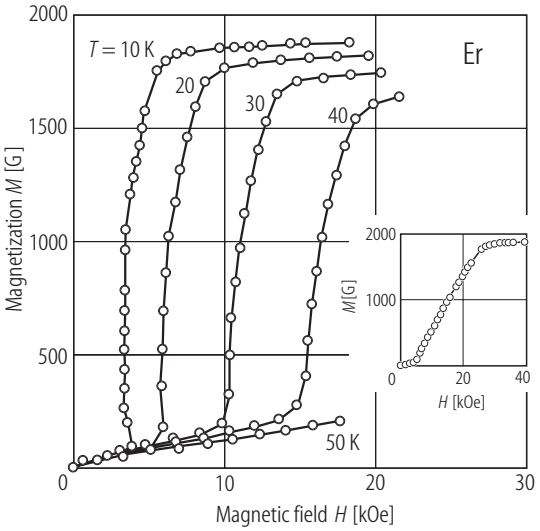

Fig. 288. Magnetization measurements for a 200 Å-single-crystal Er film grown on $Y_{39}Lu_{61}$ substrate vs. internal field at temperatures from 10 K to 50 K. Inset: Magnetization vs. applied field at 10 K without demagnetizing correction [96C].

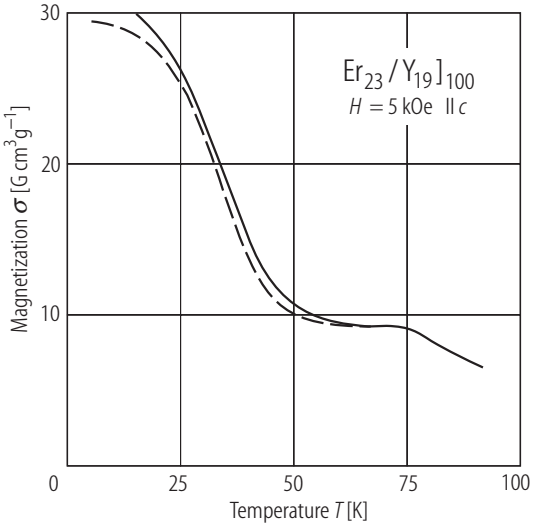

Fig. 289. Magnetization vs. temperature for $[Er_{23}/Y_{19}]_{100}$ in a 5-kOe field applied along the *c* axis. The solid and dashed curve correspond to field-cooled and zero-field-cooled data, respectively [88B].

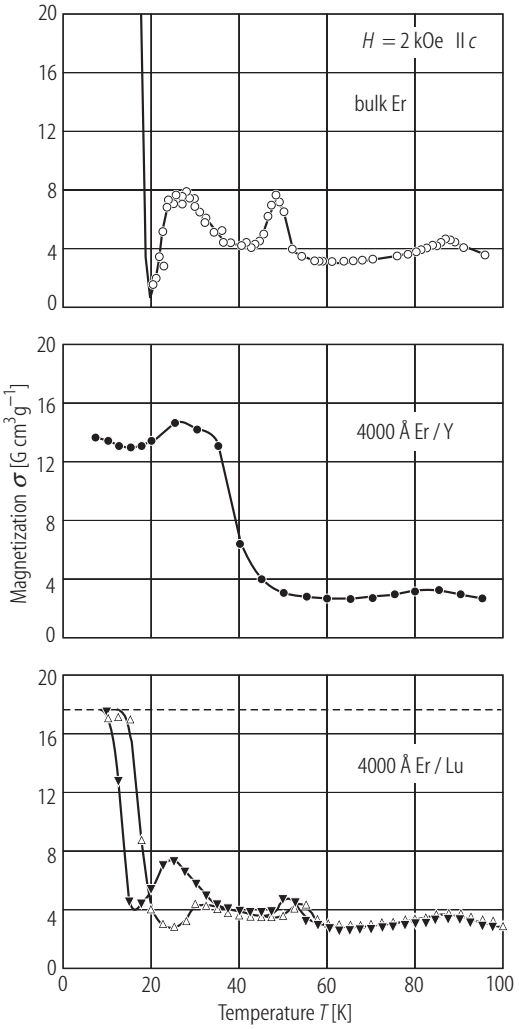

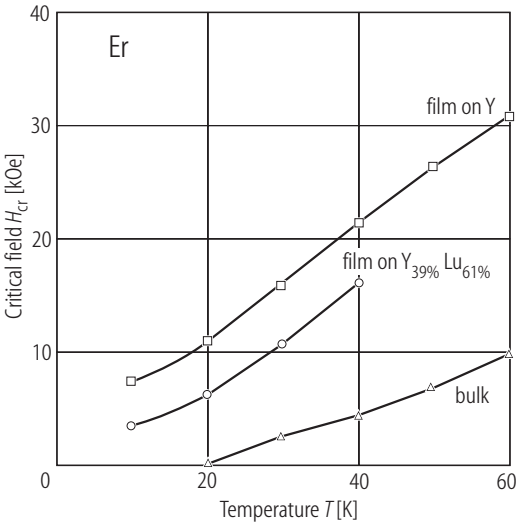

Fig. 290. Critical field H_{cr} vs. temperature for three Er samples: 1750 Å film on Y, 2000 Å film on strain-free alloy, and a bulk Er sample [96C].

Fig. 291. Magnetization as a function of temperature in a 2-kG field applied along the *c* axis for a 4000 Å Er film grown on Lu (closed symbols are field cooled and open symbols are zero-field cooled) and a 4000 Å Er film on Y (field cooled). The dashed line marks the maximum magnetization allowed by demagnetization effects in the field. Magnetization data for bulk Er are shown for comparison [91B1].

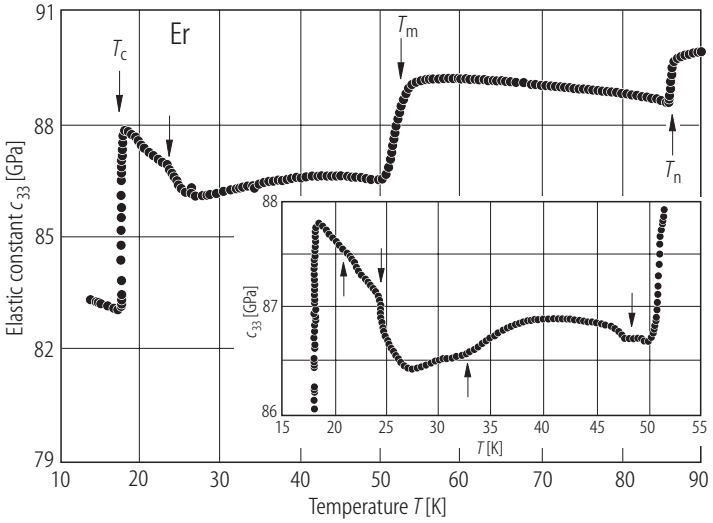

Fig. 292. The c_{33} elastic modulus of Er derived from the velocity of a longitudinal wave propagating along the *c* axis. The temperature dependence of c_{33} cooled at 1 K/min and 0.5 K/min (inset) [92E].

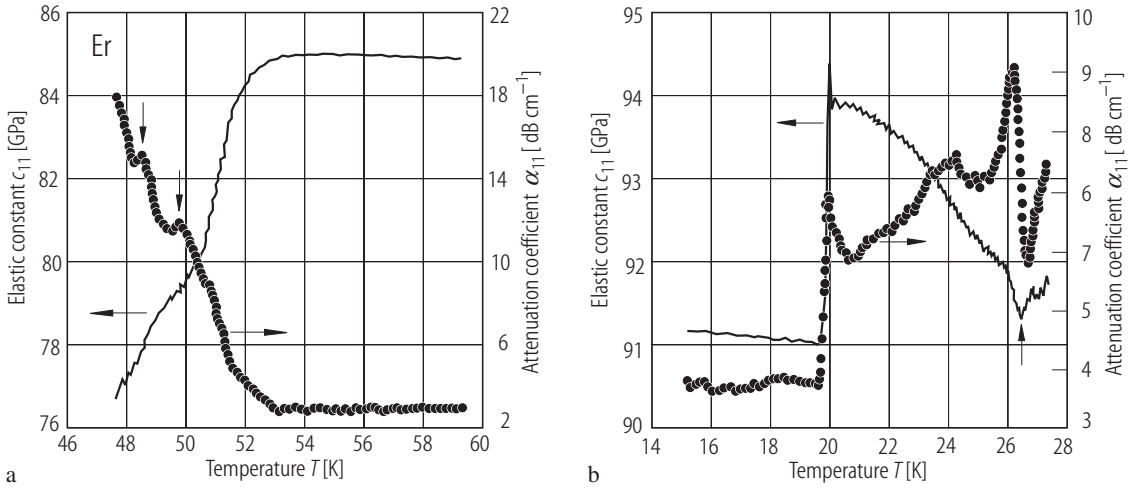

Fig. 293. The c_{11} elastic constant and the α_{11} attenuation coefficient of Er derived from a longitudinal wave propagation parallel to the basal plane. (**a**) Temperature dependence of c_{11} and α_{11} between 60 K and 46 K. (**b**) Temperature dependence of c_{11} and α_{11} between 15 K and 28 K [92E].

References

87C Cowen, R.A., Stolzman, B., Averback, R.S., Hahn, H.: J. Appl. Phys. **61** (1987) 3317

88B Borchers, J.A., Salamon, M.B., Du, R., Flynn, C.P., Rhyne, J.J., Erwin, R.W.: J. Appl. Phys. **63** (1988) 3458

89R Rhyne, J.J., Erwin, R.W., Borchers, J., Salamon, M.B., Du, R., Flynn, C.P.: Physica B **159** (1989) 111

89R1 Rhyne, J.J., Erwin, R.W., Borchers, J., Salamon, M.B., Du, R., Flynn, C.P.: Phys. Scr. T **29** (1989) 31

89Å Åström, H.U., Benediktsson, G.: J. Phys. Condens. Matter **1** (1989) 4381

90B1 Bohr, J.: J. Magn. Magn. Mater. **83** (1990) 530

91B Borchers, J.A., Salamon, M.B., Erwin, R.W., Rhyne, J.J., Du, R.R., Flynn, C.P.: Phys. Rev. B **43** (1991) 3123

91B1 Beach, R.S., Borchers, J.A., Erwin, R.W., Rhyne, J.J., Matheny, A., Flynn, C.P., Salamon, M.B.: J. Appl. Phys. **69** (1991) 4335

91G Godovikov, S.K., Nikitin, S.A., Tishin, A.M.: Phys. Lett. A **158** (1991) 265

92E Eccleston, R.S., Palmer, S.B.: J. Phys.: Condens. Matter **4** (1992) 10037

92L Lin, H., Collins, M.F., Holden, T.M., Wei, W.: Phys. Rev. B **45** (1992) 12873

92S Snigirev, O.V., Tishin, A.M., Volkozub, A.V.: J. Magn. Magn. Mater. **111** (1992) 149

93K Kawano, S., Lebech, B., Achiwa, N.: J. Phys.: Condens. Matter **5** (1993) 1535

93P1 Pecharsky, V.K., Gschneidner jr., K.A., Fort, D.: Phys. Rev. B **47** (1993) 5063

94J Jehan, D.A., McMorrow, D.F., Simpson, J.A., Cowley, R.A., Swaddling, P.P., Clausen, K.N.: Phys. Rev. B **50** (1994) 3085

95B Bulatov, A.S., Dolzhenko, V.F., Korniets, A.V.: J. Magn. Magn. Mater. **147** (1995) 403

95K Kawano, S., Sørensen, S. Aa., Lebech, B., Achiwa, N.: J. Magn. Magn. Mater. **140-144** (1995) 763

95T Tajima, K., Shinoda, Y., Tadakuma, M.: J. Magn. Magn. Mater. **140-144** (1995) 765

95W Watson, B., Ali, N.: J. Phys.: Condens. Matter **7** (1995) 4713

96C Conover, M.J., Kaldowsky, A., Flynn, C.P.: Phys. Rev. B **53** (1996) R2938

96W1 Watson, B., Ali, N.: J. Phys.: Condens. Matter **8** (1996) 1797

97H Helgsen, G., Tanaka, Y., Hill, J.P., Wochner, P., Gibbs, D., Flynn, C.P., Salamon, M.B. Phys. Rev. B **56** (1997) 2635

97W Watson, B., Ali, N.: J. Alloys Compounds **250** (1997) 662

97dM del Moral, A., Ciria, M., Arnaudas, J.I., Ward, R.C.C., Wells, M.R.: J. Appl. Phys. **81** (1997) 5311

2.1.3.11 Thulium

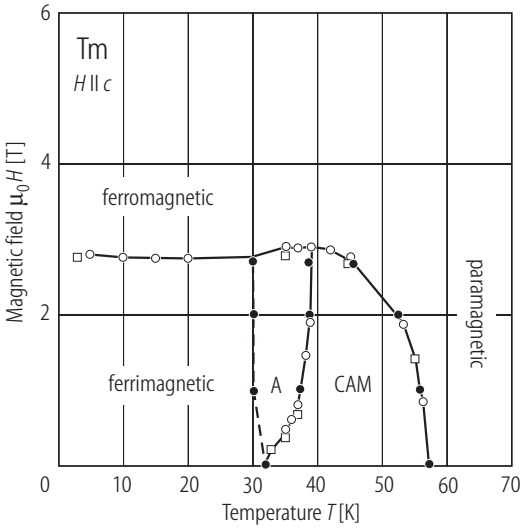

Fig. 294. Magnetic phase diagram constructed from the isothermal magnetization (squares), magnetoresistance (open circles), and resistance in a constant field (solid circles). The division of the ferromagnetic phase into two phases at nonzero field which is indicated by the dashed line, is tentative [98E].

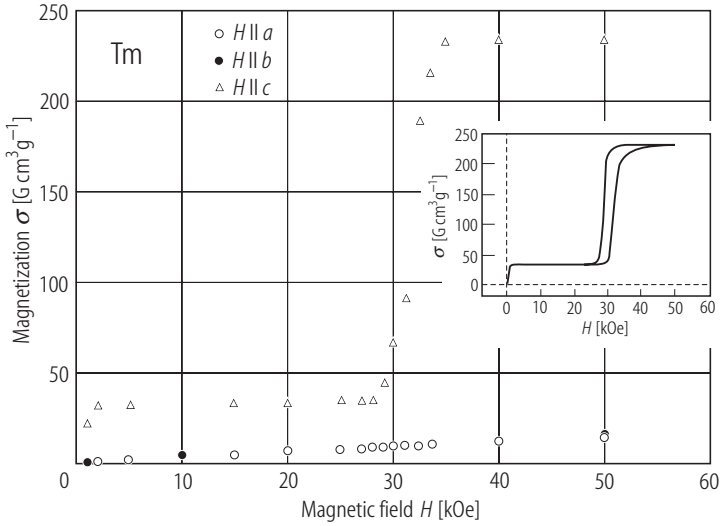

Fig. 295. Magnetic moment of Tm at 5 K measured with a SQUID magnetometer to a maximum field of 50 kOe for different crystallographic orientations: parallel *a*, *b* and *c* axis. The inset shows measurements on the same crystal at 4.2 K with a vibrating-sample magnetometer for increasing and decreasing values of the applied field. For the field parallel to the *c* axis there are two distinct saturation levels: at low fields connected with ferrimagnetic state; at higher fields moments are decoupled into ferromagnetic order [91Å].

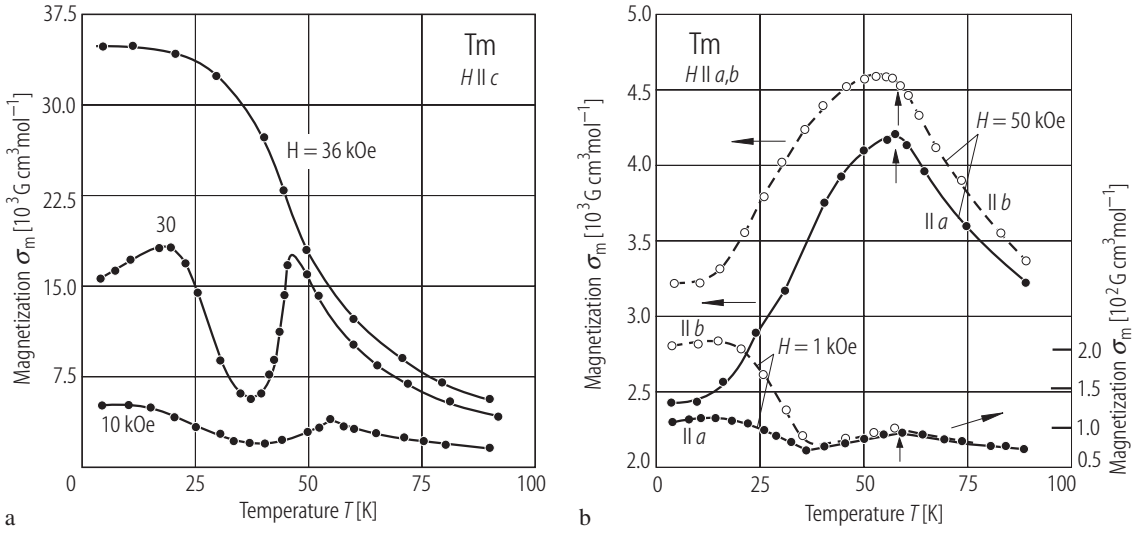

Fig. 296. (**a**) Temperature variation of the magnetization for Tm with fields applied parallel to the *c* axis; and (**b**) parallel to the *ab*-plane [90D].

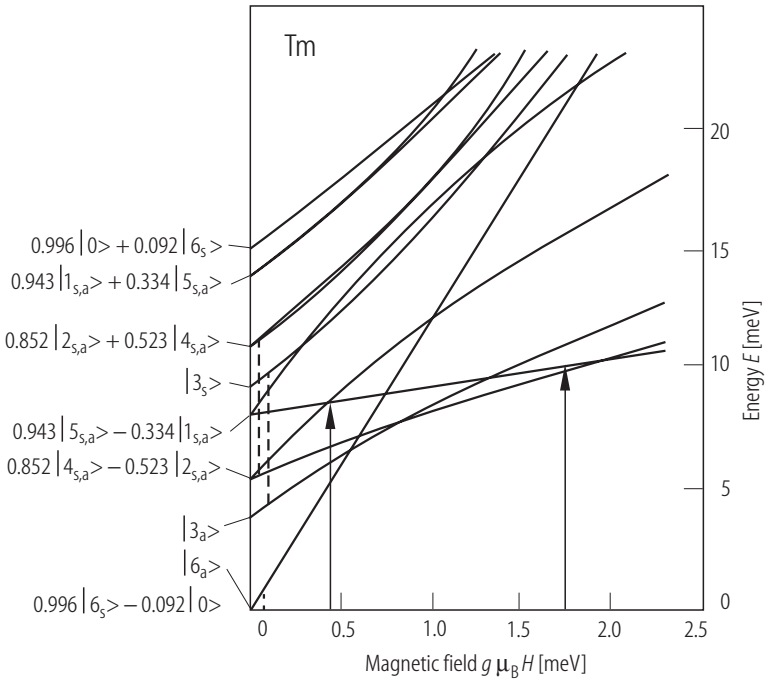

Fig. 297. Crystal-field levels in Tm calculated from the parameters $B_2^0 = -0.096$; $B_4^0 = 0$; $B_6^0 = 0.92 \cdot 10^{-5}$; $B_6^6 = 8.86 \cdot 10^{-5}$ as a function of the field $g\mu_B H$ (1 meV corresponds to 14.8 T). The state vectors to the left of the vertical axis are the zero field states of the corresponding levels. $|6_{s(a)}>$ denotes the (anti)-symmetrical combination of |+6> and |–6> states [91McE].

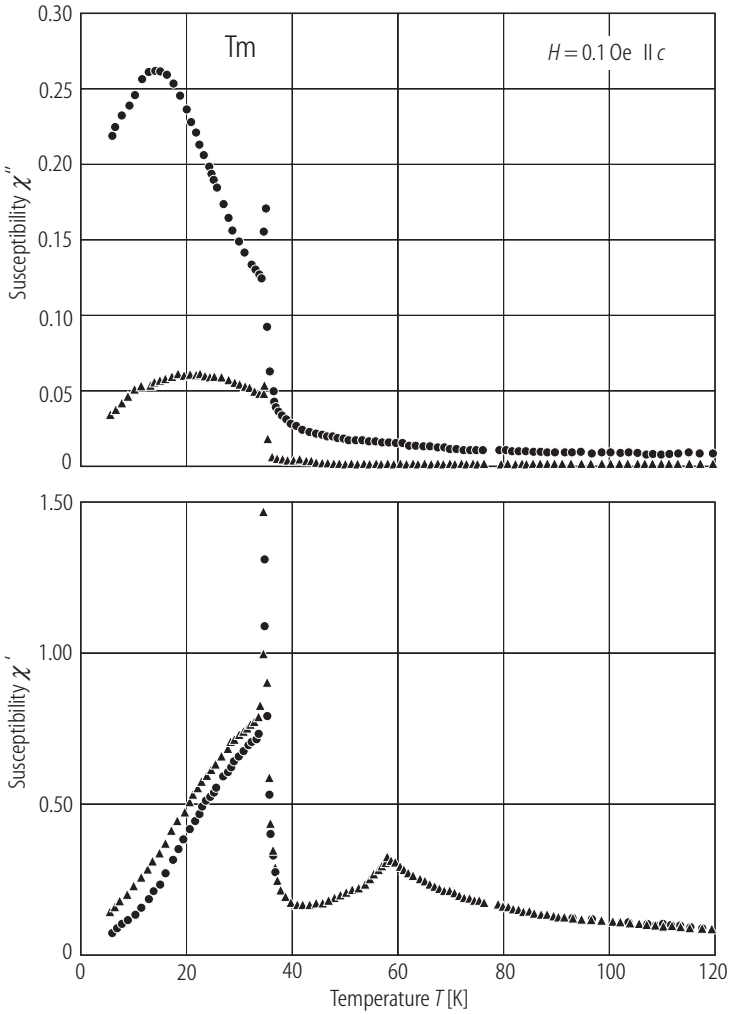

Fig. 298. ac susceptibility vs. temperature with the applied field of 0.1 Oe along the c axis for two frequencies: 100 Hz (solid triangles) and 1000 Hz (solid circles) for Tm. A cusp in χ' at 58 K marks an antiferromagnetic transition. The sharp maximum at 35 K reveals transition into the ferrimagnetic antiphase-type structure [91Å].

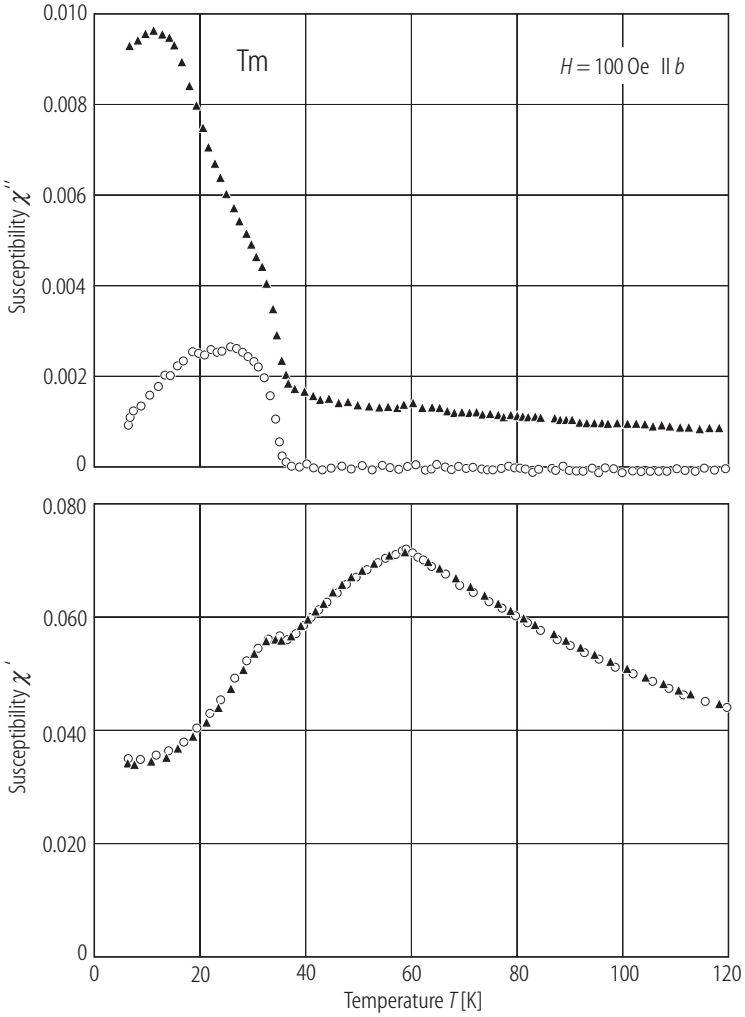

Fig. 299. ac susceptibility vs. temperature and frequency with the applied field of 100 Oe, parallel to the *b* axis: 10 Hz (open circles) and 100 Hz (solid triangles) for Tm. The strong peak in χ' at 35 K seen along the *c* axis is virtually missing for this orientation. The small anomaly at 35 K might be the sign of interaction between magnetization along *c* and the magnetic component in the basal plane [91Å].

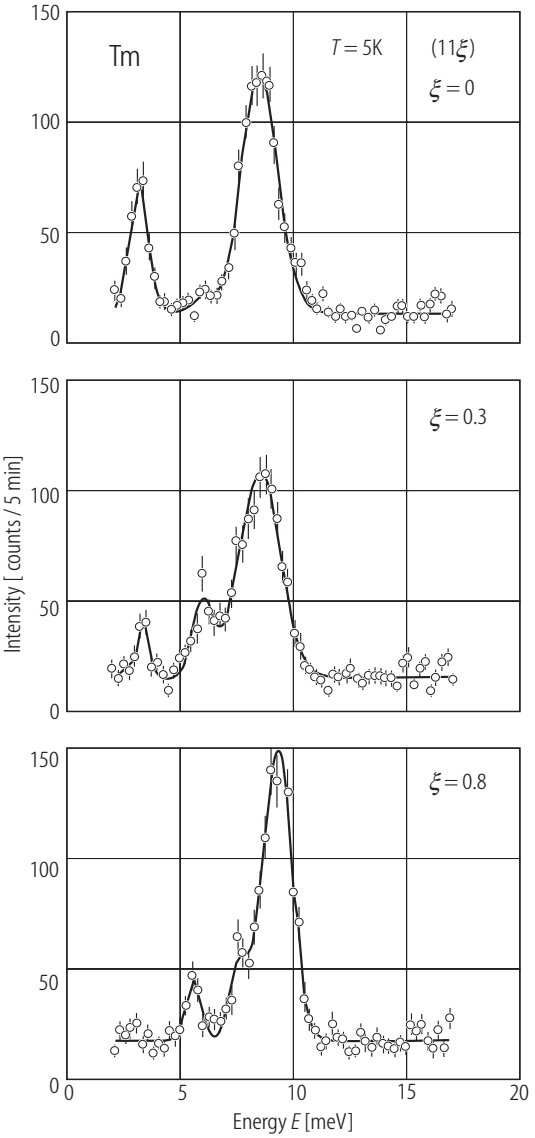

Fig. 300. Low-temperature excitation spectra for Tm single-crystal from inelastic neutron scattering measurements at 5 K. The constant κ scans at $\kappa = (1,1,\zeta)$ for ζ = 0, 0.3, 0.8 with a fixed neutron energy E_f = 14.8 meV. The three excitations are observed. The solid lines are from a fit to three Gaussian. The two lower energy excitations originate from magneto-vibrational scattering from TA phonon, higher energy excitation is magnetic. The observed gap in dispersion (≈ 8 meV) is related to the first dipolar transition in the crystal-field levels scheme [90F-B].

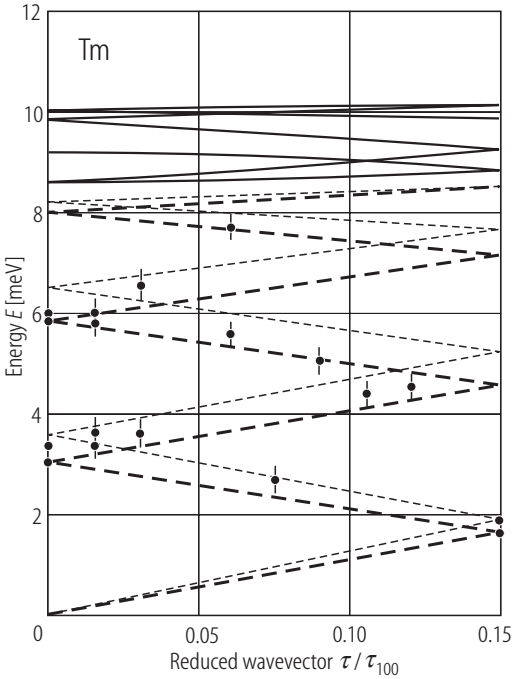

Fig. 301. Dispersion relations along the *c* direction, at zero temperature, of the spin wave (solid lines) and the transverse phonons (heavy dashed lines) in "ferromagnetic" Tm folded into the magnetic Brillouin zone of the antiferromagnetic phase.The energies of the phonons coupled to the spin waves have been adjusted so as to agree with the results calculated in the antiferromagnetic phase. The thin dashed lines show the dispersion relation assumed for the phonons in the nonmagnetic case. The circles are the experimental results [90F-B] for the phonon energies [91McE].

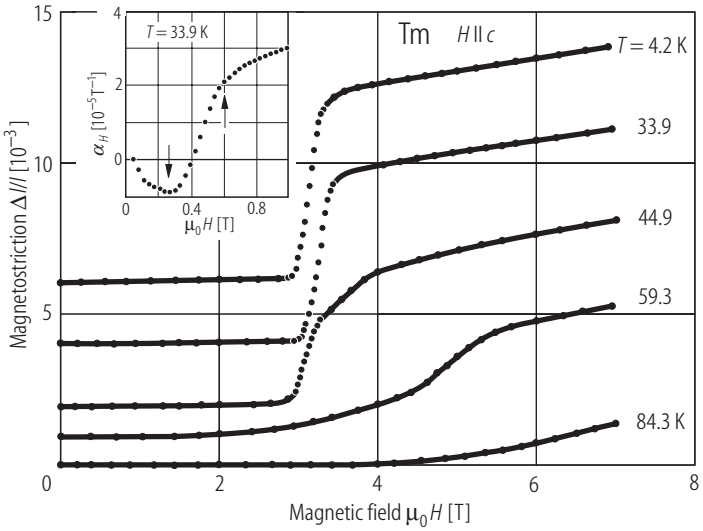

Fig. 302. Magnetostriction of Tm, measured in increasing field along the *c* axis, for various temperatures. The inset shows thermal expansion $\alpha_H = [\delta(\Delta l/l)/\delta H]_T$ at T = 33.9 K. The sudden increase in length in 3.0 T is characteristic. Arrows indicate anomalies [92Z].

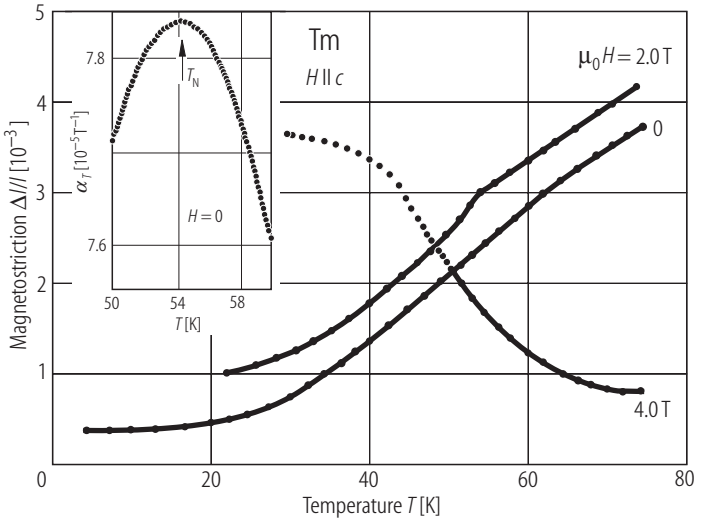

Fig. 303. Thermal expansion of Tm, measured as a function of temperature along the *c* axis at various magnetic fields $\mu_0 H$ = 0, 2.0 T and 4.0 T. The inset shows the α_T , where $\alpha_T = [\delta(\Delta l/l)/\delta T]_H$, near T_N: at 2.0 T, T_N = 52.1 K, the additional anomalies are observed at T = 31.0, 36.5 and 38.8 K [92Z].

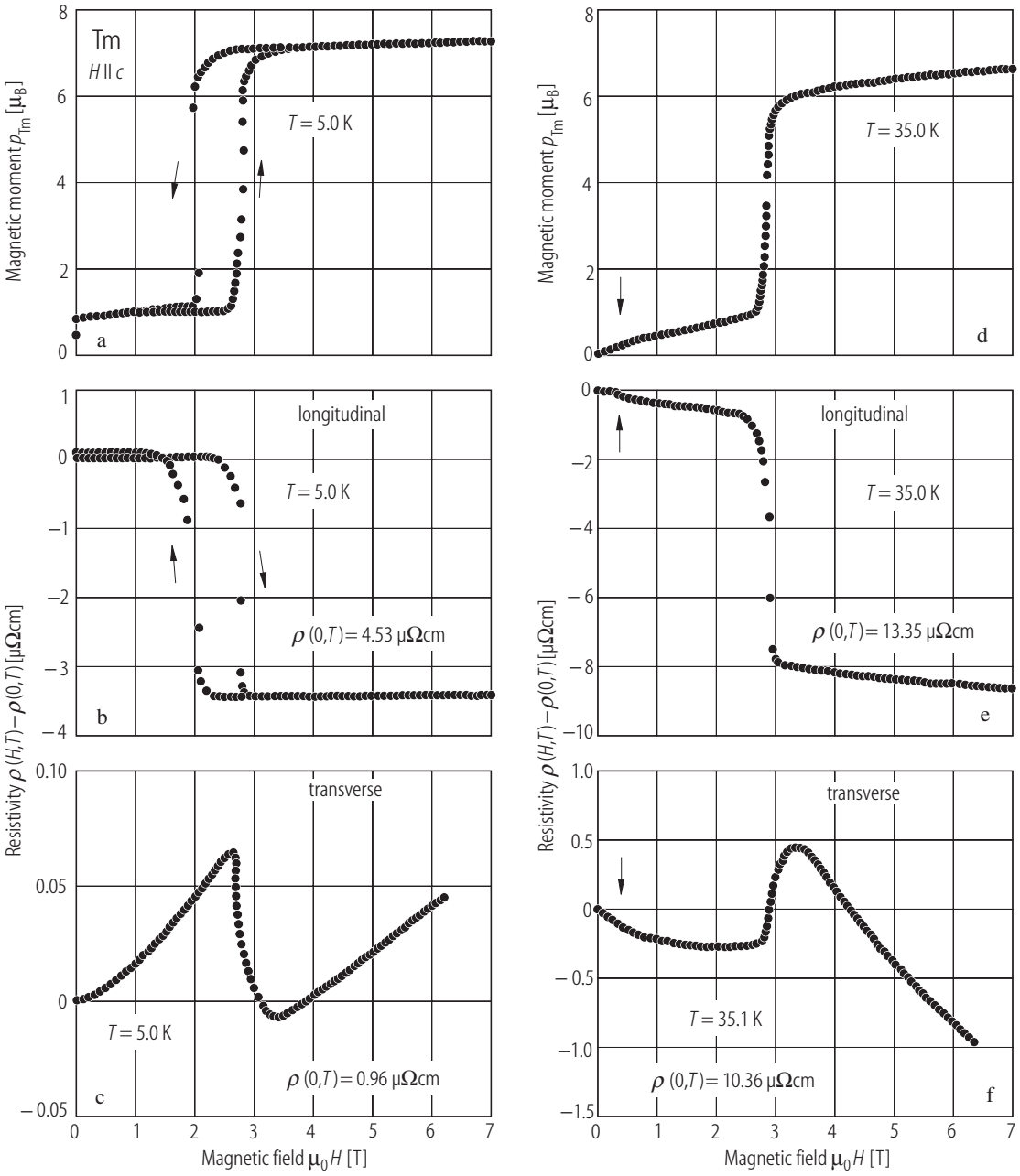

Fig. 304. Isothermal magnetization and longitudinal and transverse magnetoresistance in Tm metal at 5 K and 35 K [98E].

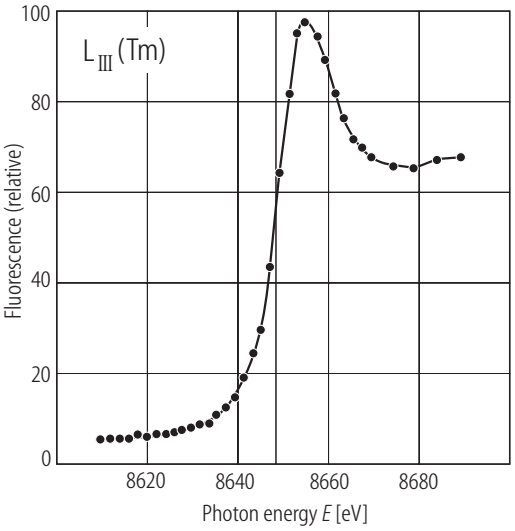

Fig. 305. Fluorescence at the centre of the Brillouin zone vs. incident photon energy through the L_{III} absorption edge. The fluorescence reflects the electric dipole transition involving 2p(3/2) → 5d(5/2) [90B].

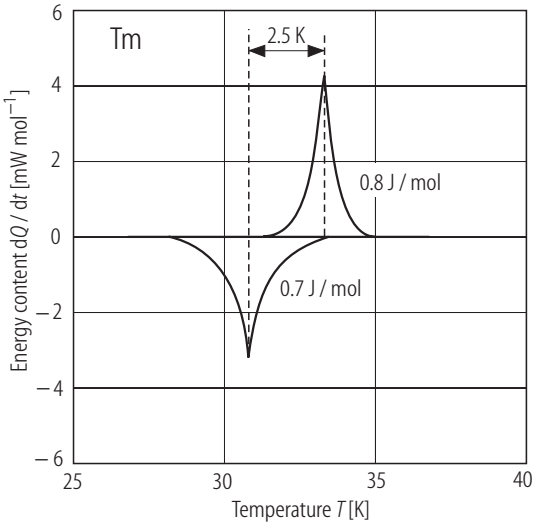

Fig. 306. The calorimetric measurements by continuously scanning the temperature. The change in energy content at the ferrimagnetic transition in Tm for increasing temperature (endothermic peak) and for decreasing temperature (exothermic peak). The integration of dQ/dt over time are shown for both peaks. The sharpness and thermal hysteresis are typical of a first-order process [91Å].

References

90B Bohr, J. Gibbs, D., Huang, K.: Phys. Rev. B **42** (1990) 4322

90D Daou, J.N., Burger, J.P., Vajda, P., Chouteau, G., Tur, R.: J. Phys.: Condens. Matter **2** (1990) 7897

90F-B Fernandez-Baca, J.A., Niclow, R.M., Rhyne, J.J.: J. Appl. Phys. **67** (1990) 5283

91McE McEwen, K.A., Steigenberger, U., Jensen, J.: Phys. Rev. B **43** (1991) 3298

91Å Åström, H.U., Noguest, J., Nicolaides, G.K., Rao, K.V., Benediktsson, G.: J. Phys.: Condens. Matter **3** (1991) 7395

92Z Zochowski, S.W., McEwen, K.A.: J. Magn. Magn. Mater. **104-107** (1992) 1515

98E Ellerby, M., McEwen, K.A., Jensen, J.: Phys. Rev. B **57** (1998) 8416

2.5 Compounds of rare earth elements and 4d or 5d elements

2.5.1 Introduction

This section 2.5 covers relevant literature published since about the year 1905 until the year 1999. The magnetic data of the same group of compounds published earlier have been compiled by A. Chelkowski and have already been published in Landolt-Börnstein, Volume 19 "Magnetic Properties of Metals", subvolume d2, pages 469-545.

The tables and figures in this section contain magnetic data on metallic or pseudometallic compounds of the rare earth group of elements which contain besides the rare earth element at least one 4d (Mo, Ru, Rh, Pd) element and/or one 5d (Re, Os, Ir, Pt) element. The compounds are summarized in two tables in subsect. 2.5.2. Table 1 is devoted to binary and pseudobinary compounds of the rare earth elements with 4d or 5d elements. Table 2 is devoted to ternary compounds which contain besides the rare element at least one 4d or 5d element and as a third one another element of the periodic system.

The compounds listed in the tables are designated by their chemical formula. The compounds are arranged in the order as their elements appear in the periodic system. Thus the rare earth elements are listed in following order

Y, La, Ce, Pr, Nd, Pm, Sm, Eu, Gd, Tb, Dy, Ho, Er, Tm, Yb, Lu,

the 4d elements in the order

Mo, Ru, Rh, Pd,

and the 5d element in the order

Re, Os, Ir, Pt.

The compounds are listed in such a way that rare-earth-rich compounds appear in the begining of each table.

The tables provide information on paramagnetic Curie temperature Θ, ferromagnetic Curie temperature T_C, Néel temperature T_N , magnetic susceptibility χ, saturation or spontaneous magnetic moment p_s and effective paramagnetic moment p_{eff} . The column "Remarks" may provide further data.

2.5.2 Survey of compounds and properties

Table 1. Binary and pseudobinary compounds of rare earth elements with 4d and 5d elements. R: rare earth element, M: 4d or 5d element, p_s refers to 4.2 K. For properties of the same compounds published earlier is refered by page number in Landolt-Börnstein NS, group III, volume 19d2, pages 469 - 545, in which also many compounds have been reviewed for which no new data would be found in the literature published in the reviewed period 1985 - 1999.

Compound	page in Vol. 19d2	Θ [K]	T_C [K]	T_N [K]	χ	p_s [μ_B]/R	p_{eff} [μ_B]/R	Remarks	Ref.
R_3M	470								
Gd_3Rh	470							XPS valence band of single crystal, pure Rh and Gd: Fig. 1; ρ vs. T: Fig. 2	95T2
		146		112	Fig. 3		14.7	$\Delta p = (p_{eff}/\text{f.u.})/3^{1/2}$	
Gd_3Pd		340	325		Fig. 4		13.27	$\Delta p = (p_{eff}/\text{f.u.})/3^{1/2}$, ρ vs. T: Fig. 5	95T2
Gd_3Ir								XPS valence band of single crystal, pure Ir and Gd: Fig. 6; ρ vs. T: Fig. 2	95T2
		169	155		Fig. 7		14.07	$\Delta p = (p_{eff}/\text{f.u.})/3^{1/2}$	
R_7M_3	471								
Ce_7Ru_3					Fig. 8			magnetization 1.5 μ_B/mol at 2 K and 5 T, C_{el}/T vs. T: Fig. 9	95T4
Ce_7Rh_3	471		6.8		Fig. 10			magnetization 6 μ_B/mol at 2 K and 5 T C_{el}/T vs. T: Fig. 11	95T4
		6.9		6.5	Fig. 12			C_m = 4.23 cm^3K/mol, the positive value of Θ is in agreement with the onset of the spontaneous magnetization	92S1
Ce_7Pd_3	471			3.6	Fig. 8			magnetization 5.8 μ_B/mol at 2 K and 5 T, C_{el}/T vs. T: Fig. 9	95T4

Compound	page in Vol. 19d2	Θ [K]	T_C [K]	T_N [K]	χ	p_s [μ_B]/R	p_{eff} [μ_B]/R	Remarks	Ref.
Ce_7Ir_3			4.45		Fig. 10			magnetization 4.8 μ_B/mol at 2 K and 5 T, C_{el}/T vs. T: Fig. 11	95T4
Ce_7Pt_3			6.85	2.85	Fig. 8			magnetization 6 μ_B/mol at 2 K and 5 T, $C_{el}T$ vs. T: Fig. 11	95T4
R_5M_3									
Ce_5Rh_3		45		4.5, 4.6	Figs. 13, 14	0.72		$\chi_0 = 7 \cdot 10^{-3}$ cm^3/Ce at, $C = 0.64$ cm^{3}K/Ce at, p_m vs. H: Figs. 15, 16, specific heat vs. T: Fig. 17	92K1
RM									
CePt								magnetic contribution to the specific heat: Fig. 18	95B1
R_3M_4	474								
Gd_3Pd_4	474	– 9.5		18	Fig. 20		8.19/Gd	another magnetic transition observed at 6 K	92T1
Yb_3Pd_4	476			3 3.2 Fig. 21			4.42	valency of Yb 2.95 suggested Mössbauer spectroscopy and neutron diffraction study, H_{hf} vs. T: Fig. 21, $p_s = 0.6$ μ_B	85P1 94B2
RM_2	475								
$LaRh_2$	476				Fig. 22			at 4.2 K $\chi_m = 1.7\ 10^{-4}$ cm^3 mol^{-1}	95O1
$CeRu_2$	476				Fig. 23			cubic Laves phase superconductor characterized by extremely small magnetic moments, static electronic magnetism occurs at $T_M = 40$ K	96H1

Compound	page in Vol. 19d2	Θ [K]	T_C [K]	T_N [K]	χ	p_s [μ_B]/R	p_{eff} [μ_B]/R	Remarks	Ref.
					Fig. 24			temperature dependence of magnetic susceptibility at $\mu_0 H = 0.1$ T	97S2
								σ vs. $\mu_0 H$: Figs. 25, 26	97D1
$CeRh_2$	477				Fig. 22			at 4.2 K $\chi_m = 7.8 \cdot 10^{-4}$ cm^3 mol^{-1}	95O1
$CeOs_2$		– 0.39 P14 1.9 P15			Fig. 27			two different crystallographic structures: C14 and C15, the C14 behaves like a normal metal with a stable Ce^{4+} valence, the C15 exhibits various features, characteristic of valence fluctuating compounds, only C14 becomes superconductive	97S1
$CePt_2$			Figs. 28, 29, 30					alloying Ir or Rh on the Pt-site decrease T_N, no magnetic order was detected for x > 0.25, the electronic part of the specific heat at temperatures higher than 10K shows a maximum dependent on x, dilution of Ce in $Ce_xPt_{1-x}Pt_2$ results in a suppression of the magnetic order and an enhanced γ_{HT}	97B1
$Ce_{1-x}Gd_xRh_2$								p_s vs. x: Fig. 31, $P(n,x)$ and $\langle p \rangle$ vs. x: Fig. 32	90T1
$PrRu_2$	477			Fig. 33					90D1
$Gd(Al_{1-x}Pd_x)_2$			Fig. 34					Curie temperatures vs. concentration from electrical resistivity measurements	94C1
$TmIr_2$		– 4 K			Fig. 35		4.49	antiferromagnetic below 0.05 K trivalent above 4 K	85W1
$YbIr_2$		– 4 K			Fig. 36		7.57	antiferromagnetic below 0.40 K, above 4 K trivalent	85W1

Compound	page in Vol. 19d2	Θ [K]	T_C [K]	T_N [K]	χ	p_s [μ_B]/R	p_{eff} [μ_B]/R	Remarks	Ref.
RM_3	479								
$CePd_3$	480							dynamical magnetic susceptibility investigation in αCE	90S6
								temperature dependence of the electrical resistivity investigations under hydrostatic pressure up to 15 kbar	90A1
RM_5	483								
$CePt_5$		– 9.44			Fig. 37 $2.20 \cdot 10^{-2}$ at 16 K		2.00	temperature independent susceptibility at 16 K, σ: Fig. 38, $\chi_0 = 9.37 \cdot 10^{-4}$ cm^3 mol^{-1}, $C = 0.500$ cm^3 K mol^{-1}	93B2
$CeAl_xPt_{5-x}$					Fig. 39			weak Kondo interaction, long-range magnetic order	97S3
x = 0		– 24							
0.5		– 11							
1		– 9							
2		– 28							
RM_{11}									
$YbGa_{7.75}Pd_{3.25}$					Fig. 40			space group Pm3m, for x ≤ 3 temperature independent Pauli paramagnets	97G1

Table 2. Ternary compounds of rare earth elements with 4d or 5d elements. R: rare earth element, M: 4d or 5d element. p_s refers to 4.2 K.

Compound	Θ [K]	T_C [K]	T_N [K]	χ	p_s [μ_B/R]	p_{eff} [μ_B/R]	Remarks	Ref.
RMM'								
R/MM' = 0.66								
Ce_2Rh_2In				Fig. 49				96K2
$Ce_2Pd_{2.04}In_{0.96}$	– 22	3.7	4.5			2.48	two magnetic transitions under an applied field $\mu_0 H = 0.01$ T	96F1
Ce_2Pd_2In	18			Figs. 41 - 44		2.48		95G1
				Fig. 47			σ vs. H: Fig. 47 and vs. H and T: Fig. 48	96K2
$Ce_2(Pd_{(1-x)}Ni_x)_2In$				Figs. 45, 46			magnetic properties change continuously from	96I1
x = 0	20					2.45	ferromagnetic for x = 0 to the temperature-	
0.25	4	4.2				2.39	independent paramagnet for x = 1	
0.50	– 39					2.46		
$Ce_2Pd_{2+x}Sn_{1-x}$							p_m vs. T and x: Fig. 57	97C1
$Ce_2Pd_{2.06}Sn_{0.94}$	– 20	3.0	4.7	Fig. 58		2.47	p_m vs. T: Fig. 59, p_m vs. H: Figs. 60, 61	96F1
$Ce_2Pd_{2.2}Sn_{0.79}$	– 34		4.2	Fig. 58		2.54	p_m vs. T: Fig. 59	96F1
Ce_2Pd_2Sn	18			Figs. 62 - 64, 44		2.62		95G1
Ce_2Pd_2Pb	– 32			Figs. 65 - 67		2.70		95G1
Ce_2Pt_2In	8.4			Fig. 50		2.49		96K2
Ce_2Pt_2Sn							p_m vs. T: Fig. 68	97C1
$Gd_2Pd_{2.02}Sn_{0.98}$			Fig. 69					98C2

Compound	Θ [K]	T_C [K]	T_N [K]	χ	p_s [μ_B/R]	p_{eff} [μ_B/R]	Remarks	Ref.
$Tb_2Pd_{2.05}Sn_{0.95}$	– 13		27.3	Fig. 70		10.15	neutron diffraction study, polycrystalline sample, T_{N2} = 20.8 K, magnetic structure between T_N and T_{N2} – incommensurate wavevector $\boldsymbol{k}_1 = (k_x\ k_x\ ½)$ (with a continuous decrease of the incommensurate component k_x from k_x = 0.115 at T = 26.3 K to k_x = 0.070 at T = 20.8 K). Below T_{N2}, a commensurate magnetic structure is observed with $\boldsymbol{k}_2 = (0\ 0\ ½)$ wavevector (k_x located to zero), magnetic structure: Fig. 71	98L1
$Tb_2Pd_{2.02}Sn_{0.98}$			Fig. 69	Figs. 72, 73			ρ vs. T: Fig. 74, p_m vs. H: Fig. 75	98C2
$Dy_2Pd_{2.02}Sn_{0.98}$			Fig. 69					98C2
Ho_2RuGe_2				Figs. 51, 53			σ: Fig. 52	96S1
$Ho_2Pd_{2.02}Sn_{0.98}$			Fig. 69					98C2
Ho_2OsGe_2				Figs. 54, 56			σ: Fig. 55	96S1
$Er_2Pd_{2.02}Sn_{0.98}$			Fig. 69	Figs. 72, 73			p_m vs. H: Fig. 75	98C2
R/MM' = 0.6								
$Ho_3Ru_2Ge_3$				Figs. 51, 53			σ: Fig. 52	96S1
R/MM' = 0.5								
YPdAl							resistivity vs. T: Fig. 76, specific heat vs. T: Fig. 77	94K1
Y_2PdSi_3							Non magnetic compound	90K3
LaRuSi							Pauli paramagnet, space group P4/nmm,	93W2

Compound	Θ [K]	T_C [K]	T_N [K]	χ	p_s [μ_B/R]	p_{eff} [μ_B/R]	Remarks	Ref.
LaRuGe							space group P4/nmm, unit cell volume: Fig. 78, Pauli paramagnet	93W2
CeRuSi	– 52			Fig. 80		2.56	space group P4/nmm, unit cell volume: Fig. 78	93W2
CeRuGe	– 73			Fig. 80		2.55	space group P4n/nmm, unit cell volume: Fig. 78	93W2
$CeRuSn_x$				Fig. 81			p_m vs. H: Fig. 82	90F2
$CeRu_{0.15}Ni_{0.85}Sn$				Fig. 83				97A1
$Ce_{0.25}U_{0.75}Ru_2$							σ vs. T: Fig. 84	92R1
CeRhGe			10	Fig. 85		2.25	p_m vs. T: Fig. 85, p_m vs. H: Fig. 87, magnetic structure Fig. 88	96B1
CeRhIn				Fig. 89				90M1
$CeRh_{1-x}Pd_xIn$				Figs. 90, 91			p_m vs. x: Figs.: 92, 93, C_p vs. T:Fig. 94, ρ/ρ(300K) vs. T: Fig. 95, valence fluctuation of Ce with x discussed, schematic representation of CeTX crystallizing in the ZrNiAl-type structure, the volume shown contains 3 unit cells and 9 Ce atoms	93B1
x = 1.00	– 48					2.49		
0.95	– 52					2.52		
0.90	– 51					2.47		
0.85	– 57					2.49		
0.80	– 60					2.51		
0.60	– 69					2.54		
$CeRh_{0.15}Ni_{0.85}Sn$				Fig. 83				97A1
CeRhSn				Fig. 96			σ_m vs. H at 4.6 K: Fig. 97	92R2

Compound	Θ [K]	T_C [K]	T_N [K]	χ	p_s [μ_B/R]	p_{eff} [μ_B/R]	Remarks	Ref.
CePdAl			Fig. 77: 2.7				resistivity vs. T: Fig. 76, heavy-fermion compound heavy fermion, frustrated magnetic structure, studied by powder neutron diffraction, space group P62m, below orders with an incommensurate antiferromagnetic propagation vector $k = (1/2,0,\tau)$, $\tau \approx 0.35$, and a longitudinal sin-wave modulated spin arrangement	94K1
CePdGa	– 35		2.2					90S2
				Fig. 98			T_K =8.8 K well defined crystal field transition at 18.9 meV and 33.8 meV, presence of CEF splitting	94A3
CePdIn			1.8	Figs. 99, 100		2.61	single crystal, Θ_a=– 65 K, Θ_c=– 43 K	90F1
CePdG	120		3.3	Figs. 116, 117				90S1
CePdSn	– 52		7	Fig. 101		2.62		88K1
			7					90S1
	– 6.3		7.0		0.88	2.7	magnetic structure: Fig. 102, simple spiral magnetic structure with the wavevector k = (0, 0.473, 0) in the temperature range 1.4 K to T_N = 7.3 K: Fig. 102a	94A5
			7 Fig. 103				neutron scattering studies on single crystal, magnetic structure below T_N is an incommensurate with propagation vector of (0, 0.473, 0) and magnetic moment of about 1 μ_B	92K2
				Fig. 104				90S2
$CePd_{0.15}Ni_{0.85}Sn$				Fig. 83				97A1
	– 176			Fig. 105		2.77		94A2

Compound	Θ [K]	T_C [K]	T_N [K]	χ	p_s [μ_B/R]	p_{eff} [μ_B/R]	Remarks	Ref.
$Ce(Pd_xNi_{1-x})Sn$			Fig. 106				neutron diffraction, single crystal, crossover from magnetic to nonmagnetic ground state in the Kondo alloy system, below 7 K incommensurate magnetic structure with propagation vector q = (0, 0.473, 0)	91K1
CeOsSi	– 29			Fig. 80		2.03	Curie-Weiss paramagnets down to 4.2 K, space group P4/nmm, unit cell volume: Fig. 78	93W2
CePtAl	6.5			Fig. 107		2.58	p_{Ce} vs. H: Fig. 108	97K2
CePtGa			3.5					90S1
			Figs. 109, 110				temperature and pressure dependence of ρ: Fig. 109, pressure dependence of T_N: Fig. 110	95U1
	– 68			Fig. 112		2.36	do not present any ordering down to 5 K, σ vs. H: Fig. 111	96K5
CePtSi				Fig. 113				90K1
$CePt_{1-x}Ni_xSi$				Fig. 114			γ vs. x: Fig. 114, correlation between γ and χ mainly reflect a lowering of the density of states of the conduction electrons at the Fermi level rather than reduced magnetic correlations suggested	96K3
$CePtSi_{1-x}Ge_x$			Fig. 115				unit cell volume, T_N and C/T vs. x: Fig. 115	92G1

Compound	Θ [K]	T_C [K]	T_N [K]	χ	p_s [μ_B/R]	p_{eff} [μ_B/R]	Remarks	Ref.
CePtSn			7.5					90S1
			7.5				ρ and S vs. T:Fig. 118	94B1
			5.5, 8	Fig. 119			antiferromagnetic Kondo lattice, crystal field splitting below 80 K of Ce^3 $J = 5/2$ state, CEF parameters $B_2^0 = 0.83$ meV, $B_2^2 = 1.53$ meV, $B_4^0 = 0.088$ meV, $B_4^2 = -0.027$ meV, $\chi_p = 4.4 \cdot 10^{-4}$ cm^3 mol^{-1} and $\lambda = -188$ mol cm^{-1}, ρ vs. ln$T$: Fig. 120	94A2
			7.8				sine modulated magnetic structure, an additional anomaly at 5.2 K	95B3
$Ce(Pt_{1-x}Ni_x)Sn$	Fig. 121		Fig. 122			Fig. 121	lattice constants: Fig. 121	92S5
$CePt_{0.15}Ni_{0.85}Sn$	– 214			Fig. 105		2.95		94A2
PrRuSi	7		73	Fig. 123		3.52	unit cell volume: Fig. 78	93W2
PrRuGe	0		62	Fig. 79		3.82	space group P4/nmm, unit cell volume: Fig. 78	93W2
PrRhSn	10			Fig. 96		3.83	σ_m vs. H at 103 K: Fig. 97	92R2
PrPdSn				Fig. 104				90S2
PrPtGa	– 18			Fig. 112		3.50	do not present any ordering down to 5 K, σ vs. H: Fig. 111	96K4
Pr_2PdSi_3	8			Fig. 125		3.47	p_m vs. H: Fig. 125, no magnetic ordering down to 4.2 K	90K3

Compound	Θ [K]	T_C [K]	T_N [K]	χ	p_s [μ_B/R]	p_{eff} [μ_B/R]	Remarks	Ref.
NdRuSi	29		74	Fig. 123		3.46	space group P4/nmm, collinear antiferromagnetic, structure which consists of ferromagnetic (001) Nd layers with moments $\perp$ to the layers, antiferromagnetically coupled along *c* axis in the sequence + – – + , unit cell volume: Fig. 78, magnetic moment vs. temperature: Fig. 126, magnetic structure: Fig. 127	93W2
NdRuGe	4		65	Fig. 79		3.91	space group P4/nmm, unit cell volume: Fig. 78	93W2
NdRhGe			14	Fig. 86		3.73	p_m vs. *T*: Fig. 86, p_m vs. *H*: Fig. 87, magnetic structure Fig. 88	96B1
NdRhSn	12			Fig. 96		3.55	σ_m vs. *H* at 30 K: Fig. 97	92R2
NdPtGa	– 15			Fig. 112		3.55	do not present any ordering down to 5 K, σ vs. *H*: Fig. 111	96K4
Nd_2PdSi_3	17	16		Fig. 125		3.54	p_m vs. *H*: Fig. 125	90K3
SmRuSi		65		Fig. 123			non Curie-Weiss behaviour, unit cell volume: Fig. 78, space group P4/nmm	93W2
							σ_s = 0.15 μ_B mol^{-1}, H_c = 12.5 kG	
		33	62.5				T_M = 16 K, T_R = 16 K	96K1
SmRuGe		45		Fig. 79			space group P4/nmm, unit cell volume: Fig. 78, non-Curie-Weiss behaviour	93W2
SmRhSi		33	73				T_M = 18 K, T_R = 23 K	96K1
SmRhGe		56					T_M = 11.5 K, T_R = 11.5 K,:Fig. 128, ρ vs. *T*: Fig. 130	96K1
SmPdIn				Figs. 134, 135			magnetic transition temperature T_c = 54 K, p_m vs. *T*: Fig. 133, p_m vs. *H*: Figs. 132, 136, ρ vs. *T*: Fig. 137, C_p vs. *T*: Fig. 138	95I1

Compound	Θ [K]	T_C [K]	T_N [K]	χ	p_s [μ_B/R]	p_{eff} [μ_B/R]	Remarks	Ref.
SmPdSn				Figs. 141, 142			ρ vs. T: Figs. 139, 140, C vs. T : Fig. 143, thermopower vs. T	95S2
EuRuGe	15					9.3	space group Pnma	93W2
EuPdIn			13				p_m vs. H: Figs. 145, 146, magnetic phase diagram: Fig. 147	98I1
GdRuGe	68					8.1	space group Pnma	93W2
GdRuSi	78	85		Fig. 124		8.58	space group P4/nmm, unit cell volume: Fig. 78, σ_s= 6.4 μ_B mol^{-1}, H_c = 0	93W2
			18.5					98I1
GdPdSn				Fig. 104				90S2
GdPtGa	34			Figs. 148, 150		7.90	ordering temperature 25 K, σ vs. H: Fig. 149	96K4
Gd_2RhSi_3	2		14			7.61		98M1
Gd_2PdSi_3	33			Fig. 151		7.97	ordering temperature 21 K	90K3
TbRuGe	44					9.7	space group Pnma	93W2
TbPdIn				Fig. 152			spin-glass behaviour, σ_m vs. T and H: Fig. 152	98N1
TbPdSn	– 11		19	Fig. 153	7.6	10.1	σ vs. T: Fig. 154, p_m vs. H: Fig. 155, Tb moment order in a sine-wave-modulated magnetic spin arrangement with the wavevector k = (0, 0.25, 0.075) below T_t	94A5
	– 11		21 23.5	Fig. 156		10.1	p_m vs. T and H: Fig. 157 critical fields: H_{c1} and H_{c2} at 4.2 K = 65 and 105 kOe, respectively	95G2
				Fig. 104				90S2

Compound	Θ [K]	T_C [K]	T_N [K]	χ	p_s [μ_B/R]	p_{eff} [μ_B/R]	Remarks	Ref.
TbPtGa			25		7.4 at 18 K		antiferromagnetic unit cell:Fig. 158, collinear antiferromagnetic structure with propagation vector k = [0,1/2,0], configuration spin sequences (+ + + +) and (– – – –) of Tb moments on sides A and B, respectively, ferromagnetic (110) planes coupled pairwise antiparallel to each other, space group Pnma	94S3
	20			Figs. 148, 150		9.70	ordering temperature 20 K, σ vs. H: Fig. 149	96K4
TbPtSn			13.8				sine modulated magnetic structure, change of magnetic structure at 10 K	95B3
			12				hexagonal phase, ZrNiAl-type of crystal structure, non-collinear magnetic structure with wavevector k = (0.726, 0.766, 1/2), magnetic moment localized on Tb^{3+} is 8.8 μ_B at 1.9 K, magnetic moment distribution: Fig. 159, magnetization vs. T: Fig. 160	96S2
Tb_2PdSi_3	28			Fig. 151		9.70	ordering temperature 19 K	90K3
DyRuGe	– 2.5					10.6	space group Pnma	93W2
DyPdIn				Fig. 161			spin-glass behaviour, σ_m vs. T and H: Fig. 161	98N1
DyPdSn	– 7		10		7.6	10.5	magnetic structure:Fig. 102, Dy^{+3} order antiferromagnetically, below T_N = 10.5 K in a sine-modulated spin arrangement of the magnetic moments with the wavevector k = (0, 0.25, 0), below T_t = 7 K two magnetic structures coexist: the sine-modulated below T_t and a spiral structure, in both structures the magnetic moments are ‖ to the b axis	94A5

Compound	Θ [K]	T_C [K]	T_N [K]	χ	p_s [μ_B/R]	p_{eff} [μ_B/R]	Remarks	Ref.
DyPtGa	10			Figs. 148, 150		10.68	ordering temperature 15 K σ vs. H: Fig. 149	96K4
Dy_2PdSi_3	4			Fig. 151		10.43	ordering temperature 7 K	90K3
HoRuGe	14					10.9	space group Pnma	93W2
				Figs. 51, 53			σ vs. H: Fig. 52	96S1
HoPdGe				Figs. 162, 164			χ': Fig. 164	96S1
HoPdSn	– 7.5		3.7		9.0	10.7	at low temperature a coexistence of two magnetic structures is observed, one with the wavevector k_1 = (0, 0.268, 0) and a second one with k_2 = (0.333,0.0635, 0,0748)	94A5
HoIrGe				Figs. 54, 56			σ:Fig. 55	96S1
HoPtGa	6			Fig. 165		10.55	do not present any ordering down to 5 K	96K4
HoPtGe				Figs. 162, 164			χ': Fig. 164	96S1
Ho_2PdSi_3	5			Fig. 166		10.58	ordering temperature 6 K	90K3
ErPdSn			5.2		9.01	9.62	square-modulated structure with wavevector $\boldsymbol{k}$ = (1/3, 1/2, 1/3)above 2.5 K changes to a single-modulated structure with $\boldsymbol{k}$ = (k_x, ½, k_z), at 1.5 K in a magnetic field H_c = 2 kOe a transition to a ferromagnetic field is obtained, p_m vs. H and T: Figs. 167, 168	95A1
ErPtGa	5			Fig. 165		9.55	do not present any ordering down to 5 K	96K4
Er_2PdSi_3	6			Fig. 166		9.50	ordering temperature 8 K	90K3
TmPtGa	– 5			Figs. 148, 150		7.40	ordering temperature 8 K σ vs. B:Fig. 149	96K4

Compound	Θ [K]	T_C [K]	T_N [K]	χ	p_s [μ_B/R]	p_{eff} [μ_B/R]	Remarks	Ref.
Tm_2PdSi_3	– 4			Fig. 166		7.30	no ordering down to 4.2 K observed	90K3
YbPdAl				Fig. 169			Yb mixed valence suggested, ρ vs. T: Fig. 170	93C1
YbPtAl	– 60		5.8	Fig. 172		4.5	dc magnetization vs. H and resistivity at 2.0 K: Fig. 173, resistivity vs. T: Fig. 171	95D1
				Fig. 174		4.5	Yb valency close to + 3	95S4
YbPtSn	0.44					4.46	T_m = 3.5 K -antiferromagnetic ordering of trivalent Yb ions suggested: Fig. 175, temperature dependence of σ_m/H at 10 kOe, p_m vs. H at 3 and 4.2 K	97K4
$(Y_xCe_{1-x})_2PdSi_3$				Figs. 176, 178			p_m vs. H: Fig. 177, no magnetic ordering observed down to 1.4 K, the Kondo effect is operative in all these alloys, strength of the Kondo effect increases with the compression of the lattice by the general replacement of Ce by Y	96M1
x = 0	– 16							
0.2	– 37							
0.5	– 45							
0.8	– 75							
R/MM' = 0.375								
$Ho_3Pd_4Ge_4$				Figs. 162, 164			σ vs. H: Fig. 163	96S1
R/MM' = 0.357								
$Dy_{1.5}Sc_{3.5}Ir_4Si_{10}$				Fig. 179				93G2
$Dy_{1.75}Sc_{3.25}Ir_4Si_{10}$				Fig. 180				93G2
$Dy_3Y_2Os_4Ge_{10}$				Fig. 181				96R1
$Dy_5Os_4Ge_{10}$				Fig. 181				96R1
$Ho_5Os_4Ge_{10}$				Figs. 54, 56			σ vs. H: Fig. 55	96S1

Compound	Θ [K]	T_C [K]	T_N [K]	χ	p_s [μ_B/R]	p_{eff} [μ_B/R]	Remarks	Ref.
R/MM' = 0.333								
$CePd_2Al$	– 23		3.3	Figs. 182, 183		2.5	Θ < 30 K, around ≈–10 K, p_m vs. H: Fig. 184, heat capacity vs. T: Fig. 185	95D2
$CePd_2(Al_{1-x}Ga_x)_3$			Fig. 186				T_N vs. coupling strength: Fig. 187	97T4
$Ce_{1-x}Y_xPd_2Ga$				Fig. 190			χ_m and ρ vs. T: Fig. 190	93D1
$CePd_2Ga$				Fig. 188			χ_m and ρ vs. T: Figs. 188, 190, p_m vs. H: Fig. 189	93D1
$Ce(Pd_xNi_{1-x})_2Sn$							ρ vs. T: Fig. 191	88K1
$CePtSi_2$			1.5				intermediate-valent system, magnetic ordering in the presence of heavy fermions, γ= 220 mJ K^{-2}	92G1
				Figs. 192, 193				96K5
$CePtGe_2$		3.75		Fig. 194		2.49	below T_C exhibits metamagnetic transition, low-temperature χ could be fitted by using a different CEF on each of the two CE sites, low-temperature C at zero and elevated H up to 10 T gave a fairly large γ(93 - 115 mJ/molCe K^2) for ferrimagnetically ordered phase and, > 257 mJ/mol Ce K^2 for the paramagnetic state, suggesting a moderately heavy fermion system	96G2
$YbPdGa_2$	– 2					4.3		96G2
$YbPtGa_2$	– 22					4.4		96G2
R/MM' = 0.2857								
$Gd_2Mo_3Si_4$	4.9	10.0		Fig. 195		8.29	σ vs. H at 5 K: Fig. 195, H_c = 8.0 kOe	95L1

Compound	Θ [K]	T_C [K]	T_N [K]	χ	p_s [μ_B/R]	p_{eff} [μ_B/R]	Remarks	Ref.
$Tb_2Mo_3Si_4$			19	Fig. 201		9.6	second magnetic transition at 2.3 K, heat capacity: Fig. 202	94A4
	11.0	19.0 and 2.3		Fig. 196		9.55	σ vs. H at 5 K: Fig. 196, H_c 8.0 kOe	95L1
$Dy_2Mo_3Si_4$	5.2	12.0		Fig. 197		10.42	σ vs. H at 5 K: Fig. 197, H_c = 2.0 kOe	95L1
$Ho_2Mo_3Si_4$	3.0	4.8		Fig. 198		10.49	σ vs. H at 5 K: Fig. 198	95L1
$Er_2Mo_3Si_4$	1.2			Fig. 199		9.51	σ vs. H at 5 K: Fig. 199	95L1
$Tm_2Mo_3Si_4$	1.7			Fig. 200		7.18	σ vs. H at 5 K: Fig. 200	95L1
R/MM' = 0.2727								
$Y_3Pt_{2.5}Ga_{8.5}$							temperature-independent paramagnetic, structure type La_3Al_{11}	94G4
$Tb_3Pt_{2.2}Ga_{8.8}$	0		20	Figs. 203, 204		10.7	structure type La_3Al_{11}	94G4
$Dy_3Pt_{2.2}Ga_{8.8}$	2			Figs. 203, 204		11.6	metamagnetic ordering temperature 20 K, structure type La_3Al_{11}, σ vs. H: Fig. 205	94G4
$Ho_3Pt_{2.2}Ga_{8.8}$	– 5		12	Figs. 206, 208		11.4	structure type La_3Al_{11}	94G4
$Er_3Pt_{2.2}Ga_{8.8}$	0			Fig. 203		10.3	ordering temperature < 5 K, structure type La_3Al_{11}	94G4
$Tm_3Pt_{2.2}Ga_{8.8}$	– 1			Fig. 206		8.5	ordering temperature < 5 K structure type La_3Al_{11}	94G4
$Yb_3Pt_{2.0}Ga_{9.0}$	– 12			Fig. 207		1.1	temperature-independent magnetic susceptibility, intermediate valence behaviour suggested, structure type La_3Al_{11}	94G4

Compound	Θ [K]	T_C [K]	T_N [K]	χ	p_s [μ_B/R]	p_{eff} [μ_B/R]	Remarks	Ref.
R/MM' = 0.25								
$(Y_{0.37}La_{0.63})_x$-$Ce_{1-x}Ru_2Si_2$				Figs. 209, 211			diluted Kondo system, magnetization : Fig. 210, simulations of $\chi(T)$ for random Kondo system	95M2
$(YLa)_{1-x}Ce_xRu_2Si_2$						Fig. 212	magnetization vs. H at 1.5 K: Fig. 212, Ce dilution progressively reduces the short- range exchange effects, resulting in continuously increasing heavy-fermion state suggested, differential susceptibility vs. H: Fig. 213, magnetic specific heat C_m vs. T: Fig. 214	95M1
$Y_xCe_{1-x}Ru_2Si_2$							p_m vs. H: Fig. 215	88H1
$LaPd_2Al_3$							NMR: Fig. 217	94F1
$La_2Rh_3Si_5$				Fig. 218			below 4 K diamagnetic	96P1

Compound	Θ [K]	T_C [K]	T_N [K]	χ	p_s [μ_B/R]	p_{eff} [μ_B/R]	Remarks	Ref.
$La_xCe_{1-x}Ru_2Si_2$							p_m vs. H: Figs. 215, 216	88H1
							p_m vs. H: Fig. 219, $\Delta l/l$ vs. B: Fig. 220, $\Delta l/l$ vs. $\int B\mathrm{d}M$: Fig. 221, $\Delta l/l$ vs. M^2: Fig. 222	88L1
			Figs. 223, 224				ρ vs. T: Figs. 223, 224, single crystals down to 20 mK, a Kondo behaviour with logarithmic slope linear with x observed for $x \geq 0.3$, variation of ρ discussed	88D1
							ρ_m vs. H: Figs. 225, 226, 227, p_m vs. H: Fig. 227	88D2
							R_H vs. T: Fig. 228, Hall resistance vs. H: Fig. 229	88D3
			Fig. 230				p_m vs. H for $H \parallel c$ at 1.5 K, $\partial p_m/\partial H$ at different temperatures: Fig. 231, magnetic phase diagram: Fig. 232 magnetic phase transition in heavy-fermion compounds studied by thermal- expansion measurements	90H1
			Fig. 233				moment amplitude from neutron diffraction vs. x Fig. 233	94B3
							theory of the magnetic instability in heavy-fermion system	96K6
$La_{1-x}Ce_xRu_2Si_2$				Figs. 234 - 236				92H1
							p_m vs. T:Fig. 237, all compounds order in structure with the incommensurate wavevector $\boldsymbol{k}$ = (0.309, 0, 0), the magnetic moment and the transition temperature decrease continuously with x, moments are directed along the c axis of the tetragonal structure	88Q1
$La_{0.3}Ce_{0.7}Ru_2Si_2$							neutron intensity vs. H: Fig. 239	90M3

Compound	Θ [K]	T_C [K]	T_N [K]	χ	p_s [μ_B/R]	p_{eff} [μ_B/R]	Remarks	Ref.
$La_{0.2}Ce_{0.8}Ru_2Si_2$							magnetic phase diagram: Fig. 240	90M3
			Fig. 241				single crystal, pressure dependence of magnetic Bragg peaks: Fig. 241, magnetic field dependence of magnetic intensities for neutron scattering vectors $\boldsymbol{Q}$ = (0.69, 0.69, 0) and (0.69, 1, 0) at 3.2 K: Fig. 243, magnetic correlations around $\boldsymbol{Q}$ vs. T: Fig. 242	90R1
							inelastic neutron scattering study of magnetic fluctuations in the heavy-fermion system, single site and intersite fluctuations have been studied between 1.4 and 100 K	92J1
			Fig. 244				moment amplitude from neutron diffraction vs. pressure: Fig. 244	94B3
$La_{0.05}Ce_{0.95}Ru_2Si_2$							p_m vs. $T^{2:}$ Fig. 245	90P2
$La_xCe_{1-x}Pd_2Si_2$			Fig. 246				resistivity and specific heat vs. T show similar behaviour	90S3
$La_{0.5}Ce_{0.5}Pd_2Si_2$	– 49		4	Figs. 248, 249		2.55	specific heat vs. T: Fig. 250	90S4
$La_{0.5}Ce_{0.5}Pd_2Ge_2$				Figs. 251, 252			p_m vs. H: Fig. 253	92B1
$La_xCe_{1-x}Ir_2Ge_2$				Fig. 254				97M1
$La_{1-x}Pr_xRu_2Si_2$				Fig. 255			p_{Pr} vs. T and H: Fig. 256	98M2
$La_{2-x}Nd_xRh_3Si_5$			Fig. 257					96P1
$La_{1-x}U_xRu_2Si_2$				Fig. 258			$T\mathrm{d}\chi_m/\mathrm{d}T$ vs. T: Fig. 258, p_m vs. H: Fig. 259	96M2
$La_{0.95}U_{0.05}Ru_2Si_2$				Fig. 260				96M2

Compound	Θ [K]	T_C [K]	T_N [K]	χ	p_s [μ_B/R]	p_{eff} [μ_B/R]	Remarks	Ref.
$CeRu_2Si_2$							magneto-thermopower vs. $H \parallel c$: Fig. 261, influence of the metamagnetic-like transition on magneto-thermopower	88A1
							p_m vs. H and p: Fig. 304, ρ_m vs. H: Figs. 305, 306, magnetostriction vs. H: Fig. 307	88M1
							p_m vs. T^2: Fig. 262	90P1
				Fig. 263				90B1
							de Haas-van Alphen effect for magnetic field ranges below and above metamagnetic transition field H_m	94A1
							single crystal heavy-fermion compound, absence of magnetic order and superconductivity, at least down to 20 mK, ρ_m vs. T: Figs. 264, 265	92L1
				Fig. 266			heavy-fermion paramagnet, metamagnetic transition ($\mu_0 H_c \approx 7.8$ T) for $H \parallel c$: Fig. 266	95T1
							single crystal, heavy-electron compound, p_m and $(\Delta\chi)^{-1}$ the reciprocal of the peak height of $\partial p_m/\partial H$: Figs. 267, 268 in low-temperature metamagnetic behaviour quite sharp at 0.1 K. $T_K \approx 20$ K	95S1
				Figs. 269, 270			single crystal, heavy fermion, tetragonal structure, non-linear susceptibility: Fig. 269	95P1
							ρ vs. H: and T: Fig. 271	97L1
$Ce(Ru_xRh_{1-x})_2Si_2$							specific heat of heavy-fermion system: Figs. 272, 273, 274	90C1

Compound	Θ [K]	T_C [K]	T_N [K]	χ	p_s [μ_B/R]	p_{eff} [μ_B/R]	Remarks	Ref.
$Ce(Ru_{1-x}Rh_x)_2Si_2$			Fig. 275				phase diagram: Figs. 275, 276, p_m vs. H: Fig. 277	92S2
			Fig. 278				single crystals, pseudo-binary system, from neutron diffraction in the intermediate phase with $0.05 \le x \le 0.25$ incommensurate magnetic modulation regarded as purely sinusoidal: Fig. 278, the magnetic moment polarized along c axis	95K1
				Fig. 279			Kondo effect exists in the intermediate concentration range $0.3 \le x \le 0.5$	98T3
$CeRu_{1.7}Rh_{0.3}Si_2$			5.5	Fig. 280			single srystal, differential susceptibility vs. H: Fig. 280, p_m vs. T: Fig. 281, phase diagram: Fig. 282, the antiferromagnetic phase has an incommensurate sinusoidal spin modulation with a wavevector $\tau = (0, 0, 0.42)$ and the magnetic moment is polarized along the c axis with the amplitude of $0.65\mu_B$/Ce	98S1
				Fig. 283			heavy-fermion which shows a SDW ordering at $T_N = 5.6$ K, p_m vs. H and $\partial p_m/\partial H$: Fig. 284, magnetostriction vs. H: Fig. 285	96T1
$CeRu_{1.5}Rh_{0.5}Si_2$			≈ 4.35 Figs. 286 - 288	Fig. 286			single crystal, commensurate magnetic structure with the wavevector $k = (0, 0, 1/2)$ and the moment oriented along c axis, which mostly corresponds to + – – + stacking sequence of ferromagnetic planes along c^*, the anomalies of χ, C_p and ρ are weak, even undetectable	94H1
$CeRu_2Si_{2-x}Ge_x$							neutron spectroscopy was used to study the spin dynamics	92R1

Compound	Θ [K]	T_C [K]	T_N [K]	χ	p_s [μ_B/R]	p_{eff} [μ_B/R]	Remarks	Ref.
$CeRu_2Si_{2-x}Ge_x$							$\boldsymbol{Q}$ (in [$2\pi/a$] modulation wavevector)	92D1
x = 0	– 13.2		-		-		-	
0.1	-		9.3		0.35		0.327	
0.2	– 1.5		9.8		1.16		0.328	
0.3	3.0		10.0		1.41		0.326	
0.5	4.1		10.2		1.20		0.327	
1.0	7.9		10.2		1.53		0.323	
2.0	11.1	9			1.76		0	
							p_{Ce} vs. T: Fig. 289, p_{Ce} vs. H: Fig. 290	
$CeRu_2(Si_{1-x}Ge_x)_2$				Fig. 292			antiferromagnetic, p_m vs. H: Fig. 291	96B2
$CeRu_2Ge_2$				Fig. 293				88B1
			Fig. 294				effect of pressure and temperature on the magnetic transition: Fig. 294	95U2
$CeRuGe_3$				Fig. 194				96G2
$CeRh_2Ge_2$			Figs. 295 - 297				effect of pressure and temperature on the magnetic transition: Figs. 295, 296, 297	95U2
$Ce(Ru_{1-x}Pd_x)_2Si_2$							magnetization vs. H: Fig. 298, differential susceptibility $\partial p_m/\partial H$ vs. H: Fig. 299	95B2
			Fig. 300	Fig. 301			magnetic specific heat C_m: Fig. 302	95K2
			Fig. 19	Fig. 303			phase diagram: Fig. 19	95S3
$Ce(Ru_{0.96}Pd_{0.04})_2Si_2$			3.1					96M4
$CeRh_2Si_2$			Fig. 308				magnetic phase diagram: Fig. 308	97G2
				Fig. 309			heavy-fermion compound	98H1
			35				C_m/T vs. T: Fig. 310,	96M3
			Figs. 310, 311				$T_N(p)/T_N(0)$ vs. p: Fig. 311	

Compound	Θ [K]	T_C [K]	T_N [K]	χ	p_s [μ_B/R]	p_{eff} [μ_B/R]	Remarks	Ref.
$Ce(Pd_{1-x}Rh_x)_2Si_2$				Figs. 312 - 314			the as-cast samples show with monotonous evolution complete miscibility in samples annealed at 1200 °C	97T5
$Ce(Pd_{1-x}Ni_x)_2Al_2$				Fig. 315			NMR study of magnetic properties	95F1
$CePd_2Si_2$							magnetic excitations in the antiferromagnetic Kondo compound	97G2
			Fig. 308				magnetic phase diagram:Fig. 308	97G2
				Fig. 309			heavy-fermion compound	98H1
$CePd_{2-x}Mn_xSi_2$			Fig. 316			Fig. 317	crystal volume and lattice parameters vs. x: Fig. 318	94G2
$CePd_2Ge_2$			Fig. 319					96O1
$CePd_2Sn_2$			0.5	Fig. 320			C_{mag} vs. T: Fig. 321, Kondo behaviour down to 50 mK	98K2
$CePt_2Si_2$							magnetostriction vs. H, for an elongation direction along $H \parallel [110]$ at 0.4 K shows an inflection point at around 2.7 T, the volume expansion exhibits two broad anomalies centred at 70 and 180 K	92D2
							single crystal, heavy-electron compound, p_m and differential susceptibility: Fig. 323, in low temperature metamagnetic, $T_K \approx 50$ K, nonmagnetic Kondo lattice system with $\gamma \approx 80$ mJ/mol K^2 intermediate valence, tetragonal $CaBe_2Ge_2$-type	95S1
$Ce_2Rh_3Si_5$				Fig. 324				90G1
$Ce_2Rh_3Ge_5$				Fig. 324				90G1

Compound	Θ [K]	T_C [K]	T_N [K]	χ	p_s [μ_B/R]	p_{eff} [μ_B/R]	Remarks	Ref.
$Ce_2Pd_3Ge_5$			3.8			2.43	orthorhombic $U_2Si_5Pd_3$-structure, specific heat, resistivity and magnetic susceptibility show antiferromagnetic ordering below 3.8 K	90G1
$Ce_2Ir_3Si_5$				Fig. 325				90G1
$Ce_2Ir_3Ge_5$				Figs. 325, 326				90G1
$PrRu_2Si_2$				Fig. 327			p_m vs. H: Fig. 328, σ vs. T: Fig. 329	92S3
$NdRu_2Si_2$			24	Figs. 330, 331	2.8		ferro-antiferro transition temperature 10 K: Fig. 330, p_m vs. H: Fig. 332	90S5
		Fig. 333	Fig. 333				$d\rho/dT$: Fig. 333	92P1
							magnetic phase diagram Fig. 334, isothermal magnetization at several temperatures Fig. 335, magnetization vs. T at several H: Fig. 336	94S1
$NdRu_2Ge_2$			17	Figs. 337, 340		4.84	p_m vs. H: Fig. 337, p_m vs. H and T along the [001] easy axis: Fig. 338, phase diagram: Fig. 339	94G1
$NdRh_2Si_2$			53				critical fields: H_{c1} and H_{c2} = 134 and 143 kOe at 4.2 K, respectively	94S2
$Nd_2Rh_3Si_5$	8.9		2.7	Fig. 218		3.69		96P1
$SmRu_2Si_2$		15.5					T_M = 11 K, T_R = 15.5 K, σ_m vs. T: Fig. 129, hysteresis loop: Fig. 131	96K1
$SmRh_2Si_2$		35	62				T_M = 10 K, T_R = 60.5 K, ρ vs. T: Fig. 128, σ_m vs. T: Fig. 130	96K1
$SmRu_2Ge_2$		15					T_R = 15.5 K, ρ vs. T: Fig. 128, σ_m vs. T: Fig. 129, hysteresis loop: Fig. 131	96K1
$SmRh_2Ge_2$		17	43				T_R = 17.5 K	96K1

Compound	Θ [K]	T_C [K]	T_N [K]	χ	p_s [μ_B/R]	p_{eff} [μ_B/R]	Remarks	Ref.
$EuPt_2Si_2$	– 30		15	Figs. 341, 342		7.7		90N1
$EuPd_2Si_2$							$\partial p_m/\partial H$ vs. H and T: Fig. 343, H_t vs. T: Fig. 344	96W1
$Eu(Pd_{1-x}Pt_x)_2Si_2$				Fig. 345			p_{Eu} vs. H: Fig. 346	96W1
$GdRu_2Si_2$	38.7		45.4 47	Fig. 347 Figs. 349, 350		8.20 8.35	p_{Gd} vs. H: Fig. 348 single crystal, at T_t = 40 K transition between the two magnetic phases: Fig. 349, p_m vs. H: Figs. 351, 352, 353; H-T phase diagram: Fig. 354	97T1 95G3
$GdRu_2Ge_2$			33				p_m vs. H: Fig. 355, C_m vs. T: Fig. 356, space group I4/mmm	96G1
$GdRu_2Sn_2$							ESR investigations	90K2
$GdRh_2Si_2$	– 2.1		106	Fig. 347		8.25	p_{Gd} vs. H: Fig. 348 p_m vs. H: Fig. 357	97T1 92S4
$GdPd_2Si_2$	– 43.9		16.5	Fig. 347		8.01	p_{Gd} vs. H: Fig. 348	97T1
$GdPd_2Ge_2$	– 34.3		9.0			8.03		93M1
$GdPd_2Sn_2$							ESR investigations	90K2
$GdOs_2Si_2$	22.6		28.5	Fig. 359		8.15	p_{Gd} vs. H: Fig. 360	97T1
$GdIr_2Si_2$	– 6.4		82.4	Fig. 359		7.94	p_{Gd} vs. H: Fig. 360	97T1
$GdIrSi_3$	– 30		15.5	Fig. 361		8.12	Mössbauer spectroscopy investigations	91S1
$GdPt_2Si_2$	– 5.6		9.3 9.90	Fig. 359		8.01	p_{Gd} vs. H: Fig. 360 C_m vs. T: Fig. 362, structure determined from neutron diffraction is modulated incommensurate antiferromagnetic type	97T1 91G1
$Gd_2Rh_3Si_5$	– 15.4		8.4	Fig. 363		8.08	C_p vs. T: Fig. 364	97P1

Compound	Θ [K]	T_C [K]	T_N [K]	χ	p_s [μ_B/R]	p_{eff} [μ_B/R]	Remarks	Ref.
$TbRu_2Si_2$			Fig. 333				dρ/dT: Fig. 333	92P1
							isothermal magnetization at several temperatures Fig. 365	94S1
			57	Fig. 366			single crystal, magnetization vs. $H \parallel c$: Fig. 367, magnetostriction vs. $H \parallel c$: Fig. 368	95T3
			57				AM structure with propagation vector $\boldsymbol{Q}$ = (τ,0,0) with τ =0.2352, at lower temperatures, it becomes antiphasic with the magnetic moments aligned along the c direction owing to the uniaxial anisotropy and reaching the maximum saturated value for free ions of 9.0 μ_B	97S5
			56	Figs. 369, 370	9		C_p vs. T: Fig. 371, χ' vs. H: Fig. 370, new phase boundaries observed at low temperatures below 4.2 K	98K1
			57	Fig. 372		8.94	single crystal, p_m vs. H: Fig. 373, metamagnetic along the c axis	95G3, 95S5
$TbRu_2Ge_2$				Fig. 374			p_m vs. H: Figs. 376, 377, H-T diagram: Fig. 375	96G1
			37				p_{Tb} vs. H: Fig. 378, magnetic structure: Fig. 379	97B3
			37				neutron diffraction, single crystal, magnetic phase transitions at 4.30, 37 and 30 K, the magnetic structures are an anti-phase structure with the propagation vector $\boldsymbol{k}_1$ = (0.235, 0, 0) (0.235 = 4/17), an amplitude modulated (AM) structure with $\boldsymbol{k}_1$ and a sinusoidal modulated structure with $\boldsymbol{k}_1$ and $\boldsymbol{k}_2$ = (0.247, 0, 0), respectively, for low, middle and high temperatures	97S5

Compound	Θ [K]	T_C [K]	T_N [K]	χ	p_s [μ_B/R]	p_{eff} [μ_B/R]	Remarks	Ref.
$TbRh_{2-x}Ru_xSi_2$							p_m vs. T: Fig. 380, phase diagram: Figs. 381, 382	93I1
x = 0.25		59		8.5				
0.5				7.5				
0.6		44.5		8.0			p_m from neutron diffraction 8.2 μ_B	
0.7		38		7.2			p_m from neutron diffraction 6.0 μ_B	
0.8		36		6.3			p_m vs. H: Fig. 383	
1.0		12		6.9			p_m from neutron diffraction 5.9 μ_B	
1.25		23		8.2			p_m from neutron diffraction 8.75 μ_B	
1.5		40		8.5			p_m from neutron diffraction 8.65 μ_B	
1.75		47		8.1			p_m vs. H: Fig. 384, dp_m/dH vs. H: Fig. 385	
$TbRh_2Si_2$							p_m vs. H: Fig. 358	92S4
							critical field vs. T: Fig. 386, p_m vs. H at different T: Fig. 388, dp_m/dH vs. H: Fig. 387	93I1
			94				critical fields: H_{c1} and H_{c2} = 80 and 190 kOe at 4.2 K, respectively	94S2
$TbRh_2Ge_2$			Fig. 375					96G1
$TbRu_{2-x}Pd_xSi_2$			Fig. 389	Fig. 390			magnetic phase diagram: Fig. 389, p_m vs. H: Fig. 391, lattice parameters: Fig. 392	96I3
$TbRh_{2-x}Pd_xSi_2$			Fig. 389	Fig. 393			p_m vs. H: Fig. 394, magnetic phase diagram: Fig. 389, lattice parameters: Fig. 392	96I3
$TbRhSi_3$	– 8		9	Fig. 395		9.4	p_m vs. H: Fig. 396, magnetic structure: Fig. 397	96J2
$TbPd_2Si_2$			16				neutron diffraction magnetic structure, orders below T_N: Fig. 398, sine- modulated structure with k = (0, 0.4057, 0.1671): Fig. 399, p_{Tb}^{3+} = 9.0 μ_B at 1.5 K $\parallel$ to the c axis, p_{Tb} vs. T: Fig. 400	97B5

Compound	Θ [K]	T_C [K]	T_N [K]	χ	p_s [μ_B/R]	p_{eff} [μ_B/R]	Remarks	Ref.
$TbPd_2Ge_2$							neutron diffraction, magnetic structure, sine-modulated structure with magnetic moments of 8.9 μ_B at 1.5 K at Tb^{3+} || to the *a* axis, propagation vector k = (0, 0.4401, 0.1158), magnetic order is confident to clusters	97B5
$TbIr_2Si_2$			75				critical fields: H_{c1} and H_{c2} = 85 and 135 kOe at 4.2 K, respectively, p_{Tb} vs. H: Fig. 401, differential magnetization vs. H: Fig. 402, magnetic phase diagram: Fig. 403	94S2
$TbIrSi_3$.	– 17		15.41	Figs. 404, 405		9.75	σ vs. T: Fig. 406, p_m vs. H: Fig. 407, magnetic structures: Fig. 408, total magnetic moments and propagation vector vs. T: Fig. 409, tetragonal cells :Fig. 410, stability conditions: Fig. 411	98B3
$TbRh_{1.5}Ir_{0.5}Si_2$			Fig. 413				p_m vs. H and T: Fig. 414, magnetic phase diagram: Fig. 412	95I2
$Tb_2Rh_3Si_5$	– 17.9		7.8	Fig. 363		10.1	C_p vs. T: Fig. 364	97P1
$DyRu_2Si_2$			29				neutron diffraction, and Mössbauer measurements, ferrimagnetic, sine-wave modulation, $\boldsymbol{Q}$ = (2/9, 0, 0): Fig. 415, magnetic moments vs. T: Fig. 416, magnetization vs. T: Fig. 417, magnetization vs. H :Fig. 418	94B4
	59		28	Fig. 366		11	single crystal, magnetization vs. H ||c: Fig. 367, magnetostriction vs. H || c: Fig. 420	95T3
$DyPd_2Si_2$			6	Fig. 421		9.93	σ vs. H: Fig. 422, magnetic structure: Fig. 423	91B1
$DyIrSi_3$	16		7.5	Fig. 424		10.4	Mössbauer spectroscopy investigations	91S1

Compound	Θ [K]	T_C [K]	T_N [K]	χ	p_s [μ_B/R]	p_{eff} [μ_B/R]	Remarks	Ref.
$DyIr_2Si_2$			40		Fig. 425		metamagnetic transition at 1.4 T at 4.5 K, moment direction in *c* axis, the magnetic structure consists of a stacking of ferromagnetic (00l) planes with a (+ – + –) sequence along *c* axis	93S1
	22		40			11.2	metamagnetic-like behaviour	
$Dy_2Rh_3Si_5$	1.2		4.5	Fig. 363		10.6	C_p vs. T: Fig. 426	97P1
$HoRu_2Si_2$	43		18	Fig. 366		11	single crystal, magnetization vs. $H \parallel c$: Fig. 367, magnetostriction vs. $H \parallel c$: Fig. 427	
$HoRu_2Ge_2$				Figs. 51, 53			σ: Fig. 52	96S1
$HoRh_2Si_2$							p_{Ho} vs. H: Fig. 428	96I2
$HoRh_{2-x}Ru_xSi_2$				Fig. 429			phase diagram: Fig. 430, σ vs. x and H: Figs. 431-434, p_{Ho} vs. x and H: Fig. 435	96I2
$HoRh_{2-x}Pd_xSi_2$				Fig. 436			phase diagram: Fig. 430, σ vs. x and H: Figs. 437 - 439	96I2
$HoPd_2Si_2$							p_{Ho} vs. H: Fig. 428	96I2
$HoPd_2Ge_2$				Figs. 162, 164			σ: Fig. 163	96S1
$HoPt_2Ge_2$				Figs. 162, 164			σ: Fig. 164	96S1
$Ho_2Ru_3Ge_5$				Figs. 51, 53			σ: Fig. 52	96S1
$Ho_2Rh_3Si_5$	0.8		2.8	Fig. 363		10.2	C_p vs. T: Fig. 426	97P1

Compound	Θ [K]	T_C [K]	T_N [K]	χ	p_s [μ_B/R]	p_{eff} [μ_B/R]	Remarks	Ref.
$ErRu_2Si_2$			6				[100] from neutron diffraction is considered to be the magnetic easy axis, magnetization in *c* plane: Figs. 440, 441, magnetization vs. θ at several magnetic fields at 2 K: Fig. 442	98T1
	3.8		5.7			9.11	neutron diffraction, and Mössbauer measurements, at low temperature metamagnetic-like behaviour, sine- modulated magnetic structure, wavevector $\boldsymbol{Q}$ = (1/5, 0, 0), moment along *b* axis: Fig. 443, σ_m vs *T*: Fig. 444, magnetization vs. *T* and vs. *H*: Fig. 445	94B4
$ErPd_2Si_2$			<4	Fig. 421		9.66	σ vs. *H*: Fig. 422	91B1
	3.4		4.8	Figs. 446, 447	8.2	958	p_m vs. *H*: Fig. 448, magnetic structure: Figs. 449, 450	94T1
$ErOs_2Si_2$	– 3		4.7				large scattering of p_{eff} but the average close to the free-ion estimate, magnetic structure is of sine-modulated with a wavevector $\boldsymbol{Q}$ = (5/17,0,0): Fig. 451, magnetization vs. *H*: Fig. 452, magnetization vs. *T*: Fig. 453	94B4
$ErIr_2Si_2$			9.5	Fig. 454	Fig. 425		moment direction in the basal plane, magnetic structure consists of stacking of a ferromagnetic (00l) plane with (+ – + –) sequence along *c* axis	93S1
$Er_2Rh_3Si_5$	4.4		2.6	Fig. 363		9.6	C_p vs. *T*: Fig. 364	97P1
$Tm_2Rh_3Si_5$	12.3			Fig. 363		7.5		97P1
R/MM' = 0.20								
$CePd_2Al_3$	– 32.6		2.8	Figs. 455, 456		2.40	C = 0.62 cm^3 K mol^{-1}, ρ vs. *T*: Fig. 457	93G1

Compound	Θ [K]	T_C [K]	T_N [K]	χ	p_s [μ_B/R]	p_{eff} [μ_B/R]	Remarks	Ref.
$CePd_2Al_3$			Fig. 217 2.9				NMR, heavy-fermion compound	94F1
$CePd_2Al_3$			Fig. 458				T_C from electrical resistivity measurements	95H1
$CePd_2Ga_3$		Fig. 459						97B2
$CePd_2Ga_3$		Fig. 460					T_C from electrical resistivity measurements	95H1
$CePd_2(Al_{1-x}Ga_x)_3$			Fig. 461				phase diagram, T_C (Δ) and T_N: Fig. 461	96L1
$CePt_2Al_3$	– 2.92			Fig. 462 $3.88 \cdot 10^{-2}$ at 16 K		2.75	σ vs. H: Fig. 38, $\chi_0 = 1.24 \cdot 10^{-4}$ cm^3 mol^{-1} at 16 K, $C = 0.830$ cm^3 K mol^{-1}	93B2
$CePt_3Al_2$	– 4.72			Fig. 462 $2.18 \cdot 10^{-2}$ at 16 K		1.92	σ vs. H: Fig. 38, $\chi_0 = 9.73 \cdot 10^{-4}$ cm^3 mol^{-1} at 16 K, $C = 0.459$ cm^3 K mol^{-1}	93B2
$CePt_4Al$	– 5.13			Fig. 37 $2.87 \cdot 10^{-2}$ at 16 K		2.37	σ vs. H: Fig. 38, $\chi_0 = 8.05 \cdot 10^{-4}$ cm^3 mol^{-1} at 16 K, $C = 0.640$ cm^3 K mol^{-1}	93B2
$CePt_4In$	– 255			Fig. 463		2.54		90M5
$PrInPt_4$	– 6			Fig. 463		3.63		90M5
$NdInPt_4$	– 8			Fig. 463		3.78		90M5
$SmInPt_4$				Fig. 463			non Curie-Weiss behaviour	90M5
$EuInPt_4$	66	53		Fig. 464		7.56		90M5
$GdInPt_4$	16	20		Fig. 465		8.03		90M5
$TbInPt_4$	5			Fig. 466		10.13		90M5
$DyInPt_4$	4			Fig. 466		10.83		90M5

Compound	Θ [K]	T_C [K]	T_N [K]	χ	p_s [μ_B/R]	p_{eff} [μ_B/R]	Remarks	Ref.
$TmInPt_4$	0			Fig. 466		7.85		90M5
R/MM' = 0.1818								
$Sm_4Si_9Ir_{13}$						1.47	space group Pnmm	95V1
$Gd_4Si_9Ir_{13}$	0.19	4.5?		Figs. 467, 468		8.09	space group Pnmm	95V1
$Tb_4Si_9Ir_{13}$	– 7.57	4.3		Figs. 469, 470		9.83	χ_m vs. H: Fig. 471, space group Pnmm	95V1
$Dy_4Si_9Ir_{13}$	1.15	4.0				10.66	space group Pnmm	95V1
$Ho_4Si_9Ir_{13}$	1.24	1.6				10.22	space group Pnmm	95V1
$Er_4Si_9Ir_{13}$	1.40	2.2				9.64	space group Pnmm	95V1
$Yb_4Si_9Ir_{13}$	– 6.63	0.5				4.09	space group Pnmm	95V1
R/MM' = 0.176								
$Ce_3Ru_4Ge_{13}$				Fig. 194				96G2
$Ce_3Pt_{23}Ge_{11}$	0.5				2.51		σ vs. H and T: Fig. 472	98T2
$Ce_3Ir_4Sn_{13}$			Figs. 473 - 475			2.45	heavy-fermion compound, three-step phase transitions at 0.6, 2.10 and 2.18 K, the phase between 0.6 and 2.1 K is paramagnetic-like and the phase below 0.6 is antiferromagnetic-like suggested Figs. 473, 474, magnetic phase diagram Fig. 475	94T2
$Eu_3Rh_4Sn_{13}$			12			8.15	susceptibility above T_N showed Curie Weiss behaviour, ^{151}Eu and ^{119}Sn Mössbauer effect over the temperature range 4.2 K to 300 K have been investigated	94T2

Compound	Θ [K]	T_C [K]	T_N [K]	χ	p_s [μ_B/R]	p_{eff} [μ_B/R]	Remarks	Ref.
$Ho_3Ru_4Ge_{13}$				Figs. 51, 53			σ vs. H: Fig. 52	96S1
$Ho_3Os_4Ge_{13}$				Figs. 54, 56			σ vs. H: Fig. 55	96S1
$Yb_3Rh_4Sn_{13}$				Fig. 476			σ vs. H: Fig. 477	97S4
R/MM' = 0.166								
$La_2Rh_3Al_9$							ρ and S vs. T: Fig. 478	97B4
$Ce_2Rh_3Al_9$	– 12.5			Fig. 479	0.98		R/R(300K) vs. T: Fig. 480, ρ and S vs. T: Fig. 478	97B4
$Ce_2Ir_3Al_9$	– 18.9			Fig. 479	0.68		R/R(300K) vs. T: Fig. 480	97B4
$Ce_2Rh_3Al_9$	6			Fig. 481			ρ vs. T: Fig. 482, S vs. T: Fig. 483	98B2
$Ce_2Ir_3Al_9$				Fig. 481			ρ vs. T: Fig. 482, S vs. T: Fig. 483	98B2
$Ce_2Rh_3Ga_9$	– 11.7			Fig. 479	1.1		R/R(300K) vs. T: Fig. 480	98B2
$Ce_2Ir_3Ga_9$				Fig. 479			R/R(300K) vs. T: Fig. 480	97B4
$Ce_2Rh_3Ga_9$				Fig. 481			ρ vs. T: Fig. 482, S vs. T: Fig. 483	98B2
$Ce_2Ir_3Ga_9$				Fig. 481			p_{Ce} vs. H: Fig. 484, ρ vs. T: Fig. 482, S vs. T: Fig. 483	98B2
R/MM' = 0.115								
$La_3Pd_{20}Si_6$				Fig. 485			no magnetic phase transition observed	97K1
$La_xCe_{3-x}Si_6Pd_{20}$							Kondo compounds, C_m vs. T and x : Figs. 487, 488, 489, 490, S_m vs. T and x: Fig. 491	97K1
$Ce_3Pd_{20}Si_6$	– 6					2.0	at 500 Oe, σ_m vs. T: Fig. 492 at 4 kOe, σ_m vs. T: Fig. 493	97T2

Compound	Θ [K]	T_C [K]	T_N [K]	χ	p_s [μ_B/R]	p_{eff} [μ_B/R]	Remarks	Ref.
$Ce_3Pd_{20}Si_6$	– 21			Fig. 485		2.62	magnetic phase transition at T_m = 0.15 K	96N1
$Pr_3Pd_{20}Si_6$	– 1.97			Figs. 485, 494		3.50	magnetic phase transition at T_m = 0.05 K	97K1
$Nd_3Pd_{20}Si_6$	– 2.37			Fig. 485		3.55	two magnetic phase transitions at T_m = 0.68 and 2.4 K: Figs. 495, 501	97K1
$Sm_3Pd_{20}Si_6$				Fig. 485			two magnetic phase transitions at T_m = 1.5 and 4.7 K: Figs. 496, 501	97K1
$Eu_3Pd_{20}Si_6$				Fig. 485			no magnetic phase transition observed	97K1
$Gd_3Pd_{20}Si_6$	1.66			Fig. 486		8.02	two magnetic phase transitions at T_m = 3.6 and 18.2 K: Figs. 497, 501	97K1
$Tb_3Pd_{20}Si_6$	2.69			Fig. 486		9.59	two magnetic phase transitions at T_m = 4 and 10.2 K: Figs. 498, 501	97K1
$Dy_3Pd_{20}Si_6$	– 3.35			Figs. 486, 500		10.8	two magnetic phase transitions at T_m = 1.75 and 5.7 K: Figs. 500, 501	97K1
$Ho_3Pd_{20}Si_6$	– 1.83			Fig. 486		10.7	two magnetic phase transitions at T_m = 0.47 and 1.95 K: Figs. 499, 501	97K1
$Er_3Pd_{20}Si_6$	– 1.72			Figs. 486, 502		9.53	magnetic phase transition at T_m = 0.35 K	97K1
$Tm_3Pd_{20}Si_6$	1.65			Figs. 486, 503		7.39	magnetic phase transition at T_m = 1.3 K: Fig. 503	97K1
$Yb_3Pd_{20}Si_6$	– 0.335			Figs. 486, 504		3.96	magnetic phase transition at T_m = 0.77 K: Fig. 504	97K1
$Ce_3Pd_{20}Ge_6$	13			Fig. 505		1.5 1.6	at 500 Oe, σ_m vs. T: Fig. 492, at 4 kOe, σ_m vs. T: Fig. 493	96N1

Compound	Θ [K]	T_C [K]	T_N [K]	χ	p_s [μ_B/R]	p_{eff} [μ_B/R]	Remarks	Ref.
$Ce_3Ge_6Pd_{20}$			Fig. 506				single crystal, possible quadrupolar ordering of the Γ_8 quartet crystalline - field ground state of Ce ion in a Kondo-lattice compound, ρ vs. T: Fig. 507, C_p vs. T and H: Figs. 508, 509	96N1, 97K3
R/MM' < 0.1								
$Y_{7.28}Re_{12}Al_{61.38}$				Fig. 510			Pauli paramagnet,structure type P6mcm, the idealized formula $Ln_8Re_{12}Al_{60}$ has the highest Ln content, the highest Al content occurs in the formula $Ln_7Re_{12}Al_{62}$	
$Y_{7+x}Re_{12}Al_{61+y}$				Fig. 510			Pauli paramagnetic	97T3
$Gd_{7.23}Re_{12}Al_{61.70}$	– 7		5	Fig. 510		7.86		97T3
$Tb_{7+x}Re_{12}Al_{61+y}$	27			Fig. 510	49.16	9.86	metamagnetic	97T3
$Dy_{7.50}Re_{12}Al_{61.17}$	15	14		Fig. 510	44.55	10.03		97T3
$Ho_{7.32}Re_{12}Al_{61.48}$	5	10		Fig. 510	43.92	10.50		97T3
$Ho_{7+x}Re_{12}Al_{61+y}$								97T3
$Er_{7+x}Re_{12}Al_{61+y}$	5	8		Fig. 510	48.45	9.79		97T3
$Lu_{7.61+x}Re_{12}Al_{61.02}$								97T3
$YbGa_{7.75}Pd_{3.25}$				Fig. 40			space group Pm3m, for $x \leq 3$ temperature independent Pauli paramagnets	97G1
$YFe_{10.8}Re_{1.2}$		460					σ vs. T: Fig. 511, σ vs. H: Figs. 512, 513	90J1
$TbFe_{10.8}Re_{1.2}$		475					σ vs. H: Fig. 512	90J1
$HoFe_{10.8}Re_{1.2}$		448					σ vs. H: Fig. 512	90J1

References

88A1 Amato, A., Jaccard, D., Sierro, J., Lapierre, F., Haen, P., Lejay, P.: J. Magn. Magn. Mater. **76-77**(1988) 263

88B1 Bohm, A., Caspary, R., Habel, U., Pawlak, L., Zuber, A., Steglich, F.: J. Magn. Magn. Mater. **76-77** (1988) 150

88D1 Djerbi, R., Haen, P., Lapierre, F., Lehmann, P., Kappler, jr., P.: J. Magn. Magn. Mater. **76-77** (1988) 260

88D2 Djerbi, R., Haen, P., Lapierre, F., Mignot, J.-M.: J. Magn. Magn. Mater. **76-77** (1988) 265

88D3 Djerbi, R., Haen, P., Lapierre, F., Mignot, J.-M., Fert, A., Hamzic, A., Kappler, J.P.: J. Magn. Magn. Mater. **76-77** (1988) 265

88H1 Haen, P., Lapierre, F., Kappler, J.P., Lejay, P., Flouquet, J., Meyer, A.: J. Magn. Magn. Mater. **76-77** (1988) 143

88K1 Kasaya, M., Tani, T., Iga, F., Kasuya, T.: J. Magn. Magn. Mater. **76-77** (1988) 278

88L1 Lacerda, A., de Visser, A., Puech, L., Lejay, P., Haen, P.: J. Magn. Magn. Mater. **76-77** (1988) 138

88M1 Mignot, J.-M., Flouquet, J., Haen, P., Lapierre, L., Puech, L., Voiron, J.: J. Magn. Magn. Mater. **76- 77** (1988) 97

88Q1 Quezel, S., Burllet, P., Jacoud, J.L., Regnault, L.P., Rossat-Mignod, J., Vettier, C., Lejay, P., Flouquet, J.: J. Magn. Magn. Mater.: **76-77** (1988) 403

90B1 Bruls, G., Weber, D., Hampel, G., Wolf, B., Kouroudis, I., Luthi, B.: Physica B **163** (1990) 41

90C1 Celemczuk, R., Bonjour, E., Rossat-Mignod, J., Chavalier, B.: J. Magn. Magn. Mater. **90-91** (1990) 477

90F1 Fujii, H., Nagasawa, M., Kawanaka, H., Inoue, T., Takabatake, T.: Physica B **165-166** (1990) 435

90F2 Fukuhara. T., Sakamoto, I., Sato, H.: Physica B **165-166** (1990) 443

90G1 Godart, C., Gupta, L., C., Tomy, C., V., Patil, S., Nagarajan, R., Beaurepaire, E.: Physica B **163** (1990) 163

90H1 Haen, P., Voiron, J., Lapierre, F., Flouquet, J., Lejay, P.: Physica B **163** (1990) 519

90J1 Jurczyk, M.: J. Magn. Magn. Mater. **89** (1990) L5

90K1 Kohler, R., Strobel, B., Kammerer, C., Grauel, A., Gottwick, U., Goring, E., Hohr, A., Sparn, G., Geibel, C., Horn, S.: J. Magn. Magn. Mater. **90-91** (1990) 428

90K2 Kaczmarska. K., Kwapulinska, E.: J. Magn. Magn. Mater. **89** (1990) L267

90K3 Kotsanidis, P., A., Yakinthos, J., K., Gamari-Seale, E.: J. Magn. Magn. Mater. **87** (1990) 199

90M1 Malik, S.K., Adroja, D.T., Pdadalia, B.D., Vijayaraghavan, R.: Physica B **163** (1990) 89

90M3 Mignot, J.-L., Jacoud, J.-L., Regnault, L.-P., Rossat-Mignod, J., Lejay, P., Boutrouille, Ph., Hennion, B., Petitgrand, D.: Physica B **163** (1990) 611

90M5 Malik, S.K., Vijayaraghan, R., Adroja, D.T., Padalia, B.D., Edelstein, A.S.: J. Magn. Magn. Mater. **92** (1990) 80

90N1 Nagarajan, R., Sampathkumaran, E., Vijayaraghavan, R.: Physica B **163** (1990) 591

90P1 Paulsen, C., Lacerda, A., Tholence, J.L., Flouquet, J.: Physica B **165-166** (1990) 433

90P2 Paulsen, C., Lacerda, A., de Visser, A., Bakker, K., Puech, L., Tholence, J.L.: J. Magn. Magn. Mater. **90-91** (1990) 408

90R1 Regnault, L.P., Jacoud, J.L., Rossat-Mignod, J., Vettier, C., Lejay, P., Flouquet, J.: J. Magn. Magn. Mater. **90-91** (1990) 398

90S1 Sakurai, J., Yamaguchi, Y., Nishigori, S., Suzuki, T., Fujita, T.: J. Magn. Magn. Mater. **90-91** (1990) 422

90S2 Sakurai, J., Yamaguchi, Y., Mibu, K., Shinjo: J. Magn. Magn. Mater. **84** (1990) 157

90S3 Sampathkumaran, E.V., Nakazawa, Y., Ishikawa, Y., Vijayaraghavan, R.: Physica B **163** (1990) 365

90S4 Steeman, R.A., Endstra, T., Mentink, S.A.M., Friikkee, E., Menovsky, A.A., Nieuwenhuys, G.J., Mydosh, J.A.: Physica B **163** (1990) 597

90S5 Schobinger-Papamantellos, P., de Mooij, D.B., Buschow, K.H.J.: J. Less-Common Met. **163** (1990) 319

91B1 Bazela, W., Leciejewicz, J., Szytula, A., Zygmunt, A.: J. Magn. Magn. Mater. **96** (1991) 114

91G1 Gignoux, D., Morin, M., Schmitt, D.: J. Magn. Magn. Mater. **102** (1991) 33

91K1 Kasaya, M., Tani, T., Suzuki, H., Ohoyama, K., Kohugi, M.: J. Phys. Soc. Jpn. **60** (1991) 2542

91S1 Sanchez, J.P., Tomala, K., Łątka, K.: J. Magn. Magn. Mater. **99** (1991) 95

92B1 Besnus, M.J., Essaihi, A., Fischer, G., Hamdaoui, N., Meyer, A.: J. Magn. Magn. Mater. **104-107** (1992) 1387

92D1 Dakin, S., Rapson, G., Rainford, B.D.: J. Magn. Magn. Mater. **108** (1992) 117
92D2 de Visser, A., Wyder, U., Schmitt, D., Zerguine, M.: J. Magn. Magn. Mater. **108** (1992) 59
92G1 Geibel, C., Kammerer, C., Seidel, B., Bredl, C.D., Grauel, A., Steglich, F.: J. Magn. Magn. Mater. **108** (1992) 207
92H1 Haen, P., Lapierre, F., Lejay, P., Voiron, J.: J. Magn. Magn. Mater. **116** (1992) 108
92J1 Jacobs, T.H., Buschow, K.H.J., Zhou, G.F., Liu, J.P., Li, X., de Boer, F.R.: J. Magn. Magn. Mater. **104-107** (1992) 1275
92K2 Kotsanidis, P., Yakinthos, J.K., Semittelou, I., Roudaut, E.: J. Magn. Magn. Mater. **116** (1992) 95
92L1 Lapierre, F., Haen, P.: J. Magn. Magn. Mater. **108** (1992) 167
92P1 Pinto, R.P., Amado, M.M., Salgueiro Silva, M., Braga, M.E., Sousa, J.B., Chavalier, B., Etourneau, J.: J. Magn. Magn. Mater. **104-107** (1992) 1235
92R1 Roy, S.B., Coles, B.R.: J. Magn. Magn. Mater. **108** (1992) 43
92R2 Routsi, Ch.D., Yakinthos, J.K., Gamari-Seale.: J. Magn. Magn. Mater. **117** (1992) 79
92S2 Sakakibara ,T., Sekine, C., Amitsuka, H., Miyako Y.: J. Magn. Magn. Mater. **108** (1992)193
92S3 Shigeoka, T., Iwata, N., Fujii, H.: J. Magn. Magn. Mater. **104-107** (1992) 1229
92S4 Szytula, A., Radwanski, R.J., de Boer, F.R.: J. Magn. Magn. Mater. **104-107** (1992) 1237
92S5 Sakurai, J., Kawamura, R., Taniguchi, T., Nishigori, S., Ikeda, S., Goshima, H., Suzuki, T., Fujita, T.: J. Magn. Magn. Mater. **104-107** (1992) 1415
93B1 Bruck, E., Nakotte, H., Bakker, K., de Boer, F.R., de Chatel, P.F.: J. Alloys Comp. **200** (1993) 79
93B2 Blazina, Z., Westwood, S.M.: J. Alloys Comp. **201** (1993) 151
93C1 Cordier, G., Friedrich, T., Henseleit, R., Grauel, A., Tegel, U., Schank, Ch., Geibel, Ch.: J. Alloys Comp. **201** (1993) 197
93D1 Das, I., Sampathkumaran, E.V., Chari, S., Gopalakrishnan, K.V.: J. Alloys Comp. **202** (1993) L7
93G1 Ghosh, K., Ramakrishnan, S., Malik, S.K., Chandra, G.: J. Alloys Comp. **202** (1993) 211
93G2 Ghosh, K., Ramakrishnan, S., Nigan, A.K., Chandra, G.: J. Appl. Phys. **73** (1993) 6637
93I1 Ivanov. V., Vinokurowa, L., Szytula, A.: J. Alloys Comp. **201** (1993)109
93M1 Mulder, F.M., Thiel, R.C., Buschow, K.H.J.: J. Alloys Comp. **202** (1993) 29
93S1 Sanchez, J.P., Blaise, A., Ressouche. E., Malamann, B., Venturini, G., Tomala, K., Kmiec, R.: J. Magn. Magn. Mater. **128** (1993) 295
93W2 Welter, R., Venturini G., Malaman, B.: J. Alloys Comp. **202** (1993) 165
94A1 Aoki, H., Uji, S., Terashima, T., Takashita, M., Onuki, Y.: Physica B **201**(1994) 231
94A2 Adroja, D.T., Rainford, B.D.: J. Magn. Magn. Mater. **135** (1994) 333
94A3 Adroja, D.T., Rainford, B.D., Malik, S.K.: Physica B **194-196** (1994) 169
94A4 Aliev, F.G., Gorelenko, Yu.K., Pryadun, V.V., Vieira, S., Villar, R., Paredes, J.: Physica B **194-196** (1994) 171
94A5 Andre, G., Bouree, F., Bombik, A., Oles, A., Sikora, W., Kolenda, M., Szytula, A., Pacyna, A., Zygmunt, A.: Acta Phys. Pol. **85** (1994) 275
94B1 Bando, U., Takabatake, T., Tanaka, H., Iwasaki, H., Fujii, H., Malik, S.K.: Physica B **194-196** (1994) 1179
94B3 Burlet, P., Regnault, L.P., Rossat-Mignod, J., Vettier, C., Flouquet, J.: J. Magn. Magn. Mater. **129** (1994) 10
94B4 Blaise, A., Kmiec, R., Malaman, B., Ressouche, E., Sanchez, J., P., Tomala, K., Venturini, G.: J. Magn. Magn. Mater. **135** (1994) 171
94F1 Fijiwara, K, Yamanashi, Y., Kumagai, K.: Physica B **199-200** (1994) 107
94G1 Garnier, A., Gignoux, D., Schmitt, D., Shigeoka, F.Y., Zhang: J. Magn. Magn. Mater. **140-144** (1994) 897
94G2 Godart, C., Flandorfer, H., Fogl, P.: Physica B **199-200** (1994) 512
94G4 Gignoux, D., Schmitt, D.: J. Magn. Magn. Mater. **129** (1994) 53
94H1 Hu, Z., Yelon, W.B.: J. Appl. Phys. **76** (1994) 6162
94K1 Kitazawa, H., Matsushita, A., Matsumoto, T., Suzuki, T.: Physica B **199-200** (1994) 28
94S1 Salgueiro da Silva, M., Sousa, J.B., Chevalier, B., Etourneau, J.: J. Appl. Phys. **76** (1994) 6344
94S2 Szytula, A., Ivanov, V., Vinokurova, L.: Acta Phys. Pol. **85** (1994)
94S3 Schäfer, W., Jansen, E., Will, G., Kosanidis, P.A., Yakinthos, J.K., Tietze-Jaensch.: J. Alloys Comp. **209** (1994) 225
94T1 Tomala, K., Sanchez, J.P., Malaman, B., Venturini, G., Blaise, A., Kmiec, R.: J. Magn. Magn. Mater. **131** (1994) 345
94T2 Takayanagi, S., Sato, H., Fakuhara, T., Wada, N.: Physica B **199-200** (1994) 49
95A1 Andre, G., Bouree, F., Guillot, M., Kolenda, M., Oles, A., Sikora, W., Szytula, A., Zygmunt, A.: J. Magn. Magn. Mater. **140-144** (1995) 879

95B2 Besnus, M.J., Braghta, A., Haen, P., Kappler, J.P., Meyer, A.: Physica B **206-207** (1995) 295
95B3 Bazela, W., Kolenda, M., Leciejewicz, J., Stuesser, N., Szytula, A., Zygmunt, A.: J. Magn. Magn. Mater. **140-144** (1995) 881
95D1 Diehl, J., Davideit, H., Klimm, S., Tegel, U., Geibel, C., Steglich, F., Horn, S.: Physica B **206-207** (1995) 344
95D2 Das, I., Sampathkumaran, E.V., Rajarajan, A.K.: J. Alloys Comp. **218** (1995) L11
95F1 Fujiwara, K., Yamanashi, Y., Kumagai, K.: Physica B **206-207** (1995) 228
95G1 Gordon, R.A., Ijiri, Y., Spencer, C.M., DiSalvo, F.J.: J. Alloys Comp. **224** (1995) 101
95G2 Guillot, M., Szytula, A., Tomkowicz, Z., Zach, R.: J. Alloys Comp. **226** (1995) 131
95G3 Garnier, A., Gignoux, D., Iwata, N., Schmitt, D., Shigeoka, T., Zhang, F.Y.: J. Magn. Magn. Mater. **140-144** (1995) 899
95H1 Hauser, R., Bauer, E., Galatanu, A., Indinger, A., Maikus, M., Kirchmayr, H., Gignoux, D., Schmitt, D.: Physica B **206-207** (1995) 231
95I1 Ito, T., Ohkubo, K., Hirasawa, T., Takeuchi, J., Hiromitsu, I., Kurisu, M.: J. Magn. Magn. Mater. **140-144** (1995) 873
95I2 Ivanov, V., Vinokurova, L., Szytula, A.: J. Alloys Comp.**218** (1995) L19
95K1 Kawarazaki, S., Kobashi, Y., Fernandez-Baca, J.A., Murayama, S., Onuki, Y., Miyako, Y.: Physica B **206-207** (1995) 298
95K2 Kusumoto, T., Takagi, S., Suzuki, H.: Physica B **206-207** (1995) 301
95L1 Le Bihan, T., Noel, H.: J. Alloys Comp. **227** (1995) 154
95M1 Meyer, A., Besuns, M.J., Haen, P., Kappler, J.P., Mathis, G.: Physica B **206-207** (1995) 304
95M2 Mydlarz, T., Talik, E., Szade, J., Heimann, J.: J. Alloys, Comp. **219** (1995) 225
95P1 Park, J.-G., Haen, P., Lapierre, F., Lejay, P., Verniere, A., Voiron, J.: Physica B **206-207** (1995) 285
95S1 Sakakibara, T., Tayama, T., Mitamura, H., Matsuhira, K., Amitsuka, H.: Physica B **206-207** (1995) 249
95S2 Sakurai, J., Kegai, K., Kuwai, T., Isikawa, Y., Nisimura, K., Mori, K.: J. Magn. Magn. Mater. **140-144** (1995) 875
95S3 Sekine, C., Sakamoto, H., Muryayama, S., Hoshi, K., Sakakibara, T.: Physica B **206-207** (1995) 291
95S4 Schank, C., Olesch, G., Kohler, J., Tegel, U., Klinger, U., Diehl, J., Klimm, S., Sparn, G., Horn, S., Geibel, C., Steglich, F.: J. Magn. Magn. Mater. **140-144** (1995) 1237
95S5 Shigeoka, T., Iwata, N., Garnier, A., Gignoux, D., Schmitt, D., Zhang, F.Y.: J. Magn. Magn. Mater. **140-144** (1995) 901
95T1 Tautz, F.S., Julian, S.R., McMulian, G.J., Lonzarich, G.G.: Physica B **206-207** (1995) 29
95T3 Takeuchi, T., Taniguchi, T., Kudoh, D., Miyako, Y.: Physica B **206-207** (1995) 398
95U1 Uwatoko, Y., Ishii, T., Oomi, G., Malik, S.K.: Physica B **206-207** (1995) 199
95U2 Uwatoko, Y., Oomi, G., Graf, T., Thompson,J.D., Canifield, P.C., Borges, H.A., Godart, C., Gupta, L.C.: Physica B **206-207** (1995) 236
95V1 Vernier, A., Lejay, P., Bordet, P., Chenavas, J., Tholence, J.L., Boucherle, J.X., Keller, N.: J. Alloys Comp. **218** (1995) 197
96B1 Bazela, W., Zygmunt, A., Szytula, A., Ressouche, E., Leciejewicz, J., Sikora, W.: J. Alloys Comp. **243** (1996) 106
96B2 Besnus, M.J., Haen, P., Mallmann, F., Kappler, J.P., Meyer, A.: Physica B **223-224** (1996) 322
96F1 Fourgeot, F., Gravereau, P., Chavelier, B., Fournes, L., Etournes, J.: J. Alloys Comp. **238** (1996) 102
96G1 Garnier, A., Gignoux, D., Schmitt., D., Shigeoka, T.: J. Magn. Magn. Mater. **157-158** (1996) 389
96G2 Gschneidner, jr., K.A., Pecharsky, V.K.: Physica B **223-224** (1996) 131
96I1 Ijiri, Y., DiSalvo, F.J.: J. Alloys Comp. **233** (1996) 69
96I2 Ivanov, V., Jaworska, T., Vinokurova, L., Mydlarz, T., Szytula, A.: J. Alloys Comp. **234** (1996) 235
96I3 Ivanov, V., Vinokurova, L., Mydlarz, T., Szytula, A.: J. Alloys Comp. **230** (1996) L5
96J2 Jaworska-Golab, T., Guillot, M., Kolenda, M., Ressouche, E., Szytula, A.: J. Magn. Magn. Mater. **164** (1996) 371
96K1 Kochetkov, Yu.V., Nikiforov, V.N., Klestov, S.A., Morozkin, A.V.: J. Magn. Magn. Mater. **157-158** (1996) 665
96K2 Kaczorowski, D., Rogl, P., Hiebl, K.: Phys.Rev. **B 54** (1996) 9891
96K3 Kolb, R., Mielke, A., Scheidt, E.W., Stewart, G.R.: J. Alloys Comp. **239** (1996) 124
96K4 Kotsanidis, P.A., Jakinthos, J.K., Schafer, W., Gamari-Seale, Hel.: J. Alloys Comp. **235** (1996) 188
96K5 Kasaya, M., Ito, M., Ono, A., Sakai, O.: Physica B **223-224** (1996) 336

96K6 Kambe, S., Raymond, S., Regnault, L-P., Flouquet, J., Lejay, P., Haen, P.: J. Phys. Soc. Jpn. **65** (1996) 3294
96L1 Ludoph, B., Süllow, S., Becker, B., Neuwenhuys, G.J., Menovsky, A.A., Mydosh, J.A.: Physica B **223-224** (1996) 351
96M1 Malik, R., Sampathkumaran, E.V.: J. Magn. Magn. Mater. **164** (1996) L13
96M2 Marumoto, K., Takeuchi, T., Miyako, Y.: Phys.Rev. **B 54** (1996) 12194
96M3 Movshovich, R., Graf, T., Mandrus, D., Hundley, M.F., Thompson, J.D., Fisher, R.A., Phillips, N.E., Smith, J.L.: Physica B **223-224** (1996) 126
96N1 Nikiforov, V.N., Koksharov, Yu.A., Mirkovic, J., Kochetkov, Yu.V.: J. Magn. Magn. Mater. **163** (1996) 184
96O1 Oomi, G., Uwatoko, Y., Sampathkumaran, E.V., Ishikawa, M.: Physica B **223-224** (1996) 303
96P1 Patil, N.G., Ghosh, K., Ramakrishnan, S.: Physica B **223-224** (1996) 392
96R1 Ramakrishnan, S., Ghosh, K.: Physica B **223-224** (1996) 154
96S1 Sologub, O., Hiebl, K., Rogl, P., Noel, H.: J. Alloys Comp. **245** (1996) L13
96S2 Szytula, A., Kolenda, M., Leciejewicz, J., Stuesser, N.: J. Magn. Magn. Mater. **164** (1996) 377
96T1 Takeuchi, T., Miyako, Y.: J. Phys Soc. Jpn. **65** (1996) 3242
96W1 Wada, H., Mitsuda, A., Shiga, M.: J. Phys. Soc. Jpn. **65** (1996) 3471
97A1 Adroja, D.T., Rainford, B.D., Houshiar, M.: J. Alloys Comp. **268** (1997) 1
97B2 Burghardt, T., Hallmann, E., Eichler, A.: Physica B **230-232** (1997) 214
97B3 Blanco, J.A., Garnier, A., Gignoux, D., Schmitt, D.: J. Alloys Comp. **275-277** (1997) 565
97B4 Buschinger, B., Geibel, C., Weiden, M., Dietrich, C., Cordier, G., Olesch, G., Kohler, J.: J. Alloys Comp. **260** (1997) 44
97B5 Bazela, W., Baran, S., Leciejewicz, J., Szytula, A., Ding, Y.: J. Cond. Matter **9** (1997) 2267
97C1 Chevalier, B., Fooyrgeot, F., Laffargue, D., Etourneau, J., Bouree, F., Roisnel, T.: Physica B **230-232** (1997) 195
97G1 Grin,Yu.N., Hiebl, K., Rogl, P., Godart, C., Alleno, E.: J. Alloys Comp. **252** (1997) 88
97G2 Grosche, F.M., Julian, S.R., Mathur, N.D., Carter, F.V., Lonzarich, G.G.: Physica B **237-238** (1997) 197
97K1 Kitagawa, J., Takeda, N., Ishikawa, W.: J. Alloys Comp. **256** (1997) 48
97K2 Kitazawa, H., Nimori, S., Tang, J., Iga, F., Donni, A., Matsumoto, T., Kido, G.: Physica B **237-238** (1997) 212
97K3 Kitakawa, J., Takeda, N., Ishikawa, M., Ishiguro, A., Komatsubara, T.: Physica B **230-232** (1997) 139
97K4 Katoh, K., Tababatake, T., Minami, A., Oguro, I., Sawa, H.: J Alloys Comp. **261** (1997) 32
97L1 Lapierre, F., Mallmann, F., Holtmeier, S., Kambe, S., Haen, P.: Physica B **230-232** (1997) 120
97M1 Malik, R., Sampathkumaran, E.V., Paulose, P.L.: Physica B **230-232** (1997) 169
97P1 Patil, N.G., Ramakrishnan, S.: Physica B **237-238** (1997) 597
97S4 Sato, H., Aoki, Y., Kobayashi, Y., Sato, H.R., Nishigaki, T., Sugswara, H., Hedo, M., Inada, Y., Onuki, Y.: Physica B **230-232** (1997) 402
97S5 Shigeoka ,T., Nishi, M., Kakurai, K.: Physica B **237-238** (1997) 572
97T1 Tung, L.D., Franse, J.J.M., Buschow, K.H.J., Brommer, P.E., Thuy, N.P.: J. Alloys Comp. **260** (1997) 35
97T2 Takeda, N., Kitagawa, J., Ishikawa, M.: Physica B **230-232** (1997) 145
97T3 Thiede, V.M.T., Gerdes, M.H., Rodewald, U.Ch., Jeitschko, W.: J. Alloys Comp. **261** (1997) 54
97T4 Tang, J., Kitazawa, H., Matsushita, A., Matsumoto, T.: Physica B **230-232** (1997) 208
97T5 Trovvarelli, O., Gomez-Berisso, M., Pedrazzini, P., Bosse, D., Geibel, C., Sereni, J.G., Steglich, F.: J. Alloys Comp. **275-277** (1997) 569
98B2 Buschinger, B., Trovarrelli, O., Weiden, M., Geibel, C., Steglich, F.: J. Alloys Comp. **275-277** (1998) 633
98B3 Bazela, W., Stusser, N., Szytula, A., Zygmunt, A.: J. Alloys Comp. **275-277** (1998) 578
98C2 Chavalier, B., Fourgeot, F., Laffargue, D., Pottgen, R., Etourneau, J.: J. Alloys Comp. **275-277** (1998) 537
98H1 Hideki Abe, Hideaki Kitazawa, Hiroyuki Suzuki, Giyuu Kido, Takehiko Matsumoto.: J. Magn. Magn. Mater. **177-181** (1998) 479
98I1 Ito, T., Nishigori, S., Hiromitsu, I., Kurisu, M.: J. Magn. Magn. Mater. **177-181** (1998) 1079
98K1 Kawae, T., Sakita, H., Hitaka, M., Takeda, K., Sigeoka, T., Iwata, N.: J. Magn. Magn. Mater. **177-181** (1998) 795
98K2 Kuwai, T., Takagi, H., Ito, H., Isikawa, Y., Sakurai, J., Nishimura, K., Paulsen, C.C.: J. Magn. Magn. Mater. **177-181** (1998) 399
98L1 Laffarggue, D., Roisnel, T., Chevalier, B., Bouree, F.: J. Alloys Comp. **262-263** (1998) 219

98M1 Mulder, F.M., Thiel, R.C., Tung, F.D., Franse, J.J.M., Buschow, K.H.J.: J. Alloys Comp. **264** (1998) 43
98M2 Marumoto, K., Takayama, F., Miyako, Y.: J. Magn. Magn. Mater. **177-181** (1998) 353
98N1 Nishigori, S., Hirooka, Y., Ito, T.: J. Magn. Magn. Mater. **177-181** (1998) 137
98S1 Sekine, C., Tayama, T., Sakakibara, T., Murayama, S., Shirotani, I., Onuki, Y.: J. Magn. Magn. Mater. **177-181** (1998) 411
98T1 Takeuchi, T., Kohyama, J.M., Kawarazaki, S., Sato, M., Miyako, Y.: **177-181** (1998) 1081
98T2 Troc, R., Kaczorowski, D., Cichorek, T., Andraka, B., Pietri, R., Seropegin, Yu.D., Gribanov, A.V.: J. Alloys Comp. **262-263** (1998) 211
98T3 Taniguchi, T., Tabata, Y., Tanabe, H., Miyako, Y.: J. Magn. Magn. Mater. **177-181** (1998) 419

2.5.3 Figures

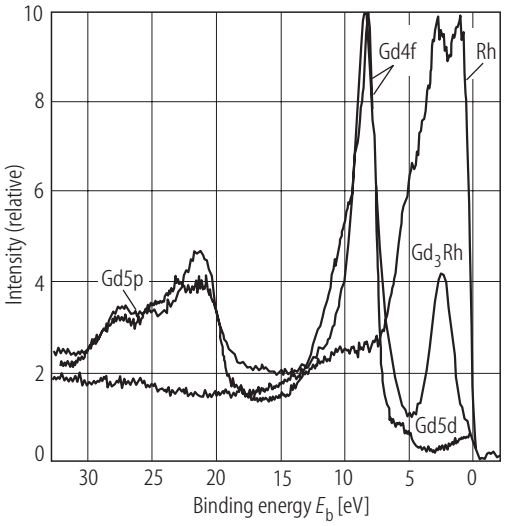

Fig. 1. Gd_3Rh. XPS valence band of single crystal (thicker line) and pure Rh and Gd [95T5].

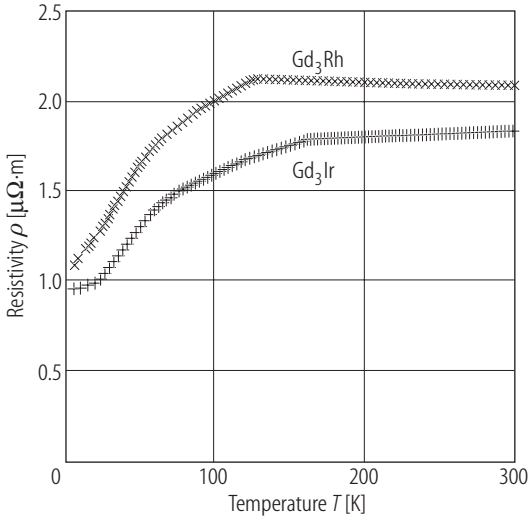

Fig. 2. Gd_3Rh, Gd_3Ir. Temperature dependence of ρ [95T5].

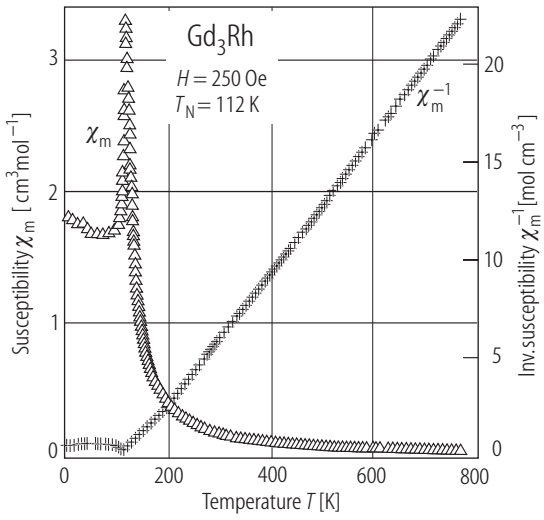

Fig. 3. Gd_3Rh. Temperature dependence of χ_m and χ_m^{-1} at H = 250 Oe [95T2].

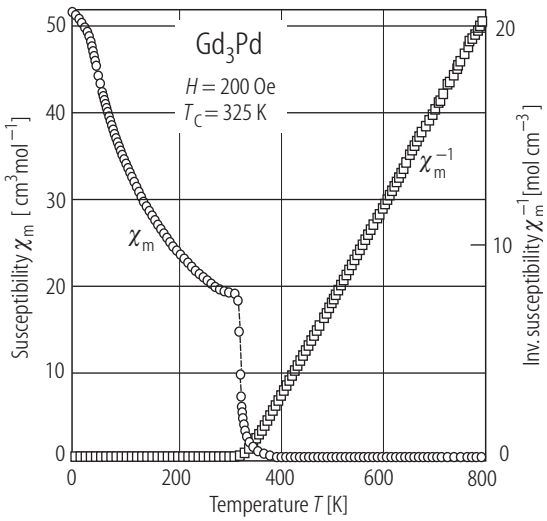

Fig. 4. Gd_3Pd. Temperature dependence of χ_m and χ_m^{-1} at 200 Oe [95T2].

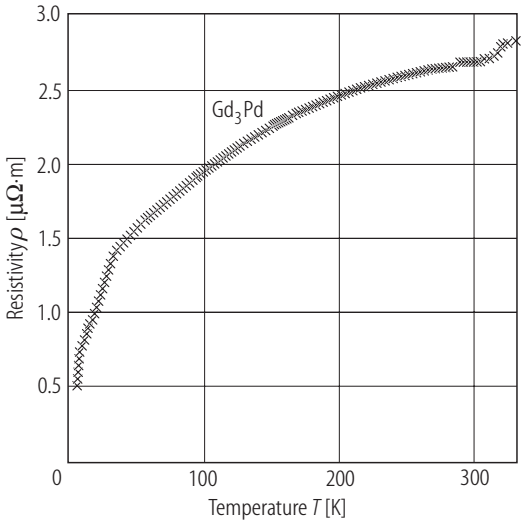

Fig. 5. Gd_3Pd. Temperature dependence of ρ [95T2].

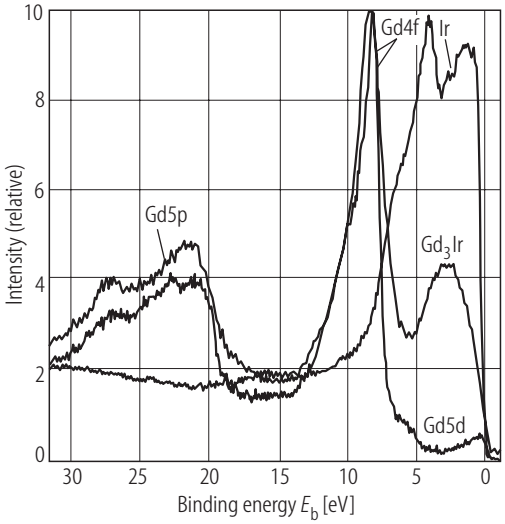

Fig. 6. Gd_3Ir. XPS valence band of single crystal (thicker line) and pure Ir and Gd [95T5].

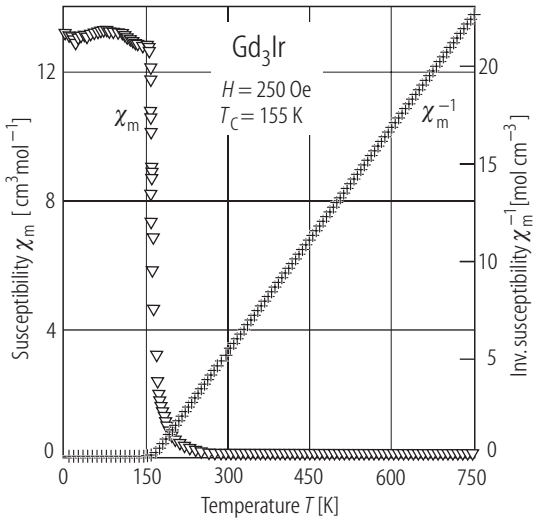

Fig. 7. Gd_3Ir. Temperature dependence of χ_m and χ_m^{-1} at 250 Oe [95T2].

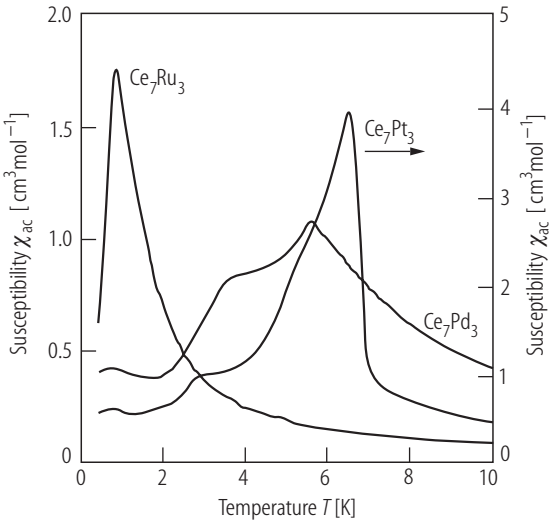

Fig. 8. Ce_7Ru_3,, Ce_7Pd_3, Ce_7Pt_3. Low temperature dependence of χ_{ac} for antiferromagnets, except for Ce_7Ru_3 [95T4].

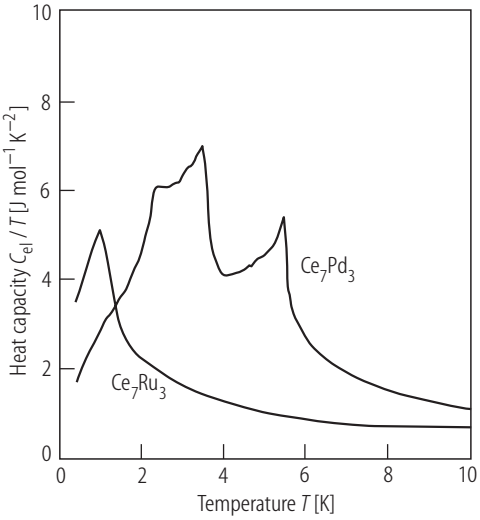

Fig. 9. Ce_7Ru_3, Ce_7Pd_3. Electronic contribution in a C_{el}/T vs. T plot. $C_{el}(T) = C_p(T)C_{ph}(T)$ [95T4].

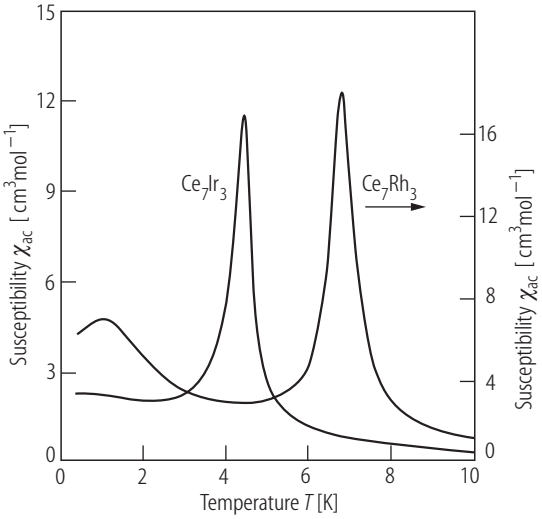

Fig. 10. Ce_7Rh_3, Ce_7Ir_3. Low temperature dependence of χ_{ac} for ferromagnets [95T4].

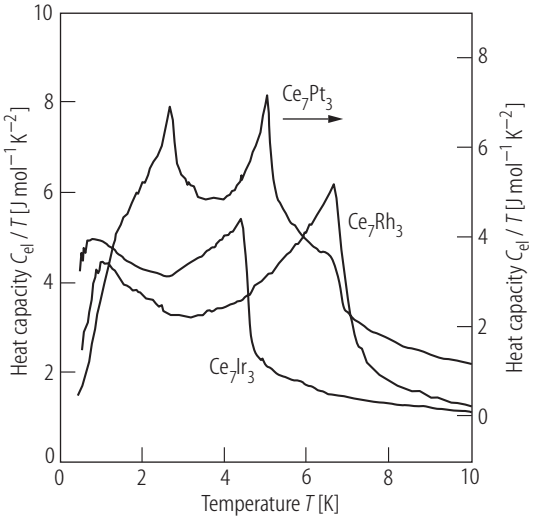

Fig. 11. Ce_7Rh_3, Ce_7Ir_3, Ce_7Pt_3. Electronic contribution in a C_{el}/T vs. T plot (see Fig. 9) [95T4].

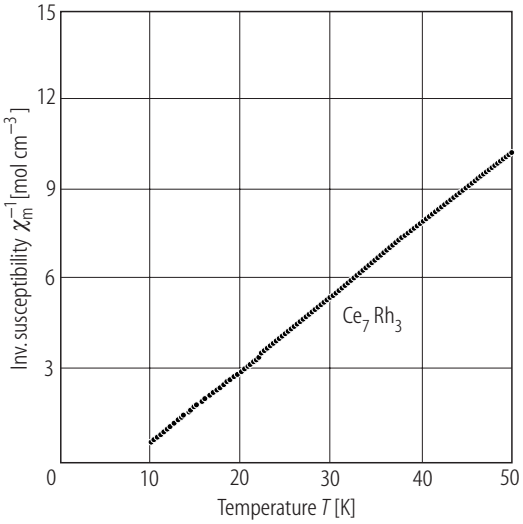

Fig. 12. Ce_7Rh_3. Temperature dependence of χ_m^{-1} [92S1].

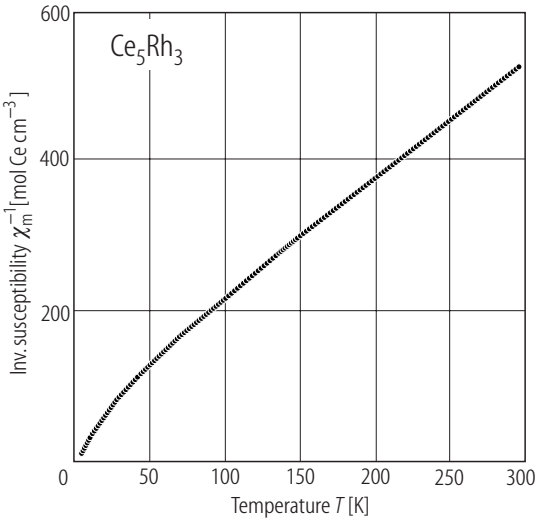

Fig. 13. Ce_5Rh_3. Temperature dependence of χ_m^{-1} [92K1].

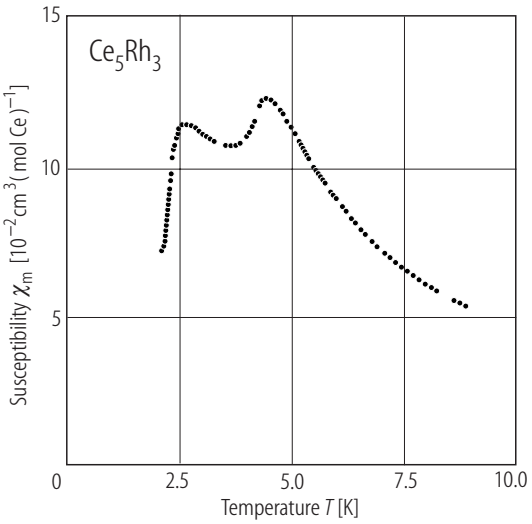

Fig. 14. Ce_5Rh_3. Low temperature dependence of χ_m [92K1].

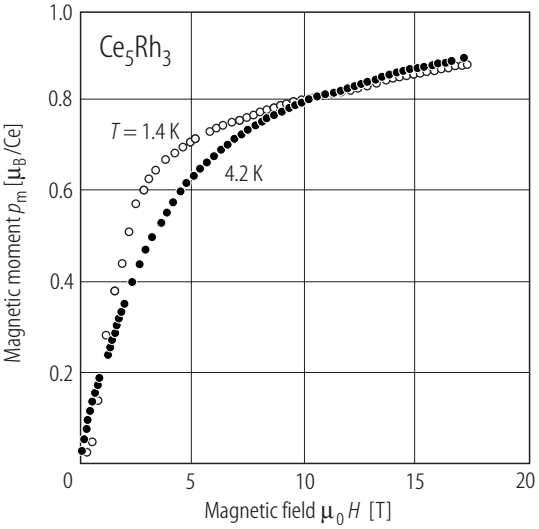

Fig. 15. Ce_5Rh_3. Magnetic field dependence of p_m at 1.4 and 4.2 K [92K1].

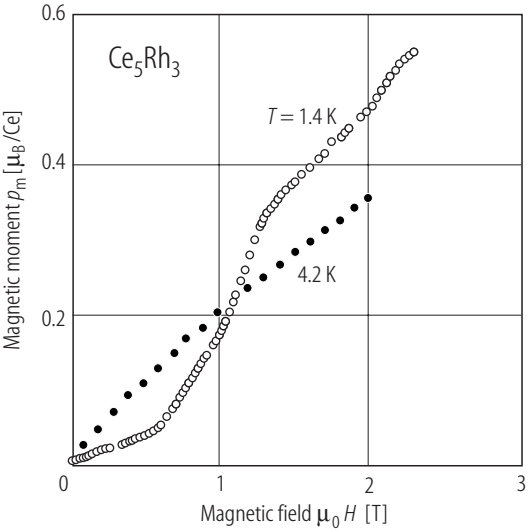

Fig. 16. Ce_5Rh_3. Low magnetic field dependence of p_m at 1.4 and 4.2 K [92K1].

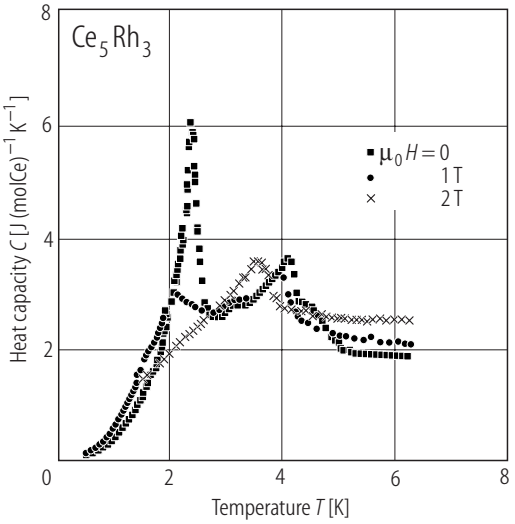

Fig. 17. Ce_5Rh_3. Low temperature specific heat for 0, 1 and 2 T [92K1].

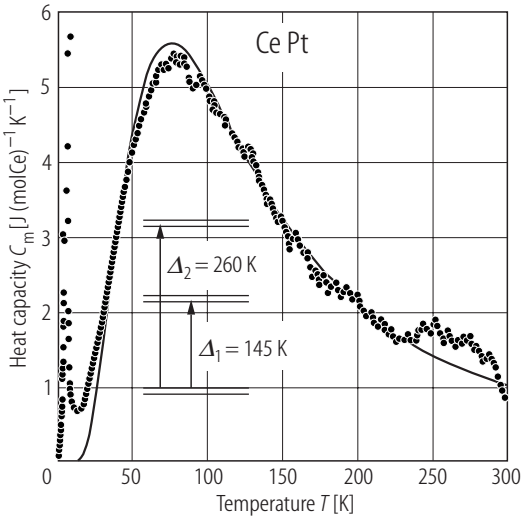

Fig. 18. CePt. Magnetic contribution to the specific heat. Solid line-theoretical calculation with Δ_1 = 145 K and Δ_2 = 260 K [95B1].

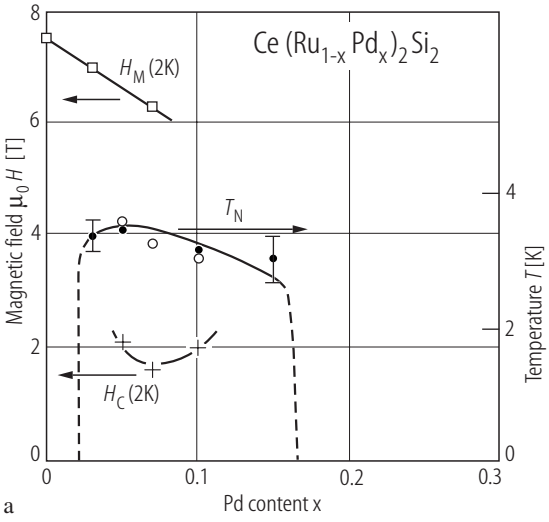

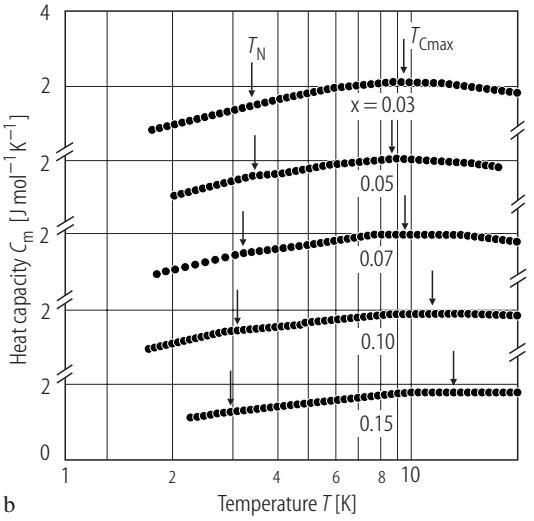

Fig. 19. $Ce(Ru_{1-x}Pd_x)_2Si_2$. Phase diagram. T_N is defined by the kink in C_m and the maximum in $\partial\chi/\partial T$. Two critical fields H_C and H_M, defined by the maximum in $\partial M/\partial H$ at 2 K, are shown [95S3].

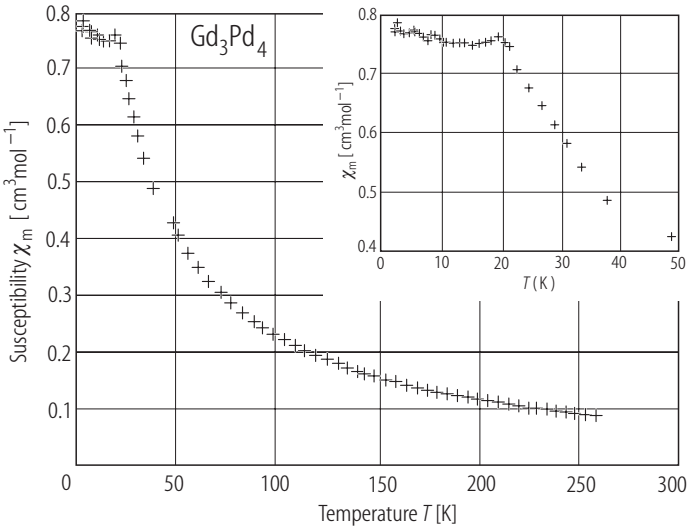

Fig. 20. Gd_3Pd_4. Temperature dependence of χ_m at low and high temperature [92T1].

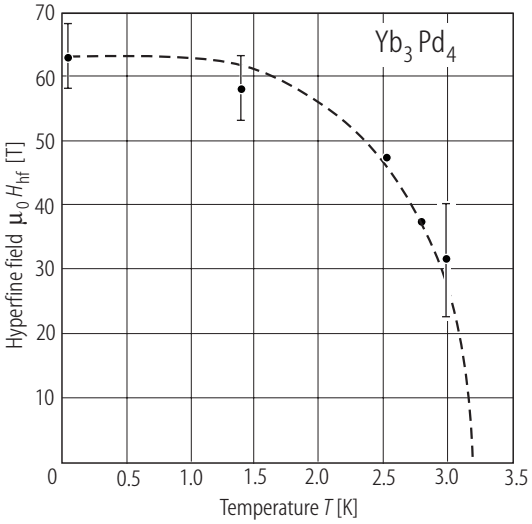

Fig. 21. Yb_3Pd_4. Temperature dependence of hyperfine field as measured by ^{170}Yb Mössbauer spectroscopy. Dashed line: mean-field S = ½ law with T_N = 3.2 K [94B2].

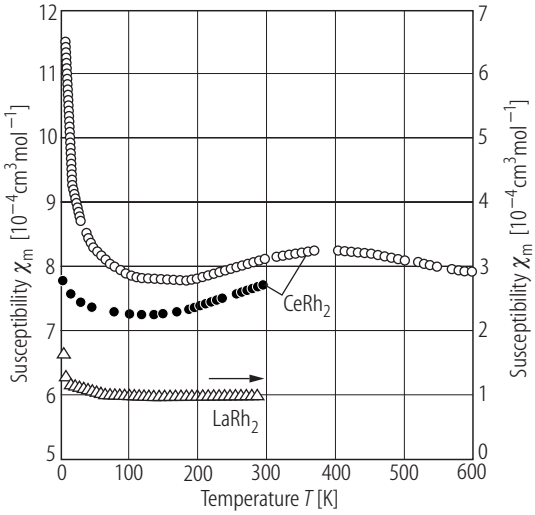

Fig. 22. $LaRh_2$, $CeRh_2$. Temperature dependence of χ_m [95O1]. Open circles: [Barberis].

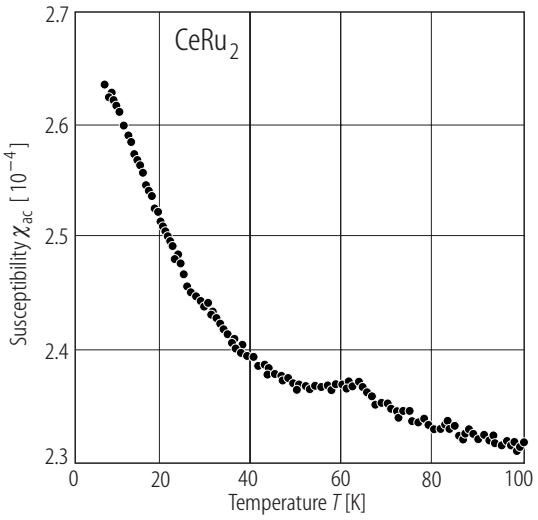

Fig. 23. $CeRu_2$. Temperature dependence of χ_{ac} [96H1].

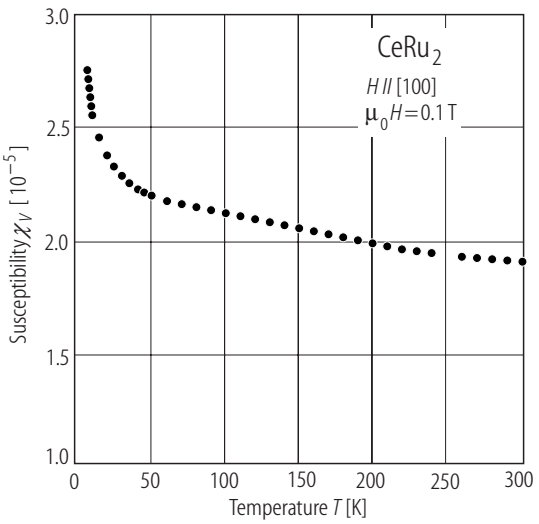

Fig. 24. $CeRu_2$. Temperature dependence of χ_V . $H \parallel$ [100] and $\mu_0 H = 0.1$ T [97S2].

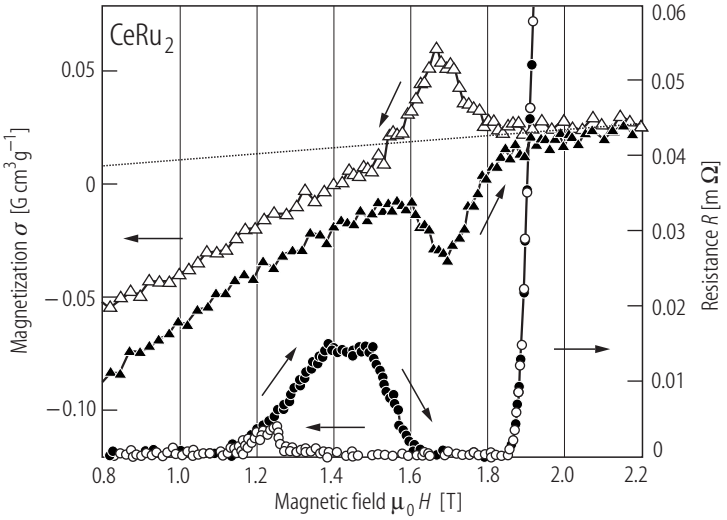

Fig. 25. $CeRu_2$. Magnetic field dependence of bulk σ and resistance R where J = 13 A cm^{-2} at 4.5 K. The dashed line is a linear fit to the reversible normal state paramagnetic magnetization with extrapolation to zero [97D1].

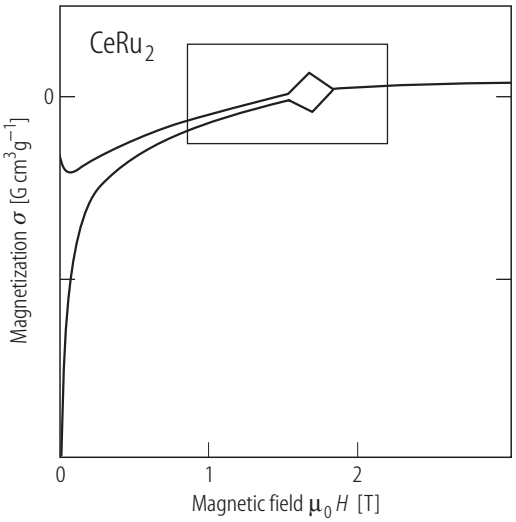

Fig. 26. $CeRu_2$. Magnetic field dependence of σ with anomaly indicated [97D1].

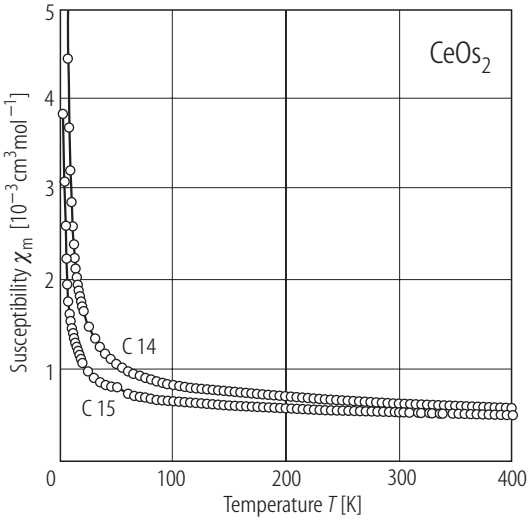

Fig. 27. $CeOs_2$. Temperature dependence of χ_m for C14 and C15 phases, respectively [97S1].

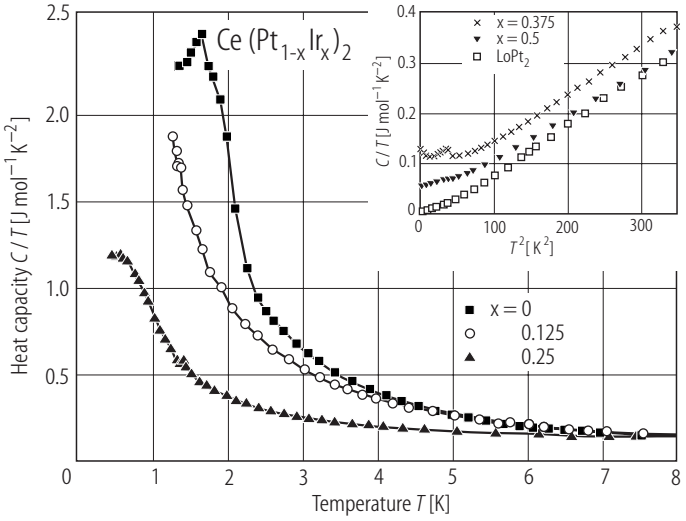

Fig. 28. $Ce(Pt_{1-x}Ir_x)_2$. Temperature dependence of C/T for different x [97B1].

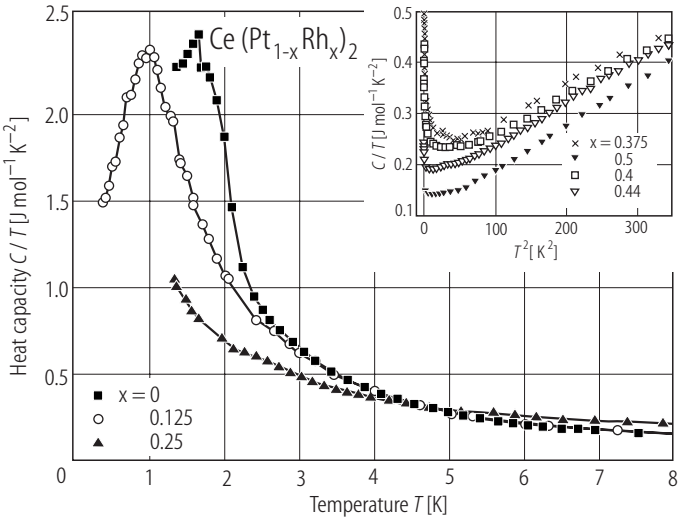

Fig. 29. $Ce(Pt_{1-x}Rh_x)_2$. Temperature dependence of C/T for different x [97B1].

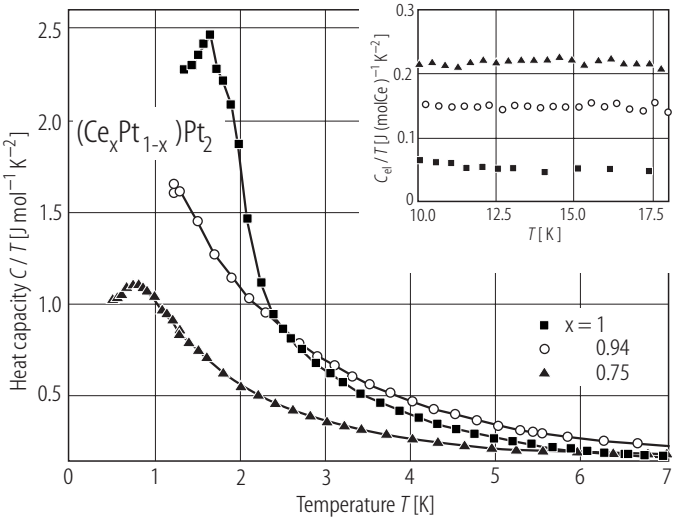

Fig. 30. $(Ce_xPt_{1-x})Pt_2$. Temperature dependence of C/T for different x [97B1].

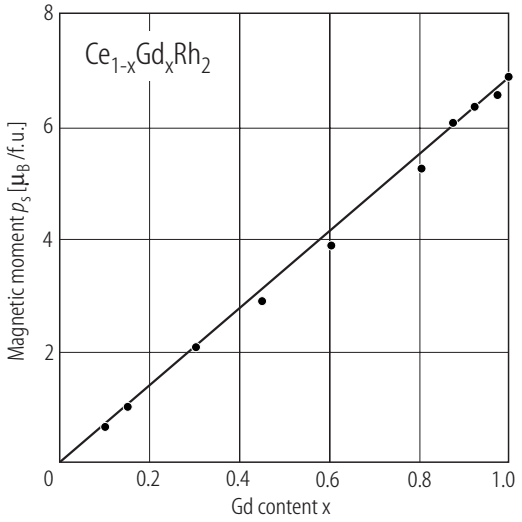

Fig. 31. $Ce_{1-x}Gd_xRh_2$. Concentration dependence of p_s [90T1].

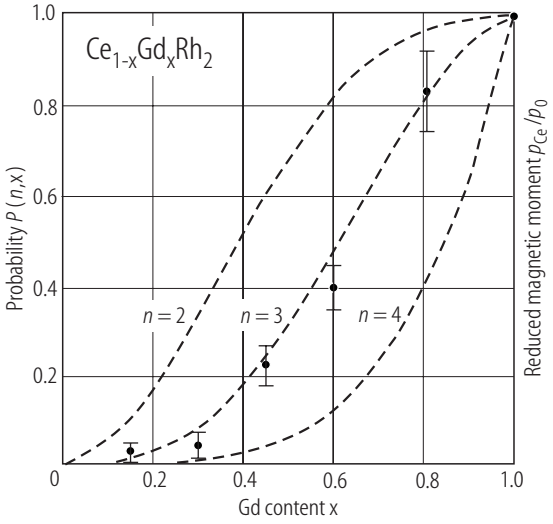

Fig. 32. $Ce_{1-x}Gd_xRh_2$. Concentration dependence of the mean reduced moment for Ce, $\langle p \rangle = p_{Ce}/p_0$ (p_0 = 2.14 μ_B for Ce^{+3}) and the probability $P(n,x)$ of finding n nearest neighbour Gd atoms to a given Ce site [90T1].

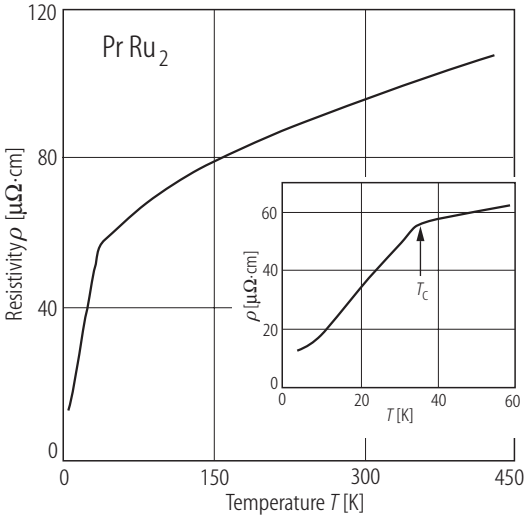

Fig. 33. $PrRu_2$. Temperature dependence of ρ. Inset: low-temperature region [90D1].

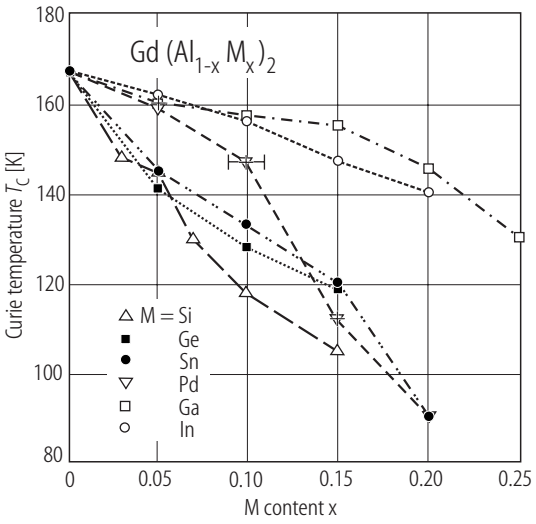

Fig. 34. $Gd(Al_{1-x}M_x)_2$. Curie temperature vs. concentration for M = Si, Ge, Sn, Pd, Ga, In from electrical resistivity [94C1].

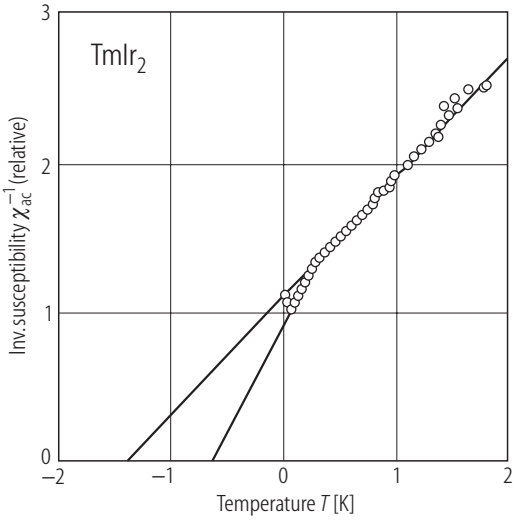

Fig. 35. $TmIr_2$. Temperature dependence of χ_{ac}^{-1} in arbitrary units [85W1].

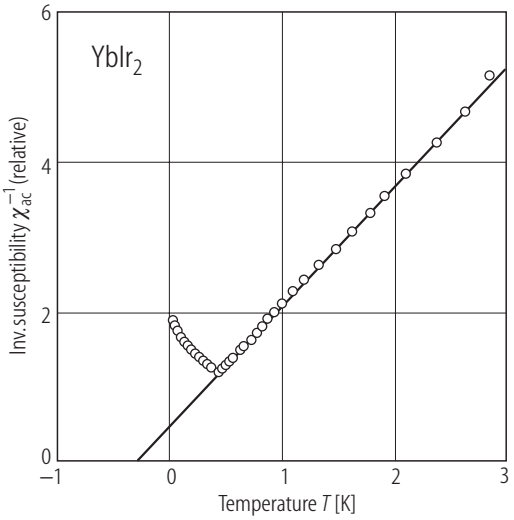

Fig. 36. $YbIr_2$. Temperature dependence of χ_{ac}^{-1} in arbitrary units [85W1].

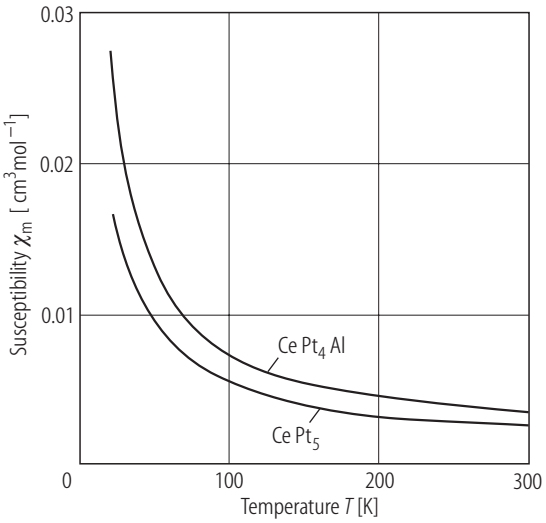

Fig. 37. $CePt_4Al$,$CePt_5$. Temperature dependence of χ_m [93B2].

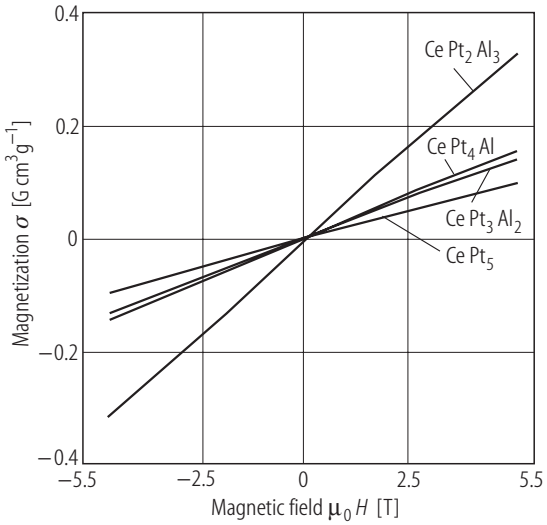

Fig. 38. $CePt_5$, $CePt_4Al$, $CePt_3Al_2$, $CePt_2Al_3$. Magnetic field dependence of σ at 16 K [93B2].

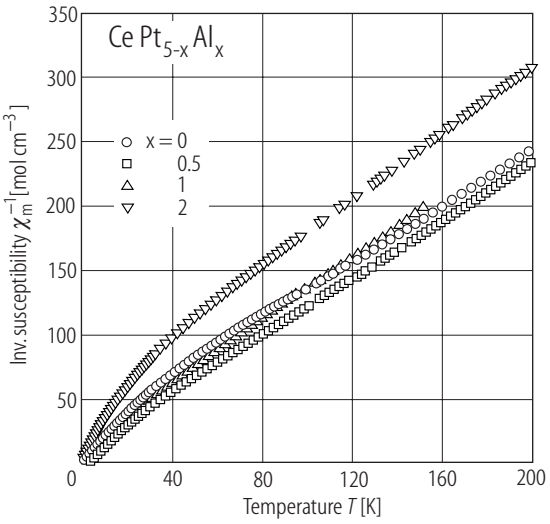

Fig. 39. $CePt_{5-x}Al_x$ Temperature dependence of χ_m^{-1} at various x [97S3].

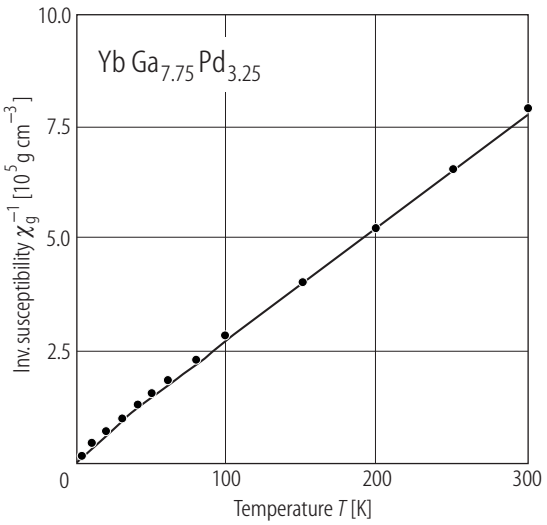

Fig. 40. $YbGa_{7.75}Pd_{3.25}$. Temperature dependence of χ_g^{-1} [97G1].

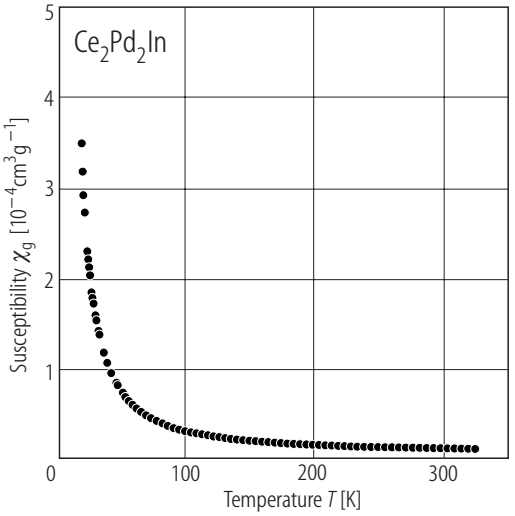

Fig. 41. Ce_2Pd_2In. Temperature dependence of χ_g [95G1].

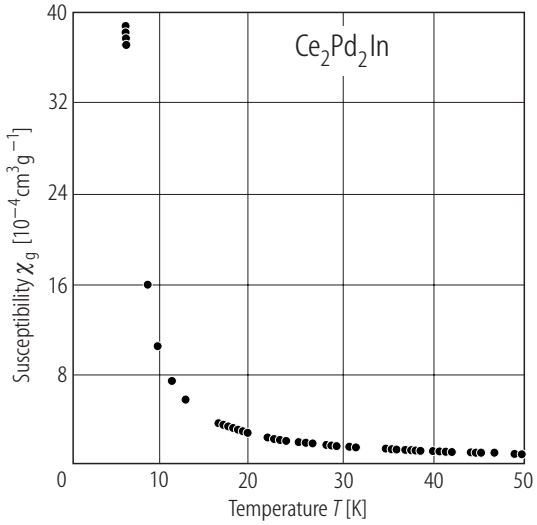

Fig. 42. Ce_2Pd_2In. Low temperature dependence of χ_g [95G1].

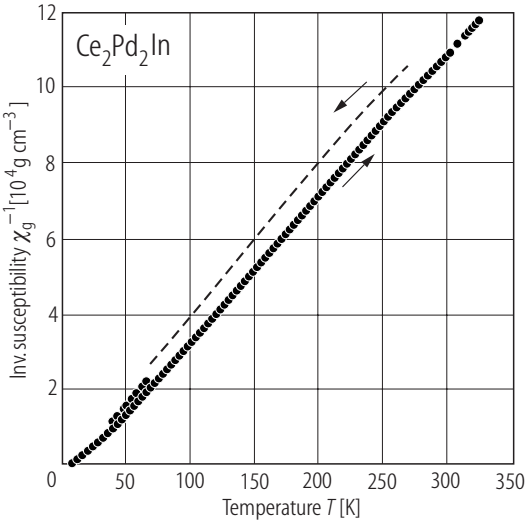

Fig. 43. Ce_2Pd_2In. Temperature dependence of χ_g^{-1} [95G1].

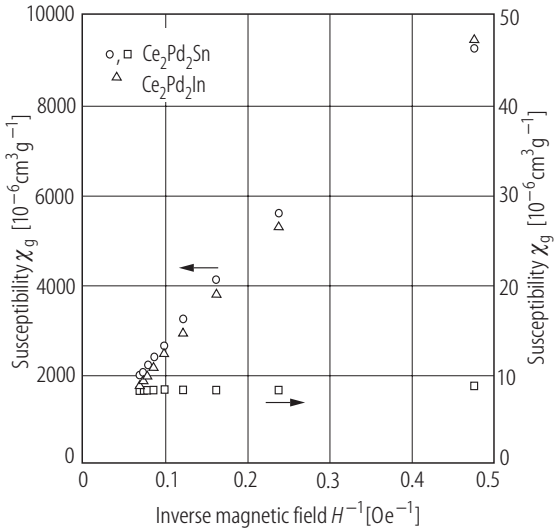

Fig. 44. Ce_2Pd_2In, Ce_2Pd_2Sn. Magnetic field dependence of χ_g at 4.2 K and for Ce_2Pd_2Sn also at 308 K [95G1].

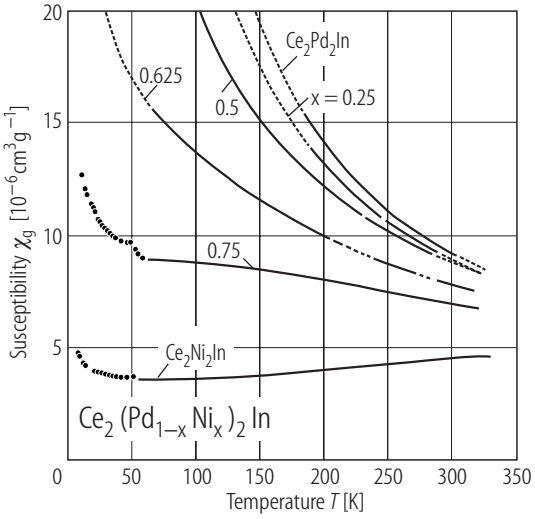

Fig. 45. $Ce_2(Pd_{1-x}Ni_x)_2In$. Temperature dependence of χ_g for various concentrations [96I1].

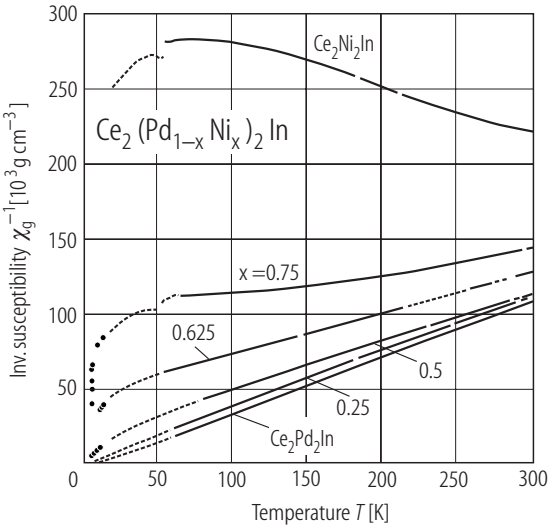

Fig. 46. $Ce_2(Pd_{1-x}Ni_x)_2In$. Temperature dependence of χ_g^{-1} for various concentrations [96I1].

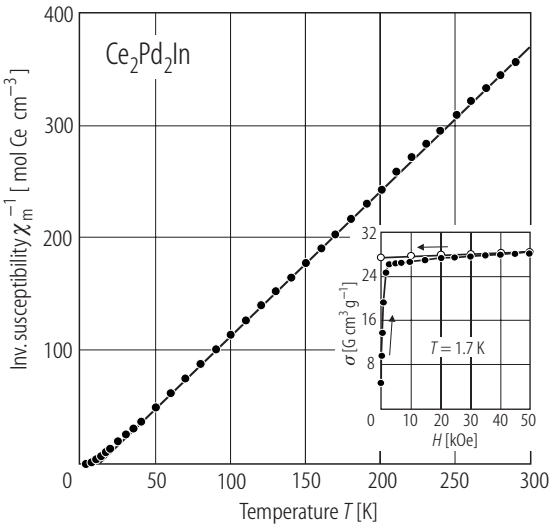

Fig. 47. Ce_2Pd_2In. Temperature dependence of χ_m^{-1}. Inset: magnetic field dependence of σ at 1.7 K [96K2].

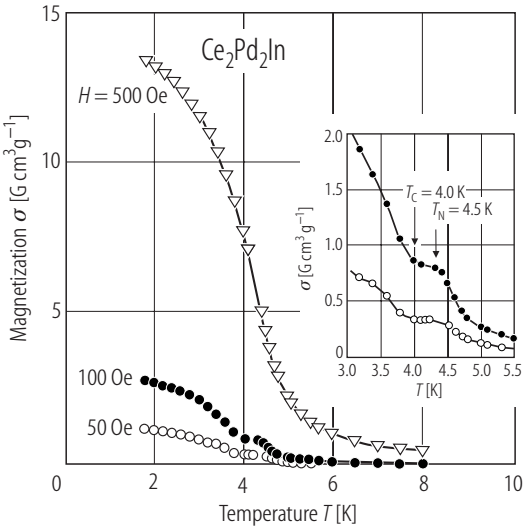

Fig. 48. Ce_2Pd_2In. Temperature dependence of σ at different H. Inset: σ in the vicinity of the magnetic phase transitions [96K2].

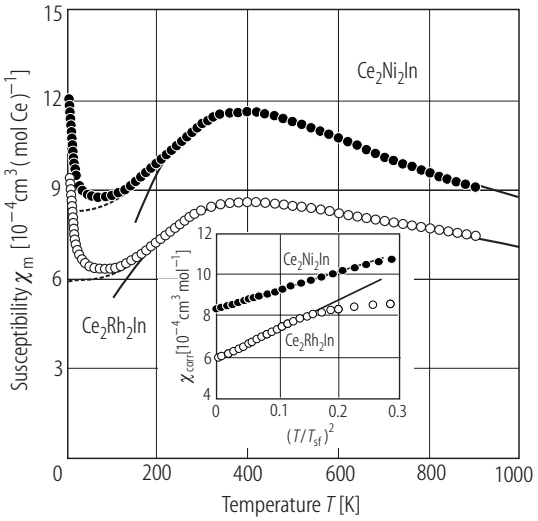

Fig. 49. Ce_2Ni_2In, Ce_2Rh_2In. Temperature dependence of χ_m. Inset: corrected susceptibility [96K2].

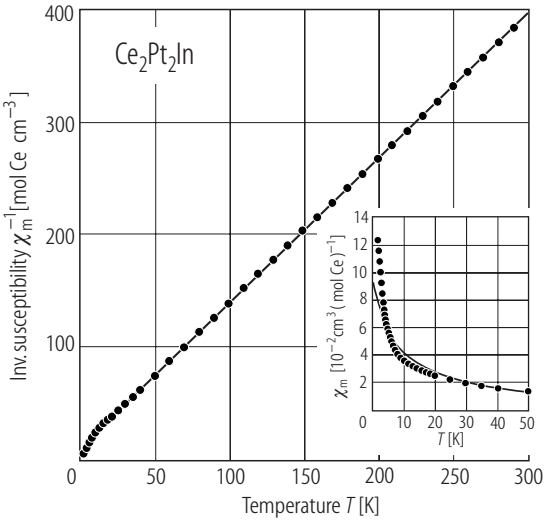

Fig. 50. Ce_2Pt_2In. Temperature dependence of χ_m and χ_m^{-1} [96K2].

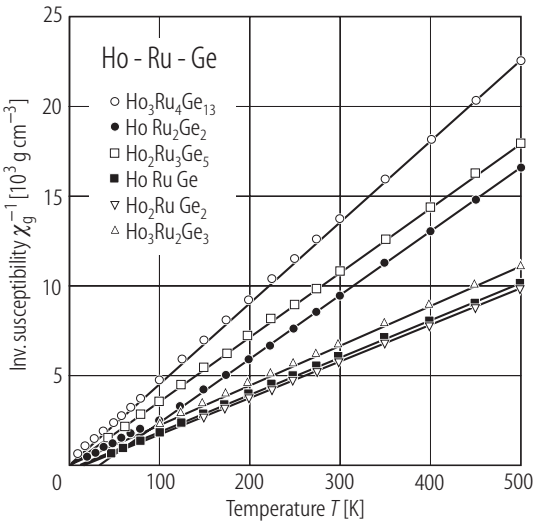

Fig. 51. $Ho_3Ru_4Ge_{13}$, $HoRu_2Ge_2$, $Ho_2Ru_3Ge_5$, HoRuGe, Ho_2RuGe_2, $Ho_3Ru_2Ge_3$. Temperature dependence of χ_g^{-1} [96S1].

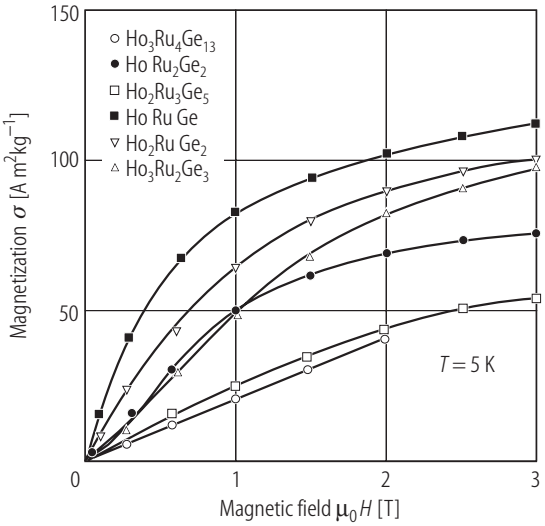

Fig. 52. $Ho_3Ru_4Ge_{13}$, $HoRu_2Ge_2$, $Ho_2Ru_3Ge_5$, HoRuGe, Ho_2RuGe_2, $Ho_3Ru_2Ge_3$. Magnetization vs. external field at $T = 5$ K [96S1].

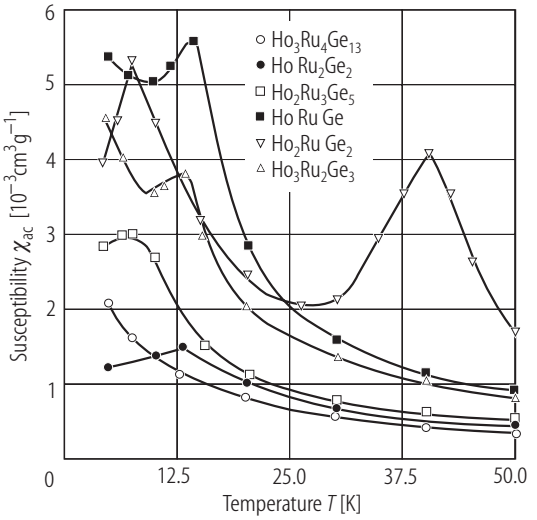

Fig. 53. $Ho_3Ru_4Ge_{13}$, $HoRu_2Ge_2$, $Ho_2Ru_3Ge_5$, HoRuGe, Ho_2RuGe_2, $Ho_3Ru_2Ge_3$. Temperature dependence of χ_{ac} [96S1].

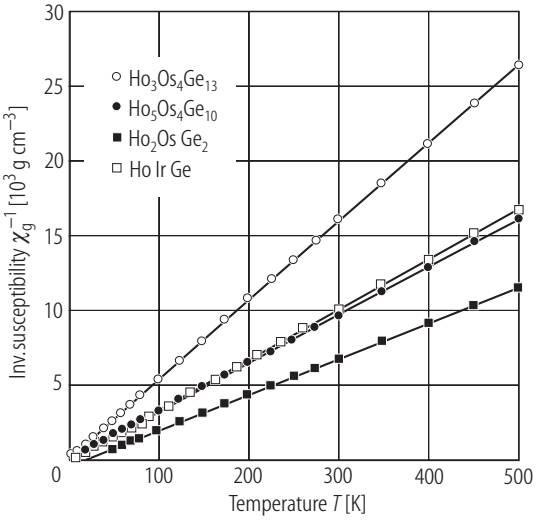

Fig. 54. $Ho_3Os_4Ge_{13}$, $Ho_5Os_4Ge_{10}$, Ho_2OsGe_2, HoIrGe. Temperature dependence of χ^{-1}_{ac}. Solid lines are calculated [96S1].

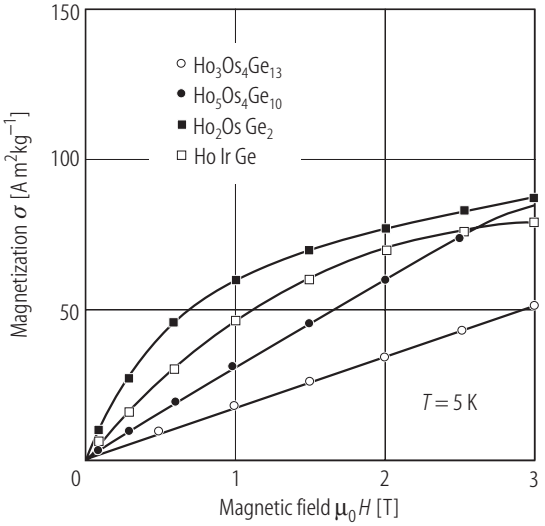

Fig. 55. $Ho_3Os_4Ge_{13}$, $Ho_5Os_4Ge_{10}$, Ho_2OsGe_2, HoIrGe. Magnetic field dependence of σ at 5 K [96S1].

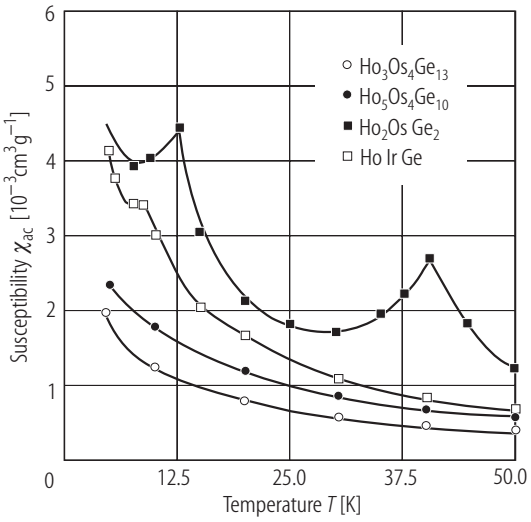

Fig. 56. $Ho_3Os_4Ge_{13}$, $Ho_5Os_4Ge_{10}$, Ho_2OsGe_2, HoIrGe. Temperature dependence of χ_{ac} [96S1].

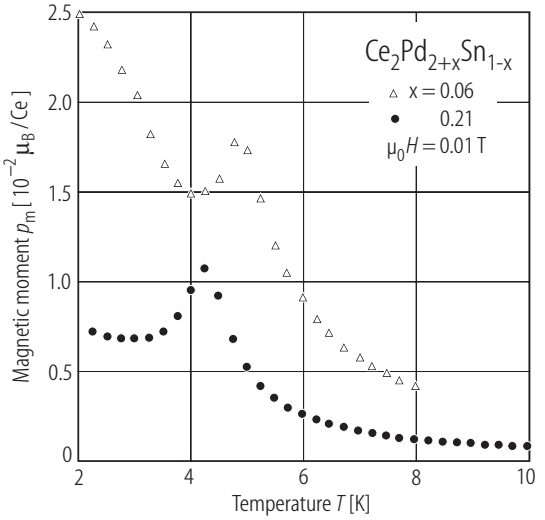

Fig. 57. $Ce_2Pd_{2+x}Sn_{1-x}$. Temperature dependence of p_m at 0.01 T for x = 0.06 and 0.21 [97C1].

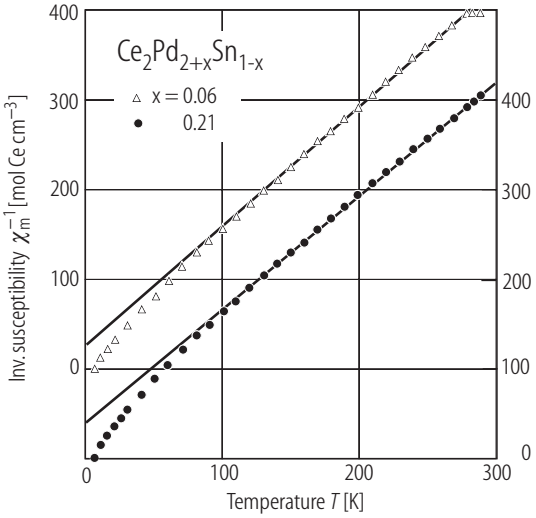

Fig. 58. $Ce_2Pd_{2+x}Sn_{1-x}$. Temperature dependence of χ_m^{-1} (for clarity the origin is shifted vertically). Solid lines are calculated [96F1].

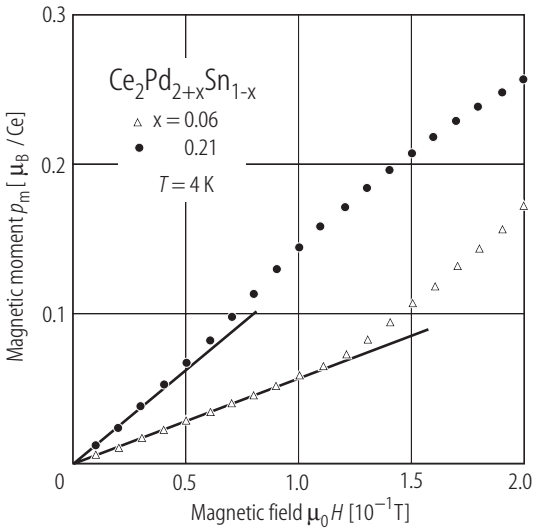

Fig. 60. $Ce_2Pd_{2+x}Sn_{1-x}$. Magnetic field dependence of p_m at 4 K [96F1].

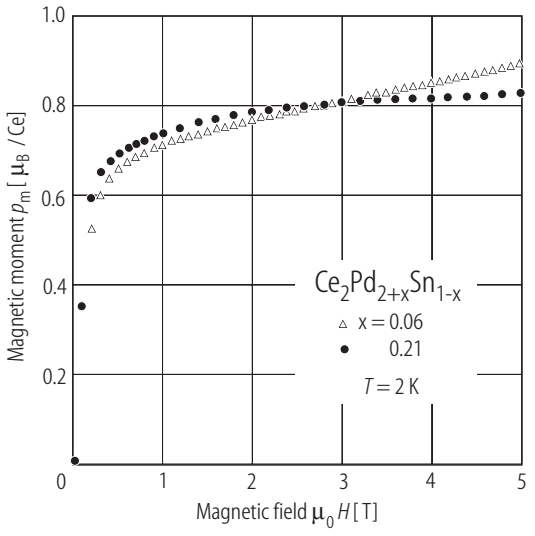

Fig. 61. $Ce_2Pd_{2+x}Sn_{1-x}$. Magnetic field dependence of p_m at 2 K [96F1].

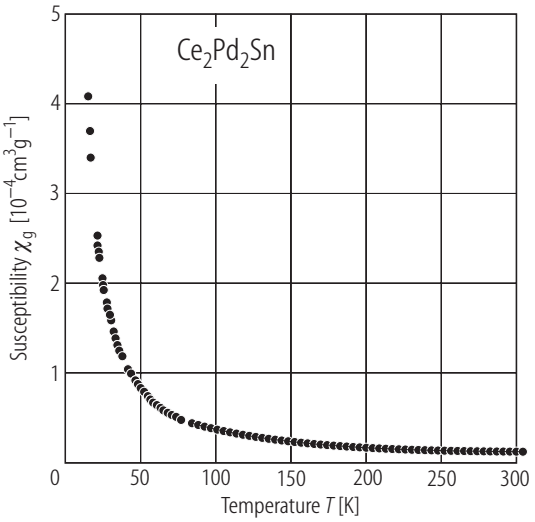

Fig. 62. Ce_2Pd_2Sn. Temperature dependence of χ_g [95G1].

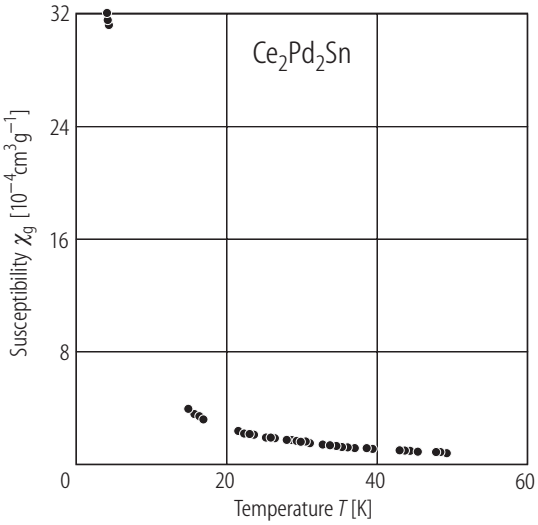

Fig. 63. Ce_2Pd_2Sn. Low temperature dependence of χ_g [95G1].

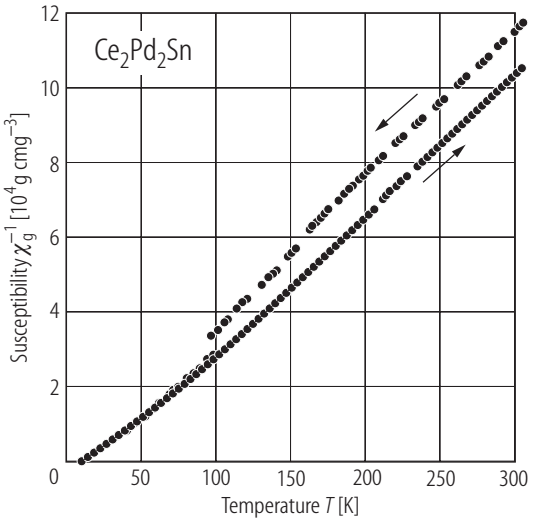

Fig. 64. Ce_2Pd_2Sn. Temperature dependence of χ_g^{-1} [95G1].

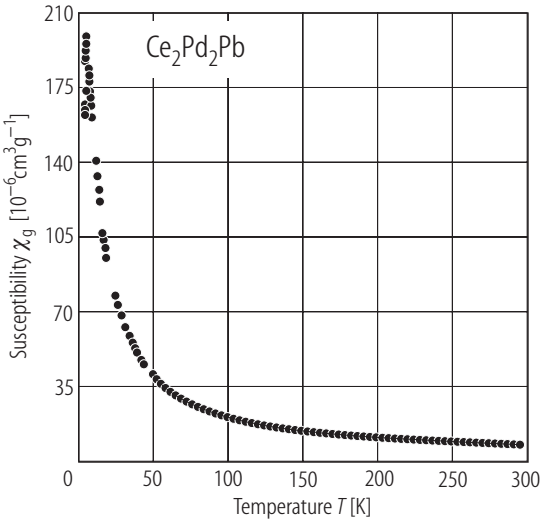

Fig. 65. Ce_2Pd_2Pb. Temperature dependence of χ_g [95G1].

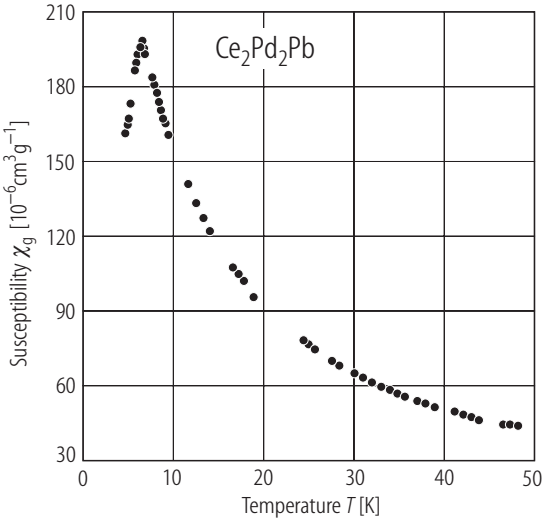

Fig. 66. Ce_2Pd_2Pb. Low temperature dependence of χ_g [95G1].

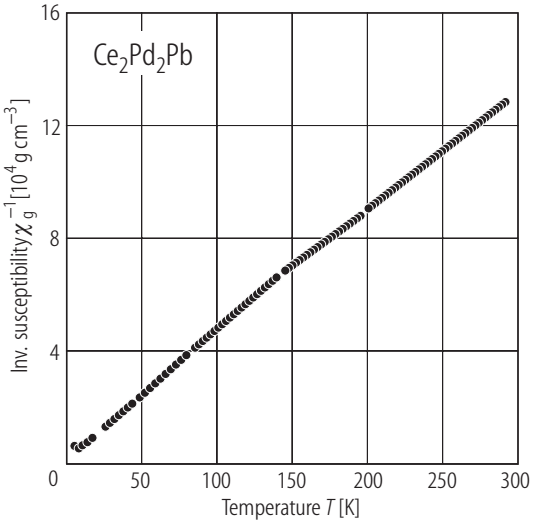

Fig. 67. Ce_2Pd_2Pb Temperature dependence of χ_g^{-1} [95G1].

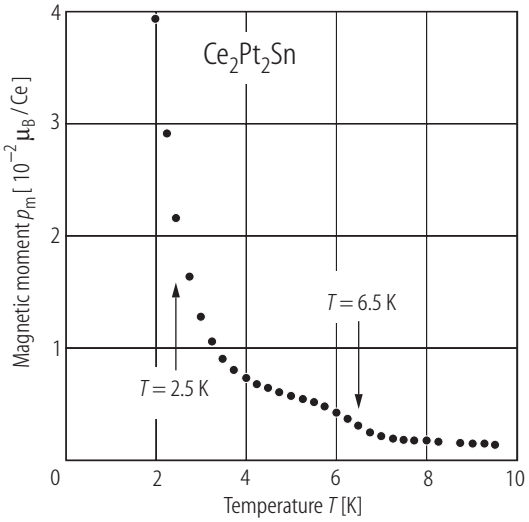

Fig. 68. Ce_2Pt_2Sn. Temperature dependence of p_m at 0.025 T [97C1].

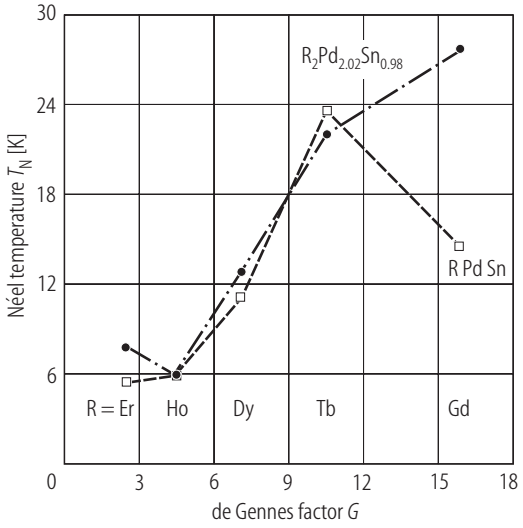

Fig. 69. $R_2Pd_{2.02}Sn_{0.98}$ and RPdSn. Néel temperature vs. de Gennes factor [98C2].

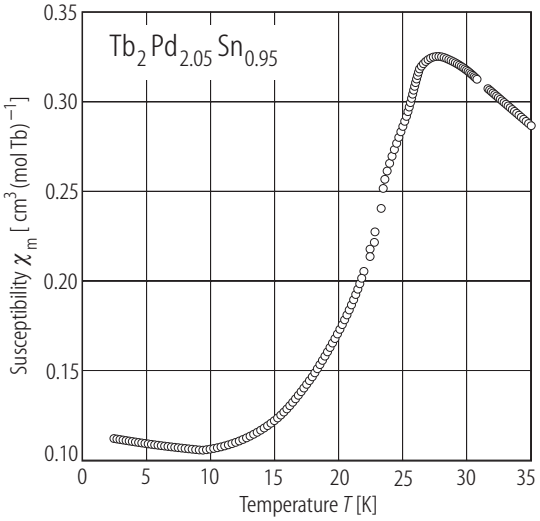

Fig. 70. $Tb_2Pd_{2.05}Sn_{0.95}$. Temperature dependence of χ_m per mol Tb [98L1].

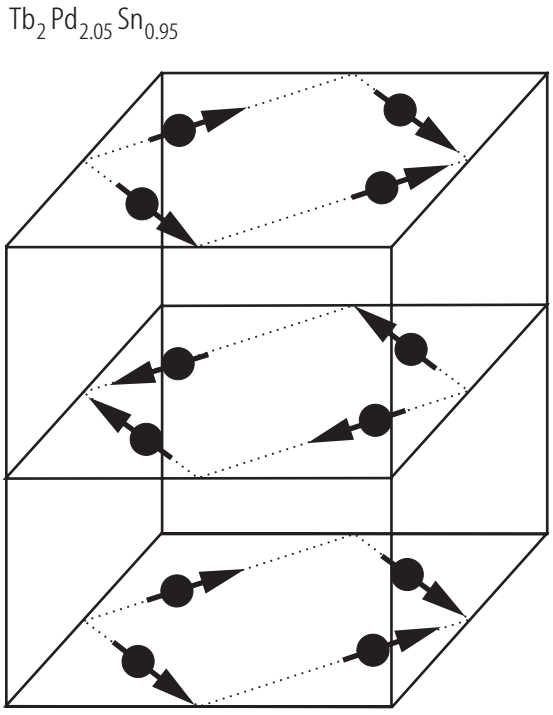

Fig. 71. $Tb_2Pd_{2.05}Sn_{0.95}$. Schematic representation of the commensurate [$\boldsymbol{k}$ = (0 0 ½)] non-collinear magnetic structure (magnetic unit cell $a\times a\times 2c$) [98L1].

References

85W1 Willis, J.O., Smith, J.L., Fisk, Z.: J. Magn. Magn. Mater. **47-48** (1985) 581
90D1 de V du Plessis, P.: Physica B **163** (1990) 603
90T1 Tari, A.: Physica B **165-166** (1990) 193
92K1 Kappler, J.P., Schmerber, G., Sereni, J.G.: J. Magn. Magn. Mater. **115** (1992) 241
92S1 Sereni, J.G., Trovarelli, O., Schmerber, G., Kappler, J.P.: J. Magn. Magn. Mater. **108** (1992) 183
92T1 Tanoue, S., Gschneidner, jr., K.A., McCallum, R.W.: J. Magn. Magn. Mater. **103** (1992) 129
93B2 Blazina, Z., Westwood, S.M.: J. Alloys Comp. **201** (1993) 151
94B2 Bonville, P., Hodges, J.A., Imbert, P., Thuery., P.: J. Magn. Magn. Mater. **136** (1994) 238
94C1 Chelkowska, G.: J. Alloys Comp. **209** (1994) 337
95B1 Burriel, R., Castro, M., Blanco, J. A., Espeso, J.I., Rodriguez Fernandez, J., Gomez-Sal, J.C., Lester, C., de Podesta, M., McEwen, K.A.: Physica B **206-207** (1995) 264
95G1 Gordon, R.A., Ijiri, Y., Spencer, C.M., DiSalvo, F.J.: J. Alloys Comp. **224** (1995) 101
95O1 Ozawa, M.,Yoshizawa, M., Sugawara, H., Onuki, Y.: Physica B **206-207** (1995) 267
95S3 Sekine, C., Sakamoto, H., Muryayama, S., Hoshi, K., Sakakibara, T.: Physica B **206-207** (1995) 291
95T2 Talik, E., Slebarski, A.: J. Alloys Comp. **223** (1995) 87
95T4 Trovarelli, O., Sereni, J.G., Schmerber, G., Kappler, J.P.: Physica B **206-207** (1995) 243
95T5 Talik, E., Neumann, M.: J. Magn. Magn. Mater. **140-144** (1995) 795
96F1 Fourgeot, F., Gravereau, P., Chavelier, B., Fournes, L., Etournes, J.: J. Alloys Comp. **238** (1996) 102
96H1 Huxley, A.D., Dalmas, P., de Reotier, P.D., Yaouanc, A., Caplan, D., Couach, M., Lejay, P., Gubbens, P.C.M., Mulders, A.M.: Phys. Rev. **B 54** (1996) 9666
96I1 Ijiri, Y., DiSalvo, F.J.: J. Alloys Comp. **233** (1996) 69
96K2 Kaczorowski, D., Rogl, P., Hiebl, K.: Phys.Rev. **B 54** (1996) 9891
96S1 Sologub, O., Hiebl, K., Rogl, P., Noel, H.: J. Alloys Comp. **245** (1996) L13
97B1 von Blanckenhagen, G.F., Lenkewitz, M., Stewart, G.R.: J. Alloys Comp. **261** (1997) 37
97C1 Chevalier, B., Fooyrgeot, F., Laffargue, D., Etourneau, J., Bouree, F., Roisnel, T.: Physica B **230-232** (1997) 195
97D1 Dilley, N.R., Herrmann, J., Han, S.H., Maple, M.B.: Physica B **230-232** (1997) 332
97G1 Grin,Yu.N., Hiebl, K., Rogl, P., Godart, C., Alleno, E.: J. Alloys Comp. **252** (1997) 88
97S1 Shugawara, H., Sato, H., Aoki, Y., Sato, H.: J. Phys. Soc. Jpn. **66** (1997) 174
97S2 Suzuki, T., Goshima, T., Sakita, S., Fujita, T., Hedo, M., Inada, Y., Yamamoto, E., Haga, Y., Onuki, Y.: Physica B **230-232** (1997) 176
97S3 Sagmeister, E., Bauer, E., Gratz, E., Michor, H., Hilscher, G.: Physica B **230-232** (1997) 148
98C2 Chavalier, B., Fourgeot, F., Laffargue, D., Pottgen, R., Etourneau, J.: J. Alloys Comp. **275-277** (1998) 537
98L1 Laffarggue, D., Roisnel, T., Chevalier, B., Bouree, F.: J. Alloys Comp. **262-263** (1998) 219

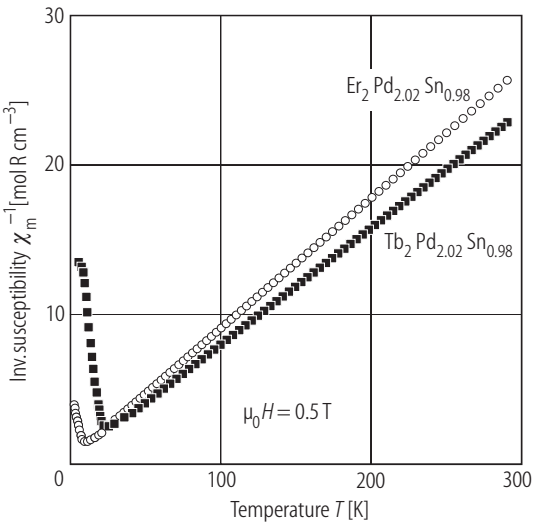

Fig. 72. $Er_2Pd_{2.02}Sn_{0.98}$, $Tb_2Pd_{2.02}Sn_{0.98}$. Temperature dependence of χ_m^{-1} at 0.5 T [98C2].

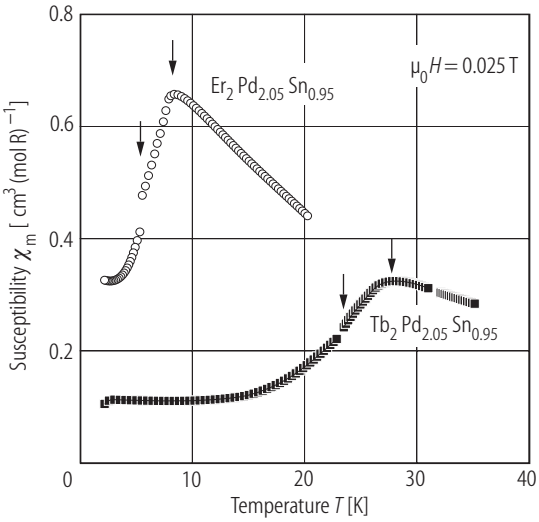

Fig. 73. $Er_2Pd_{2.05}Sn_{0.95}$, $Tb_2Pd_{2.05}Sn_{0.95}$. Temperature dependence of χ_m at 0.025 T [98C2].

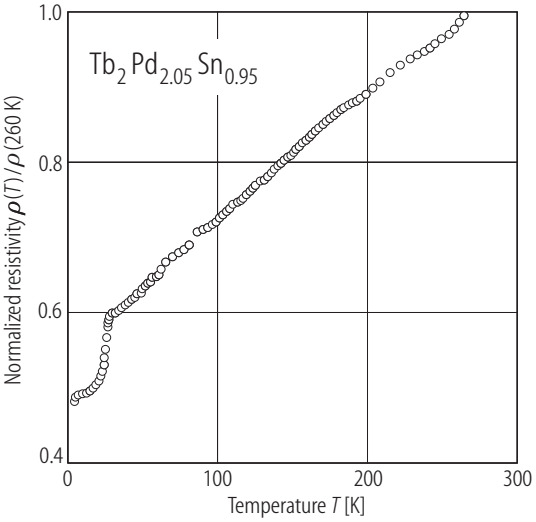

Fig. 74. $Tb_2Pd_{2.05}Sn_{0.95}$. Temperature dependence of $\rho(T)/\rho(260\ K)$ [98C2].

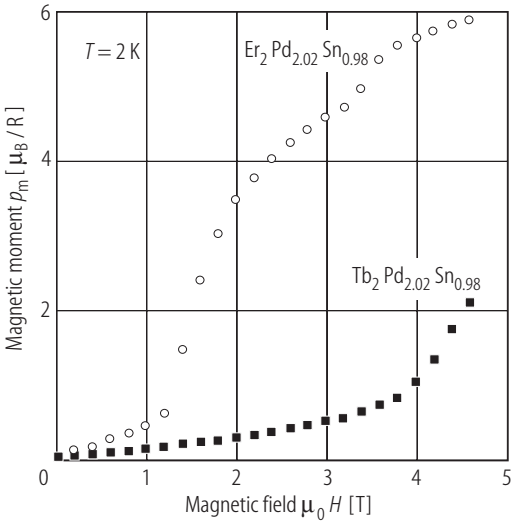

Fig. 75. $Er_2Pd_{2.02}Sn_{0.98}$, $Tb_2Pd_{2.02}Sn_{0.98}$. Magnetic field dependence of p_m at 2 K [98C2].

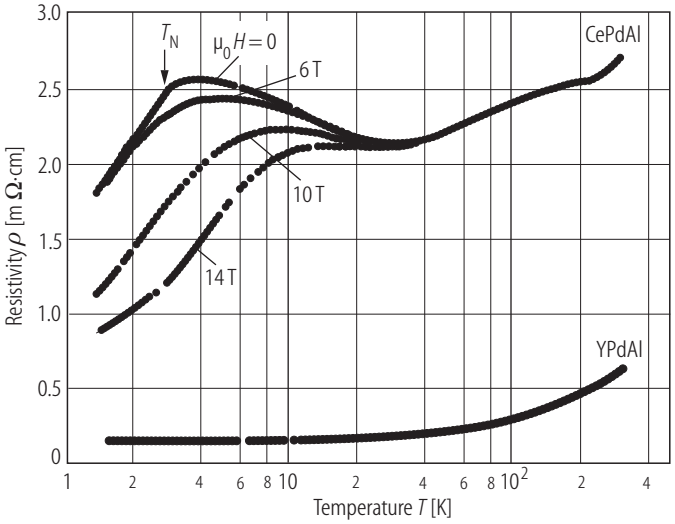

Fig. 76. YPdAl, CePdAl. Temperature dependence of the electrical resistivity at several H [94K1].

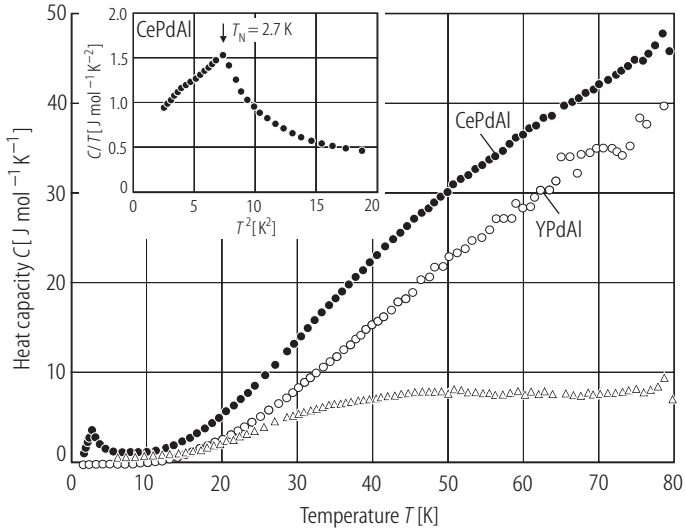

Fig. 77. YPdAl, CePdAl. Temperature dependence of the specific heat between 1.5 and 80 K. The inset shows C/T vs. T^2 for CePdAl [94K1].

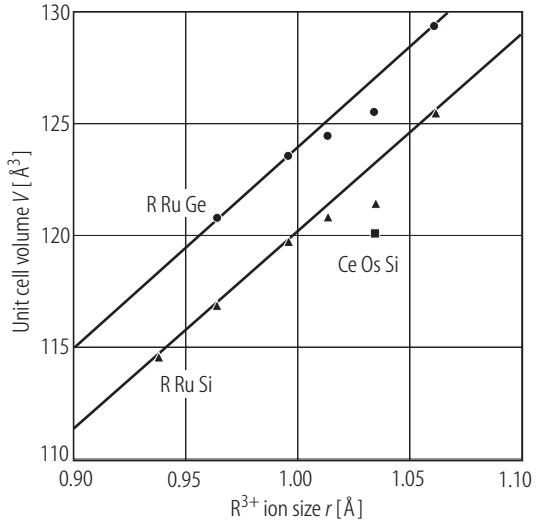

Fig. 78. CeOsSi, RRuGe (R ≡ La-Sm), RRuSi (R ≡ La-Sm, Gd) Unit cell volume vs. R^{3+} ion size [93W2].

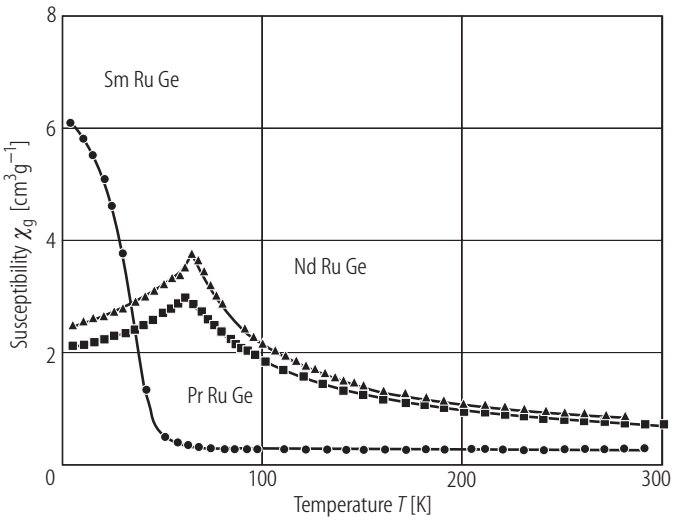

Fig. 79. PrRuGe, NdRuGe, SmRuGe. Temperature dependence of χ_g [93W2].

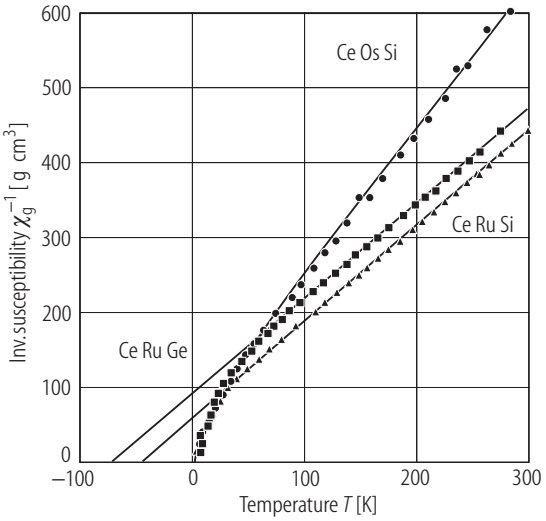

Fig. 80. CeRuGe, CeRuSi, CeOsSi. Temperature dependence of χ_g^{-1} [93W2].

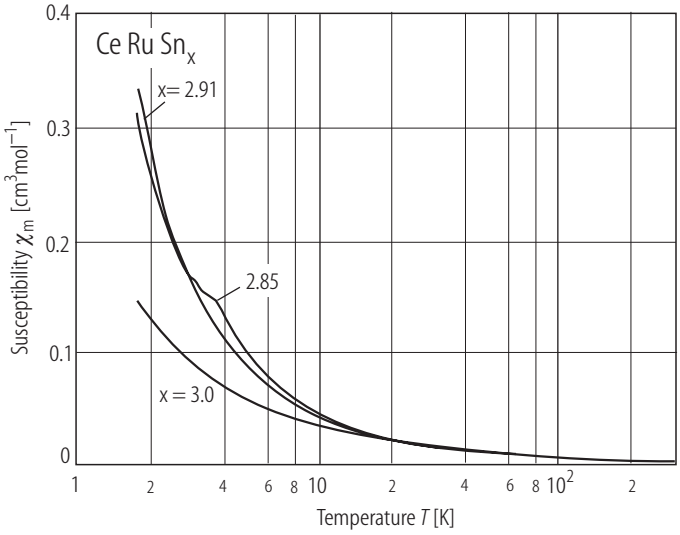

Fig. 81. CeRuSn$_x$. Temperature dependence of χ_m for different x [90F2].

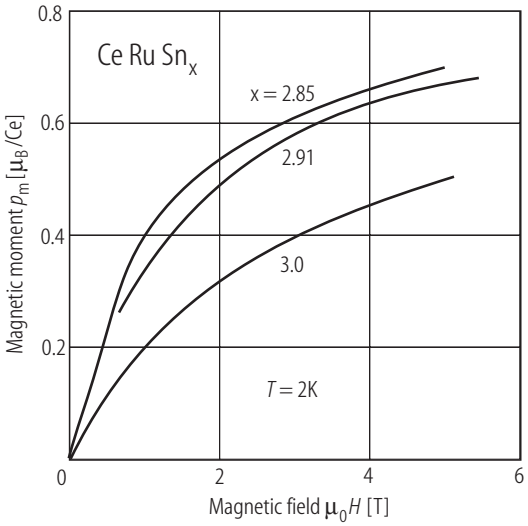

Fig. 82. $CeRuSn_x$. Magnetic field dependence of p_m at 2 K for different x [90F2].

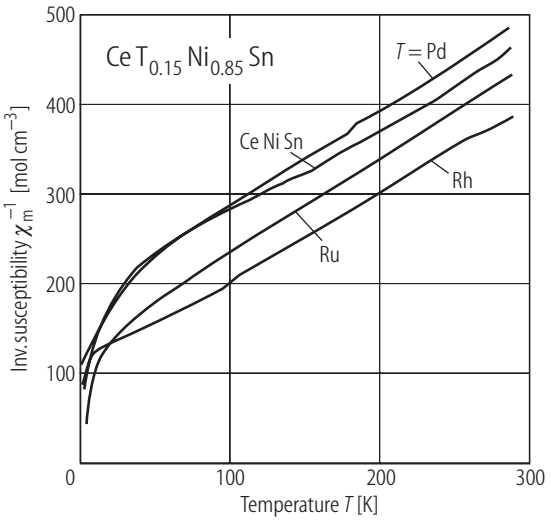

Fig. 83. CeNiSn, $CeT_{0.15}Ni_{0.85}Sn$ (T = Pd, Ru, Rh). Temperature dependence of χ_m^{-1} [97A1].

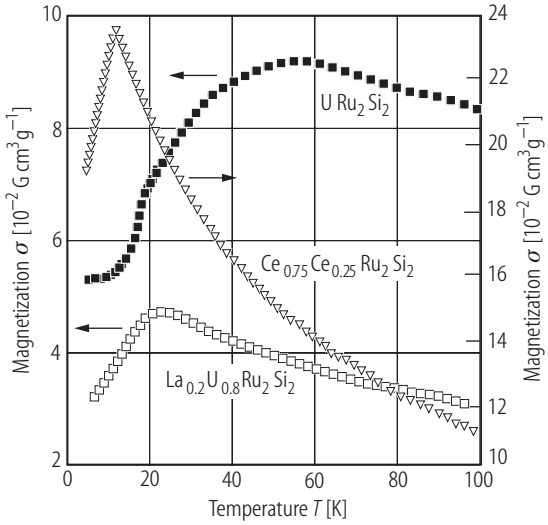

Fig. 84. $Ce_{0.25}U_{0.75}Ru_2Si_2$. Temperature dependence of σ [92R1].

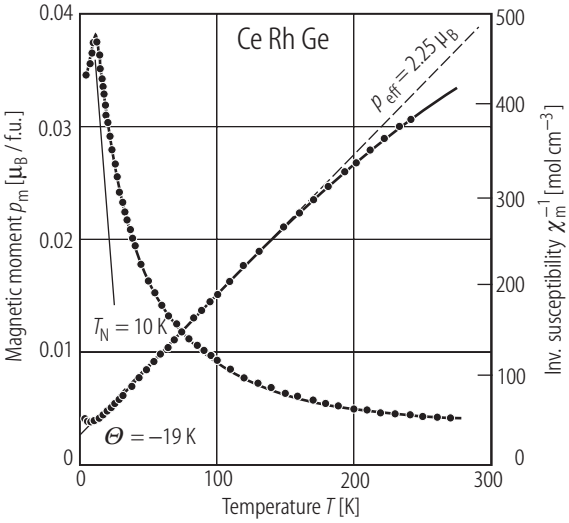

Fig. 85. CeRhGe. Temperature dependence of χ_m^{-1} and p_m [96B1].

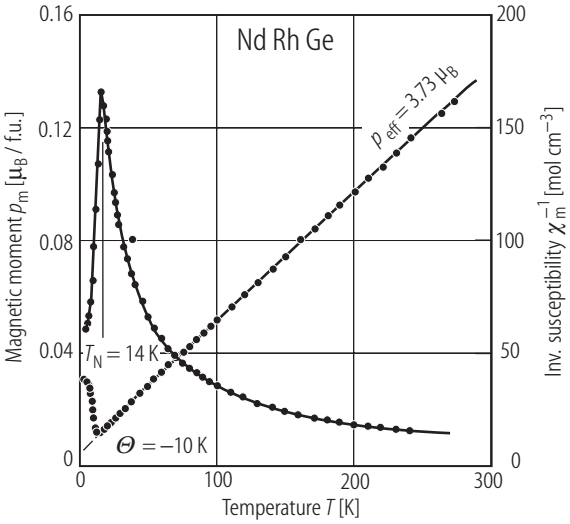

Fig. 86. NdRhGe. Temperature dependence of χ_m^{-1} and p_m [96B1].

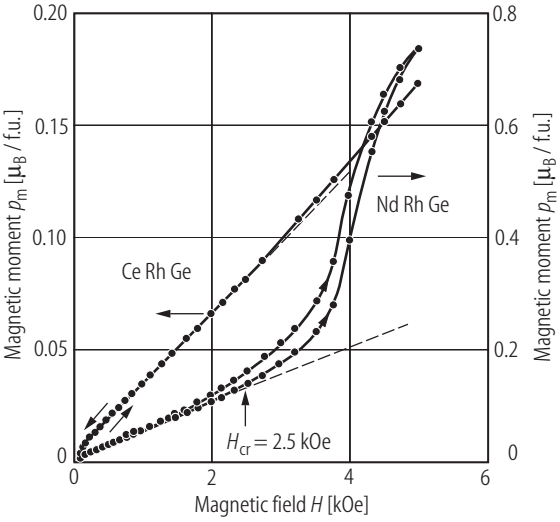

Fig. 87. CeRhGe, NdRhGe. Magnetic field dependence of p_m at 4.2 K [96B1].

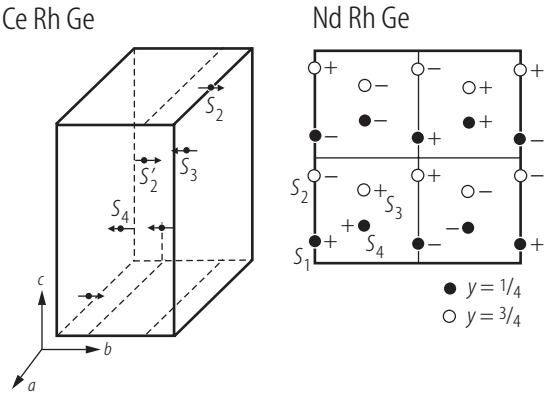

Fig. 88. CeRhGe, NdRhGe. Magnetic structure (the plus and minus indicate the direction of magnetic moments along and opposite to the *b* axis, respectively) [96B1].

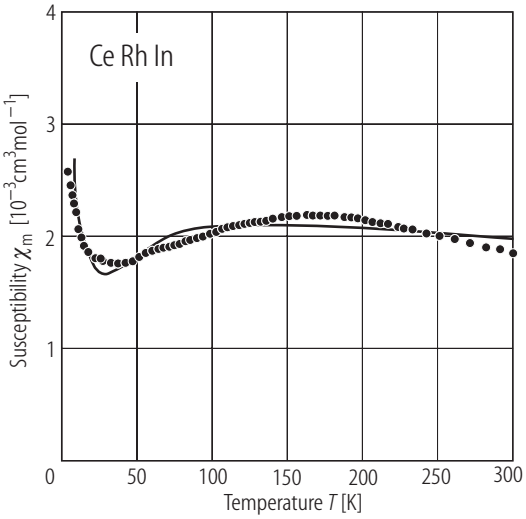

Fig. 89. CeRhIn. Temperature dependence of χ_m [90M1].

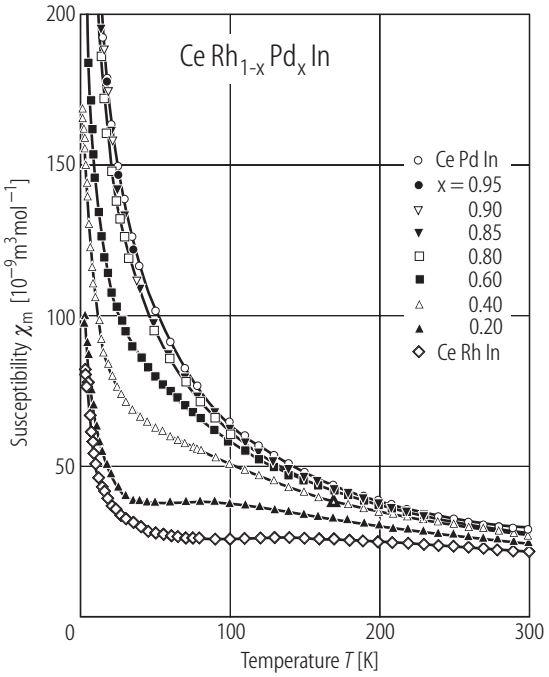

Fig. 90. $CeRh_{1-x}Pd_xIn$. Temperature dependence of χ_m. The lines are guide of eyes [93B1].

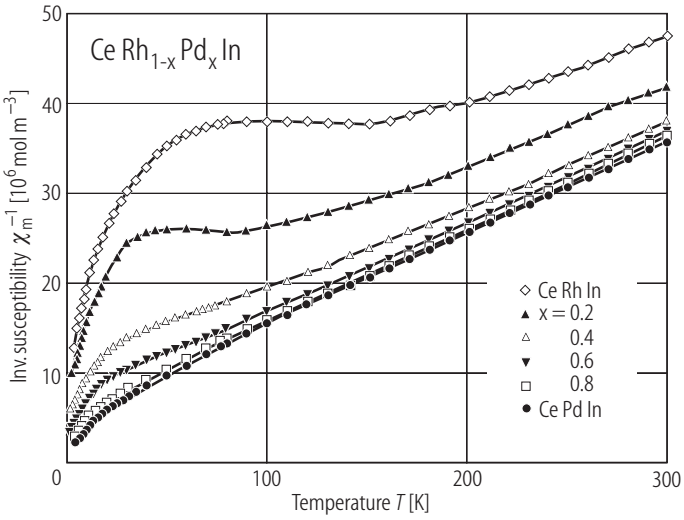

Fig. 91. $CeRh_{1-x}Pd_xIn$. Temperature dependence of χ_m^{-1} at several x [93B1].

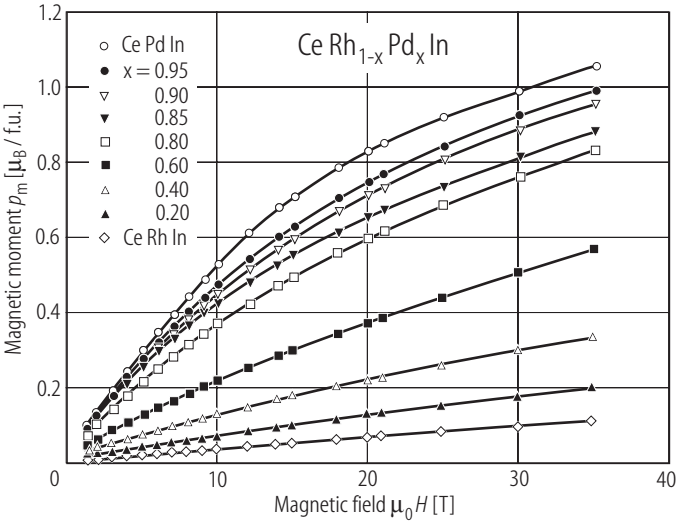

Fig. 92. $CeRh_{1-x}Pd_xIn$. Magnetic field dependence of p_m at several x [93B1].

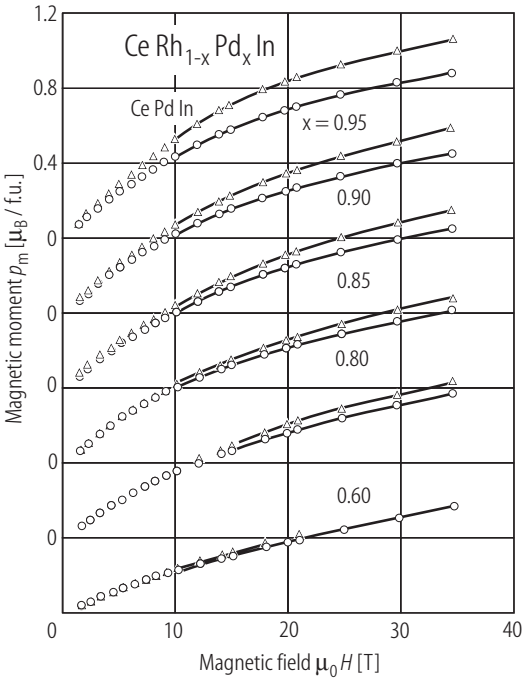

Fig. 93. $CeRh_{1-x}Pd_xIn$. Magnetic field dependence of p_m with increasing Pd concentration on powder free to be oriented in the field (triangles), and on powder fixed in random orientation by frozen alcohol (circles) [93B1].

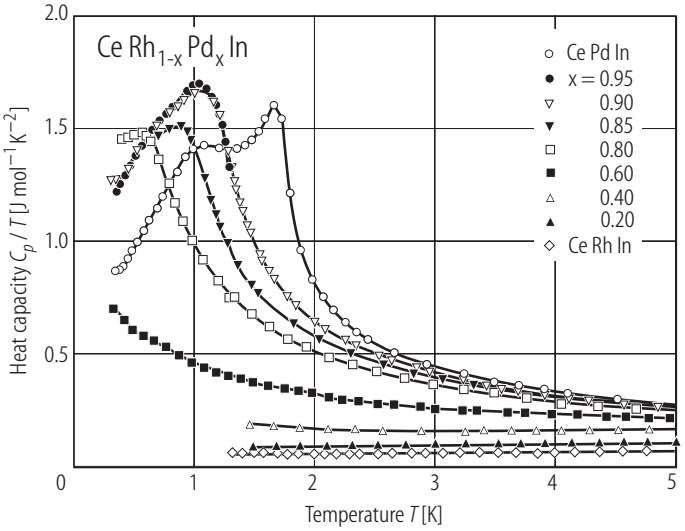

Fig. 94. $CeRh_{1-x}Pd_xIn$. Specific heat capacity C_p/T vs. T at low temperature [93B1].

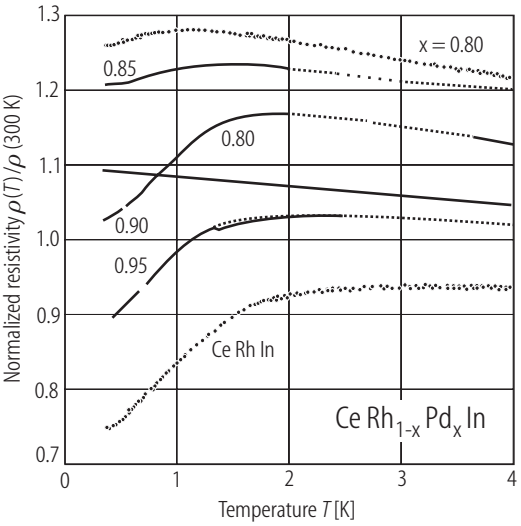

Fig. 95. $CePd_xRh_{1-x}In$. Temperature dependence of the electrical resistivity for $x \geq 0.6$ normalized to the room temperature value [93B1].

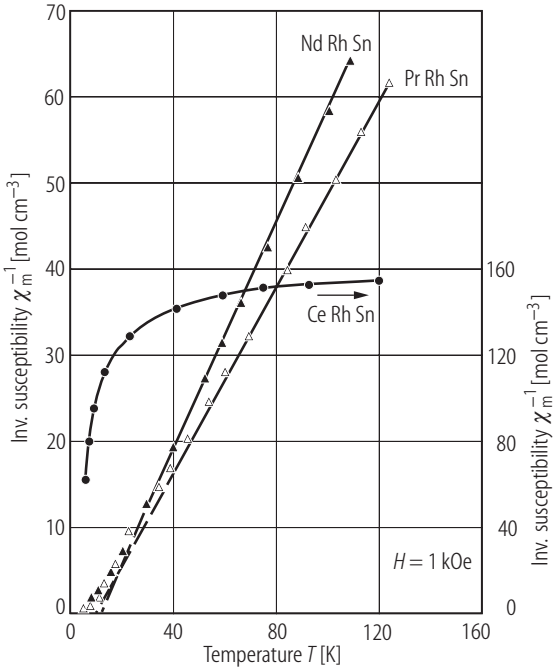

Fig. 96. CeRhSn, PrRhSn, NdRhSn. Temperature dependence of χ_m^{-1} at 1 kOe [92R2].

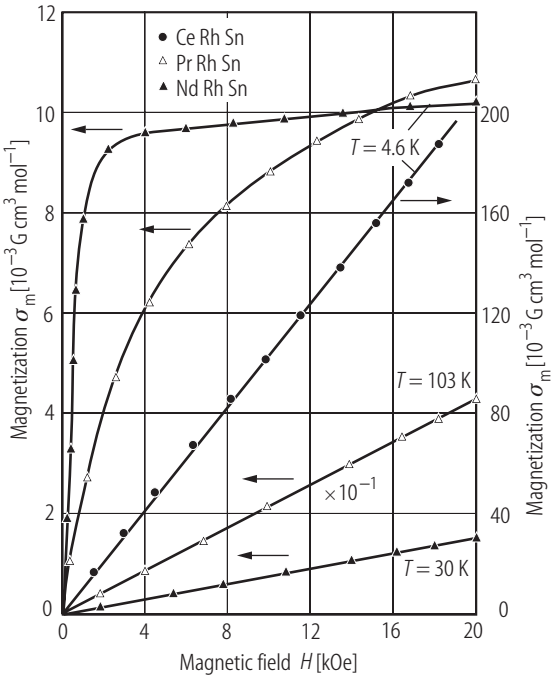

Fig. 97. CeRhSn, PrRhSn, NdRhSn. Magnetic field dependence of σ_m at different temperatures [92R2].

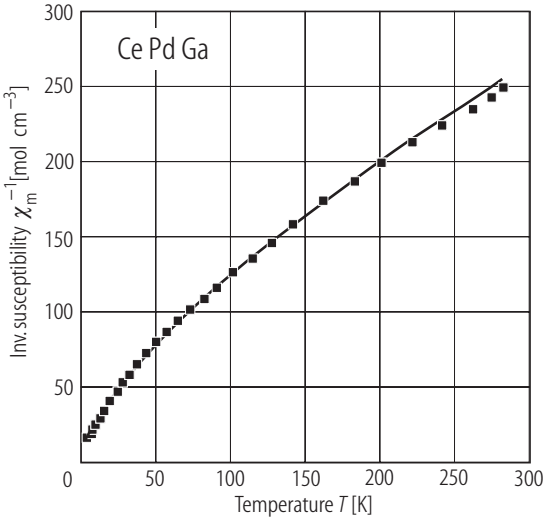

Fig. 98. CePdGa. Temperature dependence of χ_m^{-1} [94A3].

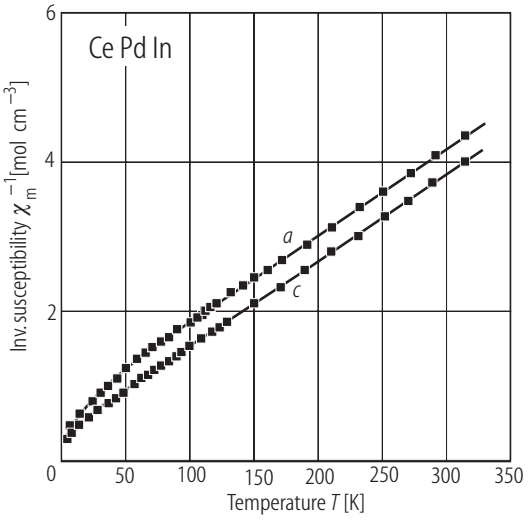

Fig. 99. CePdIn. Temperature dependence of χ_m^{-1} along *a* and *c* axes [90F1].

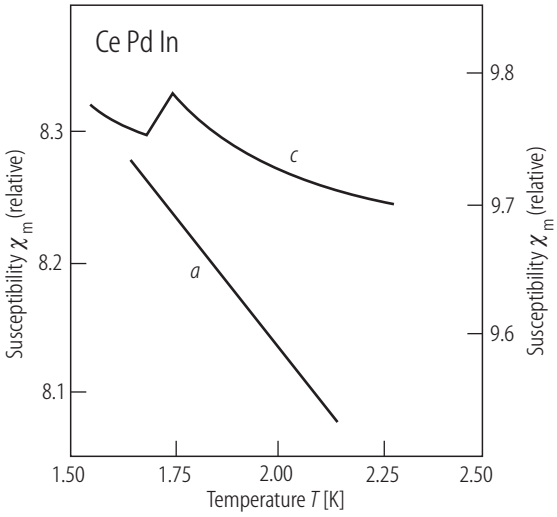

Fig. 100. CePdIn. Low temperature dependence of χ_m along the *a* and *c* axes [90F1].

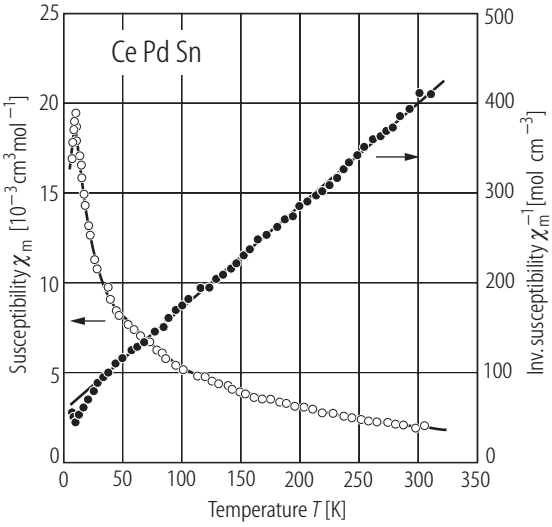

Fig. 101. CePdSn. Temperature dependence of χ_m and χ_m^{-1} [88K1].

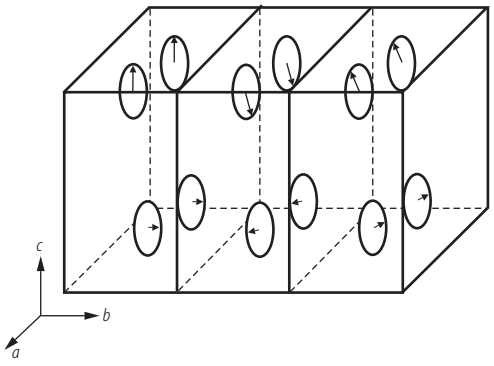

a

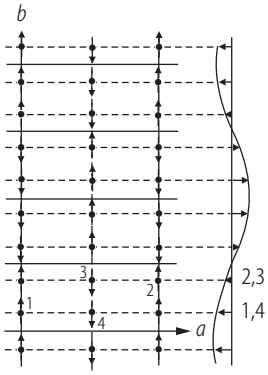

b

Fig. 102. (**a**) CePdSn, (**b**) DyPdSn. Magnetic structures [94A5].

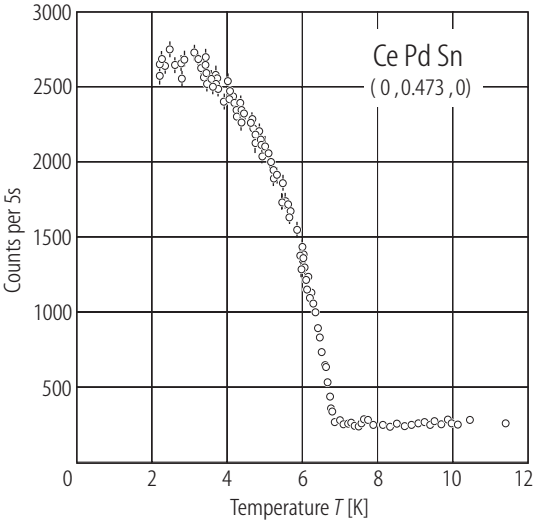

Fig. 103. CePdSn. Temperature dependence of peak intensity of the (0,0.473,0) satellite [92K2].

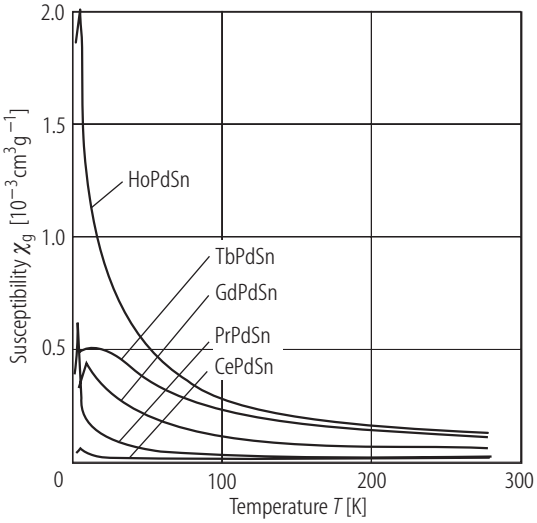

Fig. 104. RPdSn , R = Ce, Pr, Gd, Tb, Ho. Temperature dependence of χ_g [90S2].

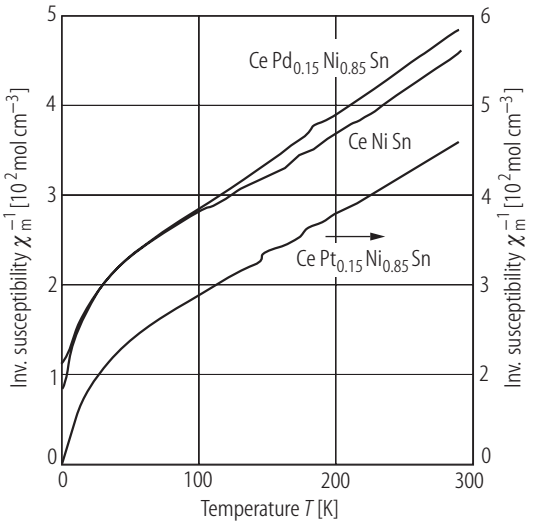

Fig. 105. CeNiSn, $CePd_{0.15}Ni_{0.85}Sn$, $CePt_{0.15}Ni_{0.85}Sn$. Temperature dependence of χ_m^{-1} [94A2].

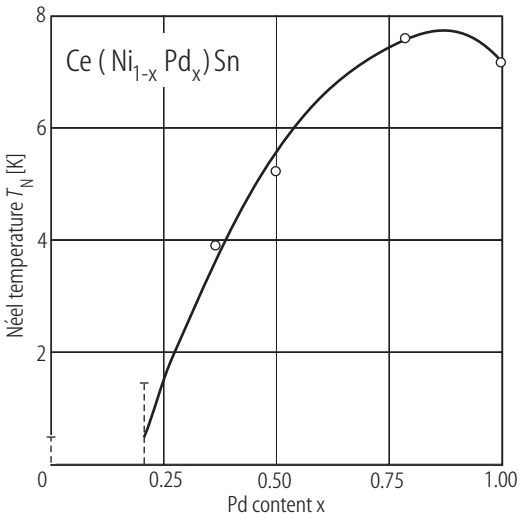

Fig. 106. $Ce(Ni_{1-x}Pd_x)Sn$. Variation of the Néel temperature with x. The solid line is drawn as visual guide. The dashed lines indicate the temperature ranges above which the magnetic order could not be observed.

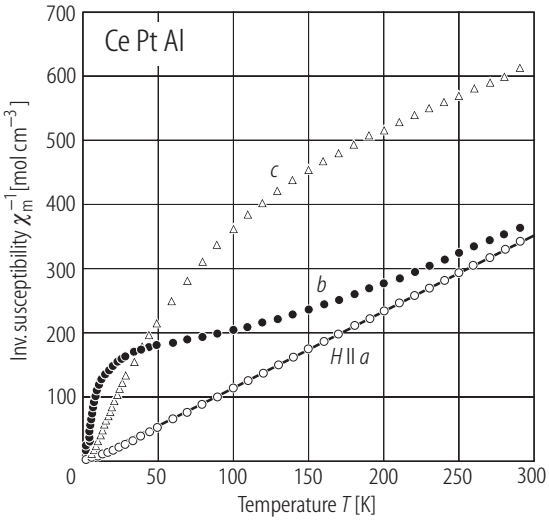

Fig. 107. CePtAl. Temperature dependence of χ_m^{-1} for single crystal along each axis at 0.1 T [97K2].

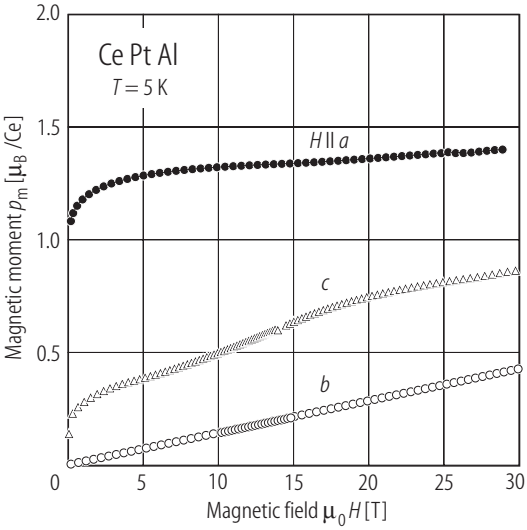

Fig. 108. CePtAl. Magnetic field dependence of p_m for each axis of the single crystal at 5 K [97K2].

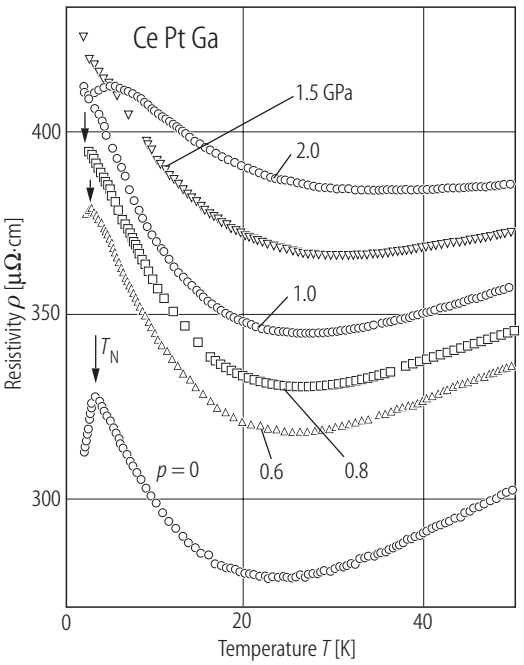

Fig. 109. CePtGa. Temperature dependence of ρ at low temperature under various pressures [95U1].

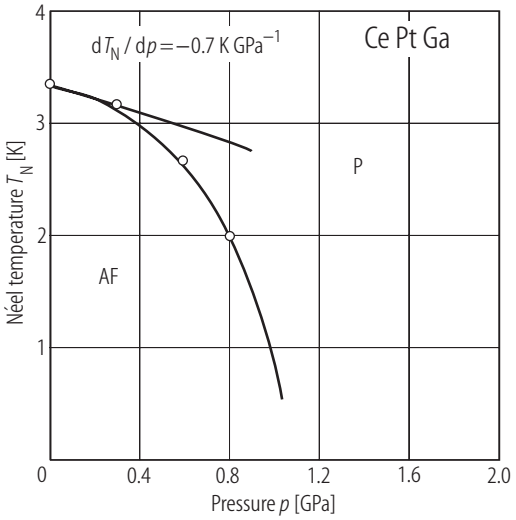

Fig. 110. CePtGa. Pressure dependence of T_N [95U1].

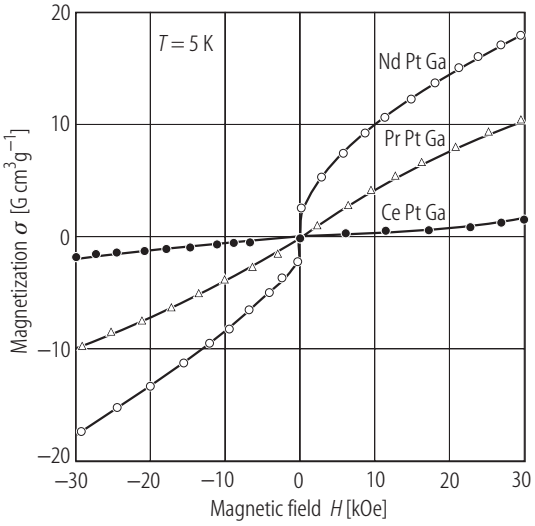

Fig. 111. CePtGa, NdPtGa, PrPtGa. Magnetic field dependence of σ at 5 K [96K5].

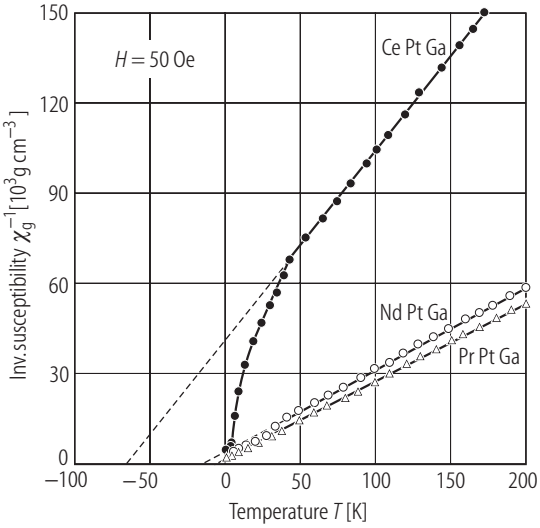

Fig. 112. CePtGa, NdPtGa, PrPtGa. Temperature dependence of χ_g^{-1} at 50 Oe [96K5].

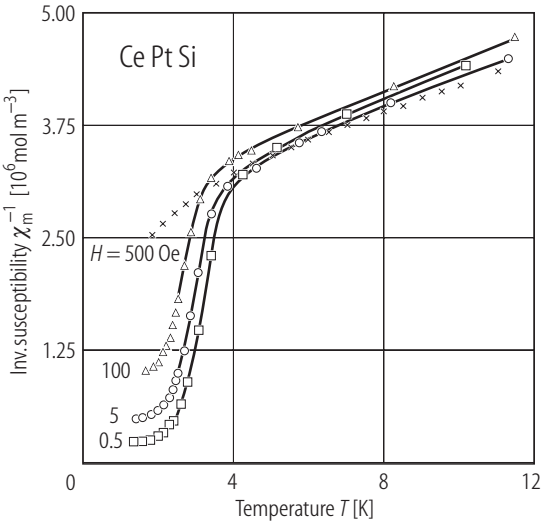

Fig. 113. CePtSi. Temperature dependence of χ_m^{-1} for various H [90K1].

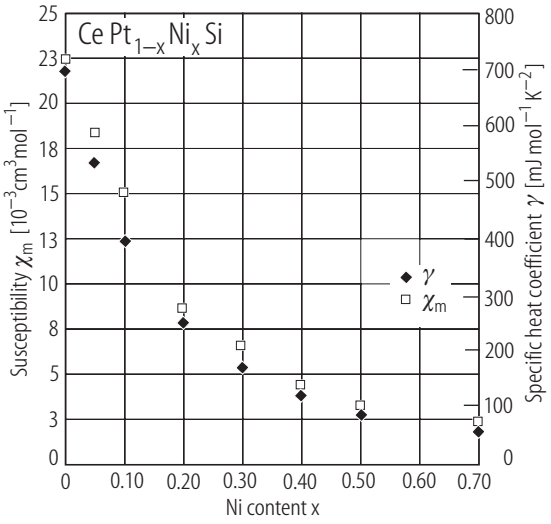

Fig. 114. CePt$_{1-x}$Ni$_x$Si. Concentration dependence of χ_m and γ [96K3].

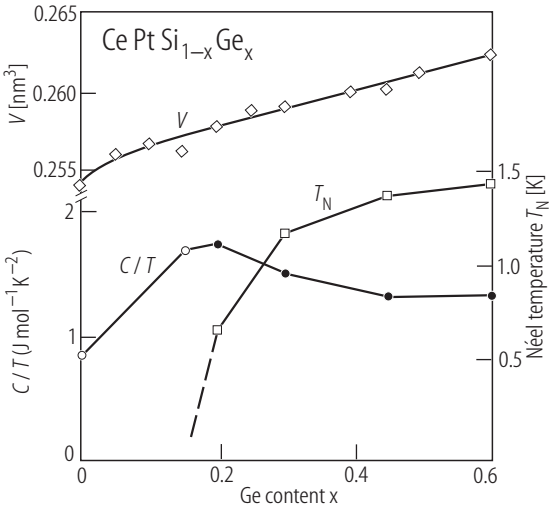

Fig. 115. CePtSi$_{1-x}$Ge$_x$. Concentration dependence of unit-cell volume, T_N and C/T. Full circles indicate that C/T was obtained in the magnetically ordered regime [92G1].

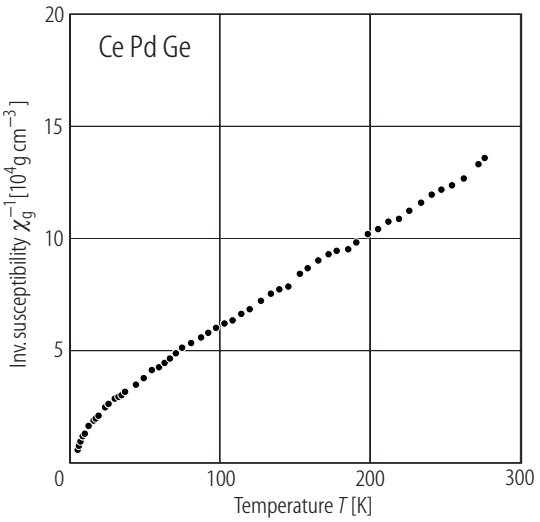

Fig. 116. CePdGe. Temperature dependence of χ_g^{-1} [90S1].

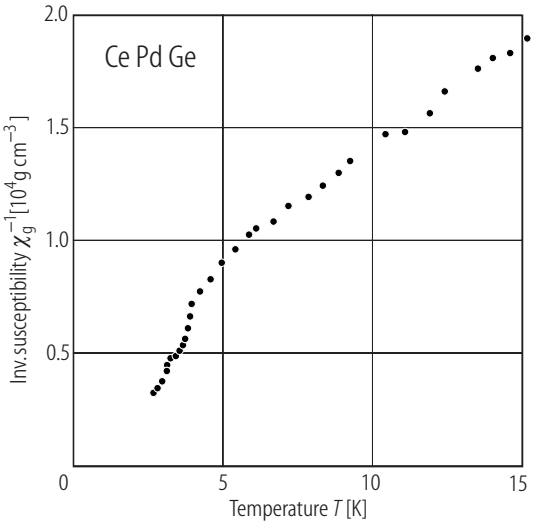

Fig. 117. CePdGe. Low temperature dependence of χ_g^{-1} [90S1].

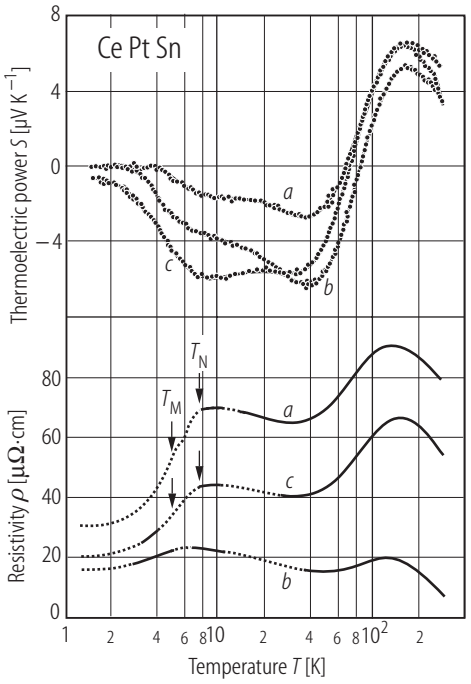

Fig. 118. CePtSn. Temperature dependence of ρ and S. Ordering temperatures T_N and T_M are indicated [94B1].

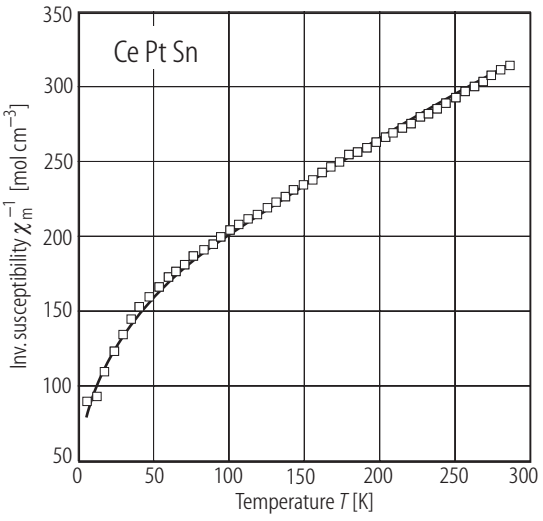

Fig. 119. CePtSn. Temperature dependence of χ_m^{-1} [94A2].

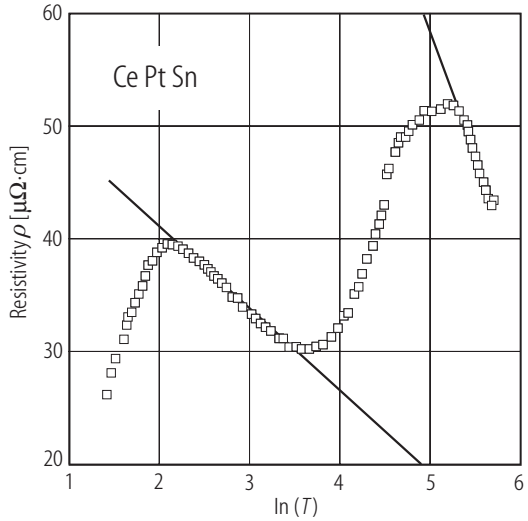

Fig. 120. CePtSn. Temperature dependence of ρ [94A2].

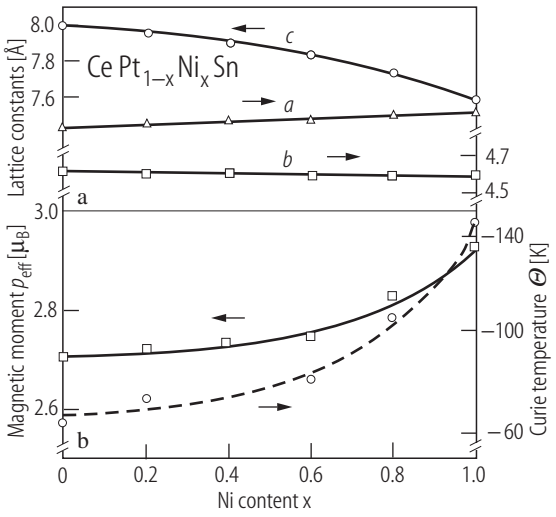

Fig. 121. $CePt_{1-x}Ni_xSn$. Concentration dependence of (**a**) lattice constant, (**b**) p_{eff} and Θ [92S5].

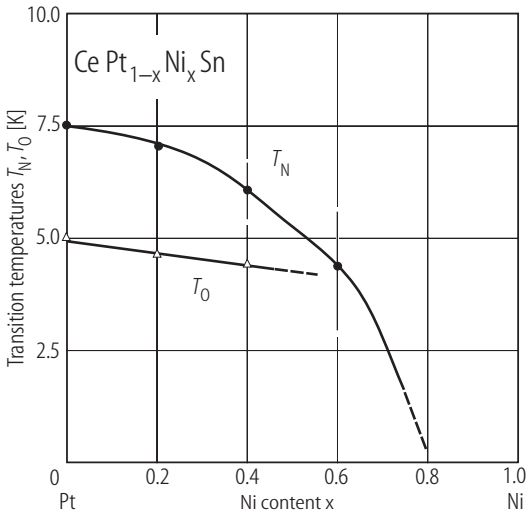

Fig. 122. $CePt_{1-x}Ni_xSn$. Concentration dependence of T_N and second magnetic transition temperature T_0 [92B1].

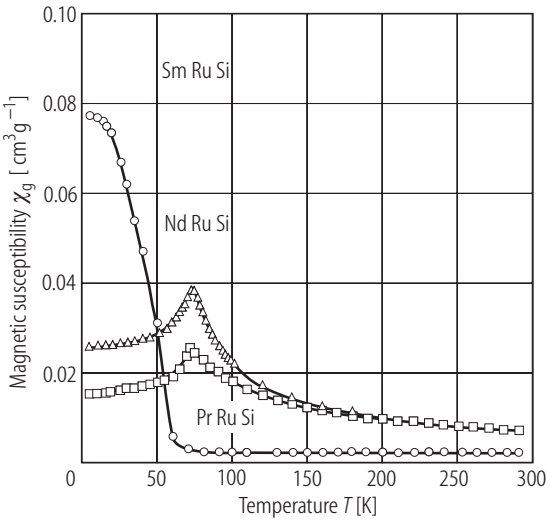

Fig. 123. PrRuSi, NdRuSi, SmRuSi. Temperature dependence of χ_g [93W2].

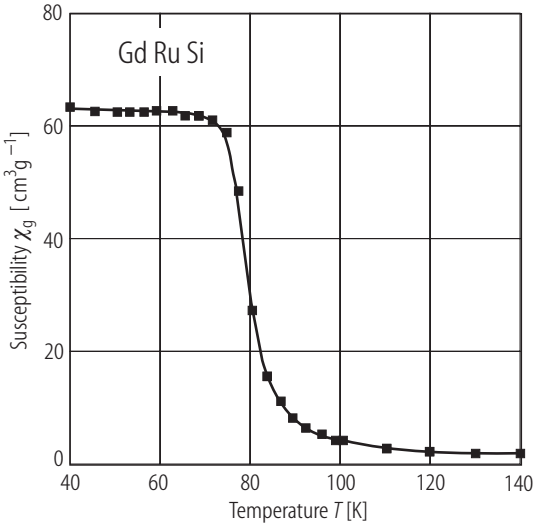

Fig. 124. GdRuSi, Temperature dependence of χ_g [93W2].

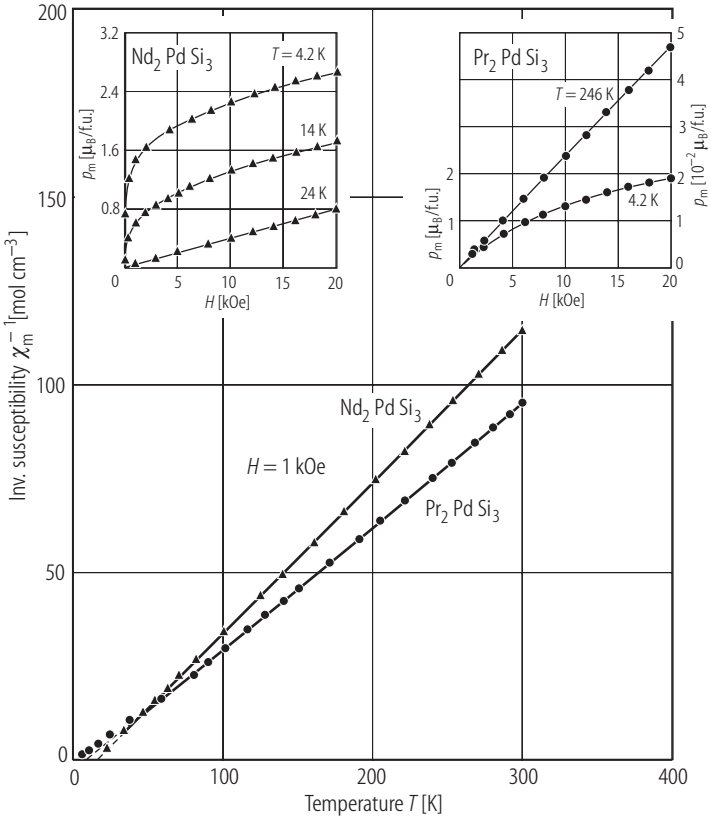

Fig. 125. Pr_2PdSi_3, Nd_2PdSi_3. Magnetic field dependence of p_m at constant temperatures and temperature dependence of χ_m^{-1} at 1 kOe [90K3].

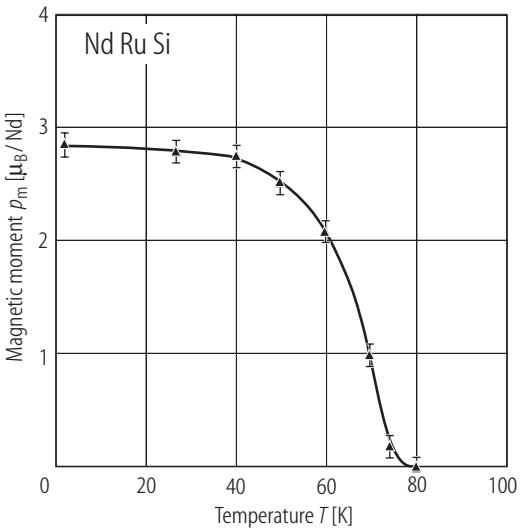

Fig. 126. NdRuSi. Temperature dependence of Nd magnetic moment [93W2].

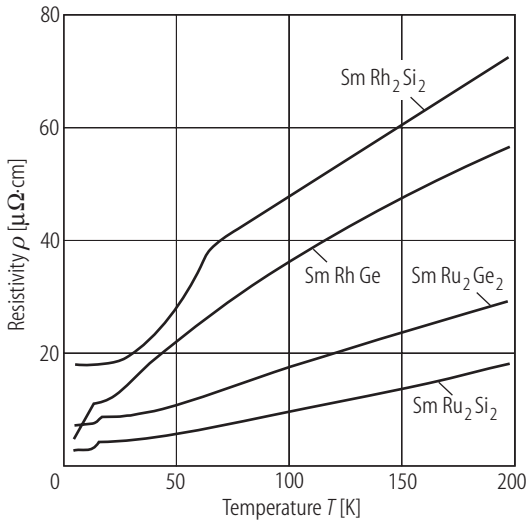

Fig. 128. $SmRu_2Si_2$, $SmRh_2Si_2$, $SmRu_2Ge_2$, SmRhGe. Temperature dependence of ρ [96K1].

For Fig. 127 see next page.

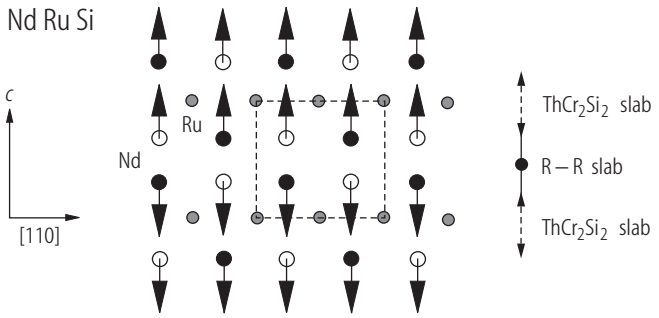

Fig. 127. NdRuSi. Magnetic structure at 2 K [93W2].

For Fig. 128 see previous page.

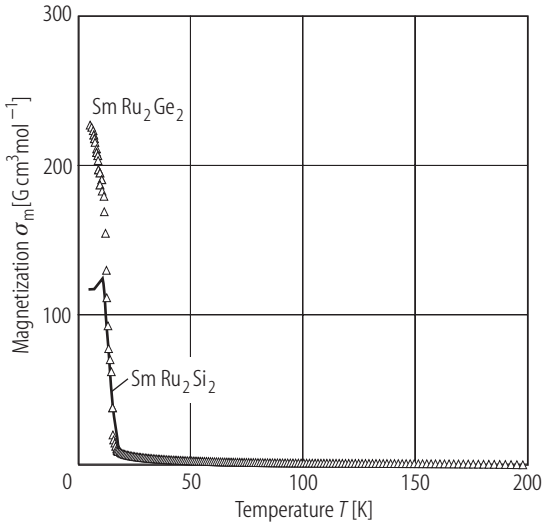

Fig. 129. $SmRu_2Si_2$, $SmRu_2Ge_2$. Temperature dependence of σ_m at 4 kOe [96K1].

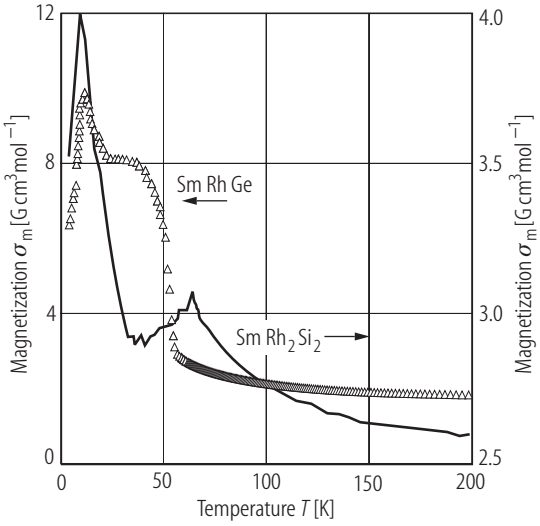

Fig. 130. $SmRh_2Si_2$, SmRhGe. Temperature dependence of σ_m at 4 kOe [96K1].

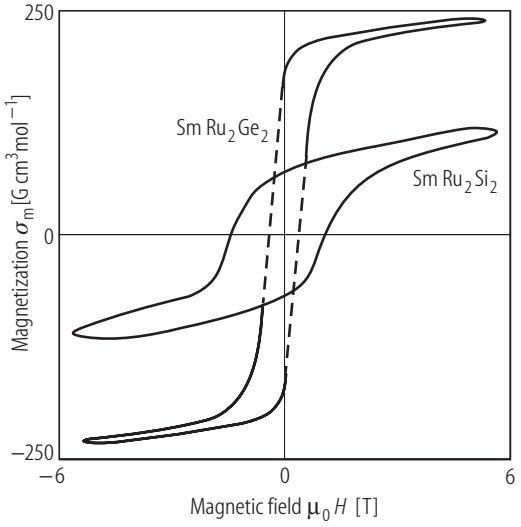

Fig. 131. $SmRu_2Si_2$, $SmRu_2Ge_2$. Hysteresis loops [96K1].

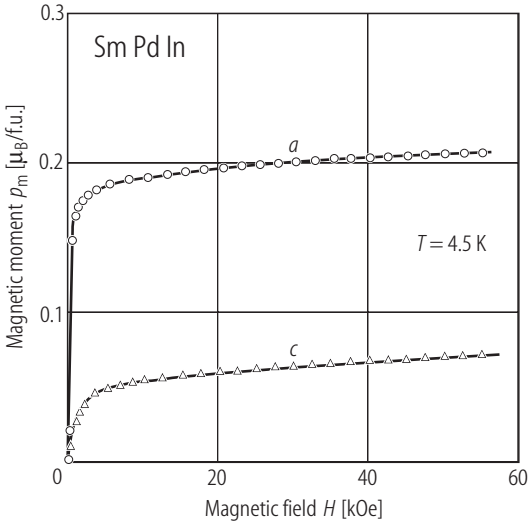

Fig. 132. SmPdIn. Magnetic field dependence of p_m at 4.5 K along the *a* and *c* axes [95I1].

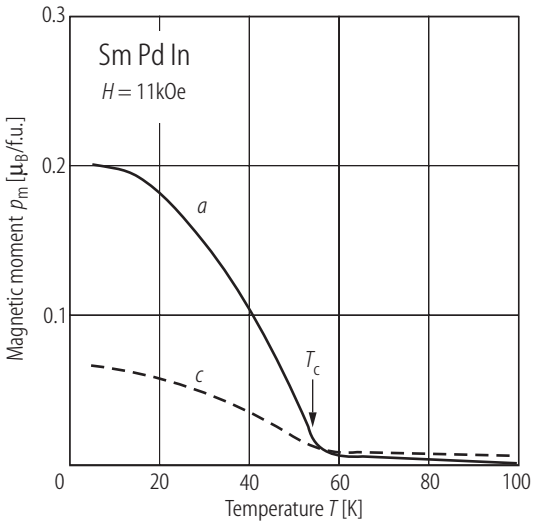

Fig. 133. SmPdIn. Temperature dependence of p_m at 11 kOe along the *a* and *c* axes [95I1].

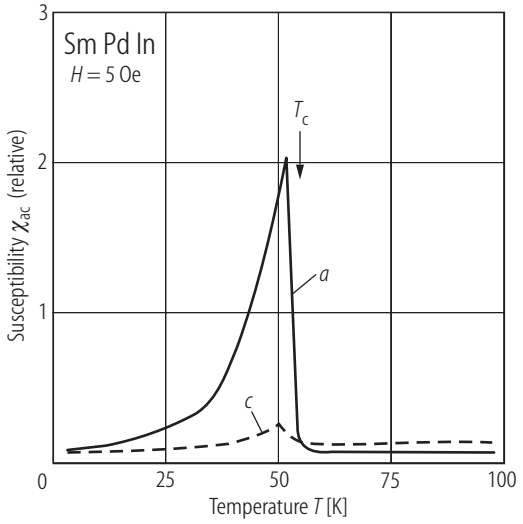

Fig. 134. SmPdIn. Temperature dependence of χ_{ac} along the *a* and *c* axes [95I1].

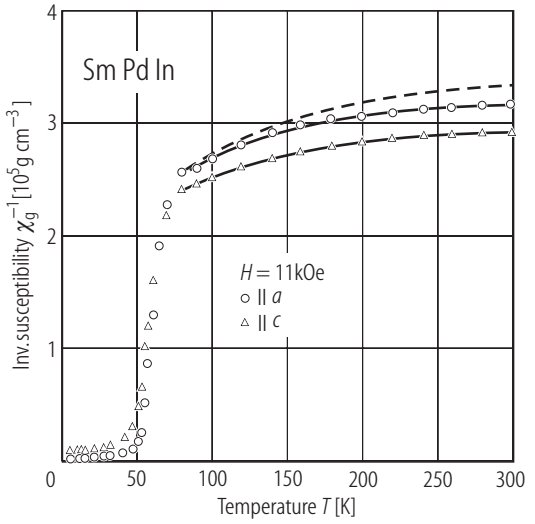

Fig. 135. SmPdIn. Temperature dependence of χ_g along the *a* and *c* axes at 11 kOe, dashed curve: theoretical [95I1].

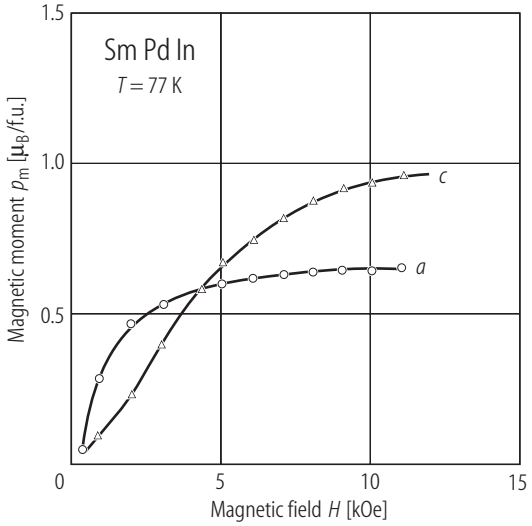

Fig. 136. SmPdIn. Magnetic field dependence of p_m for $H \parallel a$ and $H \parallel c$ [95I1].

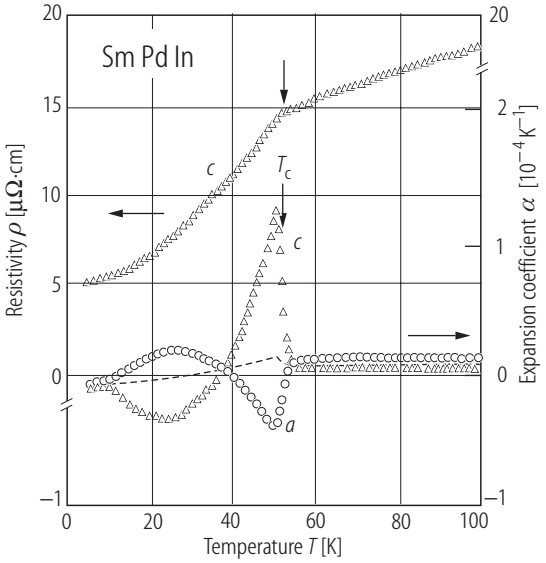

Fig. 137. SmPdIn. Temperature dependence of ρ along the *c* axis, thermal expansion coefficient along the *a* and *c* axes. Dashed curve: calculated for polycrystalline sample [95I1].

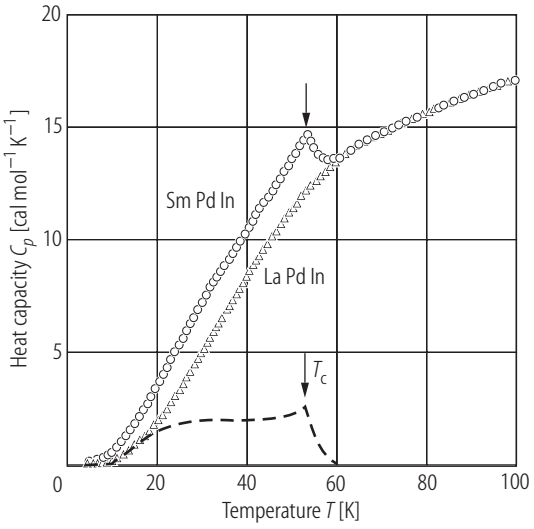

Fig. 138. LaPdIn, SmPdIn. Temperature dependence of C_p. The dashed line is the magnetic portion [95I1].

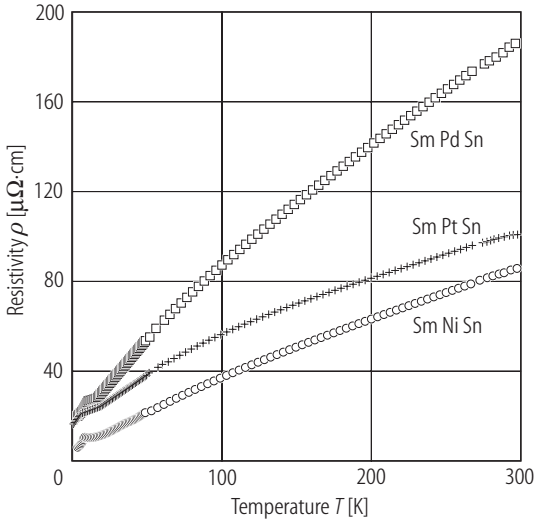

Fig. 139. SmTSn, T = Ni, Pd, Pt. Temperature dependence of ρ [95S2].

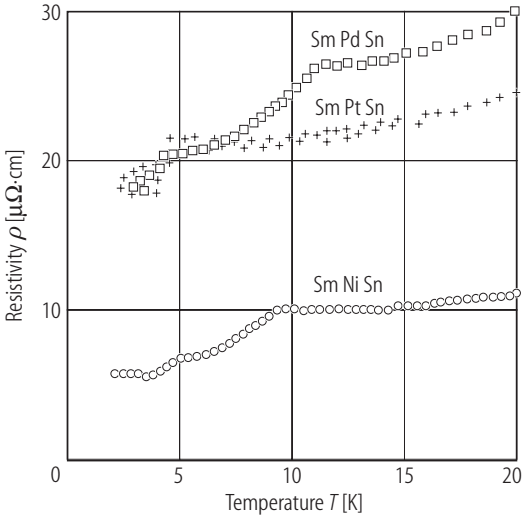

Fig. 140. SmTSn, T = Ni, Pd, Pt. Temperature dependence of ρ at low temperature [95S2].

References

88K1 Kasaya, M., Tani, T., Iga, F., Kasuya, T.: J. Magn. Magn. Mater. **76-77** (1988) 278

90F1 Fujii, H., Nagasawa, M., Kawanaka, H., Inoue, T., Takabatake, T.: Physica B **165-166** (1990) 435

90F2 Fukuhara. T., Sakamoto, I., Sato, H.: Physica B **165-166** (1990) 443

90K1 Kohler, R., Strobel, B., Kammerer, C., Grauel, A., Gottwick, U., Goring, E., Hohr, A., Sparn, G., Geibel, C., Horn, S.: J. Magn. Magn. Mater. **90-91** (1990) 428

90K3 Kotsanidis, P., A., Yakinthos, J., K., Gamari-Seale, E.: J. Magn. Magn. Mater. **87** (1990) 199

90M1 Malik, S.K., Adroja, D.T., Pdadalia, B.D., Vijayaraghavan, R.: Physica B **163** (1990) 89

90S1 Sakurai, J., Yamaguchi, Y., Nishigori, S., Suzuki, T., Fujita, T.: J. Magn. Magn. Mater. **90-91** (1990) 422

90S2 Sakurai, J., Yamaguchi, Y., Mibu, K., Shinjo: J. Magn. Magn. Mater. **84** (1990) 157

92B1 Besnus, M.J., Essaihi, A., Fischer, G., Hamdaoui, N., Meyer, A.: J. Magn. Magn. Mater. **104-107** (1992) 1387

92G1 Geibel, C., Kammerer, C., Seidel, B., Bredl, C.D., Grauel, A., Steglich, F.: J. Magn. Magn. Mater. **108** (1992) 207

92K2 Kotsanidis, P., Yakinthos, J.K., Semittelou, I., Roudaut, E.: J. Magn. Magn. Mater. **116** (1992) 95

92R1 Roy, S.B., Coles, B.R.: J. Magn. Magn. Mater. **108** (1992) 43

92R2 Routsi, Ch.D., Yakinthos, J.K., Gamari-Seale.: J. Magn. Magn. Mater. **117** (1992) 79

92S5 Sakurai, J., Kawamura, R., Taniguchi, T., Nishigori, S., Ikeda, S., Goshima, H., Suzuki, T., Fujita, T.: J. Magn. Magn. Mater. **104-107** (1992) 1415

93B1 Bruck, E., Nakotte, H., Bakker, K., de Boer, F.R., de Chatel, P.F.: J. Alloys Comp. **200** (1993) 79

93W2 Welter, R., Venturini G., Malaman, B.: J. Alloys Comp. **202** (1993) 165

94A2 Adroja, D.T., Rainford, B.D.: J. Magn. Magn. Mater. **135** (1994) 333

94A3 Adroja, D.T., Rainford, B.D., Malik, S.K.: Physica B **194-196** (1994) 169

94A5 Andre, G., Bouree, F., Bombik, A., Oles, A., Sikora, W., Kolenda, M., Szytula, A., Pacyna, A., Zygmunt, A.: Acta Phys. Pol. **85** (1994) 275

94B1 Bando, U., Takabatake, T., Tanaka, H., Iwasaki, H., Fujii, H., Malik, S.K.: Physica B **194-196** (1994) 1179

94K1 Kitazawa, H., Matsushita, A., Matsumoto, T., Suzuki, T.: Physica B **199-200** (1994) 28

95I1 Ito, T., Ohkubo, K., Hirasawa, T., Takeuchi, J., Hiromitsu, I., Kurisu, M.: J. Magn. Magn. Mater. **140-144** (1995) 873

95S2 Sakurai, J., Kegai, K., Kuwai, T., Isikawa, Y., Nisimura, K., Mori, K.: J. Magn. Magn. Mater. **140-144** (1995) 875

95U1 Uwatoko, Y., Ishii, T., Oomi, G., Malik, S.K.: Physica B **206-207** (1995) 199

96B1 Bazela, W., Zygmunt, A., Szytula, A., Ressouche, E., Leciejewicz, J., Sikora, W.: J. Alloys Comp. **243** (1996) 106

96K1 Kochetkov, Yu.V., Nikiforov, V.N., Klestov, S.A., Morozkin, A.V.: J. Magn. Magn. Mater. **157-158** (1996) 665

96K3 Kolb, R., Mielke, A., Scheidt, E.W., Stewart, G.R.: J. Alloys Comp. **239** (1996) 124

96K5 Kasaya, M., Ito, M., Ono, A., Sakai, O.: Physica B **223-224** (1996) 336

97A1 Adroja, D.T., Rainford, B.D., Houshiar, M.: J. Alloys Comp. **268** (1997) 1

97K2 Kitazawa, H., Nimori, S., Tang, J., Iga, F., Donni, A., Matsumoto, T., Kido, G.: Physica B **237-238** (1997) 212

98C2 Chavalier, B., Fourgeot, F., Laffargue, D., Pottgen, R., Etourneau, J.: J. Alloys Comp. **275-277** (1998) 537

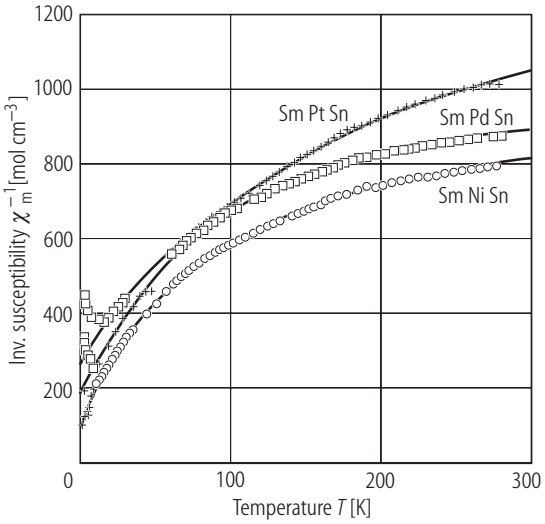

Fig. 141. SmTSn, T = Ni, Pd, Pt . Temperature dependence of χ_m^{-1} [95S2].

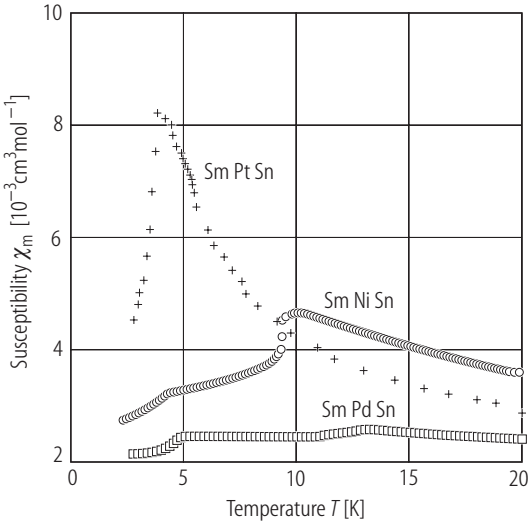

Fig. 142. SmTSn, T = Ni, Pd, Pt. Low temperature dependence of χ_m [95S2].

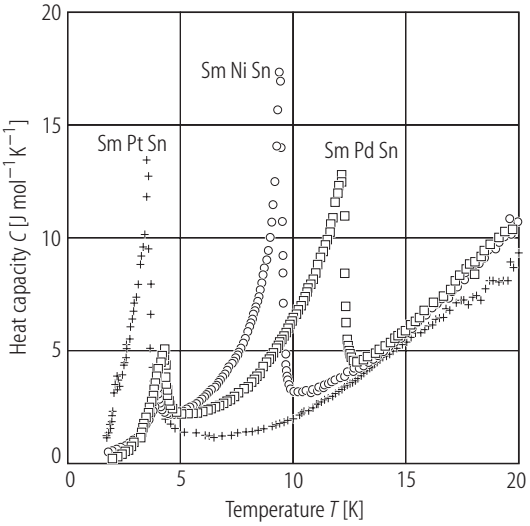

Fig. 143. SmTSn. T = Ni, Pd, Pt. Temperature dependence of specific heat [95S2].

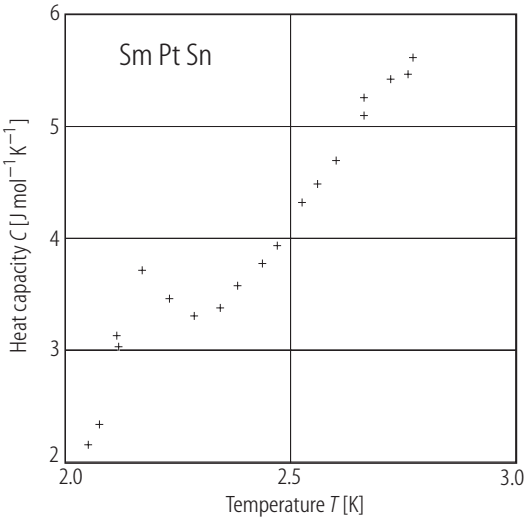

Fig. 144. SmPtSn. Low temperature dependence of specific heat [95S2].

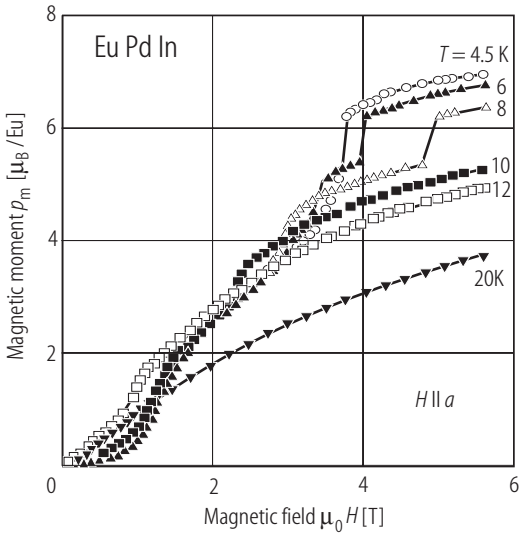

Fig. 145. EuPdIn. Magnetic field dependence of p_m along the *a* axis for several temperatures [98I1].

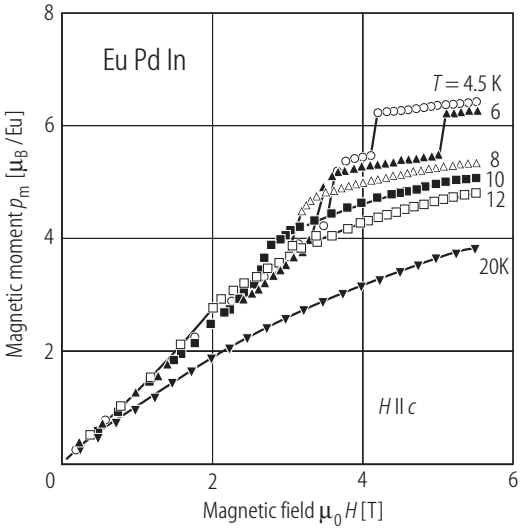

Fig. 146. EuPdIn. Magnetic field dependence of p_m along the *c* axis for several temperatures [98I1].

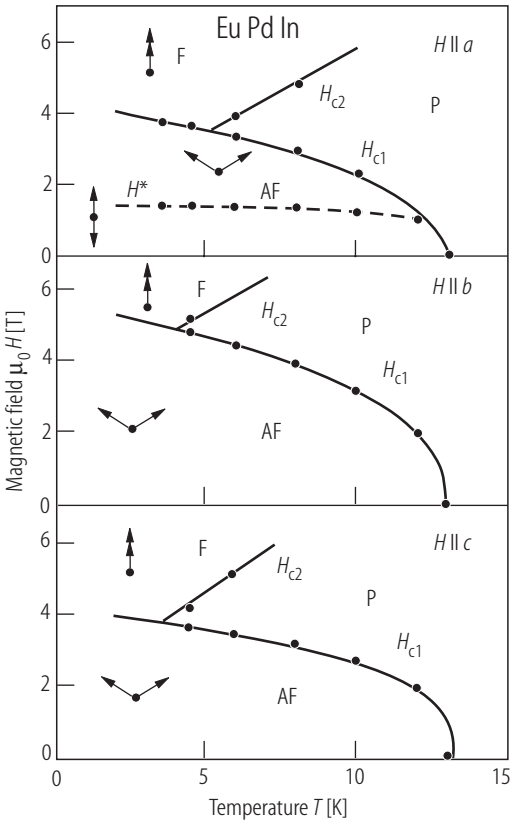

Fig. 147. EuPdIn. Magnetic phase diagram along the *a, b* and *c* axis determined by the critical fields of magnetization [98I1].

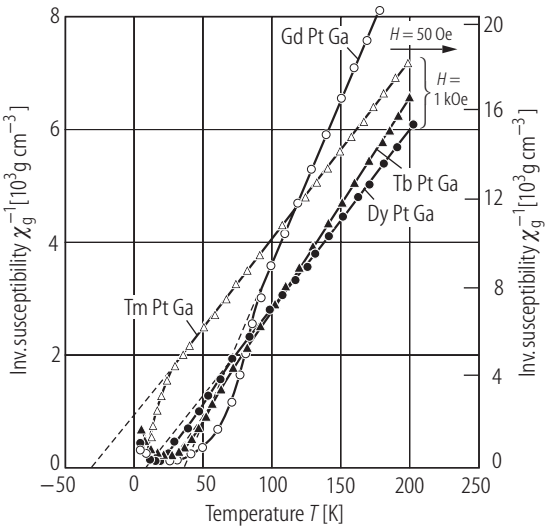

Fig. 148. GdPtGa, TbPtGa, DyPtGa, TmPtGa. Temperature dependence of χ_g^{-1} at 50 Oe for Gd and 1 kOe for Tb, Dy and Tm compounds [96K4].

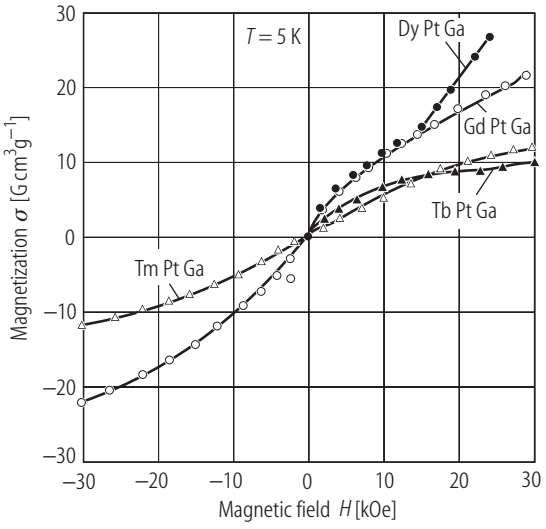

Fig. 149. GdPtGa, TbPtGa, DyPtGa, TmPtGa. Magnetic field dependence of σ at 5 K [96K4].

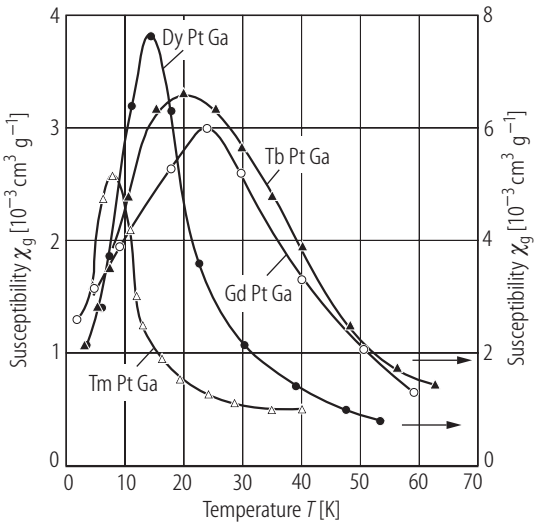

Fig. 150. GdPtGa, TbPtGa, DyPtGa, TmPtGa. Temperature dependence of χ_g [96K4].

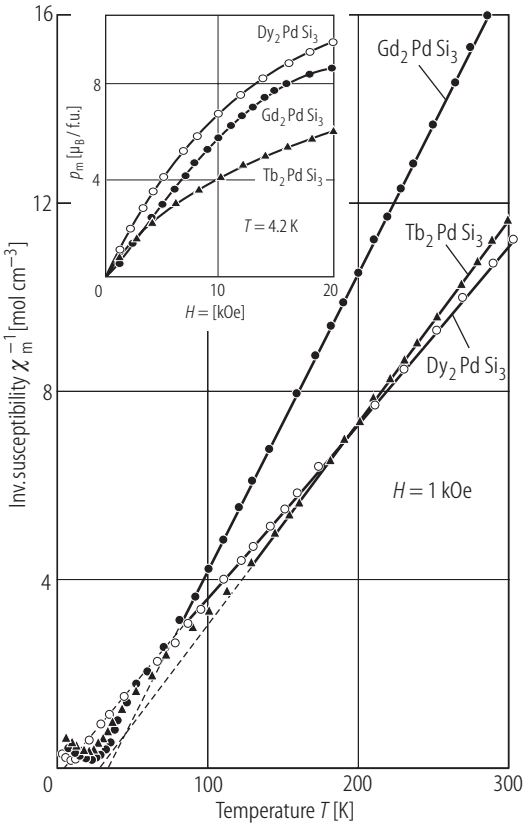

Fig. 151. Gd_2PdSi_3, Tb_2PdSi_3, Dy_2PdSi_3. Magnetic field dependence of p_m at 4.2 K (inset), and temperature dependence of χ_m^{-1} at 1 kOe [90K3].

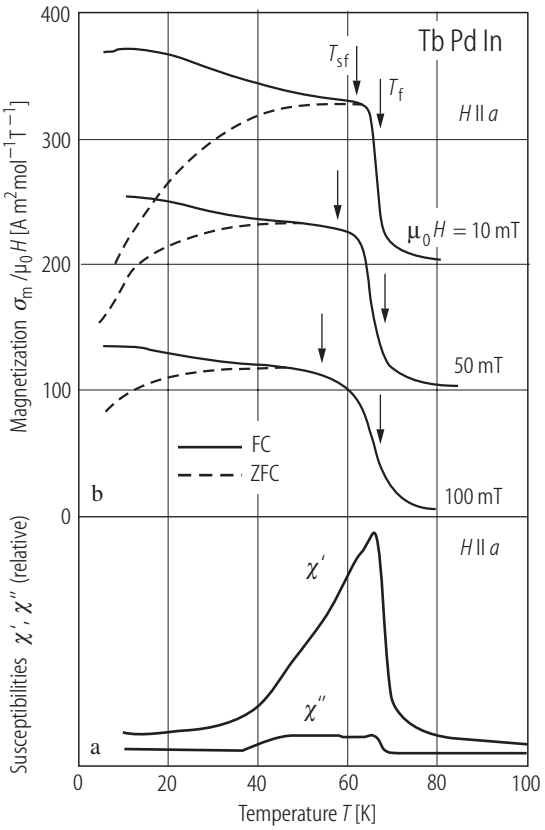

Fig. 152. TbPdIn. Temperature dependence of (**a**) χ', χ'' at $H \parallel a$ and (**b**) σ_m at different $H \parallel a$ [98N1].

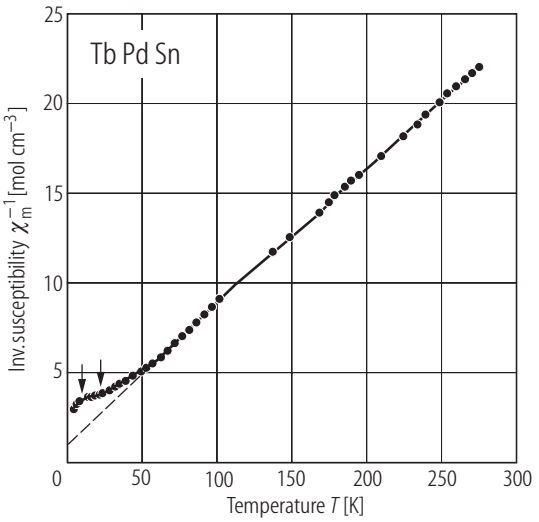

Fig. 153. TbPdSn. Temperature dependence of χ_m^{-1} [94A5].

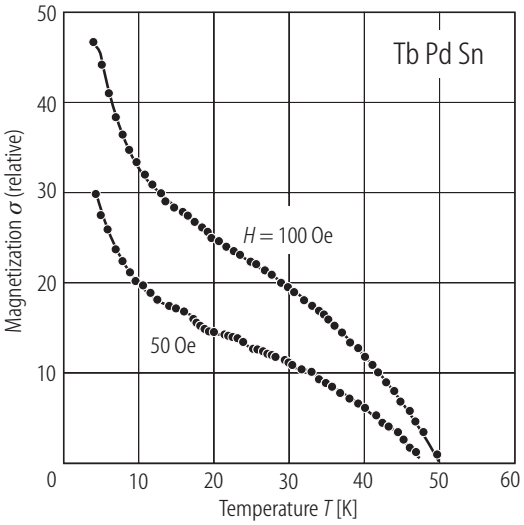

Fig. 154. TbPdSn. Temperature dependence of σ at 50 and 100 Oe [94A5].

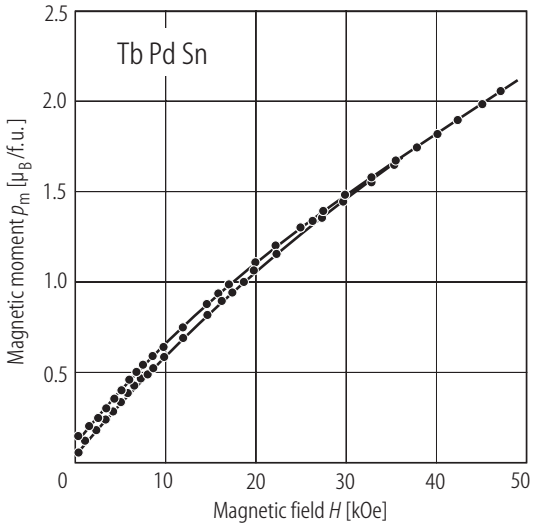

Fig. 155. TbPdSn. Magnetic field dependence of p_{FU} [94A5].

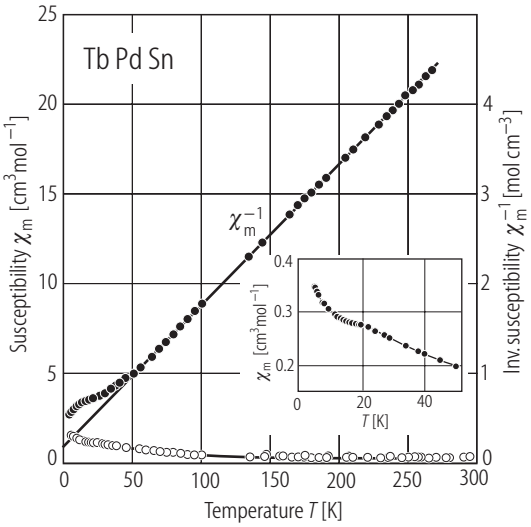

Fig. 156. TbPdSn. Temperature dependence of χ_m and χ_m^{-1} [95G2].

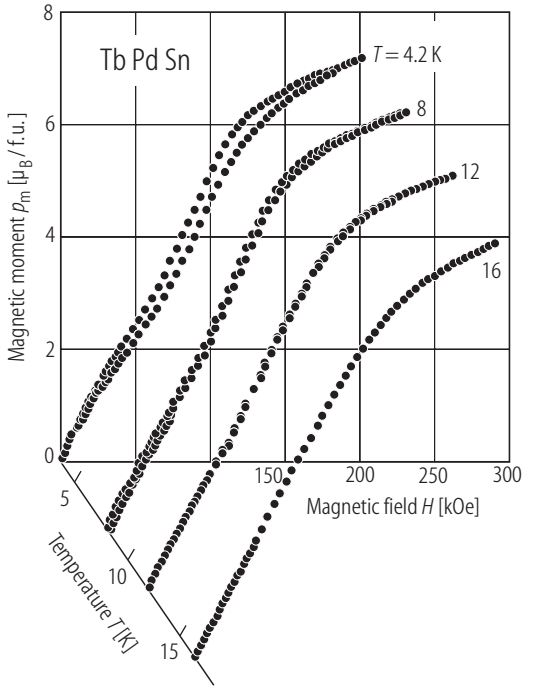

Fig. 157. TbPdSn. Magnetic field dependence of p_m at different temperatures [95G2].

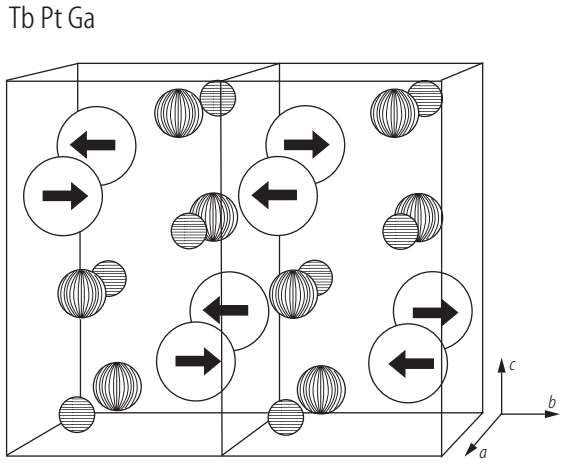

Fig. 158. TbPtGa. Antiferromagnetic unit cell, the arrows indicate the ordered Tb moments; nonmagnetic Pt and Ga atoms are shown by medium and small circles, respectively [94S3].

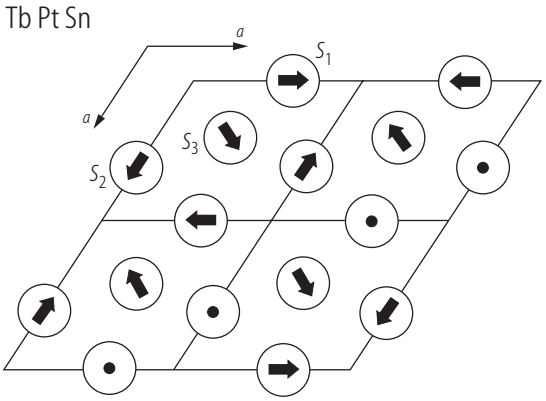

Fig. 159. TbPtSn. Schematic representation of the Tb^{3+} magnetic moment distribution in a layer, the moment directions in the adjacent layers below and above are the reverse; the magnetic unit cell is doubled along the *c* direction, the moments make an angle of 56° with the *c* axis [96S2].

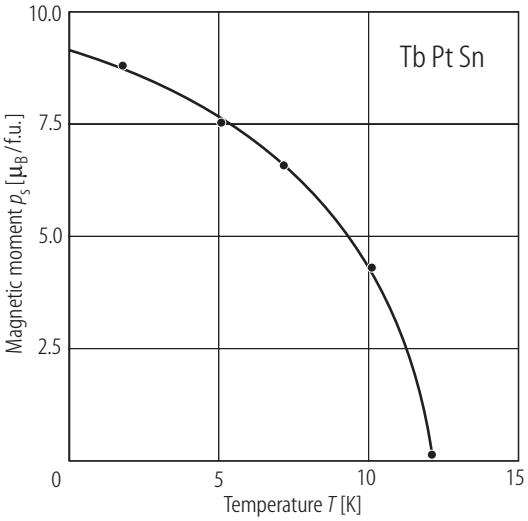

Fig. 160. TbPtSn. Temperature dependence of magnetization from neutron diffractiom [96S2].

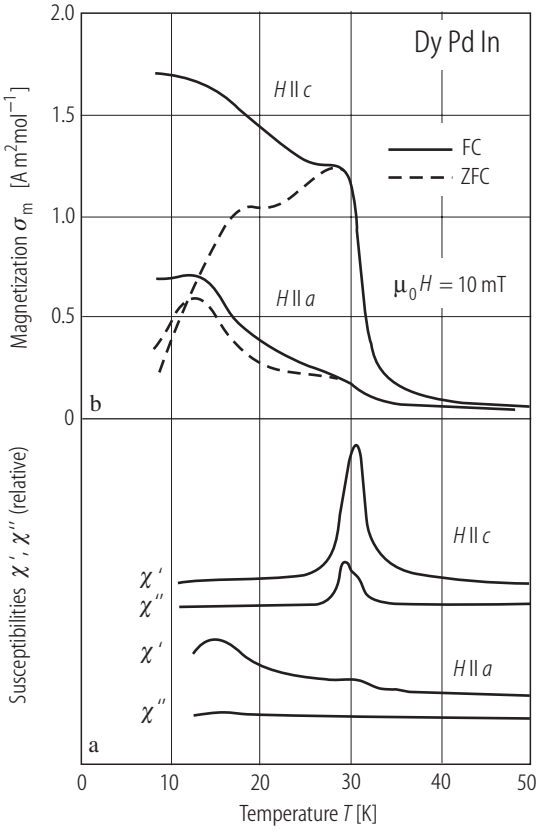

Fig. 161. DyPdIn. Temperature dependence of **(a)** χ', χ'' and **(b)** σ_m at $H \| a$ and c [98N1].

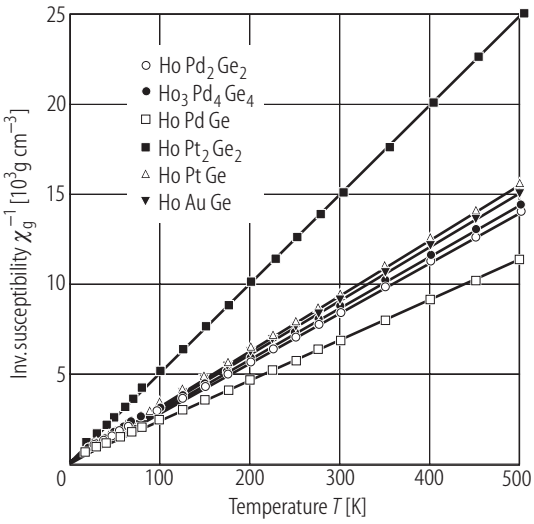

Fig. 162. $HoPd_2Ge_2$, $Ho_3Pd_4Ge_4$, HoPdGe, $HoPt_2Ge_2$, HoPtGe. Temperature dependence of χ_g^{-1}. Solid lines: calculated [96S1].

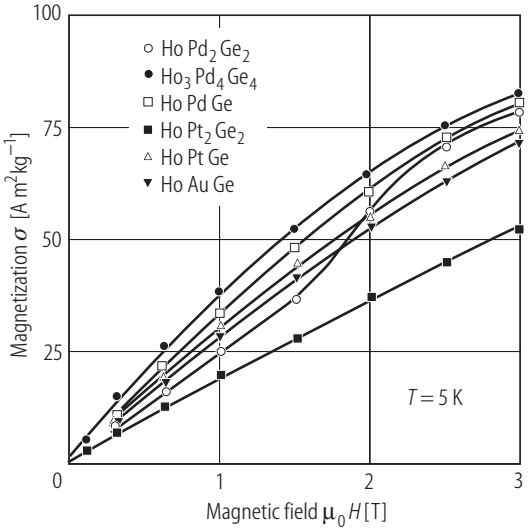

Fig. 163. $HoPd_2Ge_2$, $Ho_3Pd_4Ge_4$, HoPdGe, $HoPt_2Ge_2$, HoPtGe. Temperature dependence of σ at 5 K [96S1].

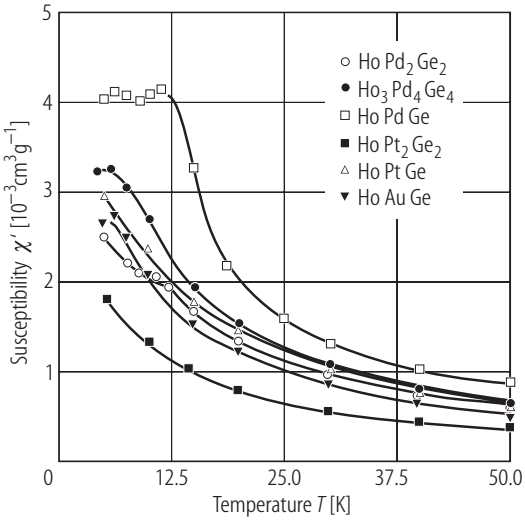

Fig. 164. $HoPd_2Ge_2$, $Ho_3Pd_4Ge_4$, HoPdGe, $HoPt_2Ge_2$, HoPtGe. Temperature dependence of χ' [96S1].

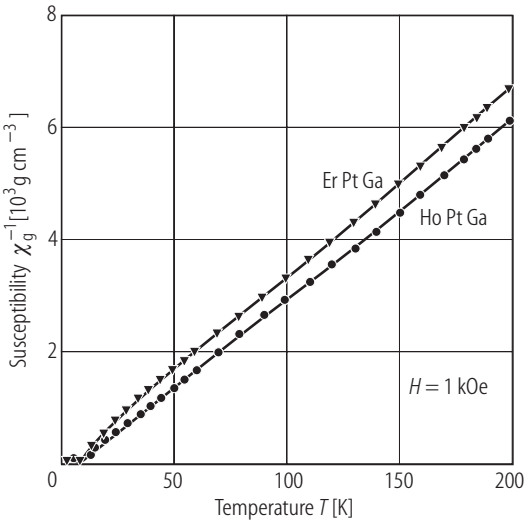

Fig. 165. HoPtGa, ErPtGa. Temperature dependence of χ_g^{-1} at $H = 1$ kOe [96K4].

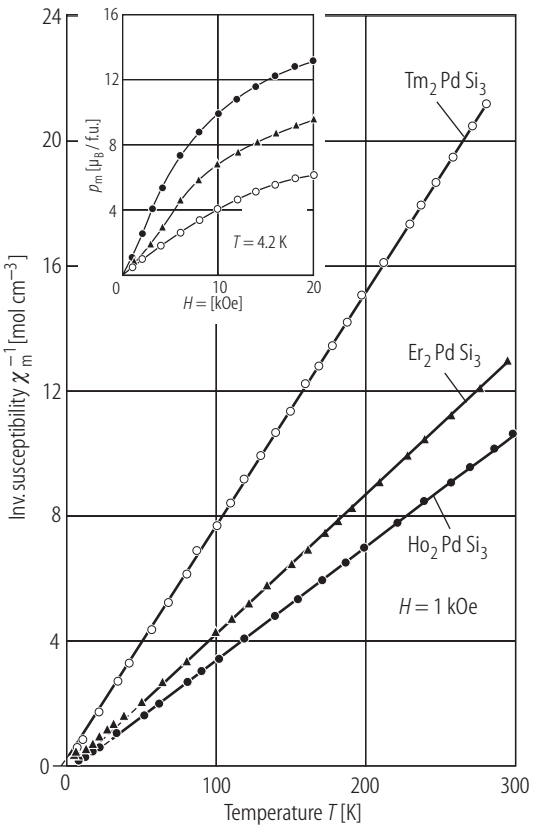

Fig. 166. Ho_2PdSi_3, Er_2PdSi_3, Tm_2PdSi_3. Magnetic field dependence of p_m at 4.2 K (inset) and temperature dependence of χ_m^{-1} at 1 kOe [90K3].

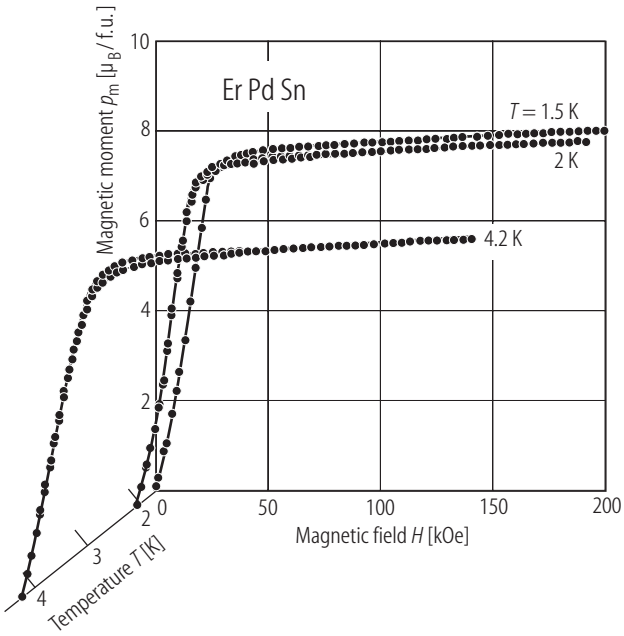

Fig. 167. ErPdSn. Magnetic field dependence of p_m at different temperatures [95A1].

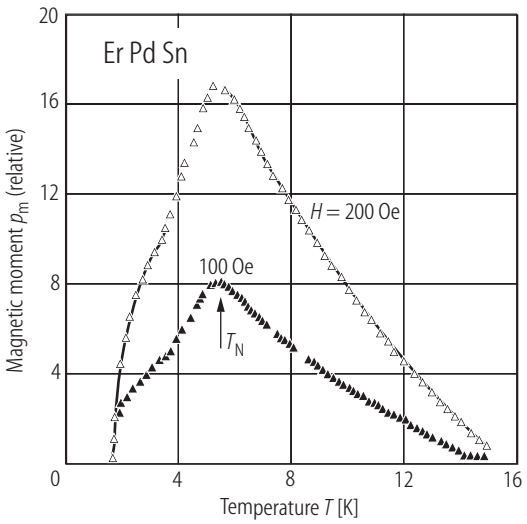

Fig. 168. ErPdSn. Temperature dependence of p_m at low temperatures and low magnetic fields. T_N = 5.2 K [95A1].

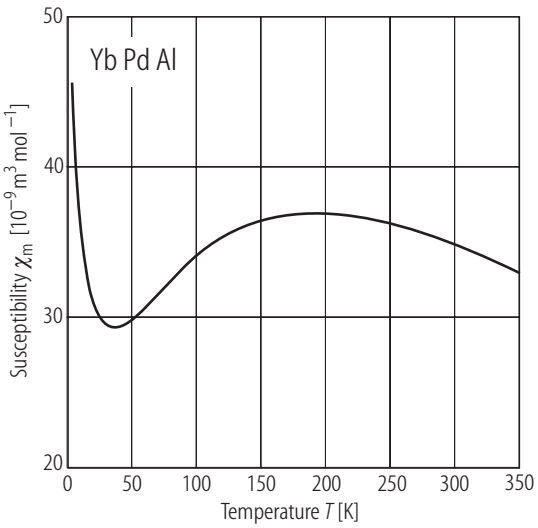

Fig. 169. YbPdAl. Temperature dependence of χ_m [93C1].

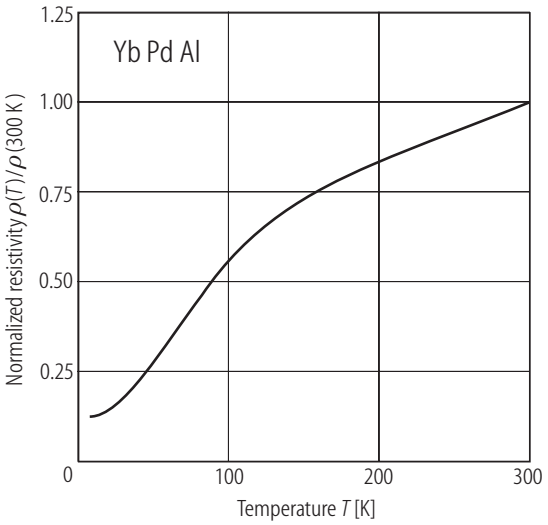

Fig. 170. YbPdAl. Temperature dependence of ρ [93C1].

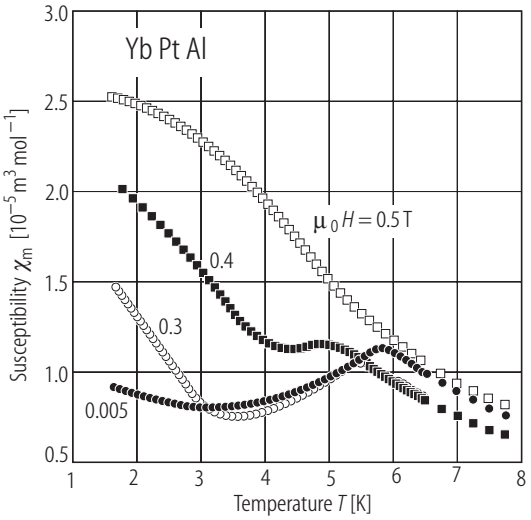

Fig. 172. YbPtAl. Temperature dependence of χ_m at $\mu_0 H$ = 0.005 T, 0.3 T, 0.4 T, and 0.5 T [95D1].

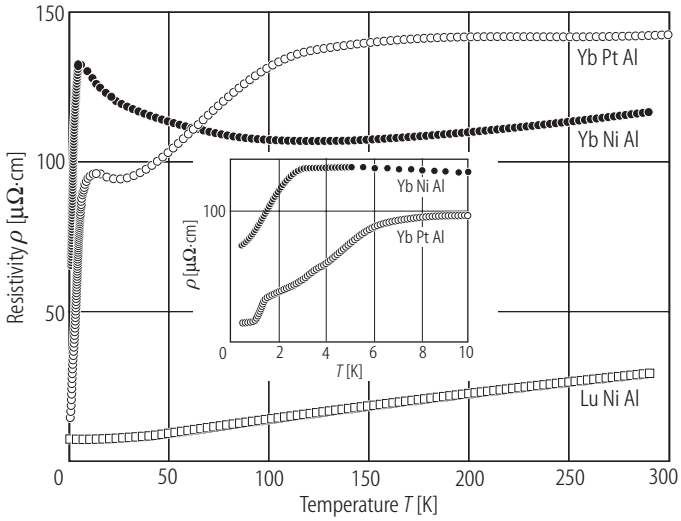

Fig. 171. YbNiAl, YbPtAl, LuNiAl. Temperature dependence of the resistivity. Inset: low-temperature region [95D1].

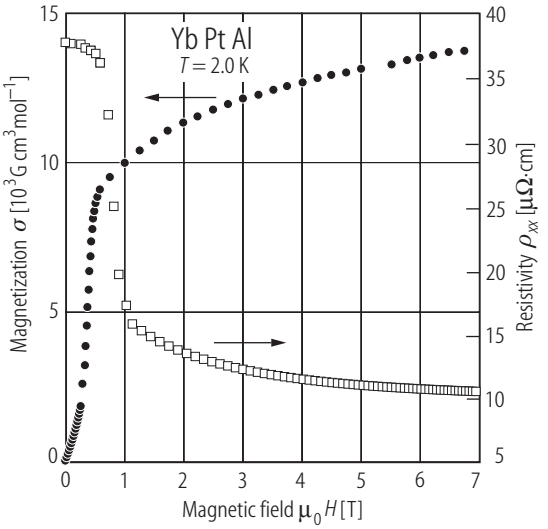

Fig. 173. YbPtAl. DC Magnetization and electrical resistivity vs. H at 2.0 K [95D1].

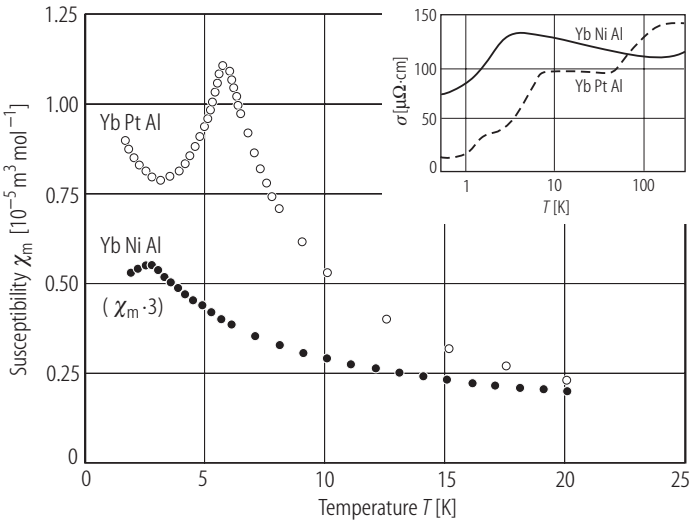

Fig. 174. YbNiAl, YbPtAl. Temperature dependence of χ_m. The values for YbNiAl are multiplied by a factor of three [95S4].

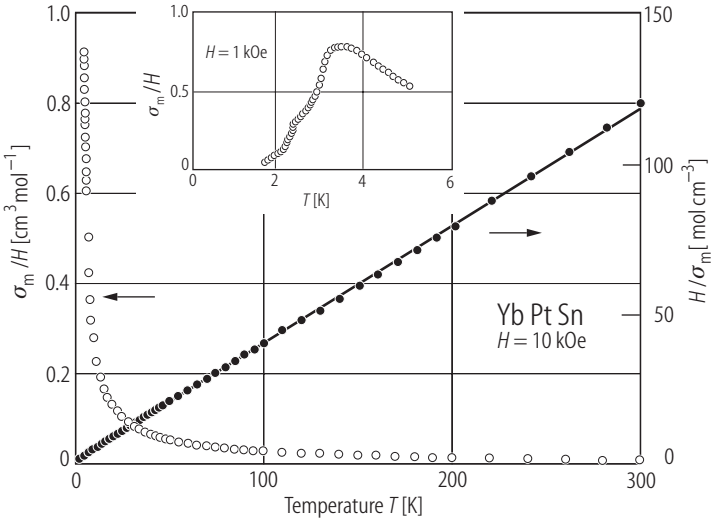

Fig. 175. YbPtSn. Temperature dependence of σ_m/H and H/σ_m, vs. T at H = 10 kOe [97K4].

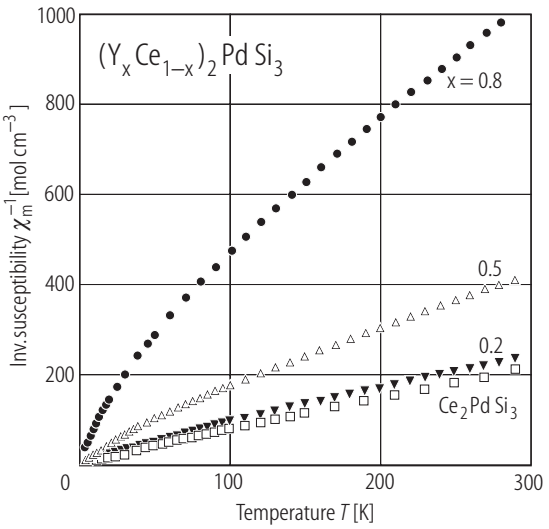

Fig. 176. $(Y_xCe_{1-x})_2PdSi_3$. Temperature dependence of χ_m^{-1} for various x [96M1].

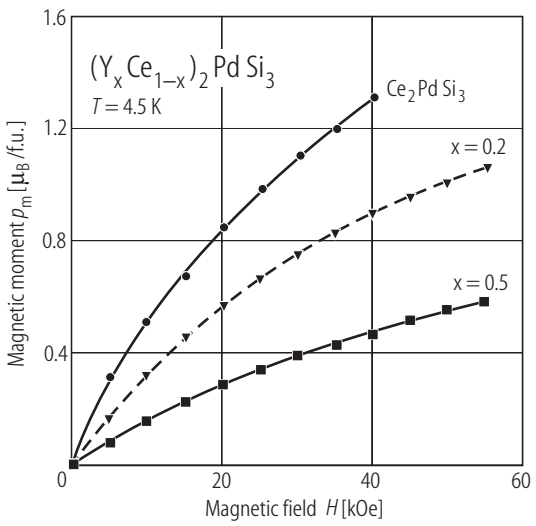

Fig. 177. $(Y_xCe_{1-x})_2PdSi_3$. Magnetic field dependence of p_m for various x at 4.5 K [96M1

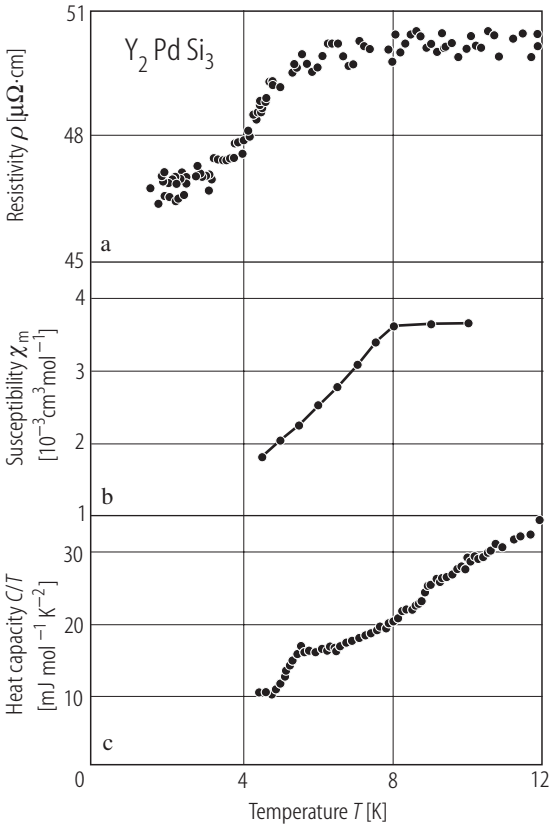

Fig. 178. Y_2PdSi_3. Temperature dependence of (**a**) ρ, (**b**) χ_m at 50 kOe, and (**c**) C/T [96M1].

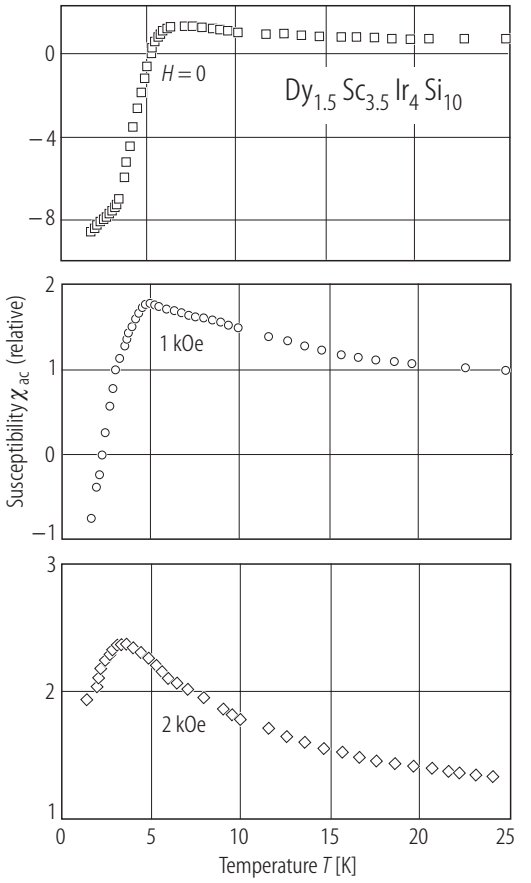

Fig. 179. $Dy_{1.5}Sc_{3.5}Ir_4Si_{10}$. Temperature dependence of ac χ_{ac} at H = 0, 1 kOe, and 2 kOe dc magnetic field [93G2].

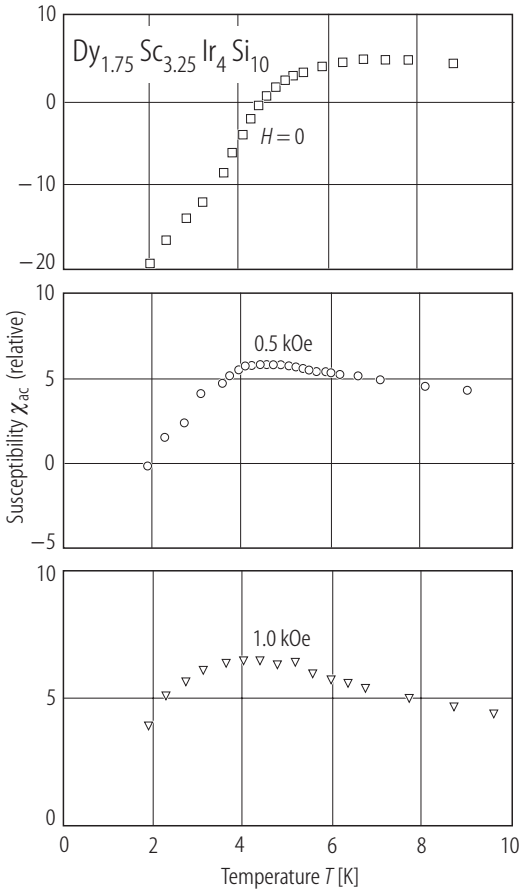

Fig. 180. $Dy_{1.75}Sc_{3.25}Ir_4Si_{10}$. Temperature dependence of ac χ_{ac} at H = 0, 0.5 kOe, and 1 kOe dc magnetic field [93G2].

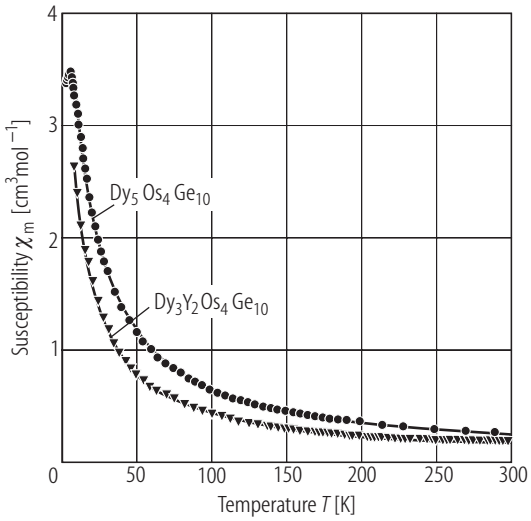

Fig. 181. $Dy_3Y_2Os_4Ge_{10}$, $Dy_5Os_4Ge_{10}$. Temperature dependence of χ_m. The solid lines are fits to the crystal-field model [96R1].

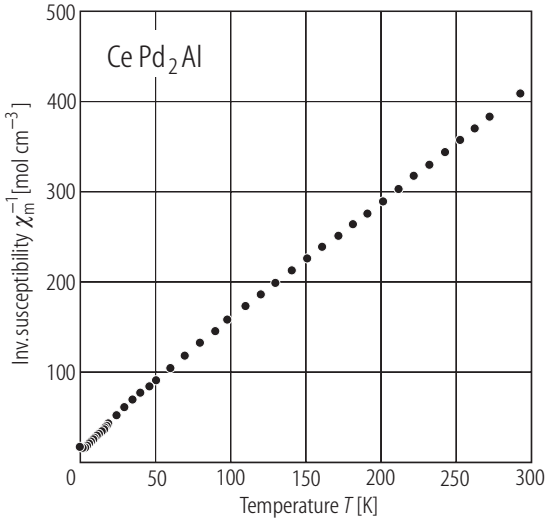

Fig. 182. $CePd_2Al$. Temperature dependence of χ_m^{-1} [95D2].

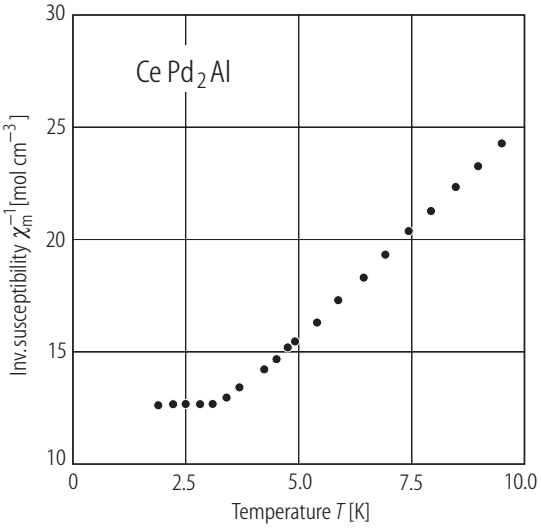

Fig. 183. $CePd_2Al$. Low-temperature dependence of χ_m^{-1} [95D2].

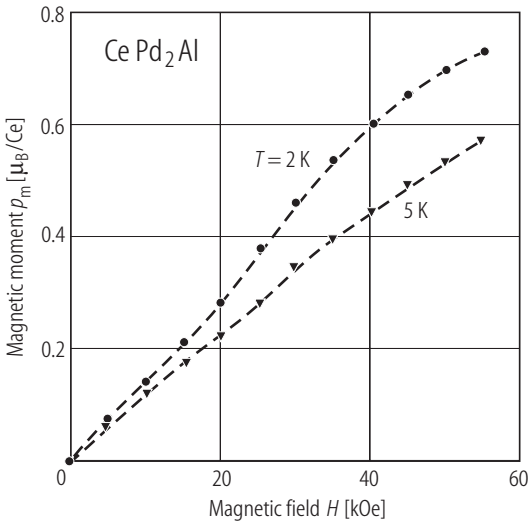

Fig. 184. $CePd_2Al$. Magnetic field dependence of p_m at 2 and 5 K [95D2].

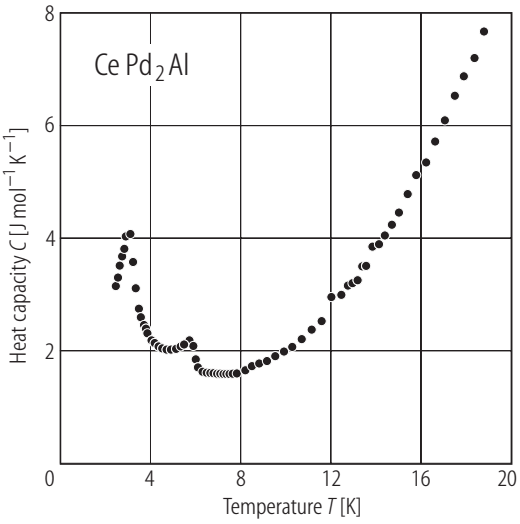

Fig. 185. $CePd_2Al$. Temperature dependence of heat capacity [95D2].

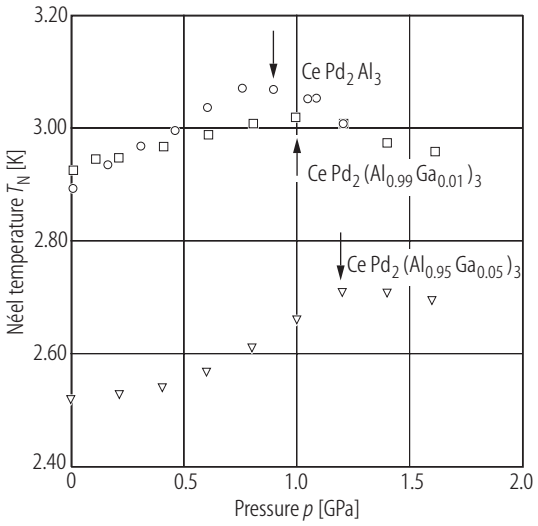

Fig. 186. $CePd_2(Al_{1-x}Ga_x)_3$. Pressure dependence of T_N. The arrows show the position of pressure p_{max} giving the maximum T_N [97T4].

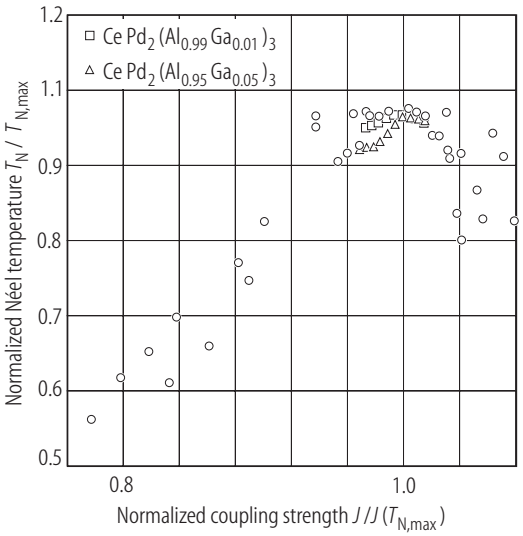

Fig. 187. $CePd_2(Al_{1-x}Ga_x)_3$. Magnetic transition temperature T_N vs. coupling strength normalized to their values where T_N exhibits a maximum value [97T4]. Circles show data from [94C2].

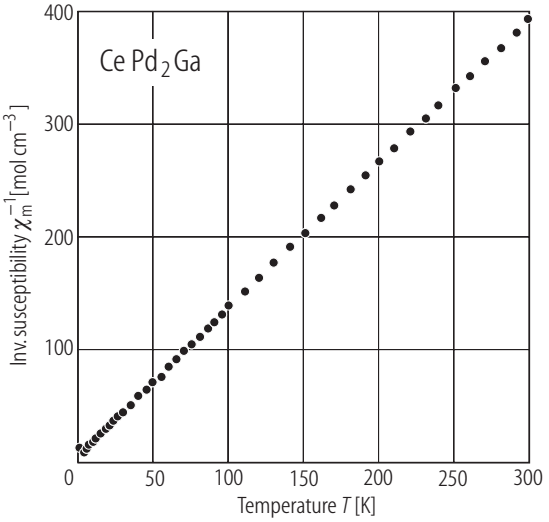

Fig. 188. $CePd_2Ga$. Temperature dependence of χ_m^{-1} [93D1].

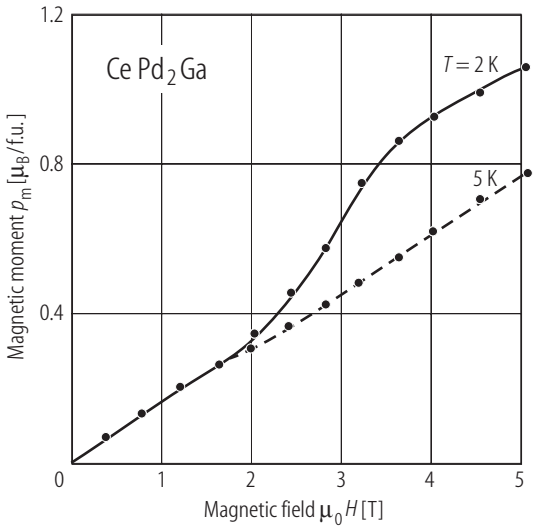

Fig. 189. $CePd_2Ga$. Magnetic field dependence of p_m [93D1].

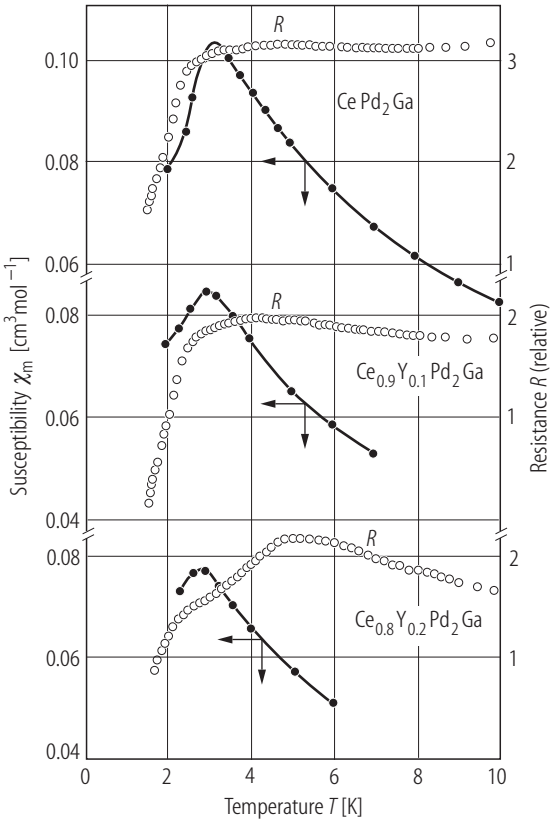

Fig. 190. $Ce_{1-x}Y_xPd_2Ga$. Temperature dependence of χ_m below 10 K. The respective electrical resistance R is also plotted in an arbitrary scale [93D1].

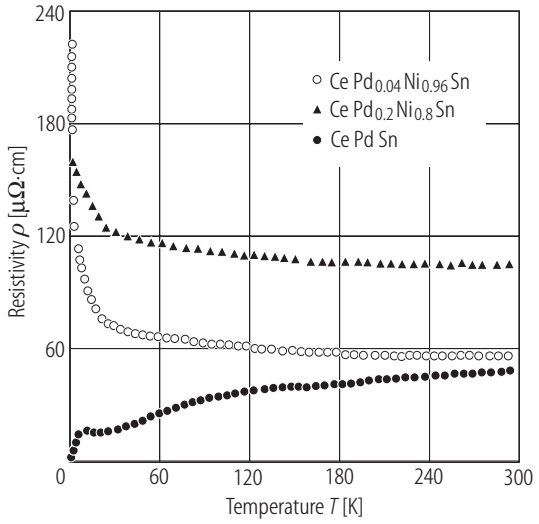

Fig. 191. $CePd_xNi_{1-x}Sn$. Temperature dependence of ρ for x = 0.04, 0.2, 1.0 [88K1].

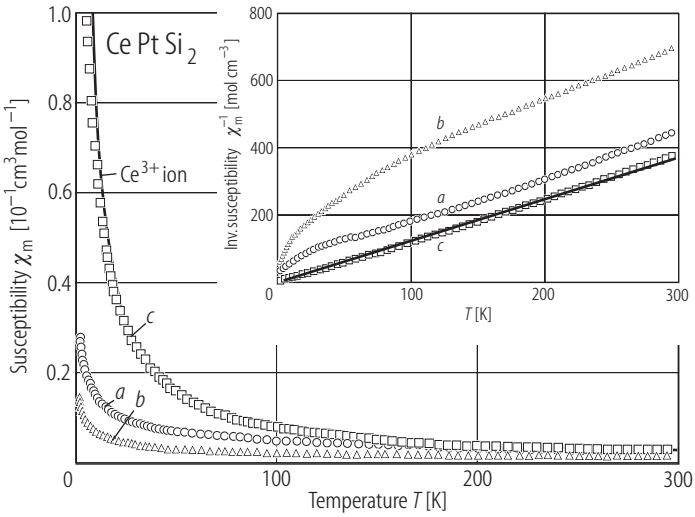

Fig. 192. $CePtSi_2$. Temperature dependence of χ_m and χ_m^{-1} along the *a, b* and *c* axis. Solid line represents $\chi_m(T)$ for Ce^{3+} free ion [96K5].

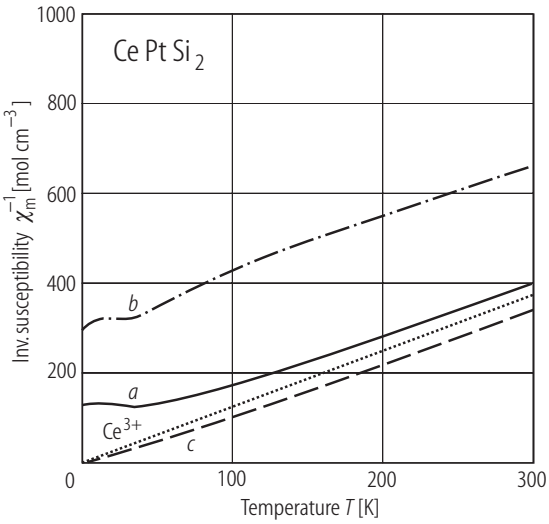

Fig. 193. $CePtSi_2$. Temperature dependence of χ_m^{-1} calculated taking into account crystalline-field effect ($T_K \approx 10$ K) [96K5].

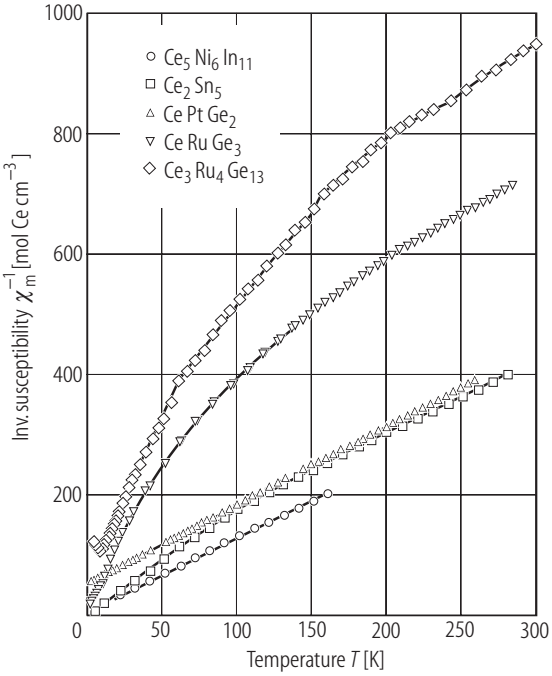

Fig. 194. $Ce_5Ni_6In_{11}$, Ce_2Sn_5, $CePtGe_2$, $CeRuGe_3$, $Ce_3Ru_4Ge_{13}$. Temperature dependence of χ_m^{-1} [96G2].

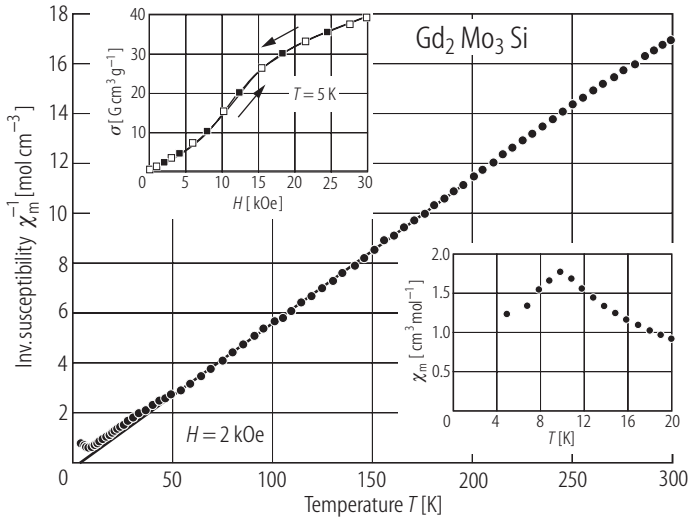

Fig. 195. $Gd_2Mo_3Si_4$. Temperature dependence of χ_m^{-1} at 2 kOe. Insets: χ_m vs. T and σ vs. H [95L1].

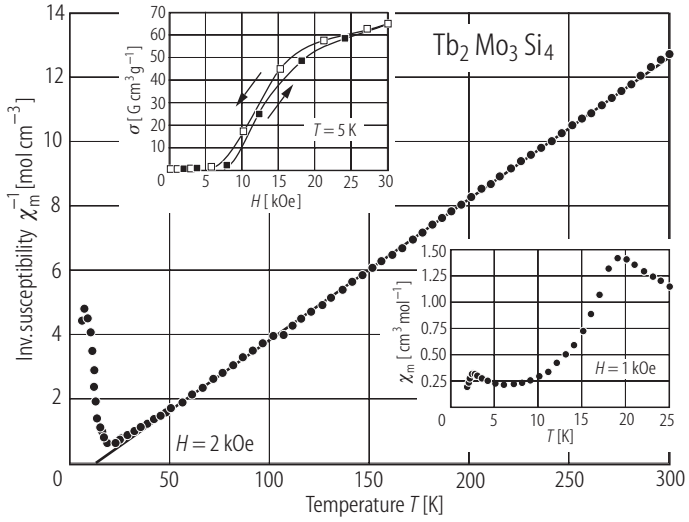

Fig. 196. $Tb_2Mo_3Si_4$. Temperature dependence of χ_m^{-1} at 2 kOe. Insets: χ_m vs. T and σ vs. H [95L1].

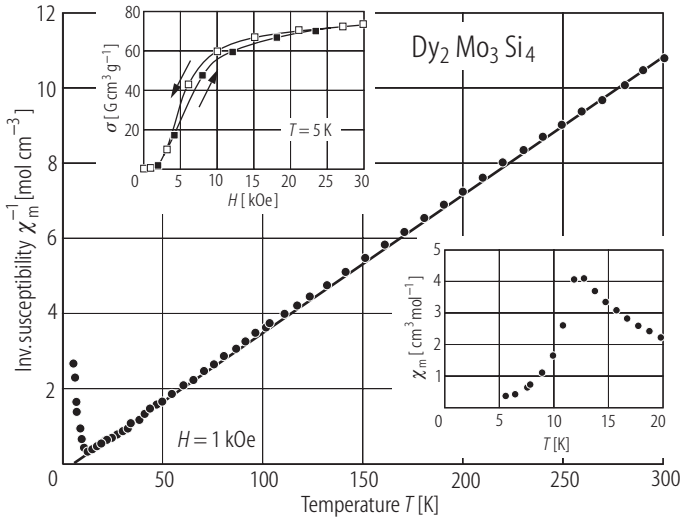

Fig. 197. $Dy_2Mo_3Si_4$. Temperature dependence of χ_m^{-1} at 1 kOe. Insets: χ_m vs. T and σ vs. H [95L1].

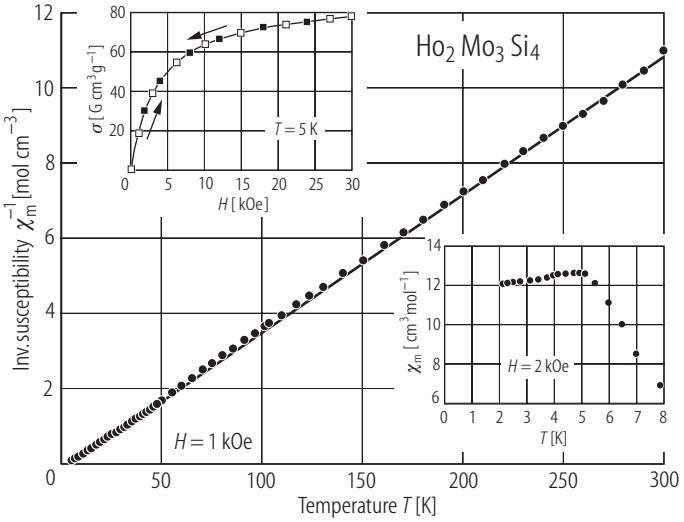

Fig. 198. $Ho_2Mo_3Si_4$. Temperature dependence of χ_m^{-1} at 1 kOe. Insets: χ_m vs. T and σ vs. H [95L1].

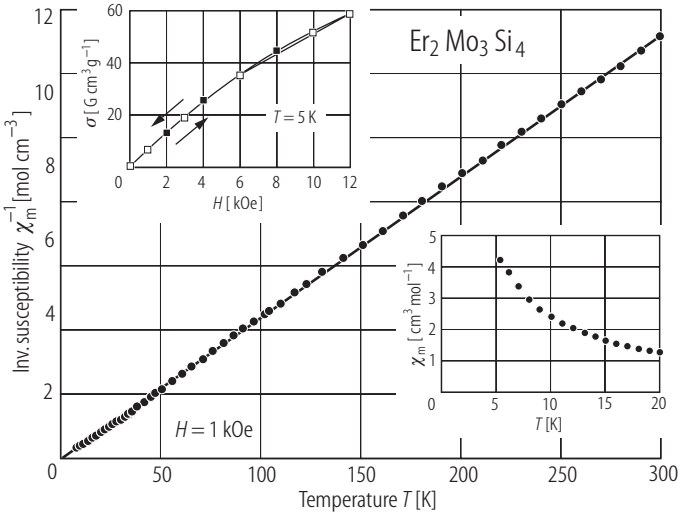

Fig. 199. $ErGd_2Mo_3Si_4$. Temperature dependence of χ_m^{-1} at 1 kOe. Insets: χ_m vs. T and σ vs. H [95L1].

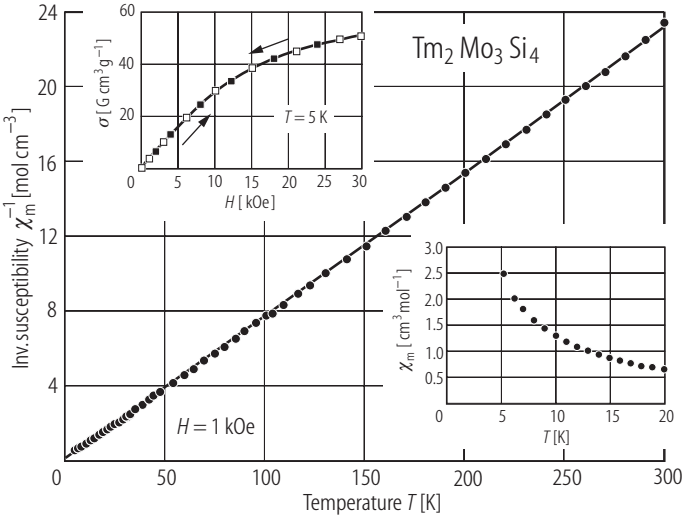

Fig. 200. $Tm_2Mo_3Si_4$. Temperature dependence of χ_m^{-1} at 1 kOe. Insets: χ_m vs. T and σ vs. H [95L1].

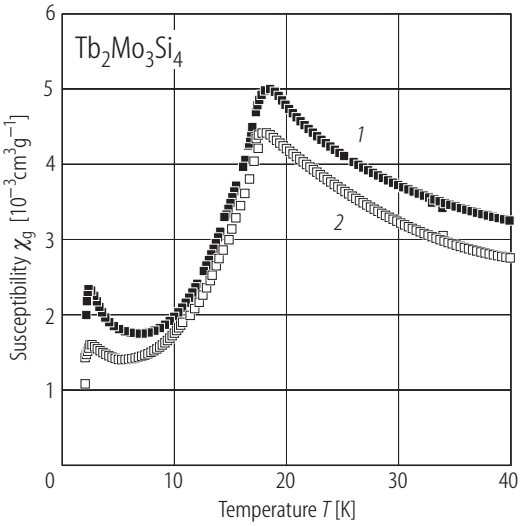

Fig. 201. $Tb_2Mo_3Si_4$. Temperature dependence of χ_g. Sample 1 annealed in vacuum at 800 K during 240 h and sample 2 at 1400 K for 1 h, respectively

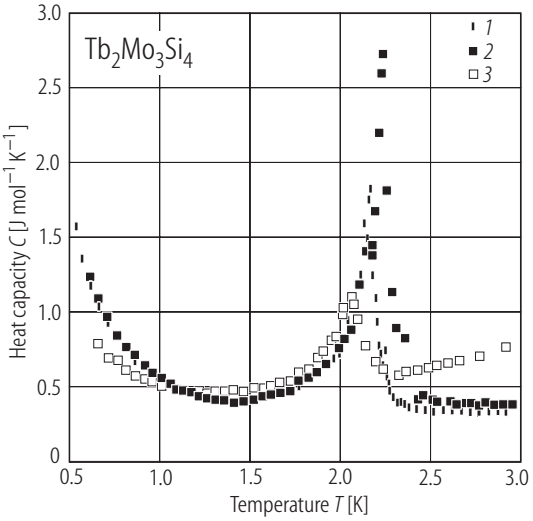

Fig. 202. $Tb_2Mo_3Si_4$. Temperature dependence of heat capacity. Sample 1 and 2 as in Fig. 201, sample 3 not annealed [94A4].

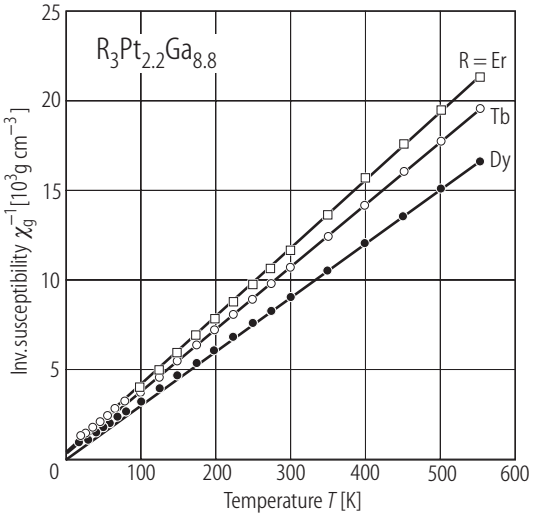

Fig. 203. $R_3Pt_{2.2}Ga_{8.8}$. R = Tb, Dy, Er. Temperature dependence of χ_g^{-1}. Solid lines: calculated [94G4].

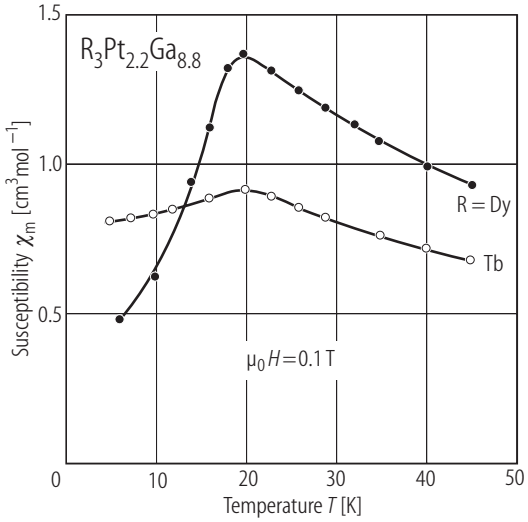

Fig. 204. $R_3Pt_{2.2}Ga_{8.8}$. R = Tb, Dy. Temperature dependence of χ_m at 0.1 T [94G4].

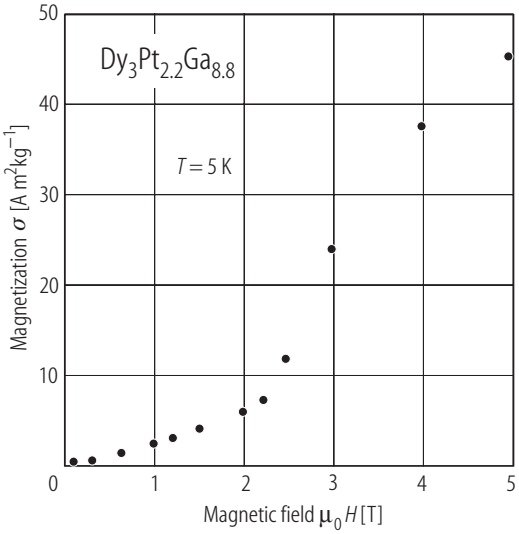

Fig. 205. $Dy_3Pt_{2.2}Ga_{8.8}$. Magnetic field dependence of σ at 5 K [94G4].

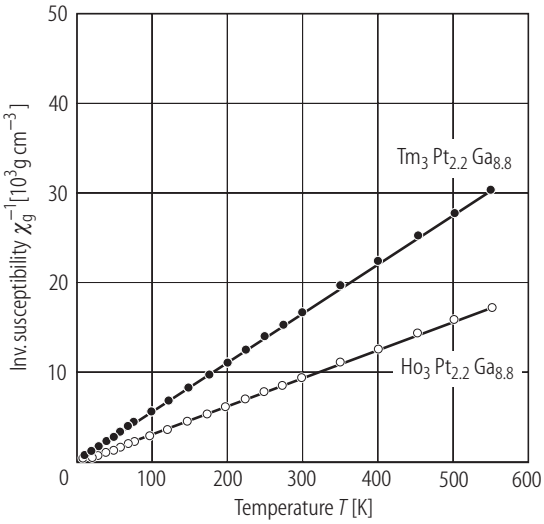

Fig. 206. $R_3Pt_{2.2}Ga_{8.8}$. R = Ho, Tm. Temperature dependence of χ_g^{-1}. Solid lines: calculated [94G4].

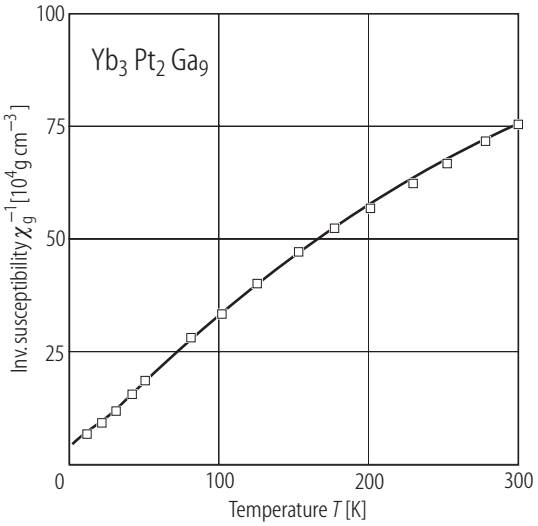

Fig. 207. $Yb_3Pt_2Ga_9$. Temperature dependence of χ_g^{-1} [94G4.].

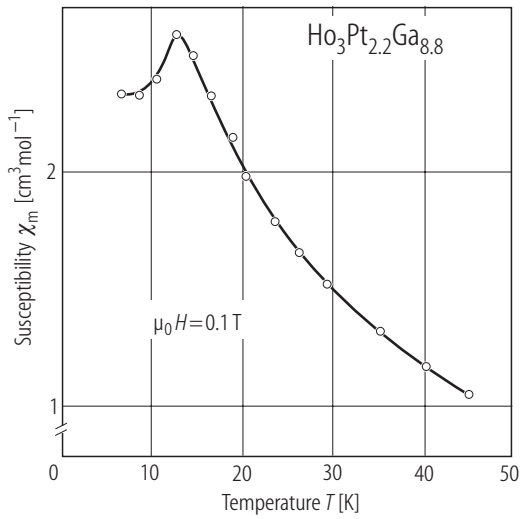

Fig. 208. $Ho_3Pt_{2.2}Ga_{8.8}$. Temperature dependence of χ_m at 0.1 T. Solid line: calculated [94G4].

References

88K1 Kasaya, M., Tani, T., Iga, F., Kasuya, T.: J. Magn. Magn. Mater. **76-77** (1988) 278

90K3 Kotsanidis, P., A., Yakinthos, J., K., Gamari-Seale, E.: J. Magn. Magn. Mater. **87** (1990) 199

93C1 Cordier, G., Friedrich, T., Henseleit, R., Grauel, A., Tegel, U., Schank, Ch., Geibel, Ch.: J. Alloys Comp. **201** (1993) 197

93D1 Das, I., Sampathkumaran, E.V., Chari, S., Gopalakrishnan, K.V.: J. Alloys Comp. **202** (1993) L7

93G2 Ghosh, K., Ramakrishnan, S., Nigan, A.K., Chandra, G.: J. Appl. Phys. **73** (1993) 6637

94A4 Aliev, F.G., Gorelenko, Yu.K., Pryadun, V.V., Vieira, S., Villar, R., Paredes, J.: Physica B **194-196** (1994) 171

94A5 Andre, G., Bouree, F., Bombik, A., Oles, A., Sikora, W., Kolenda, M., Szytula, A., Pacyna, A., Zygmunt, A.: Acta Phys. Pol. **85** (1994) 275

94C2 Cornelius, A.L., Schilling, J.S.: Phys. Rev. B **49** (1994) 3955

94G4 Gignoux, D., Schmitt, D.: J. Magn. Magn. Mater. **129** (1994) 53

94S3 Schäfer, W., Jansen, E., Will, G., Kosanidis, P.A., Yakinthos, J.K., Tietze-Jaensch.: J. Alloys Comp. **209** (1994) 225

95A1 Andre, G., Bouree, F., Guillot, M., Kolenda, M., Oles, A., Sikora, W., Szytula, A., Zygmunt, A.: J. Magn. Magn. Mater. **140-144** (1995) 879

95D1 Diehl, J., Davideit, H., Klimm, S., Tegel, U., Geibel, C., Steglich, F., Horn, S.: Physica B **206-207** (1995) 344

95D2 Das, I., Sampathkumaran, E.V., Rajarajan, A.K.: J. Alloys Comp. **218** (1995) L11

95G2 Guillot, M., Szytula, A., Tomkowicz, Z., Zach, R.: J. Alloys Comp. **226** (1995) 131

95L1 Le Bihan, T., Noel, H.: J. Alloys Comp. **227** (1995) 154

95S2 Sakurai, J., Kegai, K., Kuwai, T., Isikawa, Y., Nisimura, K., Mori, K.: J. Magn. Magn. Mater. **140-144** (1995) 875

95S4 Schank, C., Olesch, G., Kohler, J., Tegel, U., Klinger, U., Diehl, J., Klimm, S., Sparn, G., Horn, S., Geibel, C., Steglich, F.: J. Magn. Magn. Mater. **140-144** (1995) 1237

96G2 Gschneidner, jr., K.A., Pecharsky, V.K.: Physica B **223-224** (1996) 131

96K4 Kotsanidis, P.A., Jakinthos, J.K., Schafer, W., Gamari-Seale, Hel.: J. Alloys Comp. **235** (1996) 188

96K5 Kasaya, M., Ito, M., Ono, A., Sakai, O.: Physica B **223-224** (1996) 336

96M1 Malik, R., Sampathkumaran, E.V.: J. Magn. Magn. Mater. **164** (1996) L13

96R1 Ramakrishnan, S., Ghosh, K.: Physica B **223-224** (1996) 154

96S1 Sologub, O., Hiebl, K., Rogl, P., Noel, H.: J. Alloys Comp. **245** (1996) L13

96S2 Szytula, A., Kolenda, M., Leciejewicz, J., Stuesser, N.: J. Magn. Magn. Mater. **164** (1996) 377

97K4 Katoh, K., Tababatake, T., Minami, A., Oguro, I., Sawa, H.: J Alloys Comp. **261** (1997) 32

97T4 Tang, J., Kitazawa, H., Matsushita, A., Matsumoto, T.: Physica B **230-232** (1997) 208

98I1 Ito, T., Nishigori, S., Hiromitsu, I., Kurisu, M.: J. Magn. Magn. Mater. **177-181** (1998) 1079

98N1 Nishigori, S., Hirooka, Y., Ito, T.: J. Magn. Magn. Mater. **177-181** (1998) 137

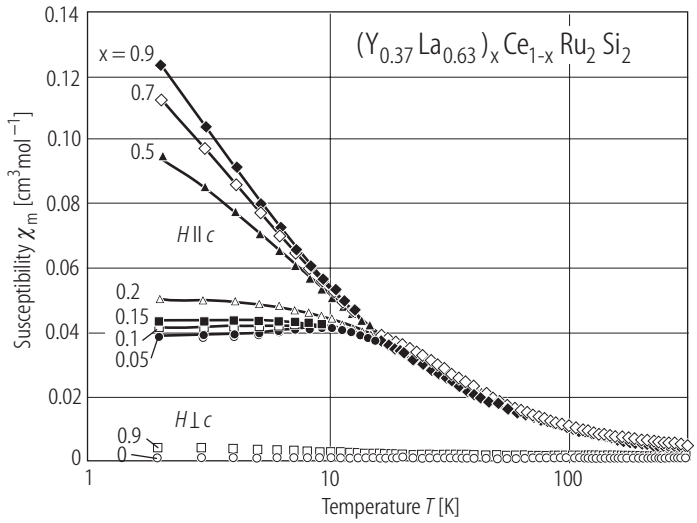

Fig. 209. $(Y_{0.37}La_{0.63})_xCe_{1-x}Ru_2Si_2$. Temperature dependence of χ_m for different x [95M2].

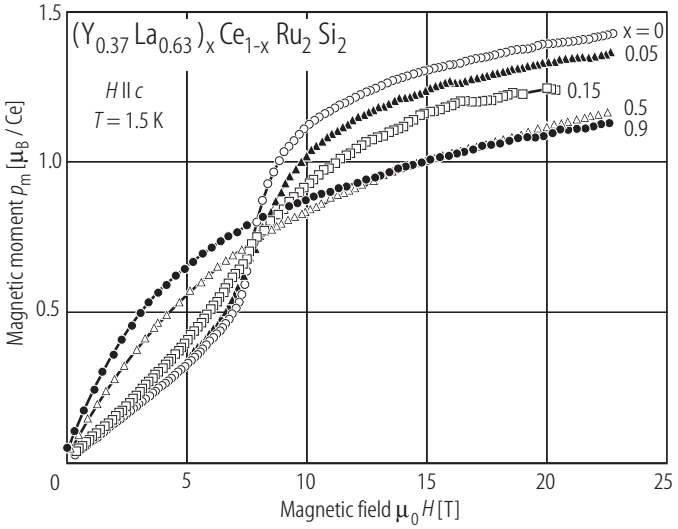

Fig. 210. $(Y_{0.37}La_{0.63})_xCe_{1-x}Ru_2Si_2$. Magnetization vs. H for different x and $H \parallel c$ at 1.5 K [95M2].

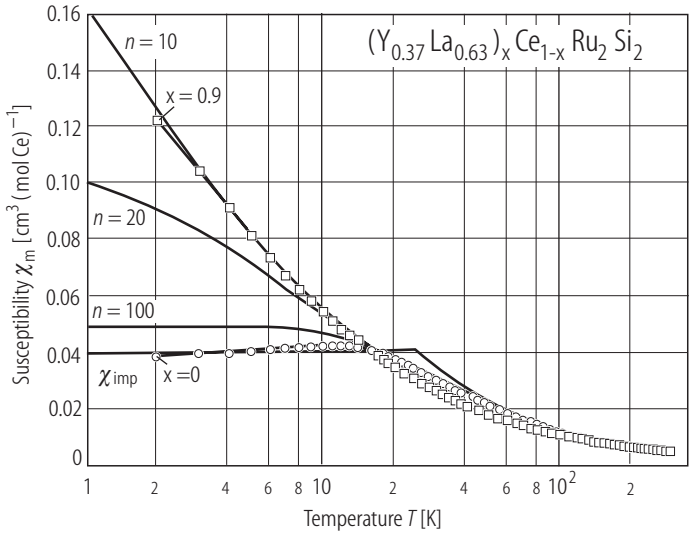

Fig. 211. $(Y_{0.37}La_{0.63})_xCe_{1-x}Ru_2Si_2$. Simulation of $\chi(T)$ for random lattice Kondo system, data for x = 0 and x = 0.9. For comparison see Fig. 209. χ_{imp}: Kondo impurity susceptibility, n: density of the Ce ions in a region of the simulations [95M2].

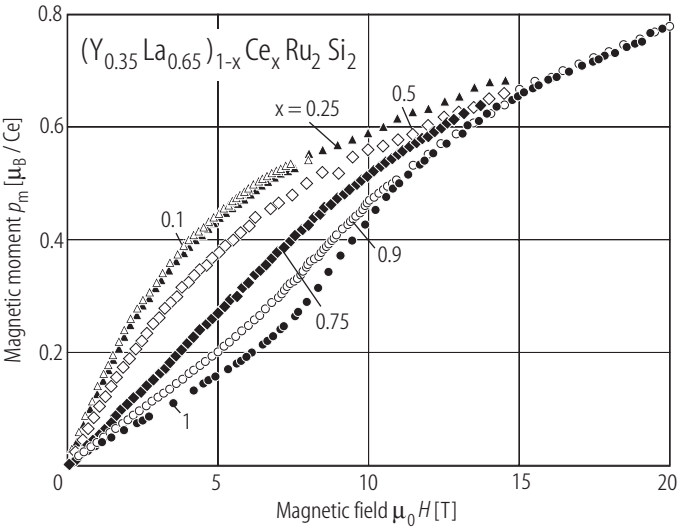

Fig. 212. $(Y_{0.35}La_{0.65})_{1-x}Ce_xRu_2Si_2$. Magnetization vs. H for different x [95M1].

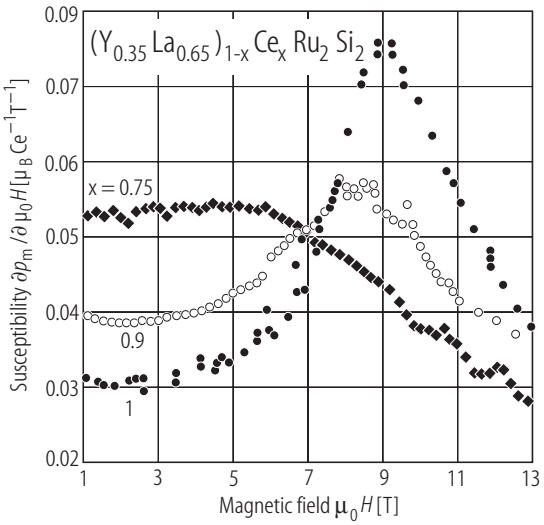

Fig. 213. $(Y_{0.35}La_{0.65})_{1-x}Ce_xRu_2Si_2$. Differential susceptibility $\partial p_m/\partial H$ vs. H for different x [95M1].

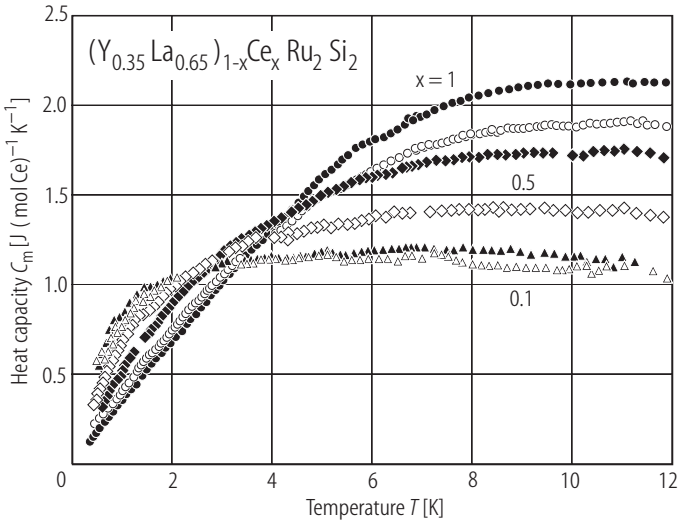

Fig. 214. $(Y_{0.35}La_{0.65})_{1-x}Ce_xRu_2Si_2$. Temperature dependence of the 4f-derived specific heat C_m [95M1].

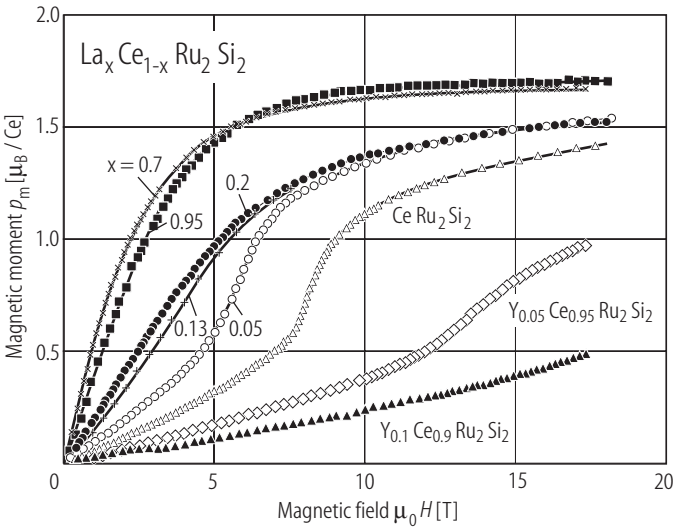

Fig. 215. $Y_yCe_{1-y}Ru_2Si_2$, $La_xCe_{1-x}Ru_2Si_2$. Magnetic field dependence of p_m in the paramagnetic region for several concentrations and $H \parallel c$ at 4.2 K, except for y = 0.05, x = 0 and 0.05 at 1.4 K, and for x = 0.2 at 6 K [88H1].

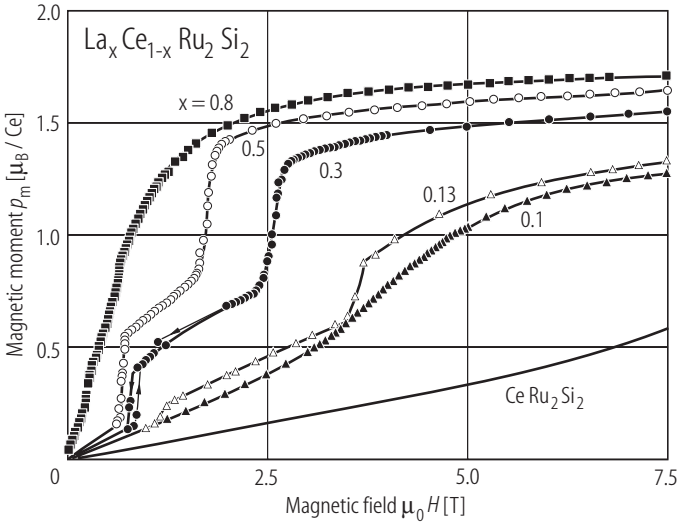

Fig. 216. $La_xCe_{1-x}Ru_2Si_2$. Magnetic field dependence of p_m below T_N (≈ 1.4 K). The continuous line represents $p_m(H \parallel c)$ for x = 0 at 1.4 K [88H1].

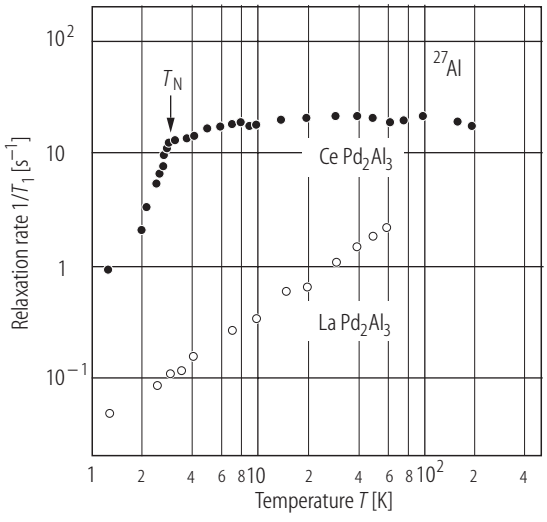

Fig. 217. $LaPd_2Al_3$, $CePd_2Al_3$. NMR, temperature dependence of $1/T_1$ for ^{27}Al [94F1].

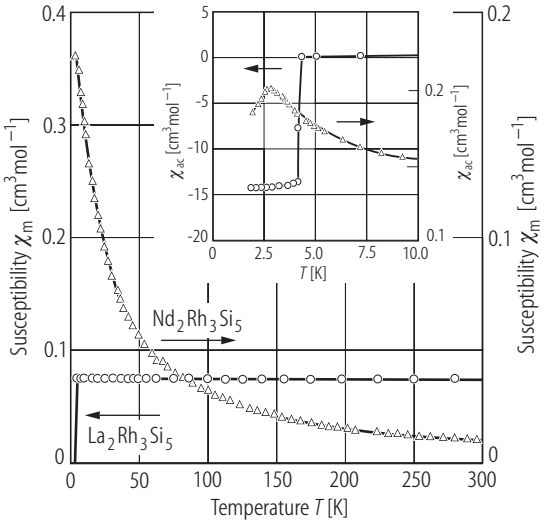

Fig. 218. $La_2Rh_3Si_5$, $Nd_2Rh_3Si_5$. Temperature dependence of χ_m and low temperature χ_{ac} [96P1].

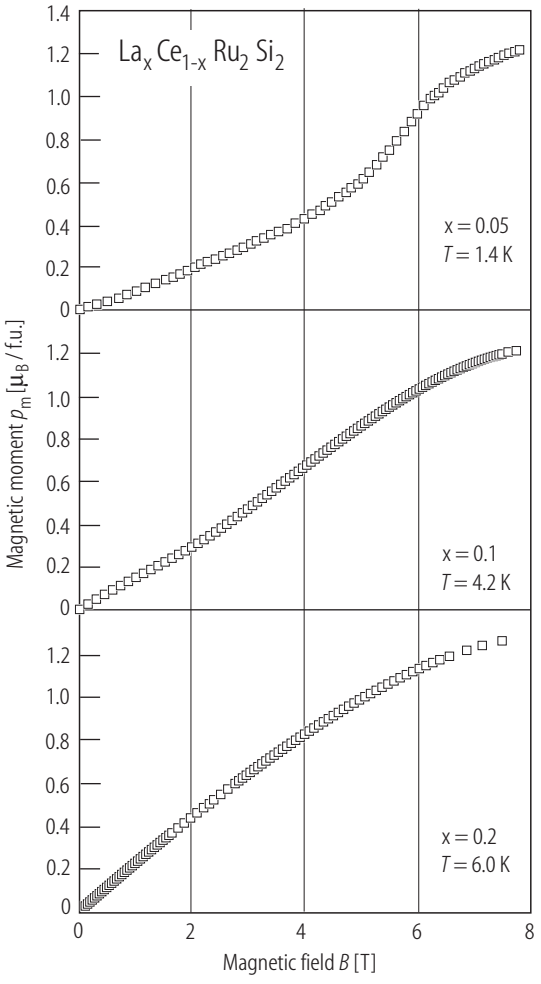

Fig. 219. $La_xCe_{1-x}Ru_2Si_2$. Magnetic field dependence of p_m along the *c* axis at 1.4 K, 4.2 K and 6.0 K for x = 0.05, 0.10 and 0.20, respectively, along the *c* axis [88L1].

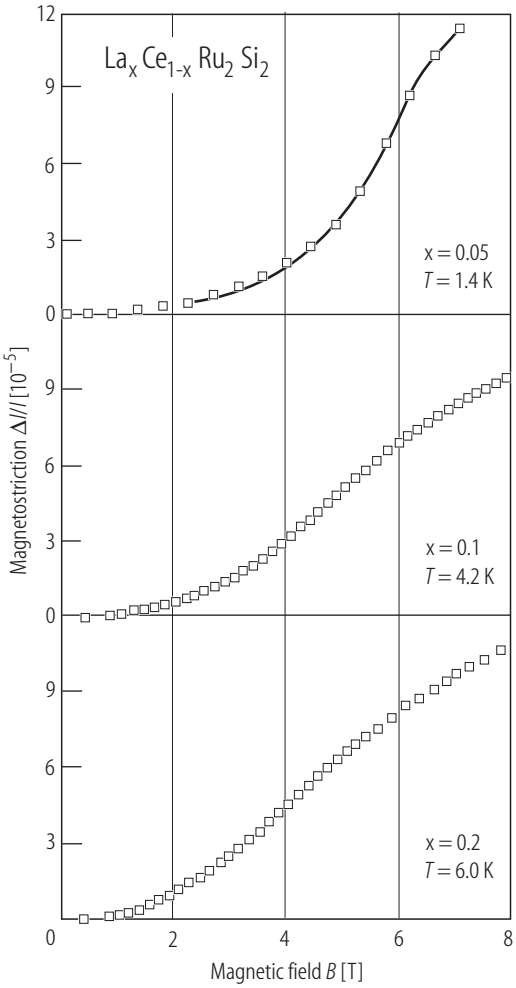

Fig. 220. $La_xCe_{1-x}Ru_2Si_2$. Magnetic field dependence of magnetostriction along the *c* axis at 1.4 K , 4.2 K and 6.0 K for x = 0.05, 0.10 and 0.20, respectively, along the *c* axis [88L1].

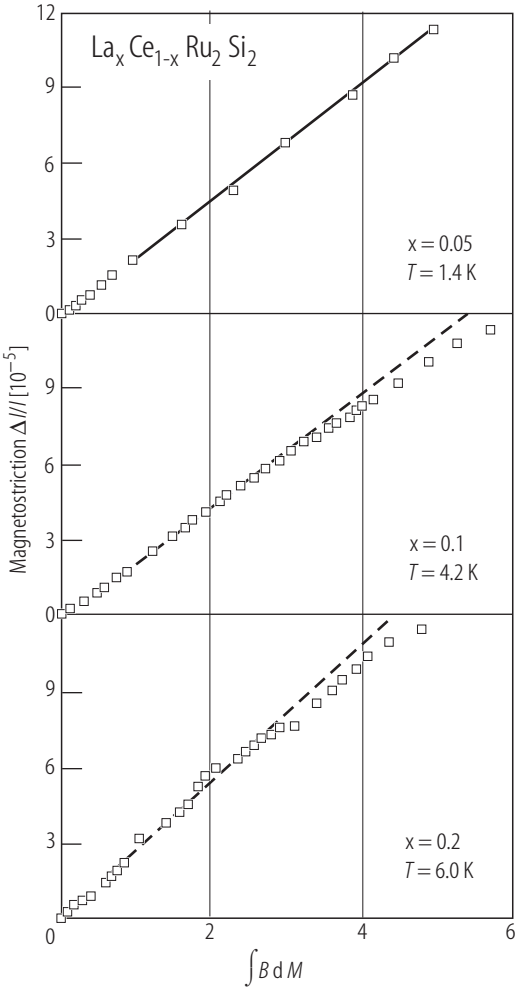

Fig. 221. $La_xCe_{1-x}Ru_2Si_2$. $\int B\mathrm{d}M$ dependence of magnetostriction at 1.4 K, 4.2 K and 6.0 K for x = 0.05, 0.10 and 0.20, respectively, along the *c* axis [88L1].

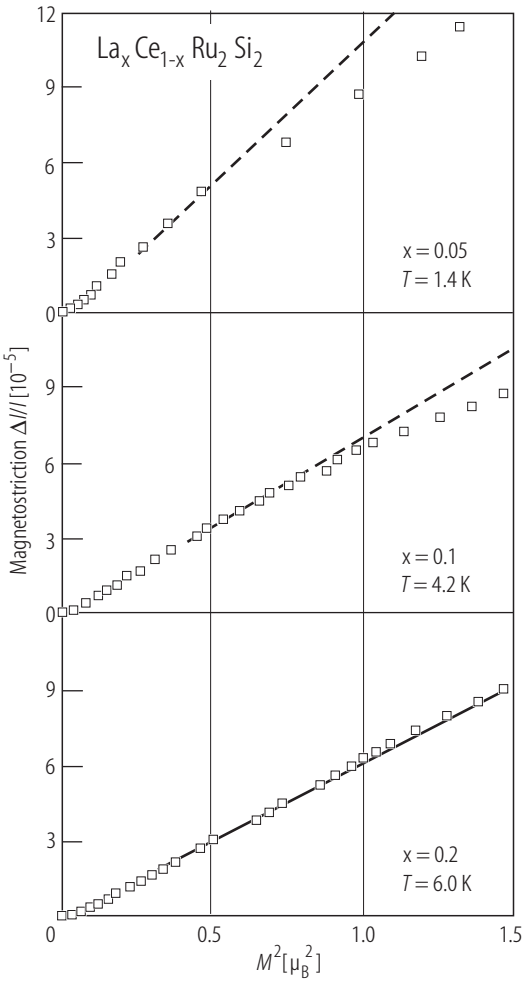

Fig. 222. $La_xCe_{1-x}Ru_2Si_2$. $M^2[\mu_B^2]$ dependence of magnetostriction at 1.4 K, 4.2 K and 6.0 K for x = 0.05, 0.10 and 0.20, respectively, along the *c* axis [88L1].

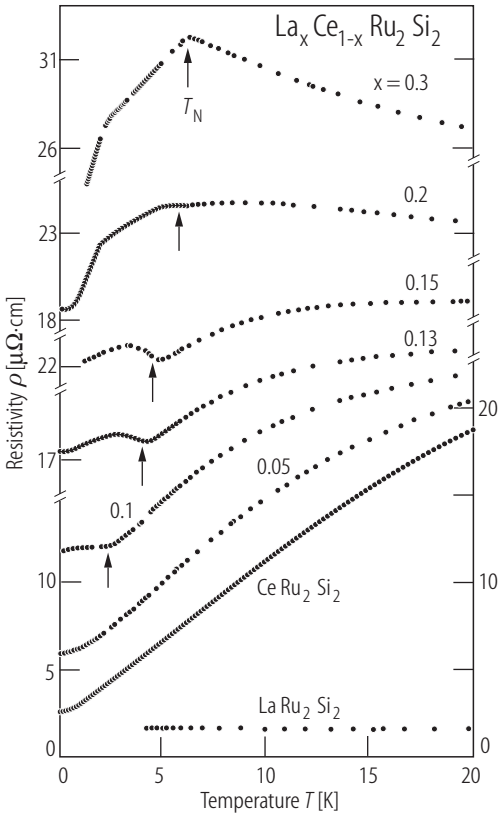

Fig. 223. $La_xCe_{1-x}Ru_2Si_2$. Temperature dependence of ρ at different x. Notice the change of scales. Néel temperatures are indicated by arrows [88D1].

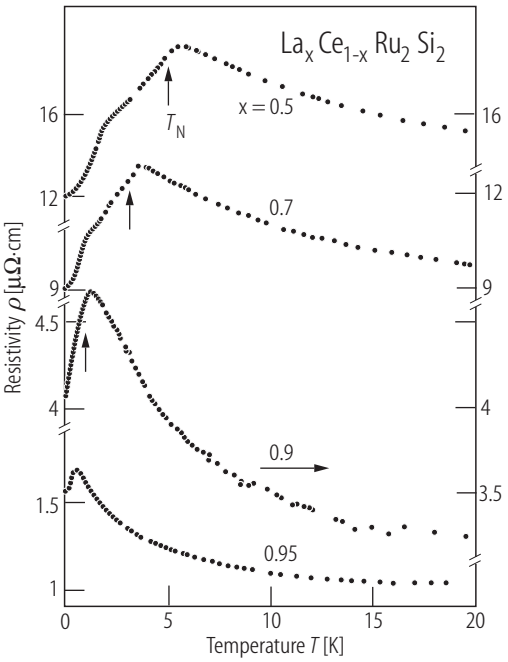

Fig. 224. $La_xCe_{1-x}Ru_2Si_2$. Temperature dependence of ρ at different x. Notice the change of scales. Néel temperatures are indicated by arrows [88D1].

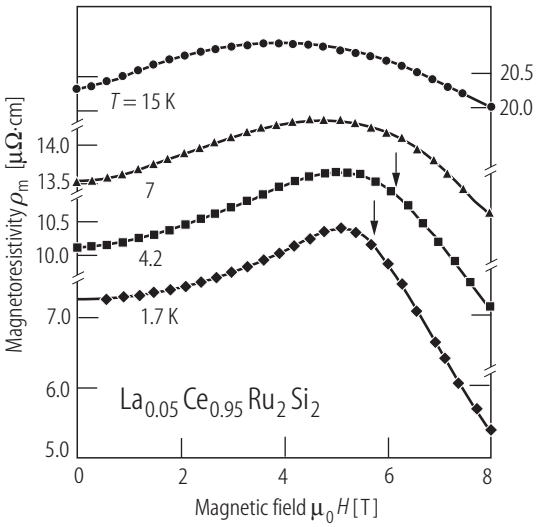

Fig. 225. $La_{0.05}Ce_{0.95}Ru_2Si_2$. Magnetic field dependence of ρ_m. Note the change of scale for each curve. For the lowest temperatures, the arrows indicate the metamagnetic field value deduced from magnetization measurements (Fig. 215) [88D2].

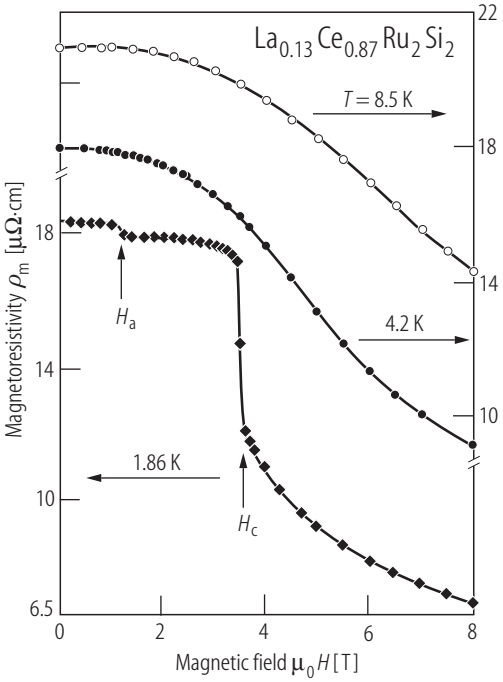

Fig. 226. $La_{0.13}Ce_{0.87}Ru_2Si_2$. Magnetic field dependence of ρ_m for 1.86 K. The two transition fields are indicated by vertical arrows [88D2].

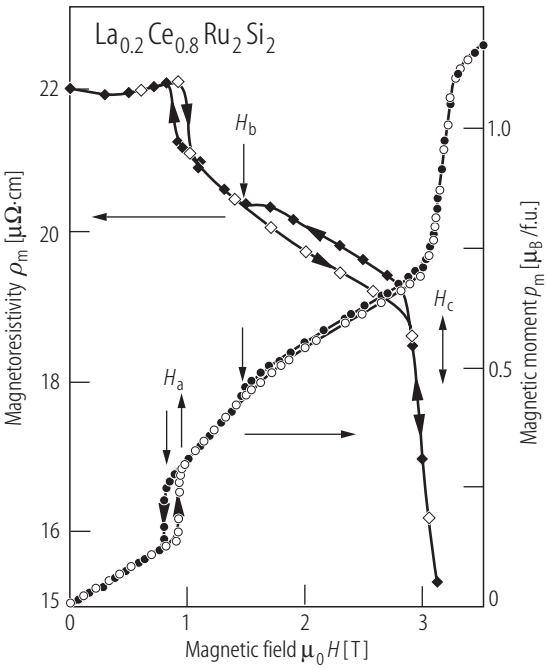

Fig. 227. $La_{0.2}Ge_{0.8}Ru_2Si_2$. Magnetic field dependence of ρ_m and p_m at 1.7 K in increasing (open symbols) and decreasing (solid symbols) H. Hysteresis is observed at H_a and between H_c and H_b [88D2].

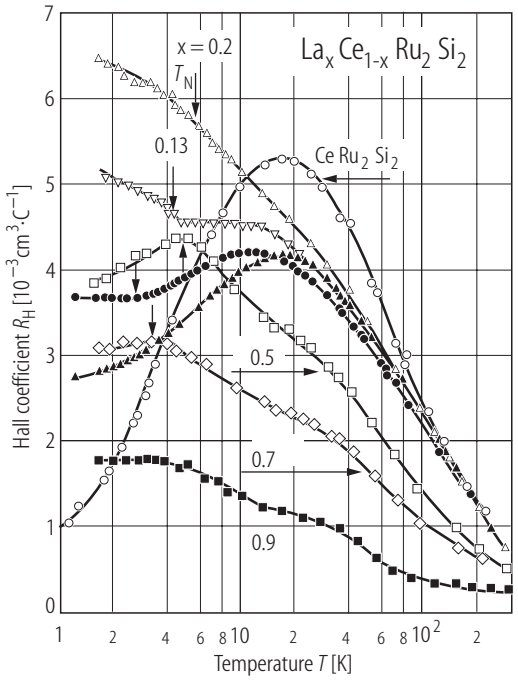

Fig. 228. $La_xCe_{1-x}Ru_2Si_2$. Temperature dependence of R_H at different x. The vertical arrows indicate T_N [88D3].

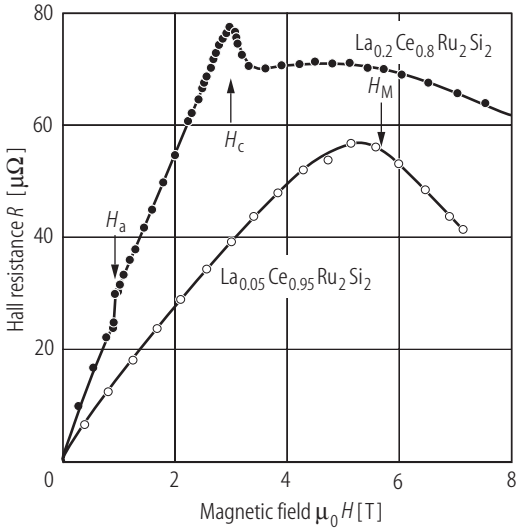

Fig. 229. $La_{0.2}Ce_{0.8}Ru_2Si_2$, $La_{0.05}Ce_{0.95}$ Ru_2Si_2. Magnetic field dependence of Hall resistance. The arrows show the transition field values derived from magnetization measurements [88D3].

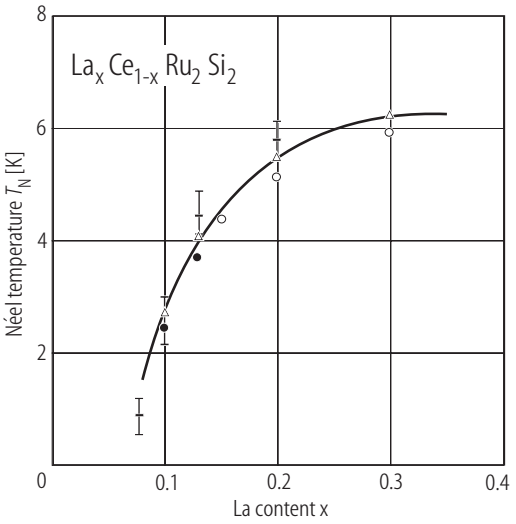

Fig. 230. $La_xCe_{1-x}Ru_2Si_2$. Concentration dependence of T_N. Different symbols refer to different measurements [90H1].

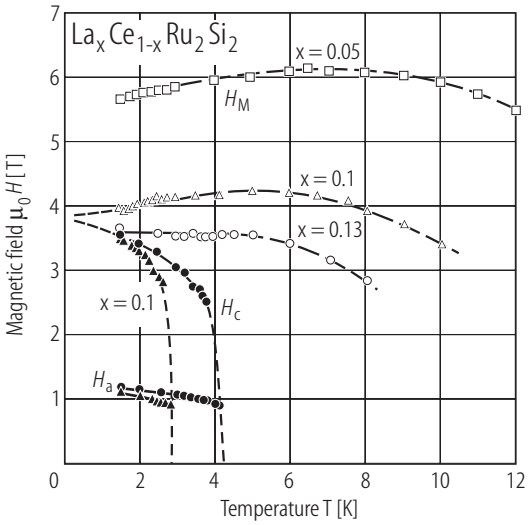

Fig. 232. $La_xCe_{1-x}Ru_2Si_2$. Magnetic phase diagram [90H1].

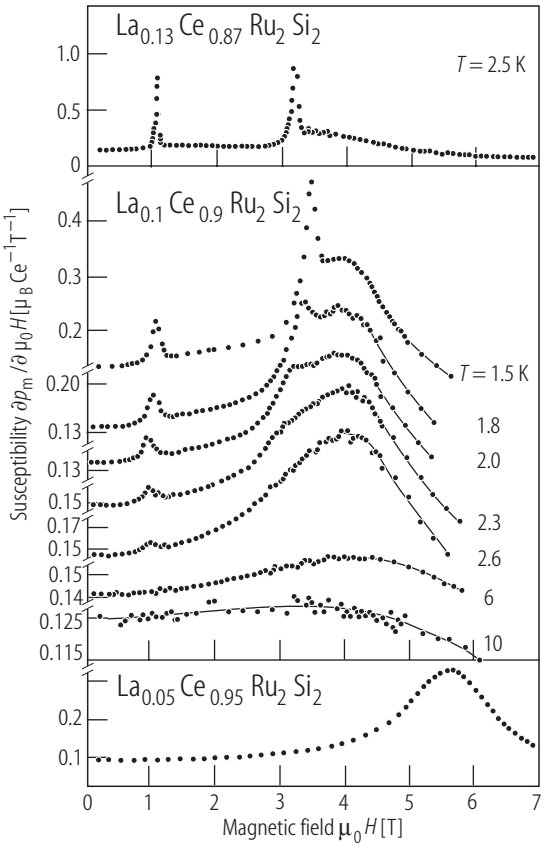

Fig. 231. $La_xCe_{1-x}Ru_2Si_2$. Magnetic field dependence of $\partial p_m/\partial H$ at different temperatures and concentrations [90H1].

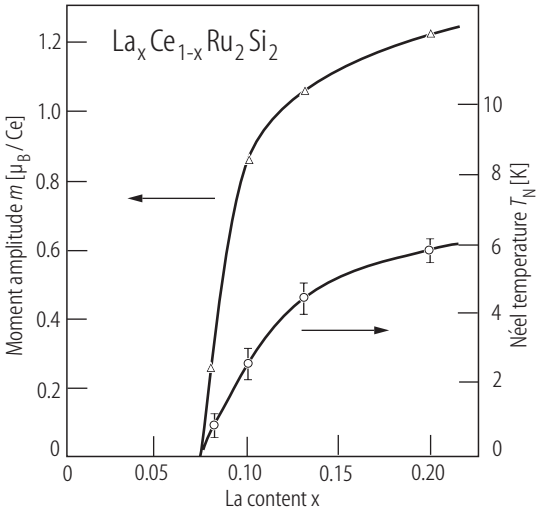

Fig. 233. $La_xCe_{1-x}Ru_2Si_2$. Concentration dependence of T_N and moment amplitude from neutron diffraction. The ordering up to x = 0.90, is incommensurate with the wavevector $\boldsymbol{k}$ = (0.309, 0, 0) [94B3].

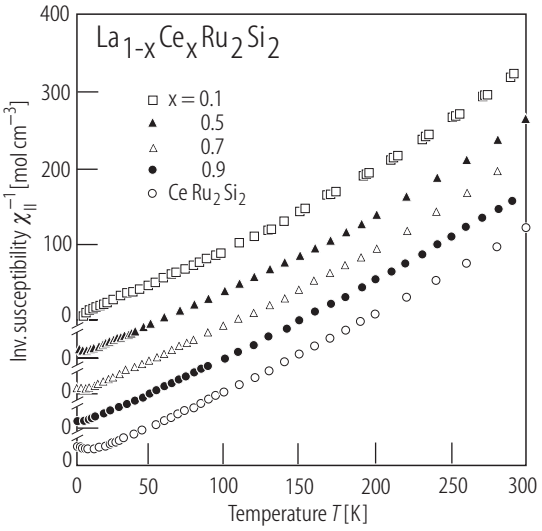

Fig. 234. $(La_{1-x}Ce_x)Ru_2Si_2$. Temperature dependence of $\chi_{\parallel}^{-1}$ for some Ce concentrations [92H1].

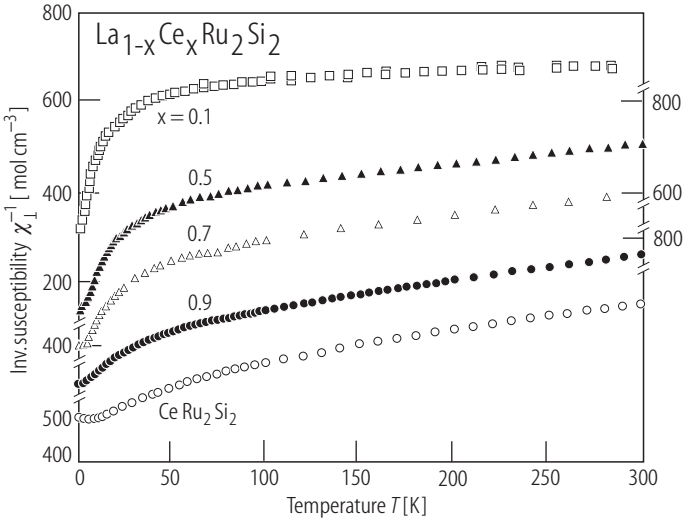

Fig. 235. $(La_{1-x}Ce_x)Ru_2Si_2$. Temperature dependence of $\chi_{\perp}^{-1}$ for some Ce concentrations [92H1].

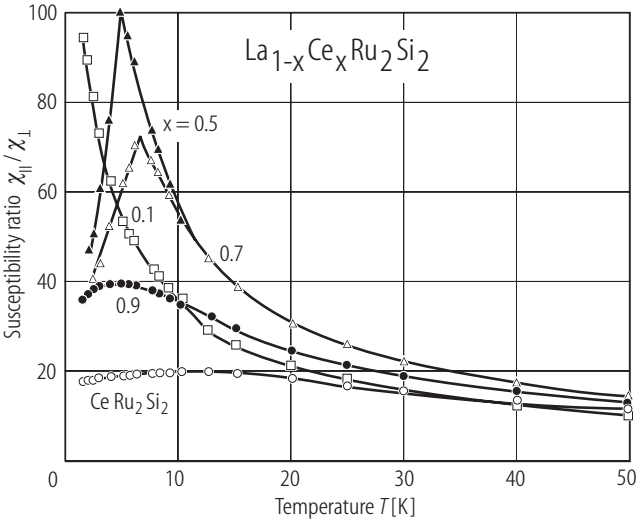

Fig. 236. $(La_{1-x}Ce_x)Ru_2Si_2$. Temperature dependence of the anisotropy ratio $\chi_{\parallel}/\chi_{\perp}$ for some Ce concentrations [92H1].

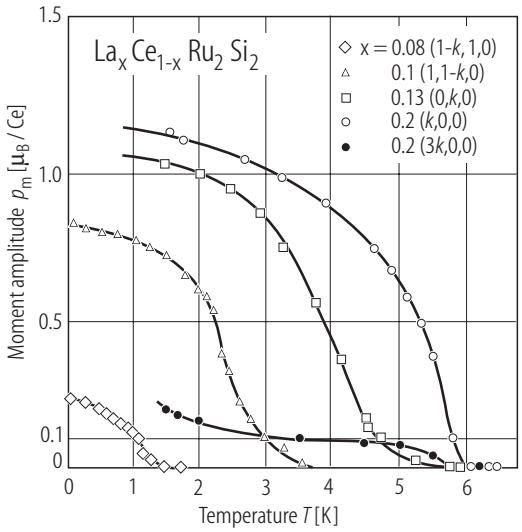

Fig. 237. $La_{1-x}Ce_xRu_2Si_2$. Temperature dependence of p_m amplitude of elastic neutron scattering [88Q1].

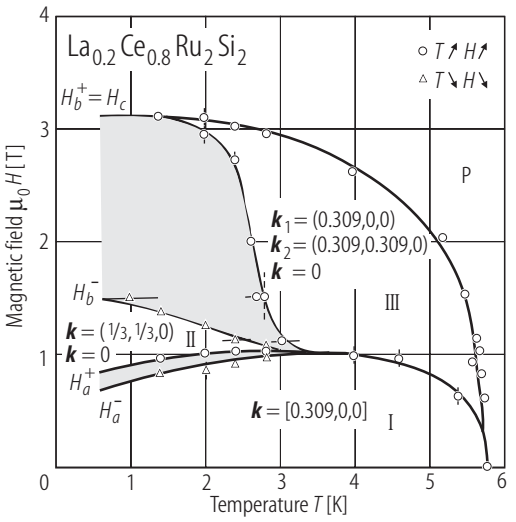

Fig. 240. $La_{0.2}Ce_{0.8}Ru_2Si_2$. Magnetic phase diagram. The hatched areas represent regions of hysteresis [90M3].

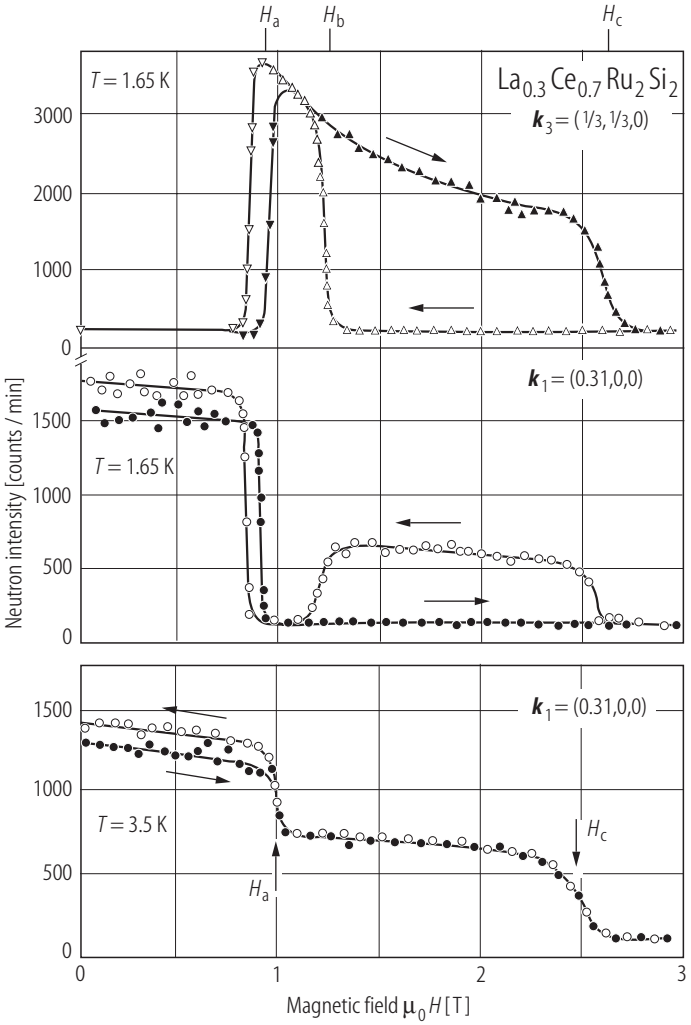

Fig. 239. $La_{0.3}Ce_{0.7}Ru_2Si_2$. Magnetic field dependence of the magnetic reflections [1.69,0,0] (circles) and [1/3,1/3,0] (triangles) at 1.65 and 3.5 K. The inverted triangles represent data for the orthogonal magnetic domain which have been scaled to the latter. Closed symbols: increasing field; open symbols: decreasing field [90M].

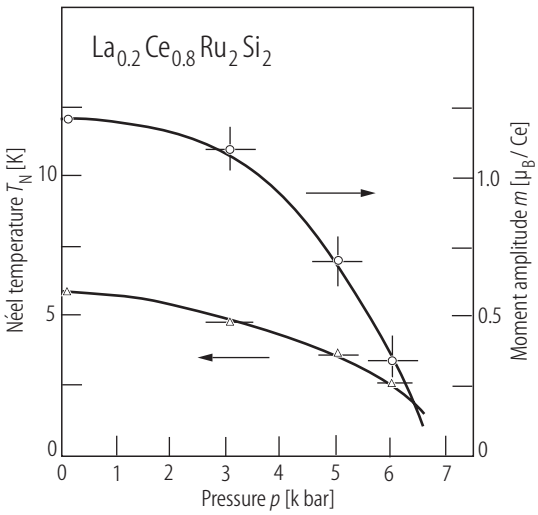

Fig. 241. $La_{0.2}Ce_{0.8}Ru_2Si_2$. Pressure dependence of T_N and neutron scattering moment amplitude [90R1].

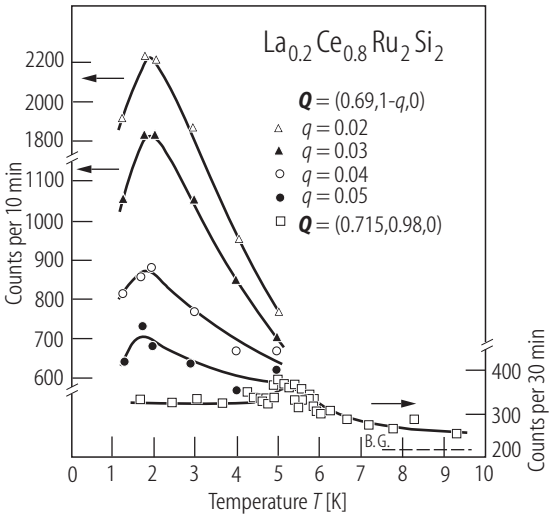

Fig. 242. $La_{0.2}Ce_{0.8}Ru_2Si_2$. Temperature dependence of magnetic correlations around $\boldsymbol{Q} = (110) - \boldsymbol{k}_1$, where $\boldsymbol{k}_1$ is the incommensurate wavevector [90R1].

For Fig. 243 see next page.

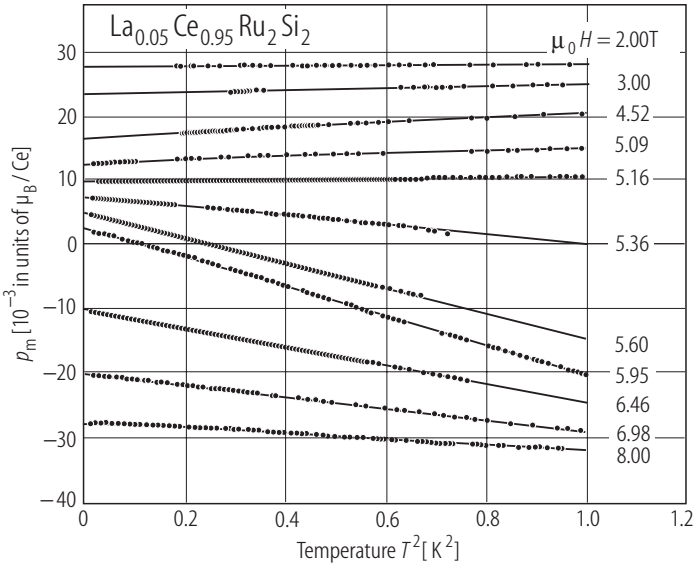

Fig. 245. $La_{0.05}Ce_{0.95}Ru_2Si_2$. Change of magnetization vs. T^2 for $H \parallel c$ at several magnetic fields [90P2, 89H1].

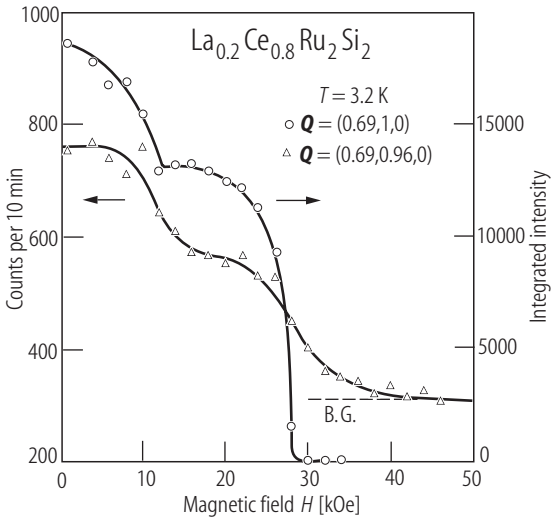

Fig. 243. $La_{0.2}Ce_{0.8}Ru_2Si_2$. Magnetic field dependence of magnetic intensities for neutron scattering vectors at 3.2 K. B.G.: background [90R1].

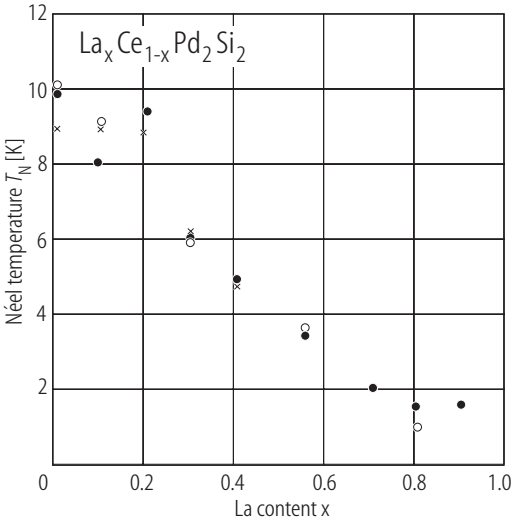

Fig. 246. $La_xCe_{1-x}Pd_2Si_2$. Concentration dependence of T_N obtained from resistivity (solid circles), susceptibility (crosses), and specific heat (open circles) investigations [90S3].

For Fig. 245 see previous page.

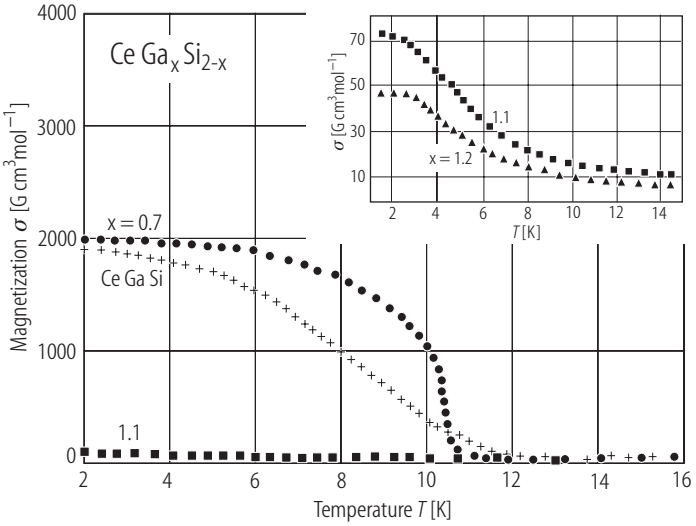

Fig. 247. $CeGa_xSi_{2-x}$. Temperature dependence of σ_m at 50 Oe [90M2].

References

88A1 Amato, A., Jaccard, D., Sierro, J., Lapierre, F., Haen, P., Lejay, P.: J. Magn. Magn. Mater. **76-77**(1988) 263

88D1 Djerbi, R., Haen, P., Lapierre, F., Lehmann, P., Kappler, jr., P.: J. Magn. Magn. Mater. **76-77** (1988) 260

88D2 Djerbi, R., Haen, P., Lapierre, F., Mignot, J.-M.: J. Magn. Magn. Mater. **76-77** (1988) 265

88D3 Djerbi, R., Haen, P., Lapierre, F., Mignot, J.-M., Fert, A., Hamzic, A., Kappler, J.P.: J. Magn. Magn. Mater. **76-77** (1988) 265

88H1 Haen, P., Lapierre, F., Kappler, J.P., Lejay, P., Flouquet, J., Meyer, A.: J. Magn. Magn. Mater. **76-77** (1988) 143

88L1 Lacerda, A., de Visser, A., Puech, L., Lejay, P., Haen, P.: J. Magn. Magn. Mater. **76-77** (1988) 138

88Q1 Quezel, S., Burllet, P., Jacoud, J.L., Regnault, L.P., Rossat-Mignod, J., Vettier, C., Lejay, P., Flouquet, J.: J. Magn. Magn. Mater.: **76-77** (1988) 403

89H1 Haen, P., Kappler, J.P., Lapierre, F., Lehmann, P., Lejay, P., Flouquet, J., Meyer, A.: J. Phys. (Paris) **49** (1989) C8-757

90B1 Bruls, G., Weber, D., Hampel, G., Wolf, B., Kouroudis, I., Luthi, B.: Physica B **163** (1990) 41

90C1 Celemczuk, R., Bonjour, E., Rossat-Mignod, J., Chavalier, B.: J. Magn. Magn. Mater. **90-91** (1990) 477

90H1 Haen, P., Voiron, J., Lapierre, F., Flouquet, J., Lejay, P.: Physica B **163** (1990) 519

90M1 Malik, S.K., Adroja, D.T., Pdadalia, B.D., Vijayaraghavan, R.: Physica B **163** (1990) 89

90M2 Moshchalkov, V.V., Petrenko, O.V., Zalyalutdinov, M.K.: Physica B **163** (1990) 395

90M3 Mignot, J.-L., Jacoud, J.-L., Regnault, L.-P., Rossat-Mignod, J., Lejay, P., Boutrouille, Ph., Hennion, B., Petitgrand, D.: Physica B **163** (1990) 611

90P1 Paulsen, C., Lacerda, A., Tholence, J.L., Flouquet, J.: Physica B **165-166** (1990) 433

90P2 Paulsen, C., Lacerda, A., de Visser, A., Bakker, K., Puech, L., Tholence, J.L.: J. Magn. Magn. Mater. **90-91** (1990) 408

90R1 Regnault, L.P., Jacoud, J.L., Rossat-Mignod, J., Vettier, C., Lejay, P., Flouquet, J.: J. Magn. Magn. Mater. **90-91** (1990) 398

90S3 Sampathkumaran, E.V., Nakazawa, Y., Ishikawa, Y., Vijayaraghavan, R.: Physica B **163** (1990) 365

90S4 Steeman, R.A., Endstra, T., Mentink, S.A.M., Friikkee, E., Menovsky, A.A., Nieuwenhuys, G.J., Mydosh, J.A.: Physica B **163** (1990) 597

92B1 Besnus, M.J., Essaihi, A., Fischer, G., Hamdaoui, N., Meyer, A.: J. Magn. Magn. Mater. **104-107** (1992) 1387

92H1 Haen, P., Lapierre, F., Lejay, P., Voiron, J.: J. Magn. Magn. Mater. **116** (1992) 108

92L1 Lapierre, F., Haen, P.: J. Magn. Magn. Mater. **108** (1992) 167

94B3 Burlet, P., Regnault, L.P., Rossat-Mignod, J., Vettier, C., Flouquet, J.: J. Magn. Magn. Mater. **129** (1994) 10

94F1 Fijiwara, K, Yamanashi, Y., Kumagai, K.: Physica B **199-200** (1994) 107

95M1 Meyer, A., Besuns, M.J., Haen, P., Kappler, J.P., Mathis, G.: Physica B **206-207** (1995) 304

95M2 Mydlarz, T., Talik, E., Szade, J., Heimann, J.: J. Alloys, Comp. **219** (1995) 225

95P1 Park, J.-G., Haen, P., Lapierre, F., Lejay, P., Verniere, A., Voiron, J.: Physica B **206-207** (1995) 285

95S1 Sakakibara, T., Tayama, T., Mitamura, H., Matsuhira, K., Amitsuka, H.: Physica B **206-207** (1995) 249

95T1 Tautz, F.S., Julian, S.R., McMulian, G.J., Lonzarich, G.G.: Physica B **206-207** (1995) 29

96M2 Marumoto, K., Takeuchi, T., Miyako, Y.: Phys.Rev. **B 54** (1996) 12194

96P1 Patil, N.G., Ghosh, K., Ramakrishnan, S.: Physica B **223-224** (1996) 392

97L1 Lapierre, F., Mallmann, F., Holtmeier, S., Kambe, S., Haen, P.: Physica B **230-232** (1997) 120

97M1 Malik, R., Sampathkumaran, E.V., Paulose, P.L.: Physica B **230-232** (1997) 169

98M2 Marumoto, K., Takayama, F., Miyako, Y.: J. Magn. Magn. Mater. **177-181** (1998) 353

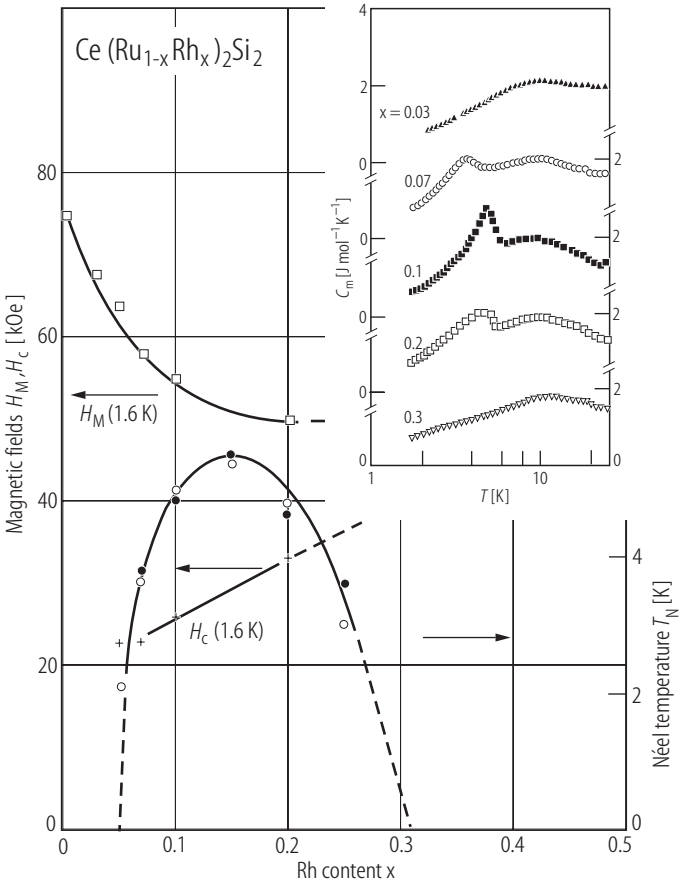

Fig. 275. $Ce(Ru_{1-x}Rh_x)_2Si_2$. Phase diagram for $0 \leq x \leq 0.5$. Inset: low-temperature specific heat of selected samples [92S2].

For Fig. 276 see next page.

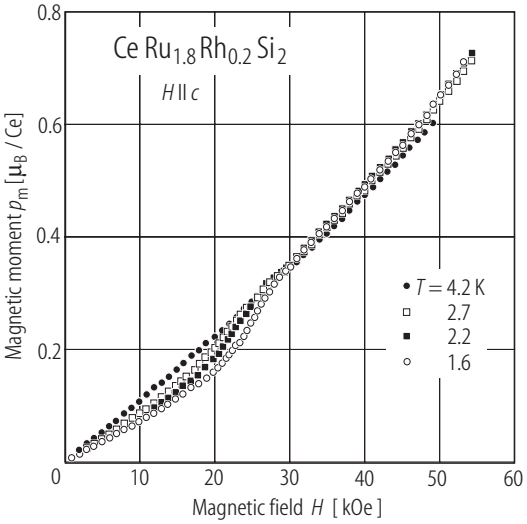

Fig. 277. $CeRu_{1.8}Rh_{0.2}Si_2$. Magnetic field dependence of p_m at temperatures below T_N = 4.2 K [92S2].

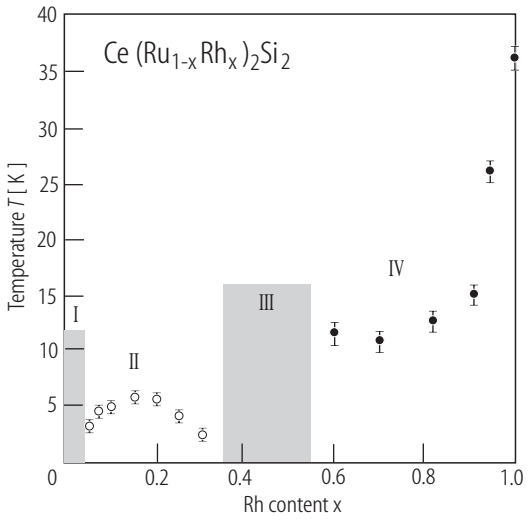

Fig. 278. $Ce(Ru_{1-x}Rh_x)_2Si_2$. Magnetic phase diagram [95K1].

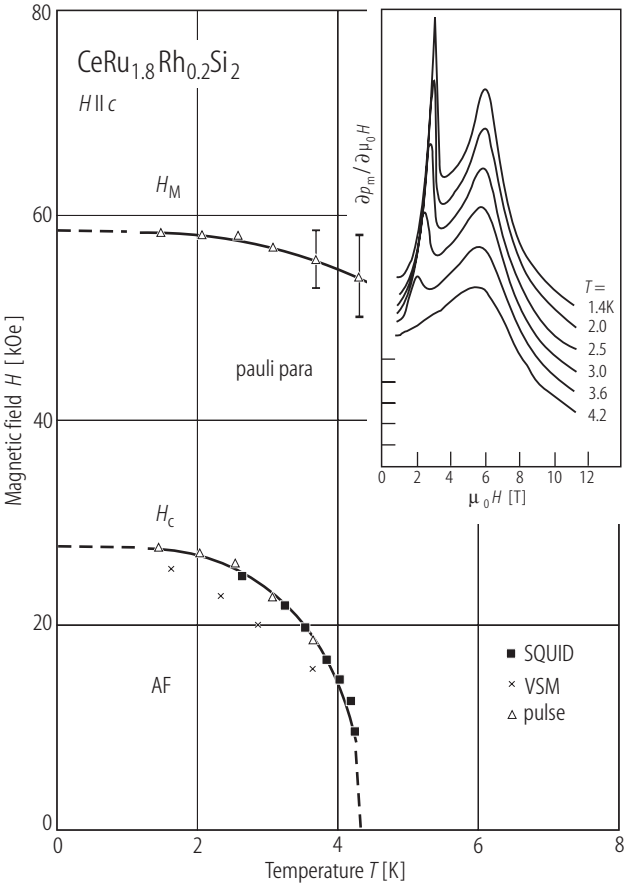

Fig. 276. $CeRu_{1.8}Rh_{0.2}Si_2$. H - T phase diagram in $H \parallel c$. H_c: critical field of the peak of $\partial p_m/\partial H$ (inset) [92S2]. SQUID: superconducting quantum interference device, VSM: vibrating sample magnetometer.

For Fig. 277 see previous page.

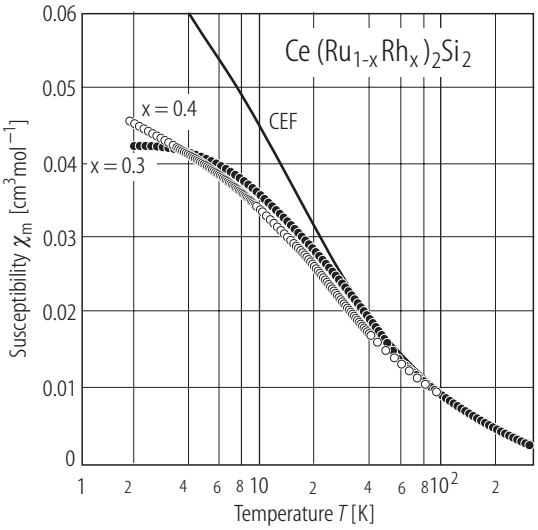

Fig. 279. $Ce(Ru_{1-x}Rh_x)_2Si_2$. Temperature dependence of χ_m for x= 0.3 and 0.4. Solid line is obtained by the CEF model [98T3].

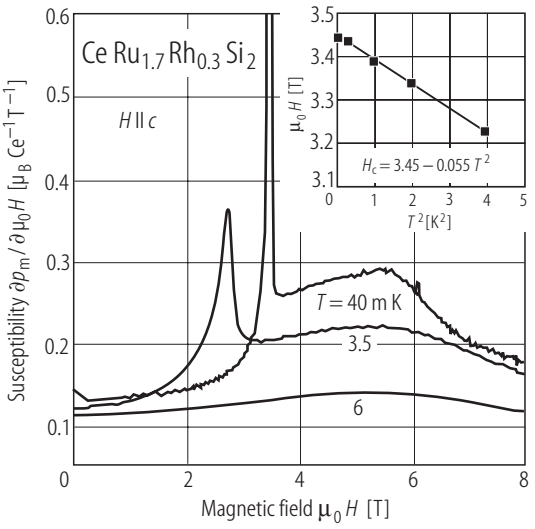

Fig. 280. $CeRu_{1.7}Rh_{0.3}Si_2$. Magnetic field dependence of differential susceptibility for $H \parallel c$ at different temperatures [98S1].

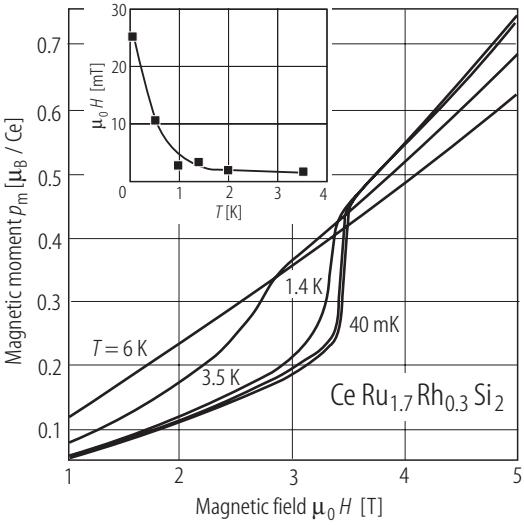

Fig. 281. $CeRu_{1.7}Rh_{0.3}Si_2$. Magnetic field dependence of p_m and temperature dependence of the field-width of hysteresis [98S1].

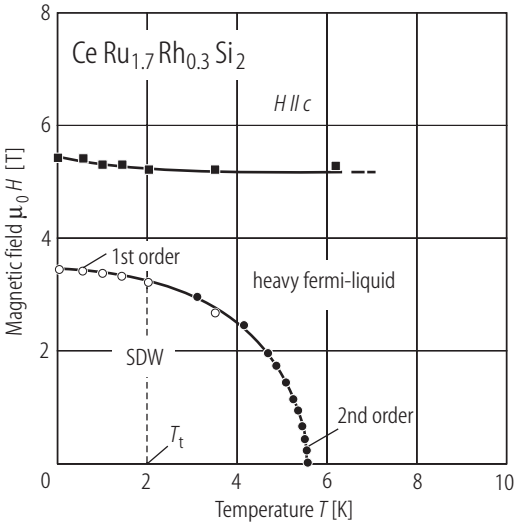

Fig. 282. $CeRu_{1.7}Rh_{0.3}Si_2$. *H-T* phase diagram [98S1].

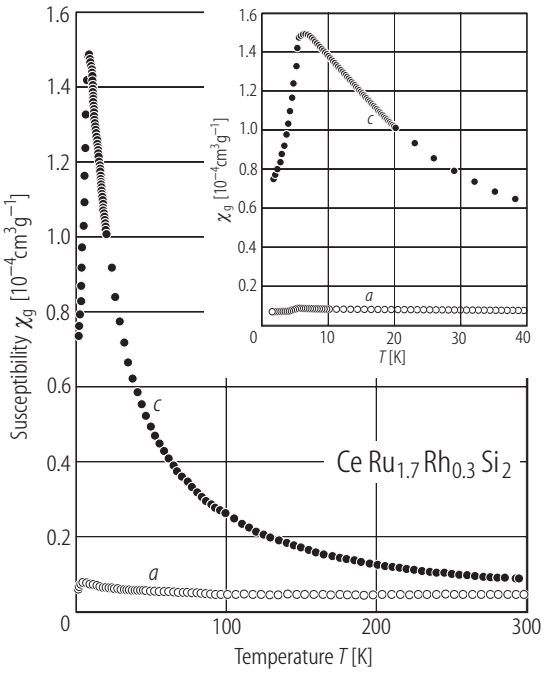

Fig. 283. $CeRu_{1.7}Rh_{0.3}Si_2$. Temperature dependence of χ_g with $H \parallel a$ and c [96T1].

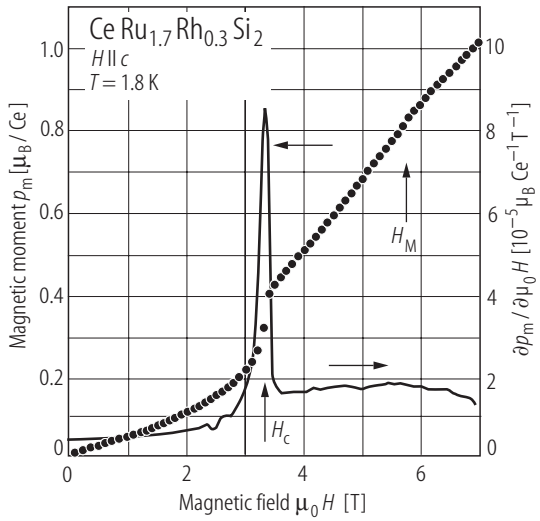

Fig. 284. $CeRu_{1.7}Rh_{0.3}Si_2$. Magnetic field and field derivative along the c axis at 1.8 K [96T1].

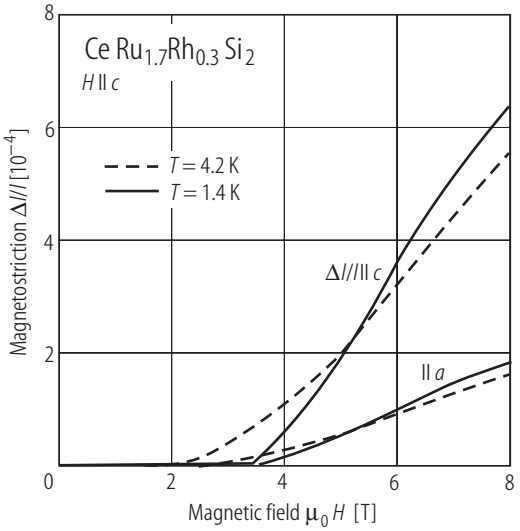

Fig. 285. $CeRu_{1.7}Rh_{0.3}Si_2$. Magnetic field dependence of the magnetostriction along the a and c axes with $H \parallel c$. Solid and dashed lines show the data at 1.4 and 4.2 K, respectively [96T1].

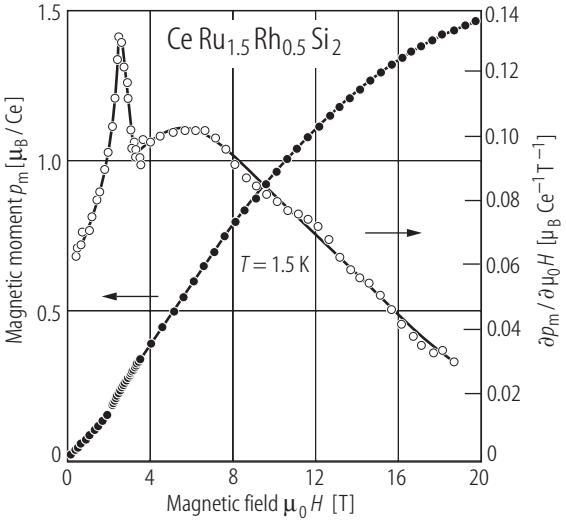

Fig. 286. $CeRu_{1.5}Rh_{0.5}Si_2$. Magnetic field dependence of magnetization of piece of single crystal ($H \parallel c$) at 1.5 K and its derivative $\partial p_m / \partial H$ vs. H [94H1].

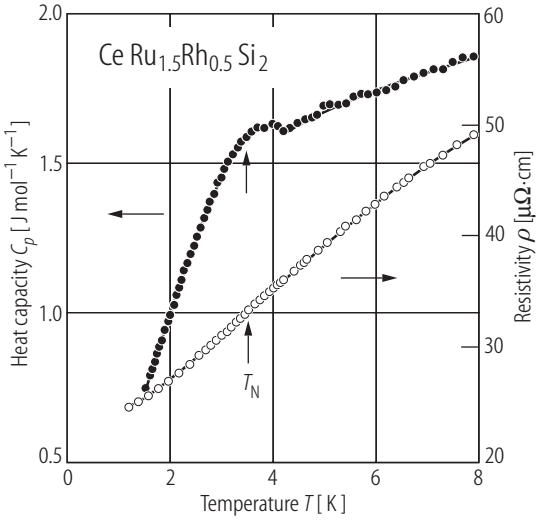

Fig. 287. $CeRu_{1.5}Rh_{0.5}Si_2$. Temperature dependence of a single crystal resistivity and polycrystal C_p [94H1].

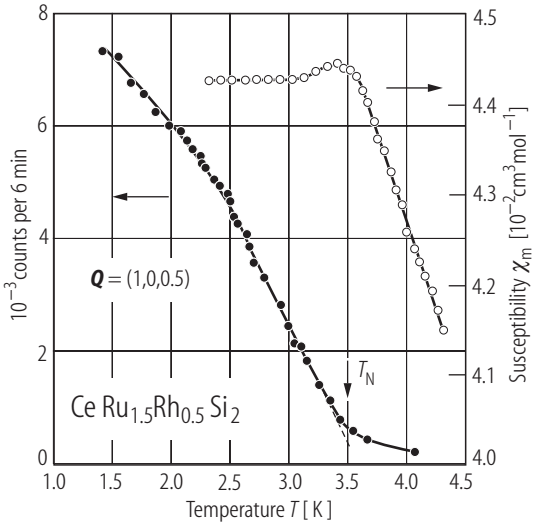

Fig. 288. $CeRu_{1.5}Rh_{0.5}Si_2$. χ_m and variations of the intensity of the (1,0,0.5) magnetic reflection vs. T [94H1].

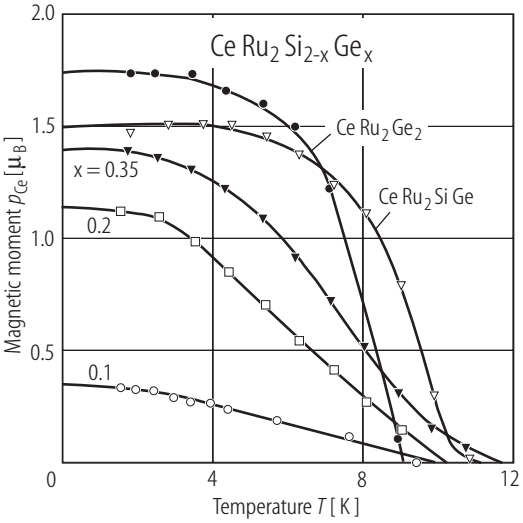

Fig. 289. $CeRu_2Si_{2-x}Ge_x$. Temperature dependence of p_{Ce} derived from powder neutron diffraction [92D1].

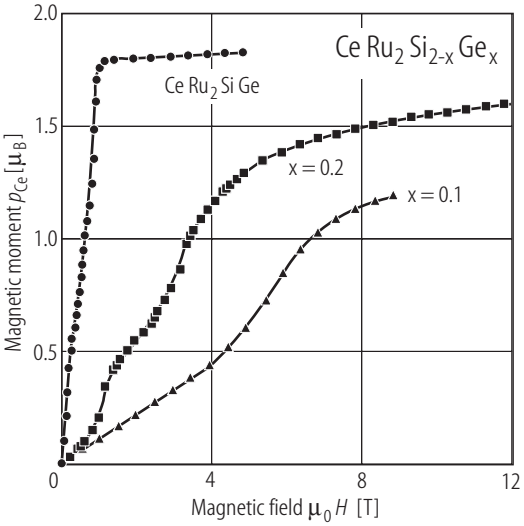

Fig. 290. $CeRu_2Si_{2-x}Ge_x$. Temperature dependence of p_{Ce} with $H \parallel c$ for single crystals with various concentrations [92D1].

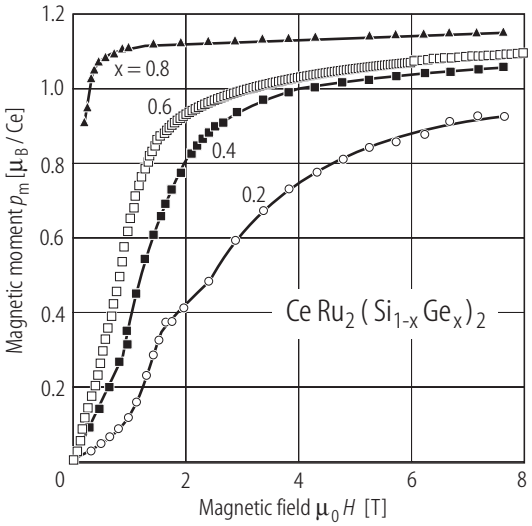

Fig. 291. $CeRu_2(Si_{1-x}Ge_x)_2$. Magnetic field dependence of magnetization of random powders for different x [96B2].

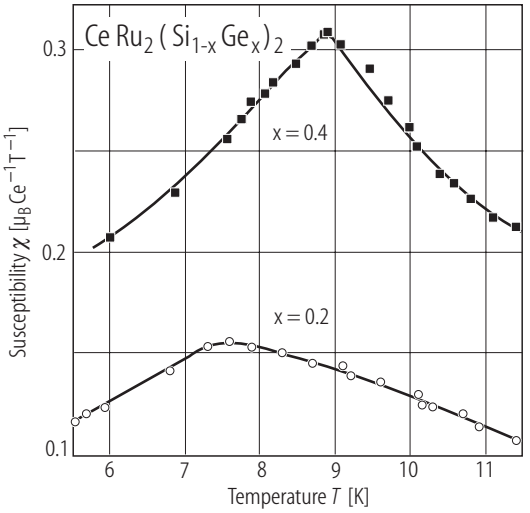

Fig. 292. $CeRu_2(Si_{1-x}Ge_x)_2$. Temperature dependence of χ for different concentrations [96B2].

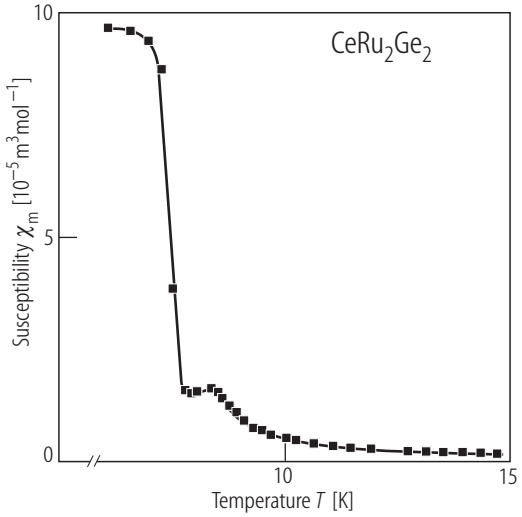

Fig. 293. $CeRu_2Ge_2$. Temperature dependence of χ_m. Solid line is guide to the eye [88B1].

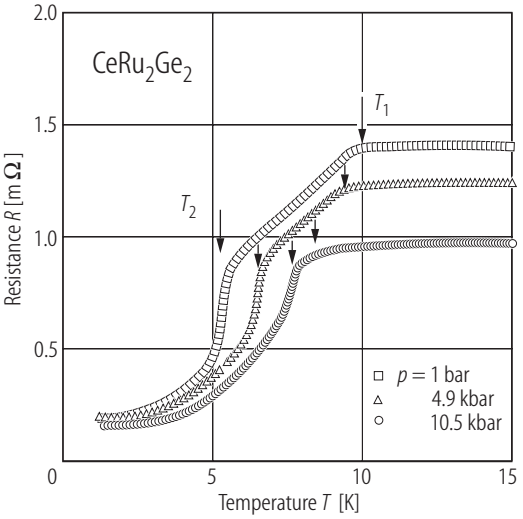

Fig. 294. $CeRu_2Ge_2$. Temperature dependence of resistance R at various pressures. Magnetic transition temperatures are indicated by arrows (see Fig. 296) [95U2].

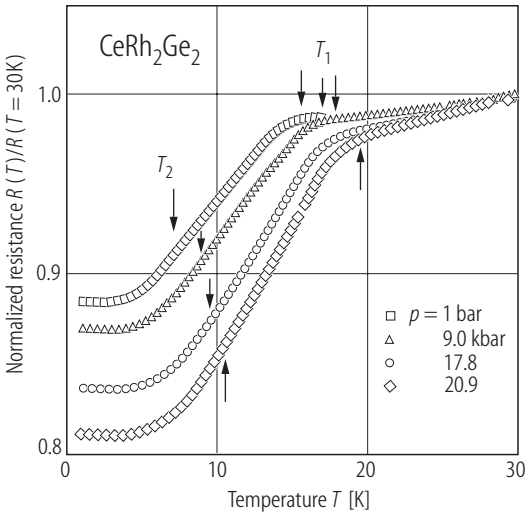

Fig. 295. $CeRh_2Ge_2$. Temperature dependence of resistivity at various pressures [95U2].

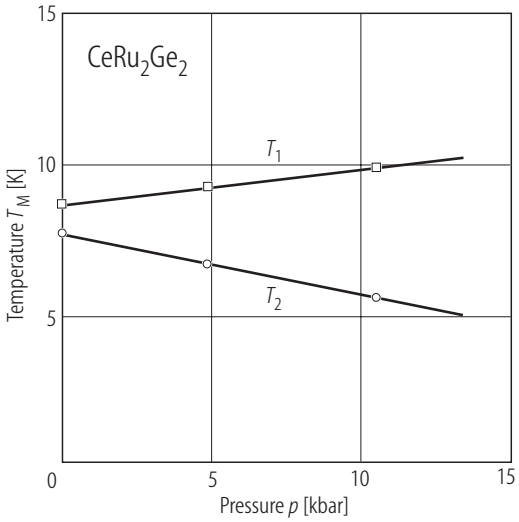

Fig. 296. $CeRu_2Ge_2$. Pressure dependence of magnetic transition temperatures from paramagnetic (T_1) to incommensurate antiferromagnetic (T_2) suggested, obtained from resistivity measurements [95U2].

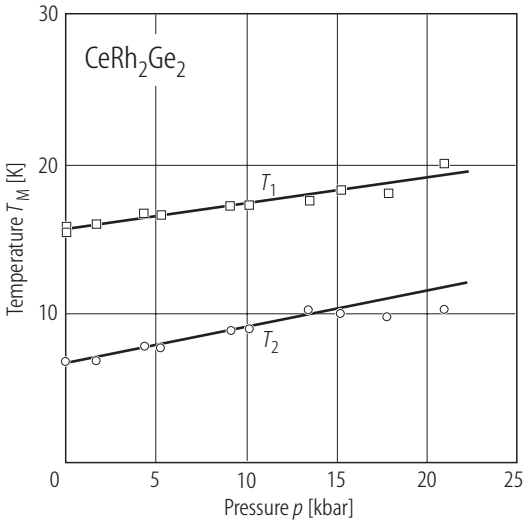

Fig. 297. $CeRh_2Ge_2$. Pressure dependence of magnetic transition temperature from paramagnetic (T_1) to commensurate antiferromagnetism (T_2) suggested, obtained from resistivity measurements [95U2].

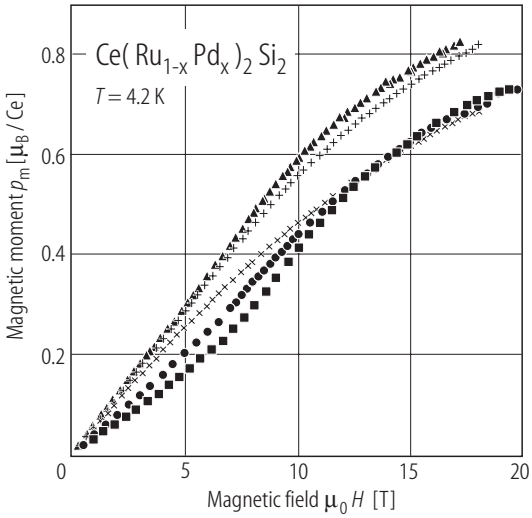

Fig. 298. $Ce(Ru_{1-x}Pd_x)_2Si_2$. Magnetic field dependence of magnetization at 4.2 K for x = 0.5 (solid triangles), 0.1 (+), 0.2 (×), 0.025 (solid circles), and x = 0 (solid squares) [95B2].

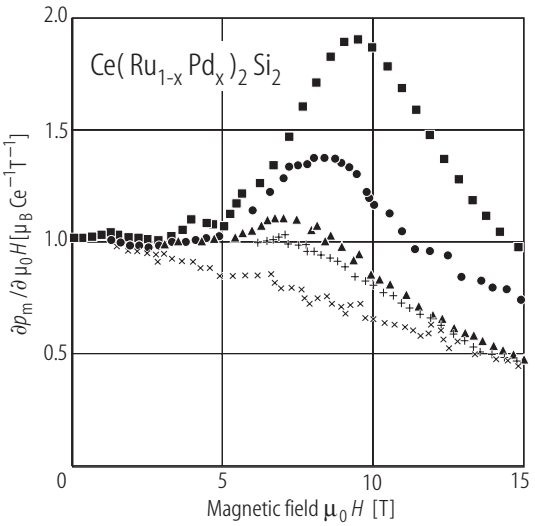

Fig. 299. $Ce(Ru_{1-x}Pd_x)_2Si_2$. Magnetic field dependence of differential susceptibility $\partial p_m/\partial H$ scaled to the low-field values. x = 0.05 (solid triangles), 0.1 (+), 0.2 (×), 0.025 (solid circles), and x = 0 (solid squares) [95B2].

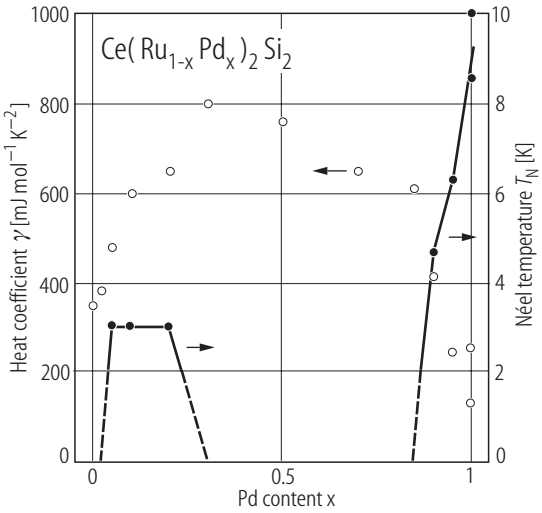

Fig. 300. $Ce(Ru_{1-x}Pd_x)_2Si_2$. Magnetic phase diagram. Solid circles: T_N, open circles: extrapolated $T \rightarrow 0$-value of $\chi(T) = C_m(T)/T$ [95K2].

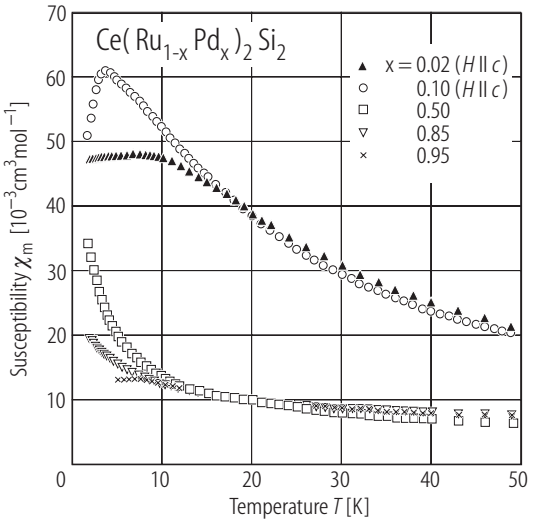

Fig. 301. $Ce(Ru_{1-x}Pd_x)_2Si_2$. Temperature dependence of χ_m for x = 0.02 ($H \parallel c$), x = 0.10 ($H \parallel c$), x = 0.50, 0.85, 0.95 [95K2].

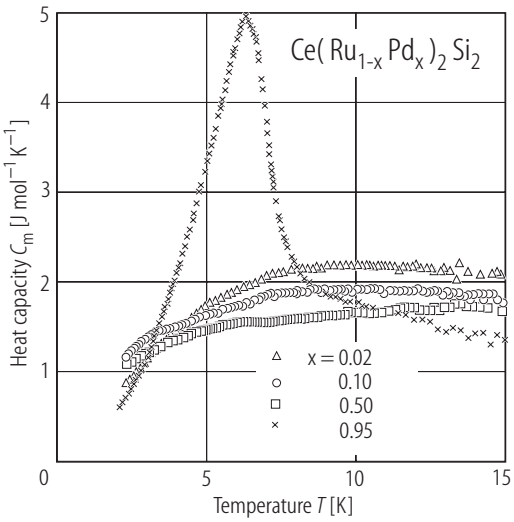

Fig. 302. $Ce(Ru_{1-x}Pd_x)_2Si_2$. Temperature dependence of the magnetic part of the specific heat C_m for x = 0.02, 0.10, 0.50, and 0.95. Samples for x = ≥ 0.30 are polycrystals [95K2].

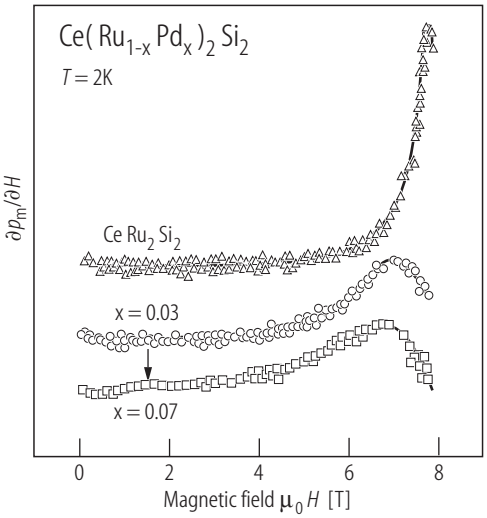

Fig. 303. $Ce(Ru_{1-x}Pd_x)_2Si_2$. Magnetic field dependence of the differential susceptibility of single crystal (for phase diagram see Fig. 19) at 2 K [95S3].

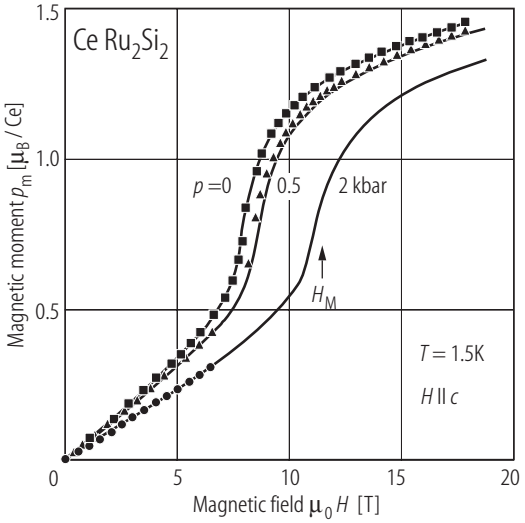

Fig. 304. $CeRu_2Si_2$. Magnetic field dependence of p_m at 1.5 K and for $H \parallel c$ axis at various pressures [88M1.

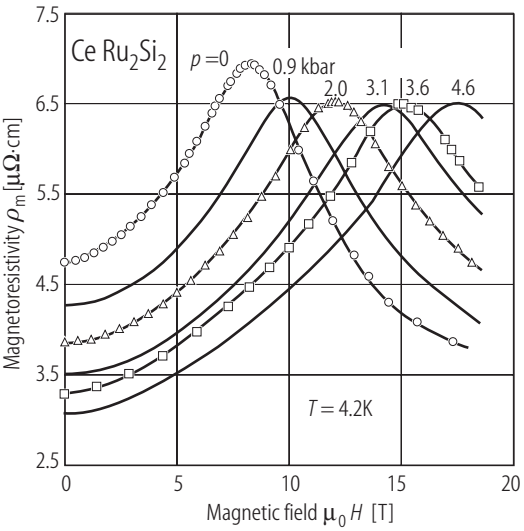

Fig. 305. $CeRu_2Si_2$. Magnetic field dependence of ρ_m at 4.2 K at various pressures ($H \parallel c$, $i \perp c$) [88M1].

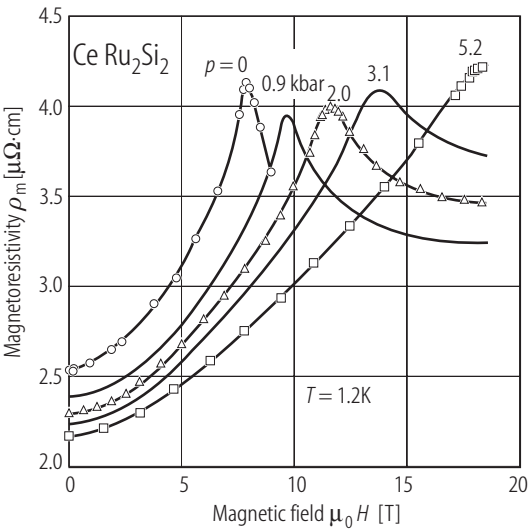

Fig. 306. $CeRu_2Si_2$. Magnetic field dependence of ρ_m at 1.2 K at various pressures ($H \parallel c$, $i \perp c$) [88M1].

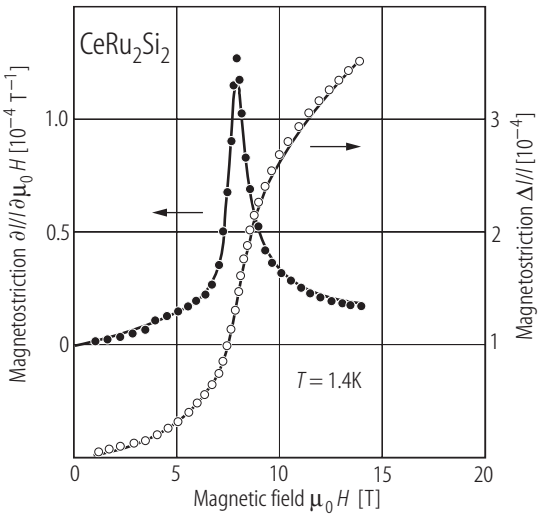

Fig. 307. $CeRu_2Si_2$. Magnetic field dependence of magnetostriction (H || c) at 1.4 K and its field derivative. Solid lines are fits according to equation $M_{sat}\Phi[H/H_s(P)]$ [88M1].

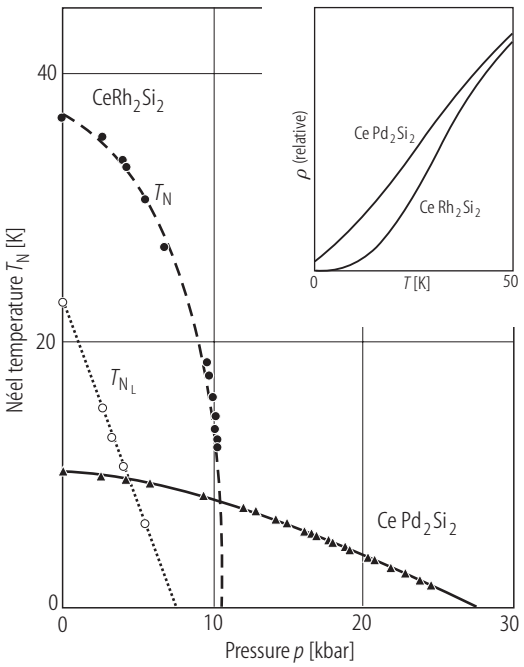

Fig. 308. $CeRh_2Si_2$, $CePd_2Si_2$. Magnetic phase diagrams [97G2].

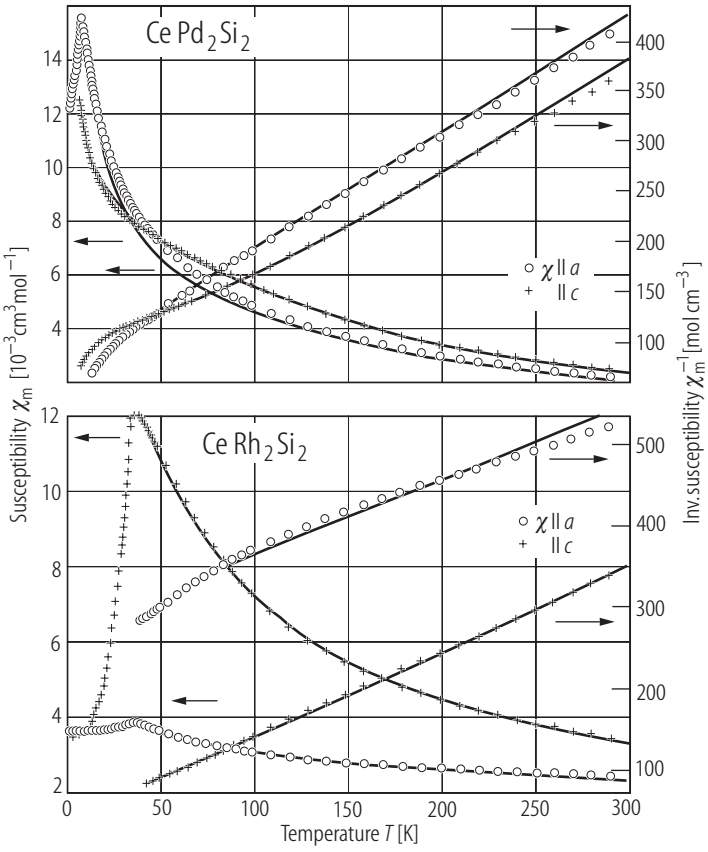

Fig. 309. $CeRh_2Si_2$, $CePd_2Si_2$. Temperature dependence of χ_m and χ_m^{-1} of single crystal samples along the a and c axis. Solid curves indicate the calculated results [98H1].

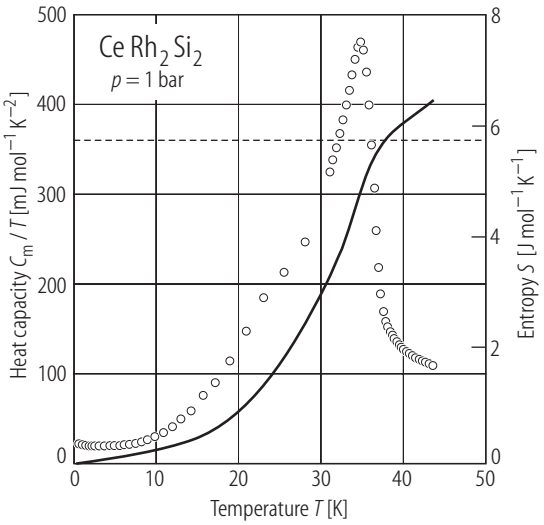

Fig. 310. $CeRh_2Si_2$. Temperature dependence of C_m/T obtained by subtracting the specific heat of $LaRh_2Si_2$ from that of $CeRh_2Si_2$. The solid curve is the magnetic entropy vs. temperature. The dotted line corresponds to $S = R \ln 2$ [96M3].

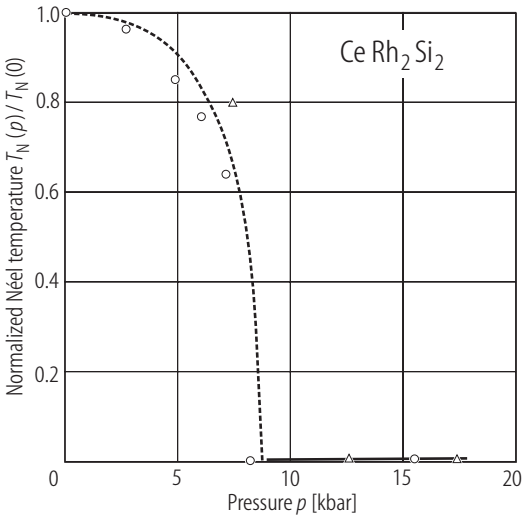

Fig. 311. $CeRh_2Si_2$. Pressure dependence of the Néel temperature normalized to its value at ambient pressure [96M3]. Triangle: [86T1]

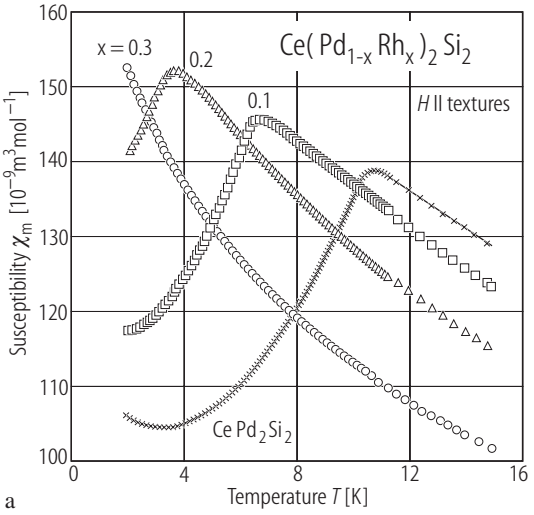

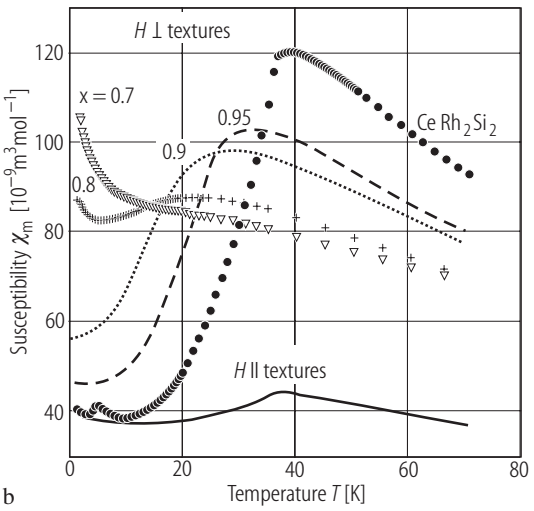

Fig. 312. $Ce(Pd_{1-x}Rh_x)_2Si_2$. Evolution of the AF transitions: Temperature dependence of: (**a**) χ_m for $x \leq 0.3$, H parallel to the direction of the textures and (**b**) χ_m for $x \geq 0.7$, H perpendicular to the direction of the textures. The full line for $CeRh_2Si_2$ || for comparison [97T5].

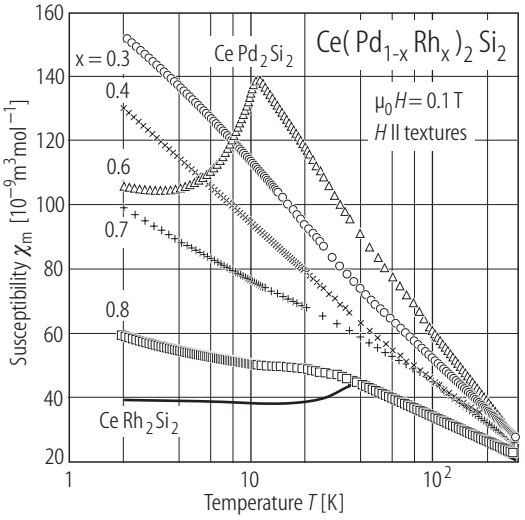

Fig. 313. $Ce(Pd_{1-x}Rh_x)_2Si_2$. Temperature dependence of χ_m at 0.1 T for H parallel to the direction of the textures [97T5].

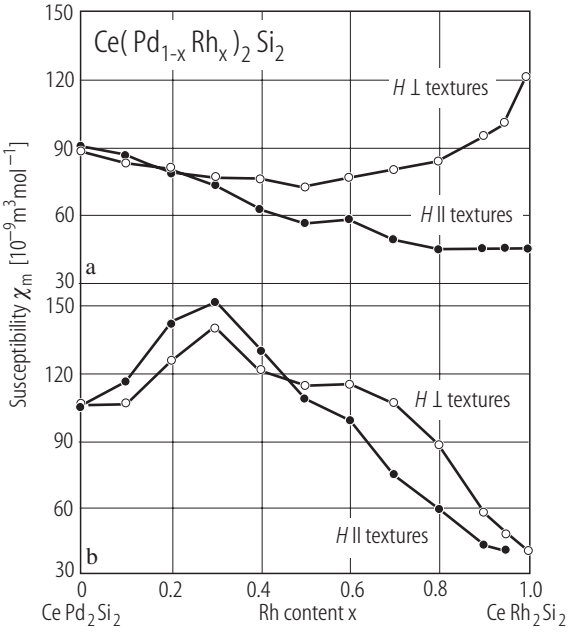

Fig. 314. $Ce(Pd_{1-x}Rh_x)_2Si_2$. Concentration dependence of $\chi_m \parallel$ (full symbols) and $\chi_m \perp$ (open symbols) at 40 K (**a**) and 2 K (**b**) [97T5].

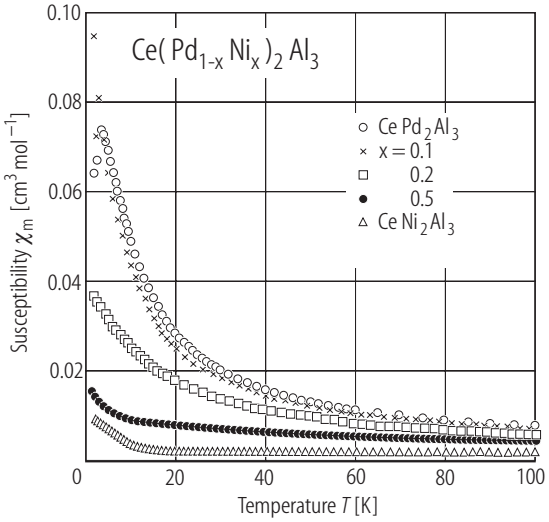

Fig. 315. $Ce(Pd_{1-x}Ni_x)_2Al_3$. Temperature dependence of χ_m for different x [95F1].

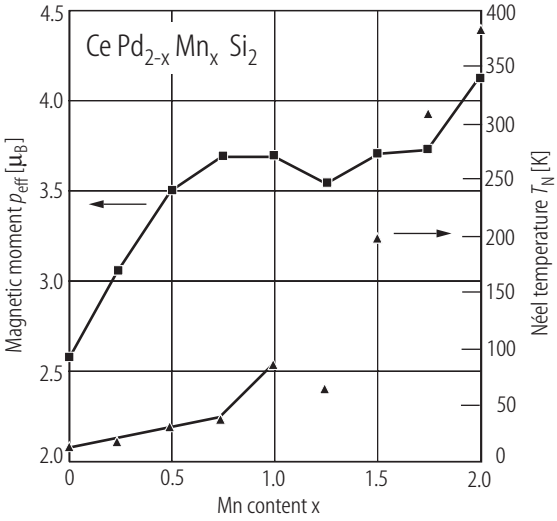

Fig. 316. $CePd_{2-x}Mn_xSi_2$. Concentration dependence of the total paramagnetic moment and Néel temperature [94G2].

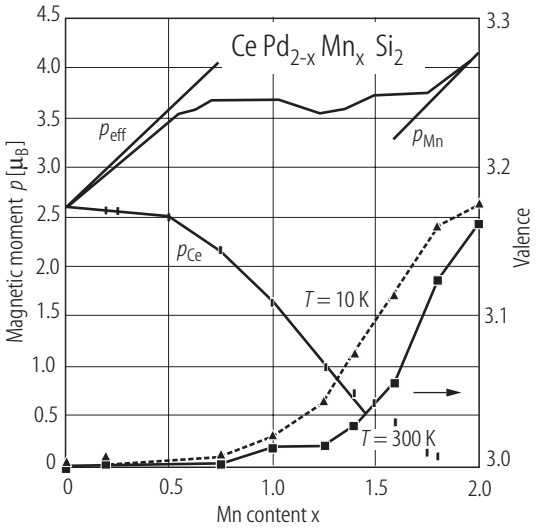

Fig. 317. $CePd_{2-x}Mn_xSi_2$. Concentration dependence of the valence at 10 and 300 K, and the total magnetic moment [94G2].

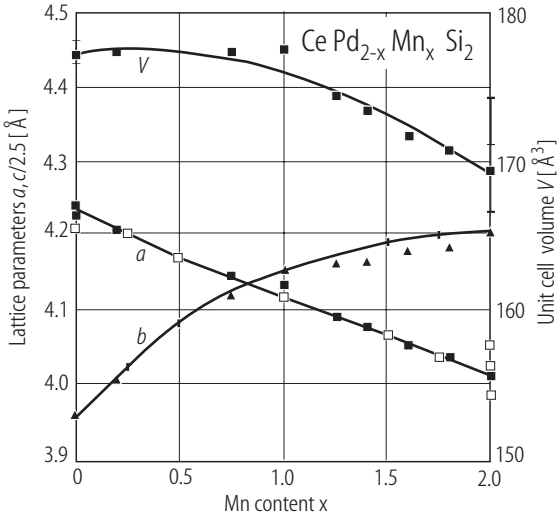

Fig. 318. $CePd_{2-x}Mn_xSi_2$. Concentration dependence of the lattice parameter and the unit cell volume [94G2].

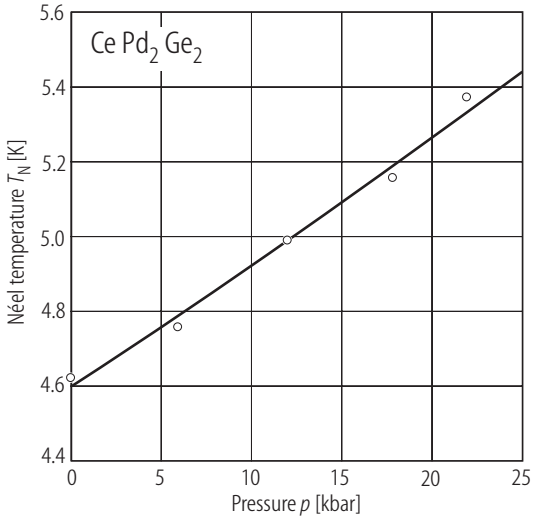

Fig. 319. $CePd_2Ge_2$. Pressure dependence of the Néel temperature [96O1].

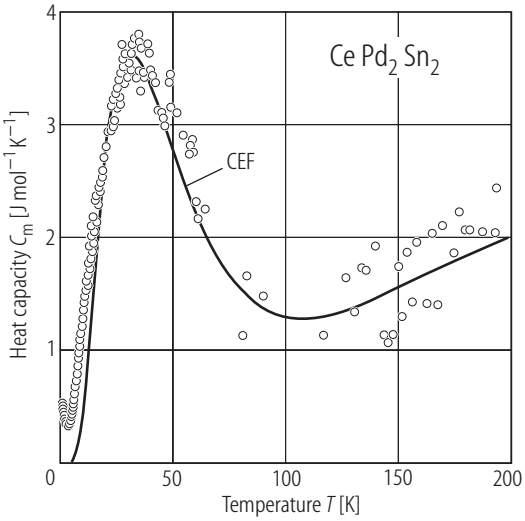

Fig. 321. $CePd_2Sn_2$. Temperature dependence of C_m. The solid curve shows the result from the calculations [98K2].

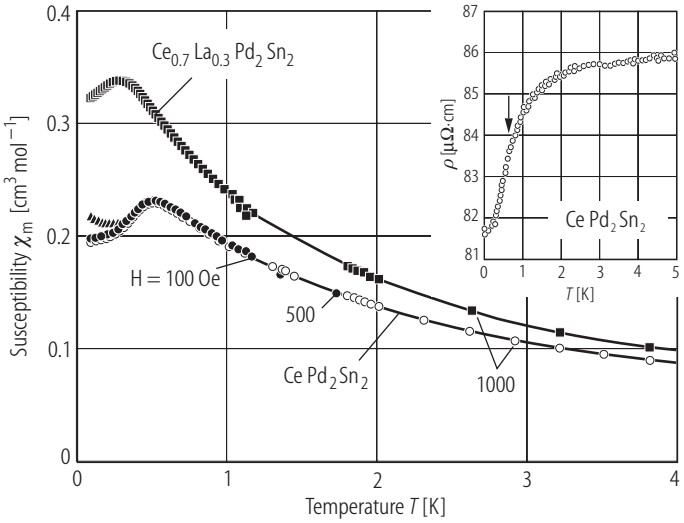

Fig. 320. $CePd_2Sn_2$, $Ce_{0.7}La_{0.3}Pd_2Sn_2$ Temperature dependence of χ_m [98K2].

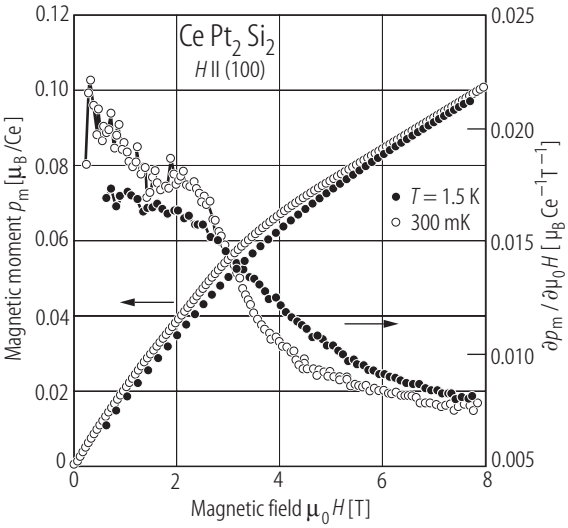

Fig. 323. $CePt_2Si_2$. Magnetization and differential susceptibility [95S1].

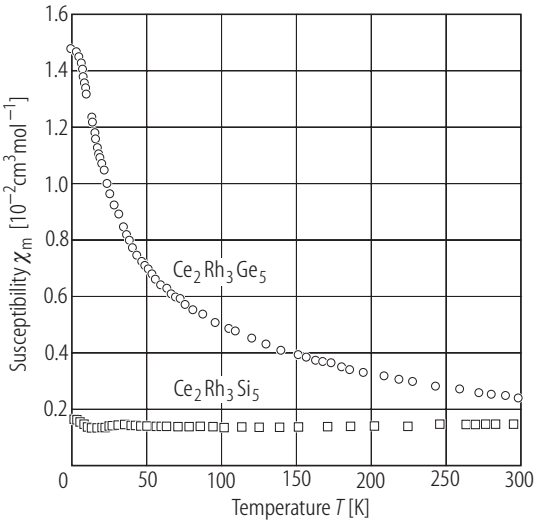

Fig. 324. $Ce_2Rh_3Ge_5$, $Ce_2Rh_3Si_5$. Temperature dependence of χ_m [90G1].

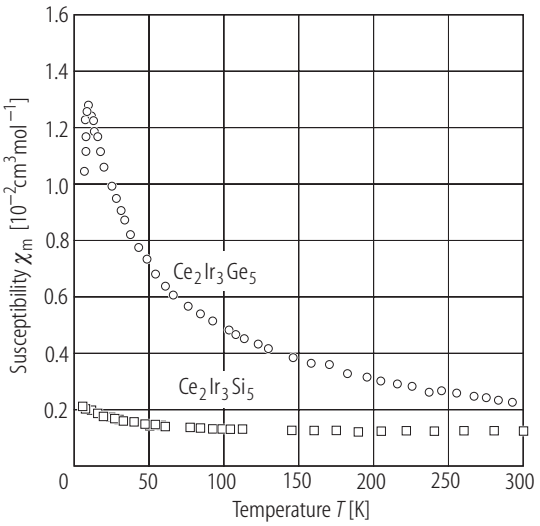

Fig. 325. $Ce_2Ir_3Ge_5$, $Ce_2Ir_3Si_5$. Temperature dependence of χ_m [90G1].

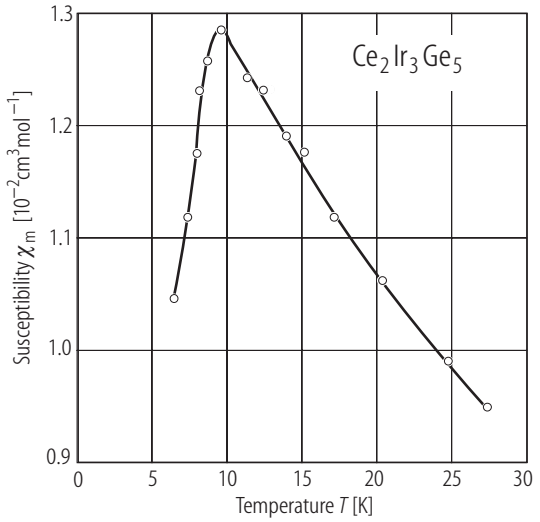

Fig. 326. $Ce_2Ir_3Ge_5$. Low temperature dependence of χ_m [90G1].

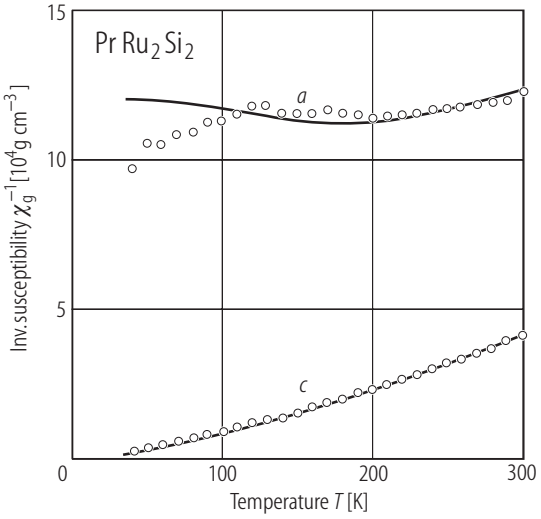

Fig. 327. $PrRu_2Si_2$. Temperature dependence of χ_g^{-1} along the *c* and *a* axis. The solid lines are calculated with the CEF parameter $B_2^0 = -14.3$ K [92S3].

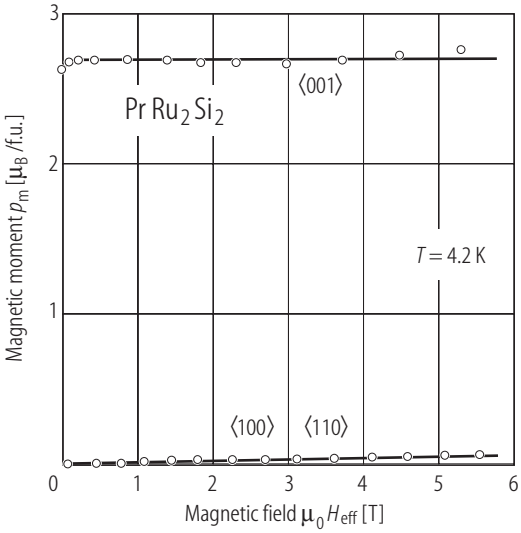

Fig. 328. $PrRu_2Si_2$. Magnetic field dependence of p_m along the main symmetry directions at 4.2 K on the single crystal [92S3].

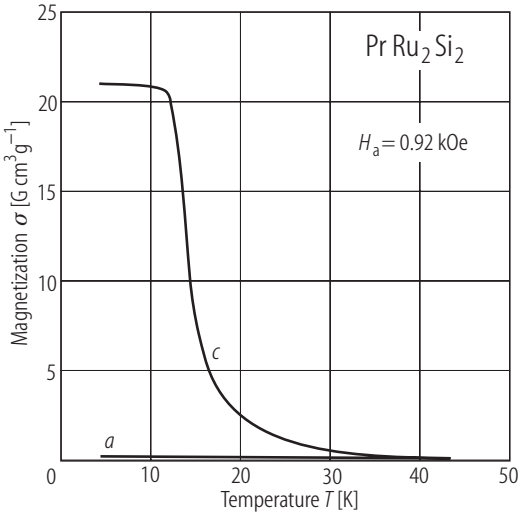

Fig. 329. $PrRu_2Si_2$. Temperature dependence of σ along the *c* and *a* axis at 0.92 kOe on single crystal [92S3].

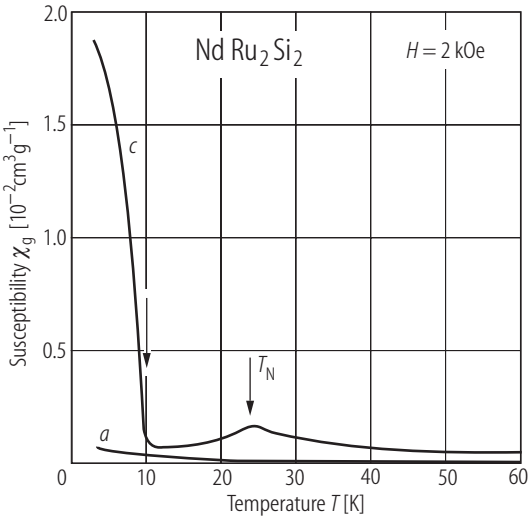

Fig. 330. $NdRu_2Si_2$. Temperature dependence of χ_g at H = 2 kOe, applied || to *a* and *c* axes on the single crystal [90S5].

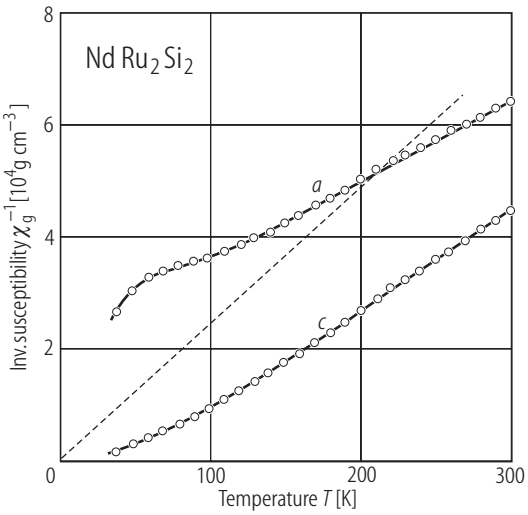

Fig. 331. $NdRu_2Si_2$. Temperature dependence of χ_g^{-1} at 2 kOe applied || to the *a* and *c*-axes on the single crystal. The broken line follows the Curie law [90S5].

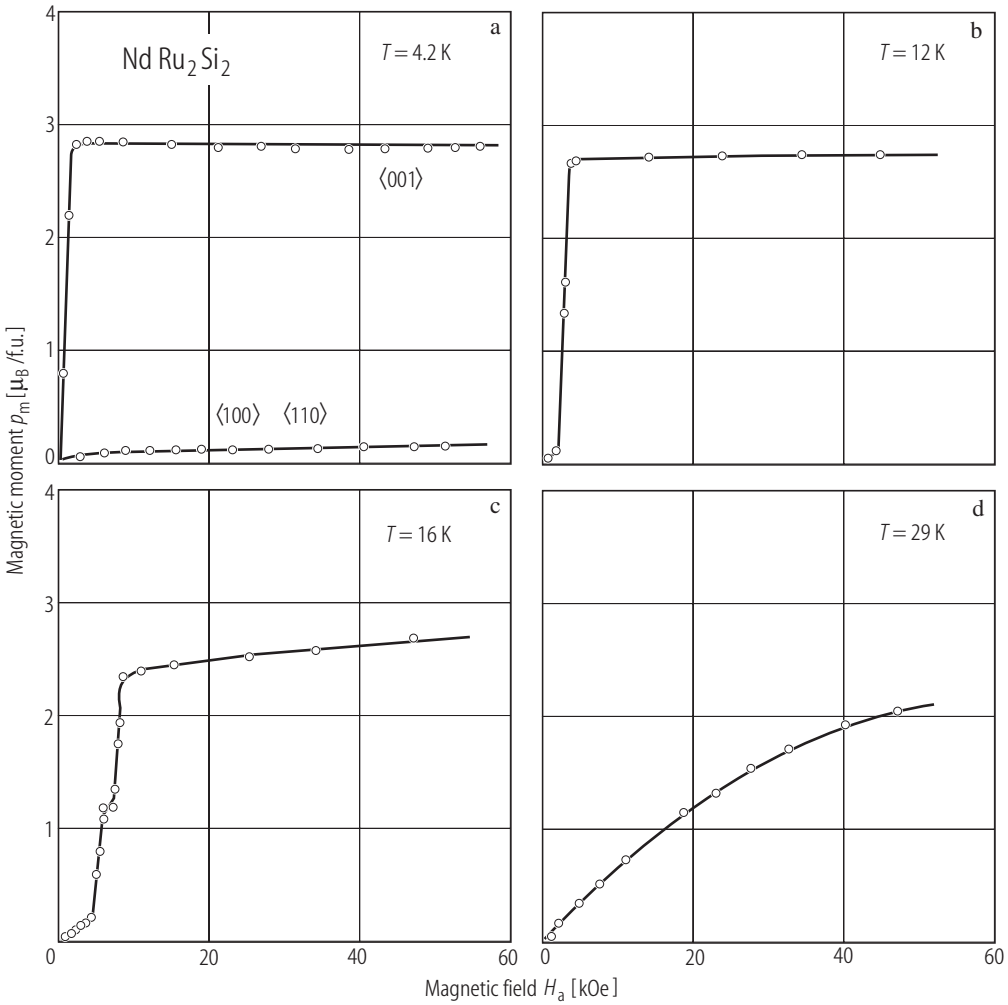

Fig. 332. $NdRu_2Si_2$. Magnetic field dependence of p_m along the *c* axis of the single crystal at 4.2 K (**a**), 12 K (**b**), 16 K (**c**) and 29 K (**d**) K. Magnetization in the *c* plane is only shown in (**a**) [90S5].

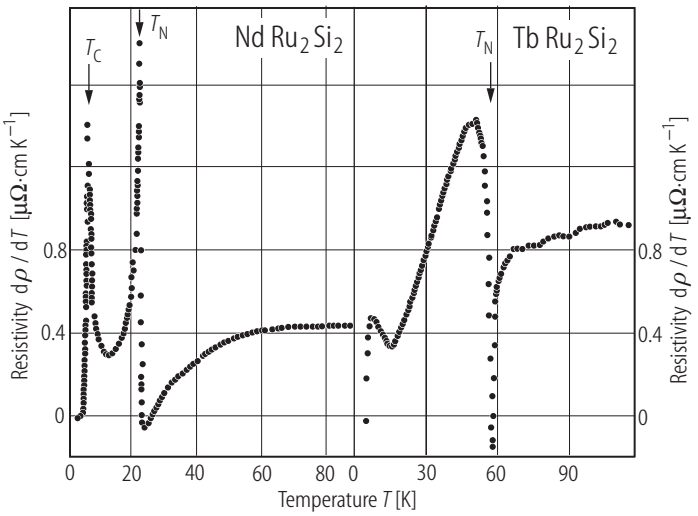

Fig. 333. $NdRu_2Si_2$, $TbRu_2Si_2$. Temperature dependence of the derivative of the electrical resistivity [92P1].

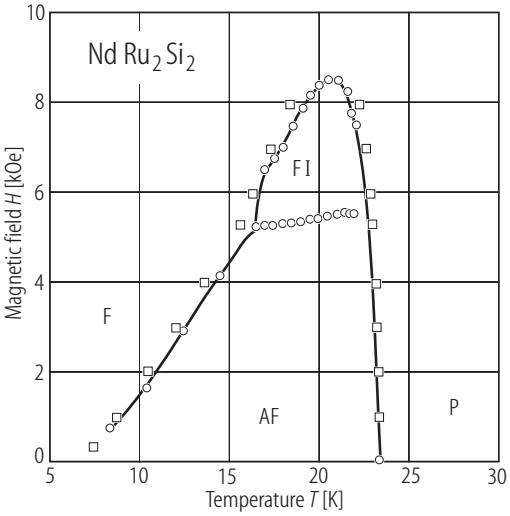

Fig. 334. $NdRu_2Si_2$. H - T magnetic phase diagram. Circles: isothermals, squares: isofields [94S1].

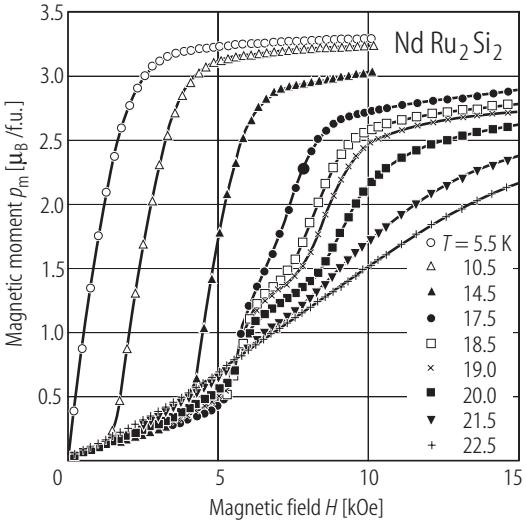

Fig. 335. $NdRu_2Si_2$. Isothermal magnetization vs. H at several temperatures [94S1].

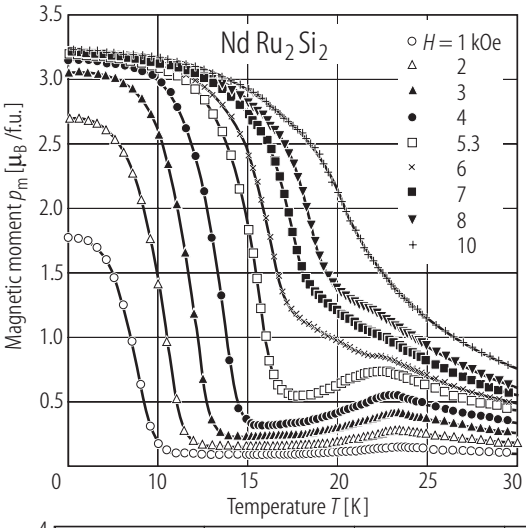

Fig. 336. $NdRu_2Si_2$. Temperature dependence of magnetization at several applied magnetic fields [94S1].

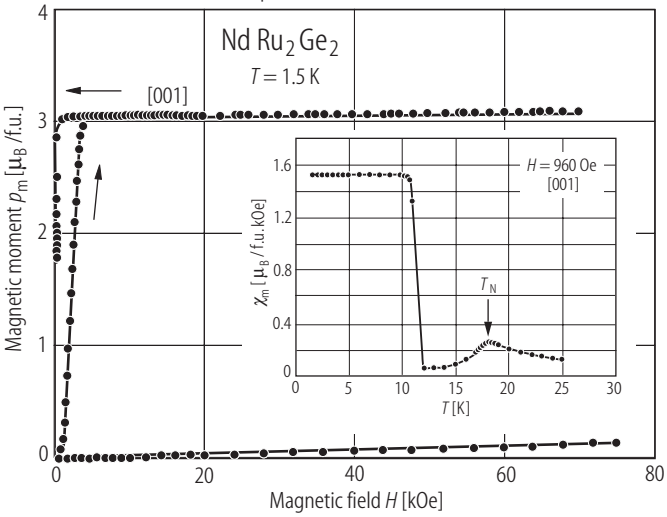

Fig. 337. $NdRu_2Ge_2$. Magnetic field dependence of p_m at 1.5 K along the three symmetry axes. Along [001] the variation corresponds to the first magnetization curve in an increasing and a decreasing field. Inset: temperature dependence of χ_m at 960 Oe along the c axis [94G1].

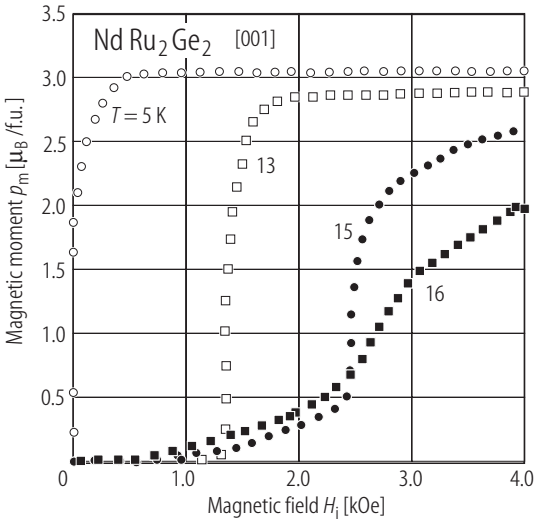

Fig. 338. $NdRu_2Ge_2$. Internal field (applied field corrected for demagnetizing field effects) dependence of magnetization at different temperatures [94G1].

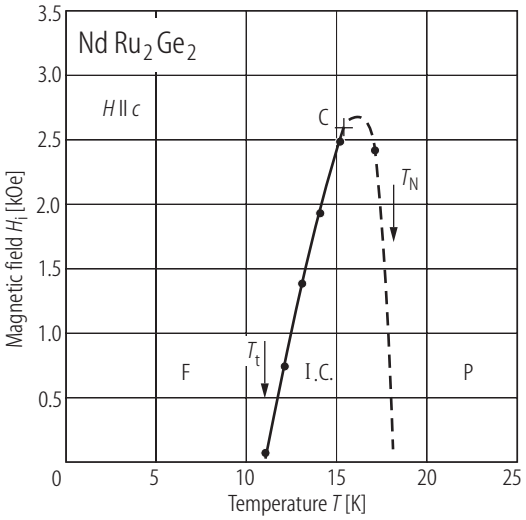

Fig. 339. $NdRu_2Ge_2$. (H,T) phase diagram. C: tricritical point. Full and dashed lines are first and second order transition, respectively. I.C. denotes the incommensurate or long-range commensurate propagation vector [94G1].

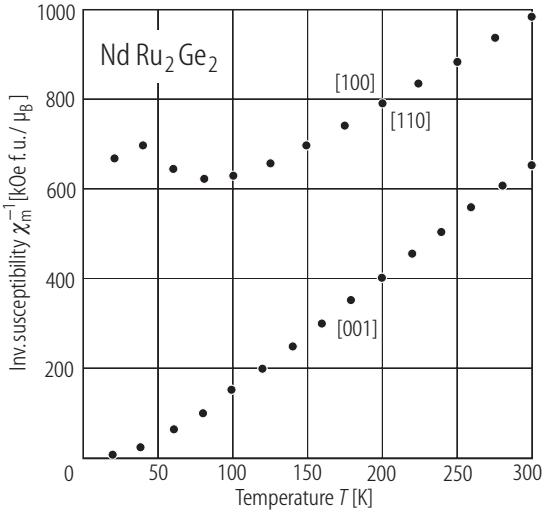

Fig. 340. $NdRu_2Ge_2$. Temperature dependence of χ_m^{-1} along the c axis [94G1].

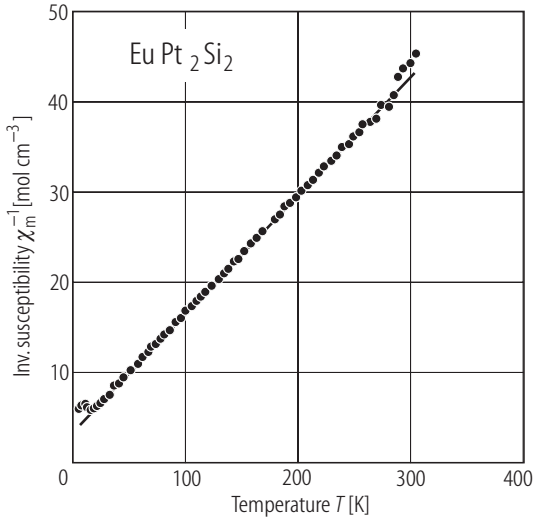

Fig. 341. $EuPt_2Si_2$. Temperature dependence of χ_m^{-1}. Continuous line: fit to the Curie-Weiss behaviour [90N1].

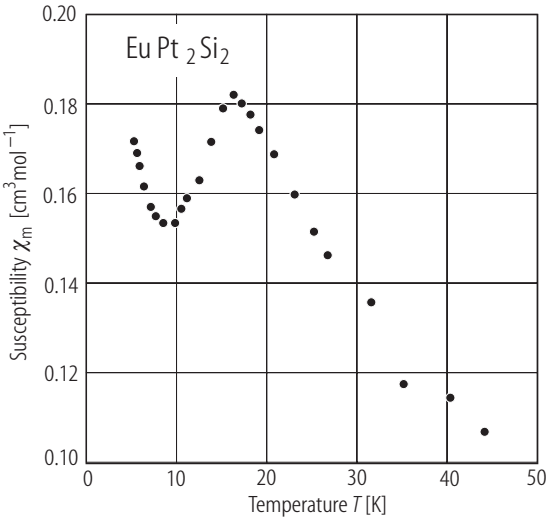

Fig. 342. $EuPt_2Si_2$. Low-temperature dependence of χ_m [90N1].

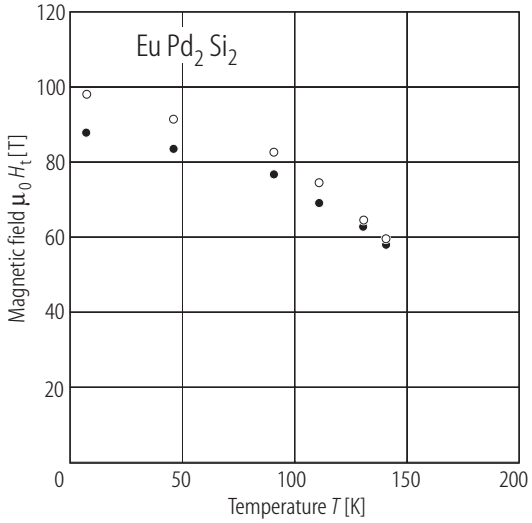

Fig. 344. $EuPd_2Si_2$. Temperature dependence of the metamagnetic transition field H_t in the increasing (open circles) and decreasing (solid circles) field process, respectively [96W1].

For Fig. 343 see next page.

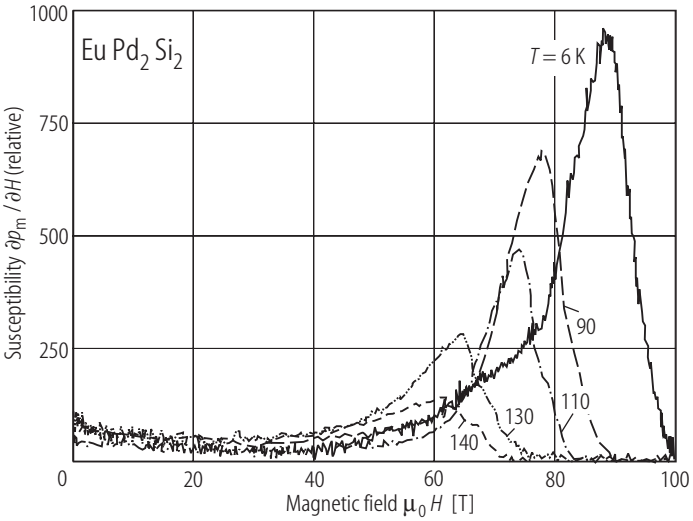

Fig. 343. $EuPd_2Si_2$. Magnetic field dependence of $\partial p_m/\partial H$ at various temperatures [96W1].

For Fig. 344 see previous page.

References

86T1 Thompson, J.D., Parks, R.D., Borges, H.: J. Magn. Magn. Mater. **54-57** (1986) 377

88B1 Bohm, A., Caspary, R., Habel, U., Pawlak, L., Zuber, A., Steglich, F.: J. Magn. Magn. Mater. **76-77** (1988) 150

88M1 Mignot, J.-M., Flouquet, J., Haen, P., Lapierre, L., Puech, L., Voiron, J.: J. Magn. Magn. Mater. **76- 77** (1988) 97

90G1 Godart, C., Gupta, L., C., Tomy, C., V., Patil, S., Nagarajan, R., Beaurepaire, E.: Physica B **163** (1990) 163

90N1 Nagarajan, R., Sampathkumaran, E., Vijayaraghavan, R.: Physica B **163** (1990) 591

90S5 Schobinger-Papamantellos, P., de Mooij, D.B., Buschow, K.H.J.: J. Less-Common Met. **163** (1990) 319

92D1 Dakin, S., Rapson, G., Rainford, B.D.: J. Magn. Magn. Mater. **108** (1992) 117

92P1 Pinto, R.P., Amado, M.M., Salgueiro Silva, M., Braga, M.E., Sousa, J.B., Chavalier, B., Etourneau, J.: J. Magn. Magn. Mater. **104-107** (1992) 1235

92S2 Sakakibara ,T., Sekine, C., Amitsuka, H., Miyako Y.: J. Magn. Magn. Mater. **108** (1992)193

92S3 Shigeoka, T., Iwata, N., Fujii, H.: J. Magn. Magn. Mater. **104-107** (1992) 1229

94G1 Garnier, A., Gignoux, D., Schmitt, D., Shigeoka, F.Y., Zhang: J. Magn. Magn. Mater. **140-144** (1994) 897

94G2 Godart, C., Flandorfer, H., Fogl, P.: Physica B **199-200** (1994) 512

94H1 Hu, Z., Yelon, W.B.: J. Appl. Phys. **76** (1994) 6162

94S1 Salgueiro da Silva, M., Sousa, J.B., Chevalier, B., Etourneau, J.: J. Appl. Phys. **76** (1994) 6344

95B2 Besnus, M.J., Braghta, A., Haen, P., Kappler, J.P., Meyer, A.: Physica B **206-207** (1995) 295

95F1 Fujiwara, K., Yamanashi, Y., Kumagai, K.: Physica B **206-207** (1995) 228

95K1 Kawarazaki, S., Kobashi, Y., Fernandez-Baca, J.A., Murayama, S., Onuki, Y., Miyako, Y.: Physica B **206-207** (1995) 298

95K2 Kusumoto, T., Takagi, S., Suzuki, H.: Physica B **206-207** (1995) 301

95S1 Sakakibara, T., Tayama, T., Mitamura, H., Matsuhira, K., Amitsuka, H.: Physica B **206-207** (1995) 249

95S3 Sekine, C., Sakamoto, H., Muryayama, S., Hoshi, K., Sakakibara, T.: Physica B **206-207** (1995) 291

95U2 Uwatoko, Y., Oomi, G., Graf, T., Thompson,J.D., Canifield, P.C., Borges, H.A., Godart, C., Gupta, L.C.: Physica B **206-207** (1995) 236

96B2 Besnus, M.J., Haen, P., Mallmann, F., Kappler, J.P., Meyer, A.: Physica B **223-224** (1996) 322

96M3 Movshovich, R., Graf, T., Mandrus, D., Hundley, M.F., Thompson, J.D., Fisher, R.A., Phillips, N.E., Smith, J.L.: Physica B **223-224** (1996) 126

96O1 Oomi, G., Uwatoko, Y., Sampathkumaran, E.V., Ishikawa, M.: Physica B **223-224** (1996) 303

96T1 Takeuchi, T., Miyako, Y.: J. Phys Soc. Jpn. **65** (1996) 3242

96W1 Wada, H., Mitsuda, A., Shiga, M.: J. Phys. Soc. Jpn. **65** (1996) 3471

97G2 Grosche, F.M., Julian, S.R., Mathur, N.D., Carter, F.V., Lonzarich, G.G.: Physica B **237-238** (1997) 197

97T5 Trovvarelli, O., Gomez-Berisso, M., Pedrazzini, P., Bosse, D., Geibel, C., Sereni, J.G., Steglich, F.: J. Alloys Comp. **275-277** (1997) 569

98H1 Hideki Abe, Hideaki Kitazawa, Hiroyuki Suzuki, Giyuu Kido, Takehiko Matsumoto.: J. Magn. Magn. Mater. **177-181** (1998) 479

98K2 Kuwai, T., Takagi, H., Ito, H., Isikawa, Y., Sakurai, J., Nishimura, K., Paulsen, C.C.: J. Magn. Magn. Mater. **177-181** (1998) 399

98S1 Sekine, C., Tayama, T., Sakakibara, T., Murayama, S., Shirotani, I., Onuki, Y.: J. Magn. Magn. Mater. **177-181** (1998) 411

98T3 Taniguchi, T., Tabata, Y., Tanabe, H., Miyako, Y.: J. Magn. Magn. Mater. **177-181** (1998) 419

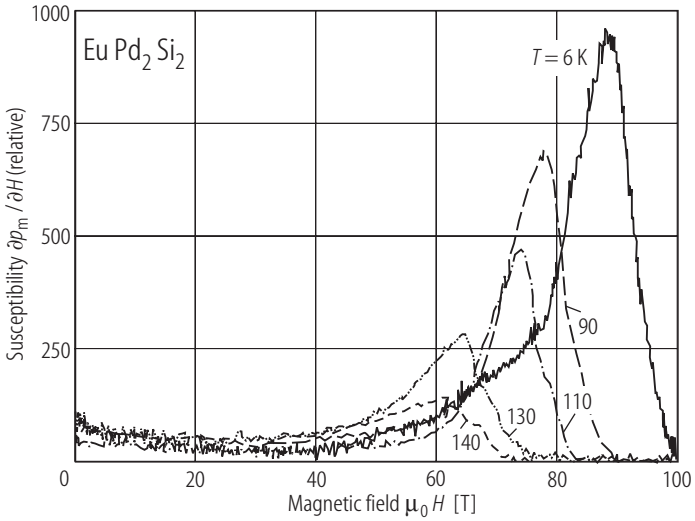

Fig. 343. $EuPd_2Si_2$. Magnetic field dependence of $\partial p_m/\partial H$ at various temperatures [96W1].

For Fig. 344 see previous page.

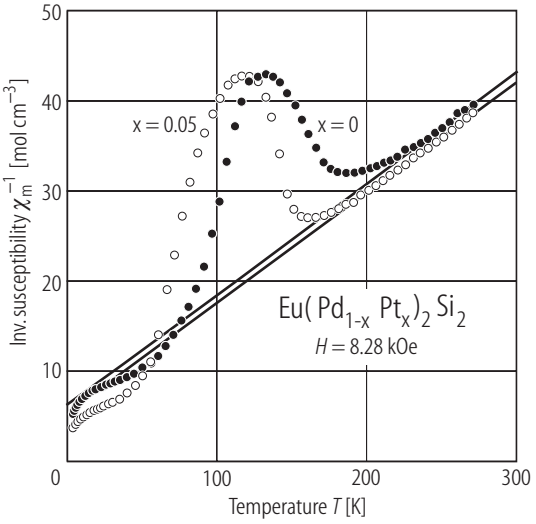

Fig. 345. $Eu(Pd_{1-x}Pt_x)_2Si_2$. Temperature dependence of χ_m^{-1} at 8.28 kOe, for x = 0 and 0.05. Solid lines show the Curie-Weiss law [96W1].

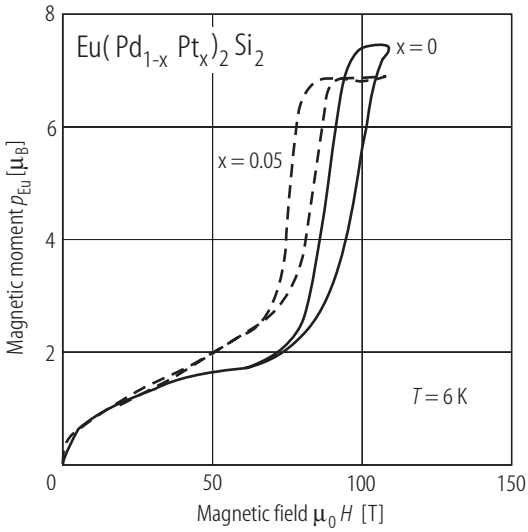

Fig. 346. $Eu(Pd_{1-x}Pt_x)_2Si_2$. Magnetic field dependence of p_{Eu} for x = 0 and 0.05 at 6 K [96W1].

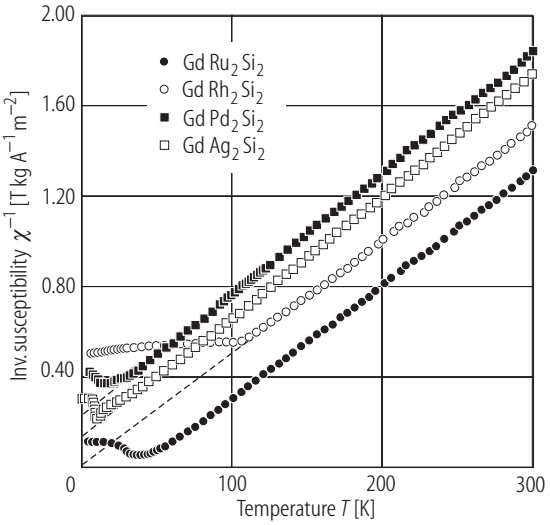

Fig. 347. $GdRu_2Si_2$, $GdRh_2Si_2$, $GdPd_2Si_2$, Temperature dependence of χ^{-1} [97T1].

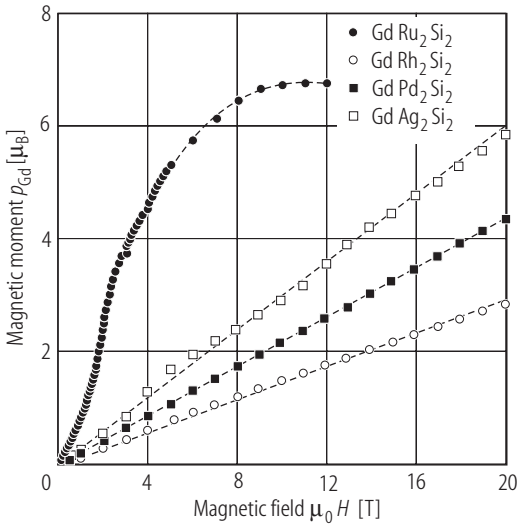

Fig. 348. $GdRu_2Si_2$, $GdRh_2Si_2$, $GdPd_2Si_2$. Magnetic field dependence of p_{Gd} at 4.2 K [97T1].

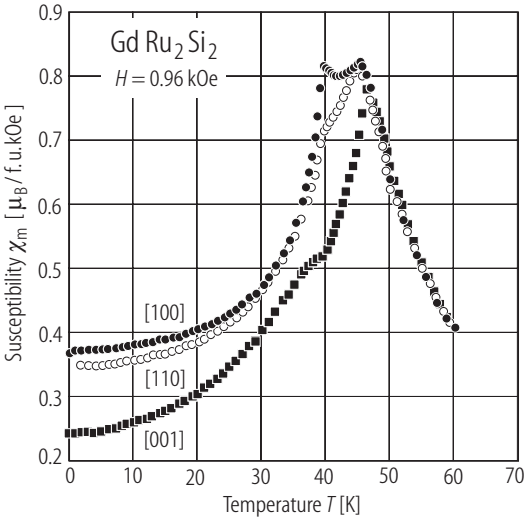

Fig. 349. $GdRu_2Si_2$. Temperature dependence of χ_m for the three main crystallographic axes at 0.96 kOe. Note that the three curves along the main crystallographic axes are superimposed [95G3].

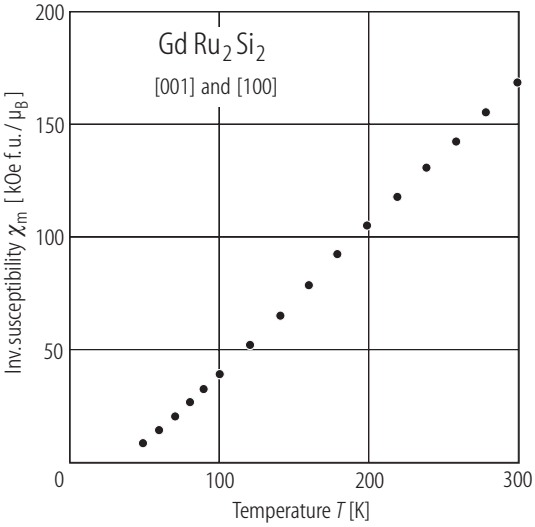

Fig. 350. $GdRu_2Si_2$. Temperature dependence of χ_m^{-1} along the [001] and [100] axes [95G3].

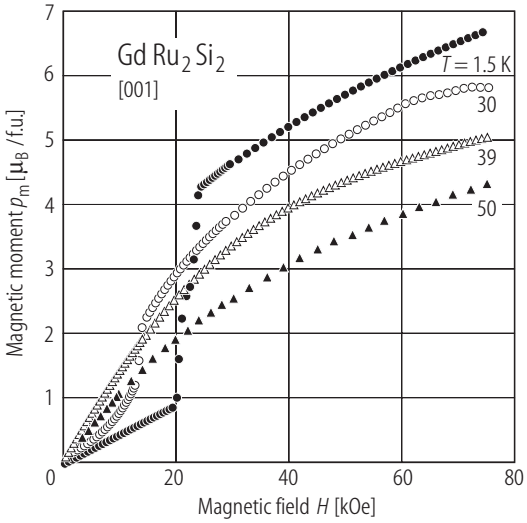

Fig. 351. $GdRu_2Si_2$. Magnetic field dependence of p_m for the H || [001] axis at different temperatures [95G3].

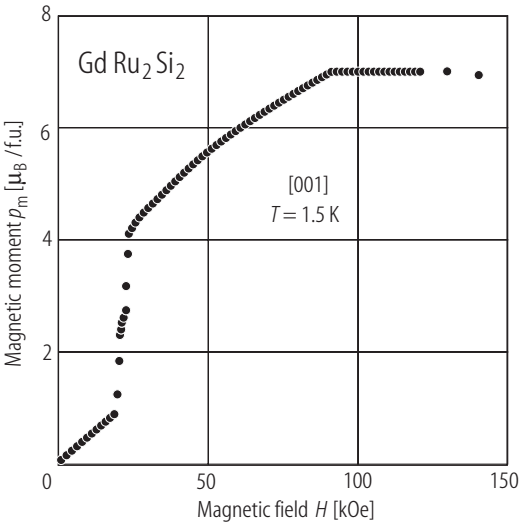

Fig. 352. $GdRu_2Si_2$. Magnetic field dependence of p_m at 1.5 K for H || [001] up to 140 kOe [95G3].

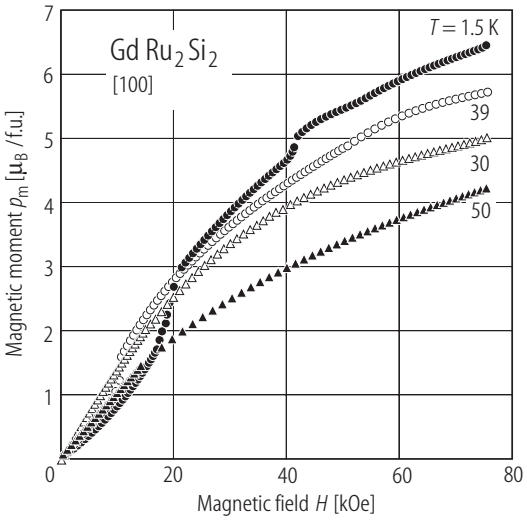

Fig. 353. $GdRu_2Si_2$. Magnetic field dependence of p_m for H || [100] at different temperatures [95G3].

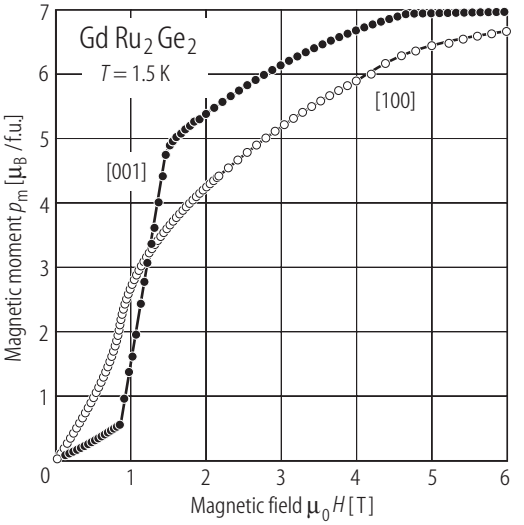

Fig. 355. $GdRu_2Ge_2$. Magnetic field dependence of p_m at 1.5 K along and perpendicular to the c axis [96G1].

For Fig. 354 see next page.

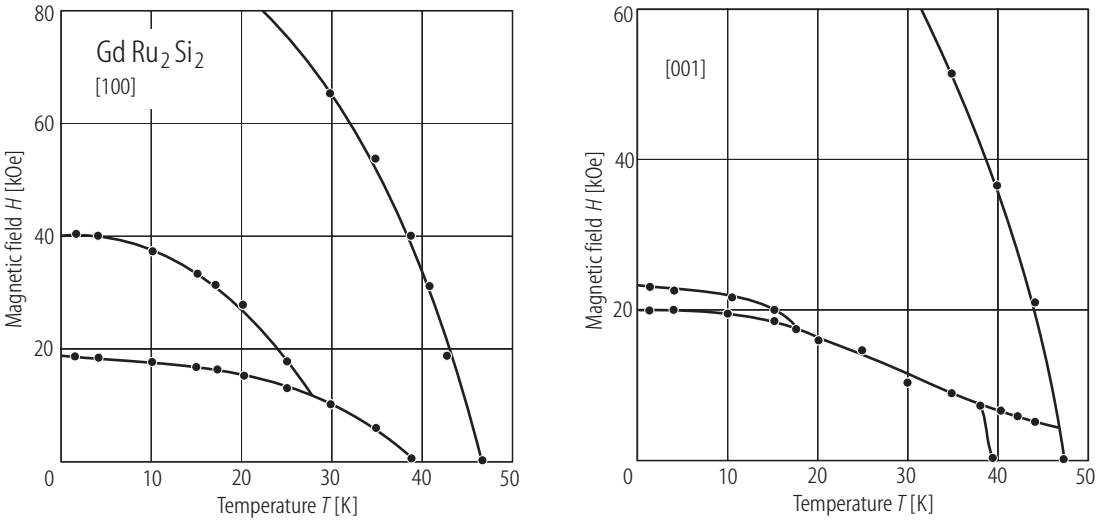

Fig. 354. $GdRu_2Si_2$. H - T phase diagrams for the H || [100] and [001] axes [95G3].

For Fig. 355 see previous page.

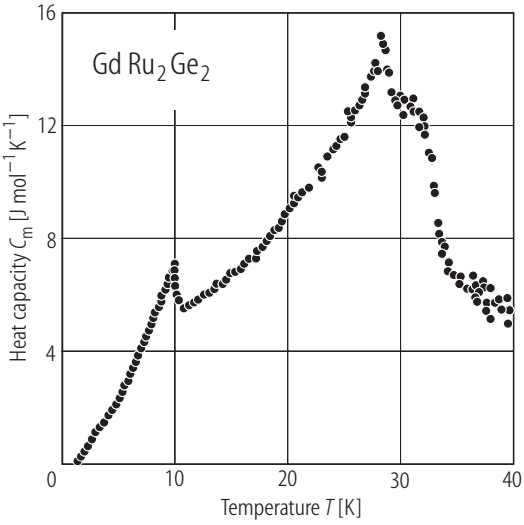

Fig. 356. $GdRu_2Ge_2$. Temperature dependence of the magnetic heat capacity C_m [96G1].

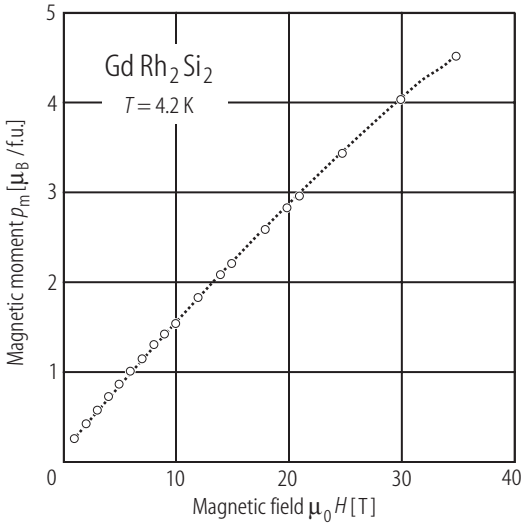

Fig. 357. $GdRh_2Si_2$. Magnetic field dependence of p_m at 4.2 K of powder particles free to rotate in the applied field [92S4].

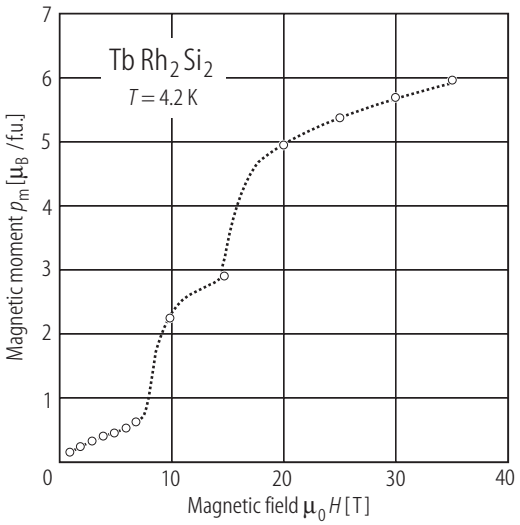

Fig. 358. $TbRh_2Si_2$. Magnetic field dependence at 4.2 K of powder particles, free to rotate in the applied field. The data above 7 T have been taken by means of a 35 T pulse in a decreasing magnetic field [92S4].

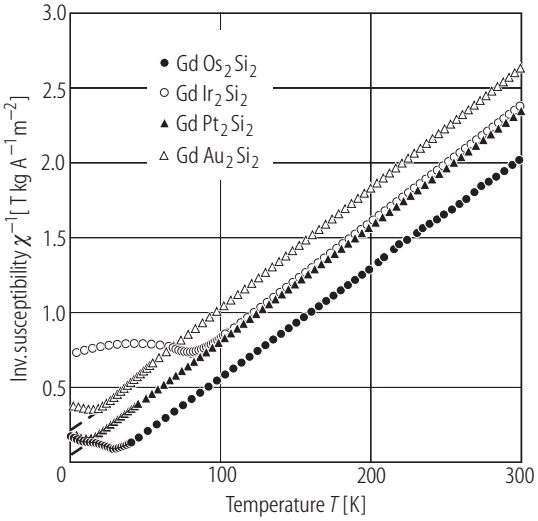

Fig. 359. $GdOs_2Si_2$, $GdIr_2Si_2$, $GdPt_2Si_2$. Temperature dependence of χ^{-1} [97T1].

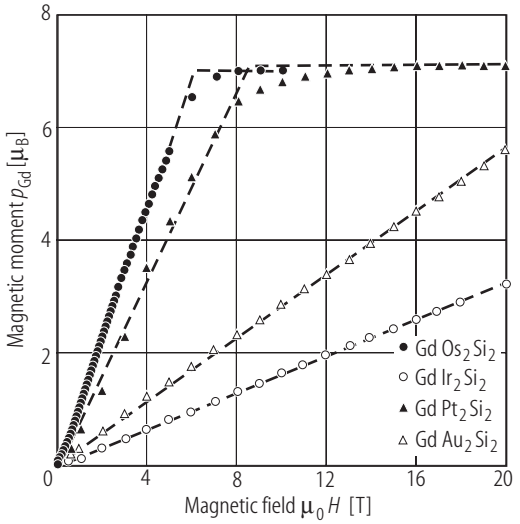

Fig. 360. $GdOs_2Si_2$, $GdIr_2Si_2$, $GdPt_2Si_2$. Magnetic field dependence of p_{Gd} at 4.2 K [97T1].

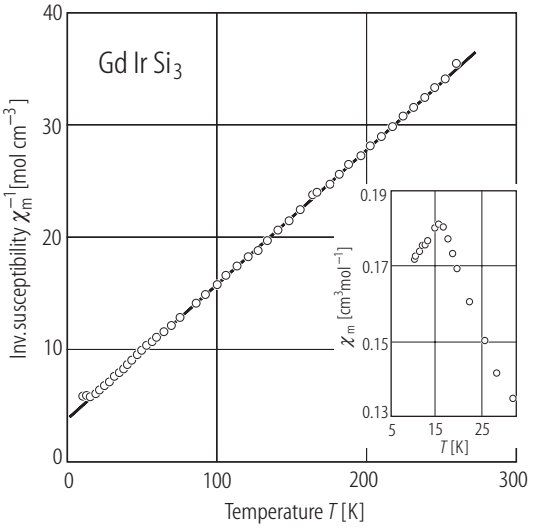

Fig. 361. $GdIrSi_3$. Temperature dependence of χ_m^{-1}. Inset: χ in the magnetic-order region [91S1].

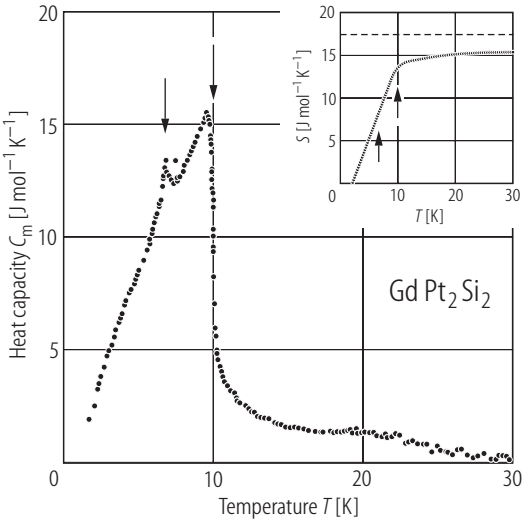

Fig. 362. $GdPt_2Si_2$. Magnetic contribution to the magnetic heat capacity. Inset: magnetic entropy; the hatched line indicates the R ln(8) limit [91G1].

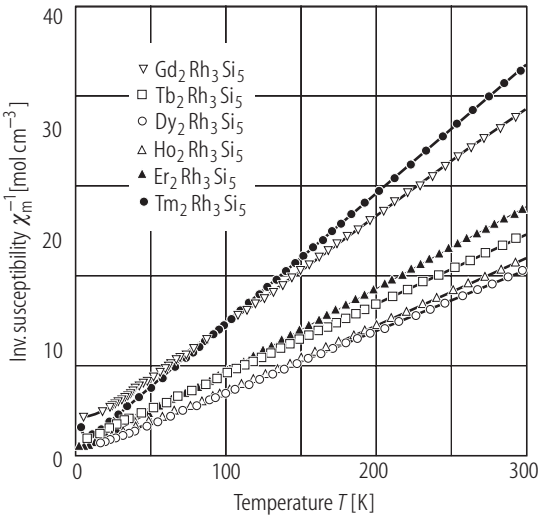

Fig. 363. $Gd_2Rh_3Si_5$, $Tb_2Rh_3Si_5$, $Dy_2Rh_3Si_5$, $Ho_2Rh_3Si_5$, $Er_2Rh_3Si_5$, $Tm_2Rh_3Si_5$. Temperature dependence of χ_m^{-1} [97P1].

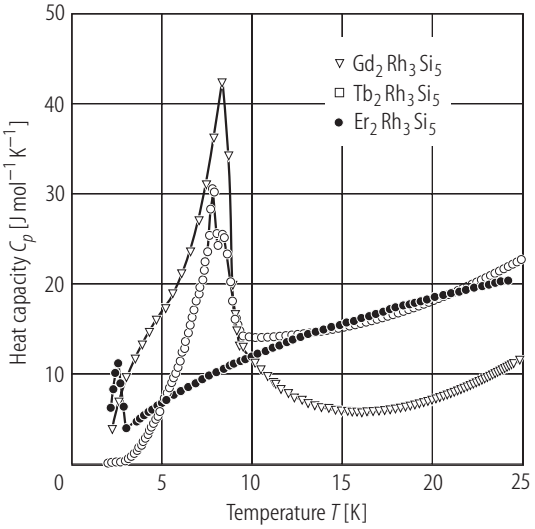

Fig. 364. $Gd_2Rh_3Si_5$, $Tb_2Rh_3Si_5$, $Er_2Rh_3Si_5$. Temperature dependence of C_p [97P1].

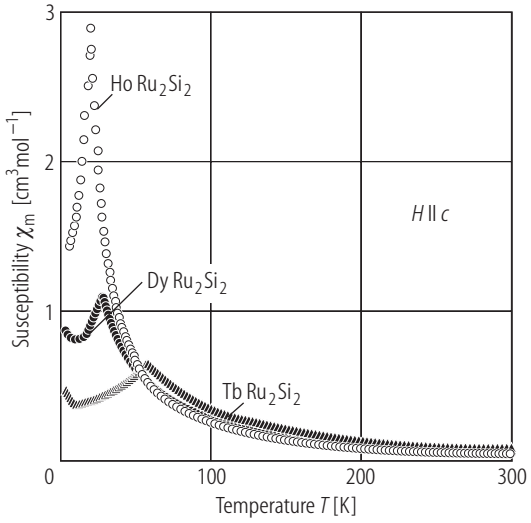

Fig. 366. $TbRu_2Si_2$, $DyRu_2Si_2$, $HoRu_2Si_2$. Temperature dependence of χ_m with the magnetic field $H \parallel c$ [95T3].

For Fig. 365 see next page.

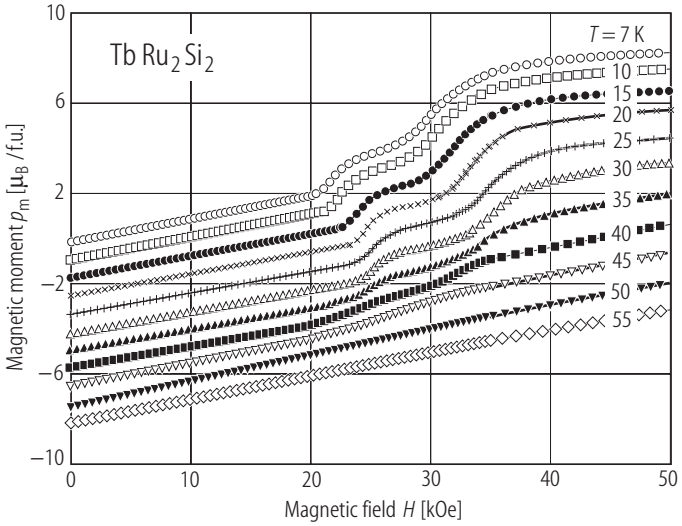

Fig. 365. $TbRu_2Si_2$. Isothermal magnetization at several temperatures [94S1].

For Fig. 366 see previous page.

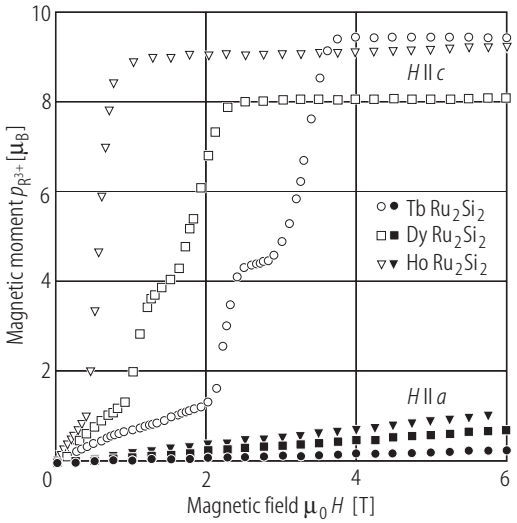

Fig. 367. $TbRu_2Si_2$, $DyRu_2Si_2$, $HoRu_2Si_2$. Magnetization vs. H. Open symbols: $H \parallel c$, solid symbols: $H \parallel a$ [95T3].

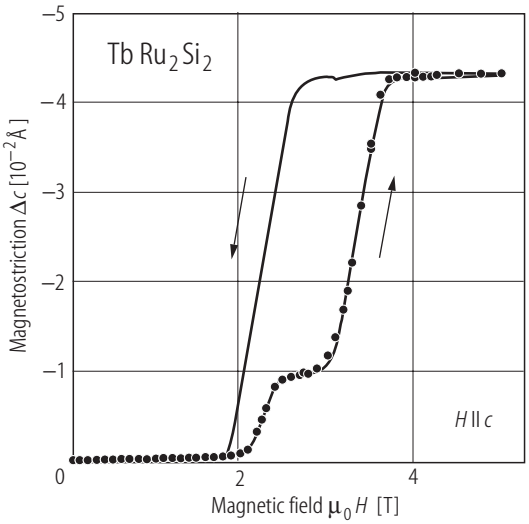

Fig. 368. $TbRu_2Si_2$. Parallel magnetostriction vs. H with $H \parallel c$. Solid circles: squared magnetization $M(H)^2$ in arbitrary units [95T3].

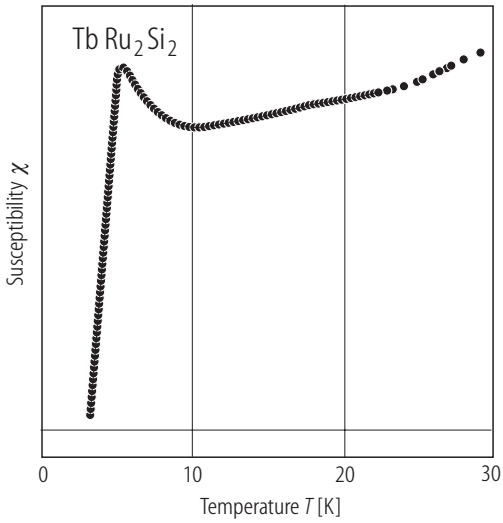

Fig. 369. $TbRu_2Si_2$. Temperature dependence of the ac susceptibility χ in zero field [98K1].

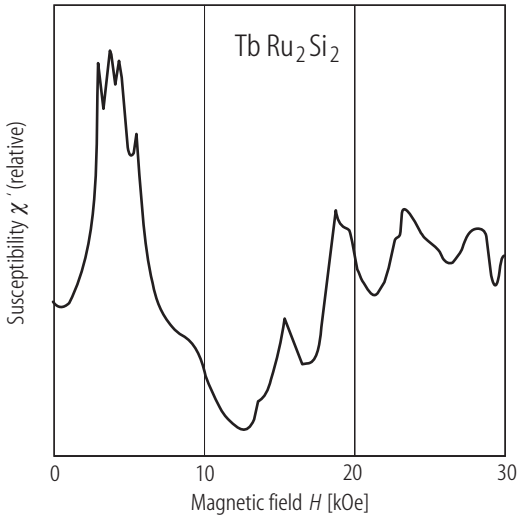

Fig. 370. $TbRu_2Si_2$. Magnetic field dependence of χ' at 3.5 K [98K1].

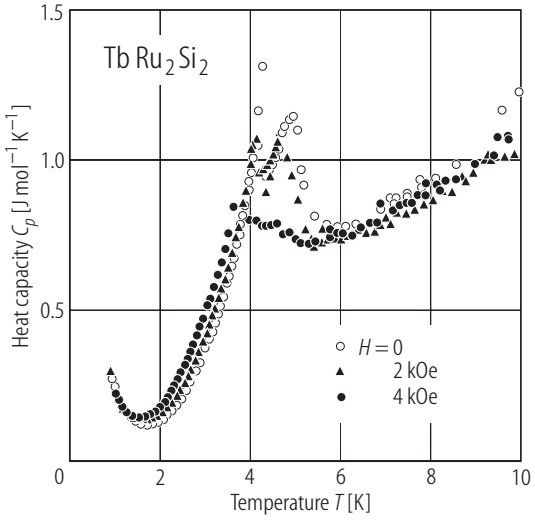

Fig. 371. $TbRu_2Si_2$. Temperature dependence of C_p [98K1].

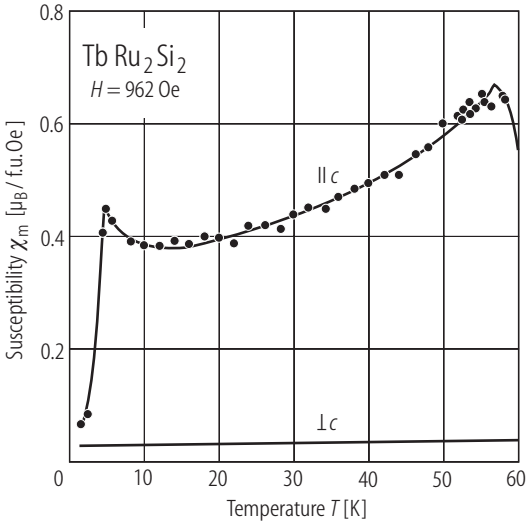

Fig. 372. $TbRu_2Si_2$. Temperature dependence of χ_m along the *c* axis and in the *c* plane at 962 Oe [95S5].

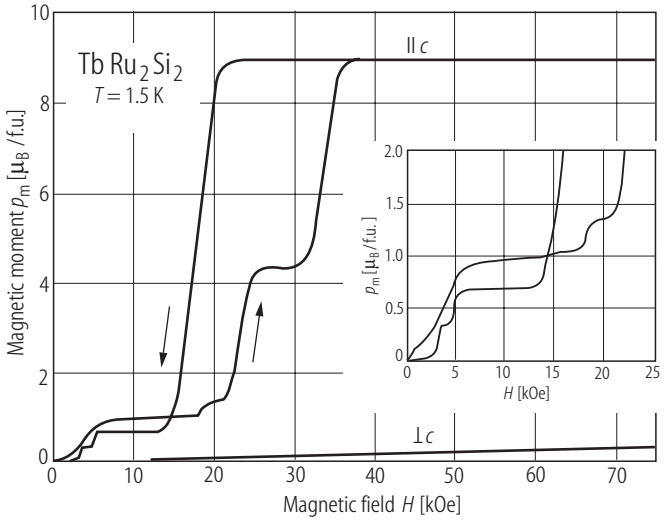

Fig. 373. $TbRu_2Si_2$. Magnetic field dependence of p_m along the c axis and in the c plane at 1.5 K [95S5].

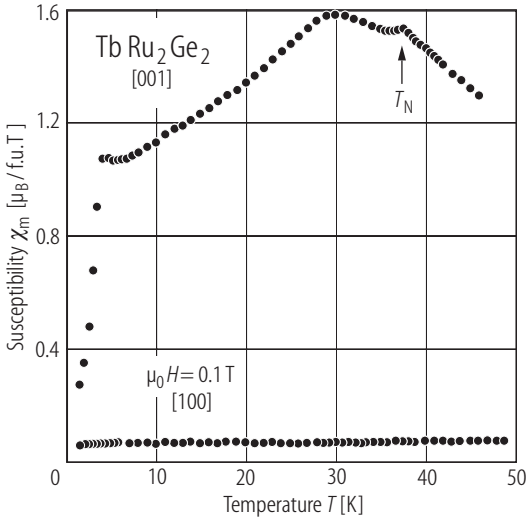

Fig. 374. $TbRu_2Ge_2$. Temperature dependence of χ_m at 0.1 T along [001] and [100] [96G1].

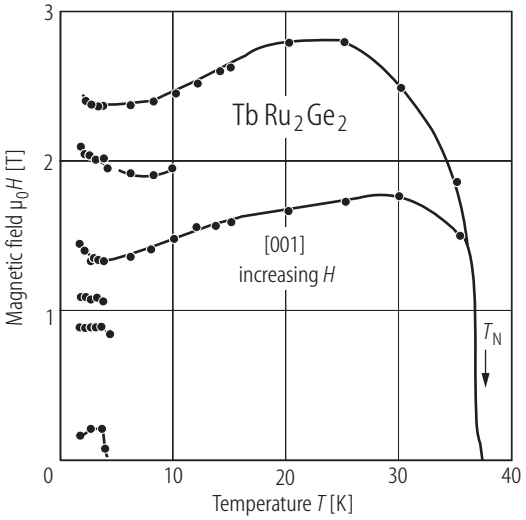

Fig. 375. $TbRu_2Ge_2$. Temperature dependence of the H - T diagram for [001] direction [96G1].

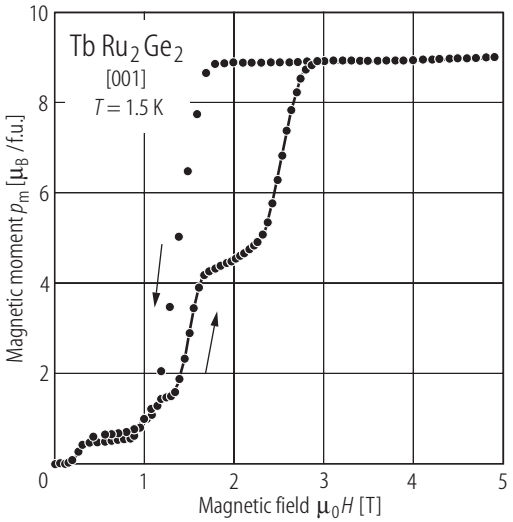

Fig. 376. $TbRu_2Ge_2$. Magnetic field dependence of p_m at 1.5 K along [001] [96G1].

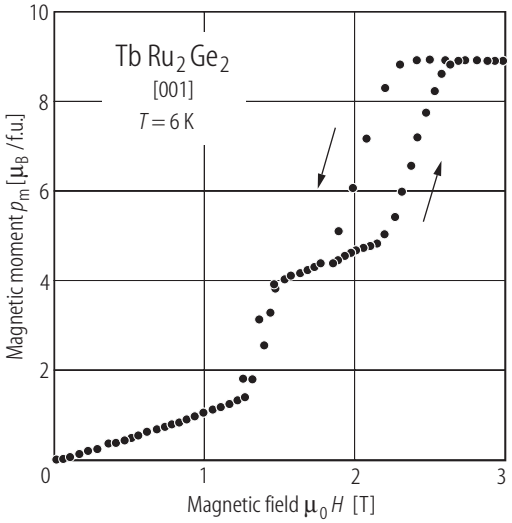

Fig. 377. $TbRu_2Ge_2$. Magnetic field dependence of p_m at 6 K [96G1].

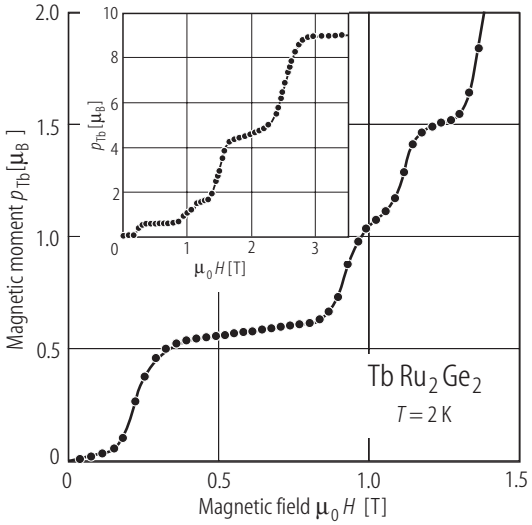

Fig. 378. $TbRu_2Ge_2$. Metamagnetic process. Low-field dependence of p_{Tb} at 2 K [97B3].

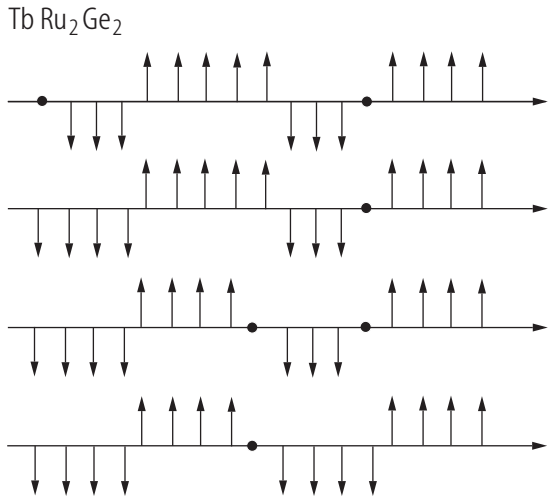

Fig. 379. $TbRu_2Ge_2$. Magnetic structure at 2 K in ZF and the three first phases. Magnetizations of 17 successive Tb planes $\perp$ to Q are represented. Black dots correspond to nonmagnetic planes [97B3].

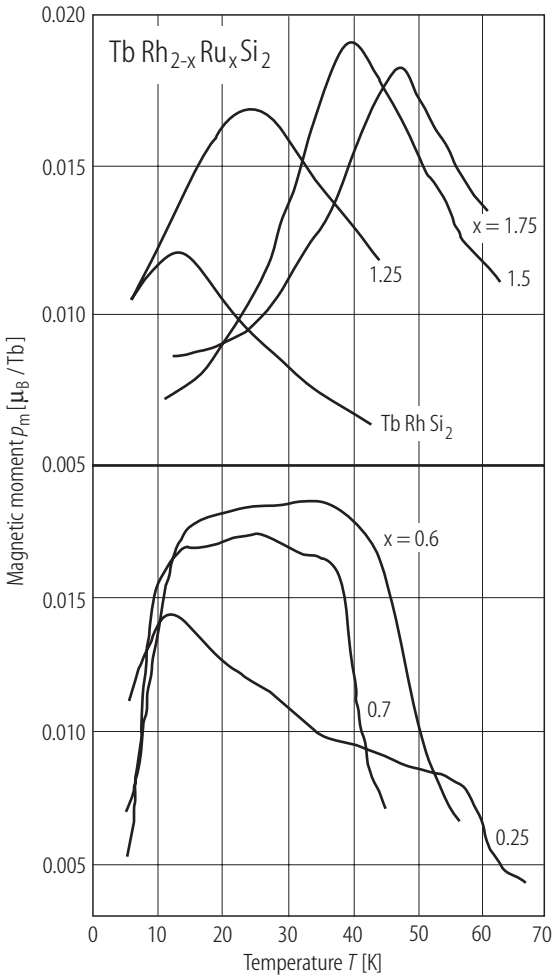

Fig. 380. $TbRh_{2-x}$ Ru_xSi_2. Temperature dependence of p_m for different x [93I1].

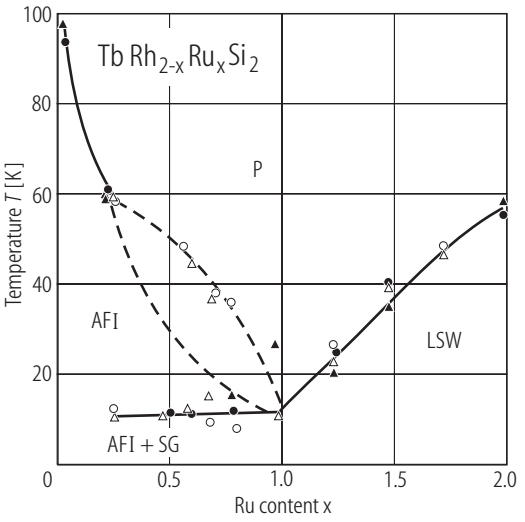

Fig. 381. $TbRh_{2-x}Ru_xSi_2$. Magnetic phase diagram in zero or low magnetic fields, determined from neutron diffraction. Solid triangles and circles: dc susceptibility; open triangles: ac susceptibility; open circles: magnetization in low magnetic fields [93I1].

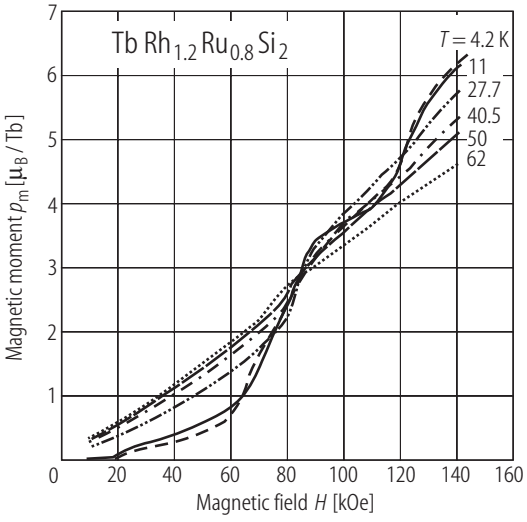

Fig. 383. $TbRh_{1.2}$ $Ru_{0.8}Si_2$. High-field magnetization at various temperatures [93I1].

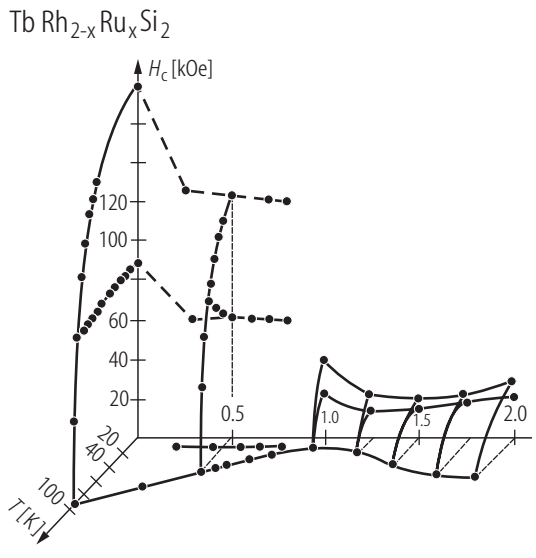

Fig. 382. $TbRh_{2-x}Ru_xSi_2$. (H,T,x) magnetic phase diagram [93I1].

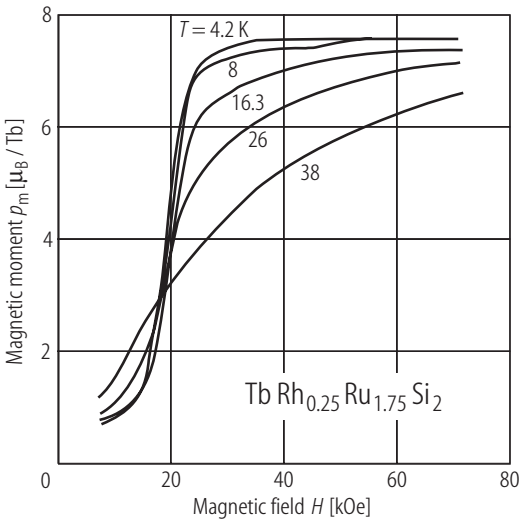

Fig. 384. $TbRh_{0.25}Ru_{1.75}Si_2$. High-field magnetization at various temperatures [93I1].

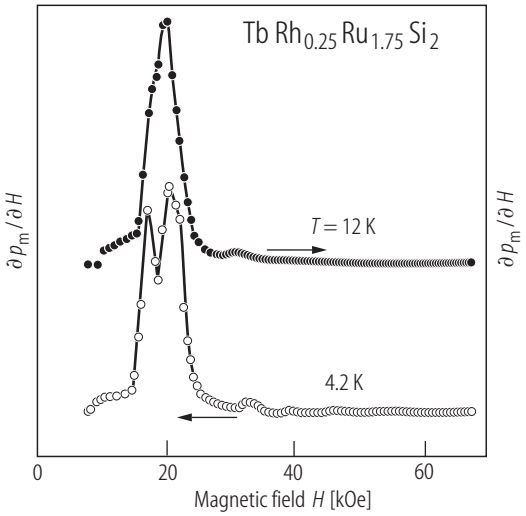

Fig. 385. $TbRh_{0.25}Ru_{1.75}Si_2$. Magnetic field dependence of differential magnetization at 4.2 and 12 K [93I1].

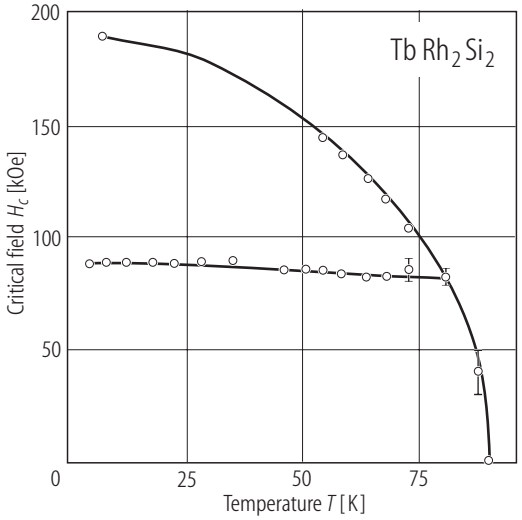

Fig. 386. $TbRh_2Si_2$. Temperature dependence of transition (critical) fields determined from $\partial p_m/\partial H$ vs. H [93I1].

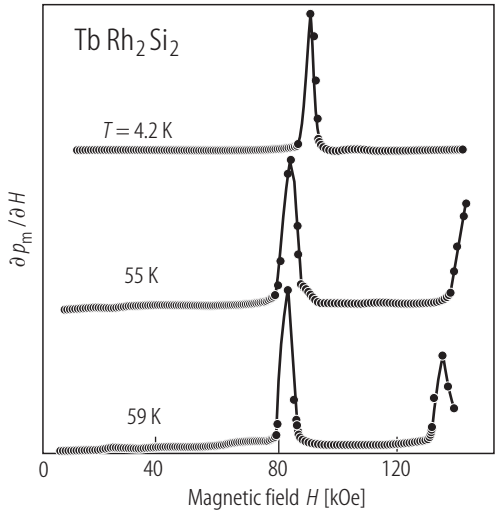

Fig. 387. $TbRh_2Si_2$. Magnetic field dependence of $\partial p_m/\partial H$ at different temperatures [93I1].

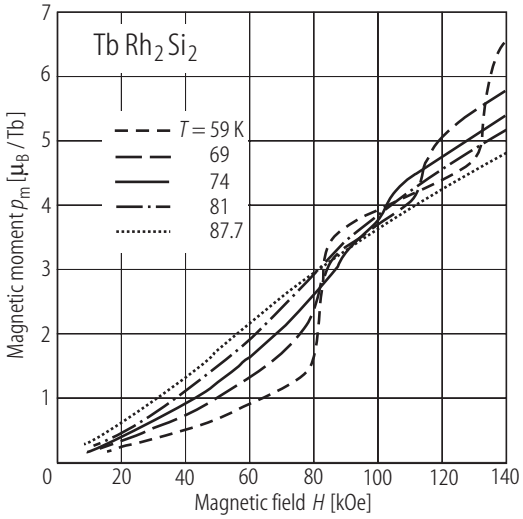

Fig. 388. $TbRh_2Si_2$. Magnetic field dependence of p_m at different temperatures [93I1].

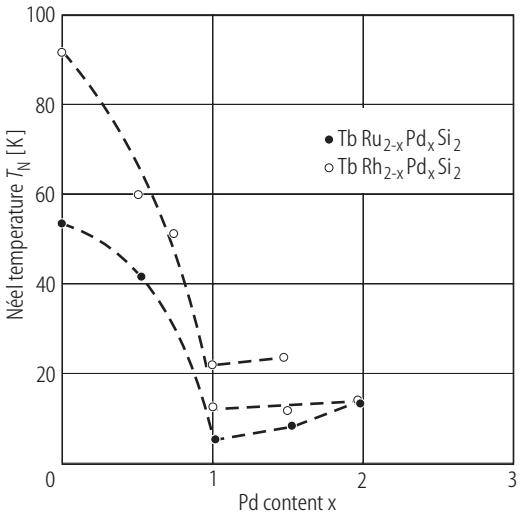

Fig. 389. $TbRu_{2-x}Pd_xSi_2$, $TbRh_{2-x}Pd_xSi_2$. Magnetic phase diagram [96I3].

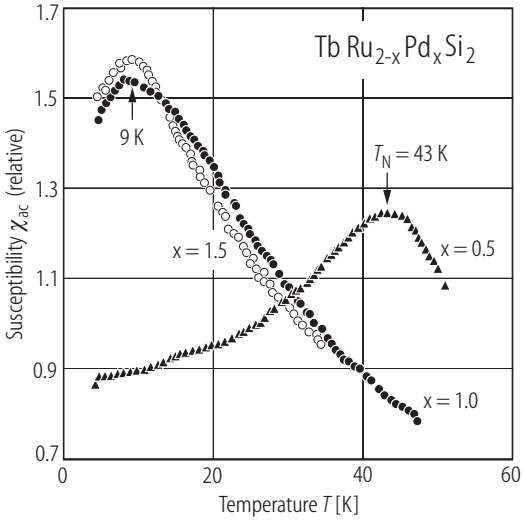

Fig. 390. $TbRu_{2-x}Pd_xSi_2$. Temperature dependence of χ_{ac} for different concentrations [96I3].

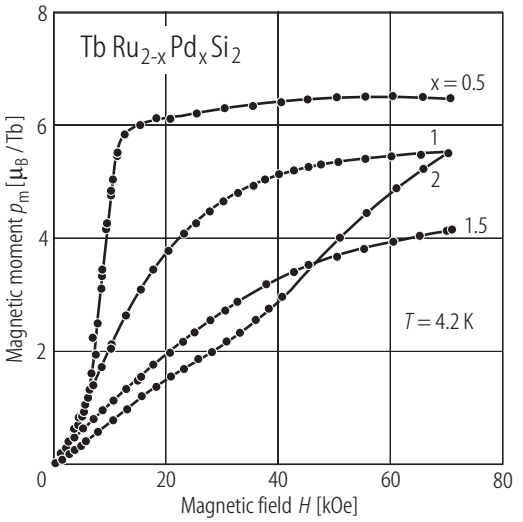

Fig. 391. $TbRu_{2-x}Pd_xSi_2$. Magnetic field dependence of p_m for various concentrations at 4.2 K [96I3].

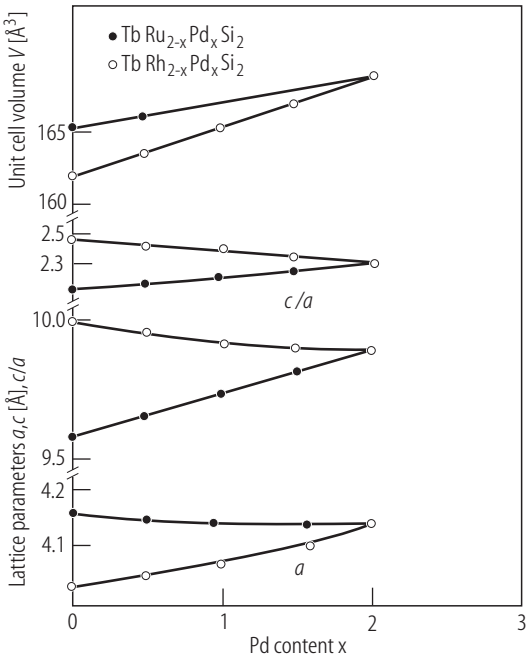

Fig. 392. $TbRu_{2-x}Pd_xSi_2$, $TbRh_{2-x}Pd_xSi_2$. Concentration dependence of the lattice constants *a* and *c* and of the ratio *a/c* of the unit cell [96I3].

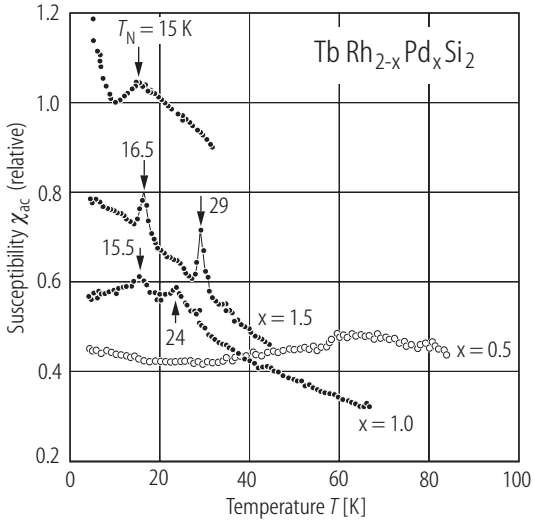

Fig. 393. $TbRh_{2-x}Pd_xSi_2$. Temperature dependence of χ_{ac} for different temperatures [96I3].

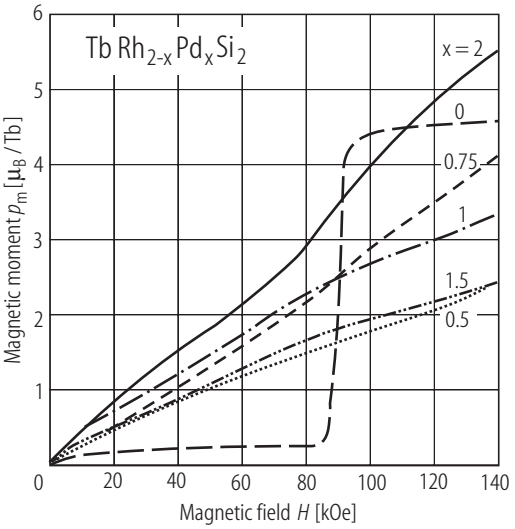

Fig. 394. $TbRh_{2-x}Pd_xSi_2$. Magnetic field dependence of p_m for various concentrations at 4.2 K [96I3].

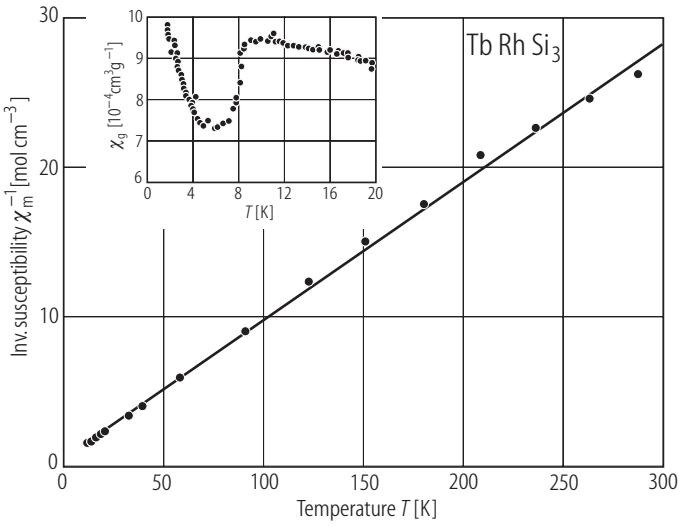

Fig. 395. $TbRhSi_3$. Temperature dependence of χ_m^{-1} and χ_g at low temperatures [96J2].

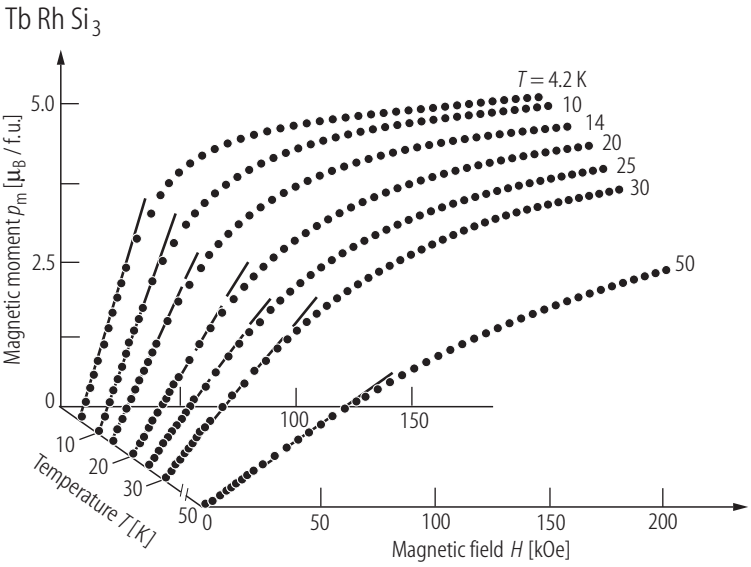

Fig. 396. $TbRhSi_3$. Magnetic field dependence of p_m at different temperatures [96J2].

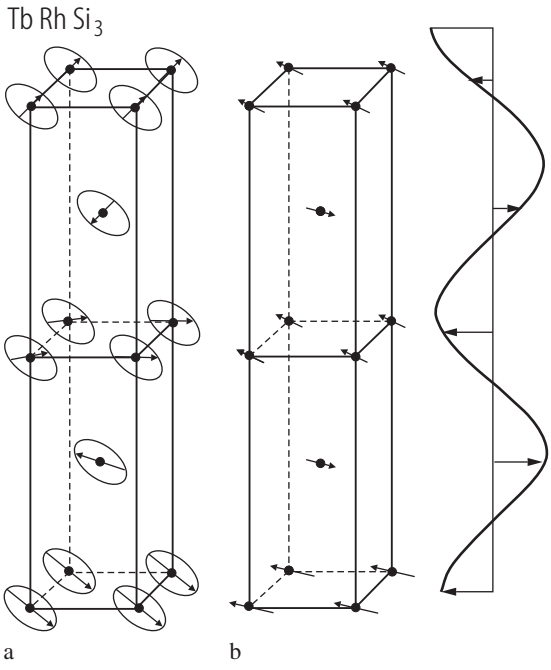

Fig. 397. $TbRhSi_3$. Magnetic structure: (**a**) helicoidal and (**b**) sine-modulated [96J2].

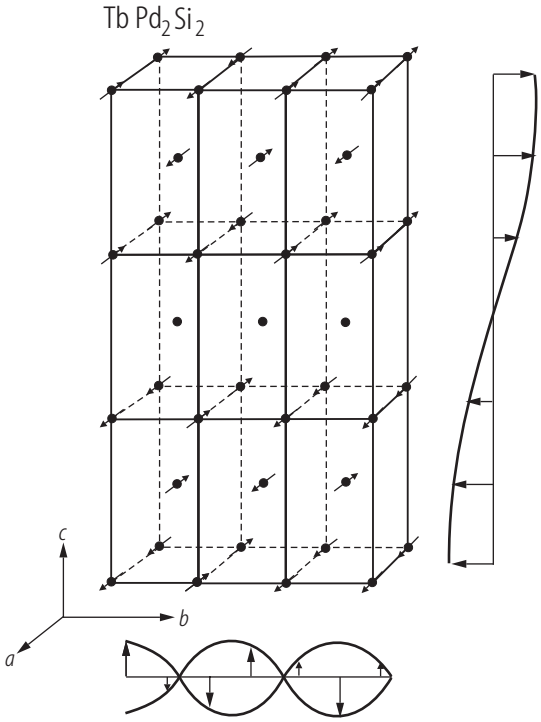

Fig. 398. $TbPd_2Si_2$. Schematic representation of the magnetic structure at 1.5 K [97B5].

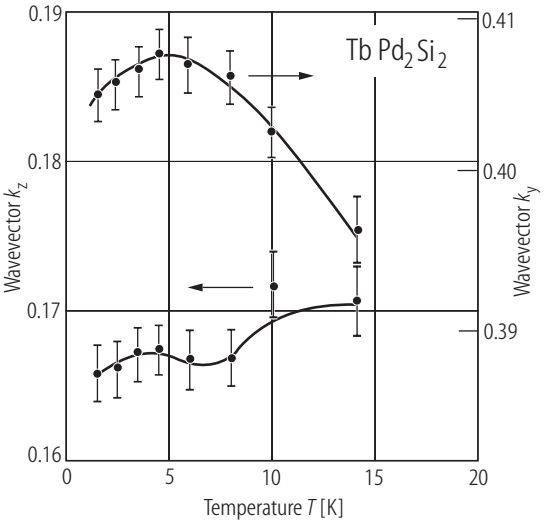

Fig. 399. $TbPd_2Si_2$. Temperature dependence of wavevector components k_z and k_y [97B5].

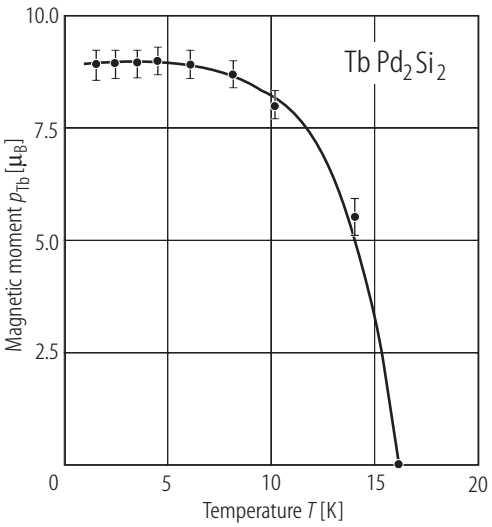

Fig. 400. $TbPd_2Si_2$. Temperature dependence of p_{Tb} [97B5].

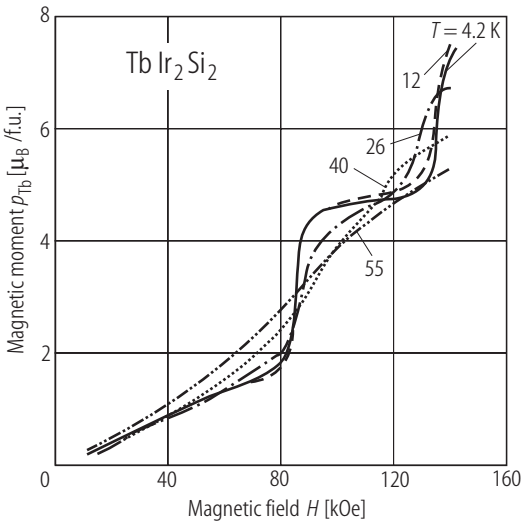

Fig. 401. $TbIr_2Si_2$. Magnetic field dependence of p_{Tb} at different temperatures [94S2].

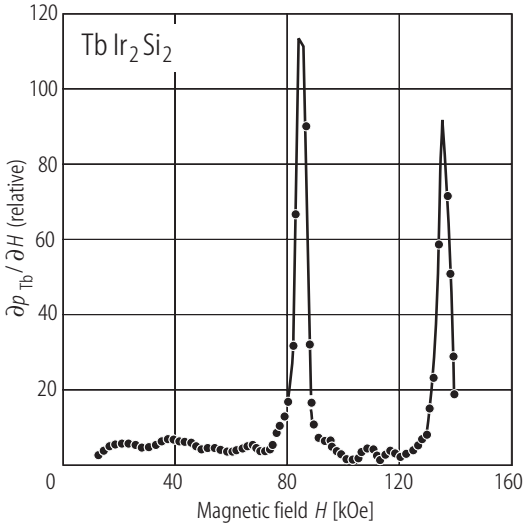

Fig. 402. $TbIr_2Si_2$. Magnetic field dependence of the differential magnetization at $T = 4.2$ K [94S2].

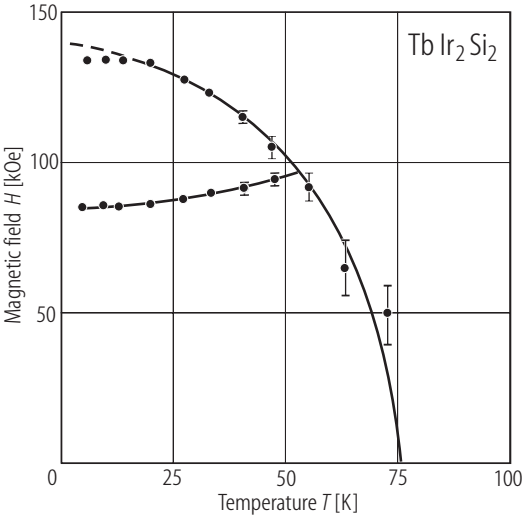

Fig. 403. $TbIr_2Si_2$. Magnetic phase diagram [94S2].

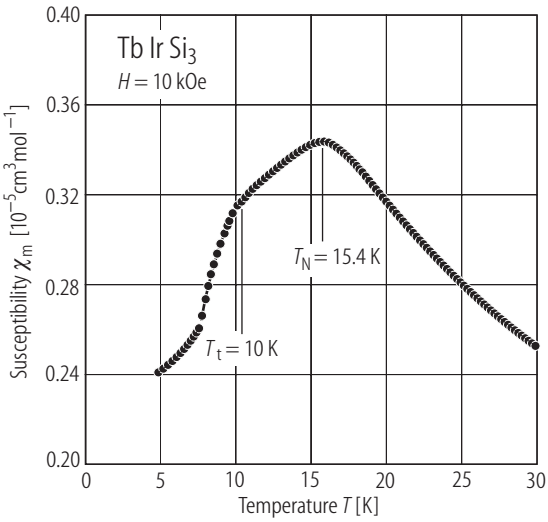

Fig. 404. $TbIrSi_3$. Temperature dependence of χ_m at 10 kOe [98B3].

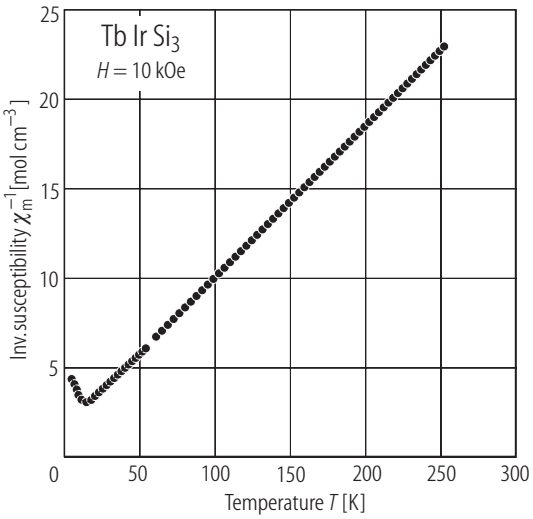

Fig. 405. $TbIrSi_3$. Temperature dependence of χ_m^{-1} at 10 kOe. T_N = 15.4 K, Θ = 17 K, p_{eff} = 9.75 μ_B/f.u. [98B3].

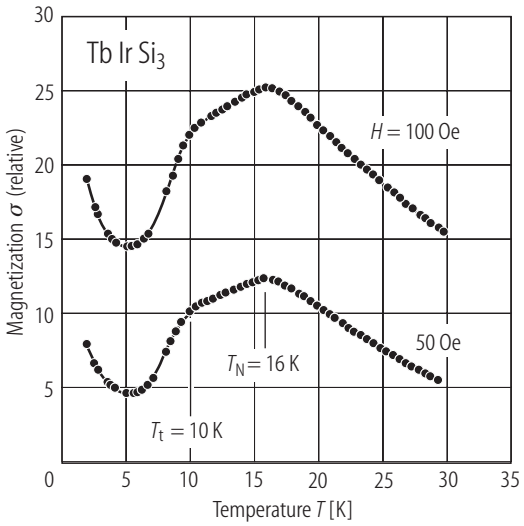

Fig. 406. $TbIrSi_3$. Temperature dependence of σ at low magnetic field [98B3].

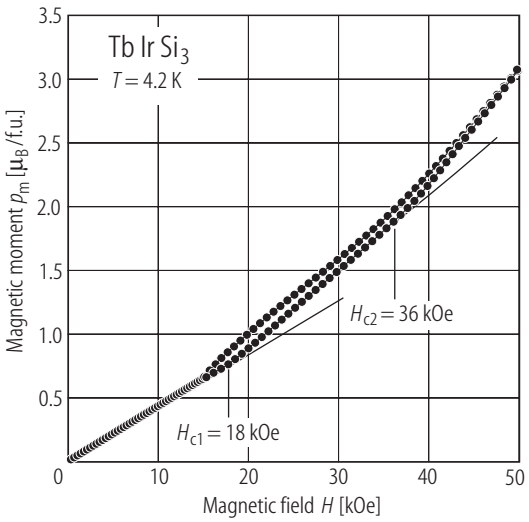

Fig. 407. $TbIrSi_3$. Magnetic field dependence of p_m at 4.2K. H_{c1} and H_{c2} denote critical fields [98B3].

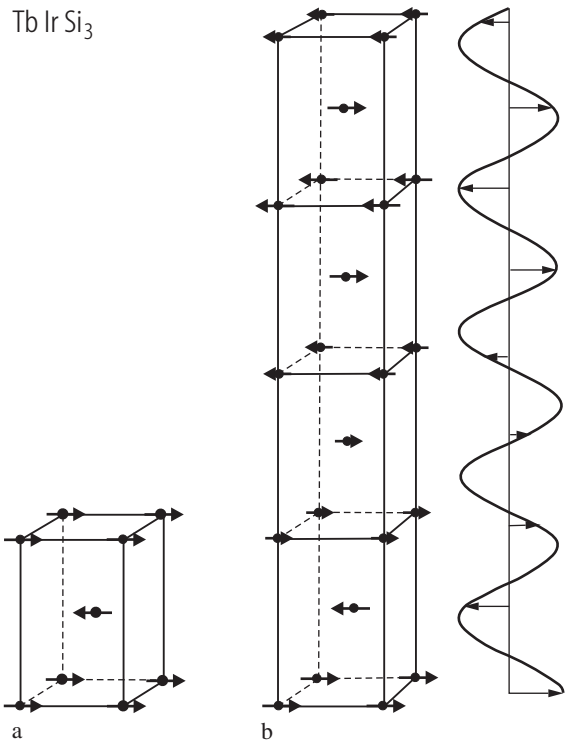

Fig. 408. $TbIrSi_3$. Magnetic structures at different temperatures (**a**) a collinear AFI-type (16 K ≤ T≤ 7.4 K), and (**b**) sine modulated (11 < T < T_N = 16 K). Only Tb atoms are presented [98B3].

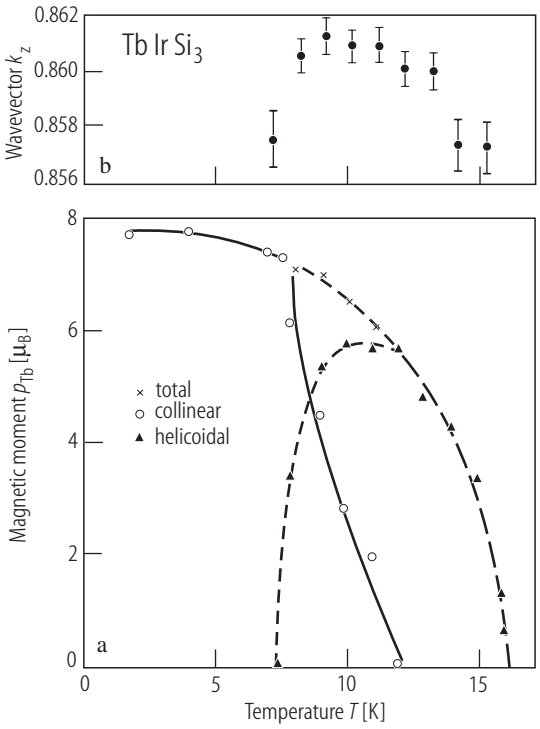

Fig. 409. $TbIrSi_3$. Temperature dependence of (**a**) total magnetic moment and collinear and helicoidal components and (**b**) propagation-vector component k_z of the magnetic moment [98B3].

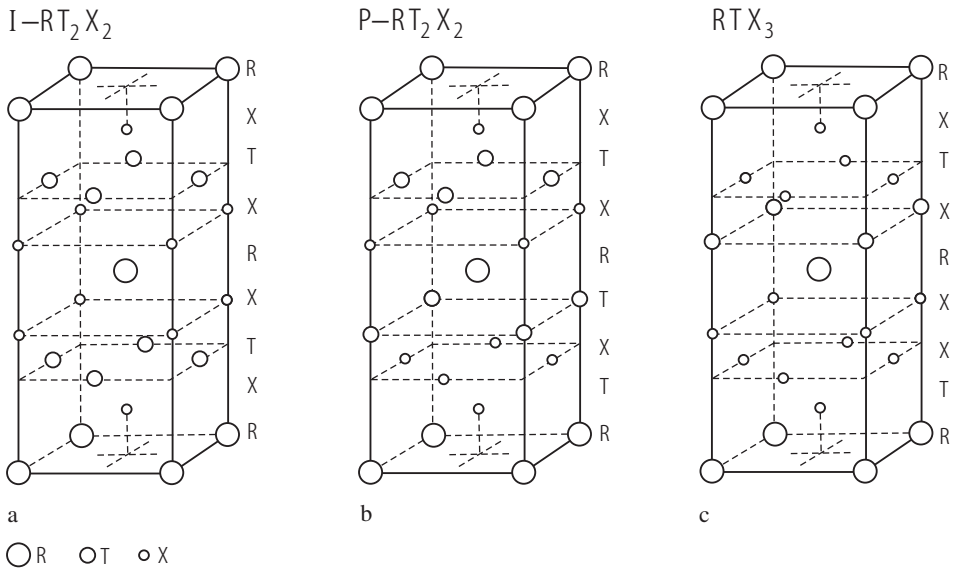

Fig. 410. The tetragonal cells of (**a**) the $ThCr_2Si_2$ -type (space group I4/mmm), (**b**) the $CaBe_2Ge_2$ -type (space group P4/nmm), and (**c**) $BaNiSn_3$ -type (space group I4/mm) [98B3].

References

91G1 Gignoux, D., Morin, M., Schmitt, D.: J. Magn. Magn. Mater. **102** (1991) 33

91S1 Sanchez, J.P., Tomala, K., Łątka, K.: J. Magn. Magn. Mater. **99** (1991) 95

92S4 Szytula, A., Radwanski, R.J., de Boer, F.R.: J. Magn. Magn. Mater. **104-107** (1992) 1237

93I1 Ivanov. V., Vinokurowa, L., Szytula, A.: J. Alloys Comp. **201** (1993)109

94S1 Salgueiro da Silva, M., Sousa, J.B., Chevalier, B., Etourneau, J.: J. Appl. Phys. **76** (1994) 6344

94S2 Szytula, A., Ivanov, V., Vinokurova, L.: Acta Phys. Pol. **85** (1994)

95G3 Garnier, A., Gignoux, D., Iwata, N., Schmitt, D., Shigeoka, T., Zhang, F.Y.: J. Magn. Magn. Mater. **140-144** (1995) 899

95S5 Shigeoka, T., Iwata, N., Garnier, A., Gignoux, D., Schmitt, D., Zhang, F.Y.: J. Magn. Magn. Mater. **140-144** (1995) 901

95T3 Takeuchi, T., Taniguchi, T., Kudoh, D., Miyako, Y.: Physica B **206-207** (1995) 398

96G1 Garnier, A., Gignoux, D., Schmitt., D., Shigeoka, T.: J. Magn. Magn. Mater. **157-158** (1996) 389

96I3 Ivanov, V., Vinokurova, L., Mydlarz, T., Szytula, A.: J. Alloys Comp. **230** (1996) L5

96J2 Jaworska-Golab, T., Guillot, M., Kolenda, M., Ressouche, E., Szytula, A.: J. Magn. Magn. Mater. **164** (1996) 371

96W1 Wada, H., Mitsuda, A., Shiga, M.: J. Phys. Soc. Jpn. **65** (1996) 3471

97B3 Blanco, J.A., Garnier, A., Gignoux, D., Schmitt, D.: J. Alloys Comp. **275-277** (1997) 565

97B5 Bazela, W., Baran, S., Leciejewicz, J., Szytula, A., Ding, Y.: J. Cond. Matter **9** (1997) 2267

97P1 Patil, N.G., Ramakrishnan, S.: Physica B **237-238** (1997) 597

97T1 Tung, L.D., Franse, J.J.M., Buschow, K.H.J., Brommer, P.E., Thuy, N.P.: J. Alloys Comp. **260** (1997) 35

98B3 Bazela, W., Stusser, N., Szytula, A., Zygmunt, A.: J. Alloys Comp. **275-277** (1998) 578

98K1 Kawae, T., Sakita, H., Hitaka, M., Takeda, K., Sigeoka, T., Iwata, N.: J. Magn. Magn. Mater. **177-181** (1998) 795

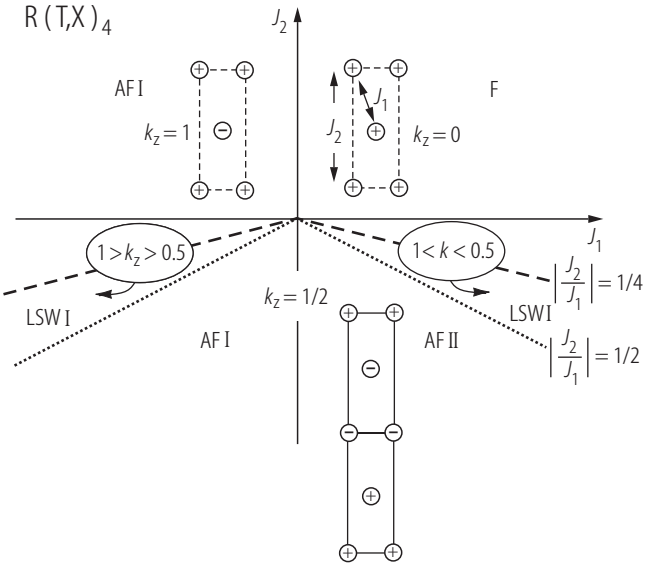

Fig. 411. $R(T,X)_4$. Stability conditions of the ternary compounds for the exchange integrals J_1 and J_2 [97W1, 97B3].

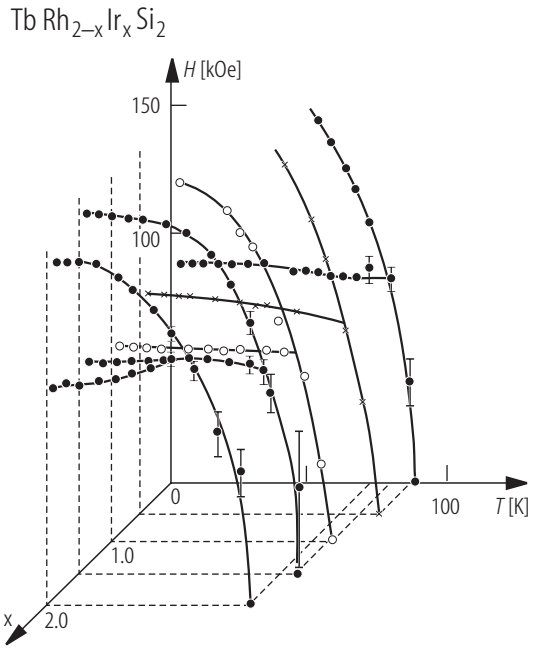

Fig. 412. $TbRh_{2-x}Ir_xSi_2$. Magnetic phase diagram (*H,T,*x) [95I2].

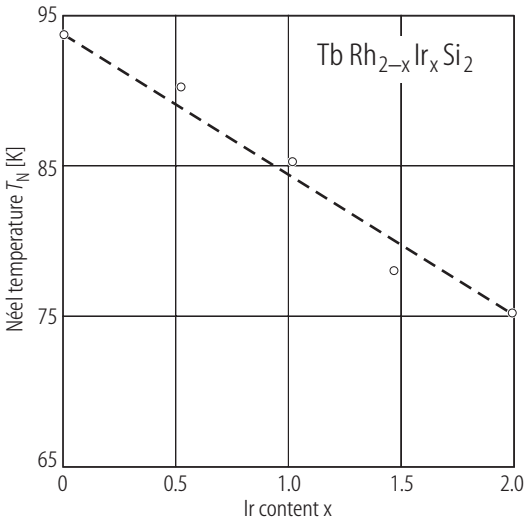

Fig. 413. $TbRh_{2-x}Ir_xSi_2$. Concentration dependence of T_N [95I2].

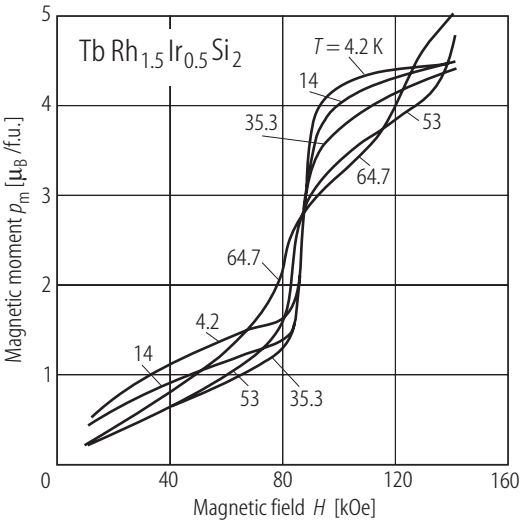

Fig. 414. $TbRh_{1.5}Ir_{0.5}Si_2$. Magnetic field dependence of high field p_m at various temperatures [95I2].

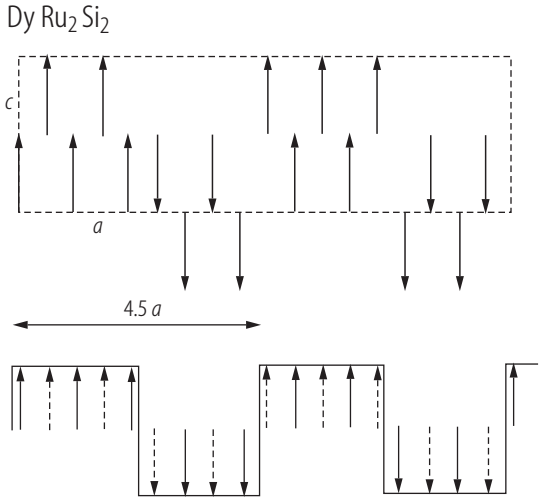

Fig. 415. $DyRu_2Si_2$. Squared magnetic structure (projection along [010]) The Dy moments are along the *c* axis [94B4].

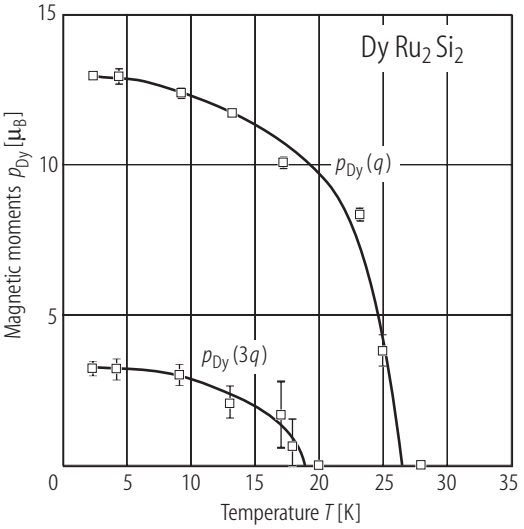

Fig. 416. $DyRu_2Si_2$. Temperature dependence of the magnetic moments associated with the first and third harmonics [94B4].

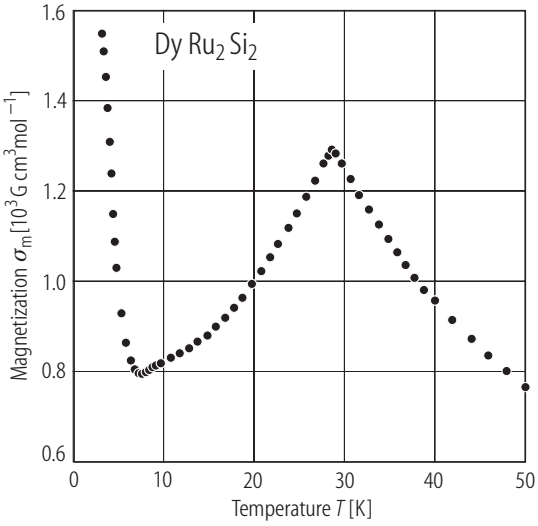

Fig. 417. $DyRu_2Si_2$. Temperature dependence of σ_m at 0.1 T [94B4].

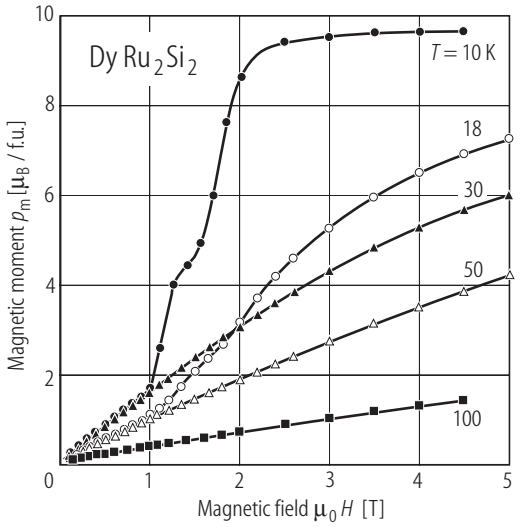

Fig. 418. $DyRu_2Si_2$. Magnetic field dependence of p_m at different temperatures [94B4].

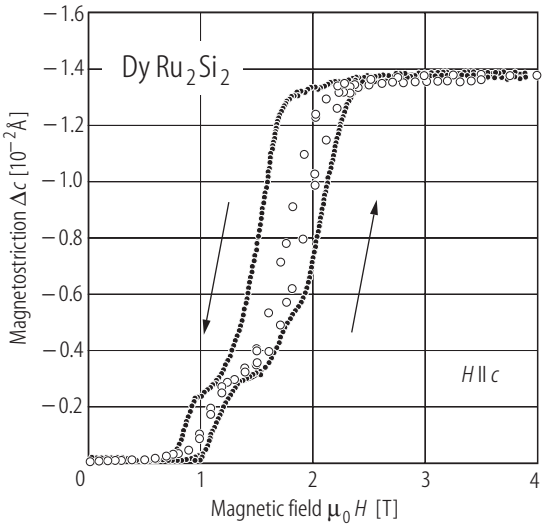

Fig. 420. $DyRu_2Si_2$. Parallel magnetostriction vs. magnetic field with $H \parallel c$. Open circles: squared magnetization $M(H)^2$ in arbitrary units [95T3].

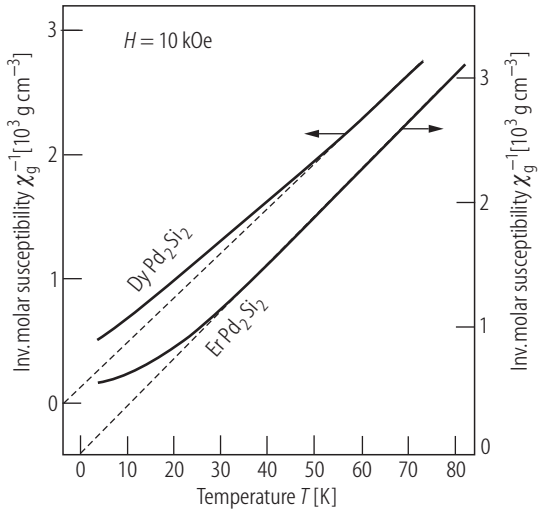

Fig. 421. $DyPd_2Si_2$, $ErPd_2Si_2$. Temperature dependence of χ_g^{-1} at 10 kOe [91B1].

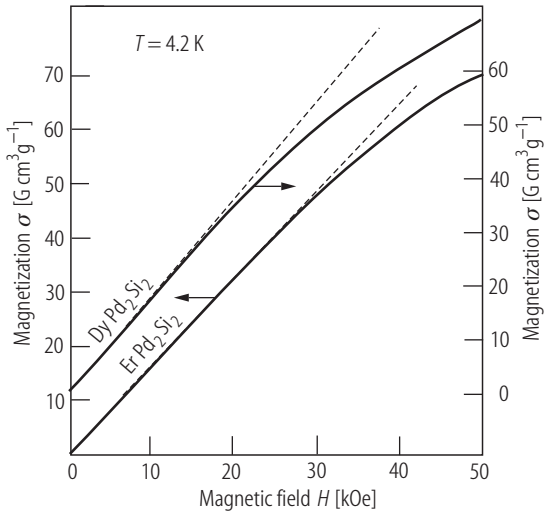

Fig. 422. $DyPd_2Si_2$. Magnetic field dependence of σ at 4.2 K [91B1].

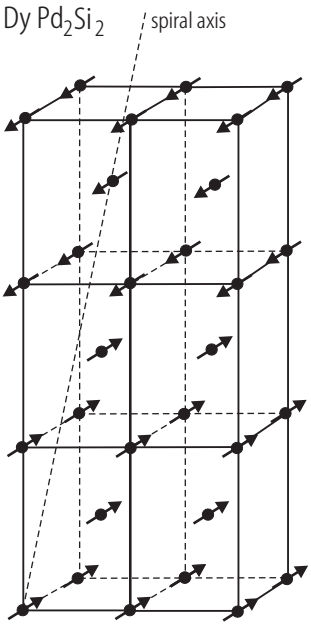

Fig. 423. $DyPd_2Si_2$. Magnetic structure [91B1].

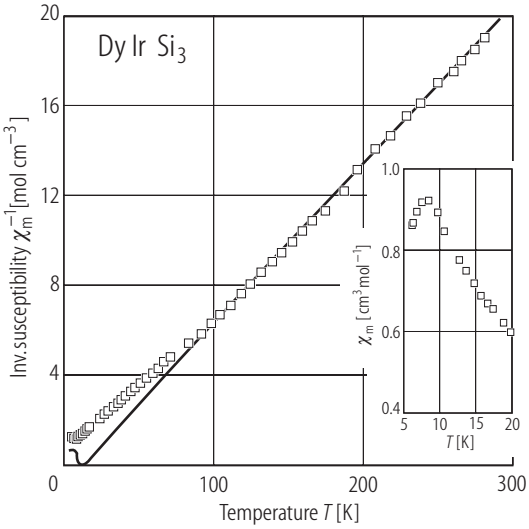

Fig. 424. $DyIrSi_3$. Temperature dependence of χ_m^{-1}. Inset: magnetic order region [91S1].

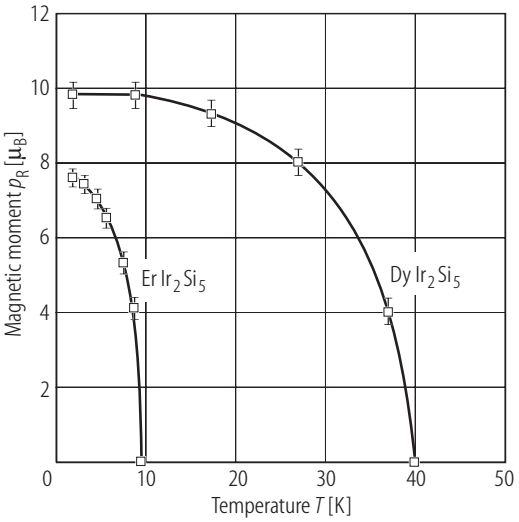

Fig. 425. $DyIr_2Si_2$, $ErIr_2Si_2$. Temperature dependence of the rare earth ordered moment [93S1].

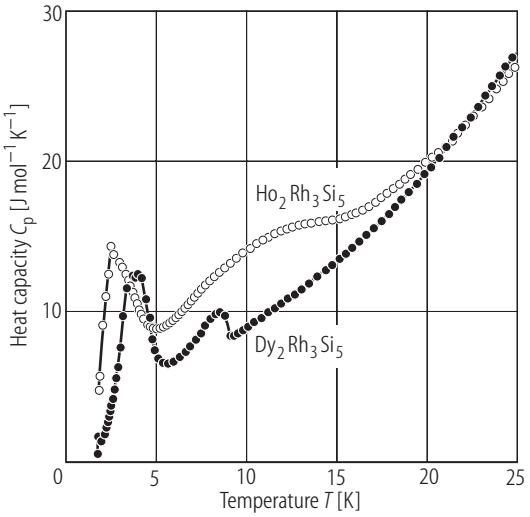

Fig. 426. $Dy_2Rh_3Si_5$, $Ho_2Rh_3Si_5$. Temperature dependence of C_p [97P1].

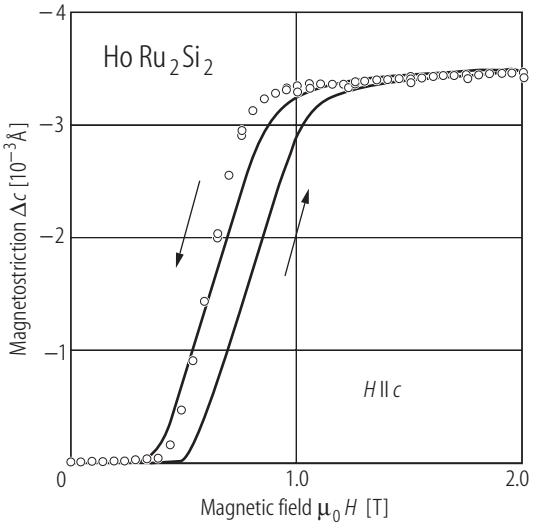

Fig. 427. $HoRu_2Si_2$. Parallel magnetostriction vs. magnetic field with $H \parallel c$. Open circles: squared magnetization $M(H)^2$ in arbitrary units [95T3].

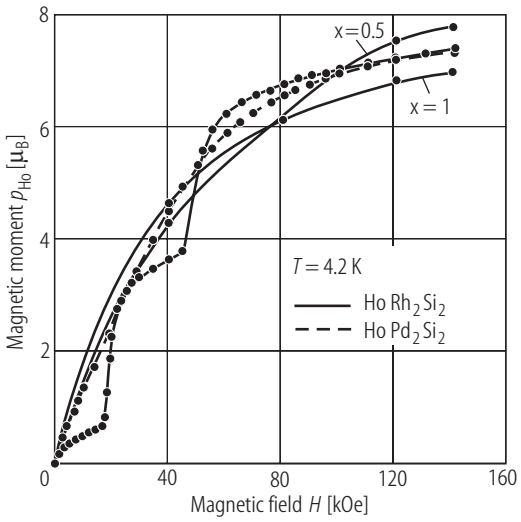

Fig. 428. $HoRh_2Si_2$, $HoPd_2Si_2$. Magnetic field dependence of p_{Ho}/at 4.2 K.

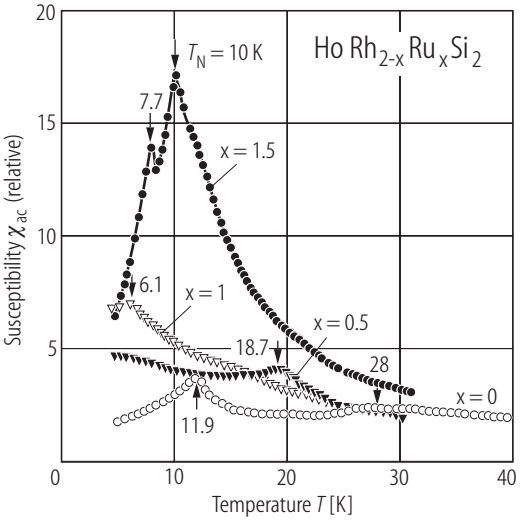

Fig. 429. $HoRh_{2-x}Ru_xSi_2$. Temperature dependence of χ_{ac} for different x [96I2].

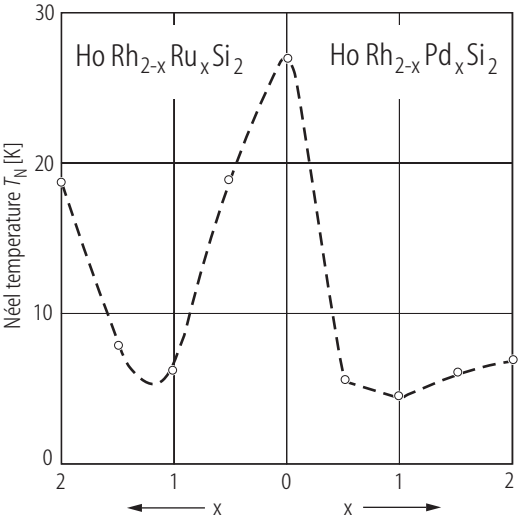

Fig. 430. $HoRh_{2-x}Pd_xSi_2$, $HoRh_{2-x}Ru_xSi_2$. Magnetic phase diagrams [96I2].

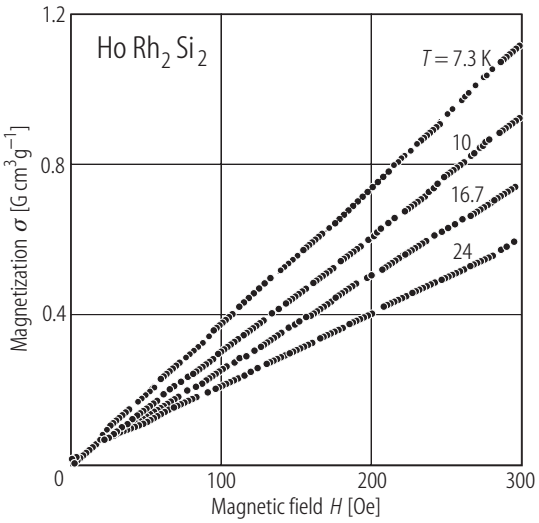

Fig. 431. $HoRh_2Si_2$. Magnetic field dependence of σ at different temperatures [96I2].

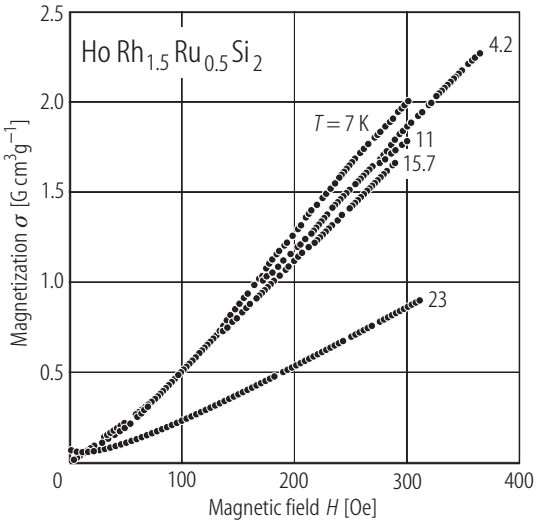

Fig. 432. $HoRh_{1.5}Ru_{0.5}Si_2$. Magnetic field dependence of σ at different temperatures [96I2].

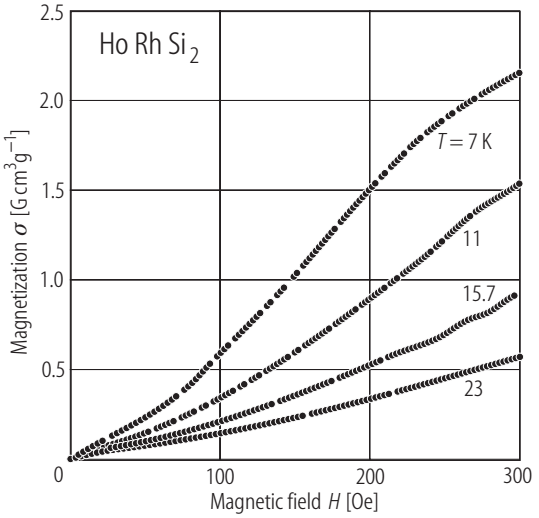

Fig. 433. $HoRhSi_2$. Magnetic field dependence of σ at different temperatures [96I2].

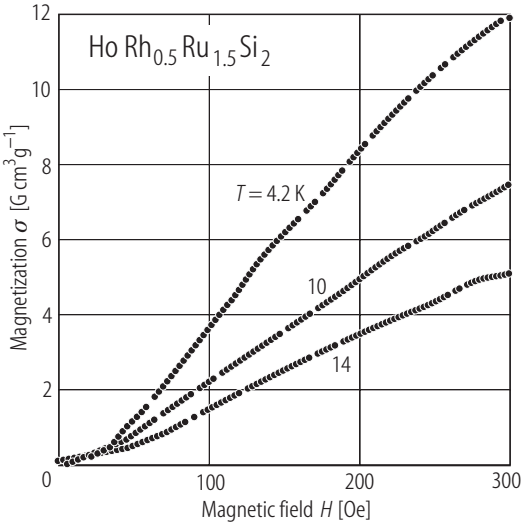

Fig. 434. $HoRh_{0.5}Ru_{1.5}Si_2$. Magnetic field dependence of σ at different temperatures [96I2].

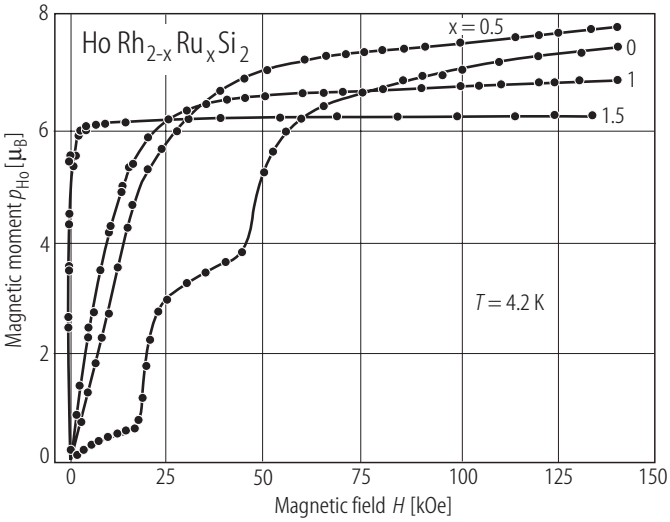

Fig. 435. $HoRh_{2-x}Ru_xSi_2$. Magnetic field dependence of p_{Ho} at 4.2 K at different concentrations [96I2].

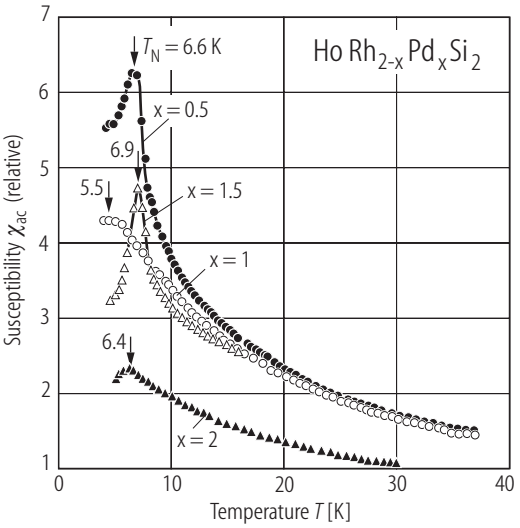

Fig. 436. $HoRh_{2-x}Pd_xSi_2$. Temperature dependence of χ_{ac} for different x [96I2].

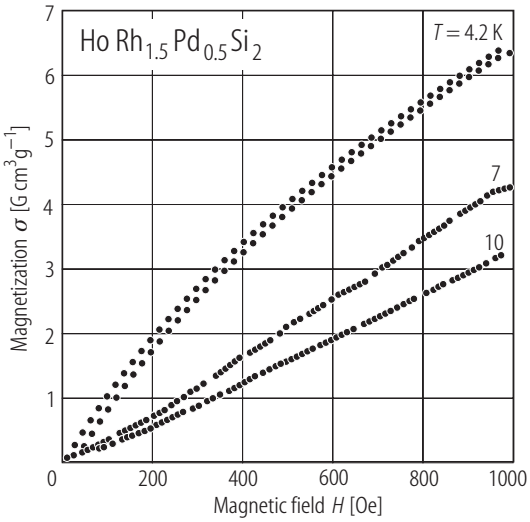

Fig. 437. $HoRh_{1.5}Pd_{0.5}Si_2$. Magnetic field dependence of σ at different temperatures [96I2].

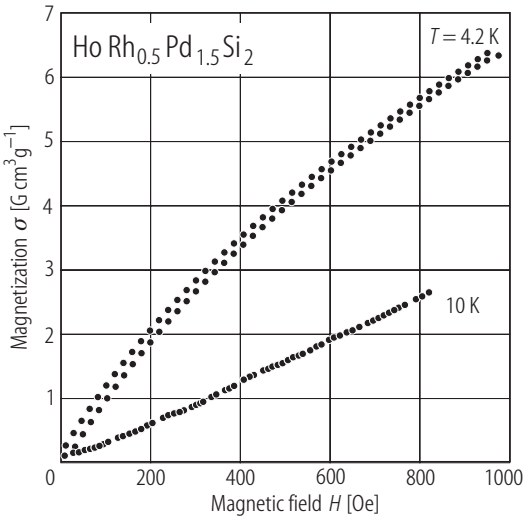

Fig. 438. $HoRh_{0.5}Pd_{1.5}Si_2$. Magnetic field dependence of σ at different temperatures [96I2].

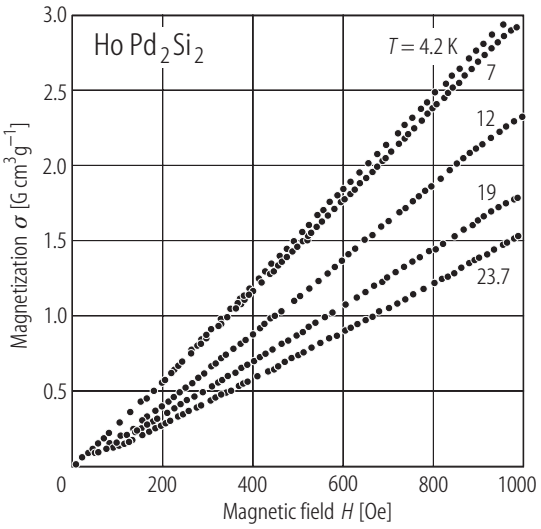

Fig. 439. $HoPd_2Si_2$. Magnetic field dependence of σ at different temperatures [96I2].

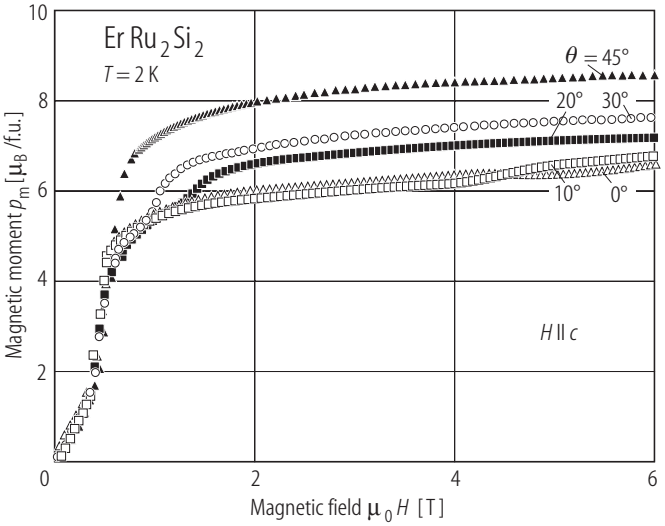

Fig. 440. $ErRu_2Si_2$. Magnetic field dependence of p_m at 2.0 K. θ: tilting angle between the [100] axis and the magnetic field direction [98T1].

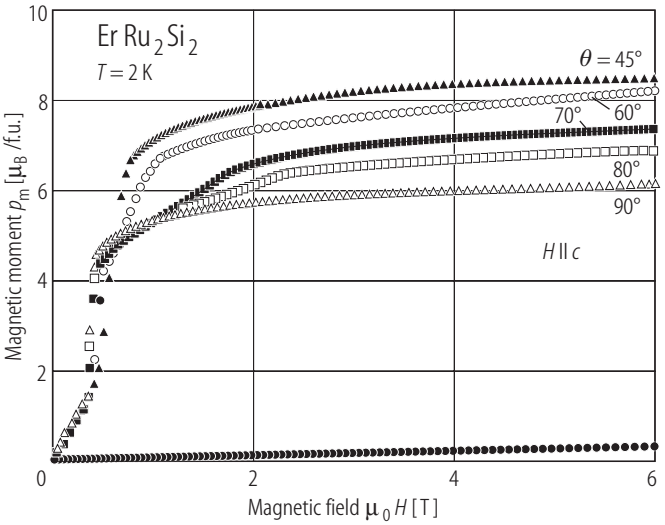

Fig. 441. $ErRu_2Si_2$. Magnetic field dependence of p_m at 2.0 K at θ between 45° and 90° [98T1].

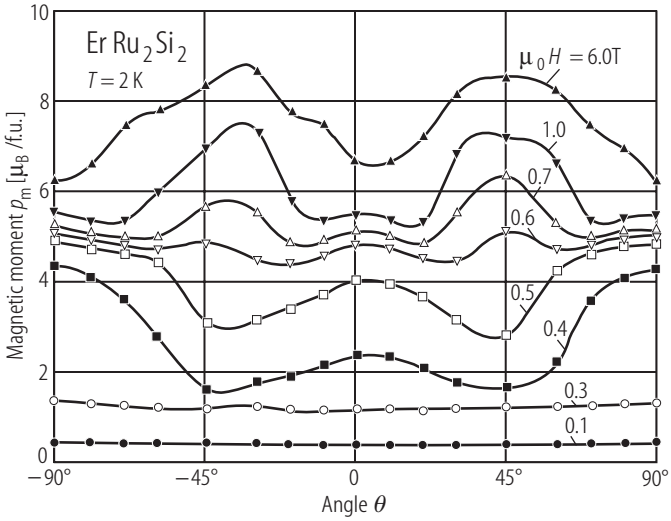

Fig. 442. $ErRu_2Si_2$. Angular dependence of p_m at several magnetic fields at 2 K [98T1].

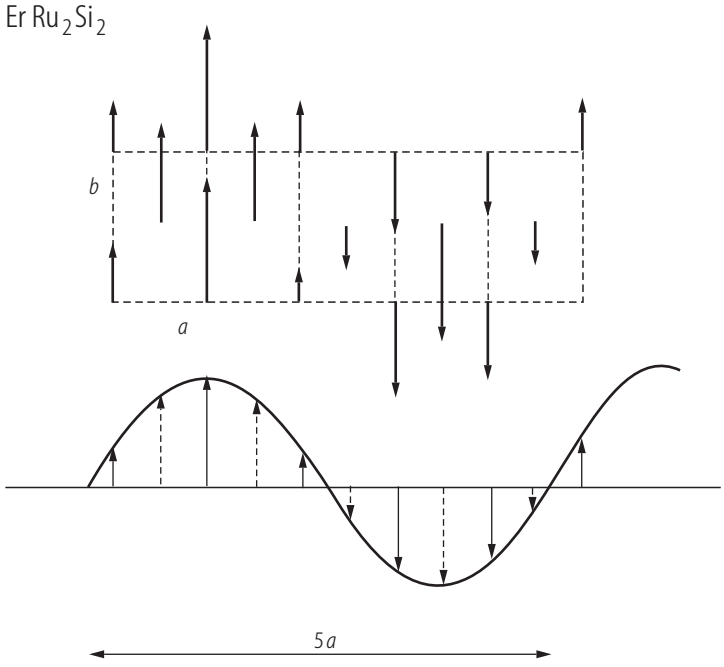

Fig. 443. $ErRu_2Si_2$. Sine modulated magnetic structure (projection along [001]); the atoms at the centre of the squares Er (1/2,1/2,1/2). Er moments are along the *b* axis [94B4].

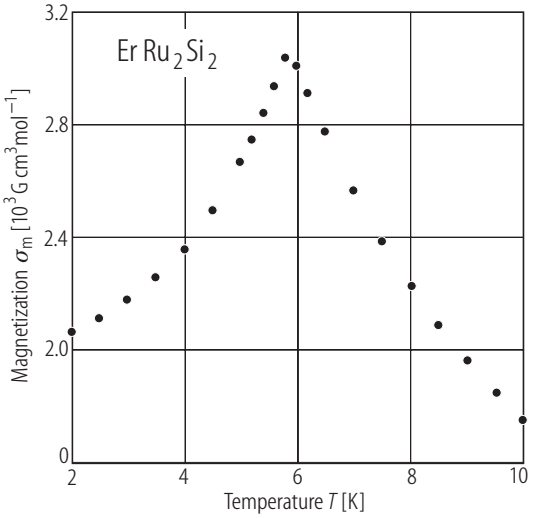

Fig. 444. $ErRu_2Si_2$. Temperature dependence of σ_m at 0.1 T [94B4].

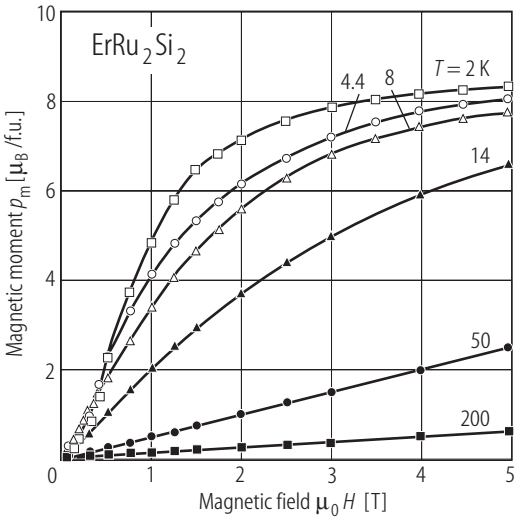

Fig. 445. $ErRu_2Si_2$. Magnetic field dependence of p_m at different temperatures [94B4].

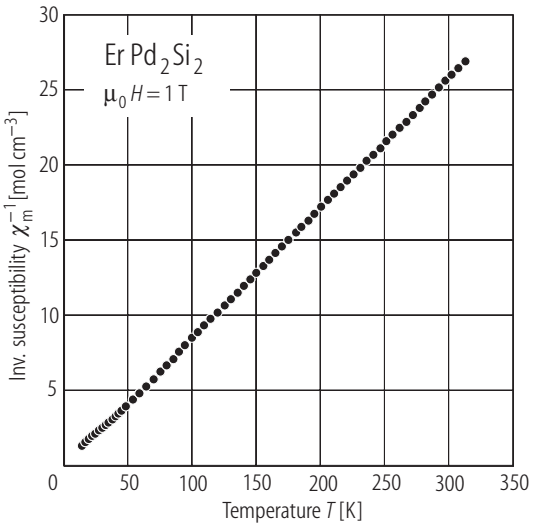

Fig. 446. $ErPd_2Si_2$. Temperature dependence of χ_m^{-1} at 1 T [94T1].

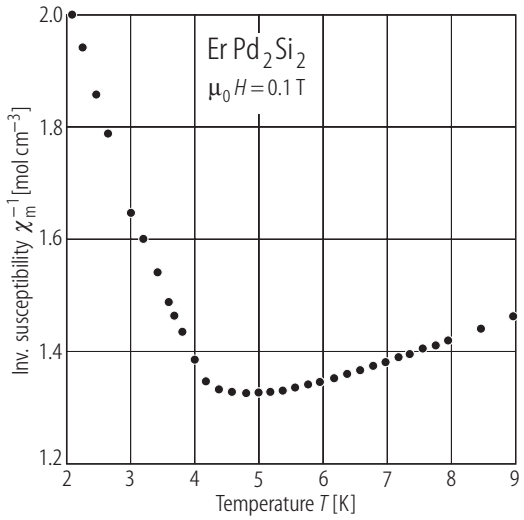

Fig. 447. $ErPd_2Si_2$. Temperature dependence of χ_m^{-1} at 0.1 T [94T1].

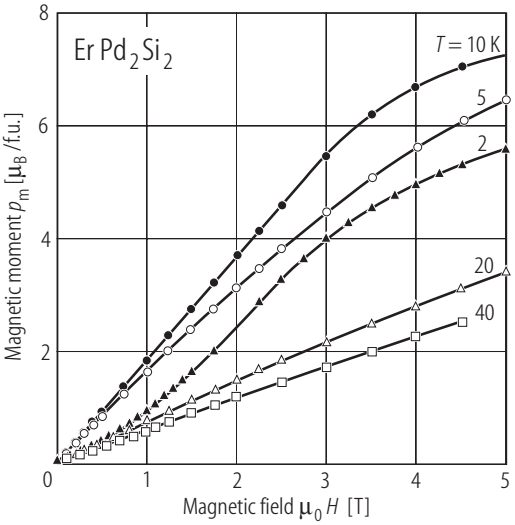

Fig. 448. $ErPd_2Si_2$. Magnetic field dependence of p_m at different temperatures [94T1].

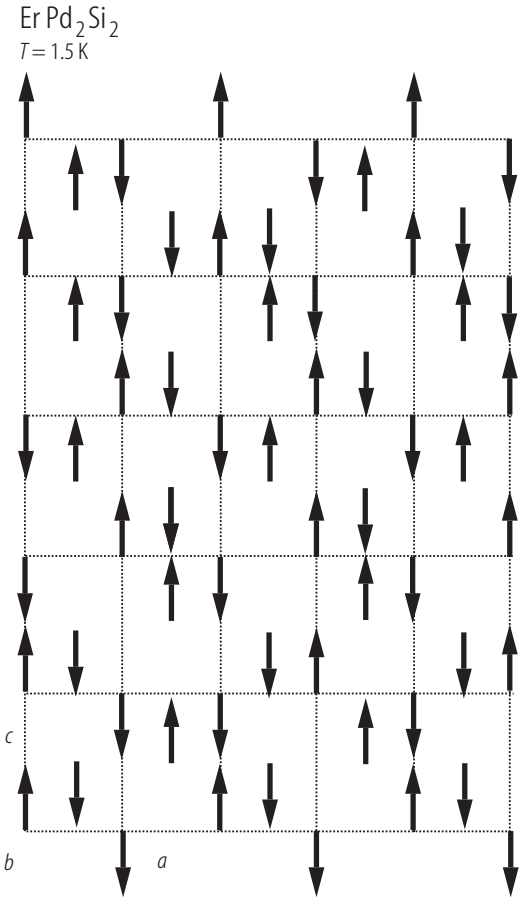

Fig. 449. $ErPd_2Si_2$. Squared magnetic structure at 1.5 K [94T1].

For Fig. 450 see next page.

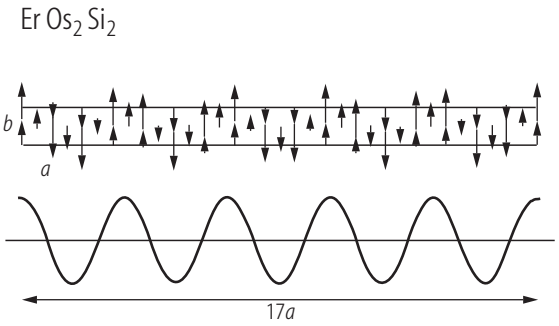

Fig. 451. $ErOs_2Si_2$. Magnetic structure (projection along [001]; the atoms at the centre of the squares are Er (1/2,1/2,1/2)). The Er moments are along the *b* axis [94B4].

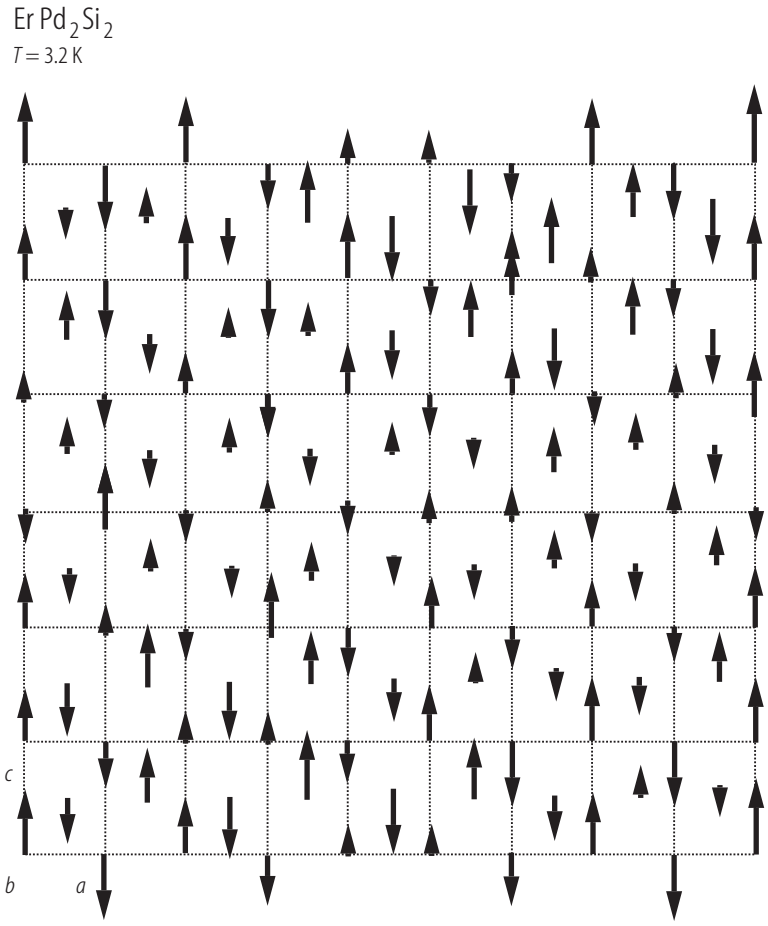

Fig. 450. $ErPd_2Si_2$. Magnetic superstructure at 3.2 K [94T1].

For Fig. 451 see previous page.

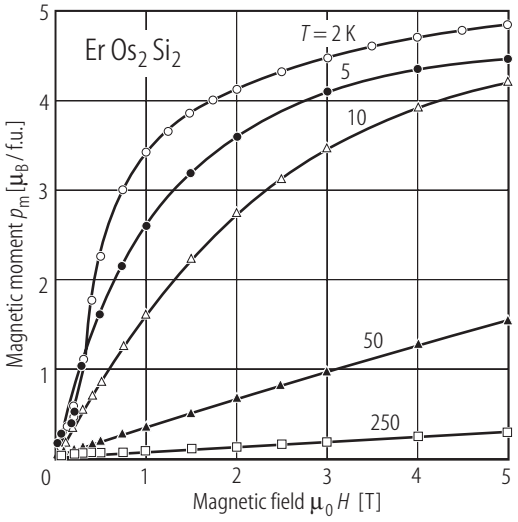

Fig. 452. $ErOs_2Si_2$. Magnetic field dependence of p_m at different temperatures [94B4].

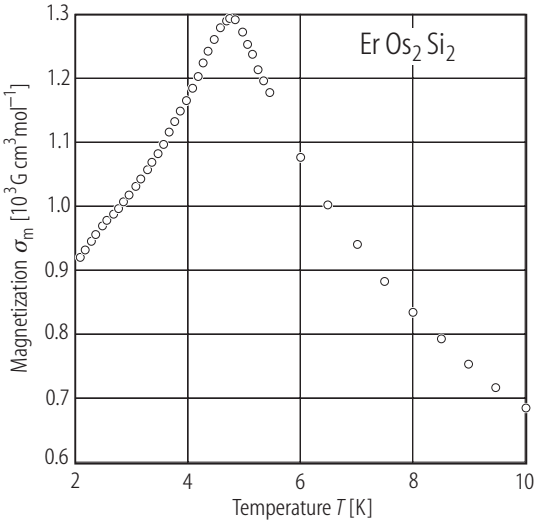

Fig. 453. $ErOs_2Si_2$. Temperature dependence of σ_m at 0.1 T [94B4].

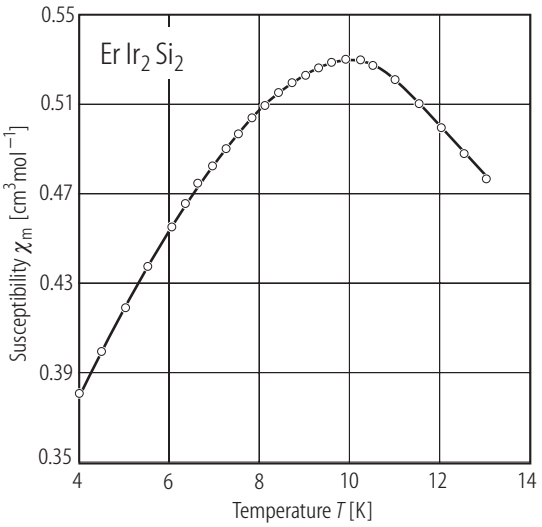

Fig. 454. $ErIr_2Si_2$. Temperature dependence of χ_m at 0.1 T [93S1].

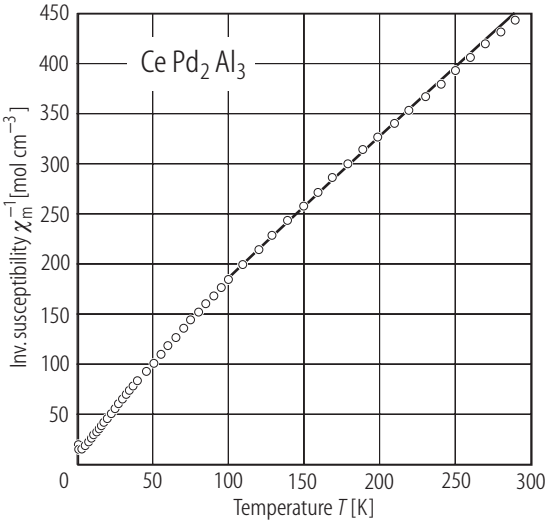

Fig. 455. $CePd_2Al_3$. Temperature dependence of χ_m^{-1} [93G1].

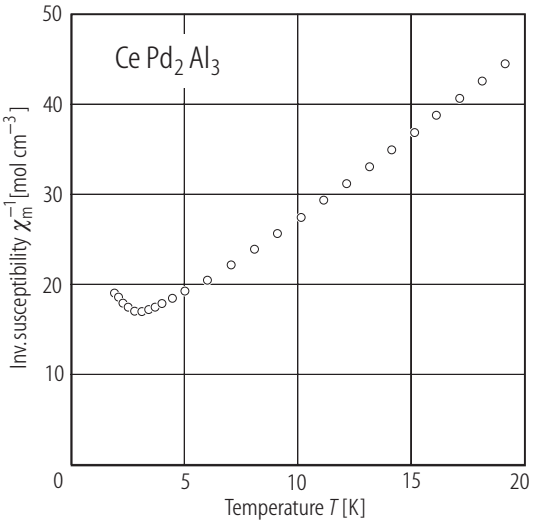

Fig. 456. $CePd_2Al_3$. Low-temperature dependence of χ_m^{-1} [93G1].

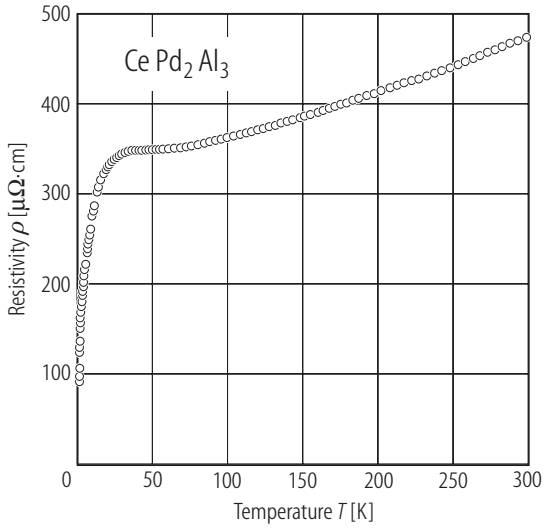

Fig. 457. $CePd_2Al_3$. Temperature dependence of ρ [93G1].

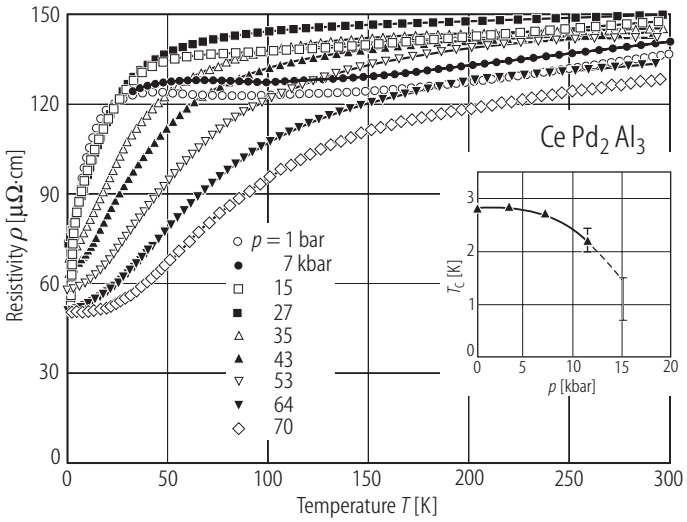

Fig. 458. $CePd_2Al_3$. Temperature and pressure dependence of resistivity. Inset: T_C vs. p [95H1].

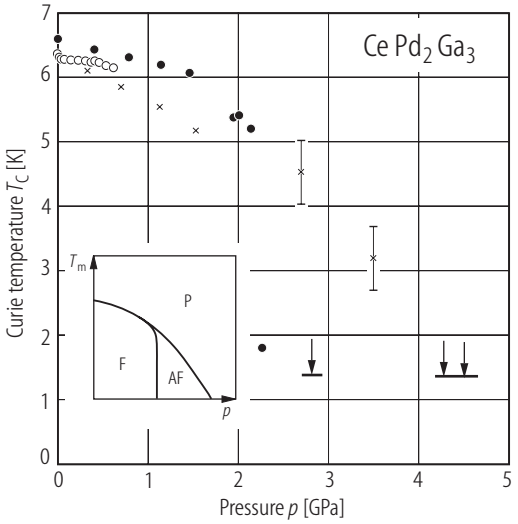

Fig. 459. $CePd_2Ga_3$. Pressure dependence of the magnetic ordering temperature [97B2].

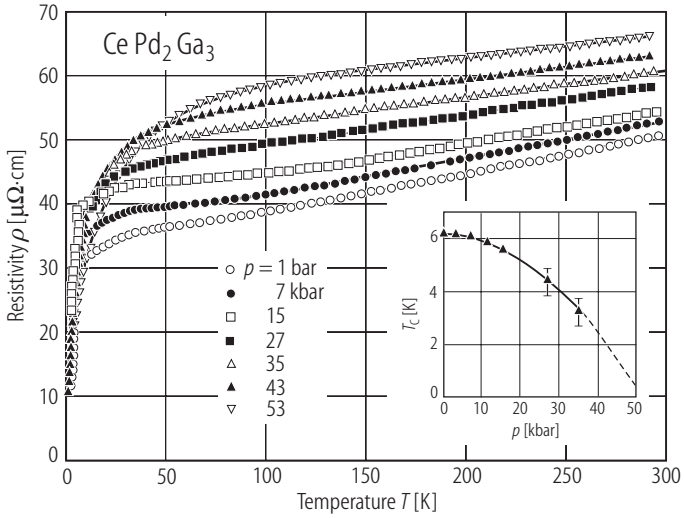

Fig. 460. $CePd_2Ga_3$. Temperature and pressure dependence of resistivity. Inset: T_C vs. p [95H1].

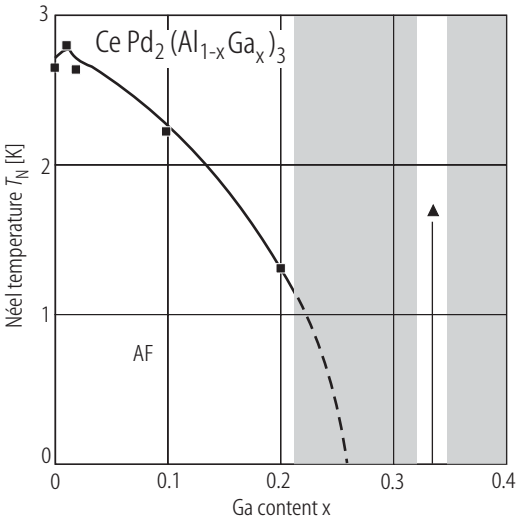

Fig. 461. $CePd_2(Al_{1-x}\ Ga_x)_3$. Phase diagram of T_N vs. Ga concentration. Full triangle denotes T_C. The shaded area covers the composition region where no homogeneous samples could be obtained [96L1].

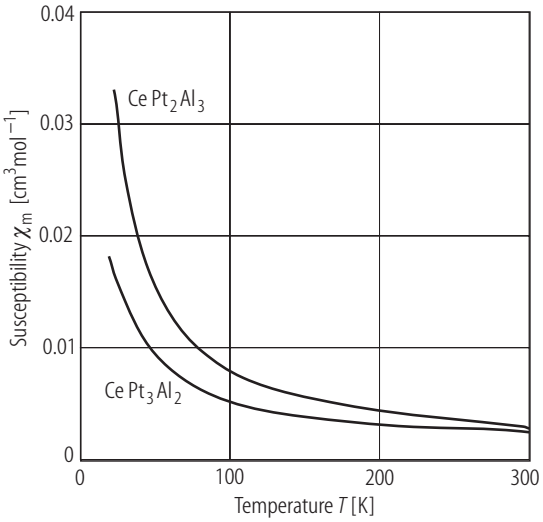

Fig. 462. $CePt_3Al_2$, $CePt_2Al_3$. Temperature dependence of χ_m [93B2].

For Fig. 463 see next page.

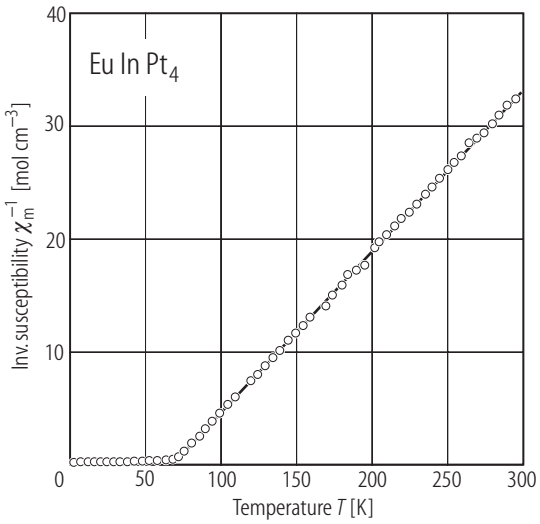

Fig. 464. $EuInPt_4$. Tenperature dependence of χ_m^{-1}.

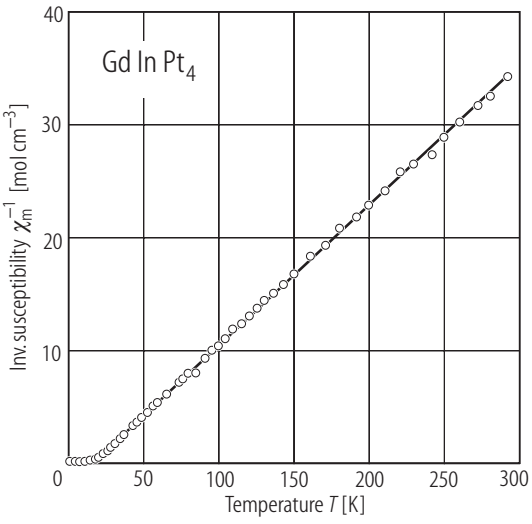

Fig. 465. $GdInPt_4$. Temperature dependence of χ_m^{-1}.

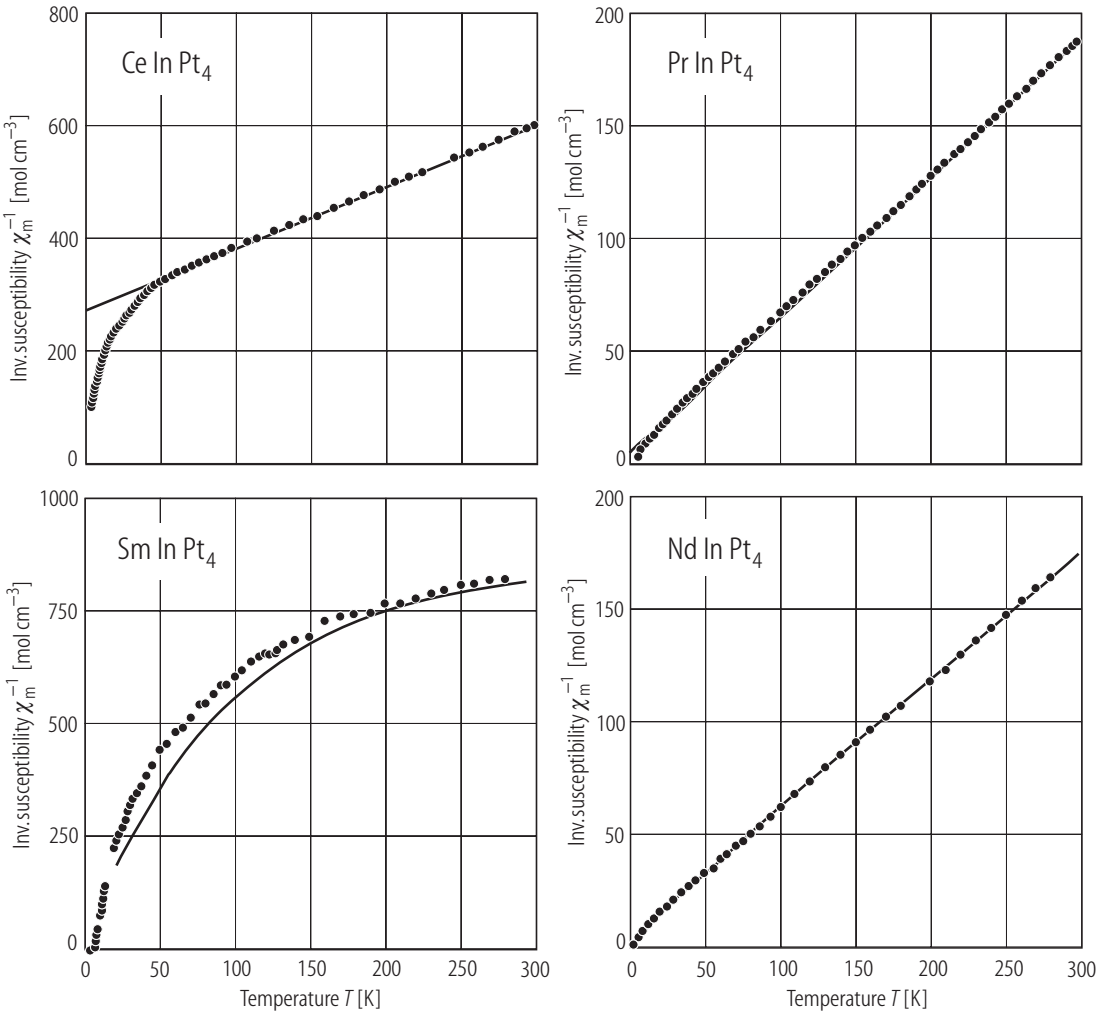

Fig. 463. $CeInPt_4$, $PrInPt_4$, $NdInPt_4$, $SmInPt_4$. Temperature dependence of χ_m^{-1} [90M5].

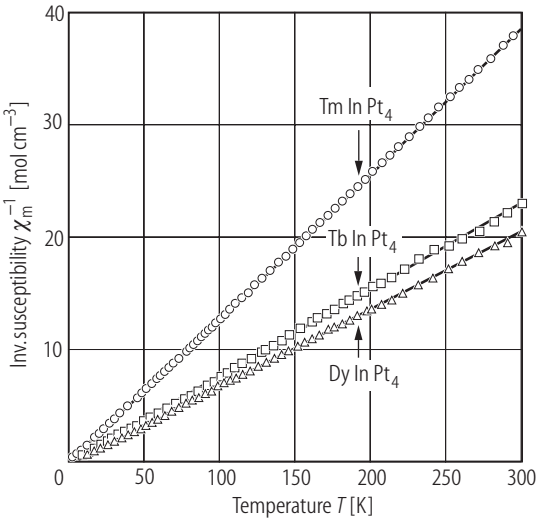

For Figs. 464 and 465 see previous page.

Fig. 466. $TmInPt_4$, $TbInPt_4$, $DyInPt_4$. Temperature dependence of χ_m^{-1} [90M5].

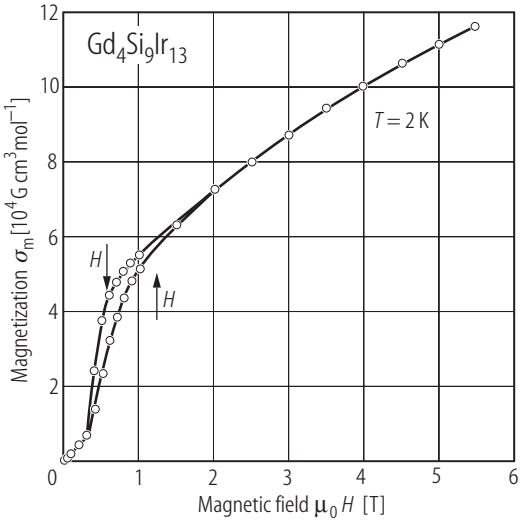

Fig. 467. $Gd_4Si_9Ir_{13}$. Magnetic field dependence of σ_m at 2 K [95V1].

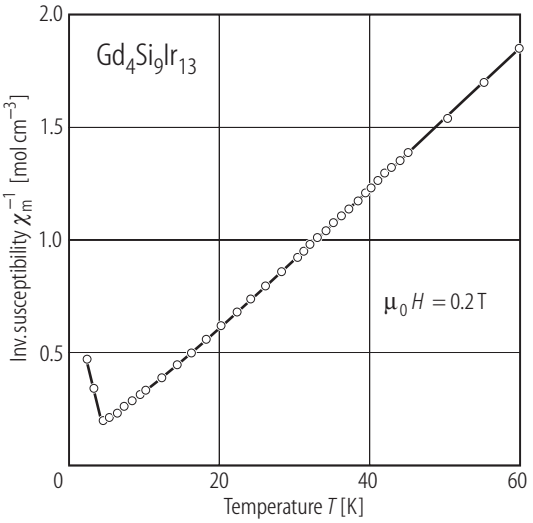

Fig. 468. $Gd_4Si_9Ir_{13}$. Temperature dependence of χ_m^{-1} at 0.2 T [95V1].

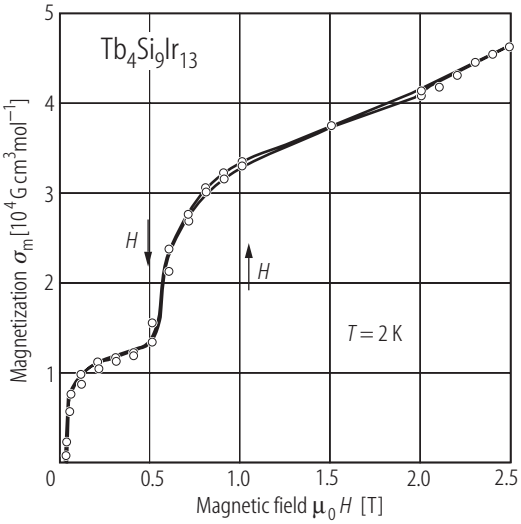

Fig. 469. $Tb_4Si_9Ir_{13}$. Magnetic field dependence of σ_m at 2 K [95V1].

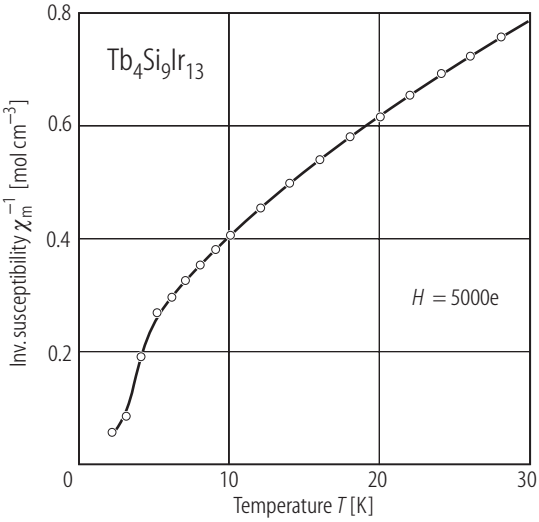

Fig. 470. $Tb_4Si_9Ir_{13}$. Low temperature dependence of χ_m^{-1} (the sample has been cooled down under 500 Oe [95V1]).

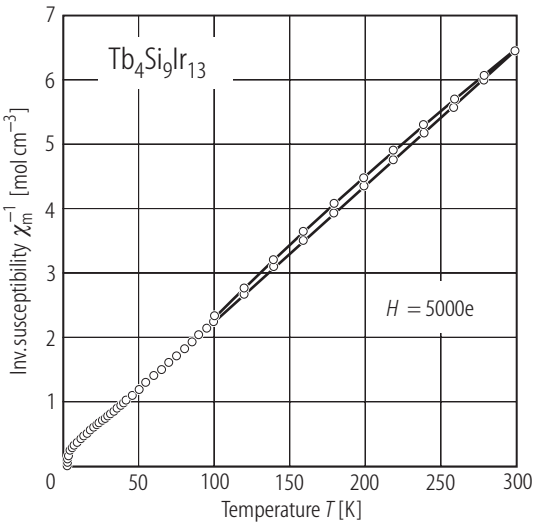

Fig. 471. $Tb_4Si_9Ir_{13}$. Temperature dependence of χ_m^{-1} at 500 Oe [95V1].

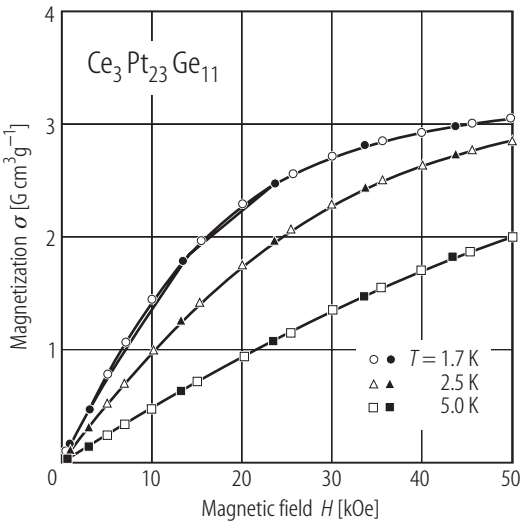

Fig. 472. $Ce_3Pt_{23}Ge_{11}$. Magnetic field dependence of σ at 5 K for several temperatures. Open and solid symbols denote increasing and decreasing field, respectively [98T2].

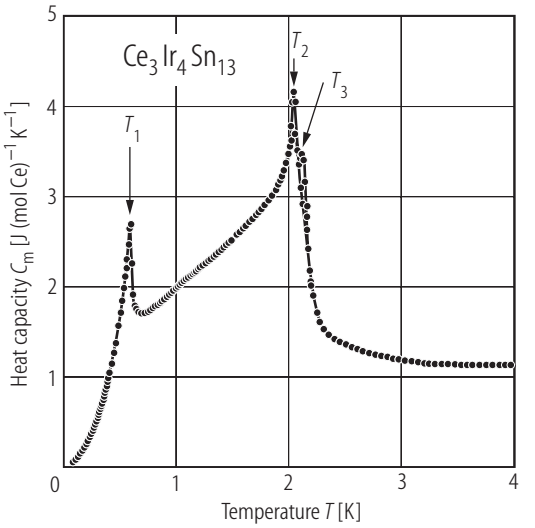

Fig. 473. $Ce_3Ir_4Sn_{13}$. Temperature dependence of the specific heat [94T2].

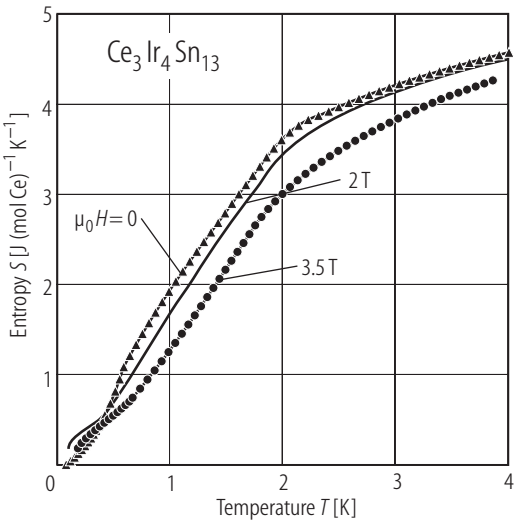

Fig. 474. $Ce_3Ir_4Sn_{13}$. Temperature dependence of the entropy. At low temperature lattice contribution to the specific heat is very small and the magnetic contribution is dominating [94T2].

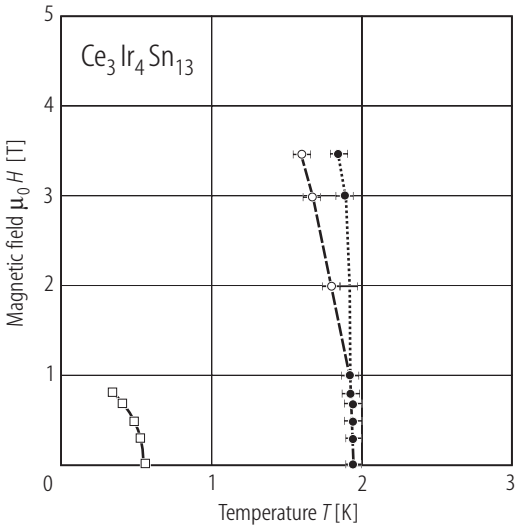

Fig. 475. $Ce_3Ir_4Sn_{13}$. Magnetic phase diagram [94T2].

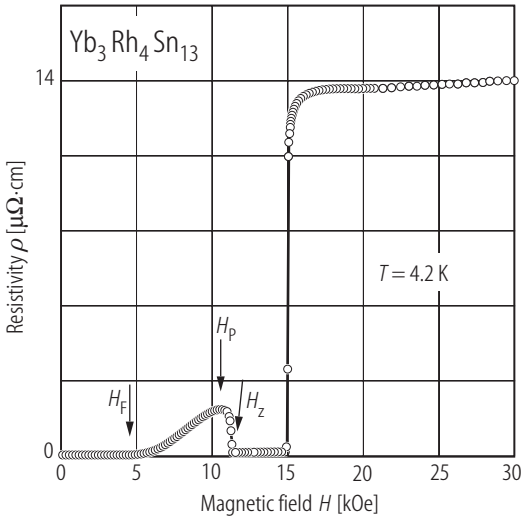

Fig. 476. $Yb_3Rh_4Sn_{13}$. Magnetic field dependence of the electrical resistivity at 4.2 K [97S4].

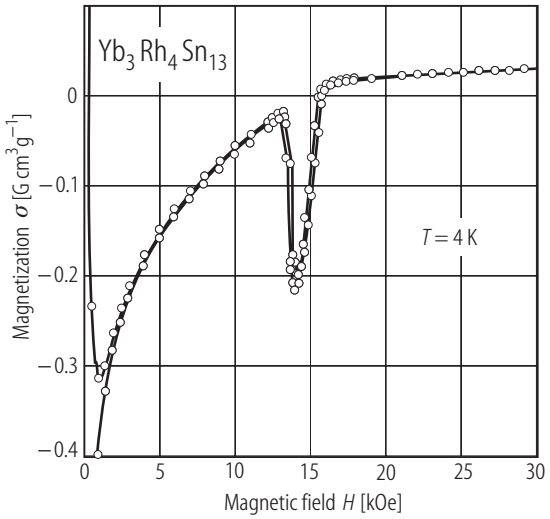

Fig. 477. $Yb_3Rh_4Sn_{13}$. Magnetic field dependence of σ at 4 K [97S4].

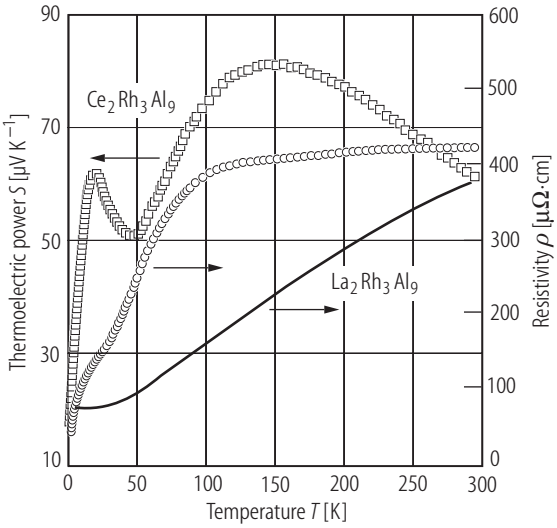

Fig. 478. $La_2Rh_3Al_9$, $Ce_2Rh_3Al_9$. Temperature dependence of S and ρ [97B4].

References

90M5 Malik, S.K., Vijayaraghan, R., Adroja, D.T., Padalia, B.D., Edelstein, A.S.: J. Magn. Magn. Mater. **92** (1990) 80

91B1 Bazela, W., Leciejewicz, J., Szytula, A., Zygmunt, A.: J. Magn. Magn. Mater. **96** (1991) 114

91S1 Sanchez, J.P., Tomala, K., Łątka, K.: J. Magn. Magn. Mater. **99** (1991) 95

93B2 Blazina, Z., Westwood, S.M.: J. Alloys Comp. **201** (1993) 151

93G1 Ghosh, K., Ramakrishnan, S., Malik, S.K., Chandra, G.: J. Alloys Comp. **202** (1993) 211

93S1 Sanchez, J.P., Blaise, A., Ressouche. E., Malamann, B., Venturini, G., Tomala, K., Kmiec, R.: J. Magn. Magn. Mater. **128** (1993) 295

94B4 Blaise, A., Kmiec, R., Malaman, B., Ressouche, E., Sanchez, J., P., Tomala, K., Venturini, G.: J. Magn. Magn. Mater. **135** (1994) 171

94T1 Tomala, K., Sanchez, J.P., Malaman, B., Venturini, G., Blaise, A., Kmiec, R.: J. Magn. Magn. Mater. **131** (1994) 345

94T2 Takayanagi, S., Sato, H., Fakuhara, T., Wada, N.: Physica B **199-200** (1994) 49

95H1 Hauser, R., Bauer, E., Galatanu, A., Indinger, A., Maikus, M., Kirchmayr, H., Gignoux, D., Schmitt, D.: Physica B **206-207** (1995) 231

95I2 Ivanov, V., Vinokurova, L., Szytula, A.: J. Alloys Comp.**218** (1995) L19

95T3 Takeuchi, T., Taniguchi, T., Kudoh, D., Miyako, Y.: Physica B **206-207** (1995) 398

95V1 Vernier, A., Lejay, P., Bordet, P., Chenavas, J., Tholence, J.L., Boucherle, J.X., Keller, N.: J. Alloys Comp. **218** (1995) 197

96I2 Ivanov, V., Jaworska, T., Vinokurova, L., Mydlarz, T., Szytula, A.: J. Alloys Comp. **234** (1996) 235

96L1 Ludoph, B., Süllow, S., Becker, B., Neuwenhuys, G.J., Menovsky, A.A., Mydosh, J.A.: Physica B **223-224** (1996) 351

97B2 Burghardt, T., Hallmann, E., Eichler, A.: Physica B **230-232** (1997) 214

97B3 Blanco, J.A., Garnier, A., Gignoux, D., Schmitt, D.: J. Alloys Comp. **275-277** (1997) 565

97B4 Buschinger, B., Geibel, C., Weiden, M., Dietrich, C., Cordier, G., Olesch, G., Kohler, J.: J. Alloys Comp. **260** (1997) 44

97P1 Patil, N.G., Ramakrishnan, S.: Physica B **237-238** (1997) 597

97S4 Sato, H., Aoki, Y., Kobayashi, Y., Sato, H.R., Nishigaki, T., Sugswara, H., Hedo, M., Inada, Y., Onuki, Y.: Physica B **230-232** (1997) 402

97W1 Wang, Yin-gang, Yang, Fuming, Chen, Changpin, Wang, Qidong: J. Alloys Comp.**257** (1997) 19

98T1 Takeuchi, T., Kohyama, J.M., Kawarazaki, S., Sato, M., Miyako, Y.: **177-181** (1998) 1081

98T2 Troc, R., Kaczorowski, D., Cichorek, T., Andraka, B., Pietri, R., Seropegin, Yu.D., Gribanov, A.V.: J. Alloys Comp. **262-263** (1998) 211

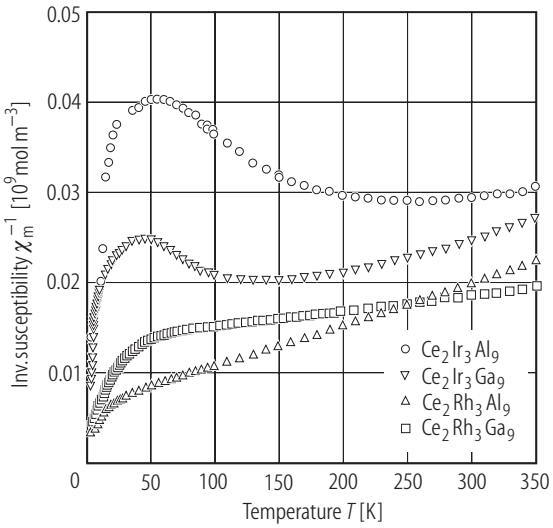

Fig. 479. $Ce_2Ir_3Al_9$, $Ce_2Ir_3Ga_9$, $Ce_2Rh_3Al_9$, $Ce_2Rh_3Ga_9$. Temperature dependence of χ_m^{-1} [97B4].

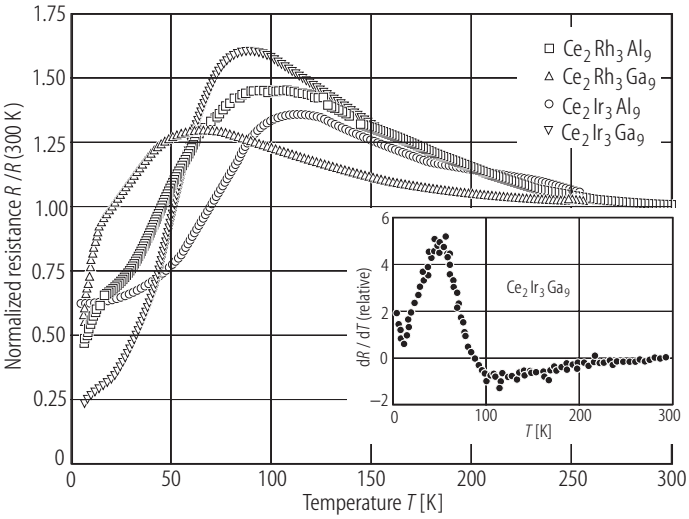

Fig. 480. $Ce_2Rh_3Al_9$, $Ce_2Rh_3Ga_9$, $Ce_2Ir_3Al_9$, $Ce_2Ir_3Ga_9$. Temperature dependence of R/R(300 K) [97B4].

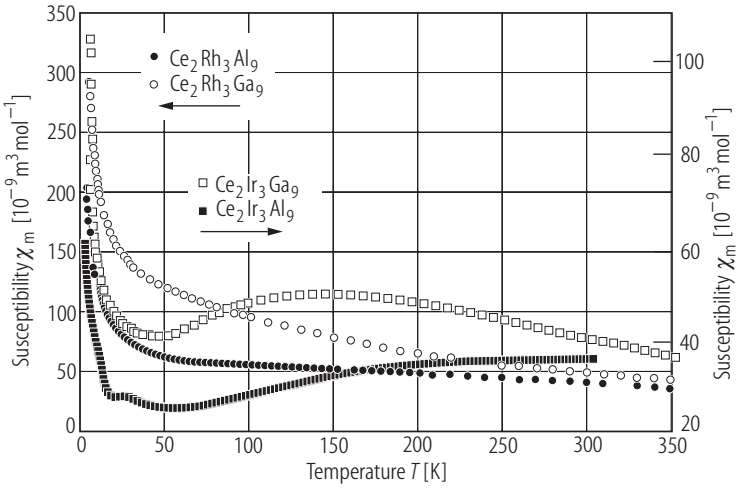

Fig. 481. $Ce_2Rh_3Al_9$, $Ce_2Rh_3Ga_9$, $Ce_2Ir_3Ga_9$, $Ce_2Ir_3Al_9$. Temperature dependence of χ_m. Note two scales [98B2].

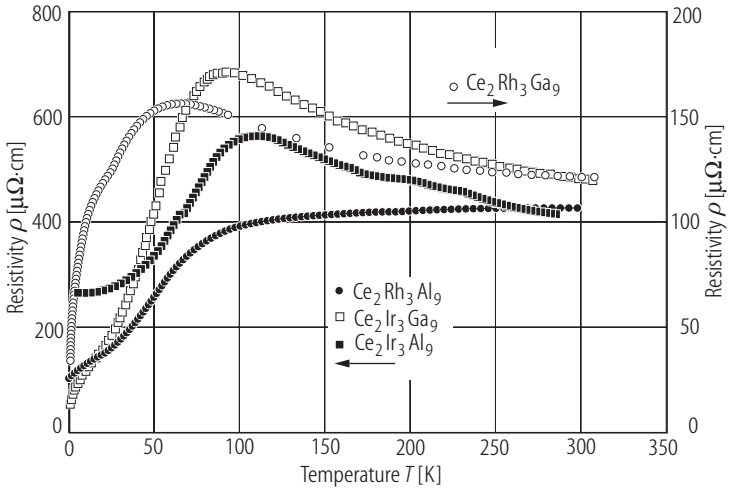

Fig. 482. $Ce_2Rh_3Al_9$, $Ce_2Ir_3Ga_9$, $Ce_2Ir_3Al_9$. Temperature dependence of ρ [98B2].

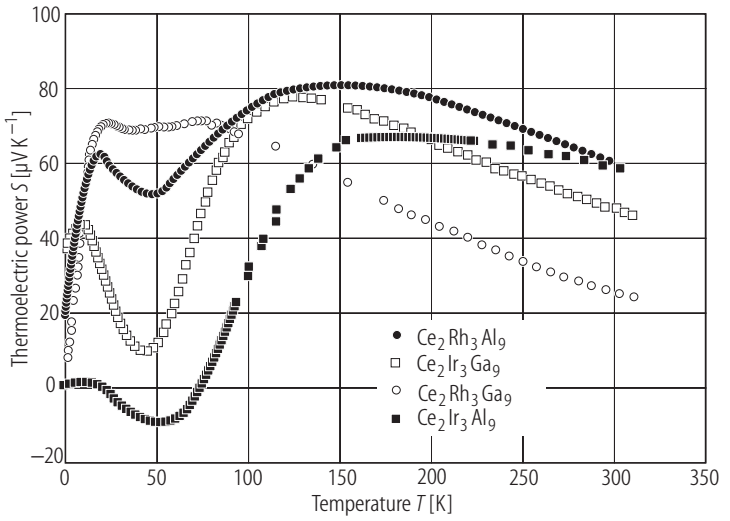

Fig. 483. $CeRh_3Al_9$, $Ce_2Ir_3Ga_9$, Ce_2Rh_3, $Ce_2Ir_3Al_9$. Temperature dependence of thermoelectric power S [98B2].

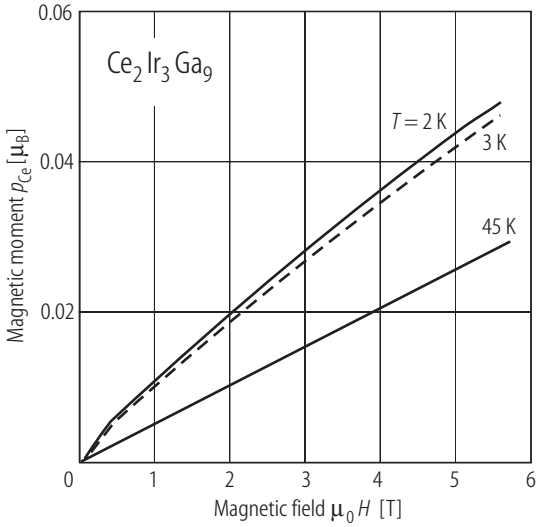

Fig. 484. $Ce_2Ir_3Ga_9$. Magnetic field dependence of p_{Ce} at 2, 3 and 45 K [98B2].

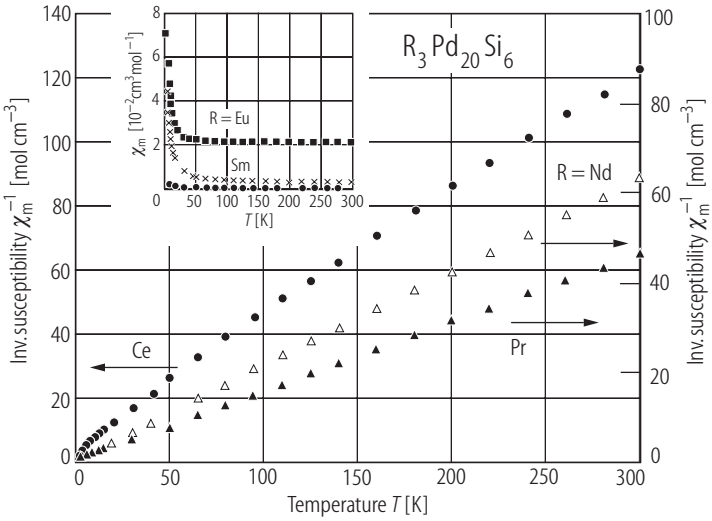

Fig. 485. $R_3Pd_{20}Si_6$, R = Ce, Pr, Nd. Temperature dependence of χ_m^{-1}. Inset: χ_m for R = La, Sm and Eu [97K1].

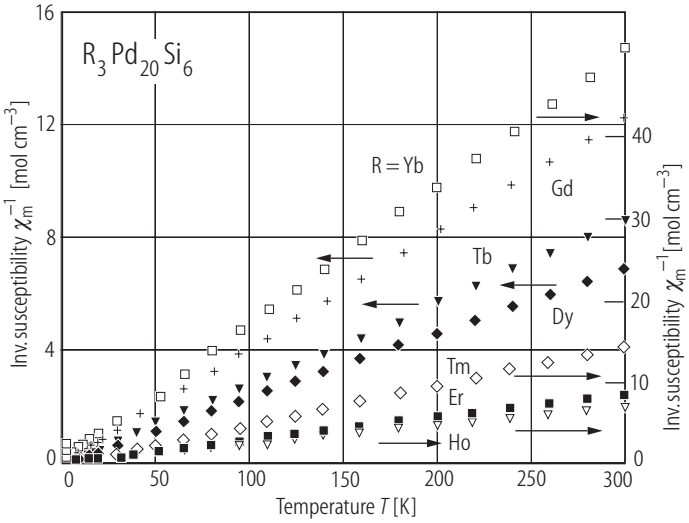

Fig. 486. $R_3Pd_{20}Si_6$, R = Gd, Tb, Dy, Ho, Er, Tm, Tb. Temperature dependence of χ_m^{-1} [97K1].

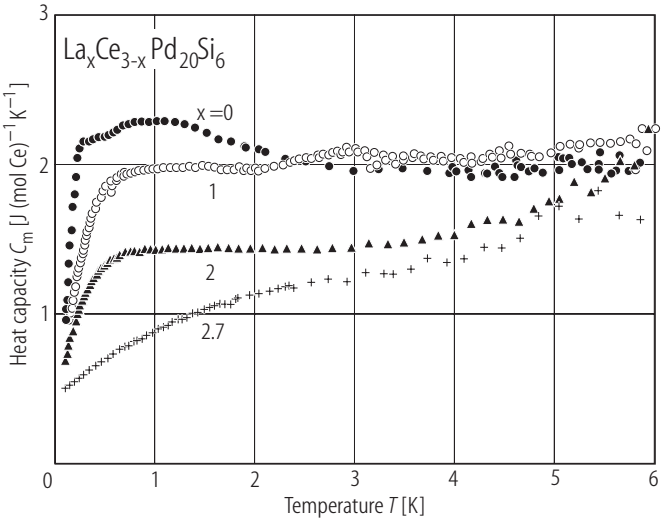

Fig. 487. $La_xCe_{3-x}Pd_{20}Si_6$. Temperature dependence of C_m for different x [97T2].

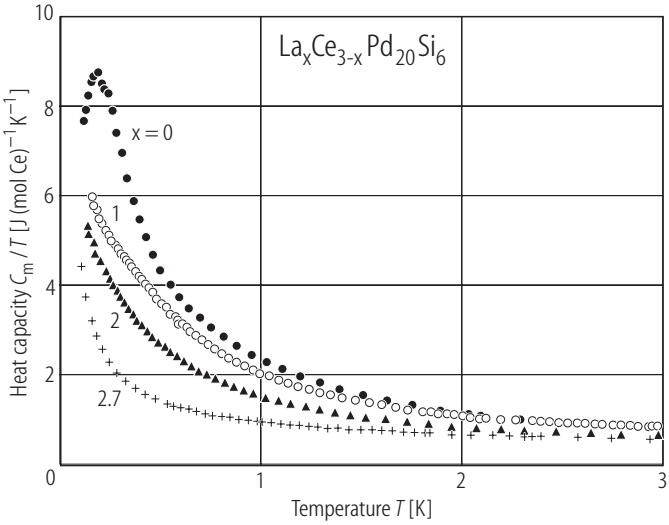

Fig. 488. $La_xCe_{3-x}Pd_{20}Si_6$. Temperature dependence of C_m/T for different x [97T2].

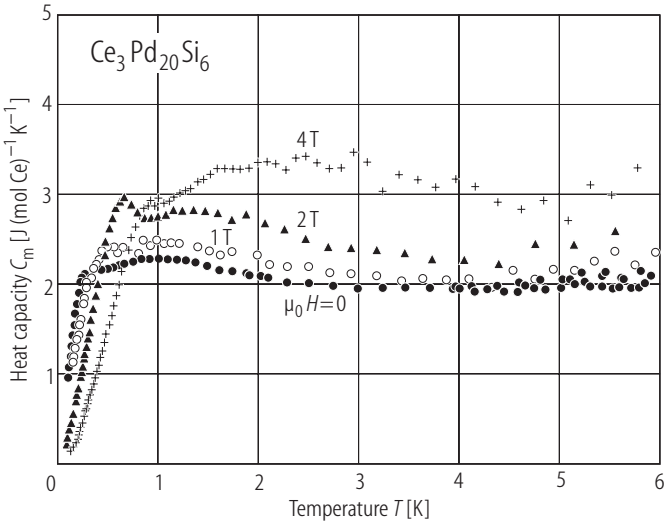

Fig. 489. $Ce_3Pd_{20}Si_6$. Temperature dependence of C_m for different H [97T2].

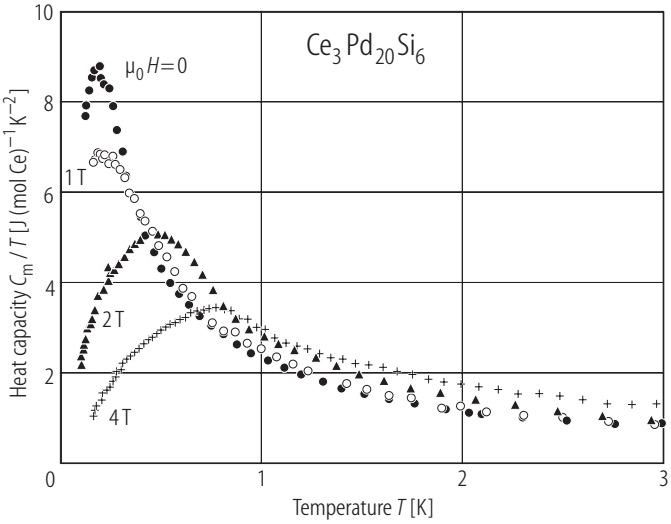

Fig. 490. $Ce_3Pd_{20}Si_6$. Temperature dependence of C_m/T for different H [97T2].

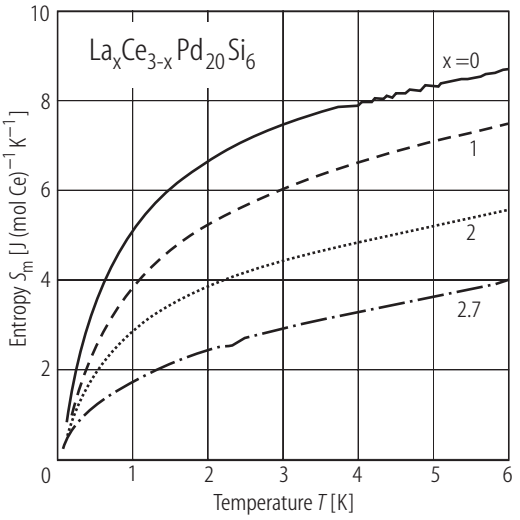

Fig. 491. $La_xCe_{3-x}Pd_{20}Si_6$. Temperature dependence of magnetic entropy S_m for different x [97T2].

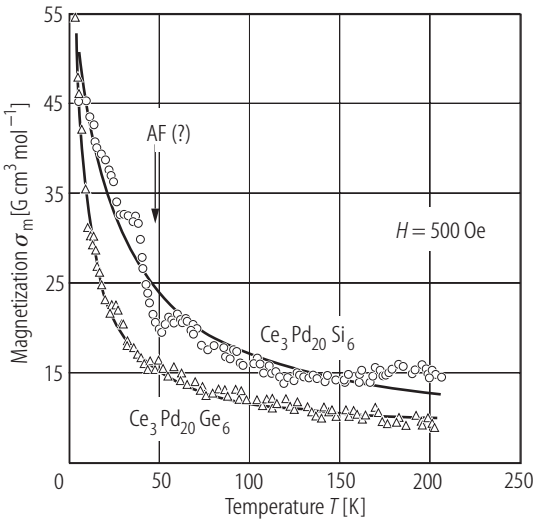

Fig. 492. $Ce_3Pd_{20}Si_6$, $Ce_3Pd_{20}Ge_6$. Temperature dependence of σ_m at 500 Oe [96N1].

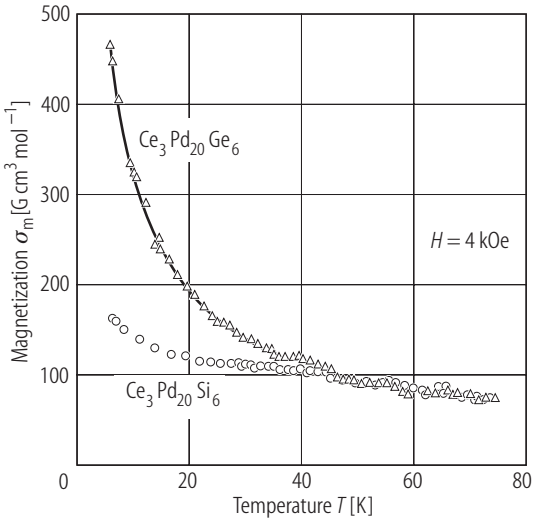

Fig. 493. $Ce_3Pd_{20}Si_6$, $Ce_3Pd_{20}Ge_6$. Temperature dependence of σ_m at 4 kOe [96N1].

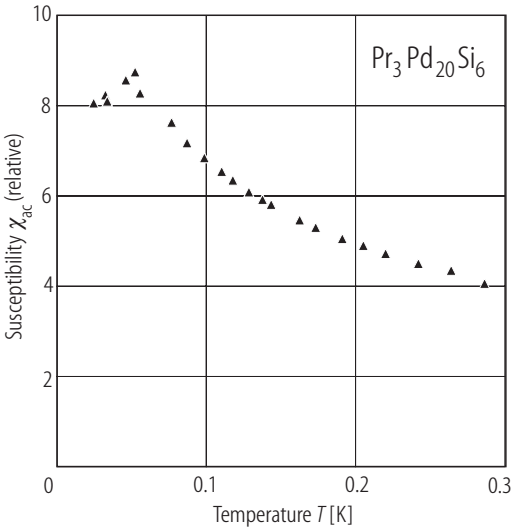

Fig. 494. $Pr_3Pd_{20}Si_6$. Low-temperature dependence of χ_{ac} [97K1].

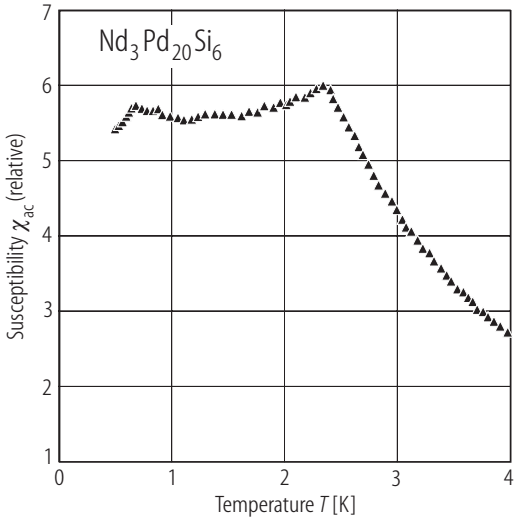

Fig. 495. $Nd_3Pd_{20}Si_6$. Low-temperature dependence of χ_{ac} [97K1].

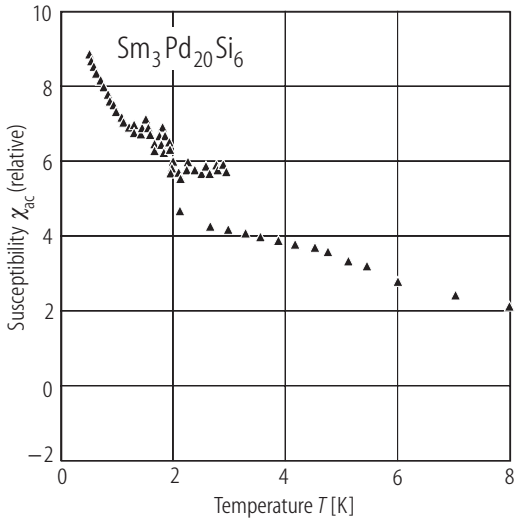

Fig. 496. $Sm_3Pd_{20}Si_6$. Low-temperature dependence of χ_{ac} [97K1].

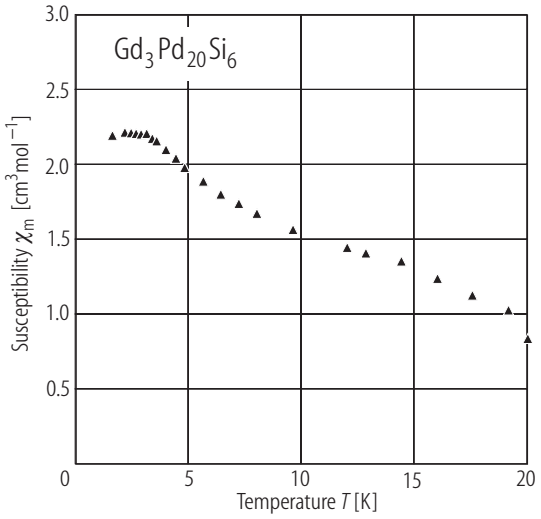

Fig. 497. $Gd_3Pd_{20}Si_6$. Low-temperature dependence of χ_m [97K1].

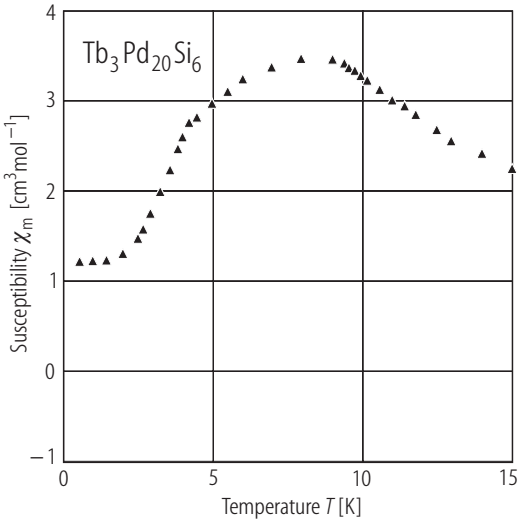

Fig. 498. $Tb_3Pd_{20}Si_6$. Low-temperature dependence of χ_m [97K1].

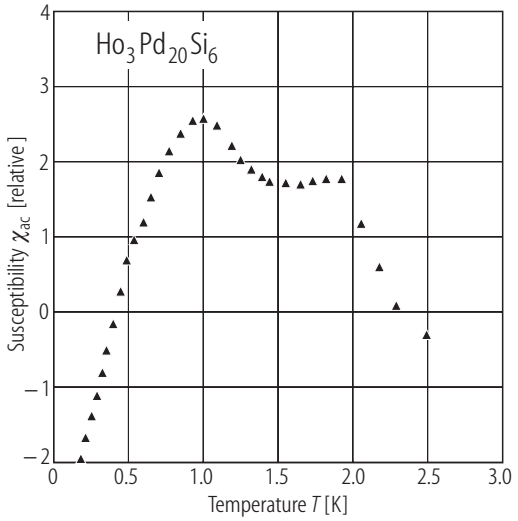

Fig. 499. $Ho_3Pd_{20}Si_6$. Low-temperature dependence of χ_{ac} [97K1].

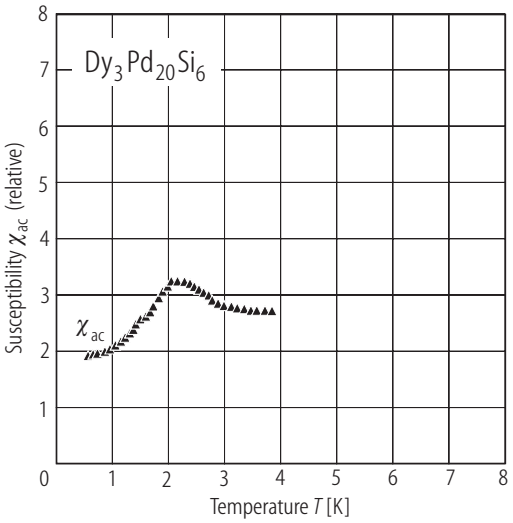

Fig. 500. $Dy_3Pd_{20}Si_6$. Low-temperature dependence of χ_{ac} [97K1].

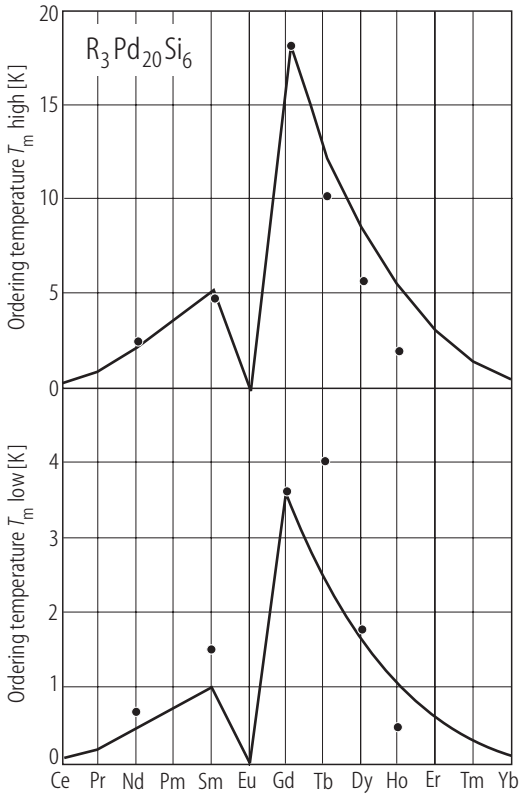

Fig. 501. $R_3Pd_{20}Si_6$. Magnetic ordering temperatures of R = Nd, Sm, Gd, Tb, Dy, Ho. This compounds have two magnetic phase transitions T_m^{high} and T_m^{low} at relatively low temperatures (see Figs. 495 - 500). The solid curves represent the predictions of de Gennes scaling normalized at Gd [97K1].

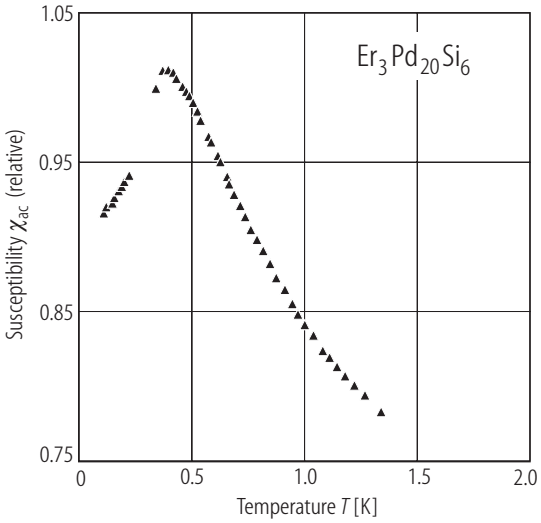

Fig. 502. $Er_3Pd_{20}Si_6$. Low-temperature dependence of χ_{ac} [97K1].

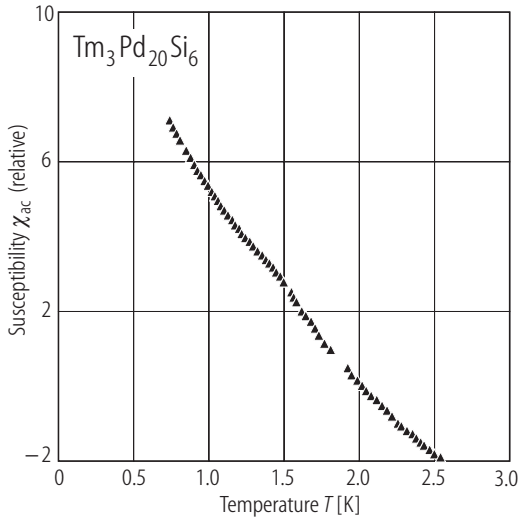

Fig. 503. $Tm_3Pd_{20}Si_6$. Low-temperature dependence of χ_{ac} [97K1].

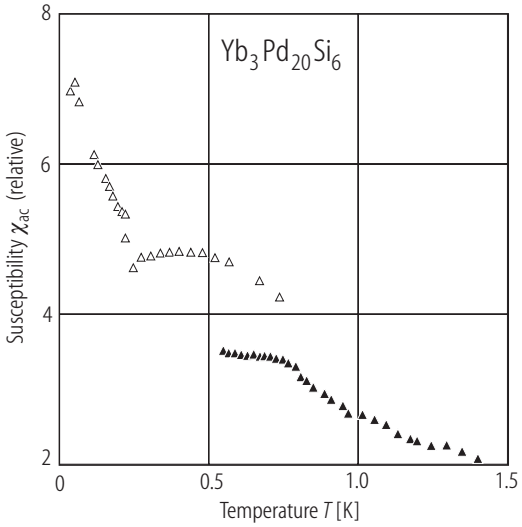

Fig. 504. $Yb_3Pd_{20}Si_6$. Low-temperature dependence of χ_{ac} [97K1].

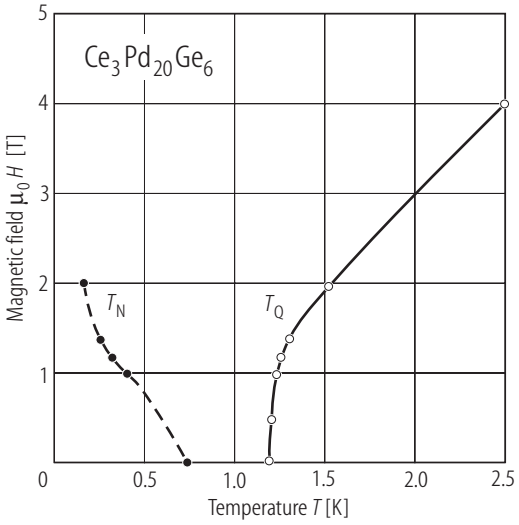

Fig. 506. $Ce_3Pd_{20}Ge_6$. Magnetic phase diagram. T_Q: supposed quadrupolar ordering temperature [97K3].

For Fig. 505 see next page.

For Fig. 504 see previous page.

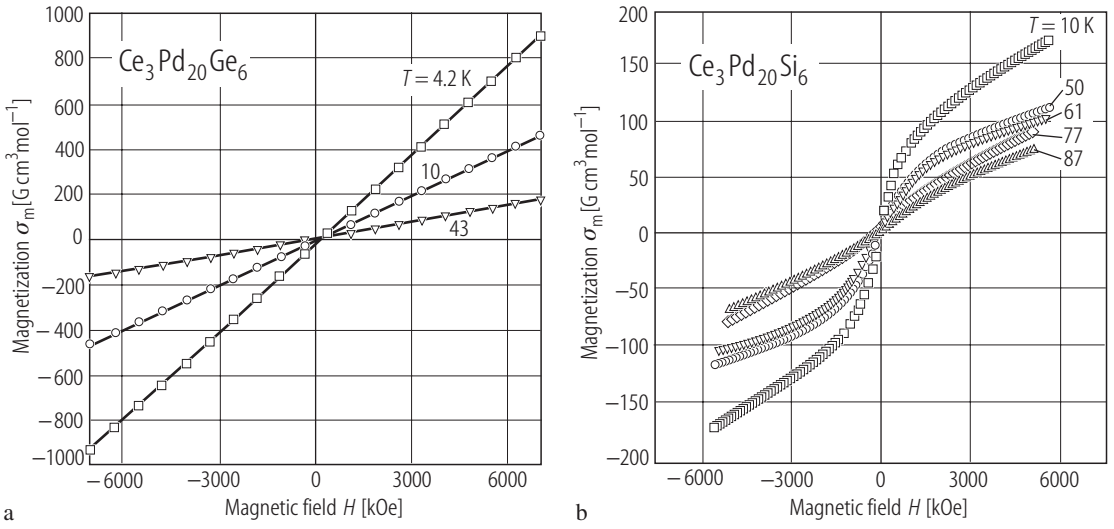

Fig. 505. (**a**) $Ce_3Pd_{20}Ge_6$, (**b**) $Ce_3Pd_{20}Si_6$. Magnetic field dependence of σ_m at various temperatures [96N1].

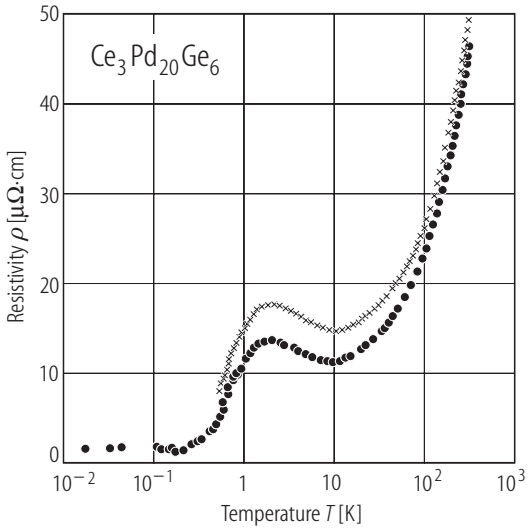

Fig. 507. $Ce_3Pd_{20}Ge_6$. Temperature dependence of ρ for polycrystalline (circles) and single crystalline sample (crosses) [97K3].

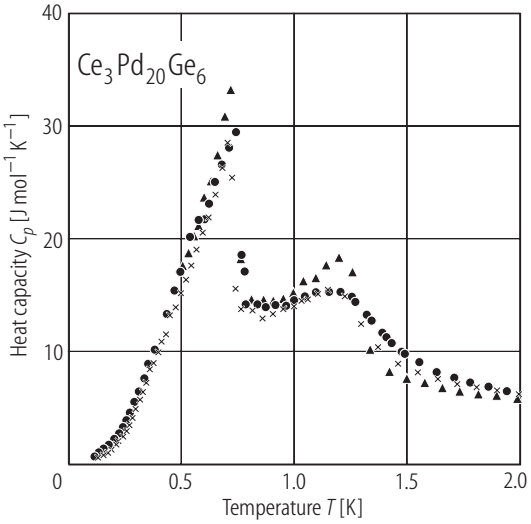

Fig. 508. $Ce_3Pd_{20}Ge_6$. Temperature dependence of C_p for polycrystalline (circles) and two single crystalline samples (crosses and triangles) [97K3].

For Fig. 509 see next page.

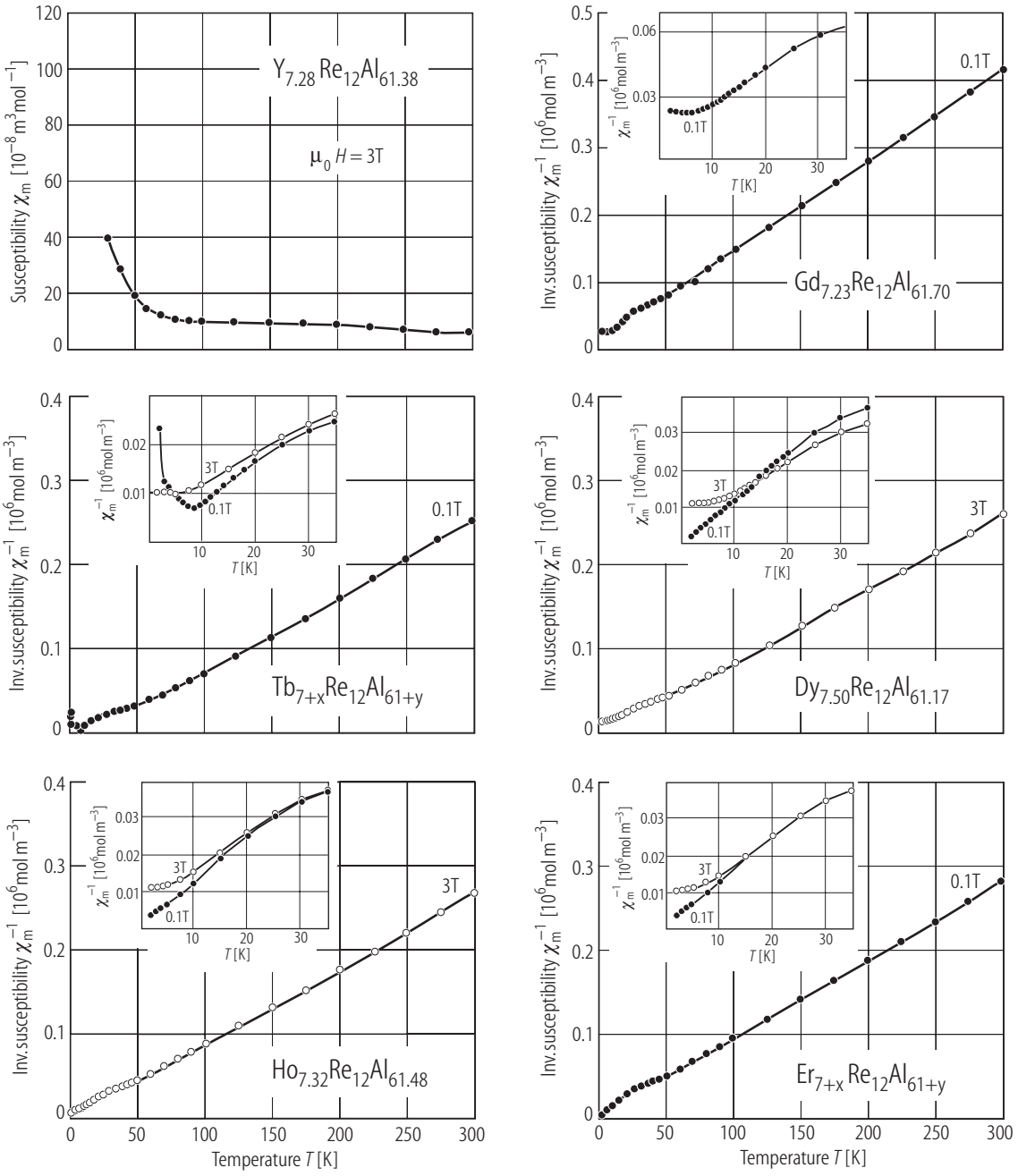

Fig. 510. $R_{7+x}Re_{12}Al_{61+y}$. R = Y, Gd, Tb, Dy, Ho, Er. Temperature dependence of χ_m^{-1}. The idealized formula $R_8Re_{12}Al_{60}$ has the highest R content, the highest Al content occurs in the formula $R_7Re_{12}Al_{62}$, [97T3].

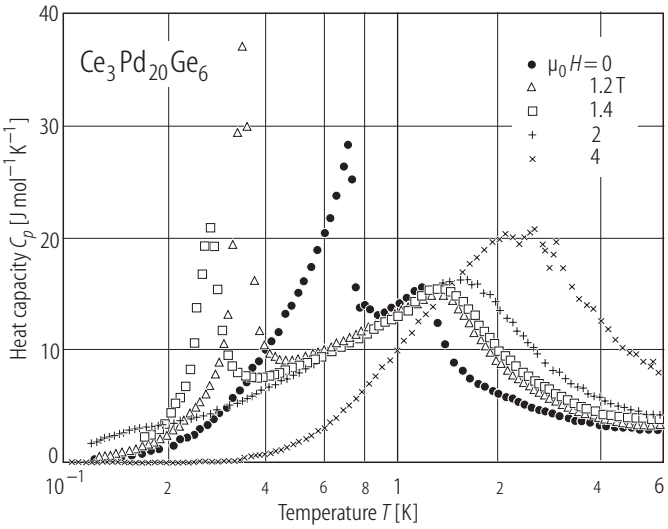

Fig. 509. $Ce_3Pd_{20}Ge_6$. Temperature dependence of C_p at different magnetic fields [97K3].

For Fig. 510 see previous page.

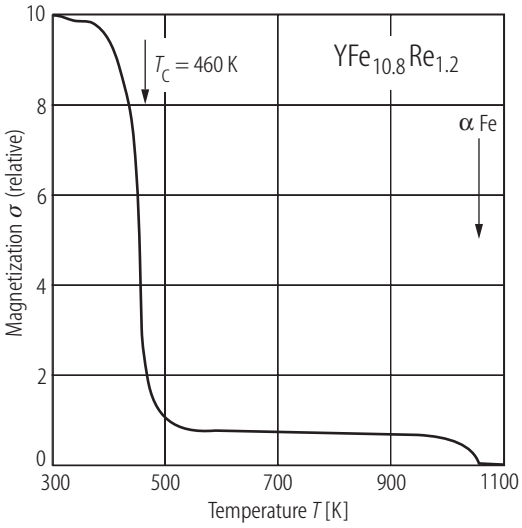

Fig. 511. $YFe_{10.8}Re_{1.2}$. Temperature dependence of magnetization in 2 kOe [90J1].

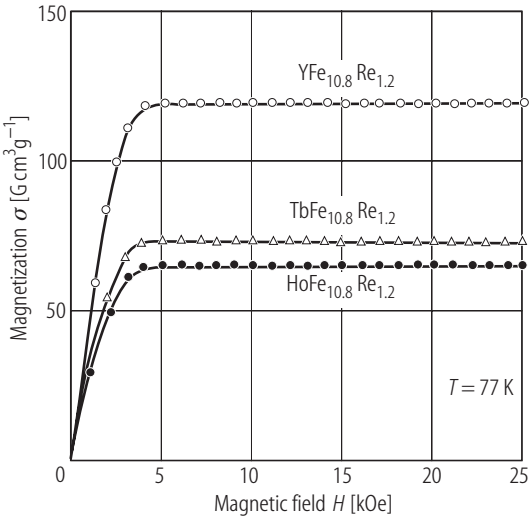

Fig. 512. $RFe_{10.8}Re_{1.2}$. R = Y, Tb, Ho. Magnetic field dependence of σ at 77 K [90J1].

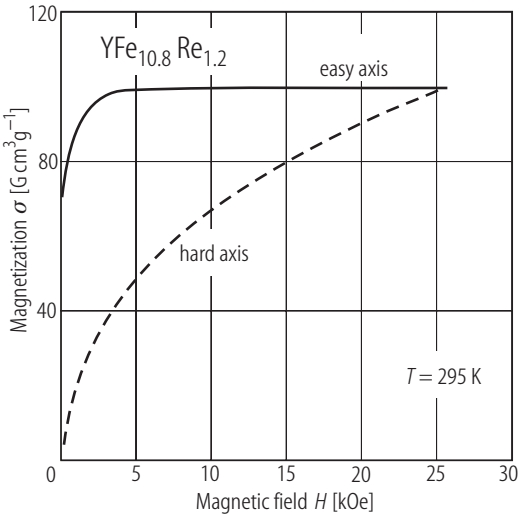

Fig. 513. $YFe_{10.8}Re_{1.2.}$ Magnetic field dependence of σ for aligned powder samples with H along the easy axis at 295 K [90J1].

References

90J1 Jurczyk, M.: J. Magn. Magn. Mater. **89** (1990) L5

96N1 Nikiforov, V.N., Koksharov, Yu.A., Mirkovic, J., Kochetkov, Yu.V.: J. Magn. Magn. Mater. **163** (1996) 184

97B4 Buschinger, B., Geibel, C., Weiden, M., Dietrich, C., Cordier, G., Olesch, G., Kohler, J.: J. Alloys Comp. **260** (1997) 44

97K1 Kitagawa, J., Takeda, N., Ishikawa, W.: J. Alloys Comp. **256** (1997) 48

97K3 Kitakawa, J., Takeda, N., Ishikawa, M., Ishiguro, A., Komatsubara, T.: Physica B **230-232** (1997) 139

97T2 Takeda, N., Kitagawa, J., Ishikawa, M.: Physica B **230-232** (1997) 145

97T3 Thiede, V.M.T., Gerdes, M.H., Rodewald, U.Ch., Jeitschko, W.: J. Alloys Comp. **261** (1997) 54

98B2 Buschinger, B., Trovarrelli, O., Weiden, M., Geibel, C., Steglich, F.: J. Alloys Comp. **275-277** (1998) 633

2.7 Compounds of rare earth elements and Be, Mg, Zn, Cd, or Hg

2.7.1 Introduction

The present work is a continuation of the previous review of Morin in the same series [89M1]. General considerations about crystallography, metallurgy and basic magnetic couplings have then been omitted to avoid redundancy. As far as the ternary compounds are concerned, only non magnetic alloyed atoms have been considered. This allowed us to focus ourselves to the fundamental aspects of the only 4f magnetism, as for the binary systems. The importance of studies on monocrystalline materials has been still growing (see subsects. 2.7.2 and 2.7.3). Besides, new series have been elaborated and magnetically characterized on polycrystalline samples. Some particular series or compounds such as the RX and RX_2 series have been detailed elsewhere (Table 1). In the present review, the same organization as the previous one has been followed, i.e. compounds are successively presented according to their stoichiometry. Subsects. 2.7.2 to 2.7.5 are then devoted to the RX, RX_2, R_2X_{17} and RBe_{13} series, respectively. Other X-rich compounds are gathered in subsect. 2.7.6 while the ternary systems are considered in subsect. 2.7.7.

Table 1. General reviews.

Subject	Reference
Compounds of RE and Be, Mg, Zn, Cd, Hg	89M1
Quadrupolar interactions	90M1
Metamagnetism in intermetallic systems	95G2
Magnetic properties of rare earth compounds	97G1
Thermodynamic data of rare earth alloys	94C1
High pressure studies of anomalous Ce and Yb compounds	94T1

2.7.2 RX compounds

The main studies performed on these cubic CsCl-type compounds are devoted to the Mg and Zn series, and more particularly to measurements carried out on single crystals or under hydrostatic pressure (Figs. 1 - 28). Using single crystals allows one to obtain very specific information on the magnetic couplings, the effects of which may strongly depend on the direction under investigation because of the presence of magnetocrystalline anisotropy. On the other hand, many previous studies have shown the importance of magnetoelastic and two-ion quadrupolar interactions in these series [90M1]. Applying a pressure then leads to influence the magnetic properties through the magnetoelasticity. This effect is especially important in cerium compounds, owing to the weakly localized character of the 4f electron which may give rise to Kondo or heavy fermion behaviour [92C1]. The role of the 5d conduction electrons in the pressure dependence of the exchange interactions has been also investigated in GdMg and GdZn compounds through band structure calculations [96B2]. As far as the two-ion quadrupolar interactions are concerned, the main previous studies were limited to ferroquadrupolar-type couplings, in the RZn series and the Tm-based compounds [89M1]. Later, they have been extended to CeMg and CeZn compounds (Table 2). In more recent works, antiferroquadrupolar interactions have been thoroughly investigated, through their effects on the antiferromagnetic moment arrangements. In particular, it has been shown that multiaxial (non collinear) structures can be stabilized by this type of coupling, even under an external field [95A1, 96A1]. Finally, some progress has been realized about the structural transformations in the RCd series (Figs. 29 - 32) [87K1].

References

89M1 Morin, P., in: Magnetic Properties of Metals (Wijn, H.P.J., ed.), Landolt-Börnstein, New Series, Berlin, Heidelberg, New York: Springer, Vol. 19e2 **1989**, p. 1

90M1 Morin, P., Schmitt, D., in: Ferromagnetic Materials (Buschow, K.H.J., Wohlfarth, E.P., eds.), Amsterdam: North-Holland, Vol. 5 **1990**, Chap. 1, p. 1

94C1 Colinet, C., Pasturel, A., in: Handbook on the Physics and Chemistry of Rare Earths (Gschneidner Jr., K.A., Eyring, L., Lander, G.H., Choppin, G.R., eds.), Amsterdam: Elsevier, Vol. 19 **1994**, Chap. 134, p. 479

94T1 Thompson, J.D., Lawrence, J.M., in: Handbook on the Physics and Chemistry of Rare Earths (Gschneidner Jr., K.A., Eyring, L., Lander, G.H., Choppin, G.R., eds.), Amsterdam: Elsevier, Vol. 19 **1994**, Chap. 133, p. 383

95G2 Gignoux, D., Schmitt, D., in: Handbook on the Physics and Chemistry of Rare Earths (Gschneidner Jr., K.A., Eyring, L., eds.), Amsterdam: Elsevier, Vol. 20 **1995**, Chap. 138, p. 293

97G1 Gignoux, D., Schmitt, D., in: Handbook of Magnetic Materials (Buschow, K.H.J., ed.), Amsterdam: Elsevier, Vol. 10 **1997**, Chap. 2, p. 239

2.7 Compounds of rare earth elements and Be, Mg, Zn, Cd, or Hg

2.7.1 Introduction

The present work is a continuation of the previous review of Morin in the same series [89M1]. General considerations about crystallography, metallurgy and basic magnetic couplings have then been omitted to avoid redundancy. As far as the ternary compounds are concerned, only non magnetic alloyed atoms have been considered. This allowed us to focus ourselves to the fundamental aspects of the only 4f magnetism, as for the binary systems. The importance of studies on monocrystalline materials has been still growing (see subsects. 2.7.2 and 2.7.3). Besides, new series have been elaborated and magnetically characterized on polycrystalline samples. Some particular series or compounds such as the RX and RX_2 series have been detailed elsewhere (Table 1). In the present review, the same organization as the previous one has been followed, i.e. compounds are successively presented according to their stoichiometry. Subsects. 2.7.2 to 2.7.5 are then devoted to the RX, RX_2, R_2X_{17} and RBe_{13} series, respectively. Other X-rich compounds are gathered in subsect. 2.7.6 while the ternary systems are considered in subsect. 2.7.7.

Table 1. General reviews.

Subject	Reference
Compounds of RE and Be, Mg, Zn, Cd, Hg	89M1
Quadrupolar interactions	90M1
Metamagnetism in intermetallic systems	95G2
Magnetic properties of rare earth compounds	97G1
Thermodynamic data of rare earth alloys	94C1
High pressure studies of anomalous Ce and Yb compounds	94T1

2.7.2 RX compounds

The main studies performed on these cubic CsCl-type compounds are devoted to the Mg and Zn series, and more particularly to measurements carried out on single crystals or under hydrostatic pressure (Figs. 1 - 28). Using single crystals allows one to obtain very specific information on the magnetic couplings, the effects of which may strongly depend on the direction under investigation because of the presence of magnetocrystalline anisotropy. On the other hand, many previous studies have shown the importance of magnetoelastic and two-ion quadrupolar interactions in these series [90M1]. Applying a pressure then leads to influence the magnetic properties through the magnetoelasticity. This effect is especially important in cerium compounds, owing to the weakly localized character of the 4f electron which may give rise to Kondo or heavy fermion behaviour [92C1]. The role of the 5d conduction electrons in the pressure dependence of the exchange interactions has been also investigated in GdMg and GdZn compounds through band structure calculations [96B2]. As far as the two-ion quadrupolar interactions are concerned, the main previous studies were limited to ferroquadrupolar-type couplings, in the RZn series and the Tm-based compounds [89M1]. Later, they have been extended to CeMg and CeZn compounds (Table 2). In more recent works, antiferroquadrupolar interactions have been thoroughly investigated, through their effects on the antiferromagnetic moment arrangements. In particular, it has been shown that multiaxial (non collinear) structures can be stabilized by this type of coupling, even under an external field [95A1, 96A1]. Finally, some progress has been realized about the structural transformations in the RCd series (Figs. 29 - 32) [87K1].

Table 2. CeMg, CeZn compounds. Elastic constant ½(c_{11}-c_{12}) at room temperature, magnetoelastic coefficient B_1, two-ion quadrupolar coefficient K_1 and total quadrupolar coefficient G_1 for the tetragonal symmetry.

Compound	½(c_{11}-c_{12}) [GPa]	B_1 [K/atom]	K_1 [mK/atom]	G_1 [mK/atom]	Figures	Ref.
CeMg	8.4	108	30 ± 40	80	3, 4	88M1, 90A1
CeZn	13.5	218	20 ± 60	400	3, 4	88M1, 90A1

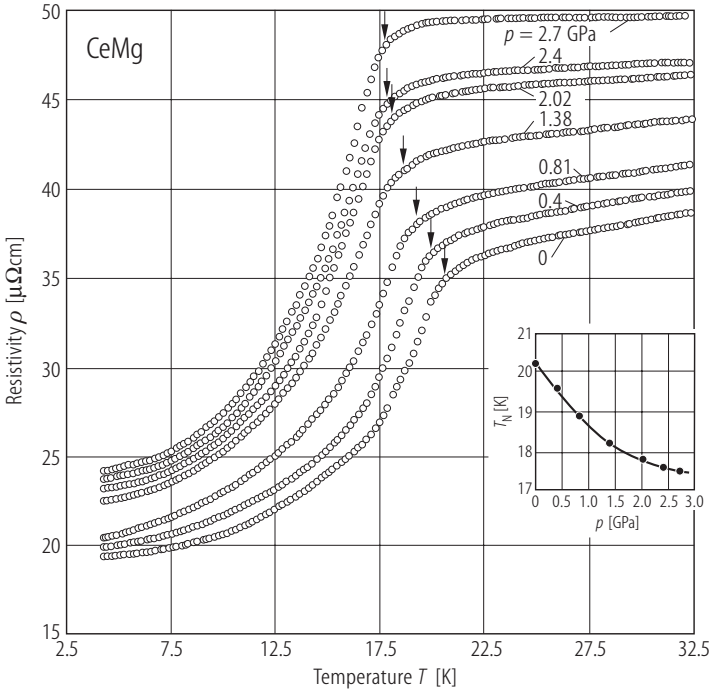

Fig. 1. CeMg. Electrical resistivity vs. temperature at various pressures. The arrows show the Néel temperatures T_N. The inset shows the pressure dependence of T_N [87K3].

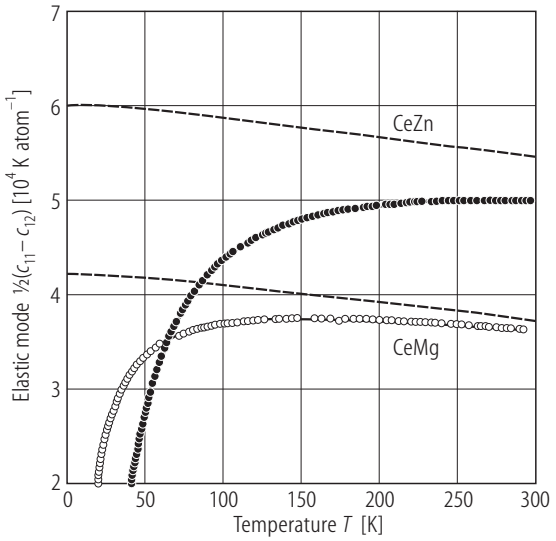

Fig. 3. CeMg, CeZn. Shear elastic mode vs. temperature obtained by ultrasonic velocity measurements. Dashed lines are the lattice background deduced from LaMg and LaZn. Full lines are calculated within the quadrupolar model. 10^4 K/atom = 2.325 and 2.696 GPa for CeMg and CeZn, respectively [88M1].

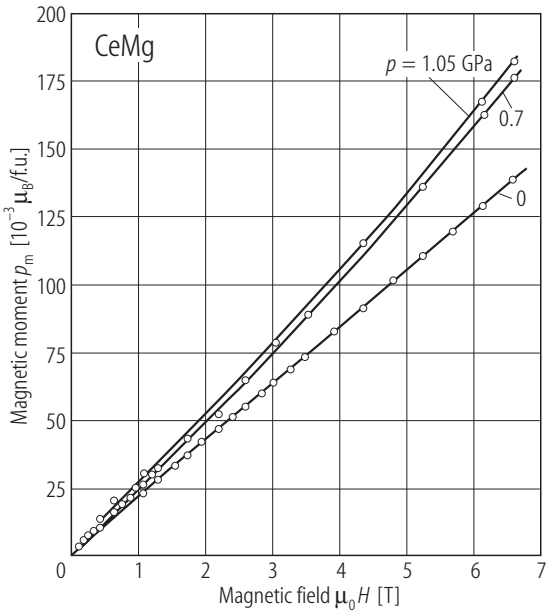

Fig. 2. CeMg. Isothermal magnetization curves vs. magnetic field at T = 4.2 K for various pressures [87K3].

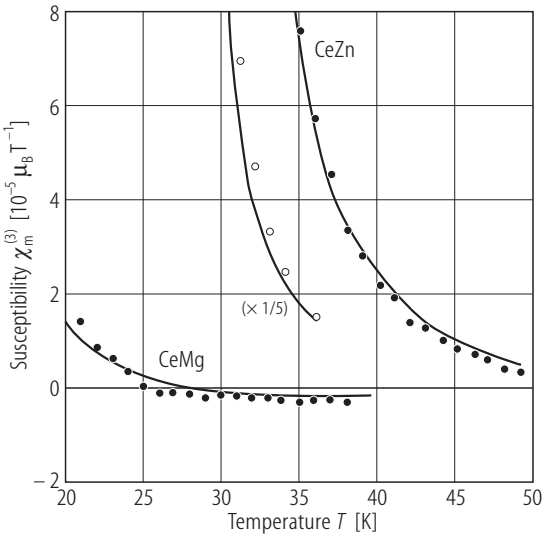

Fig. 4. CeMg, CeZn. Third-order paramagnetic susceptibility $\chi_m^{(3)}$ vs. temperature for a magnetic field applied along the [001] axis (tetragonal symmetry). $\chi_m^{(3)}$ represents the initial curvature of the magnetization curves. Full lines are calculated for the quadrupolar coefficients G_1 = 80 and 400 mK/atom for CeMg and CeZn, respectively [90A1].

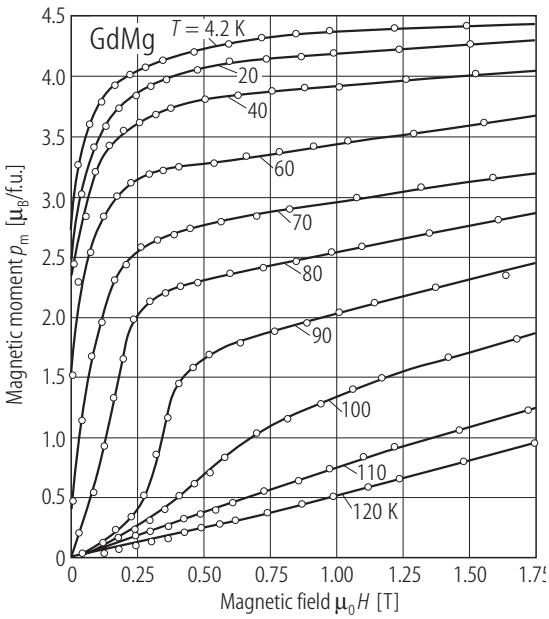

Fig. 5. GdMg. Isothermal magnetization curves vs. magnetic field at p = 1.3 GPa for various temperatures [86L2].

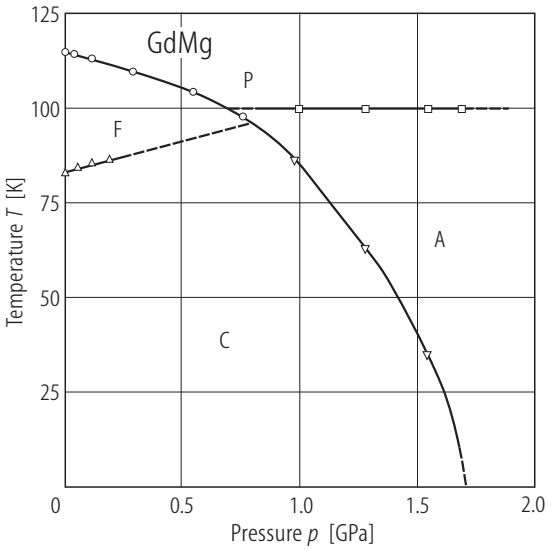

Fig. 6. GdMg. Pressure - temperature magnetic phase diagram. P: paramagnetic; F: ferromagnetic; C: canted; A: antiferromagnetic [86L2].

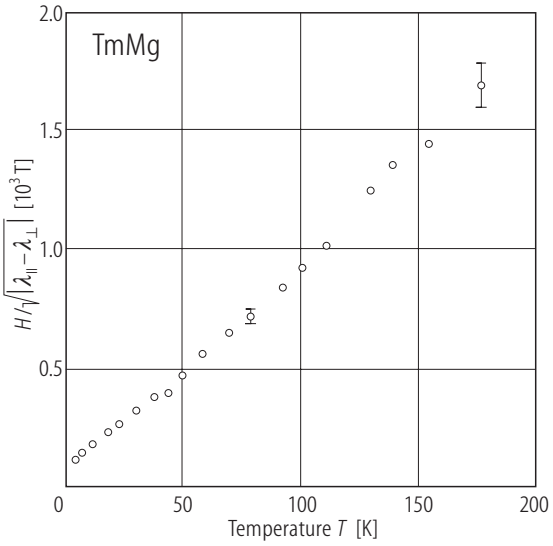

Fig. 7. TmMg. Reciprocal parastriction susceptibility, $H/\sqrt{|\lambda_{\parallel}-\lambda_{\perp}|}$ vs. temperature for a magnetic field applied along the [001] axis. The changes of length, $\lambda_{\parallel}$ and $\lambda_{\perp}$, are measured parallel and perpendicular to H [86G1].

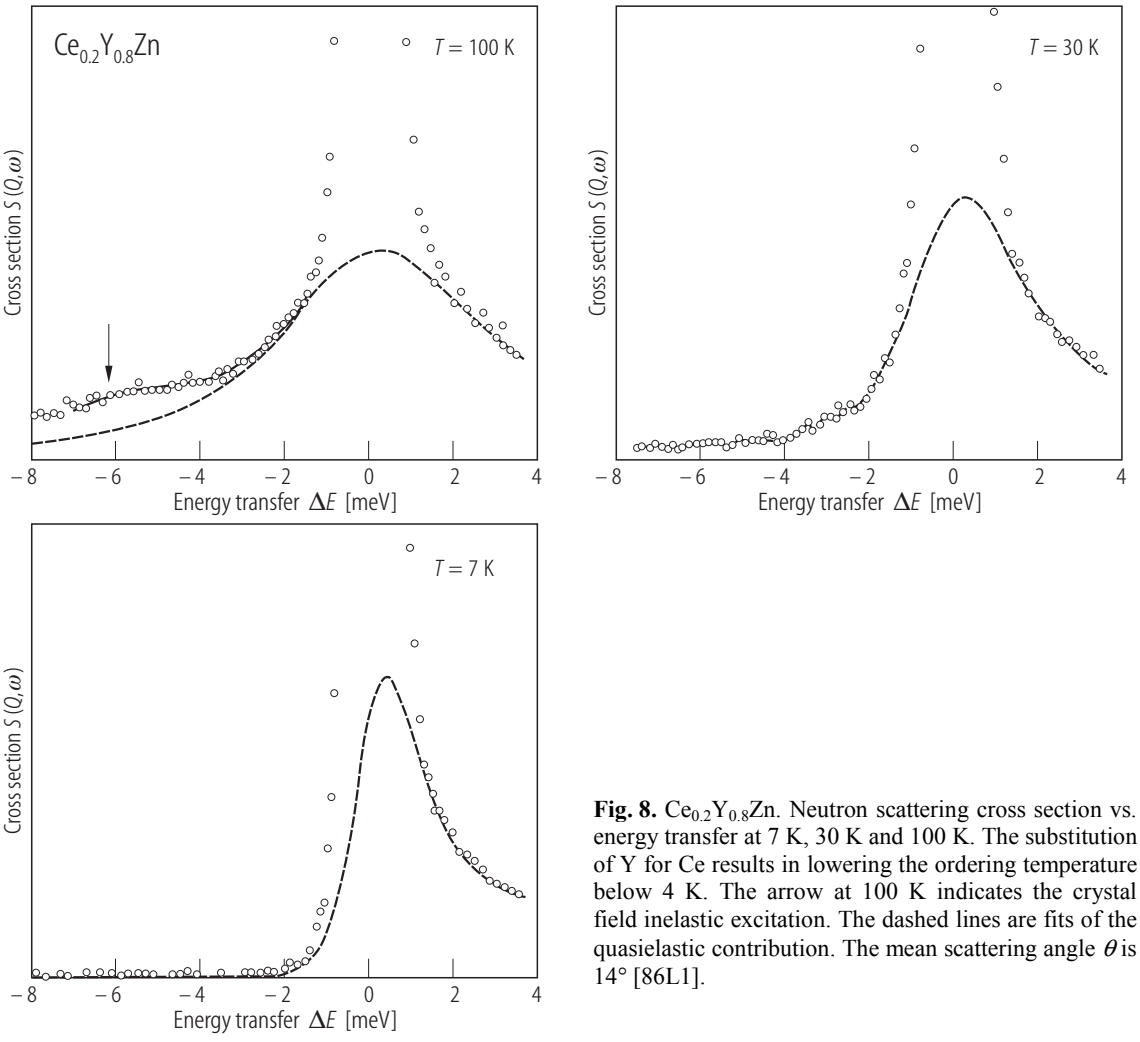

Fig. 8. $Ce_{0.2}Y_{0.8}Zn$. Neutron scattering cross section vs. energy transfer at 7 K, 30 K and 100 K. The substitution of Y for Ce results in lowering the ordering temperature below 4 K. The arrow at 100 K indicates the crystal field inelastic excitation. The dashed lines are fits of the quasielastic contribution. The mean scattering angle θ is 14° [86L1].

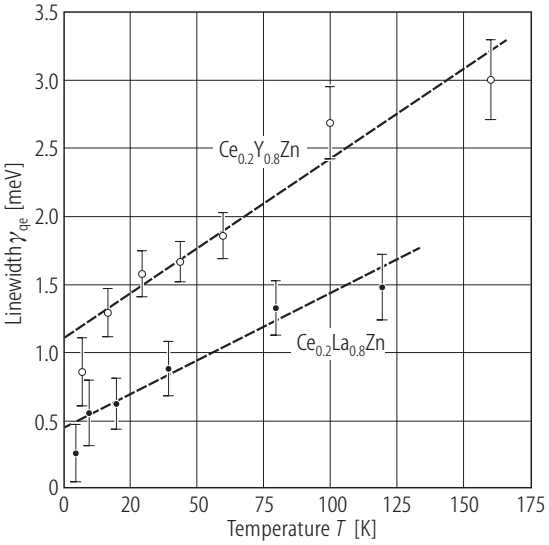

Fig. 9. $Ce_{0.2}Y_{0.8}Zn$, $Ce_{0.2}La_{0.8}Zn$. Linewidth of the quasielastic contribution to the neutron scattering cross section vs. temperature [86L1].

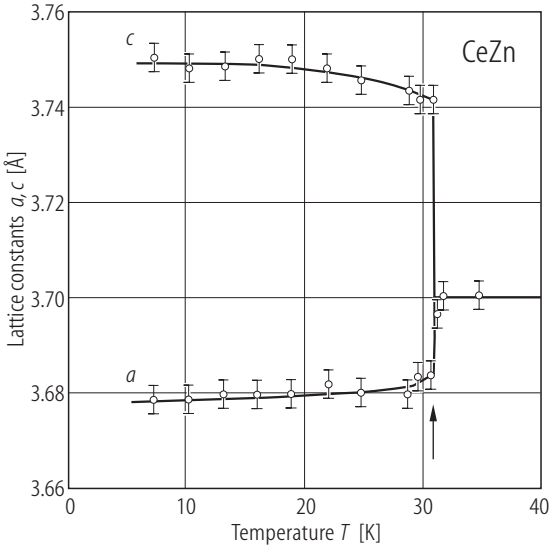

Fig. 11. CeZn. Lattice constants a, c vs. temperature, deduced from the position of the (200) and (002) nuclear reflections measured by powder neutron diffraction. The arrow indicates the Néel temperature T_N (first order transition). The symmetry is cubic above T_N and tetragonal below T_N [89U1].

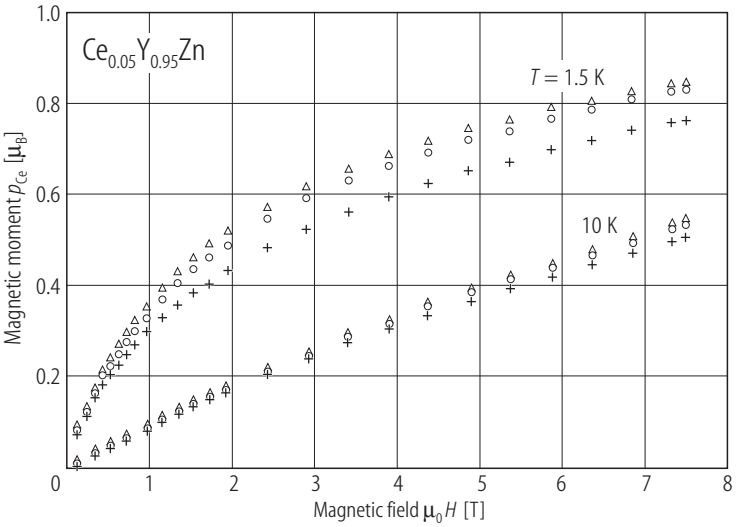

Fig. 10. $Ce_{0.05}Y_{0.95}Zn$. Magnetization curves vs. magnetic field at 1.5 and 10 K for a single crystal. The field is applied along Δ [111], o [110] or + [001] direction. The Néel temperature is below 1.5 K [86L1].

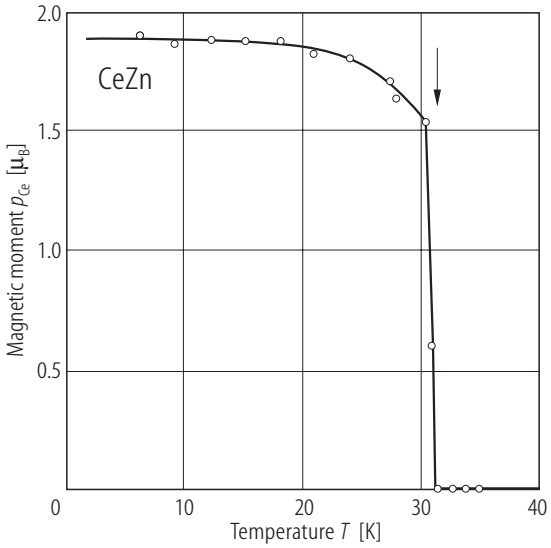

Fig. 12. CeZn. Ordered magnetic moment vs. temperature, deduced from the (10½) magnetic reflection measured by powder neutron diffraction. The arrow indicates the Néel temperature. The moment direction is [001] [88U1].

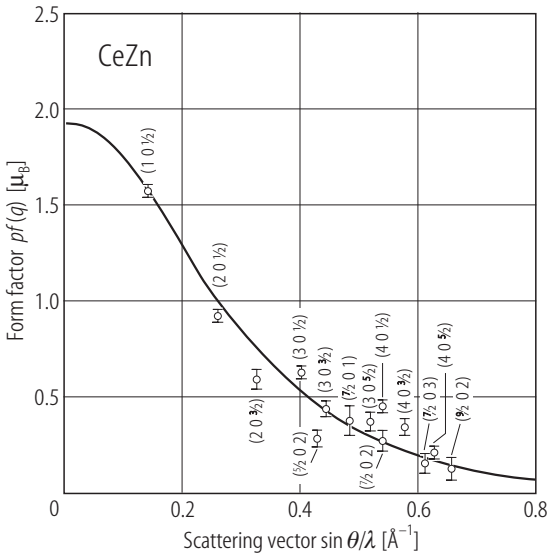

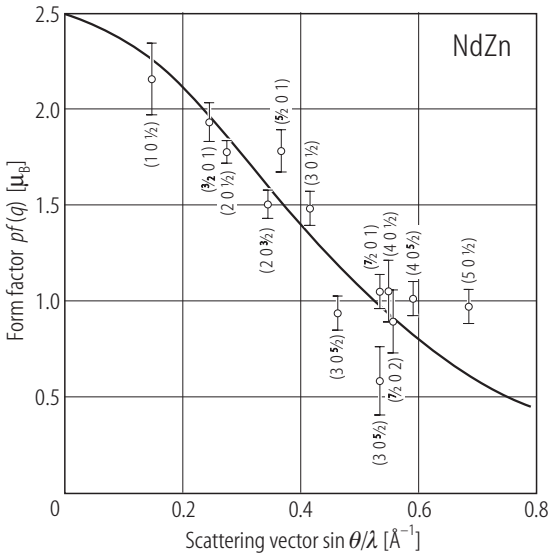

Fig. 13. CeZn, NdZn. Effective magnetic amplitude $pf(q)$ vs. scattering vector $q/(4\pi) = \sin(\theta)/\lambda$ measured by neutron diffraction at 8 K for CeZn and 4.2 K for NdZn. p is the ordered moment and $f(q)$ the magnetic form factor. The reflections (h,k,l) measured are indicated [87F1].

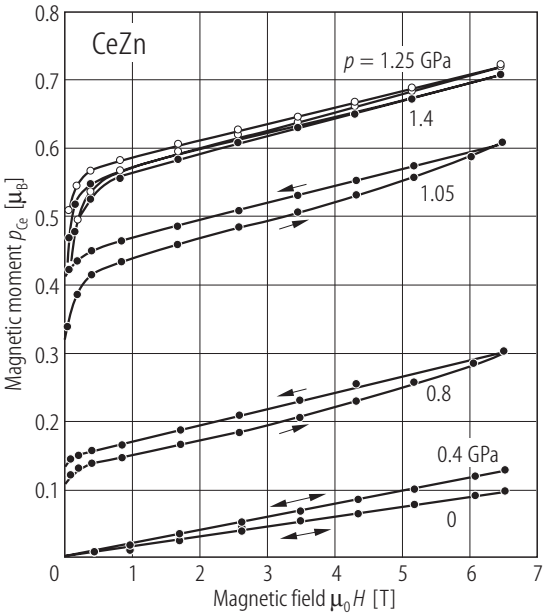

Fig. 14. CeZn. Magnetization curves vs. magnetic field at 4.2 K for the pressures indicated. Note the hysteresis above 0.8 GPa [86K1].

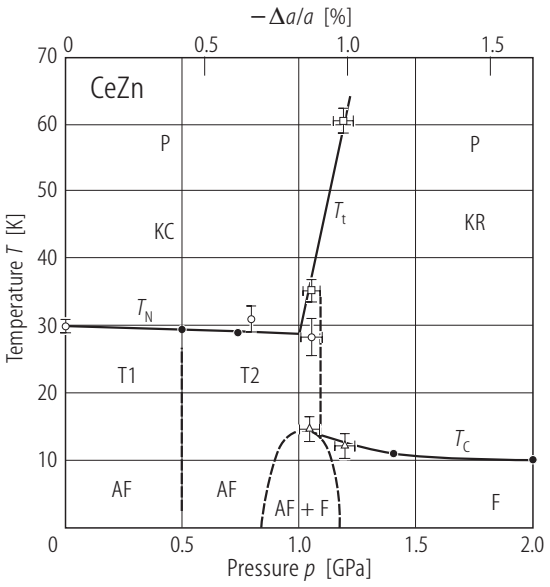

Fig. 16. CeZn. Pressure - temperature magnetic and structural phase diagram. P: paramagnetic; F: ferromagnetic; AF: antiferromagnetic; T1: tetragonal symmetry, $c/a > 1$; T2: tetragonal symmetry, $c/a < 1$; KC: cubic Kondo state; KR: rhomboedral Kondo state. T_C, T_N, T_t as in Fig. 15 [90S1].

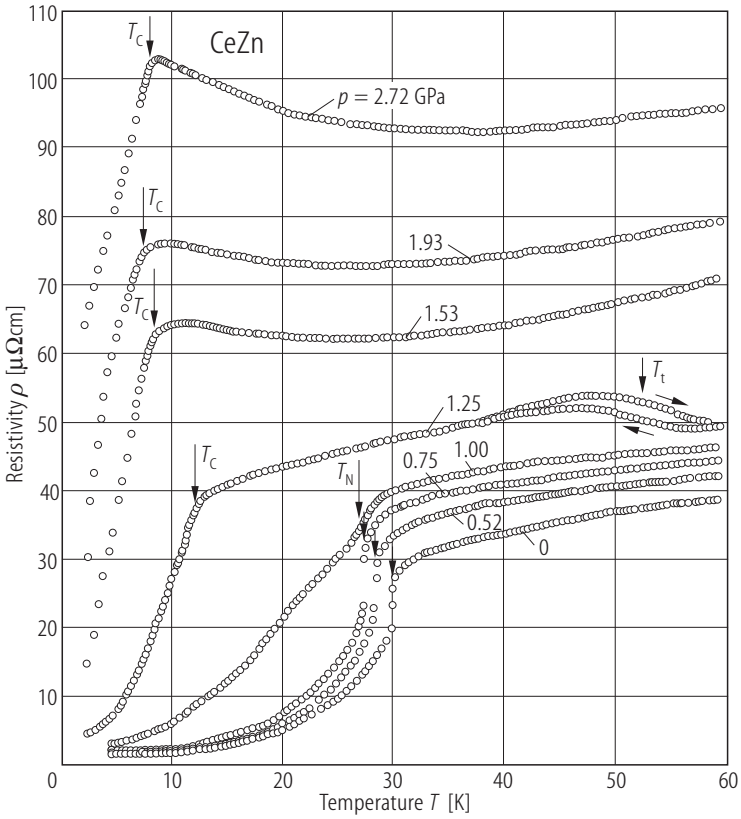

Fig. 15. CeZn. Electrical resistivity vs. temperature at various pressures, as indicated. T_C: Curie temperature, T_N: Néel temperature, T_t: structural transition temperature [86K1].

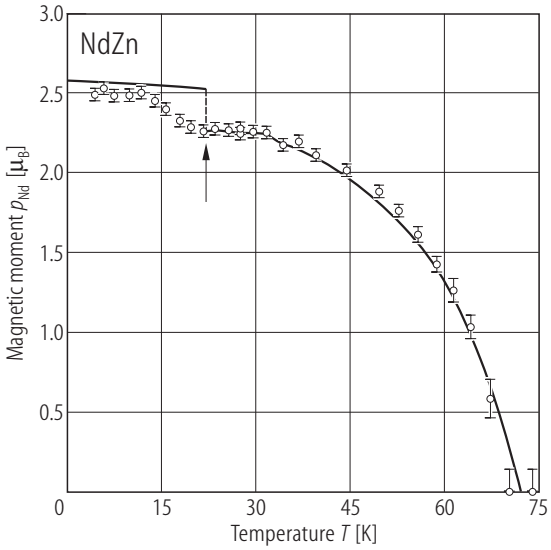

Fig. 17. NdZn. Ordered magnetic moment vs. temperature, deduced from the (10½) magnetic reflection measured by neutron diffraction. The arrow indicates the spin reorientation transition at T_{sr} = 18 K. The moment direction is [110] and [111] below and above T_{sr}, respectively [87F1].

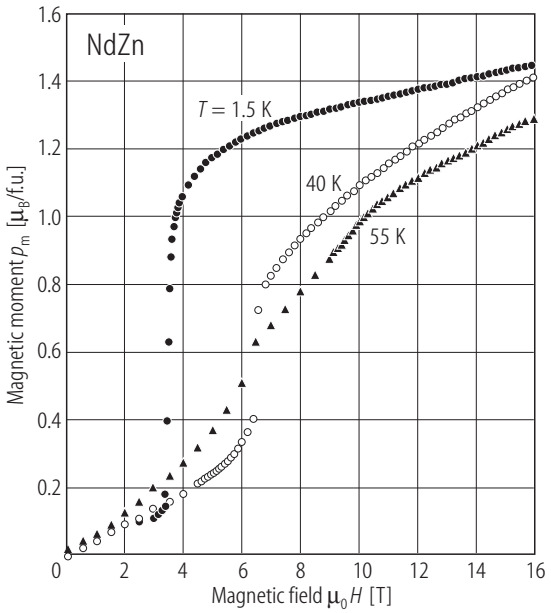

Fig. 18. NdZn. Magnetization curves vs. magnetic field applied along the [110] direction at T = 1.5 K, 40 K and 55 K. The field-induced metamagnetic transitions correspond to changes of antiferromagnetic moment configuration [95A2].

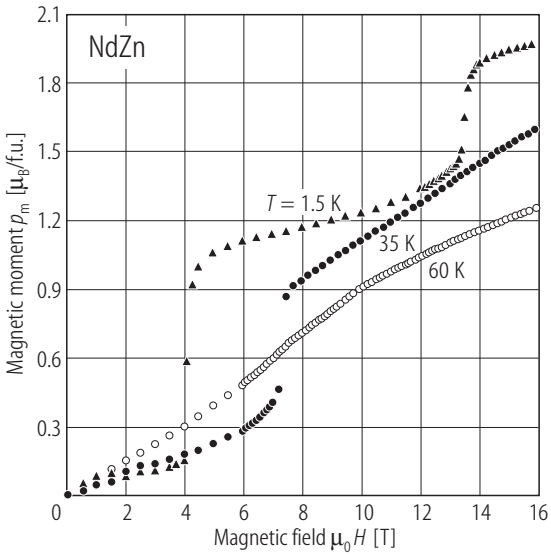

Fig. 19. NdZn. Magnetization curves vs. magnetic field applied along the [111] direction at T = 1.5 K, 35 K and 60 K [95A2].

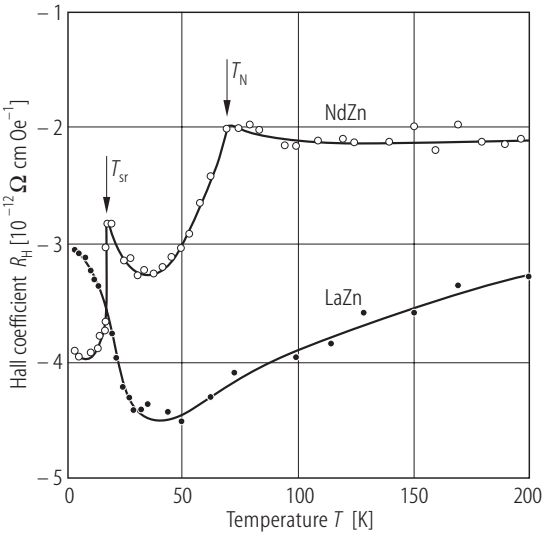

Fig. 21. NdZn, LaZn. Hall coefficient vs. temperature. Arrows indicate the Néel temperature T_N and the spin reorientation temperature T_{sr} [86H1].

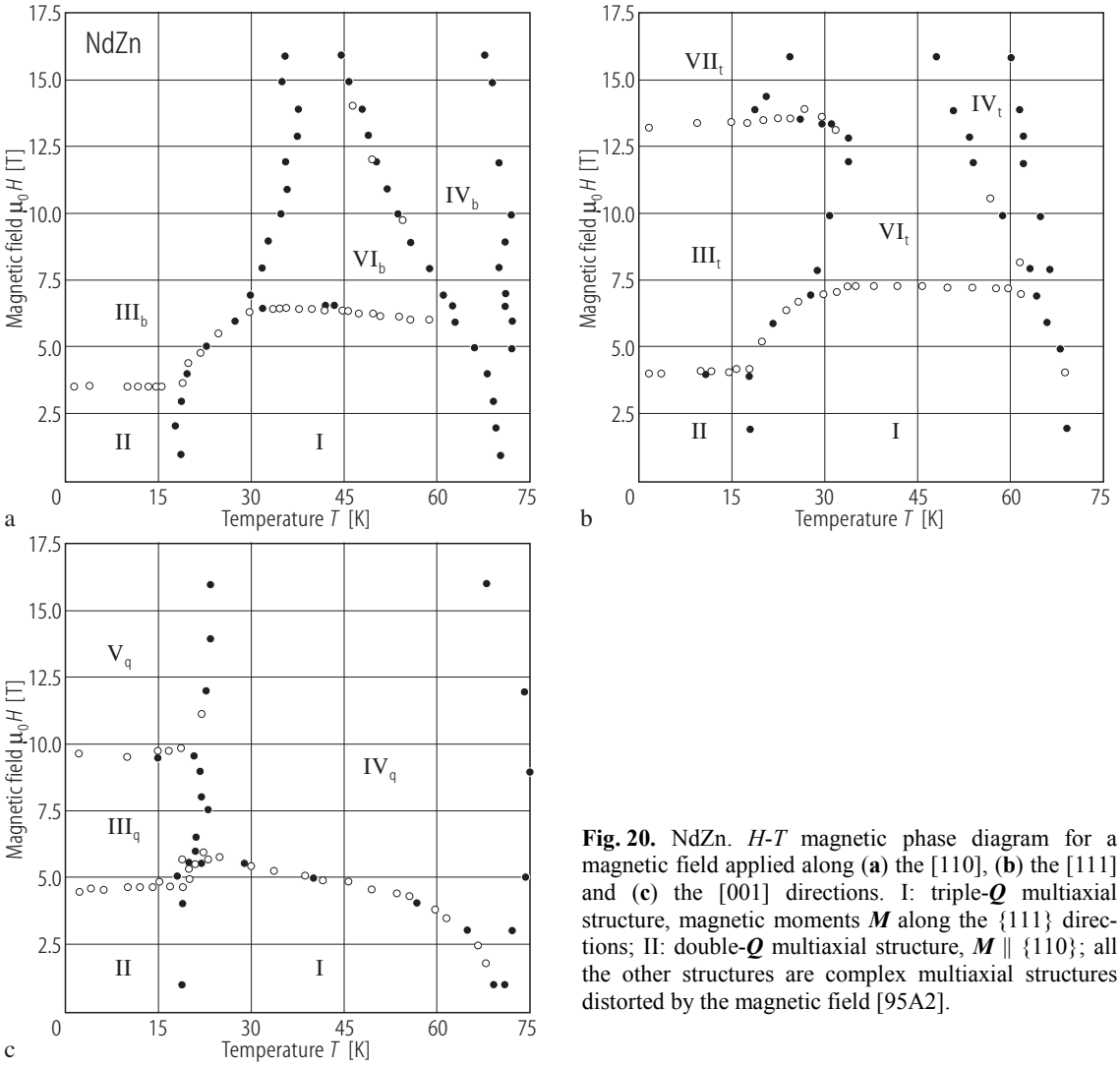

Fig. 20. NdZn. *H-T* magnetic phase diagram for a magnetic field applied along (**a**) the [110], (**b**) the [111] and (**c**) the [001] directions. I: triple-***Q*** multiaxial structure, magnetic moments ***M*** along the {111} directions; II: double-***Q*** multiaxial structure, ***M*** ∥ {110}; all the other structures are complex multiaxial structures distorted by the magnetic field [95A2].

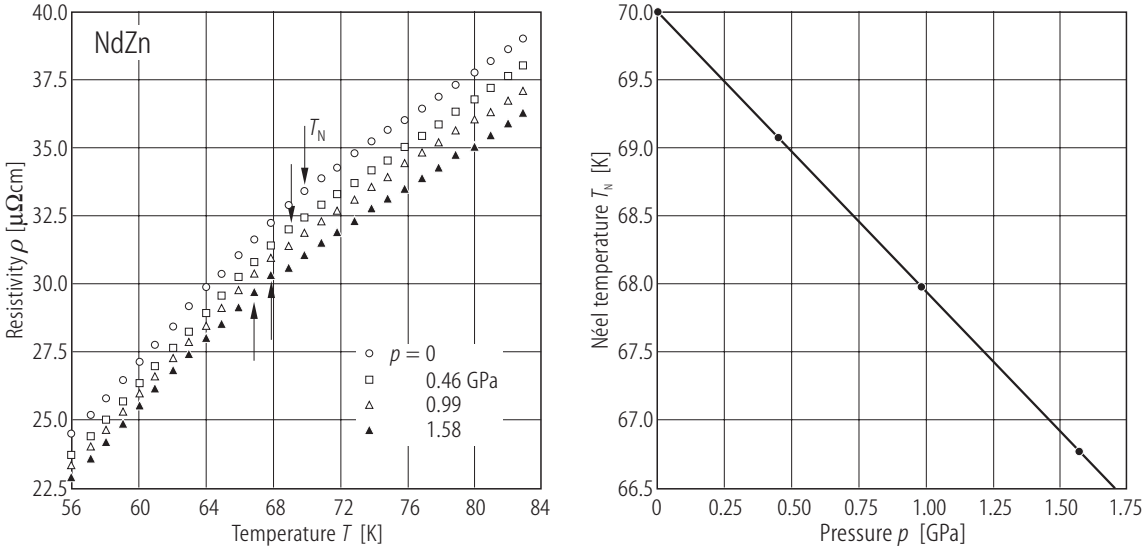

Fig. 22. NdZn. Electrical resistivity vs. temperature at various pressures around the Néel temperature T_N. Right figure: T_N vs. pressure [95K2].

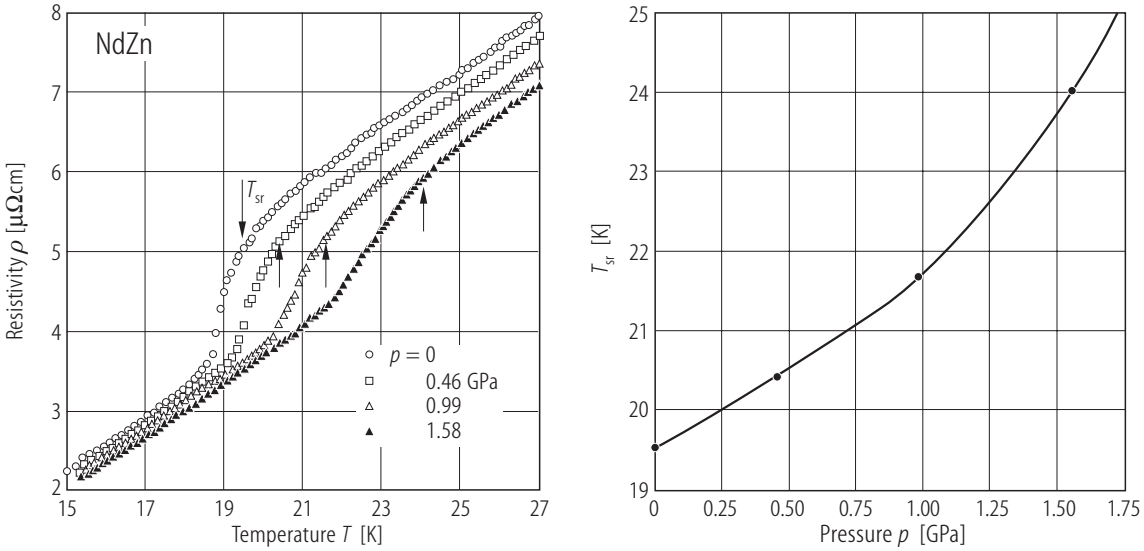

Fig. 23. NdZn. Electrical resistivity vs. temperature at various pressures around the spin reorientation temperature T_{sr}. Right figure: T_{sr} vs. pressure [95K2].

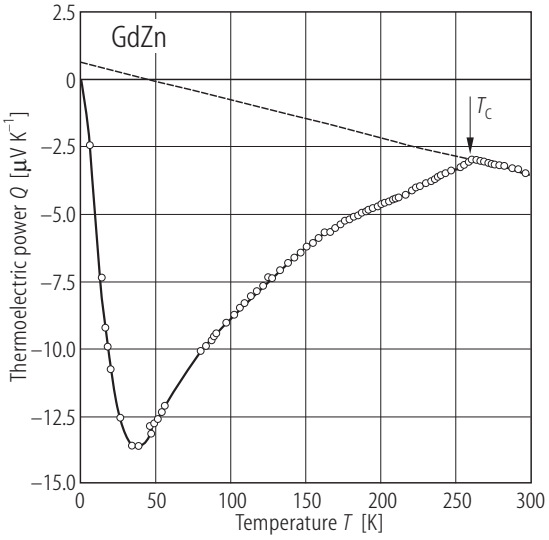

Fig. 24. GdZn. Thermoelectric power referred to copper vs. temperature. T_C is the Curie temperature [88P1].

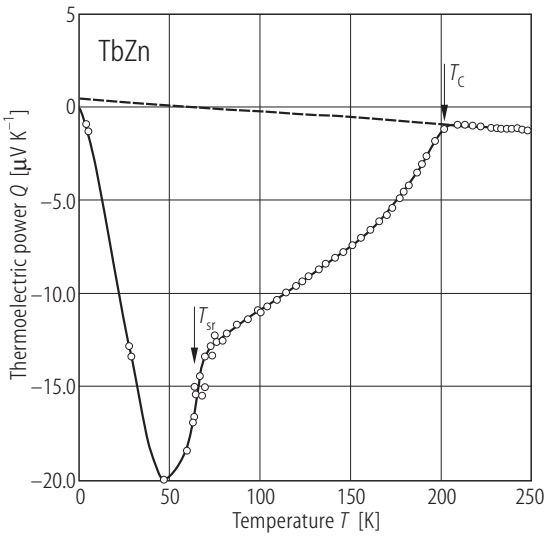

Fig. 26. TbZn. Thermoelectric power referred to copper vs. temperature. T_C is the Curie temperature, T_{sr} the spin reorientation temperature. The moment direction is [110] and [001] below and above T_{sr}, respectively [88P1].

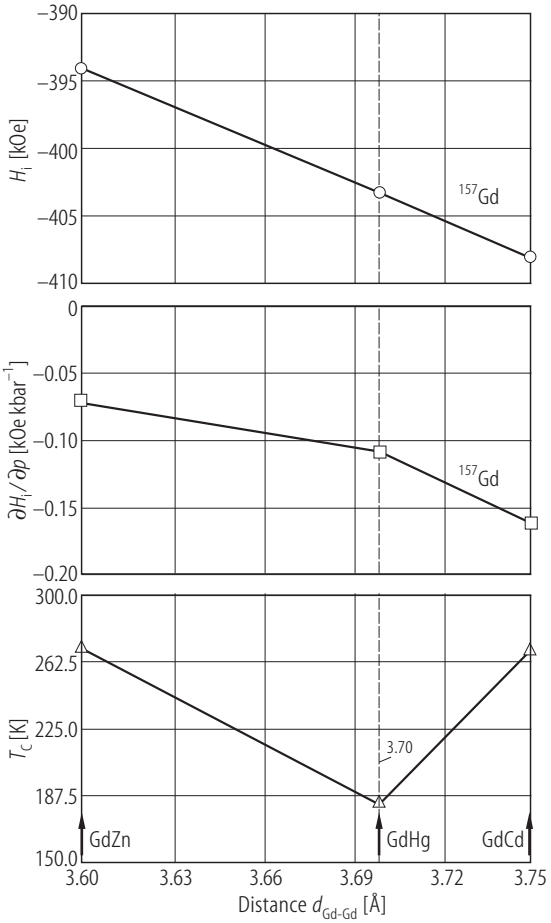

Fig. 25. GdZn, GdHg, GdCd. Effective magnetic field H_i(Gd), its pressure derivative and Curie temperature T_C vs. next-nearest Gd-Gd distance, obtained by high pressure NMR measurements [87K2].

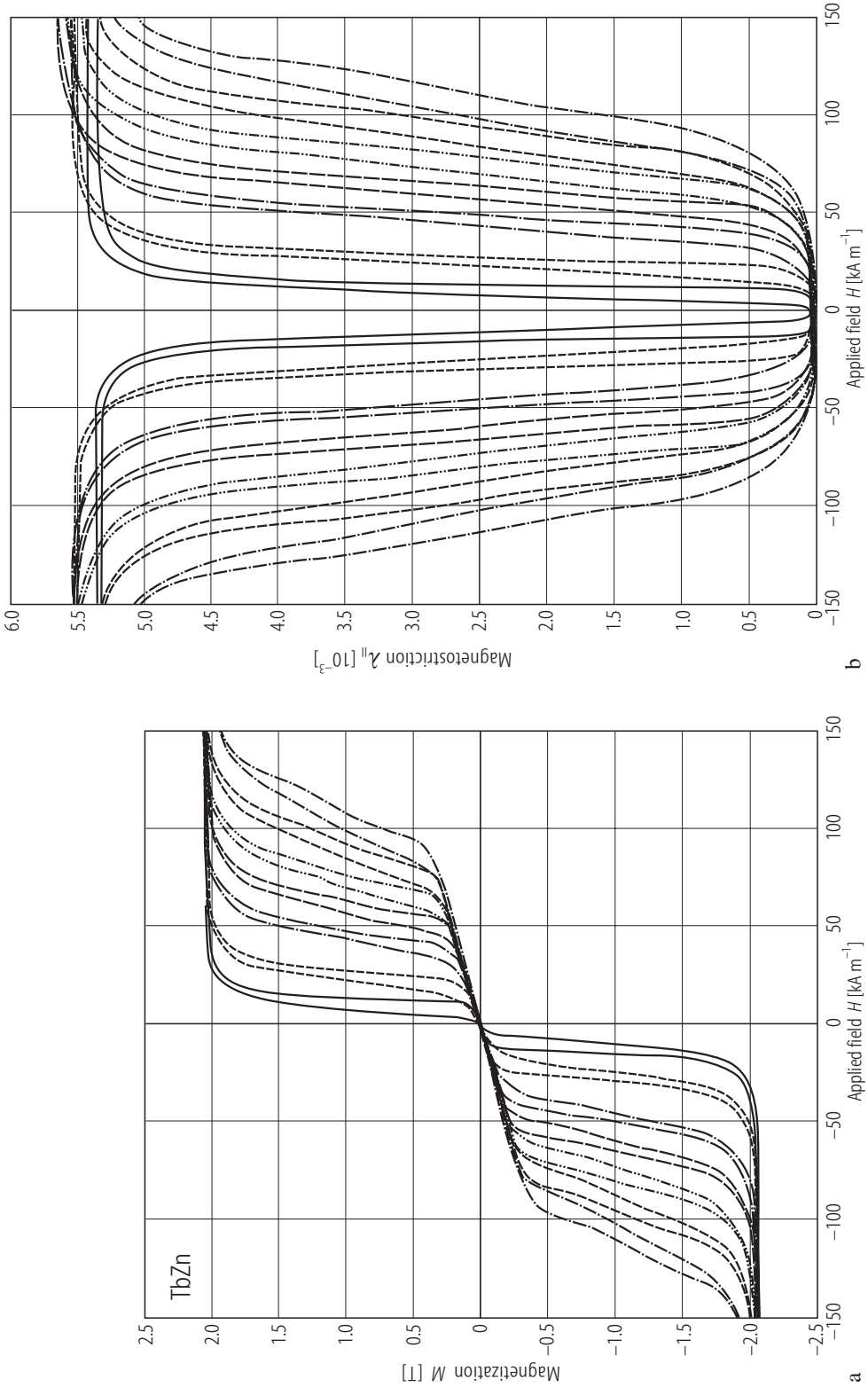

Fig. 27. TbZn. (**a**) Magnetization and (**b**) magnetostriction vs. magnetic field applied along the [100] easy axis at 77 K and for various compressive stresses: ——5.3, – – –13.3, –·–· 24.6, ---- 31.1, ·····37.5, ···· 44, and ·–·–· 50.5 MPa [95C1].

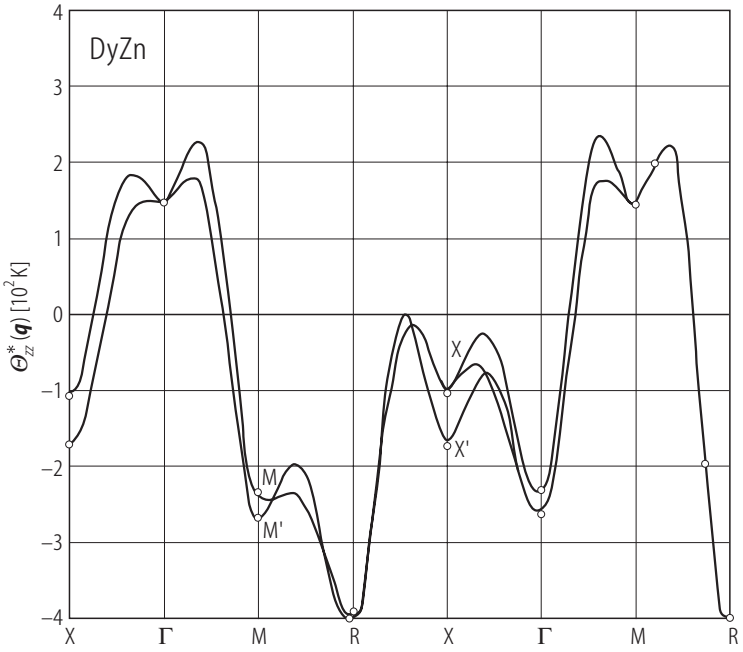

Fig. 28. DyZn. Ab-initio calculated Fourier transform
$\theta_{zz}^*(q) = 1/3J(J+1)\, J_{zz}(q)$
of the two-ion anisotropic bilinear exchange coupling constants $J_{zz}(R_{ij})$ for the main symmetry directions of the cubic Brillouin zone [86S1].

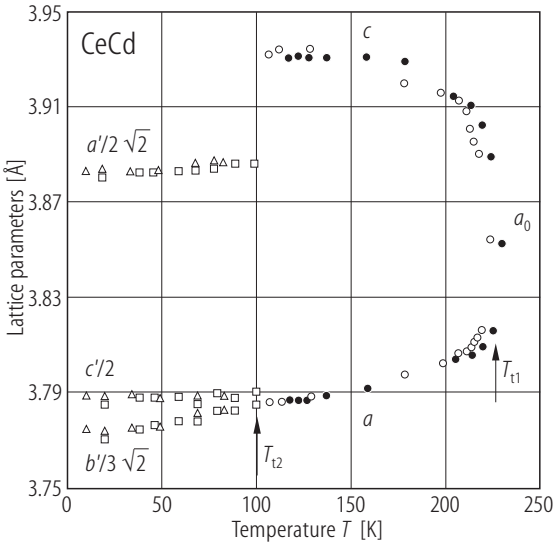

Fig. 29. CeCd. Lattice parameters vs. temperature, determined by X-ray diffraction measurements on single crystal. The structure is cubic above T_{t1} = 220 K, tetragonal between T_{t1} and T_{t2} = 100 K and orthorhombic below T_{t2}. Full circles and squares: increasing temperature; open circles and triangles: decreasing temperature [88N1].

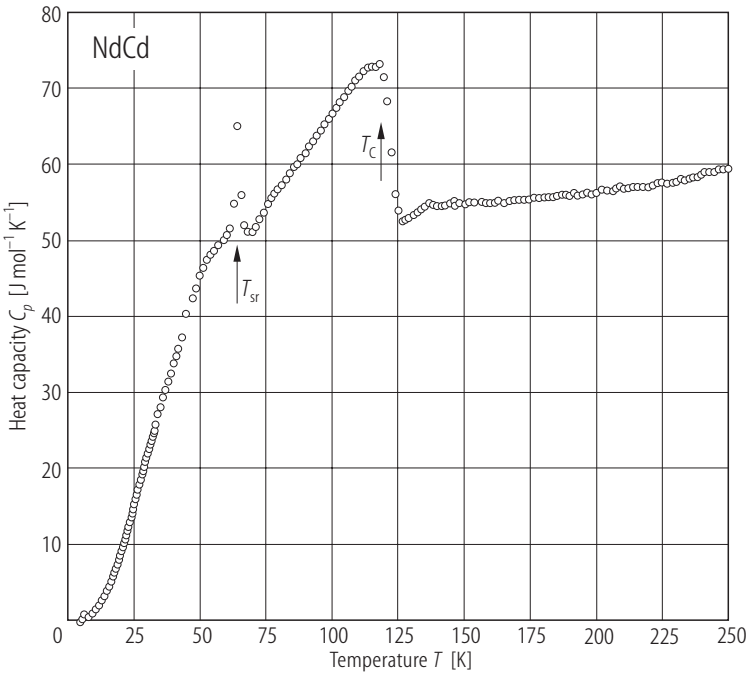

Fig. 30. NdCd. Heat capacity vs. temperature. T_C = 121 K is the Curie temperature, T_{sr} = 62.5 K the spin reorientation temperature. The moment direction is [110] and [111] below and above T_{sr}, respectively [90A1].

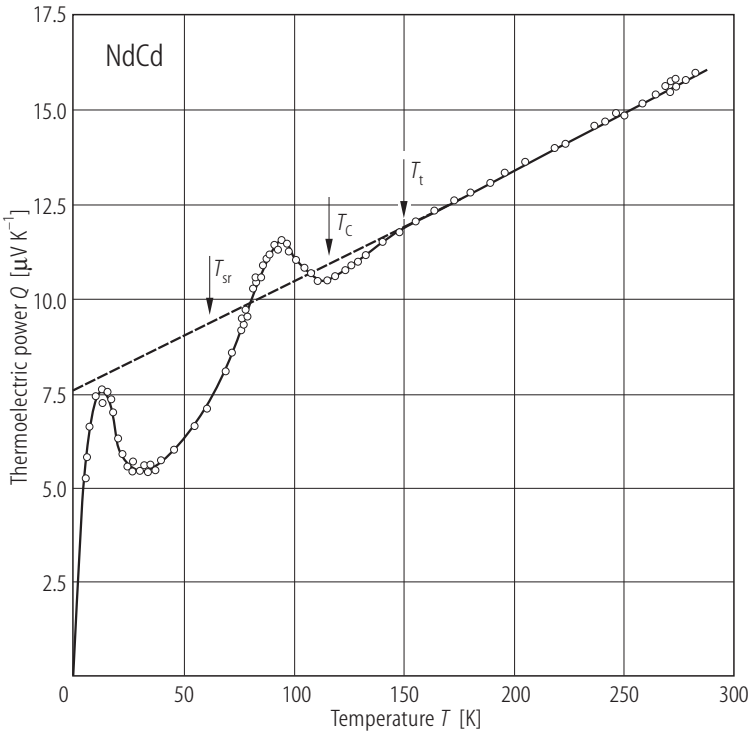

Fig. 31. NdCd. Thermoelectric power referred to Cu vs. temperature. T_C is the Curie temperature, T_{sr} the spin reorientation temperature and T_t a structural transition temperature [88P1].

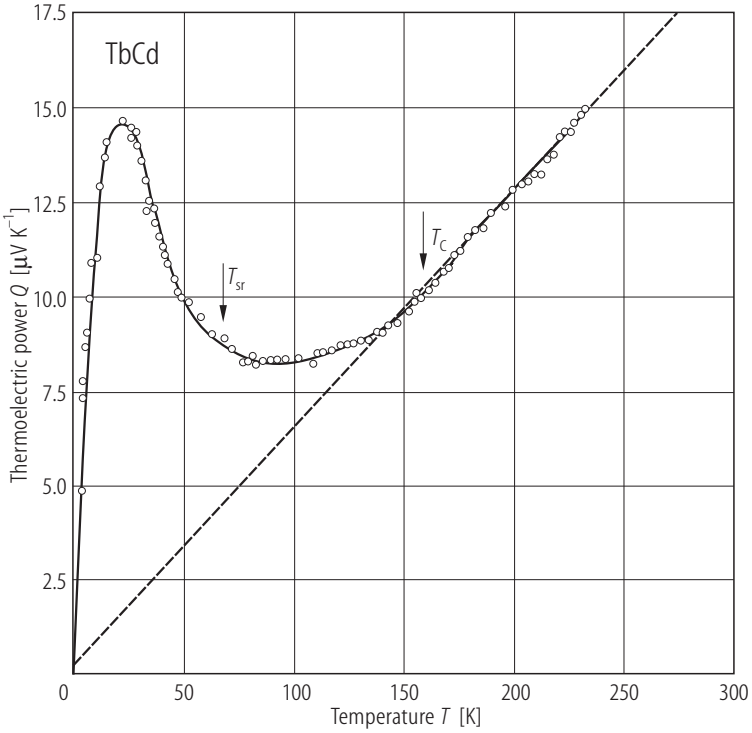

Fig. 32. TbCd. Thermoelectric power referred to copper vs. temperature. T_C is the Curie temperature, T_{sr} the spin reorientation temperature. The moment direction is [110] and [001] below and above T_{sr}, respectively [88P1].

2.7.3 RX_2 compounds

The interest for the RX_2 compounds has been renewed owing to the availability of single crystals, in particular in the RZn_2 orthorhombic series (Figs. 33 - 53) [97G1]. In these recent studies, anisotropic metamagnetic processes have been shown to occur [95G2], due to the existence of long-range competing interactions and frustration in the presence of magnetocrystalline anisotropy leading to the existence of collinear incommensurate or long-period commensurate magnetic structures (Table 3). The case of $DyZn_2$ is worth being emphasized, this compound exhibiting a conversion axis phenomenon similar to $DyCu_2$ [94H1]: under certain conditions of field and temperature, a hard magnetization direction acquires the characteristics of another axis (metamagnetic behaviour), and conversely. These effects seem to be strongly related to quadrupolar interactions and magnetostriction.

References

86G1 Giraud, M., Morin, P., Rouchy, J., Schmitt, D.: J. Magn. Magn. Mater. **59** (1986) 255

86H1 Hiraoka, T.: J. Phys. Soc. Jpn. **55** (1986) 4417

86K1 Kadomatsu, H., Tanaka, H., Kurisu, M., Fujiwara, H.: Phys. Rev. B **33** (1986) 4799

86L1 Lahiouel, R., Galera, R.M., Murani, A.P., Pierre, J., Siaud, E.: Z. Phys. B **62** (1986) 457

86L2 Liu, W.L., Kurisu, M., Kadomatsu, H., Fujiwara, H.: J. Phys. Soc. Jpn. **55** (1986) 33

86S1 Schmitt, D.: J. Magn. Magn. Mater. **54-57** (1986) 461

87F1 Fujii, H., Uwatoko, Y., Motoya, K., Ito, Y., Okamoto, T.: J. Magn. Magn. Mater. **63-64** (1987) 114

87K1 Kadomatsu, H., Kurisu, M., Fujiwara, H.: J. Phys. F **17** (1987) L305

87K2 Kasamatsu, Y., Tohyama, T., Kojima, K., Hihara, T.: J. Magn. Magn. Mater. **70** (1987) 294

87K3 Kurisu, M., Tanaka, H., Kadomatsu, H., Fujiwara, H.: J. Phys. Soc. Jpn. **56** (1987) 1127

88M1 Morin, P., Rouchy, J., Miyako, Y., Nishioka, T.: J. Magn. Magn. Mater. **76-77** (1988) 319

88N1 Nakazato, M., Wakabayashi, N., Kitai, T.: J. Phys. Soc. Jpn. **57** (1988) 953

88P1 Pinto, R.P., Amado, M.M., Braga, M.E., Sousa, J.B., Morin, P., Aléonard, A.: J. Magn. Magn. Mater. **72** (1988) 152

88U1 Uwatoko, Y., Fujii, H., Nishi, M., Motoya, K., Ito, Y.: J. Magn. Magn. Mater. **76-77** (1988) 411

89M1 Morin, P., in: Magnetic Properties of Metals (Wijn, H.P.J., ed.), Landolt-Börnstein, New Series, Berlin, Heidelberg, New York: Springer, Vol. 19 e2 **1989**, p. 1

89U1 Uwatoko, Y., Fujii, H., Nishi, M., Motoya, K., Ito, Y.: Solid State Commun. **72** (1989) 941

90A1 Aléonard, R., Morin, P.: J. Magn. Magn. Mater. **84** (1990) 255

90M1 Morin, P., Schmitt, D., in: Ferromagnetic Materials (Buschow, K.H.J., Wohlfarth, E.P., eds.), Amsterdam: North-Holland, Vol. 5 **1990**, Chap. 1, p. 1

90S1 Shigeoka, T., Uwatoko, Y., Fujii, H., Reberlsky, L., Shapiro, S.M., Asai, K.: Phys. Rev. B **42** (1990) 8394

92C1 Continenza, A., Monachesi, P.: Phys. Rev. B **46** (1992) 6217

95A1 Amara, M., Morin, P.: Physica B **205** (1995) 379

95A2 Amara, M., Morin, P., Burlet, P.: Physica B **210** (1995) 157

95K2 Kurisu, M., Kadomatsu, H., Fujiwara, H., Hiraoka, T.: J. Magn. Magn. Mater. **140-144** (1995) 1146

96A1 Amara, M., Morin, P.: Physica B **222** (1996) 61

96B2 Buschow, K.H.J., Grechnev, G.E., Hjelm, A., Kasamatsu, Y., Panfilov, A.S., Svechkarev, I.V.: J. Alloys Compounds **244** (1996) 113

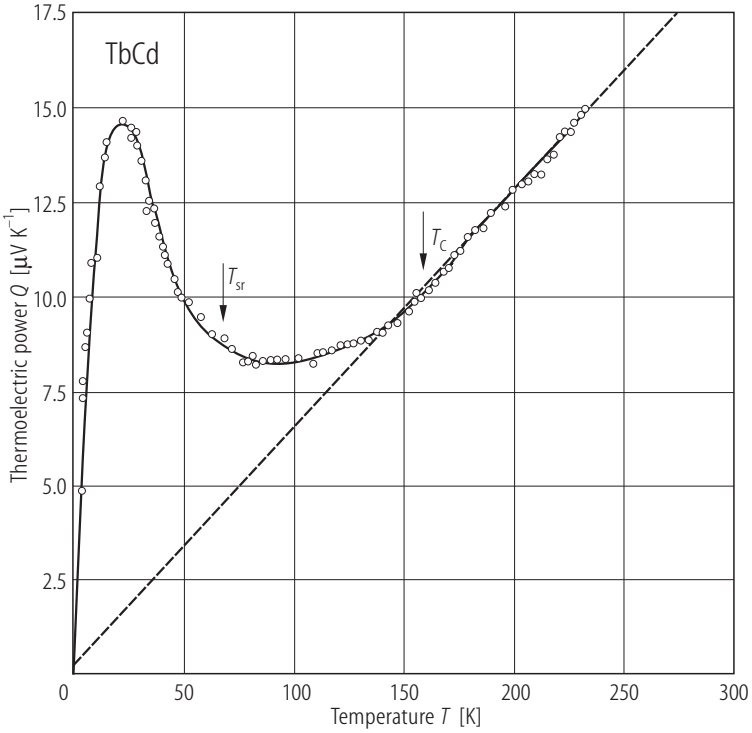

Fig. 32. TbCd. Thermoelectric power referred to copper vs. temperature. T_C is the Curie temperature, T_{sr} the spin reorientation temperature. The moment direction is [110] and [001] below and above T_{sr}, respectively [88P1].

2.7.3 RX_2 compounds

The interest for the RX_2 compounds has been renewed owing to the availability of single crystals, in particular in the RZn_2 orthorhombic series (Figs. 33 - 53) [97G1]. In these recent studies, anisotropic metamagnetic processes have been shown to occur [95G2], due to the existence of long-range competing interactions and frustration in the presence of magnetocrystalline anisotropy leading to the existence of collinear incommensurate or long-period commensurate magnetic structures (Table 3). The case of $DyZn_2$ is worth being emphasized, this compound exhibiting a conversion axis phenomenon similar to $DyCu_2$ [94H1]: under certain conditions of field and temperature, a hard magnetization direction acquires the characteristics of another axis (metamagnetic behaviour), and conversely. These effects seem to be strongly related to quadrupolar interactions and magnetostriction.

Table 3. RZn_2 compounds. T_N, T_t: Néel, transition temperature; ***Q***: propagation vector; ***M***: magnetization; p_s: magnetic moment.

Compound	T_N, T_t [K]	***Q*** (reduced unit)	Comments	Figures	Ref.
$CeZn_2$	7.5 T_t = 7.2	(0,0,τ) ($T > T_t$) τ = 0.6… 0.5 (7.5…5 K) (0,0,1) ($T < T_t$)	p_s = 1.6 μ_B (4.2 K) ***M*** || ***b*** phase mixing (< T_t, sample dependent)	33 - 39	88K1, 92G1
$PrZn_2$	23 T_t= 10	(0,0,0.449) ($T > T_t$) (0,0,1/2) ($T < T_t$)	***M*** || ***a*** at 8.3 K p_s = 2.3 μ_B and ***M*** $\perp$ ***c*** at 33° of ***a***	40 - 42	92K1, 95O1
$NdZn_2$	23	complex antiferromagnetic	***M*** || ***b***	43, 44	90K2
$SmZn_2$	45	antiferromagnetic	no Curie-Weiss behaviour		70D1
$EuZn_2$	30	antiferromagnetic	Eu^{2+} state		75D1
$GdZn_2$	68	antiferromagnetic			70D1
$TbZn_2$	75 T_t = 60	(0,0,τ) ($T > T_t$) τ = 0.394 … 0.439 (75…60 K) (0,0,0.5) ($T < T_t$)	***M*** || ***b*** p_s = 8.15 μ_B (4.2 K)	45, 46	72D1
$DyZn_2$	38 T_t = 32	(0,0,0.45) ($T > T_t$) (0,0,0.5) ($T < T_t$)	p_s = 9.7 μ_B (4.2 K) ***M*** at 16° of ***b*** Conversion axis phenomenon	45, 47 - 50	90O1
$HoZn_2$	14 T_t = 6	(0,0,0.441)	p_s = 9.4 μ_B (4.2 K) ***M*** || ***b***	45, 51	95K1
$ErZn_2$	13	complex antiferromagnetic		45, 52	75D1
$TmZn_2$	5.2	antiferromagnetic		53	75D1

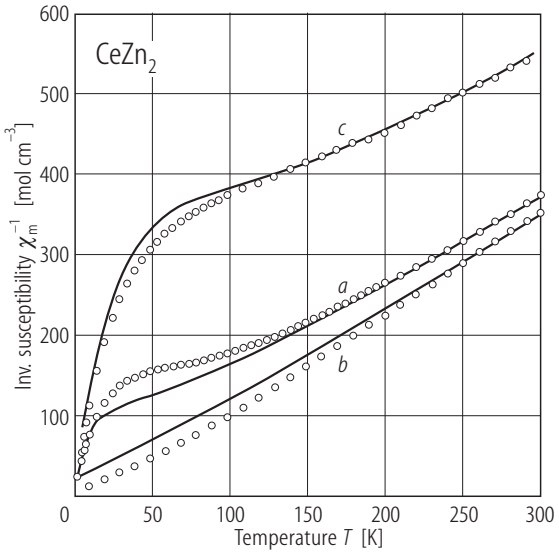

Fig. 33. $CeZn_2$. Reciprocal magnetic molar susceptibility vs. temperature along the *a*, *b* and *c* axes of the orthorhombic unit cell. Lines are calculated in a crystal field model [88V1].

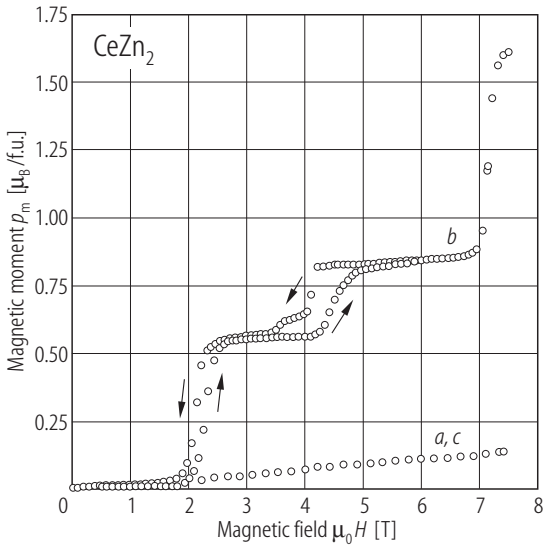

Fig. 34. $CeZn_2$. Magnetization vs. applied magnetic field at T = 1.5 K. Note the three-step metamagnetic process along the *b* easy axis. The curves are superimposed along *a* and *c* directions [92G1].

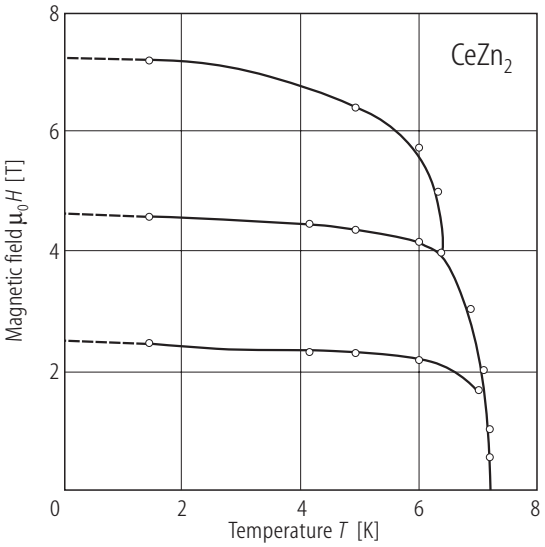

Fig. 35. $CeZn_2$. Magnetic field-temperature phase diagram for the *b* direction. The two field-induced phases correspond to structures where a part of the moments antiparallel to the field have flipped [92G1].

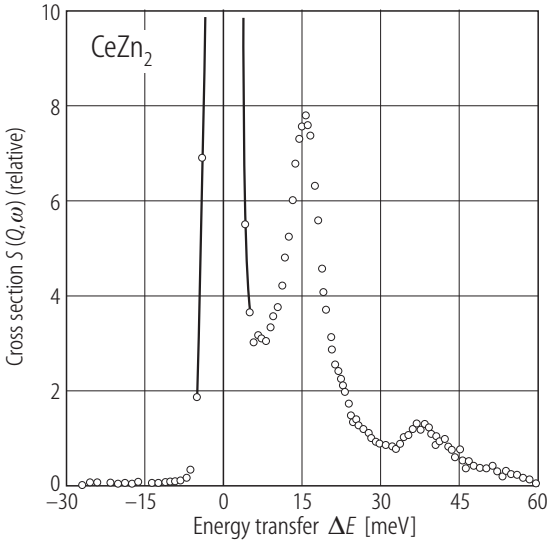

Fig. 36. $CeZn_2$. Neutron scattering cross section vs. energy transfer at 10 K for an incident neutron energy E_i = 68 meV. Two crystal field excitations can be observed at ΔE = 15.7 and 37.5 meV [92M2].

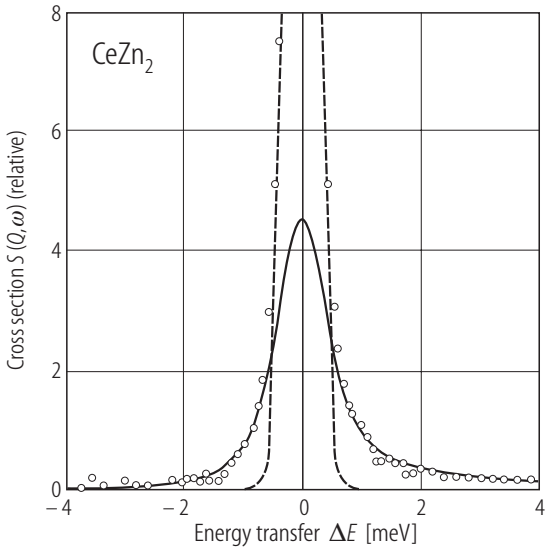

Fig. 37. $CeZn_2$. Quasielastic scattering cross section vs. energy transfer at 30 K for an incident neutron energy $E_i = 4.6$ meV. The mean scattering angle is 35°. Dashed line: elastic incoherent contribution; continuous line: quasielastic contribution [93O2].

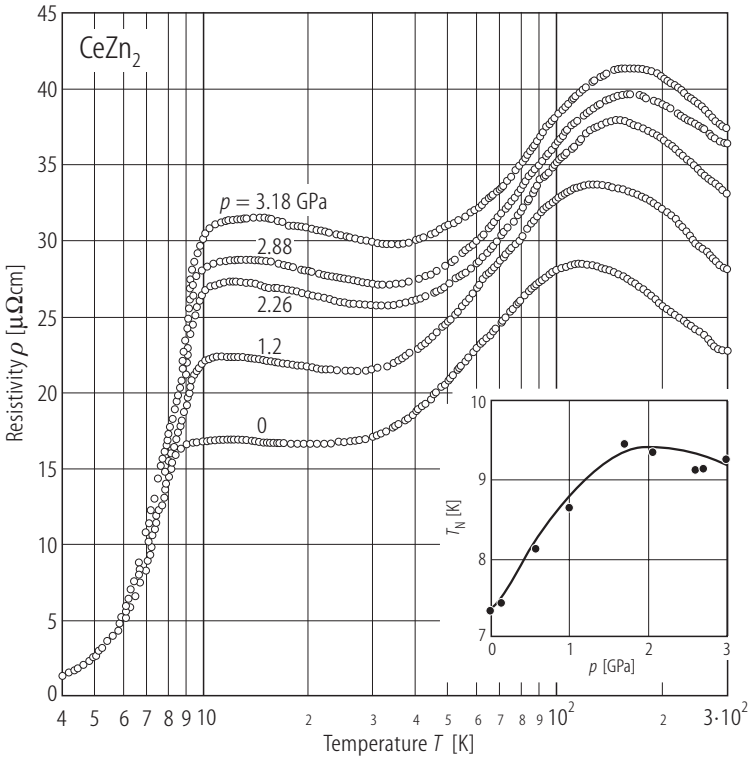

Fig. 38. $CeZn_2$. Magnetic contribution to the electrical resistivity vs. temperature at various pressures. $LaZn_2$ has been taken as the non-magnetic reference. Inset: Néel temperature vs. pressure [88K1].

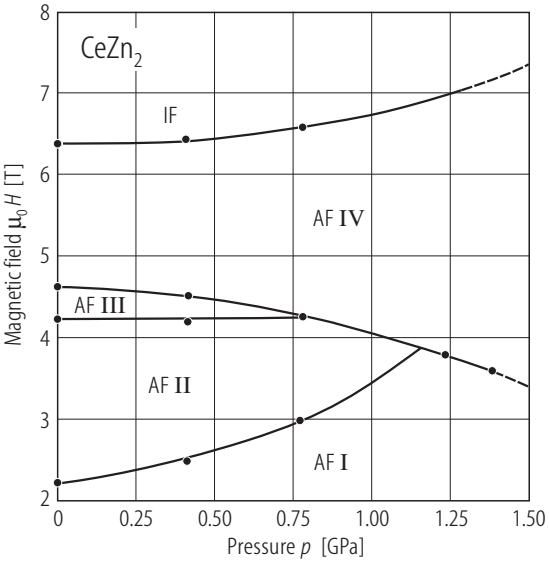

Fig. 39. $CeZn_2$. Field-pressure magnetic phase diagram at 4.2 K for the *b* axis. IF: induced ferromagnetic; AF: antiferromagnetic; the net resultant moments are (I) $M = 0$, (II) $M = M_s/3$, (III) $M = 7M_s/18$ and (IV) $M = M_s/2$, M_s being the saturated magnetization [88K1].

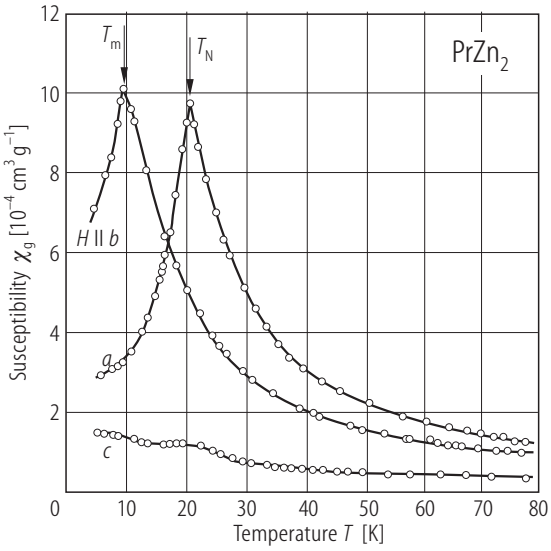

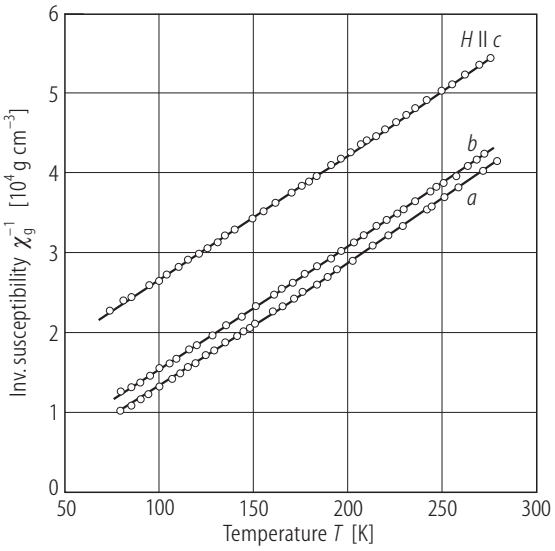

Fig. 40. $PrZn_2$. Magnetic mass susceptibility vs. temperature along the *a*, *b* and *c* axes of the orthorhombic unit cell. T_N is the Néel temperature; a change of magnetic structure occurs at T_m. Right figure: reciprocal mass susceptibility vs. temperature for the three symmetry directions [92K1].

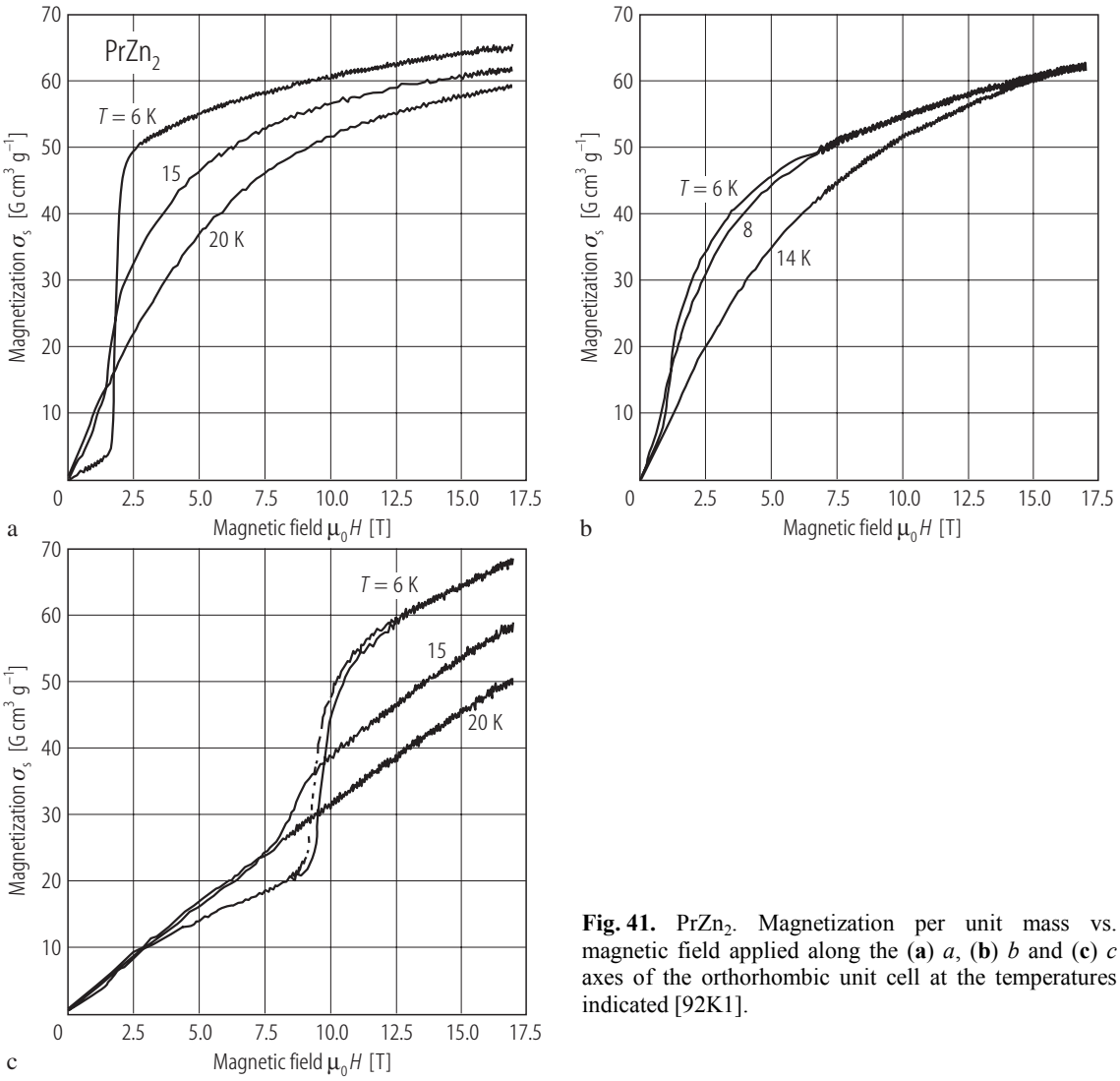

Fig. 41. $PrZn_2$. Magnetization per unit mass vs. magnetic field applied along the (**a**) *a*, (**b**) *b* and (**c**) *c* axes of the orthorhombic unit cell at the temperatures indicated [92K1].

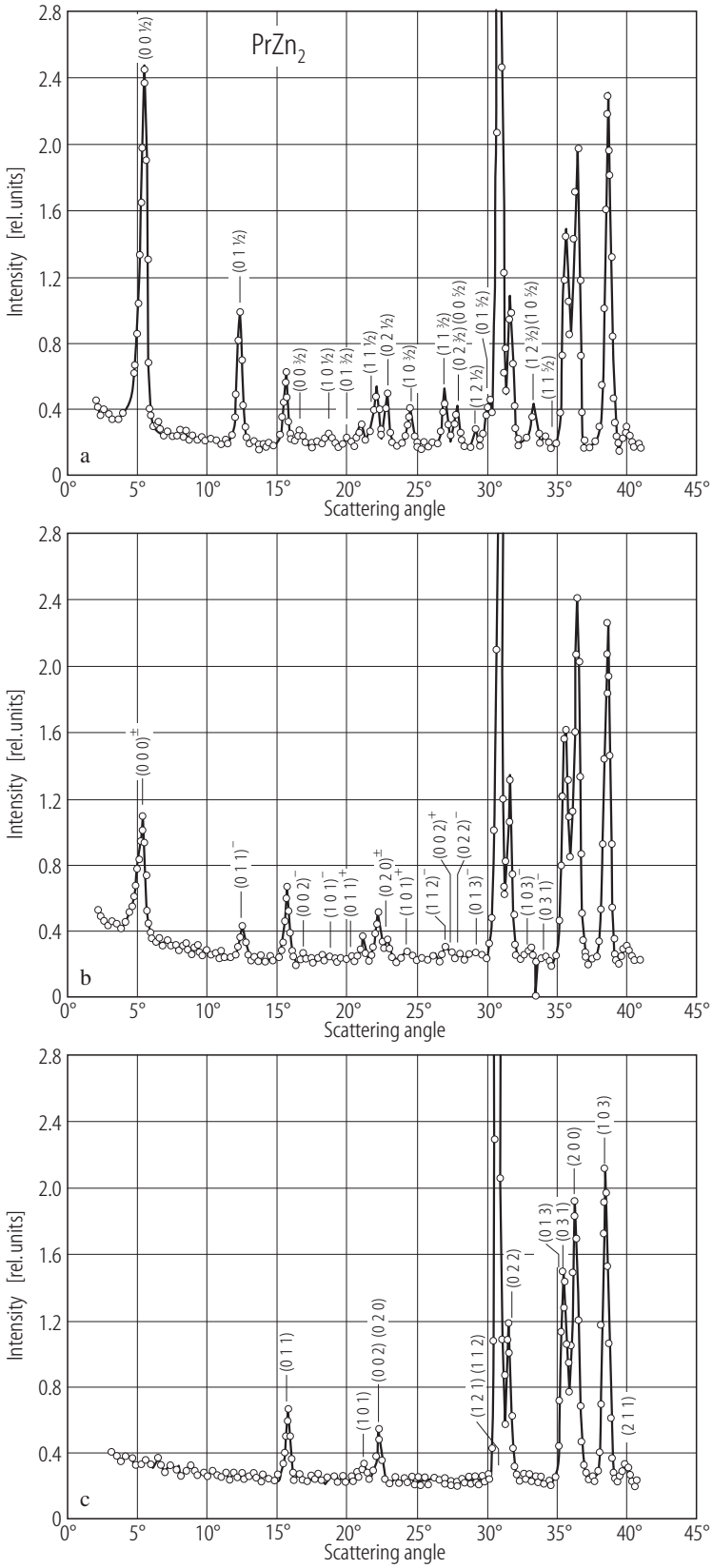

Fig. 42. $PrZn_2$. Neutron diffraction patterns vs. scattering angle at (**a**) T = 8.3 K, (**b**) 15.3 K and (**c**) 78 K. Labels are the indexation of the nuclear or magnetic reflections [95O1].

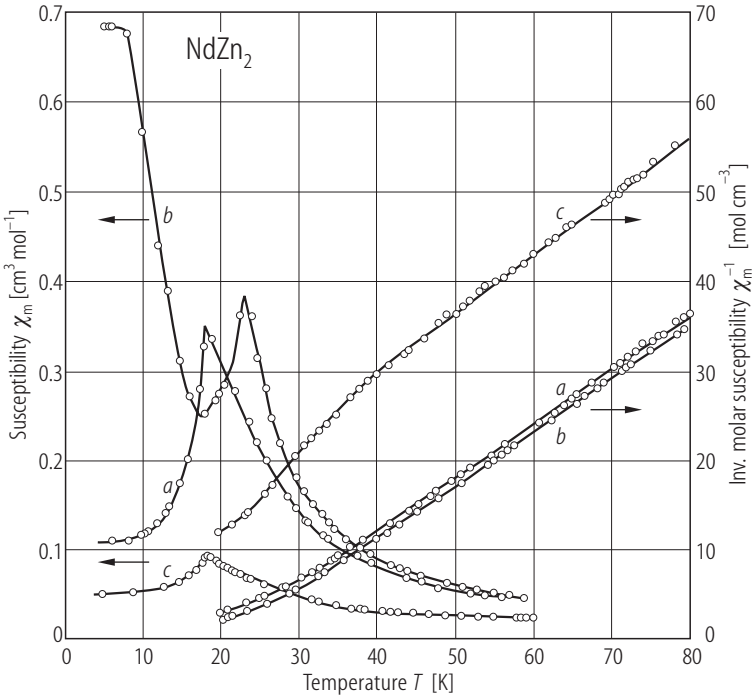

Fig. 43. $NdZn_2$. Magnetic molar susceptibility (left scale) and reciprocal susceptibility (right scale) vs. temperature along the *a*, *b* and *c* axes of the orthorhombic unit cell [90K2].

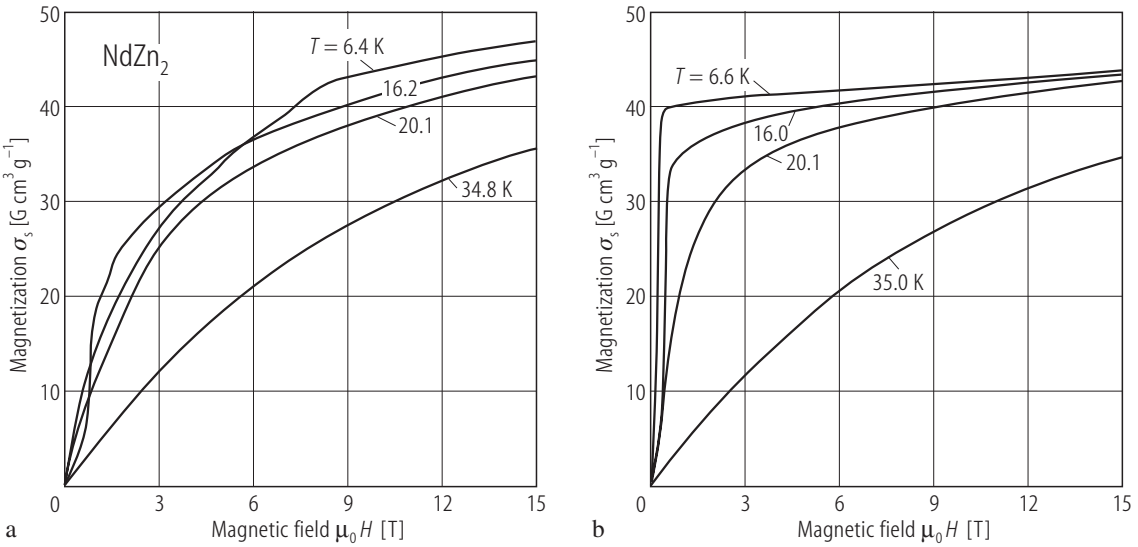

Fig. 44. $NdZn_2$. Magnetization per unit mass vs. magnetic field applied along the (**a**) *a* and (**b**) *b* axes of the orthorhombic unit cell at the temperatures indicated [90K2].

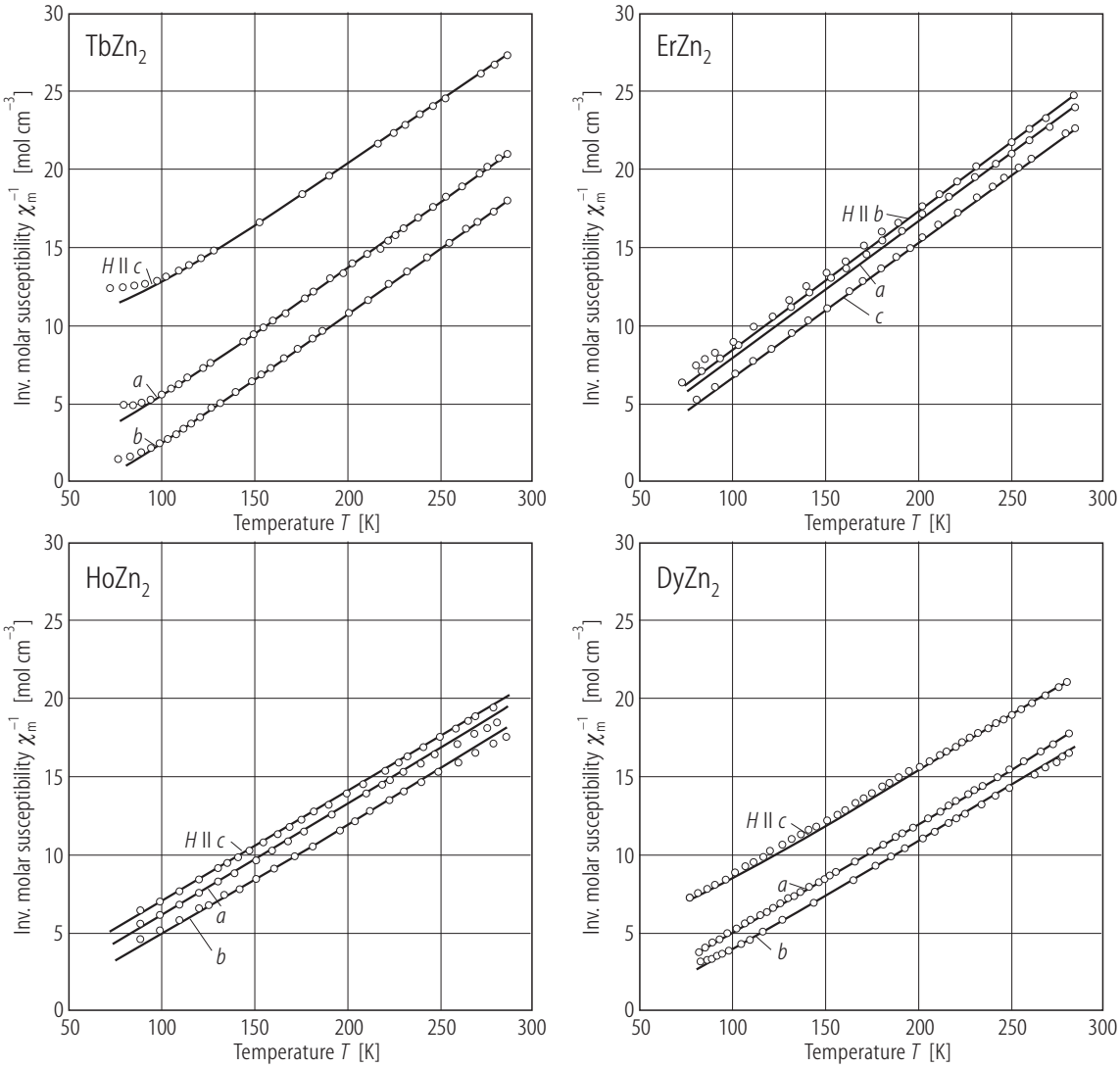

Fig. 45. $TbZn_2$, $ErZn_2$, $HoZn_2$, $DyZn_2$. Reciprocal magnetic molar susceptibility vs. temperature along the *a*, *b* and *c* axes of the orthorhombic unit cell. Lines are calculated in a crystal field model [95K1].

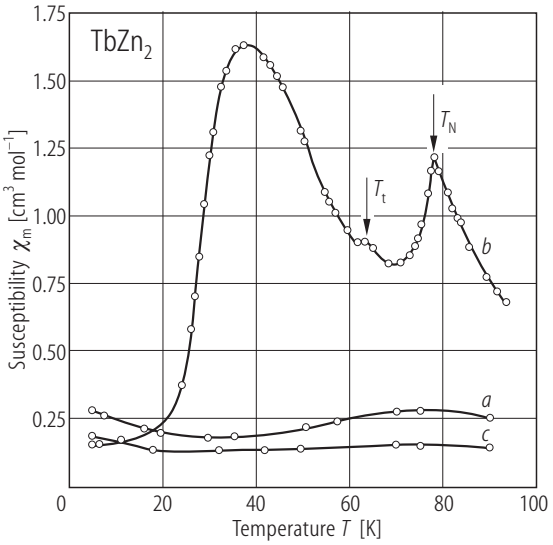

Fig. 46. $TbZn_2$. Magnetic molar susceptibility vs. temperature along the *a*, *b* and *c* crystallographic axes. T_N is the Néel temperature. A change of magnetic structure occurs at the transition temperature T_t = 60 K [90K2].

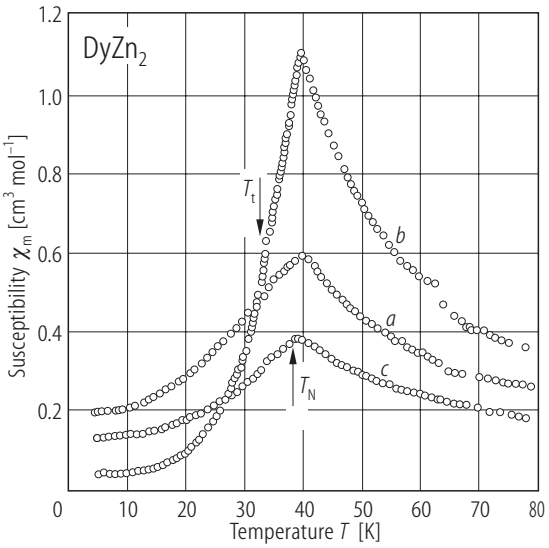

Fig. 48. $DyZn_2$. Magnetic molar susceptibility vs. temperature along the a, *b* and *c* crystallographic axes. T_N is the Néel temperature. A change of magnetic structure occurs at the transition temperature T_t = 32 K [90O1].

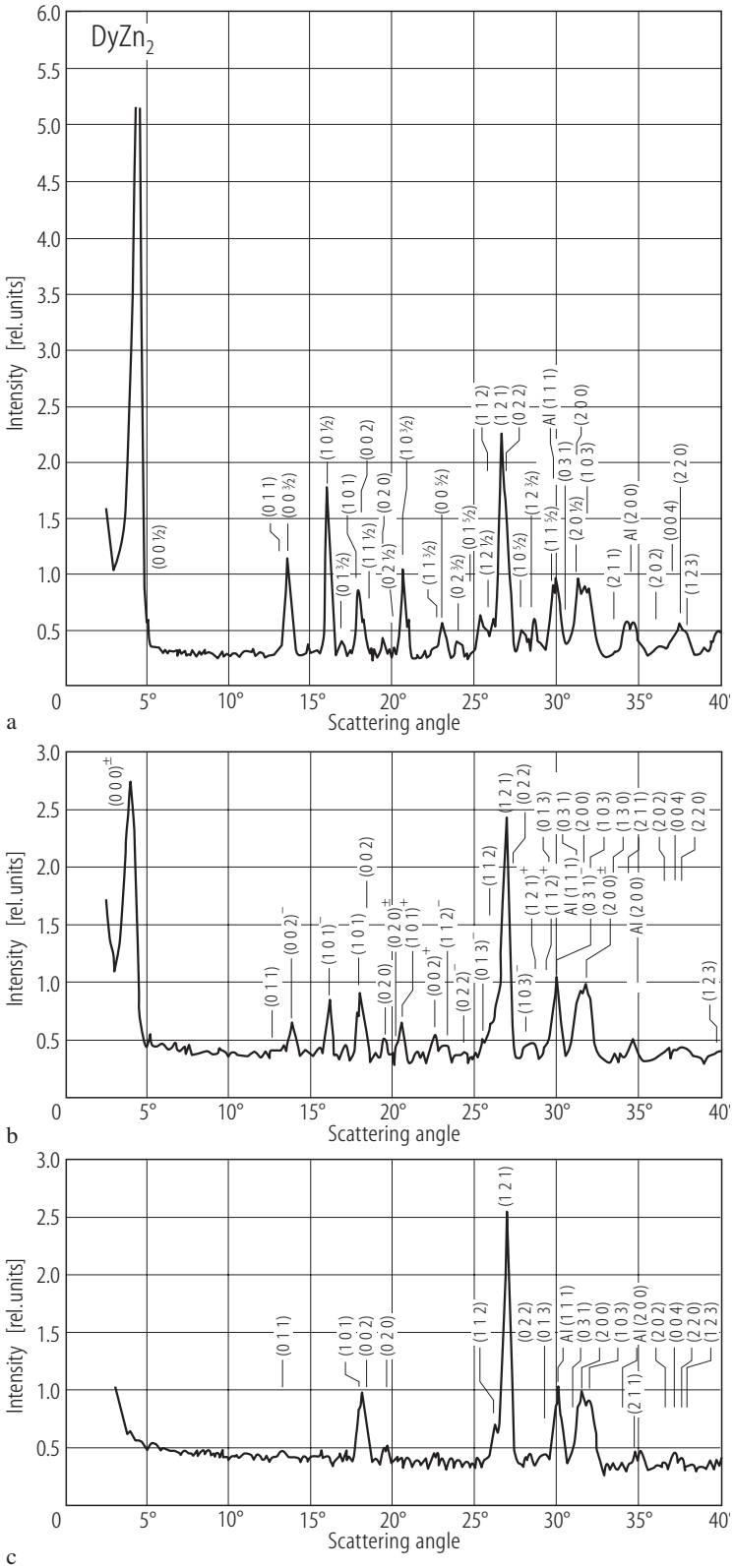

Fig. 47. $DyZn_2$. Neutron diffraction patterns vs. scattering angle at (**a**) T = 4.2 K, (**b**) 30 K and (**c**) 78 K. Labels are the indexation of the nuclear or magnetic reflections [90O1].

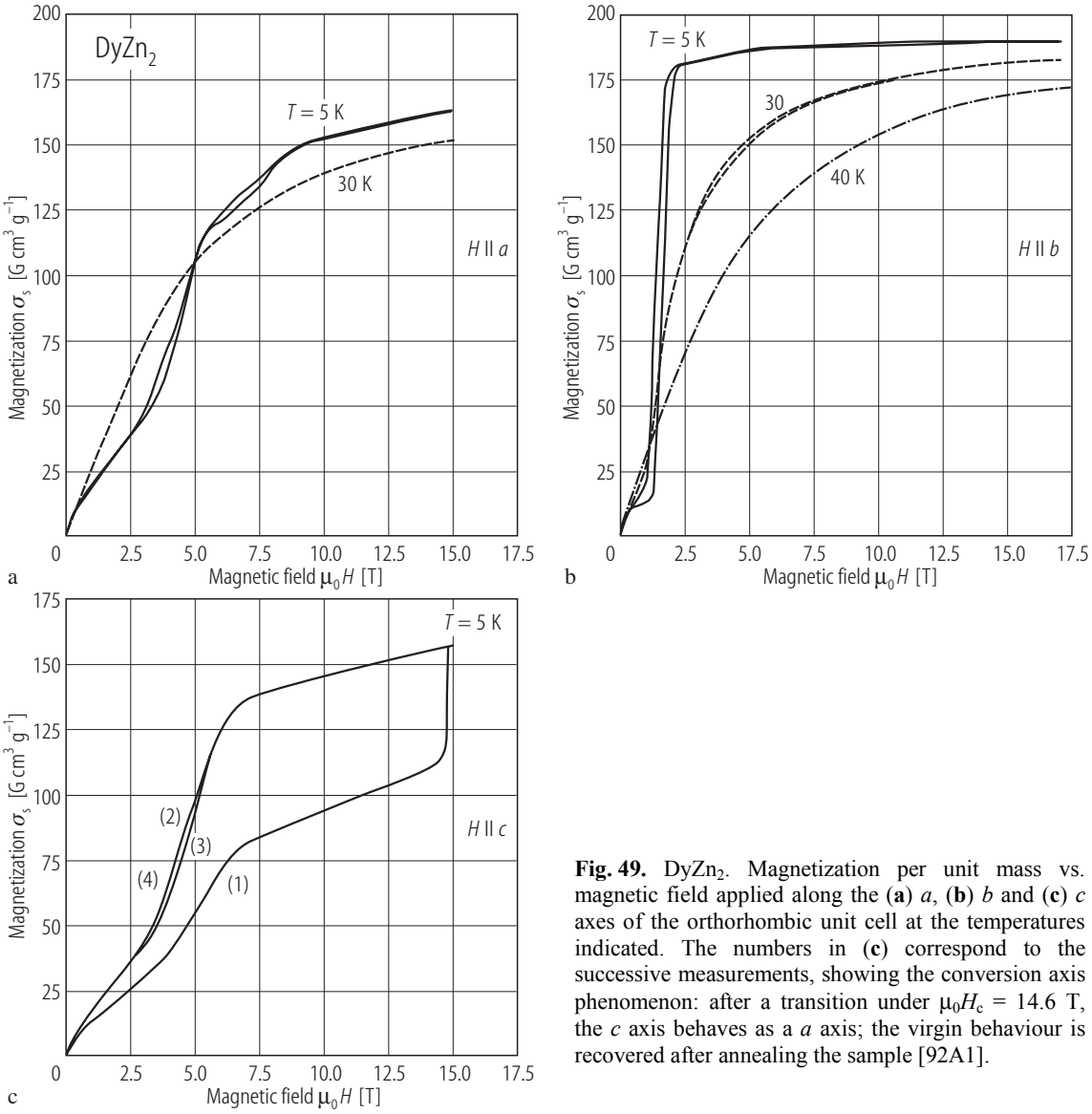

Fig. 49. $DyZn_2$. Magnetization per unit mass vs. magnetic field applied along the (**a**) *a*, (**b**) *b* and (**c**) *c* axes of the orthorhombic unit cell at the temperatures indicated. The numbers in (**c**) correspond to the successive measurements, showing the conversion axis phenomenon: after a transition under $\mu_0 H_c$ = 14.6 T, the *c* axis behaves as a *a* axis; the virgin behaviour is recovered after annealing the sample [92A1].

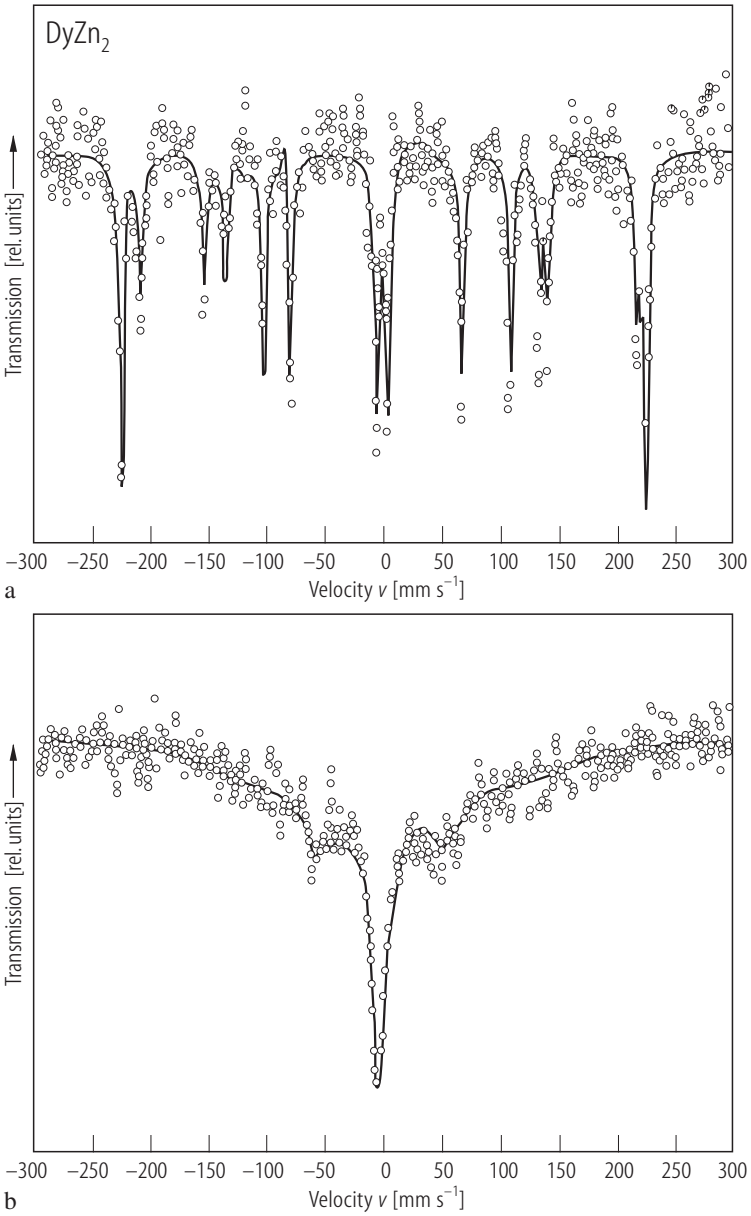

Fig. 50. $DyZn_2$. Mössbauer spectra measured at (**a**) T = 5 K and (***b***) 32.9 K [93O1].

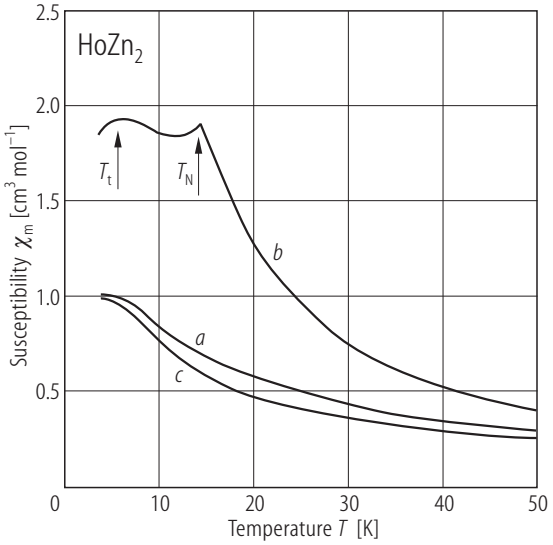

Fig. 51. $HoZn_2$. Magnetic molar susceptibility vs. temperature along the *a*, *b* and *c* crystallographic axes. T_N is the Néel temperature. A change of magnetic structure occurs at the transition temperature T_t = 6 K [95K1].

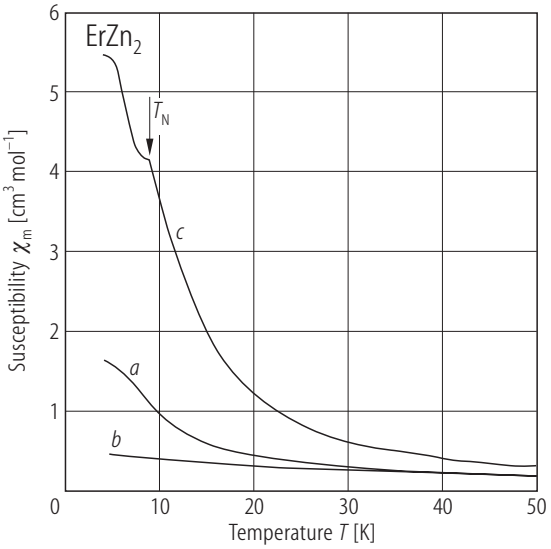

Fig. 52. $ErZn_2$. Magnetic molar susceptibility vs. temperature along the *a*, *b* and *c* crystallographic axes. T_N is the Néel temperature [90K2].

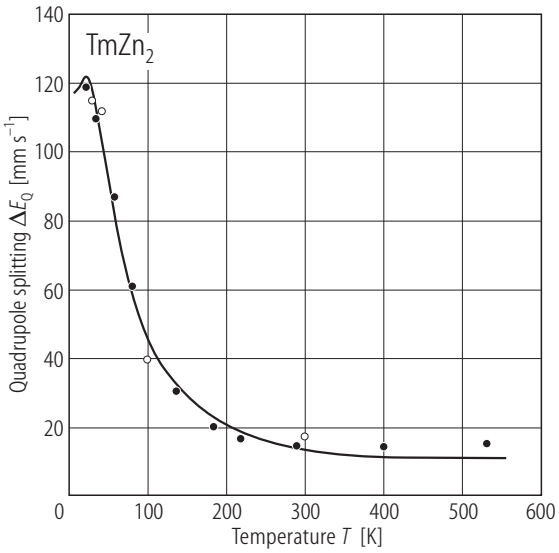

Fig. 53. $TmZn_2$. Quadrupole splitting vs. temperature. The line is calculated in a crystal field model [88S3].

References

70D1 Debray, D.K., Wallace, W.E., Ryba, E.: J. Less-Common Met. **22** (1970) 19

72D1 Debray, D., Sougi, M., Meriel, P.: J. Chem. Phys. **56** (1972) 4325

75D1 Debray, D., Wortmann, B.F., Methfessel, S.: Phys. Status Solidi (a) **30** (1975) 713

88K1 Kurisu, M., Yamashita, M., Kadomatsu, H., Fujiwara, H.: Physica B **149** (1988) 78

88S3 Stewart, G.A., Kaindl, G.: Hyperfine Interactions **40** (1988) 429

88V1 Voiron, J., Morin, P., Gignoux, D., Aléonard, R.: J. Phys. (Paris) Colloq. **49** (1988) C8-419

90K2 Kitai, T., Kaneko, T., Abe, S., Tomiyoshi, S., Nakagawa, Y.: J. Magn. Magn. Mater. **90-91** (1990) 55

90O1 Ohashi, M., Kitai, T., Kaneko, T., Yoshida, H., Yamaguchi, Y., Abe, S.: J. Magn. Magn. Mater. **90-91** (1990) 585

92A1 Abe, S., Kaneko, T., Ohashi, M., Nakagawa, Y., Kitai, T.: J. Magn. Magn. Mater. **104-107** (1992) 1403

92G1 Gignoux, D., Morin, P., Voiron, J., Burlet, P.: Phys. Rev. B **46** (1992) 8877

92K1 Kaneko, T., Kitai, T., Abe, S., Ohashi, M., Nakagawa, Y.: Physica B **177** (1992) 295

92M2 Morin, P., Gignoux, D., Voiron, J., Murani, A.P.: Physica B **180-181** (1992) 173

93O1 Onodera, H., Kitai, T., Ohashi, M., Yamaguchi, Y., Kaneko, T.: Hyperfine Interactions **78** (1993) 451

93O2 Osakabe, T., Kohgi, M., Ohoyama, K., Kitai, T.: Physica B **186-188** (1993) 574

94H1 Hashimoto, Y., Kindo, K., Takeuchi, T., Senda, K., Date, M., Yamagishi, A.: Phys. Rev. Lett. **72** (1994) 1922

95G2 Gignoux, D., Schmitt, D., in: Handbook on the Physics and Chemistry of Rare Earths (Gschneidner Jr., K.A., Eyring, L., eds.), Amsterdam: Elsevier, Vol. 20 **1995**, Chap. 138, p. 293

95K1 Kitai, T.: J. Phys. Soc. Jpn. **64** (1995) 3403

95O1 Ohashi, M., Kitai, T., Kaneko, T., Abe, S., Funahashi, S., Yamaguchi, Y.: J. Magn. Magn. Mater. **140-144** (1995) 1119

97G1 Gignoux, D., Schmitt, D., in: Handbook of Magnetic Materials (Buschow, K.H.J., ed.), Amsterdam: Elsevier, Vol. 10 **1997**, Chap. 2, p. 239

2.7.4 R_2X_{17} compounds

The only new magnetic results have been obtained with zinc. The magnetic behaviour has been investigated in the whole series and its antiferromagnetic nature confirmed (Figs. 54 - 64 and Table 4). The de Gennes law is far to be followed for some particular compounds (see the values of Θ for Ce_2Zn_{17} and of T_N for Gd_2Zn_{17} and Tb_2Zn_{17}). Only Ce_2Zn_{17} has been studied on a single crystal (Figs. 61, 62). Five compounds in the series exhibit a transition in the ordered range, probably related to a change of the magnetic structure which remains to be confirmed by neutron diffraction experiments. A close similarity can be observed between the heat capacity anomalies and the temperature derivatives of the electrical resistivity (see e.g. Figs. 55 and 56).

Table 4. R_2Zn_{17} compounds. Θ: paramagnetic Curie temperature; p_{eff}: effective paramagnetic moment; T_N: Néel temperature, T_t: transition temperature in ordered range.

Compound	Θ [K]	p_{eff} [μ_B]	T_N [K]	T_t [K]	Figures	Ref.
Ce_2Zn_{17}	– 24.0	2.31	1.7		61, 62	87O1
Pr_2Zn_{17}	– 5.5	3.76	2.2	1.7	55, 56, 59, 63	93M1, 94G1
Nd_2Zn_{17}	– 16.7	3.66	1.1		57	93M1, 94G1
Sm_2Zn_{17}	– 41.5	1.11	4.1	3.3	55	87O1
Gd_2Zn_{17}	– 58.4	8.27	9.0		54, 58	94G1, 96M1
Tb_2Zn_{17}	– 60.7	9.45	22.7	7.2	54, 60	87O1, 93M1
Dy_2Zn_{17}	– 21.0	10.96	8.8		54	93M1, 94G1
Ho_2Zn_{17}	– 12.5	10.82	3.0	2.5	55, 64	87O1, 94G1
Er_2Zn_{17}	– 5.8	9.66	1.6	1.4		93M1, 94G1
Tm_2Zn_{17}	– 6.3	7.87	0.8			87O1
Yb_2Zn_{17}		0				94G1

For Figs. 54 and 55 see next page.

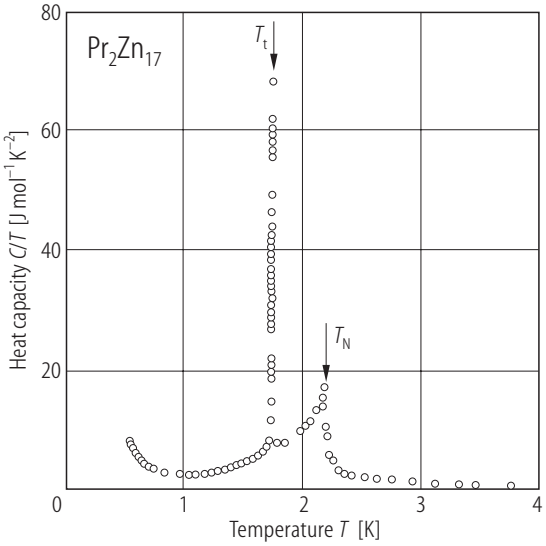

Fig. 56. Pr_2Zn_{17}. Heat capacity divided by temperature vs. temperature. The arrows show the Néel temperature T_N and the transition temperature T_t in the ordered range [93M1].

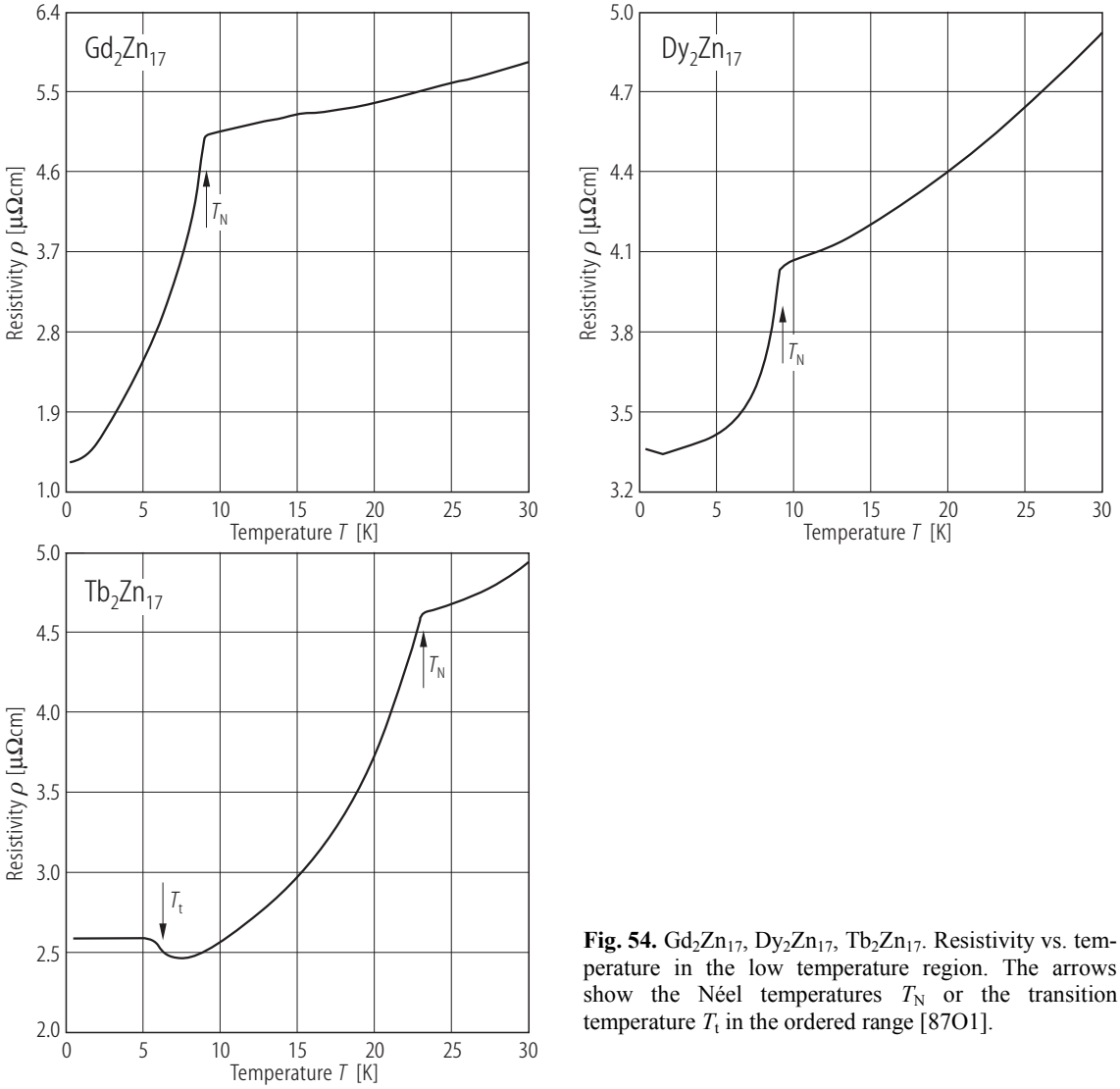

Fig. 54. Gd_2Zn_{17}, Dy_2Zn_{17}, Tb_2Zn_{17}. Resistivity vs. temperature in the low temperature region. The arrows show the Néel temperatures T_N or the transition temperature T_t in the ordered range [87O1].

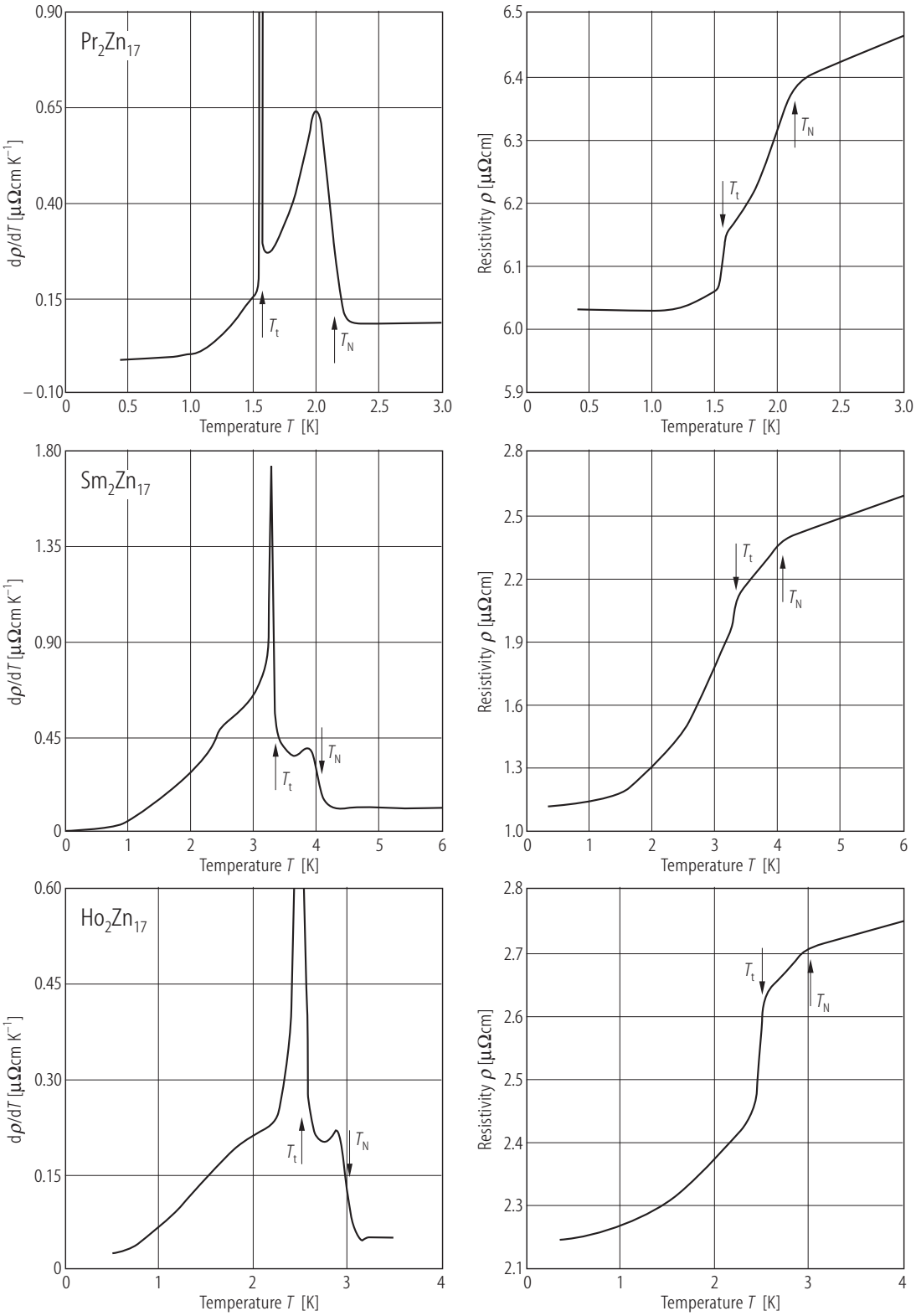

Fig. 55. Pr_2Zn_{17}, Sm_2Zn_{17}, Ho_2Zn_{17}. Temperature derivative of the resistivity (left part) and resistivity at low temperature (right part). The arrows show the Néel temperatures T_N or the transition temperatures T_t in the ordered range [87O1].

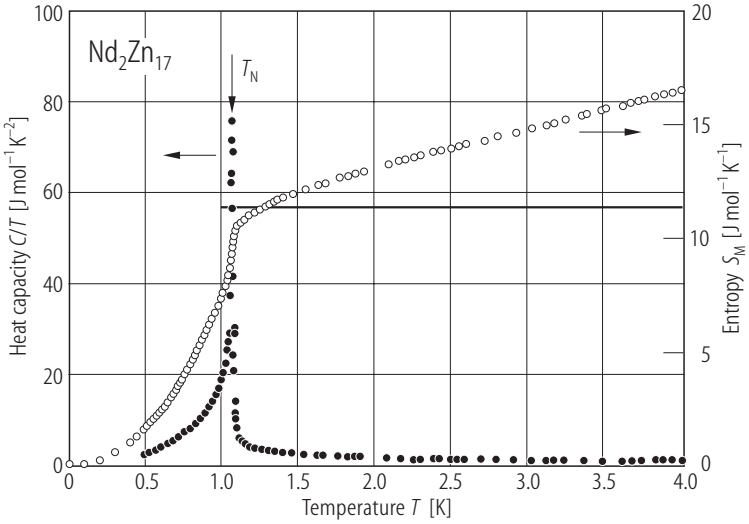

Fig. 57. Nd_2Zn_{17}. Heat capacity divided by temperature vs. temperature (left scale); magnetic entropy vs. temperature (right scale). The Néel temperature T_N is indicated. The horizontal line corresponds to an entropy of $2R\ln(2)$ [93M1].

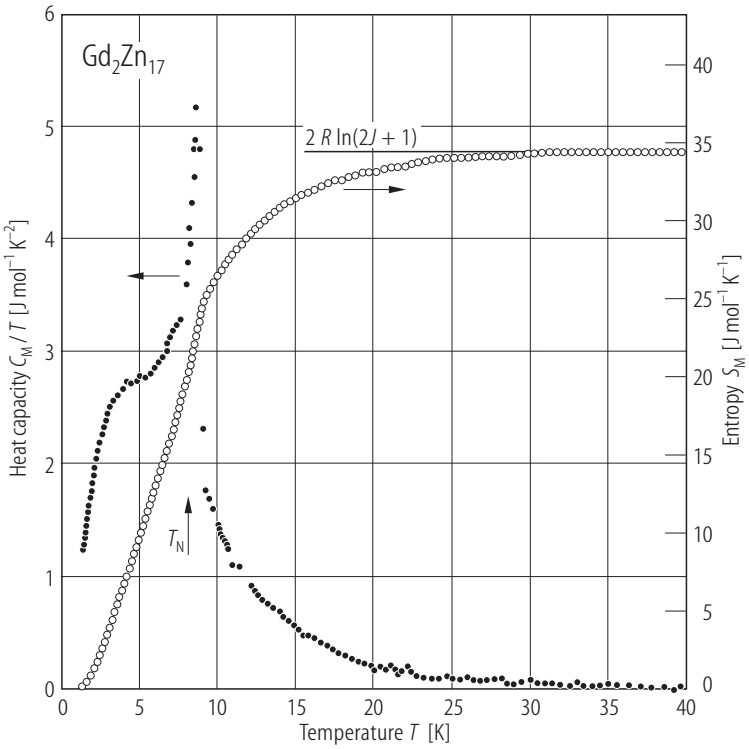

Fig. 58. Gd_2Zn_{17}. Magnetic heat capacity divided by temperature vs. temperature (left scale); magnetic entropy vs. temperature (right scale). The Néel temperature T_N is indicated. The horizontal line corresponds to an entropy of $2R\ln(2J+1)$ [96M1].

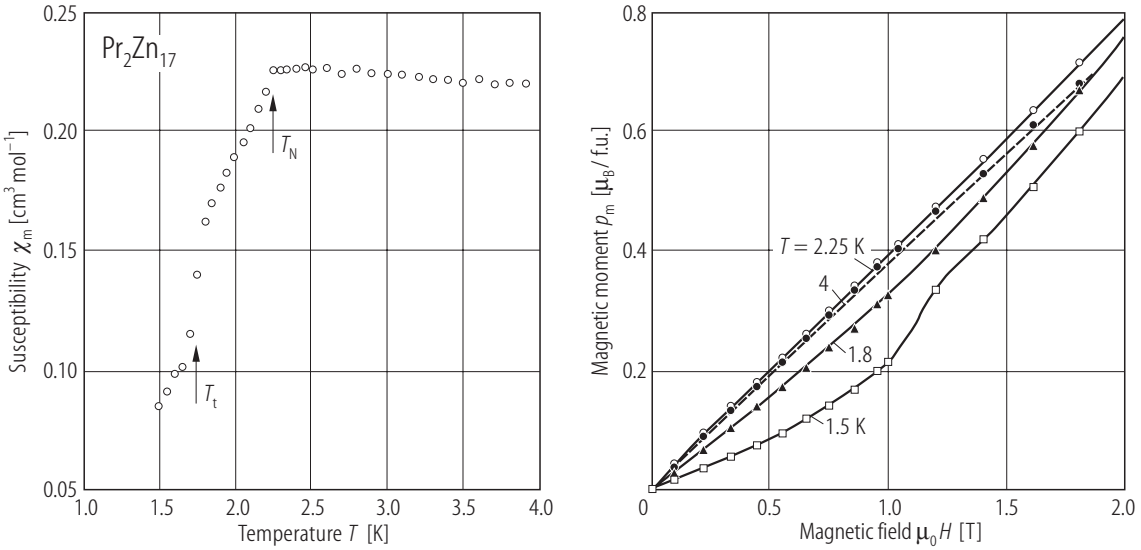

Fig. 59. Pr_2Zn_{17}. Magnetization vs. magnetic field at various temperatures. Left figure: magnetic susceptibility vs. temperature. T_N is the Néel temperature and T_t the transition temperature in the ordered range [94G1].

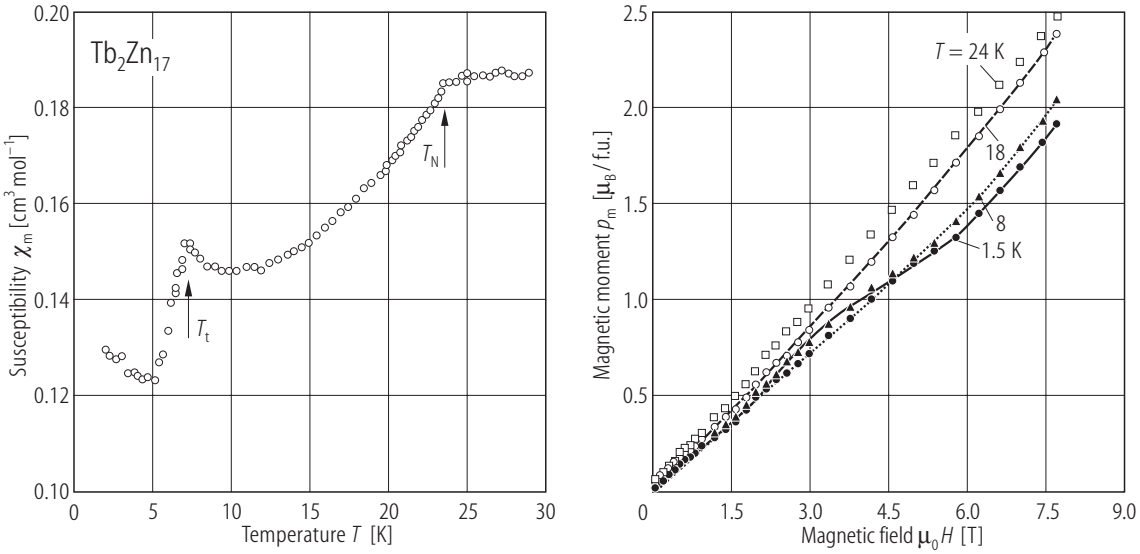

Fig. 60. Tb_2Zn_{17}. Magnetization vs. magnetic field at various temperatures. Left figure: magnetic susceptibility vs. temperature. T_N is the Néel temperature and T_t the transition temperature in the ordered range [94G1].

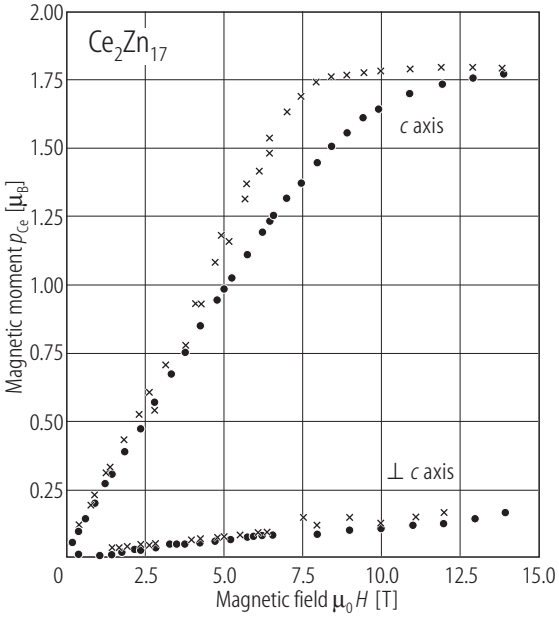

Fig. 61. Ce_2Zn_{17}. Magnetization vs. magnetic field at 1.3 K (crosses) and 4.2 K (full circles) parallel and perpendicular to the *c* axis of a single crystal [87S1].

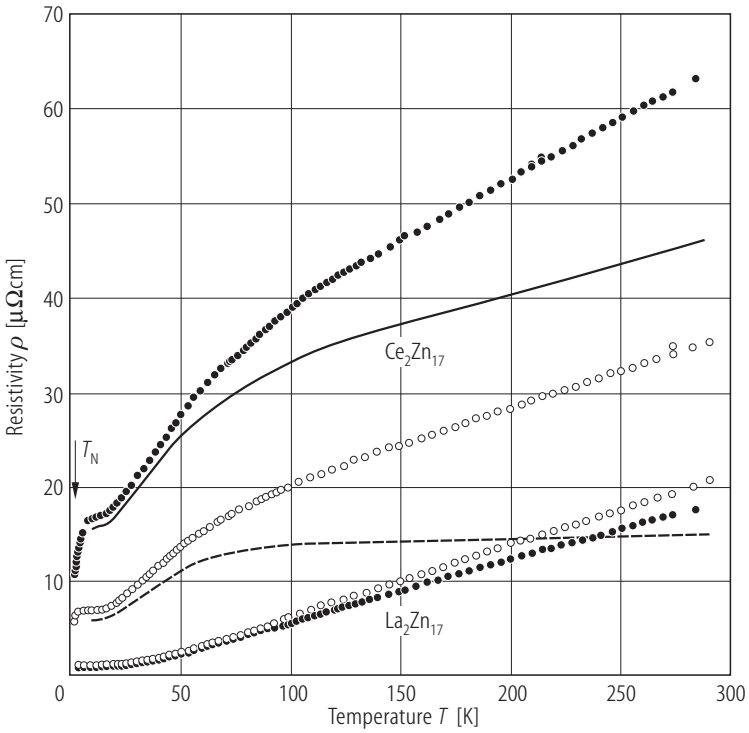

Fig. 62. Ce_2Zn_{17}, La_2Zn_{17}. Electrical resistivity vs. temperature for a current flow *J* parallel (full circles) and perpendicular (open circles) to the *c* axis of a single crystal. The magnetic part is shown by a solid line ($J \parallel c$) and a broken line ($J \perp c$). T_N is the Néel temperature [88S2].

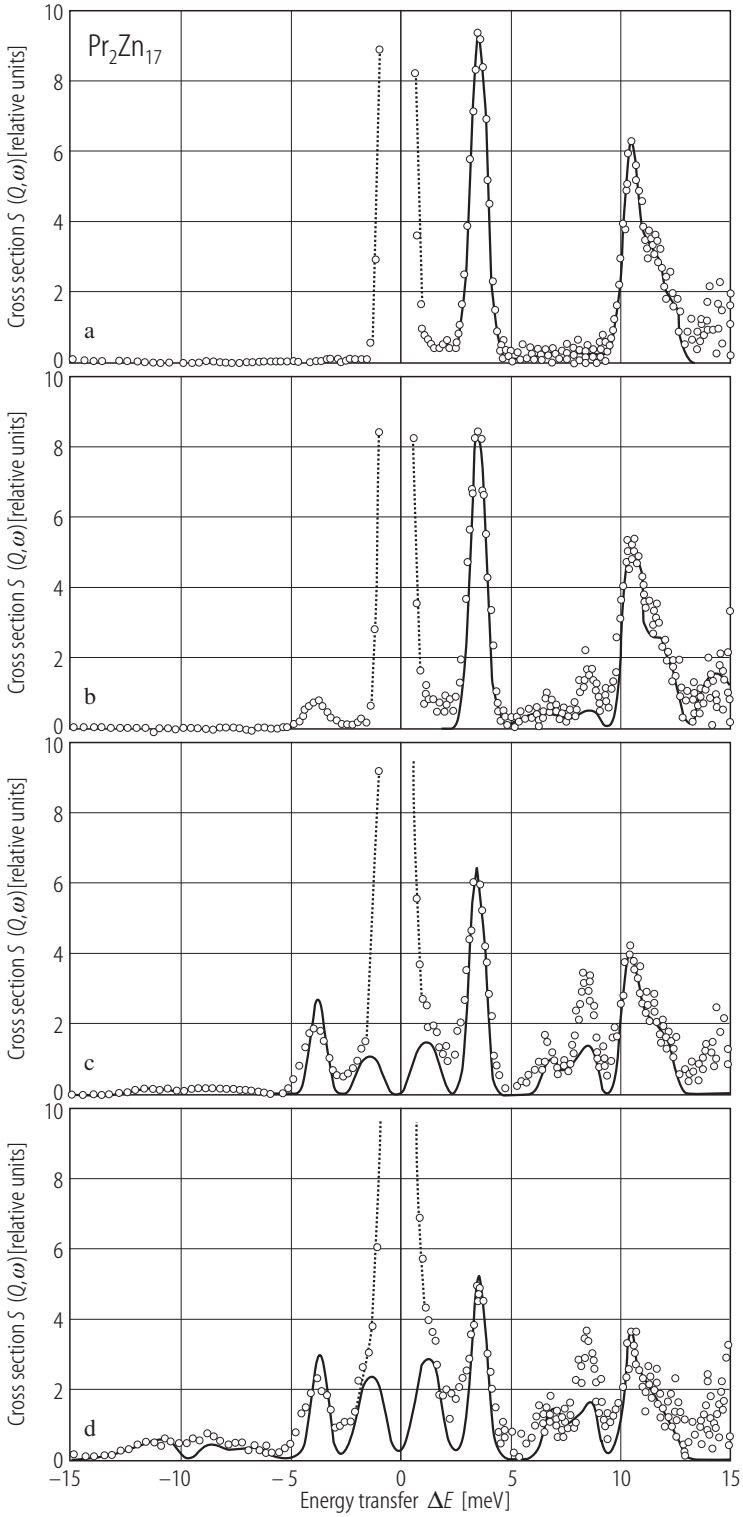

Fig. 63. Pr_2Zn_{17}. Neutron scattering cross section vs. energy transfer at (**a**) T = 4 K, (**b**) 20 K, (**c**) 50 K and (**d**) 75 K. Dashed line is experimental, continuous line is calculated in a crystal field model [95G1].

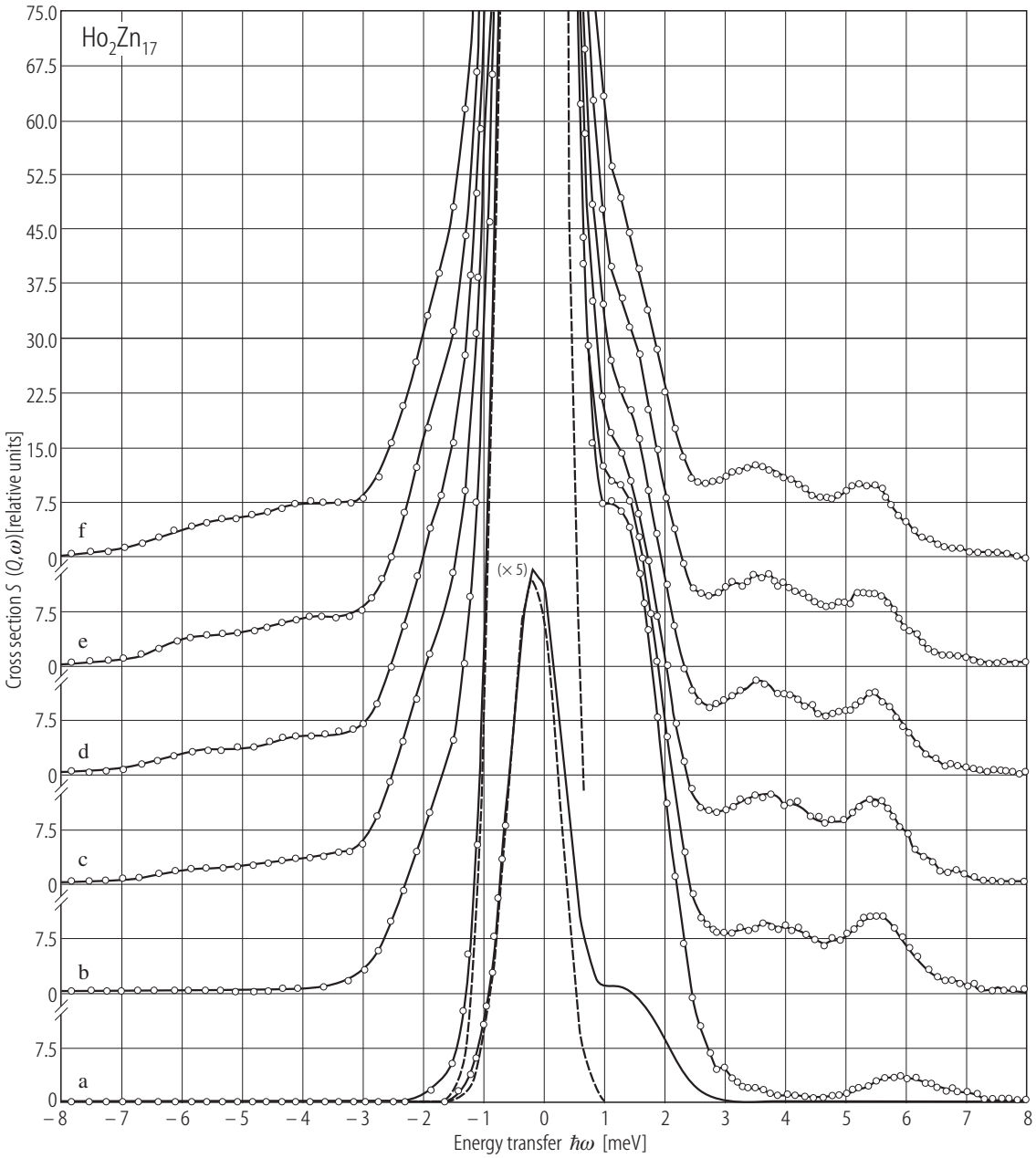

Fig. 64. Ho_2Zn_{17}. Neutron scattering cross section vs. energy transfer at (**a**) T = 4 K, (**b**) 20 K, (**c**) 40 K, (**d**) 60 K, (**e**) 80 K and (**f**) 100 K. The scattering angle is 16°. The dashed line corresponds to the elastic peak alone [95G1].

References

87O1 Olivier, M., Siegrist, T., McAlister, S.P.: J. Magn. Magn. Mater. **63-64** (1987) 281

87S1 Sato, N., Kontani, M., Abe, H., Adachi, K.: J. Magn. Magn. Mater. **70** (1987) 372

88S2 Sato, N., Kontani, M., Abe, H., Adachi, K.: J. Phys. Soc. Jpn. **57** (1988) 1069

93M1 Marquina, C., Kim-Ngan, N.H., Bakker, K., Radwanski, R.J., Jacobs, T.H., Buschow, K.H.J., Franse, J.J.M., Ibarra, M.R.: J. Phys.: Condens. Matter **5** (1993) 2009

94G1 Gignoux, D., Schmitt, D., Garcia-Landa, B., Ibarra, M.R., Marquina, C.: J. Alloys Compounds **210** (1994) 91

95G1 Garcia-Landa, B., Ibarra, M.R., Algarabel, P.A., Moze, O.: Phys. Rev. B **51** (1995) 15132

96M1 Marquina, C., Kim-Ngan, N.H., Buschow, K.H.J., Franse, J.J.M., Ibarra, M.R.: J. Magn. Magn. Mater. **157-158** (1996) 403

2.7.5 RBe_{13} compounds

Most of the recent studies in this series have been devoted to the unstable cerium ion. In particular, the substitution of La for Ce allows one to change the degree of valence instability of this ion which becomes trivalent for a concentration lower than 5% [89T2]. The magnetic behaviour of $CeBe_{13}$ has been investigated through various experiments: heat capacity [85B1, 90K1], point-contact spectroscopy [87N1] and photoemission [93L1]. Note that a single crystal was grown for this latter experiment. In the heavy rare earth series, few new studies have been performed (Figs. 65 - 70). Besides, a model including three exchange parameters, i.e. one within the ferromagnetic (001) planes and two between nearest and next-nearest (001) planes, has been developed to explain the occurrence of commensurate or incommensurate helicoidal structures as well as the evolution of the periodicity as a function of the temperature according to the change of crystal field anisotropy [91B1].

Table 5. RBe_{13} compounds. T_N, T_t: Néel, transition temperature; $\boldsymbol{Q}$: propagation vector; $\boldsymbol{M}$: magnetic moment; Θ: paramagnetic Curie temperature.

Compound	T_N, T_t [K]	$\boldsymbol{Q}$ (reduced unit)	Comments	Figures	Ref.
$CeBe_{13}$	non magnetic		mixed valence		90K1, 93L1
$PrBe_{13}$	no ordering		singlet ground state $\Theta = -8$ K		90K1
$NdBe_{13}$	2.6 ?		$\Theta = 2.5$ K, no ordering at 1.2 K [86V1]		75B1
$SmBe_{13}$	8.8				75B1
$EuBe_{13}$	non magnetic		Eu^{3+} state ($J = 0$)		75B1
$GdBe_{13}$	26	(0,0,0.284)	helical ($\boldsymbol{M} \perp \boldsymbol{c}$) $p_s = 6.6\ \mu_B$ (1.4 K) $\Theta = 25$ K	65 - 67	91B1, 91R1
$TbBe_{13}$	16.5 $T_t = 8.5$	(0,0,τ) ($> T_t$) (0,0,1/3) ($< T_t$)	helical ($\boldsymbol{M} \perp \boldsymbol{c}$) $p_s = 8.8\ \mu_B$ (4.2 K) $\tau(T) = 0.312 \ldots 0.333$ $\Theta = 14$ K	65	91B1
$DyBe_{13}$	10	(0,0,1/3)	helical ($\boldsymbol{M} \perp \boldsymbol{c}$) $p_s = 8.75\ \mu_B$ (1.5 K) $\Theta = 13$ K	65	91B1
$HoBe_{13}$	6 $T_t = 4.5$	(0,0,τ) ($> T_t$) (0,0,1/3) ($< T_t$)	helical ($\boldsymbol{M} \perp \boldsymbol{c}$) $p_s = 8.4\ \mu_B$ (1.4 K) $\tau(T) = 0.328$ (4.9 K) $\Theta = 6$ K		85V1, 91B1
$ErBe_{13}$	3	(0,0,1/3)	$\Theta = 6$ K	65	91B1
$TmBe_{13}$	no ordering		singlet ground state		81C1
$YbBe_{13}$	1.28	antiferromagnetic	Γ_7 ground state Kondo behaviour	68 - 70	86B1

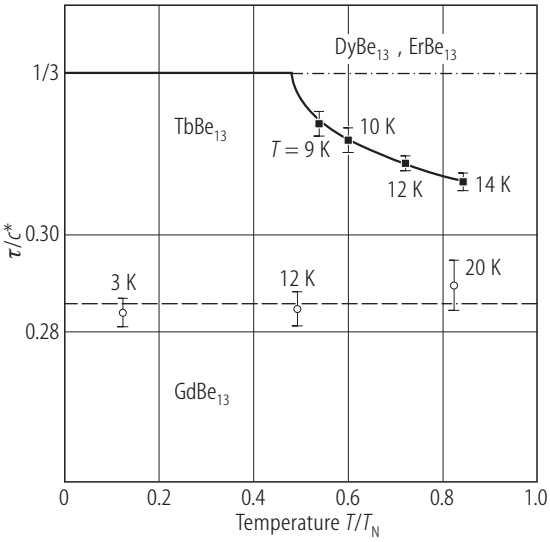

Fig. 65. RBe_{13}. z-component τ (in unit of c^*) of the magnetic propagation vector vs. temperature. τ is incommensurate for Gd, locks onto the commensurate value 1/3 below $T_N/2$ for Tb, and is 1/3 in the whole temperature range for Dy and Er [91B1].

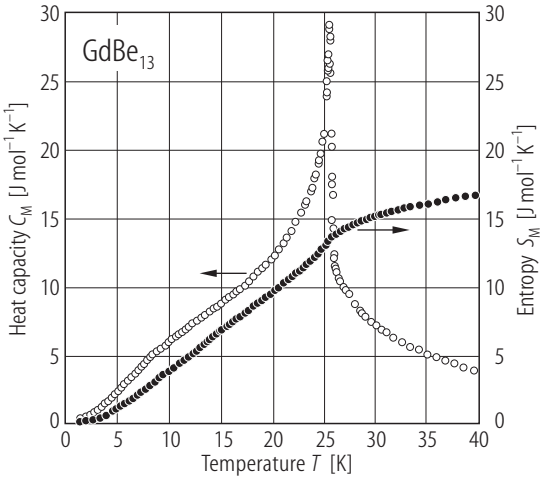

Fig. 66. $GdBe_{13}$. Magnetic contribution to the heat capacity (left scale) and corresponding entropy (right scale) vs. temperature [96B1].

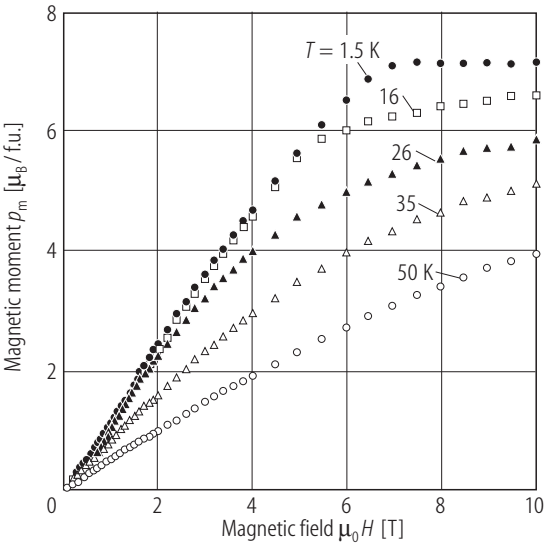

Fig. 67. $GdBe_{13}$. Magnetization curves vs. magnetic field at various temperatures.

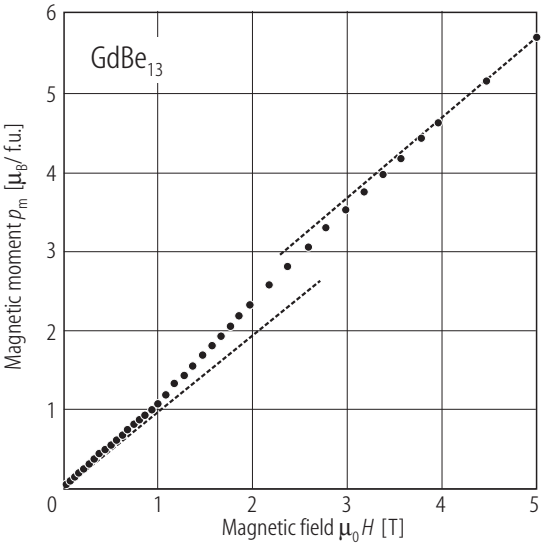

Right figure: detail of the 1.5 K curve in low field (the process is reversible) [96B1].

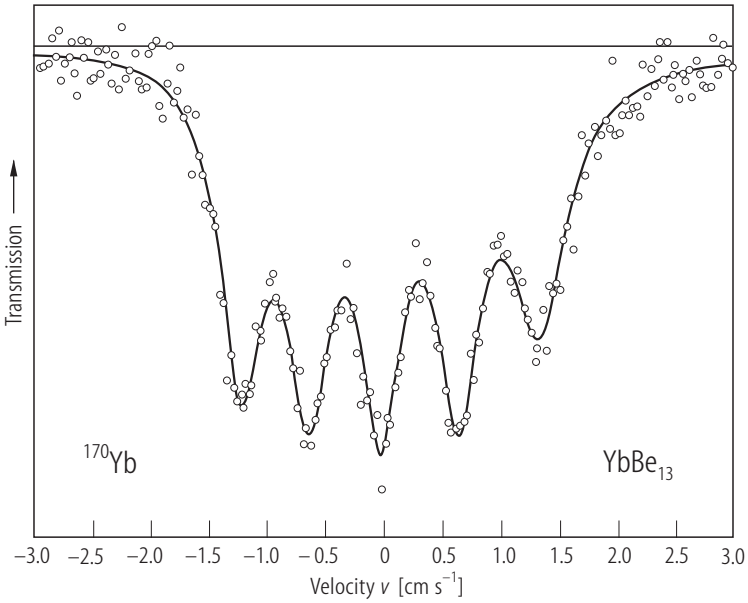

Fig. 68. YbBe$_{13}$. ^{170}Yb Mössbauer absorption spectrum at 0.05 K [86B1].

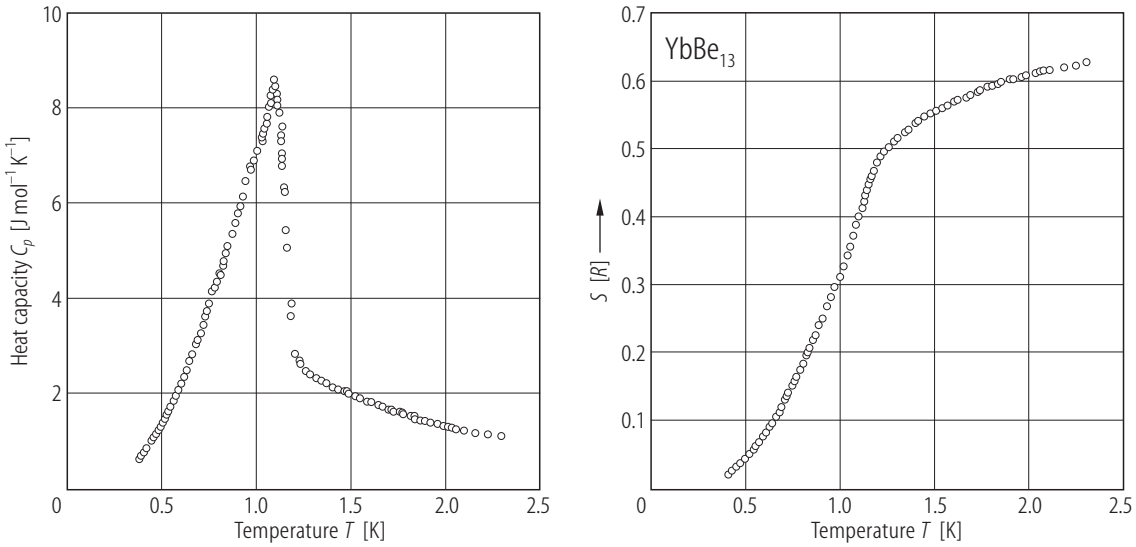

Fig. 69. YbBe$_{13}$. Heat capacity vs. temperature. Right figure: entropy (in unit of R) vs. temperature [86R1].

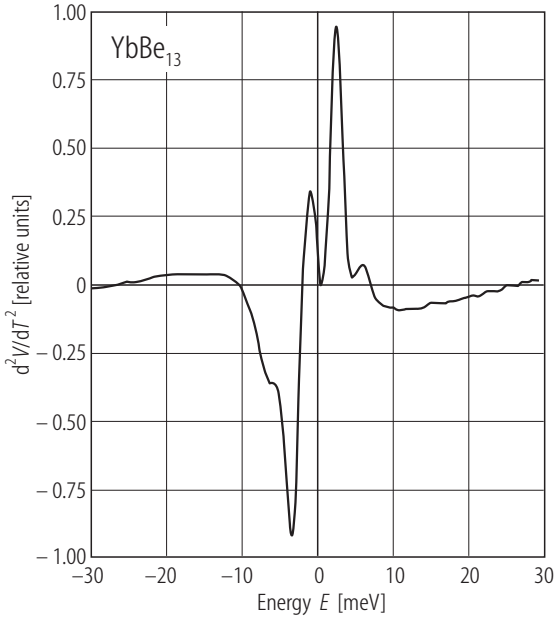

Fig. 70. $YbBe_{13}$. d^2V/dT^2 spectrum of point contact vs. energy (corresponding to the applied voltage) at 1.6 K [87N1].

2.7.6 Other X-rich compounds

Apart from the rare earth series quoted above, the other X-rich compounds have been little investigated in the past decade (Figs. 71 - 78). The main studies involve cerium ion in relation with its possible Kondo or heavy fermion behaviour. Several binary compounds with magnesium as well as the corresponding pseudo-ternary (diluted) compounds Ce-Y-Mg have been investigated, showing magnetic results consistent with a normal Ce^{3+}state [96F1]. Some anomalous effects nevertheless are present, as shown in $CeMg_3$ through the temperature dependence of the thermoelectric power (Fig. 71) [88S1] and of the quasielastic linewidth in neutron scattering spectra [87L1]. Compounds with cadmium at different stoichiometries have also been studied and do not exhibit heavy fermion behaviour (Table 6). Finally, a study of the pseudo-ternary compounds $Eu_xSr_{1-x}Mg_{5.2}$, $(Eu_xSr_{1-x})_3Mg_{13}$ and $Eu(Mg_{1-x}Al_x)_{5.2}$ has been performed in relation with the magnetism of europium clusters [88L1, 92L1], while the magnetic behaviour of the pseudo-ternary compounds YbM_xGa_{4-x} (M = Zn, Cd) is characterized by a non-magnetic Yb^{2+} groundstate [95G3].

Table 6. X-rich compounds. T_N: Néel temperature; Θ: paramagnetic Curie temperature; p_{eff}: effective paramagnetic moment.

Compound	T_N [K]	Θ [K]	p_{eff} [μ_B]	Comments	Figures	Ref.
$CeCd_2$	≈ 20	– 56	2.65	two peaks at 18.5 and 22 K in the heat capacity curve		89T1
$CeCd_3$	2	– 52	2.60			89T1
$Ce_{13}Cd_{58}$	< 1.3	– 12	2.60			89T1
$CeCd_6$	< 1.3	– 9.5	2.53			89T1
$CeCd_{11}$	< 1.3	– 7.8	2.57		77	89T1
$PrCd_{11}$	< 1.2	≈ 0	≈ 3.58		78	92M1
$CeZn_{11}$	2.0	– 1.83	2.34		76	93N1

References

75B1 Bucher, E., Maita, J.P., Hull, G.W., Fulton, R.C., Cooper, A.C.: Phys. Rev. B **11** (1975) 440
81C1 Clad, R., Bouton, J.M., Herr, A.: C.R. Acad. Sci. (Paris) **292** (1981) 999
85B1 Besnus, M.J., Kappler, J.P., Meyer, A.: Physica B **130** (1985) 127
85V1 Vigneron, F., Bonnet, M., Becker, P.: Physica B **130** (1985) 366
86B1 Bonville, P., Imbert, P., Jéhanno, G.: J. Phys. F **16** (1986) 1873
86R1 Ramirez, A.P., Batlogg, B., Fisk, Z.: Phys. Rev. B **34** (1986) 1795
86V1 Vigneron, F.: Chem. Scr. (Sweden) **26A** (1986) 93
87N1 Nowack, A., Wohlleben, D., Fisk, Z.: J. Magn. Magn. Mater. **63-64** (1987) 680
89T2 Tchoffo, F., Lemius, B., Domngang, S.: J. Phys. Soc. Jpn. **58** (1989) 2264
90K1 Kim, J.S., Andraka, B., Jee, C.S., Roy, S.B., Stewart, G.R.: Phys. Rev. B **41** (1990) 11073
91B1 Bourée-Vigneron, F.: Phys. Scr. (Sweden) **44** (1991) 27
91R1 Roy, S.B., Stewart, G.R.: J. Magn. Magn. Mater. **99** (1991) 235
93L1 Lawrence, J.M., Arko, A.J., Joyce, J.J., Blyth, R.I.R., Bartlett, R.J., Canfield, P.C., Fisk, Z., Riseborough, P.S.: Phys. Rev. B **47** (1993) 15460
96B1 Besnus, M.J., Fraga, G.L.F., Schmitt, D.: J. Alloys Compounds **235** (1996) 59

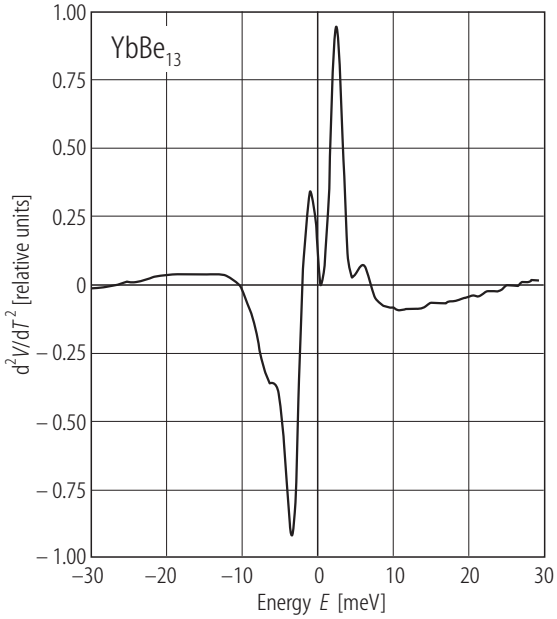

Fig. 70. $YbBe_{13}$. d^2V/dT^2 spectrum of point contact vs. energy (corresponding to the applied voltage) at 1.6 K [87N1].

2.7.6 Other X-rich compounds

Apart from the rare earth series quoted above, the other X-rich compounds have been little investigated in the past decade (Figs. 71 - 78). The main studies involve cerium ion in relation with its possible Kondo or heavy fermion behaviour. Several binary compounds with magnesium as well as the corresponding pseudo-ternary (diluted) compounds Ce-Y-Mg have been investigated, showing magnetic results consistent with a normal Ce^{3+}state [96F1]. Some anomalous effects nevertheless are present, as shown in $CeMg_3$ through the temperature dependence of the thermoelectric power (Fig. 71) [88S1] and of the quasielastic linewidth in neutron scattering spectra [87L1]. Compounds with cadmium at different stoichiometries have also been studied and do not exhibit heavy fermion behaviour (Table 6). Finally, a study of the pseudo-ternary compounds $Eu_xSr_{1-x}Mg_{5.2}$, $(Eu_xSr_{1-x})_3Mg_{13}$ and $Eu(Mg_{1-x}Al_x)_{5.2}$ has been performed in relation with the magnetism of europium clusters [88L1, 92L1], while the magnetic behaviour of the pseudo-ternary compounds YbM_xGa_{4-x} (M = Zn, Cd) is characterized by a non-magnetic Yb^{2+} groundstate [95G3].

Table 6. X-rich compounds. T_N: Néel temperature; Θ: paramagnetic Curie temperature; p_{eff}: effective paramagnetic moment.

Compound	T_N [K]	Θ [K]	p_{eff} [μ_B]	Comments	Figures	Ref.
$CeCd_2$	≈ 20	– 56	2.65	two peaks at 18.5 and 22 K in the heat capacity curve		89T1
$CeCd_3$	2	– 52	2.60			89T1
$Ce_{13}Cd_{58}$	< 1.3	– 12	2.60			89T1
$CeCd_6$	< 1.3	– 9.5	2.53			89T1
$CeCd_{11}$	< 1.3	– 7.8	2.57		77	89T1
$PrCd_{11}$	< 1.2	≈ 0	≈ 3.58		78	92M1
$CeZn_{11}$	2.0	– 1.83	2.34		76	93N1

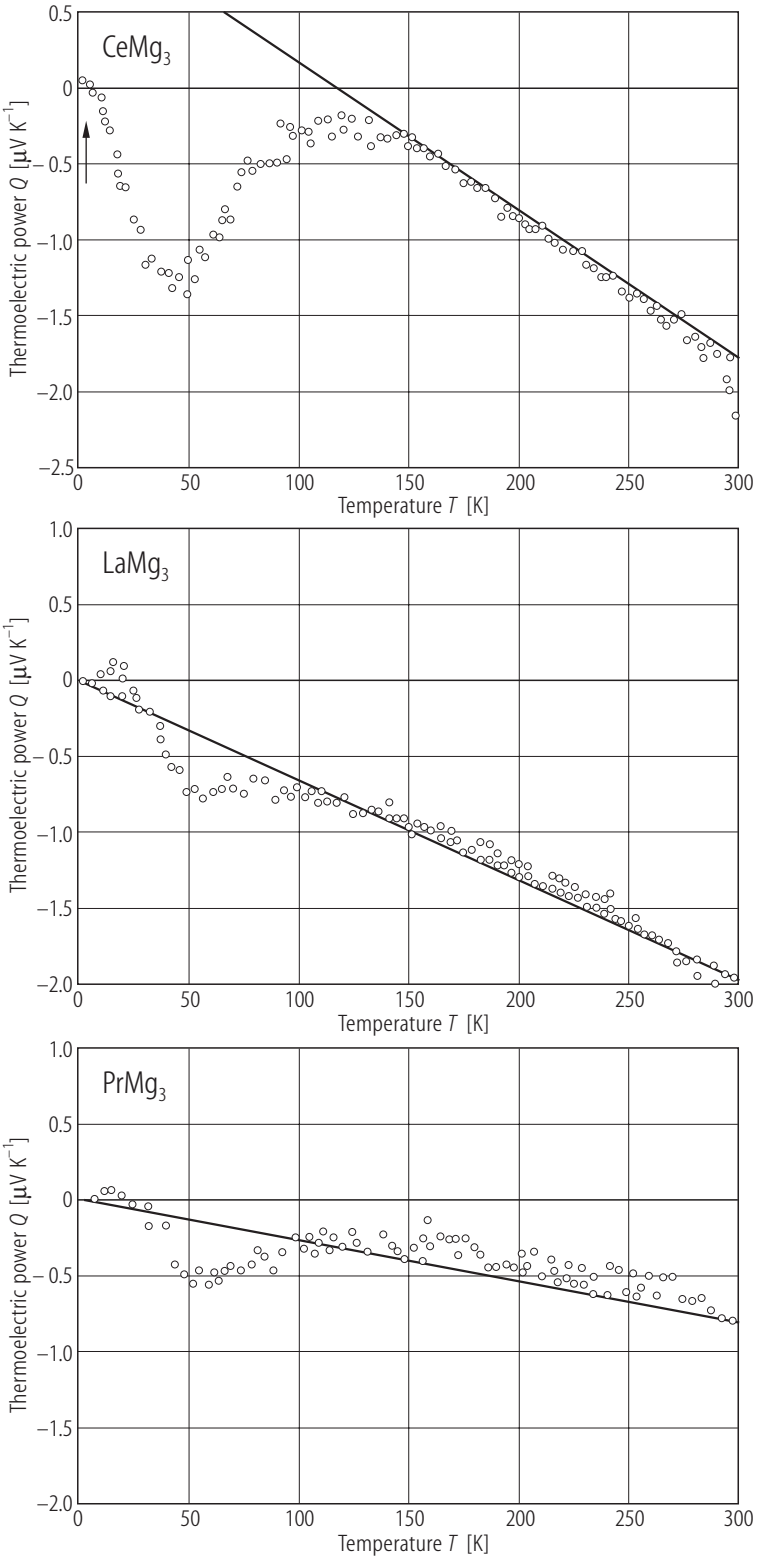

Fig. 71. $LaMg_3$, $CeMg_3$, $PrMg_3$. Thermoelectric power vs. temperature. The straight lines are fits of the linear portions between 150 K and 300 K. The arrow indicates the Néel temperature T_N = 3.4 K for $CeMg_3$ [88S1].

For Fig. 72 see p. 397.

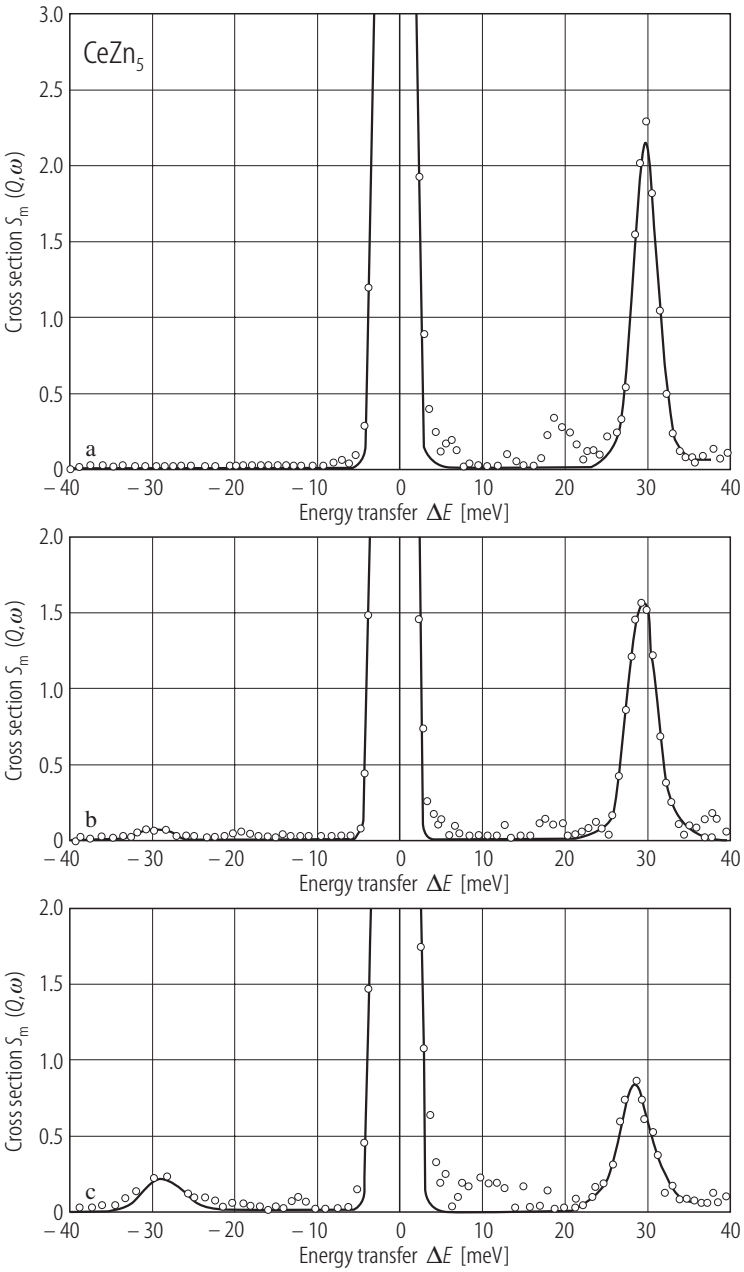

Fig. 73. $CeZn_5$. Magnetic neutron scattering cross section vs. energy transfer at (**a**) T = 8 K, (**b**) 120 K and (**c**) 250 K. The incident neutron energy is E_0 = 67 meV. Continuous lines are least square fits [90G1].

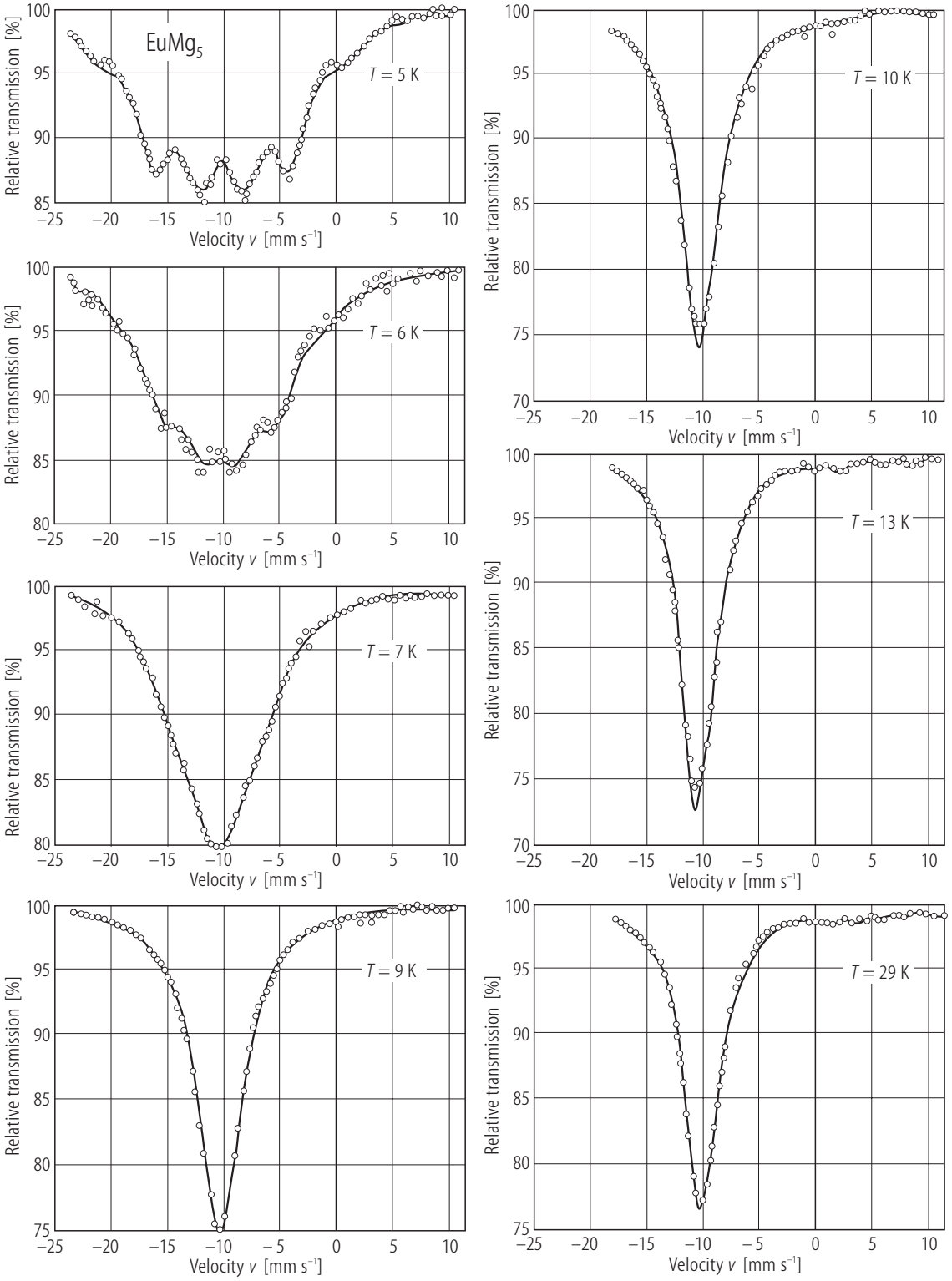

Fig. 74. $EuMg_5$. ^{151}Eu Mössbauer absorption spectra at various temperatures. The lines are calculated [86E1].

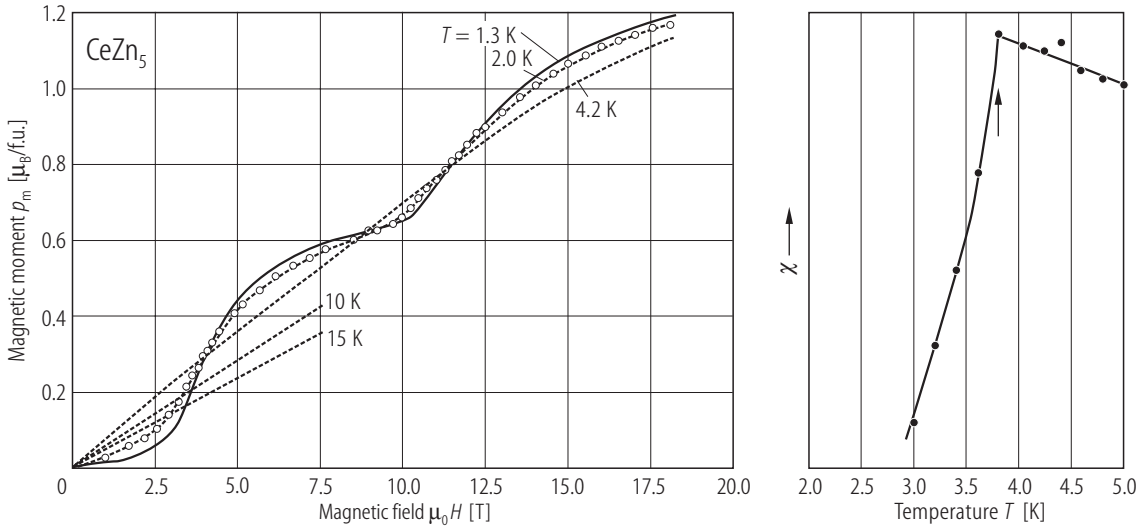

Fig. 72. $CeZn_5$. Magnetization curves vs. magnetic field at various temperatures, showing the two-step metamagnetic process in the antiferromagnetic phase. Right figure: detail of the susceptibility around the Néel temperature T_N = 3.8 K [87G1].

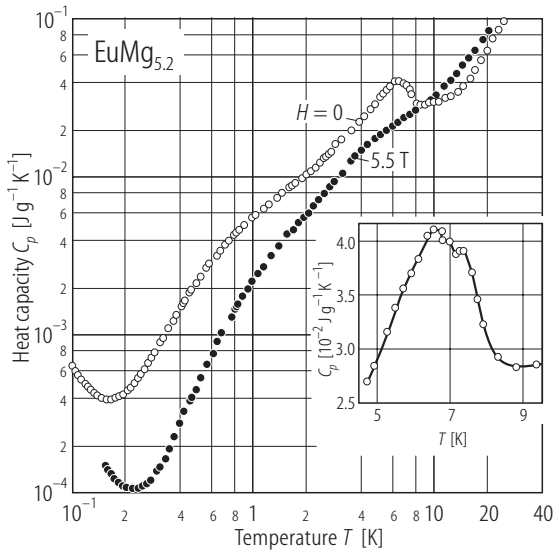

Fig. 75. $EuMg_{5.2}$. Heat capacity vs. temperature (logarithmic scale) for the magnetic fields indicated. Inset: detail of heat capacity around the Néel temperature T_N = 7.8 K (linear scale) [88L1].

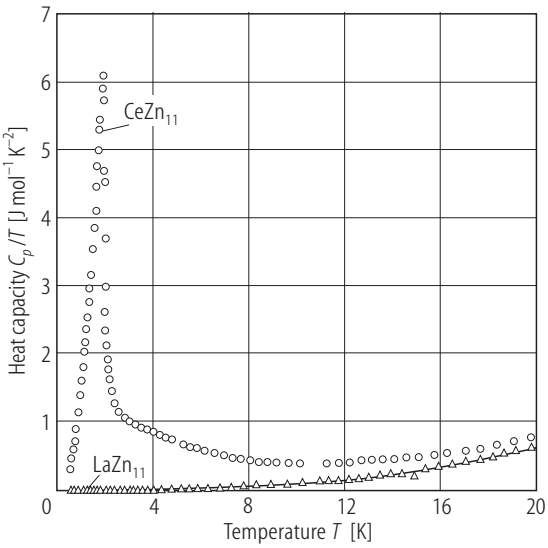

Fig. 76. $LaZn_{11}$, $CeZn_{11}$. Heat capacity divided by temperature vs. temperature. The large peak shows the Néel temperature T_N = 2 K for $CeZn_{11}$ [93N1].

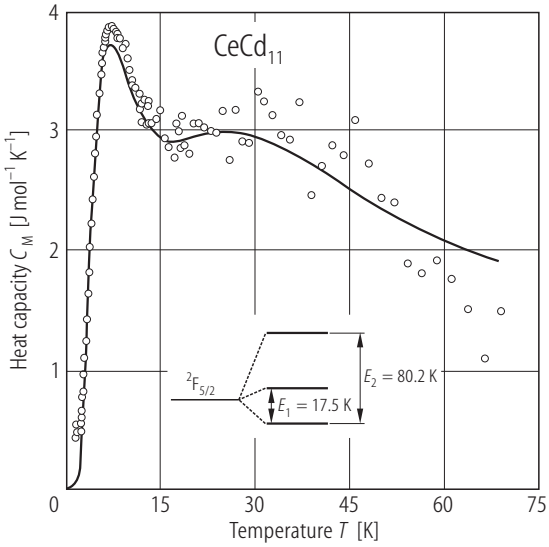

Fig. 77. $CeCd_{11}$. Magnetic contribution to the heat capacity vs. temperature. Line is calculated in a crystal field model. Inset: crystal field splitting of the $^2F_{5/2}$ ground multiplet of the Ce^{3+} ion [88T1].

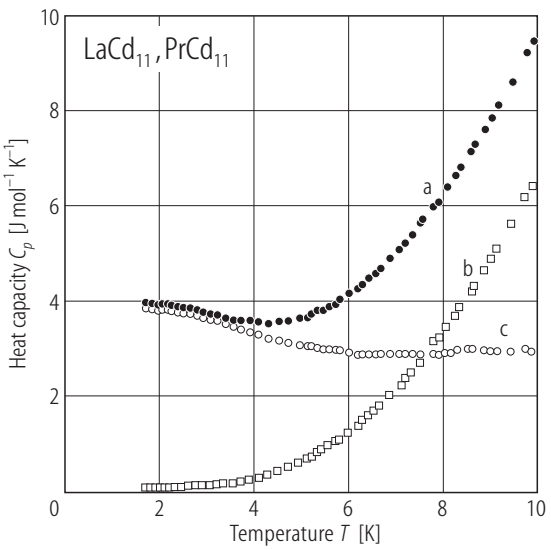

Fig. 78. $LaCd_{11}$, $PrCd_{11}$. Heat capacity vs. temperature for (a) $PrCd_{11}$, (b) $LaCd_{11}$ and (c) difference between (a) and (b) [92M1].

2.7.7 Ternary compounds

Among the ternary rare earth compounds which include at least one of the five elements Be, Mg, Zn, Cd or Hg, those with magnetic d elements (Fe, Co,...) have not been considered here. Among the other compounds, it turns out that the only series which has received a high interest during the last decade was tabulated with unknown structure in the previous review (Table 24 of [89M1]): indeed, in the R-Mg-Zn system, a new group of quasicrystalline phases has been discovered with a composition close to $R_8Mg_{42}Zn_{50}$ (Figs. 79 - 87) [94T2, 94Z1]. These stable icosahedral phases correspond to the unknown Z-phase [82P1] previously listed and identified *before* the discovery of quasicrystals in 1984 [84S1]. The main interest for these new systems in the science of quasicrystals was the *absence* of aluminium and transition metals and the *presence* of rare earth. Their crystal structure has been investigated with the help of the maximum entropy method in six-dimensional space [96Y1] while their primary solidification area has been determined in the ternary phase diagram [97L1]. Their magnetic properties, despite some aspects reminiscent of those observed in spin glasses (Fig. 79), actually exhibit pecularities specific to their quasicrystalline nature, in particular as far as their *quasimagnetic* structures are concerned (Figs. 81, 82) [97C1]. The recent discovery of a decagonal quasicrystalline phase in the same ternary system [97S2] leads to conclude that these compounds will be still thoroughly investigated in the future.

Except for the above R-Mg-Zn system, no further magnetic studies have been performed on the ternary compounds listed in the previous review [89M1]. Besides, few new other ternary series have been synthesized during the last decade. A first family includes the equiatomic compounds RMX, with R = Eu and Yb, M = Mg, Zn Cd or Hg and X = Si, Ge, Sn or Pb, but no magnetic data are available [91M1, 93M2]. Another series is the $R_xM_{1-x}Sb_2$ system (M = Zn or Cd), where metal deficiency has been found in some cases [95S1, 96W1]: the only magnetic data have been obtained for R = Ce (Table 7, Fig. 88). The last novel family investigated is the R_6ZnSb_{15} series in which antiferromagnetism has been found for the Gd compound (Table 7, Fig. 89).

References

86E1 El Massalami, M., de Groot, H.J.M., Thiel, R.C., de Jongh, L.J.: Hyperfine Interactions **28** (1986) 667

87L1 Lopes, L.C., Coqblin, B.: J. Magn. Magn. Mater. **63-64** (1987) 213

88L1 Lueken, H., Brauers, T., Erassme, J., Deussen, M., Löhneysen, H.v., Schröder, A., Wosnitza, J., Sauer, C.: J. Less-Common Met. **142** (1988) 221

88S1 Sakurai, J., Yamaguchi, Y., Galera, R.M., Pierre, J.: J. Phys. (Paris) Colloq. **49** (1988) C8-787

89T1 Tang, J., Gschneidner Jr., K.A.: J. Less-Common Met. **149** (1989) 341

90G1 Gignoux, D., Schmitt, D., Bauer, E., Murani, A.P.: J. Magn. Magn. Mater. **88** (1990) 63

92L1 Lueken, H., Scheins, W., Handrick, K.: J. Less-Common Met. **183** (1992) 271

92M1 Malik, S.K., Tang, J., Gschneidner Jr., K.A.: J. Magn. Magn. Mater. **109** (1992) 316

93N1 Nakazawa, Y., Ishikawa, M., Noguchi, S., Okuda, K.: J. Phys. Soc. Jpn. **62** (1993) 3003

95G3 Grin, Y., Hiebl, K., Rogl, P.: J. Alloys Compounds **227** (1995) L4

96F1 Flandorfer, H., Kosticas, A., Rogl, P., Godart, C., Giovannini, M., Saccone, A., Ferro, R.: J. Alloys Compounds **240** (1996) 116

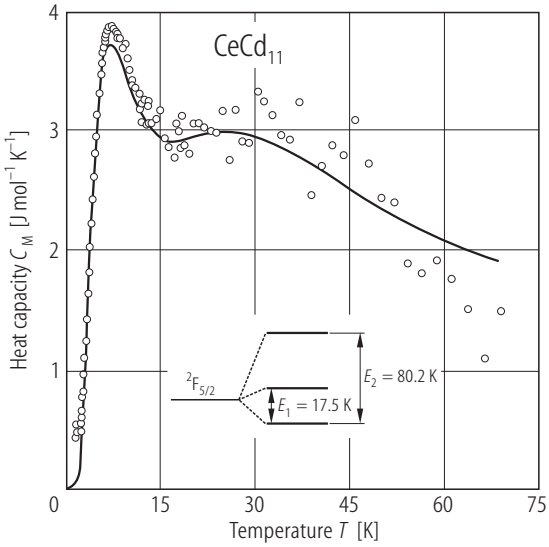

Fig. 77. $CeCd_{11}$. Magnetic contribution to the heat capacity vs. temperature. Line is calculated in a crystal field model. Inset: crystal field splitting of the $^2F_{5/2}$ ground multiplet of the Ce^{3+} ion [88T1].

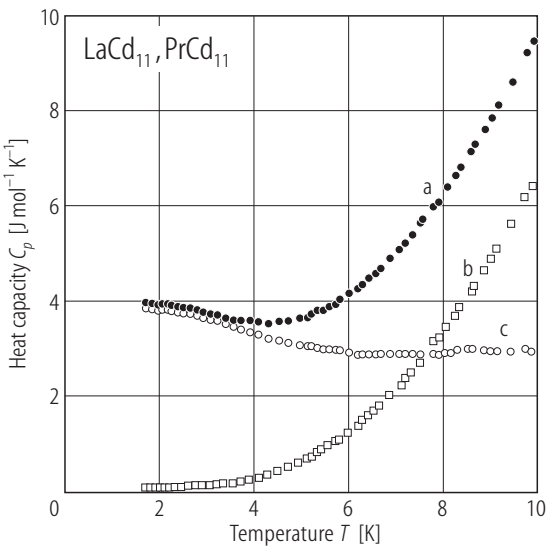

Fig. 78. $LaCd_{11}$, $PrCd_{11}$. Heat capacity vs. temperature for (a) $PrCd_{11}$, (b) $LaCd_{11}$ and (c) difference between (a) and (b) [92M1].

2.7.7 Ternary compounds

Among the ternary rare earth compounds which include at least one of the five elements Be, Mg, Zn, Cd or Hg, those with magnetic d elements (Fe, Co,...) have not been considered here. Among the other compounds, it turns out that the only series which has received a high interest during the last decade was tabulated with unknown structure in the previous review (Table 24 of [89M1]): indeed, in the R-Mg-Zn system, a new group of quasicrystalline phases has been discovered with a composition close to $R_8Mg_{42}Zn_{50}$ (Figs. 79 - 87) [94T2, 94Z1]. These stable icosahedral phases correspond to the unknown Z-phase [82P1] previously listed and identified *before* the discovery of quasicrystals in 1984 [84S1]. The main interest for these new systems in the science of quasicrystals was the *absence* of aluminium and transition metals and the *presence* of rare earth. Their crystal structure has been investigated with the help of the maximum entropy method in six-dimensional space [96Y1] while their primary solidification area has been determined in the ternary phase diagram [97L1]. Their magnetic properties, despite some aspects reminiscent of those observed in spin glasses (Fig. 79), actually exhibit pecularities specific to their quasicrystalline nature, in particular as far as their *quasimagnetic* structures are concerned (Figs. 81, 82) [97C1]. The recent discovery of a decagonal quasicrystalline phase in the same ternary system [97S2] leads to conclude that these compounds will be still thoroughly investigated in the future.

Except for the above R-Mg-Zn system, no further magnetic studies have been performed on the ternary compounds listed in the previous review [89M1]. Besides, few new other ternary series have been synthesized during the last decade. A first family includes the equiatomic compounds RMX, with R = Eu and Yb, M = Mg, Zn Cd or Hg and X = Si, Ge, Sn or Pb, but no magnetic data are available [91M1, 93M2]. Another series is the $R_xM_{1-x}Sb_2$ system (M = Zn or Cd), where metal deficiency has been found in some cases [95S1, 96W1]: the only magnetic data have been obtained for R = Ce (Table 7, Fig. 88). The last novel family investigated is the R_6ZnSb_{15} series in which antiferromagnetism has been found for the Gd compound (Table 7, Fig. 89).

Table 7. Ternary compounds. T_N: Néel temperature; Θ: paramagnetic Curie temperature; p_{eff}: effective paramagnetic moment.

Compound	T_N [K]	Θ [K]	p_{eff} [μ_B]	Comments	Figures	Ref.
$CeZn_{0.6}Sb_2$	2.0	– 11.0	2.6	Ce^{3+} state	88	96F2
$CeZnBi_2$	< 5	0.4	2.15	Ce^{3+} state	88	96F2
Ce_6ZnSb_{15}	< 5	– 10	2.7			96S1
Pr_6ZnSb_{15}	< 5	– 13	3.6		89	96S1
Sm_6ZnSb_{15}	< 5			No Curie-Weiss behaviour	89	96S1
Gd_6ZnSb_{15}	15	– 34	7.7		89	96S1

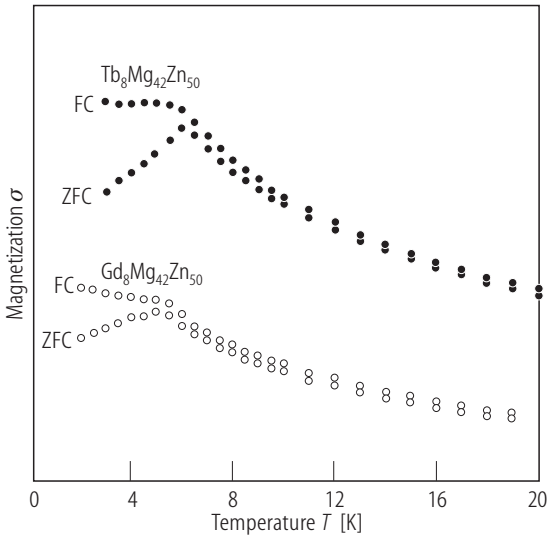

Fig. 79. $Gd_8Mg_{42}Zn_{50}$, $Tb_8Mg_{42}Zn_{50}$. Field-cooled (FC) and zero-field-cooled (ZFC) magnetization vs. temperature in a magnetic field of 30 Oe [95H2].

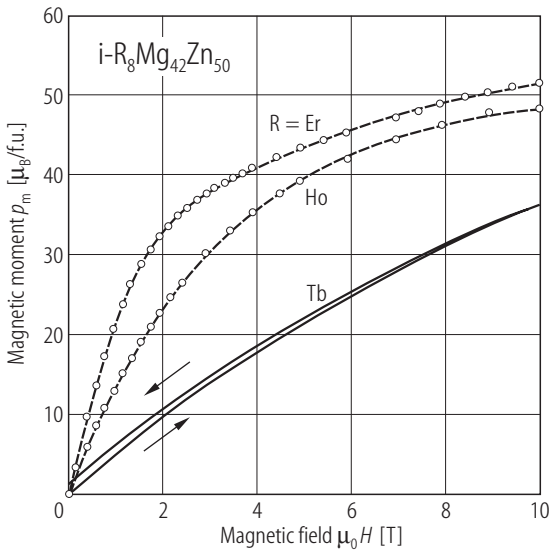

Fig. 80. $Tb_8Mg_{42}Zn_{50}$, $Ho_8Mg_{42}Zn_{50}$, $Er_8Mg_{42}Zn_{50}$. Magnetization vs. magnetic field at 1.5 K. Note the small hysteresis for the Tb compound [97C2].

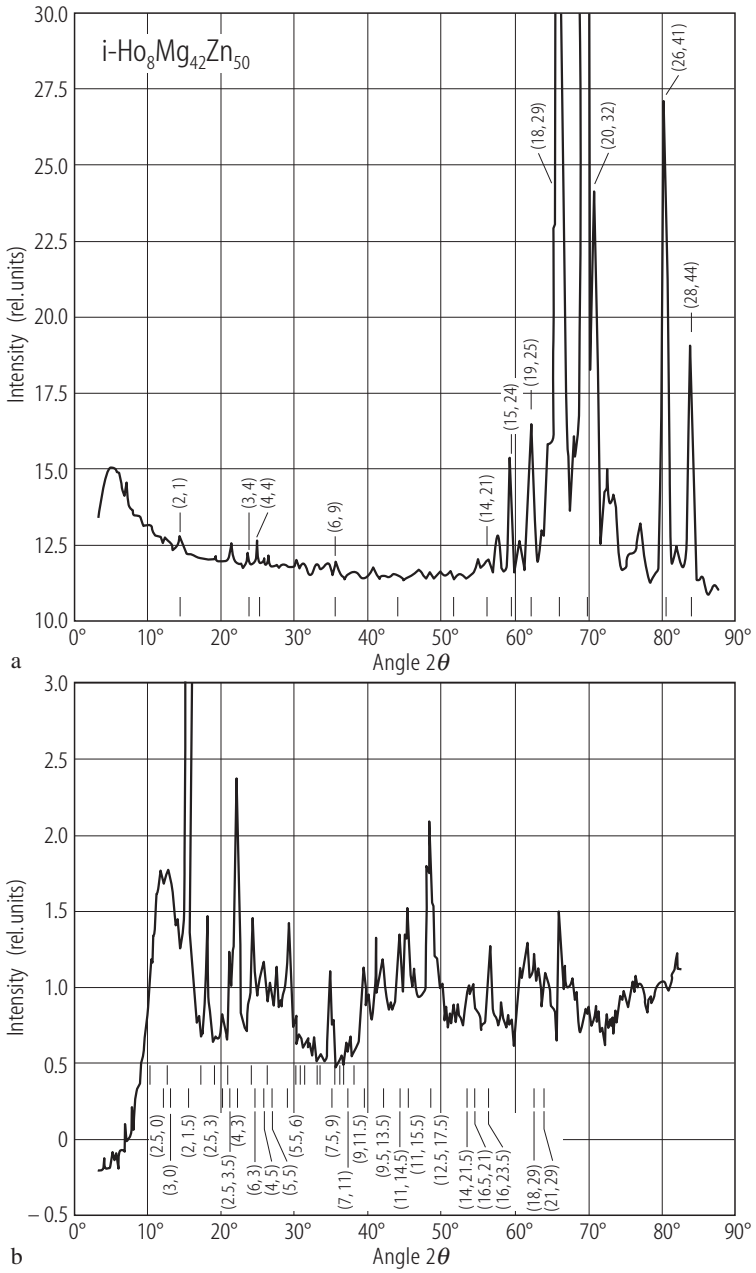

Fig. 81. i-$Ho_8Mg_{42}Zn_{50}$. (**a**) Neutron diffraction pattern vs. scattering angle at 15 K; labels (N, M) follow the two-index notation for nuclear reflections in icosahedral systems. (**b**) Difference between spectra obtained at 1.5 and 15 K; the labels correspond to the strongest (N_{mag} – 0.125, M_{mag} – 0.0625) magnetic reflections [97C1].

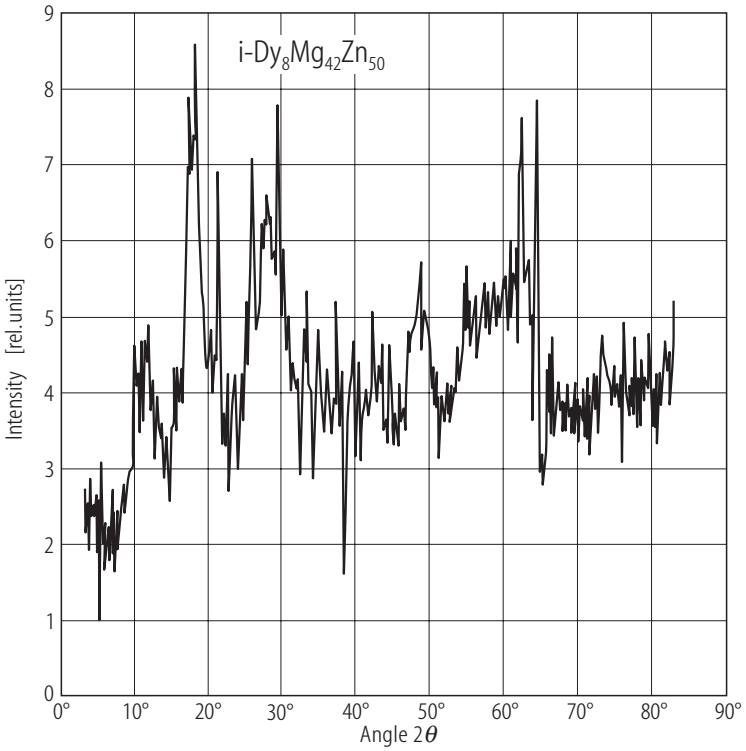

Fig. 82. i-$Dy_8Mg_{42}Zn_{50}$. Difference between neutron diffraction patterns obtained at 1.5 K and 15 K vs. scattering angle; the narrow reflections and the broad peaks are of magnetic origin [98C1].

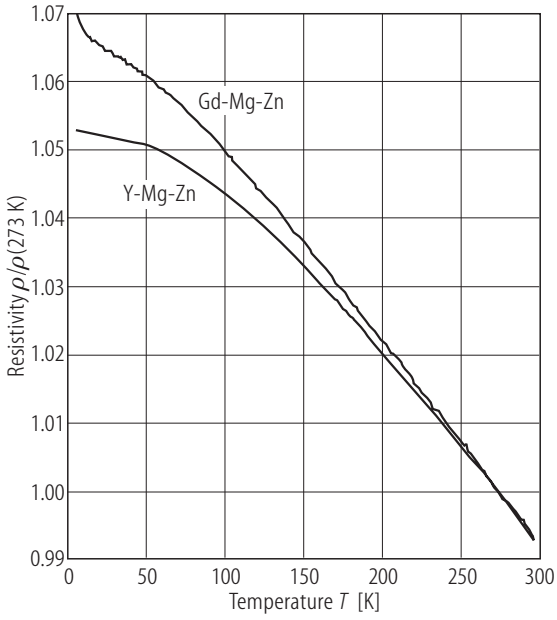

Fig. 83. Gd-Mg-Zn, Y-Mg-Zn icosahedral phases. Resistivity normalized to the value at 273 K vs. temperature [97K1].

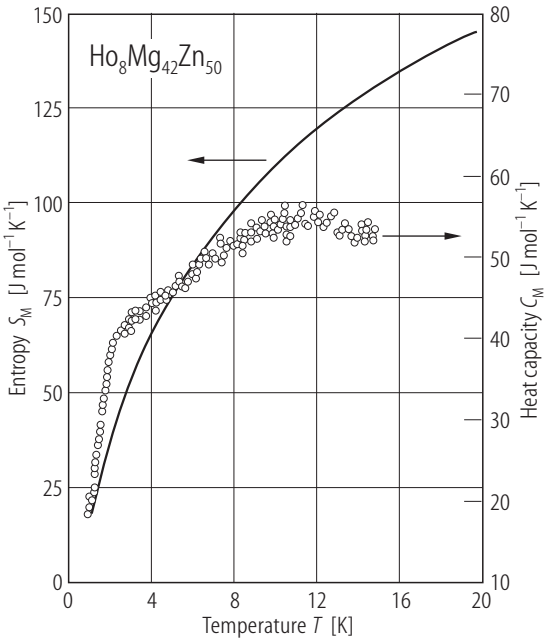

Fig. 85. $Ho_8Mg_{42}Zn_5$. Magnetic entropy (left scale) and magnetic contribution to the heat capacity (right scale) vs. temperature [99C1].

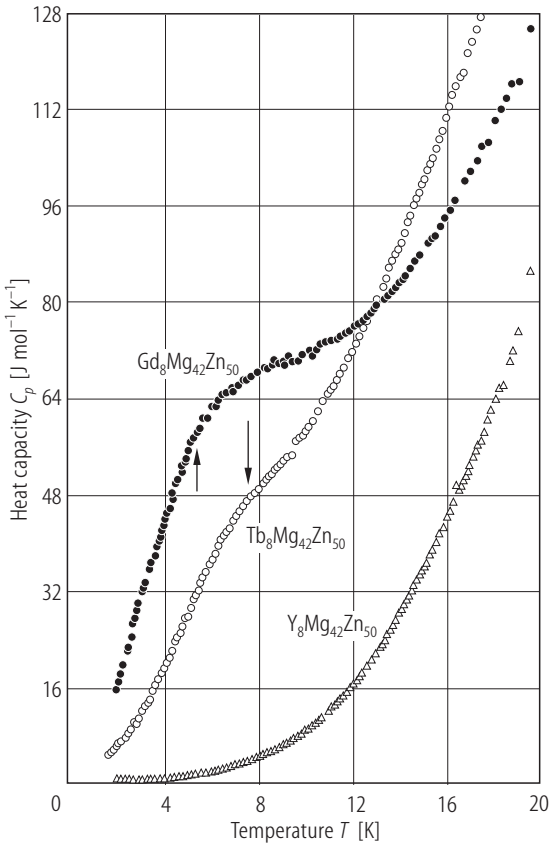

Fig. 84. $Gd_8Mg_{42}Zn_{50}$, $Tb_8Mg_{42}Zn_{50}$, $Y_8Mg_{42}Zn_{50}$. Heat capacity vs. temperature; the arrows indicate the spin freezing temperatures T_f determined by ac magnetic susceptibility measurement [95H1].

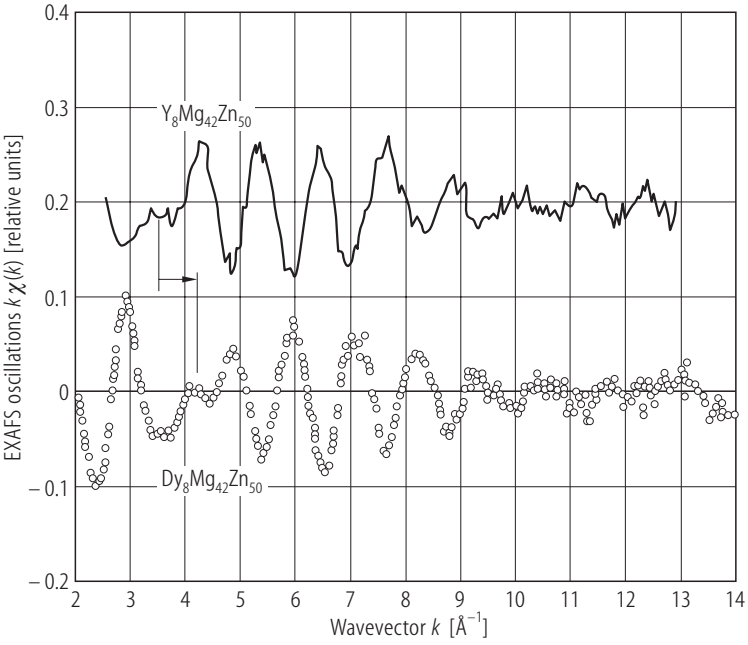

Fig. 86. $Y_8Mg_{42}Zn_{50}$, $Dy_8Mg_{42}Zn_{50}$. EXAFS oscillations vs. wavevector for the K edge of Y (upper curve) and the L3 edge of Dy (lower curve); the arrow shows the phase shift arising from the different nature of the atoms emitting the photoelectron [99C1].

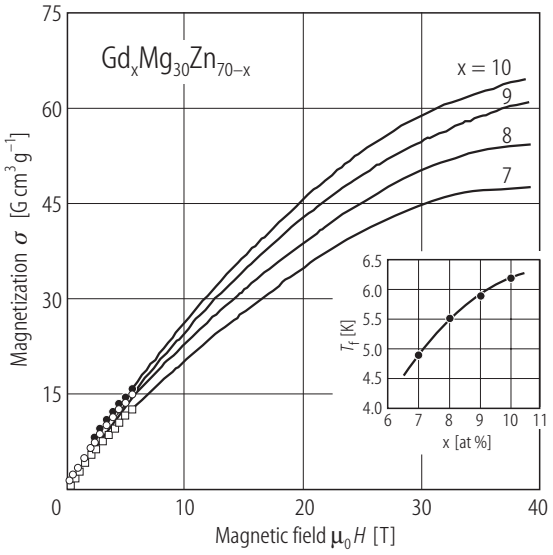

Fig. 87. $Gd_xMg_{30}Zn_{70-x}$. Magnetization vs. magnetic field at 4.2 K for various Gd concentrations x. Inset: Spin freezing temperature T_f vs. Gd concentration x [97S1].

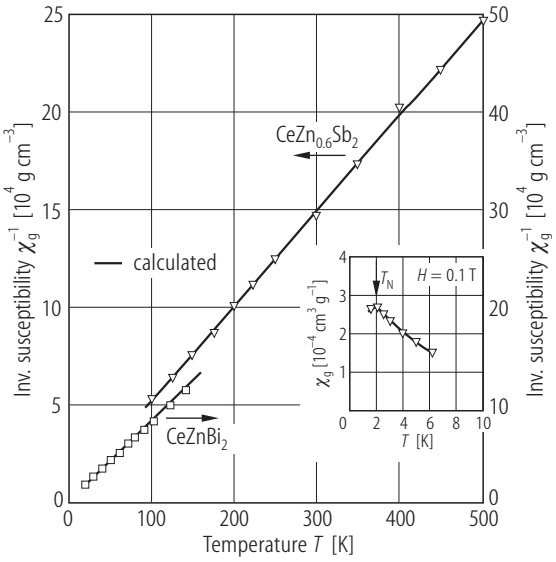

Fig. 88. $CeZn_{0.6}Sb_2$, $CeZnBi_2$. Reciprocal mass susceptibility vs. temperature for the Sb (left scale) and the Bi (right scale) compound. Lines are calculated. Inset: mass susceptibility for the Sb compound measured in a field of 0.1 T; T_N is the Néel temperature [96F2].

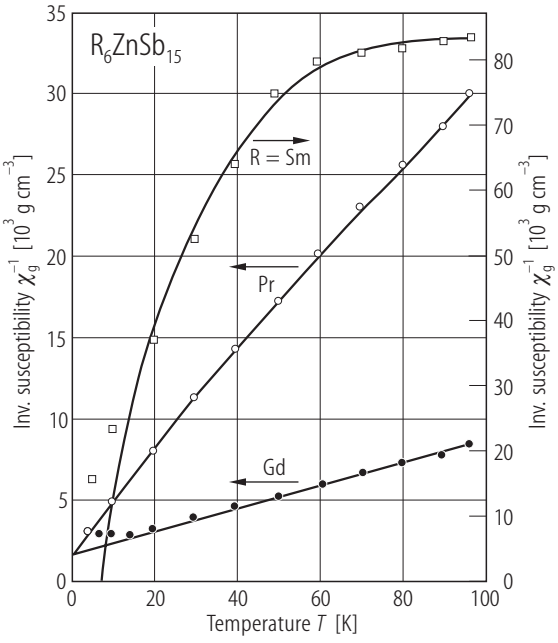

Fig. 89. Pr_6ZnSb_{15}, Sm_6ZnSb_{15}, Gd_6ZnSb_{15}. Reciprocal mass susceptibility vs. temperature. Lines are calculated [96S1].

References

82P1 Padezhnova, E.M., Mel'Nik, E.V., Miliyevskiy, R.A., Dobatkina, T.V., Kinzhibalo, V.V.: Russ. Metall. (Engl. Trans.) **4** (1982) 185

84S1 Schechtman, D., Blech, I., Gratias, D., Cahn, J.W.: Phys. Rev. Lett. **53** (1984) 1951

89M1 Morin, P., in: Magnetic Properties of Metals (Wijn, H.P.J., ed.), Landolt-Börnstein, New Series, Berlin, Heidelberg, New York: Springer, Vol. 19 e2 **1989**, p. 1

91M1 Merlo, F., Pani, M., Fornasini, M.L.: J. Alloys Compounds **171** (1991) 329

93M2 Merlo, F., Pani, M., Fornasini, M.: J. Alloys Compounds **196** (1993) 145

94T2 Tsai, A.P., Niikura, A., Inoue, A., Masumoto, T., Nishida, Y., Tsuda, K., Tanaka, M.: Philos. Mag. Lett. **70** (1994) 169

94Z1 Zhao, D., Tang, Y., Luo, Z., Wang, R., Shen, N., Zhang, S.: J. Phys.: Condens. Matter **6** (1994) 7329

95H1 Hattori, Y., Fukamichi, K., Suzuki, K., Niikura, A., Tsai, A.P., Inoue, A., Masumoto, T.: J. Phys.: Condens. Matter **7** (1995) 4183

95H2 Hattori, Y., Niikura, A., Tsai, A.P., Inoue, A., Masumoto, T., Fukamichi, K., Aruga-Katori, H., Goto, T.: J. Phys.: Condens. Matter **7** (1995) 2313

95S1 Sologub, O., Hiebl, K., Rogl, P., Bodak, O.: J. Alloys Compounds **227** (1995) 40

96F2 Flandorfer, H., Sologub, O., Godart, C., Hiebl, K., Leithe-Jasper, A., Rogl, P., Noël, H.: Solid State Commun. **97** (1996) 561

96S1 Sologub, O., Vybornov, M., Rogl, P., Hiebl, K., Cordier, G., Woll, P.: J. Solid State Chem. **122** (1996) 266

96W1 Wollesen, P., Jeitschko, W., Brylak, M., Dietrich, L.: J. Alloys Compounds **245** (1996) L5

96Y1 Yamamoto, A., Weber, S., Sato, A., Kato, K., Ohshima, K.I., Tsai, A.P., Niikura, A., Hiraga, K., Inoue, A., Masumoto, T.: Philos. Mag. Lett. **73** (1996) 247

97C1 Charrier, B., Ouladdiaf, B., Schmitt, D.: Phys. Rev. Lett. **78** (1997) 4637

97C2 Charrier, B., Schmitt, D.: J. Magn. Magn. Mater. **171** (1997) 106

97K1 Kondo, R., Hashimoto, T., Edagawa, K., Takeuchi, S., Takeuchi, T., Mizutani, U.: J. Phys. Soc. Jpn. **66** (1997) 1097

97L1 Langsdorf, A., Ritter, F., Assmus, W.: Phil. Mag. Lett. **75** (1997) 381

97S1 Saito, H., Fukamichi, K., Goto, T., Tsai, A.P., Inoue, A., Masumoto, T.: J. Alloys Compounds **252** (1997) 6

97S2 Sato, T.J., Abe, E., Tsai, A.P.: Jpn. J. Appl. Phys. **36** (1997) L1038

98C1 Charrier, B., Ouladdiaf, B., Schmitt, D.: Physica B **241-243** (1998) 733

99C1 Charrier, B., Schmitt, D., in: Aperiodic '97 (de Boissieu, M., Verger-Gaugry, J.L., Currant, R., eds.), Singapour: World Scientific, **1999**, p. 733